Quantification of the Cavitating Propulsor-Induced Underwater Sound Pressure in the Far-Field as well as on the Ship Hull based on Turbulence Resolved Flow Simulations and Acoustic Analogy

Vom Promotionsausschuss der

Technischen Universität Hamburg

zur Erlangung des akademischen Grades

Doktor-Ingenieur (Dr.-Ing.)

genehmigte Dissertation

von

Julian Kimmerl

aus

München

2024

1. Gutachter: Prof. Dr.-Ing. Moustafa Abdel-Maksoud

2. Gutachter: Prof. Dr.-Ing. Stefan Krüger

Vorsitzender des Prüfungsausschusses: Prof. Dr.-Ing. Jürgen Grabe

Tag der mündlichen Prüfung: 13.05.2024

DOI: https://doi.org/10.15480/882.9643

ORCID: https://orcid.org/0000-0002-2484-6532

Summary

Underwater radiated noise of propulsor-hull combinations is an important challenge for protection of the environment and military applications. Up to now, only single acoustic sources and propellers in open water condition have been investigated in detail. For geometrically complex and cavitating propulsor flow in behind ship condition with volumetric sound sources, the finite volume method is the only viable simulation approach and requires high mesh resolution at the locations of known acoustic sources, such as the trailing vortices of the propeller. However, due to simplifications typically utilized in the marine industry, the incompressible, isothermal Eulerian mixture model, requires additional means to estimate far-field noise, such as coupled acoustic analogies. The limitations in capturing the volumetric sound sources of this combined approach are inclined flow, slipstream interactions with obstacles, and upstream wake fueling slipstream distortions, as the propeller slipstream flow is not rotationally symmetric to the rotational axis.

In this work the physical mechanisms for generation of far-field underwater noise are explained, with a focus on the volumetric sources turbulence and cavitation and their interaction, followed by a summary of the underlying process of propagation of sound and the model of acoustic analogies. A combination of methods specific to the posed problem is developed next, with a wall resolved implicit Large Eddy simulation to capture most turbulent length scales in combination with the Volume-of-Fluid Eulerian mixture model and the OpenFOAM Schnerr-Sauer phase transition model. To realize the propeller rotation, a multi reference frame or a dynamic mesh functionality with sliding mesh interface is used. To resolve the propeller slipstream phenomena for the above mentioned cases that are limited by the current technology, a manual and automatic AMR method is implemented based on Q-criterion and vapor regions. The permeable surface Ffowcs-Williams-Hawkings method is implemented to deal with the acoustic part of the simulation and the only viable placement of the passive surface is determined as being directly connected to the geometry of the sliding mesh interface for complex cases with numerical resource restrictions.

Different test cases with increasing complexity are investigated beginning with hydrofoils, open water propellers, propeller-rudder combinations and ending with propulsor-hull combinations that consist of a twin-screw mega yacht, a single screw container vessel and a double ended ferry with a SCHOTTEL SRE propulsor centrally located at each end. The test cases are evaluated with the developed methods regarding turbulence, with a focus on trailing vortices, sheet and trailing vortex cavitation and structure interaction in the propeller slipstream and validated with model test results, where available. Numerical and physical phenomena occurring with these specific test cases that affect acoustic sources are identified and described, such as the time-dependent flow within a cavitating tip vortex of a propeller. Next the simulation approach is validated regarding the correct prediction underwater sound with open water propeller test cases and compared with full-scale measurements, leading to good agreement for propellers and acceptable agreement for the full-scale cases. Pressure pulses at propeller blade frequencies in wetted and cavitating condition on the hull are well predicted by the incompressible pressure with errors of approximately $+/-0.1kPa$ and far-field noise determined with the acoustic analogy reaches satisfactory agreement with deviations of around $+/-10dB$ depending on the frequency. However, the current approach is technologically plagued by numerical issues, which reduce stability, introduce errors for interpolation between moving and stationary meshes, as well as between refinement timesteps for AMR, and additional unknown sources most likely attributed to numerics. Depending on the spurious noise source they mainly affect higher frequency noise in cavitating condition in full scale. Besides, more advanced and intuitive methods to evaluate the near- and far-field pressure field are developed that lead to better interpretability of underwater acoustics.

While the developed approach and evaluation methods are promising regarding accuracy and numerical resources, further research is required to improve the consistency of the results and the stability of the simulations significantly in order to facilitate the approach widely in an industry environment.

Table of Contents

List of Figures

List of Tables

List of Abbreviations

Here the abbreviations used in the text and figures are listed alphabetically.

ABS	American Bureau of Shipping (company)
AMI	Arbitrary Mesh Interface
AMR	Adaptive Mesh Refinement
awt	All y^+ wall treatment
BEM	Boundary Element Method
BV	Bureau Veritas (company)
Cav	Cavitating
CavQRef	Cavitating with Q-criterion refinement
CCS	China Classification Society (company)
CFD	Computational Fluid Dynamics
CFL	Courant-Friedrichs-Lewy Number (see also List of Symbols)
CNR-INM	Consiglio Nazionale delle Ricerche - Istituto di ingegneria del mare (Institute of Marine Engineering)
CPA	Closest Point of Approach
CPU	Central Processing Unit
d	Days
dB	Decibel (see also List of Symbols)
DES	Detached Eddy Simulation
DNV	Det Norske Veritas (company)
ESD	Energy Saving Device
EU	European Union
Exp	Experiment
FEM	Finite Element Method
FFT	Fast Fourier Transform
FS	Full Scale
FVM	Finite Volume Method
FWH	Ffowcs-Williams Hawkings
GHz	Gigahertz
GRF	Generalized Reference Frame
HPC	High-Performance Computing
Hull	Hull geometry
HullR	Hull geometry with rudder
HyPNoS	Hydrodynamic Propeller Noise Monitoring System
Hz	Hertz (see also List of Symbols)
ICES	International Council for the Exploration of the Seas
IDDES	Improved Delayed Detached Eddy Simulation
ILES	Implicit LES
IMO	International Maritime Organization
ISO	International Organization for Standardization
ITTC	International Towing Tank Conference
KFWH	Kirchhoff FWH
KR	Korean Register (company)
LDV	Laser Doppler velocimetry

LES	Large Eddy Simulation
MarTERA	Maritime and Marine Technologies for a new ERA
MRF	Multiple Reference Frames
MS	Model Scale
MSL	Monopole Source Level
NA	Not Available
NACA	National Advisory Committee for Aeronautics
NATO	North Atlantic Treaty Organization
NB	Narrow Band
NoiseLES	Entwicklung eines hybriden Verfahrens zur Berechnung der Schallabstrahlung von Schiffspropellern
NoR	No Rudder
Oct	Octave
OpenFOAM	Open Source Field Operation and Manipulation
PEM	Permanent Magnet Motor
PFWH	Permeable surface FWH, identical to KFWH
PIMPLE	Combination of PISO and SIMPLE Solution Algorithms, PISO: Pressure-Implicit with Splitting of Operators, SIMPLE: Semi-Implicit Method for Pressure Linked Equations
PIV	Particle Image Velocimetry
POD	Proper Orthogonal Decomposition
PPTC	Potsdam Propeller Test Case
ProNoVi	Analysis Methods and Design Measures for the Reduction of Noise and Vibration Induced by Marine Propellers
PS	Pressure side of a lifting surface
QI	Quasi-infinite domain
Qref	Approach with AMR of the Q-criterion
R	Rudder
RANS	Reynolds-averaged Navier–Stokes equations
Red-Emi	Reduction of hydroacoustic Emission from propulsion systems
RINA	Registro Italiano Navale (company)
RMS	Root mean square
RNL	Radiated Noise Level
rot	Rotations
SBN	Structure-borne noise
SL	Source Level
SPL	Sound Pressure Level
SRE	SCHOTTEL EcoPeller
SS	Suction side of a lifting surface
SST	Shear Stress Transport
SSTLM	Langtry-Menter's local correlation-based transition model
SVA	Schiffbau-Versuchsanstalt Potsdam
TKE	Turbulence Kinetic Energy
TUHH	Hamburg University of Technology
UNIGE	University of Genoa
URN	Underwater Radiated Noise

UTC	Coordinated universal time
VOF	Volume-Of-Fluid
VTT	Valtion teknillinen tutkimuskeskus, Technical Research Centre of Finland Ltd
WALE	Wall Adapting Local Eddy-viscosity
wl	Waterline

List of Symbols

Here the mathematical symbols in the text are listed in order of appearance to increase legibility. Duplicate symbols are listed at their first appearance:

Symbol	Unit	Explanation
f, F	Hz	Frequency
r	m	Distance in space, Radius
λ	m	Wavelength
k	$m^2/s^2, 1/m$	Turbulent kinetic energy, Axial wavenumber
ϵ	m^2/s^3	Turbulent kinetic energy dissipation rate
ω	$1/s$	Turbulence specific dissipation rate, Rotation rate, Angular frequency
u_Θ	m/s	Angular Velocity
Γ	m^2/s	Circulation
a	m	Radius of solid body rotation with respect to vortex core
Ω_{ij}	$1/s$	Antisymmetric rotation rate tensor
S_{ij}	$1/s$	Symmetric strain rate tensor
Q	$1/s^2, m^3/s$	Q-criterion, Acoustic volume flow rate
T	K	Temperature
p_v, p_{Sat}	Pa	Water vapor saturation pressure
T_r	K	Temperature at the triple point of water
T_f	K	Temperature at point F in Fig. 7
R	m	Radius of a microscopic bubble with time derivatives $\dot{R}$ and $\ddot{R}$, Propeller radius, Resistance of a medium against acoustic flow
p_B	Pa	Pressure at a microscopic bubble interface
p	Pa	Local pressure
σ_{st}	N/m	Microscopic bubble surface tension
μ	Kg/ms	Liquid dynamic viscosity
$\vec{x}, x_i, (x, y, z)$	m	Location vector
ρ	Kg/m^3	Material density
n	$Hz, -$	Rotation rate, Mode number
D, D_P	m	Diameter (of a propeller)
σ_u	$-$	Cavitation number with respect to flow velocity
σ_n	$-$	Cavitation number with respect to rotation rate (of a propeller)
d_l	m	Liquid vortex core diameter
d_v	m	Vapor vortex core diameter
ρ_l	Kg/m^3	Liquid vortex core density
ρ_v	Kg/m^3	Vapor vortex core density
B	m	Wing span of a lifting surface
β	$-$	Empirical vortex roll-up parameter
η	m	Cavitation radius
r_0	m	Baseline vortex cavity radius
$\hat{\eta}$	m	Baseline amplitude of vortex cavity radius
ξ	m	Radial local coordinate direction, Longitudinal helix coordinate

φ	m	Circumferential local coordinate direction
ψ	m	Axial local coordinate direction
t	s, °	Time
i	$-$	Integer frequency counter
x_i	$-$	Integer event counter
y_i	m	Local hydrofoil coordinate system
u_∞, u_A, U_∞, V_A, U^*	m/s	Bulk flow velocity/Inflow velocity
Ma	$-$	Local Mach number
c	m/s	Speed of sound
L, d_{Ref}	m	Characteristic length of a fluid mechanics problem
v_p, c	m/s	Phase velocity of a wave
Z	$Pa\,s/m^3$	Acoustic Impedance
p'	Pa	Acoustic pressure
$\mathcal{F}$	$-$	Fourier transform operator
Z_0	Kg/m^2s	Characteristic specific acoustic impedance
Z_{water}	$Pa\,s/m^3$	Acoustic Impedance of water
Z_{air}	$Pa\,s/m^3$	Acoustic Impedance of air
$\square$	$-$	Differential wave operator
T_{ij}	N/m^2	Lighthill stress tensor
S	m	Surface description
y	m	Acoustic source location
x	m	Acoustic observer location
Θ, Θ_0	°	Angle in local coordinate system around axis 1
Ψ	°	Angle in local coordinate system around axis 2
Φ	°	Angle in local coordinate system around axis 3
ρ_0	Kg/m^3	Quiescent medium material density / reference density
$\vec{U}$ (u, v, w)	m/s	Velocity
u_n	m/s	Local fluid normal velocity
v_n	m/s	Local normal velocity of a boundary surface and its time derivative $\dot{v}_n$
n_i	m	Local normal vector to boundary surface
P_{ij}	Pa	Fluid compressive stress tensor
δ	$-$	Dirac function
H	$-$	Heaviside function
$\overline{u}$	m/s	Mean velocity
u', u'_i	m/s	Temporal velocity fluctuation
τ	Pa	Fluid shear stress
ρ_m	Kg/m^3	Mixture density
μ_t	Kg/ms	Eddy viscosity
F_S	Kg/m^2s^2	External forces in Navier-Stokes equations
α, α_l	$-$	Water volume phase fraction, Later in the text used equivalently to $\alpha = 0.5$
ρ_1	Kg/m^3	Material density of species 1
ρ_2	Kg/m^3	Material density of species 2
γ	$-$	Intermittency
Re	$-$	Reynolds number
$Re_{\Theta,\mathrm{t}}$	$-$	Transition momentum thickness Reynolds number
F_1, F_2	$-$	Blending factors for wall distance
y^+	$-$	Dimensionless wall distance
k_l	m^2/s^2	Laminar kinetic energy
G	$-$	Example filter kernel

Δ	$-, m$	Filter size, Cell Size
$\overline{\Delta}$	m	Physical space filter length
k_c	m^2/s^2	Cutoff turbulent kinetic energy
B_{ij}	Pa	Subgrid stress tensor
g_i	m/s^2	Local gravitational field vector
D_{ij}	$1/s$	Strain rate tensor
$\tilde{B}$	Pa	Remaining unknown quantity of the subgridscale influence onto the resolved turbulent structures
CFL	$-$	CFL number
O	$-$	Order operator
k_T	$-$	Propeller thrust coefficient
k_Q	$-$	Propeller torque coefficient
$\vec{U}, \vec{u}$	m/s	Velocity
u_c	m/s	Compression velocity
S_α	$1/s$	Additional source term in phase transport equation
C_α	$-$	Empirical constant
V_v	$1/m^3$	Discrete volume element consisting of vapor
V_l	$1/m^3$	Discrete volume element consisting of liquid
α_{Nuc}	$-$	Initial nuclei volume phase fraction
V_{Nuc}	$1/m^3$	Initial nuclei volume
n_0	$1/m^3$	Nuclei density
d_{Nuc}	m	Initial nuclei diameter
α_v	$-$	Vapor volume phase fraction
r_{Rb}	m	Nucleation site radius
$\dot{m}^+, \dot{m}^-, \dot{m}_\alpha$	$Kg/m^3 s$	Mass transfer rate
C_V	$-$	Vaporization coefficient
C_c	$-$	Condensation coefficient
p_{Coeff}	$Kg/m^3 s$	Auxiliary variable for mass transfer rate
$\dot{V}^+, \dot{V}^-, \dot{V}$	$1/m^3 s$	Volume transfer rate
S_p	$1/m^3 s$	Implicit volume transfer term
S_U	$1/m^3 s$	Explicit volume transfer term
$\overline{p}$	Pa	Mean local pressure
p'_T	Pa	Thickness or pseudo-thickness contribution to acoustic pressure
p'_L	Pa	Loading or pseudo-loading contribution to acoustic pressure
p'_Q	Pa	Non-linear quadrupole contributions to acoustic pressure
t^*	s, °	Time at which noise is generated
t_{ret}	s, °	Retarded time
M_r	$-$	Mach number of the permeable surface in the vectorial direction from the surface element to the receiver and its time derivative $\dot{M}_r$
u_r	m/s	Surface velocity in receiver direction
tr	$-$	Trace operator
$P_{ij}{}'$	Pa	Perturbation stress tensor
$\vec{l}$	Pa	Pressure force at the permeable surface in direction r or M with its time derivatives $\dot{l}$
H	$-$	Hanning window
a_1	$-$	Conversion factor for single sided spectra
a_2	$-$	Energy correction factor for the Hanning window
$\widetilde{p'}$	$-$	Convoluted acoustic pressure
f_s	Hz	sampling frequency
θ	°	Phase angle
z_c	$-$	Example complex number

$p'_{peak,i}$	Pa	Peak value of incompressible hull pressure pulses at propeller blade harmonic frequencies, where i is the integer data point in the Fourier transformed series describing the harmonic under investigation
Subscript m	$-$	Model scale
Subscript s	$-$	Full scale
σ_m	$-$	Model scale cavitation number
σ_s	$-$	Full scale cavitation number
SPL	dB	Sound pressure level
p_{ref}	Pa	Reference pressure for URN measurements of $1 \cdot 10^{-6}\ Pa$
r_{ref}	m	Standardized distance of $1m$
SL	dB	Source level
RNL	dB	Radiated noise level
MSL	dB	Monopole source level
f_0	Hz	Center band frequency
SL_{1Hz}	dB	Source level on $1Hz$ frequency band
$SL_{1/3\ octave}$	dB	Source level on 1/3 octave frequency band
r_S	m	Radius of a sphere
v	m/s	Velocity of a solid body in a fluid
p_{rgh}	Pa	OpenFOAM field dynamic pressure without hydrostatic part
d	m	Distance
r_{AMI}	m	Radius of the AMI interface (See list of Abbreviations)
$l_{upstream}$	m	Extent of the referenced surface upstream from the origin
$l_{downstream}$	m	Extent of the referenced surface downstream from the origin
f_{int}	$-$	Estimation of resolved turbulence of an LES from RANS precursor simulation
l_0	m	Turbulent integral length scale
k_{res}	m^2/s^2	Resolved turbulent kinetic energy
Δ_{Max}	m	FVM cell size
τ	s	Random time scale
R_L	$-$	Empirically determined ratio of turbulence to FVM cell size
λ_T	m	Inertial subrange length
ν	m^2/s	Kinematic viscosity
r_b	m	Minimum bubble radius generated by a propeller
r/R	$-$	Radii section of a propeller
U_x, V_x	m/s	Velocity component in x direction of the coordinate system
Δ_{CPU}	$-$	Processor imbalance
$nCells_i$	$-$	number of cells in each subdomain n
c	m	Chord length of a hydrofoil or propeller radius section, Compactness of the helix-directional cross section of the vortex cavity
s	m	Span of a hydrofoil, Finite line element of closed loop integration
α_{OA}	°	Angle of attack of a fluid dynamic profile
C_f	$-$	Lift coefficient
Q_{min}, Q_{max}	$1/s^2$	Q-criterion limits for automatic AMR
C_D	$-$	Drag coefficient
σ	$-$	Standard deviation
f_{FO}	Hz	Shedding frequency
J	$-$	Advance coefficient
l	m	Width of a cavitation tunnel
L_S	m	Length of a vessel
P	W	Power of a vessel, Perimeter of the cavitating vortex on helix-directional cross section
h	m	Wave height

V_i	m/s	Velocity component in i direction of the coordinate system
σ_i	m/s	Standard deviation of velocity component in i direction of the coordinate system
wa, wx	m/s	Axial velocity deficit in wake field
f_h	m	Function that describes the geometric location of the helix trajectory of a tip vortex
L_Q	m	Length of the tip vortex on a helix trajectory
ΔT	s	Timescale of one propeller rotation
t_i	$-$	Designation of station along helix trajectory of tip vortex
A	m^2	Cross-section of the cavitating vortex in helix trajectory direction
U_n	m/s	Velocity normal to helix trajectory intersections of the cavitating tip vortex
C	$-$	Coefficient for damping function (vortex cavitation analysis)
δ	$-$	Coefficient for damping function (vortex cavitation analysis)
Λ	$-$	Logarithmic decrement (vortex cavitation analysis)
ζ	$-$	Lehr damping factor (vortex cavitation analysis)
A_n	$-$	Amplitude at n-th maximum (vortex cavitation analysis)
T_D	$-$	Distance between two maxima (vortex cavitation analysis), originally oscillation period
$U\_rel, \overrightarrow{U_{rel}}$	m/s	Relative velocity in helix intersection plane, meaning a subtraction of bulk flow velocity and propeller rotation
$rc0$	m	Radius of vortex core solid body rotation
$\alpha_{0.5}$	$-$	Water volume phase fraction $\alpha = 0.5$
Γ_{Tip}	m^2/s	Bound circulation in the tip vortex
Γ_{Hub}	m^2/s	Bound circulation in the hub vortex
$\dot{V}$	m^3/s	Volume flow rate
$\dot{m}$	Kg/s	Mass flow rate
n_{Cells}	$-$	Total number of cells in a specific FVM mesh
$f_{z=i}$	$kPa, -$	Property associated with the frequency f at blade harmonic i

1 Introduction

This chapter offers an overview of the starting point of this research including the motivation for silent marine vessels, a summary of the state of the art regarding the experimental and numerical investigation of underwater radiated noise and the different approaches to tackle the challenge of simulating underwater radiated noise within the context of marine propulsion machinery. In this work, two aspects of underwater noise are considered, the emission of the propulsion system into the hull and into the fluid domain. The novel solution approach followed in this particular research is identified from open research questions of previous works and outlined together with its corresponding limitations and exclusions. Finally, the structure of this text, i.e. the successive chapters, is exposited.

1.1 Motivation for silent propulsion

Machinery noise is an everyday occurrence, which also pertains to marine vessels. Here, the onboard noise has historically been a substantial issue as it directly affects the human end user of the vessel, such as passengers and crew. Noise sources on a ship may include engines, gearboxes, pumps and other aggregates, which typically have tonal emission characteristics with peak frequencies of less than $f_e < 1kHz$. Gears under load for example are emitting primarily with their respective gear mesh frequencies, while electric engines are generating harmonics from magnetic excitation depending on type, i.e. asynchronous, synchronous, or PEM motor. Besides the engine, with sound emissions that are relatively independent of the operation point and may only change with loading, the main source of vibration on a vessel is typically the propulsion system. It requires special consideration, as the characteristics onboard not only depend on the current operation point, but also on the installation and the underwater geometry of the vessel structure around it. Furthermore, a propulsion system can be separated into multiple sources of noise, particularly mechanical and hydrodynamic noise. While the mechanical noise is originating from similar sources as described above, the hydrodynamic interaction caused by a rotating lifting surface generates additional noise from displacement of water, induced turbulence in the flow, or cavitation which enters the hull structure over different noise transmission paths, such as the powertrain, the propulsion unit housing, or through the water between propulsor and hull. In general, it is worthwhile to invest time in the design stage of a vessel and propulsion system, as well as the propeller, to create a silent vessel, if the requirements demand it, as it is always more economical to design a silent system beforehand, than attempt to correct the acoustic properties of an existing system, which is truly its own field of research.

While onboard noise and vibration might have been the dominant concern for end users of a propulsion product, there are two primary external drivers for the adoption of silent marine propulsion regarding underwater radiated noise and thus the associated development of methods to simulate a propulsors noise emission into the fluid, instead of onto the vessel hull: the first is embedded in the larger context of the preservation of the environment, which entails the worlds water bodies, and the second concerns military reconnaissance activities. Naturally, there are correlations between onboard noise and underwater radiated noise [1] , which may be exploited in the implementation of live onboard URN monitoring systems that use vibration data at the hull plate structure in the vicinity of the propulsion system, such as in the research project HyPNoS.

While airborne radiated noise and its detrimental effect on biological organisms has been considered an environmental concern since at least the beginning of the process of industrialization, anthropogenic underwater noise generation in the context of the protection of the environment has neither attracted general focus nor research interest until relatively recently. Although measurements confirmed the increase of underwater background noise levels in correlation with the utilization of the world oceans for global shipping [2] [3] [4] , only recent studies by marine biologists [5] [6] [7] [8] associated unusual reactions of marine life to it. As visual sensory input is quickly losing applicability with increasing water depth, since the solar radiation light waves are absorbed by water molecules, underwater life evolved to utilize sound for their way of life, such as for communication, navigation, and in general predator-prey interaction. This fact is particularly concerning with respect to marine mammals such as from the class

of cetaceans, i.e. orcinus orca or balaenoptera physalus. [9] [10] There has been an increasing consciousness in governmental bodies and even in general society, whenever there have been reports of individuals and groups perishing regionally after anthropogenic acoustically taxing activities, such as by construction work or military endeavors. The general consensus is that due to the assumed impact of sound on an integral part of the marine life, further studies regarding its sources are advisable. The most well-known research project regarding the environmental impact of URN due to being one of the first projects to address this issue was the ICES (International Council for the Exploration of the Sea) project which investigated the impact of fishery research vessels on the behavior of the fish under observation, with its final report ICES 209 being published in 1995 [11]. It gave suggestions which are still being employed until this day, not due to its relevance but its popularity as being one of the first publications to offer a noise emission guideline in the form of a limit curve for vessel signatures and thereby giving clear engineering instructions on the system design. Subsequently, the United Nations IMO focused on this topic specifically since 2009 [12] [13], declaring underwater noise by commercial shipping a topic of concern, which was followed by international governing organizations such as the EU commission [14] [15] [16] in their own non-mandatory guidelines. This spurred interest from standardization bodies such as classification societies, with DNV Silent class adopting and expanding on the ICES limit curves [17] and RINA DOLPHIN class being the first to provide practically realizable and implementable rules in the form of signatures similar to the original ICES publication for different types of vessels with high noise sensitivity such as fishery, environmental or seismic ships. In Fig. 1 both the original limit curve from the ICES 209 report and the DNV modification are compared with different frequency normalizations, which leads to completely different characteristics of the plots, although they contain the same values for frequencies of $f > 25Hz$. Most classification societies, such as ABS, BV, KR, and CCS, have adopted similar rules at this point and it is expected that all societies will over the next few years.

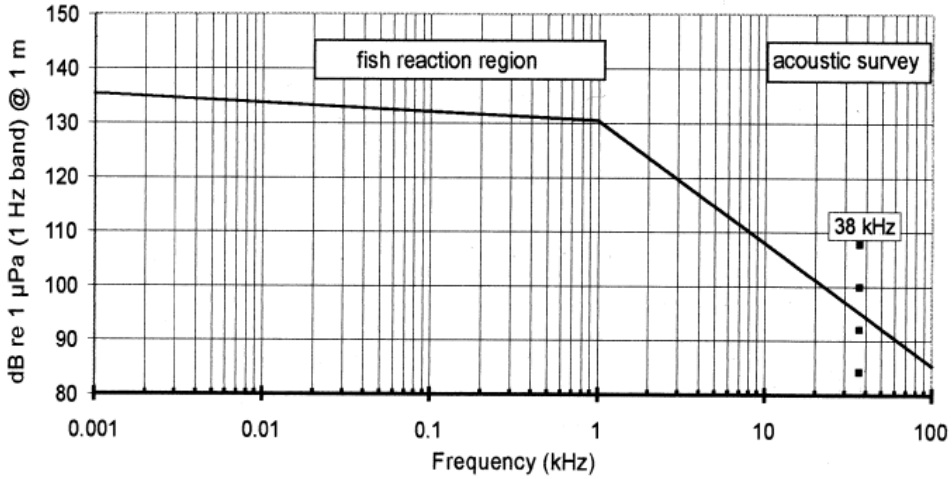

(a) ICES 209 limit curve [11]

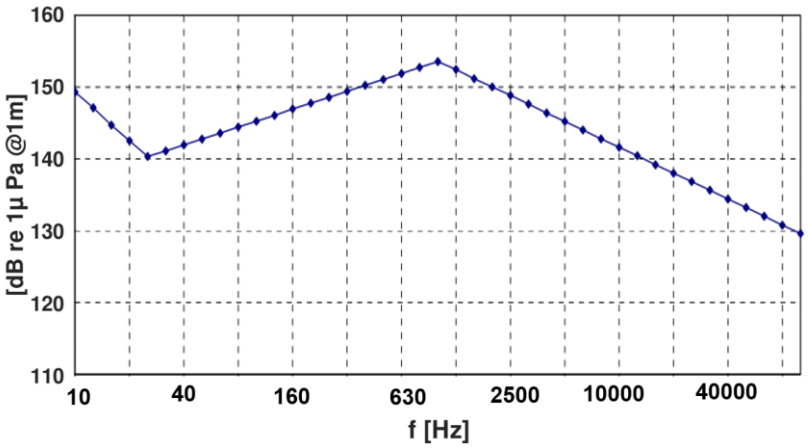

(b) DNV Silent R (Research) [17]

Fig. 1: ICES 209 limit curve and adopted DNV class guidelines

More in the past, research interest has been raised on underwater radiated noise in naval applications, where acoustic detection plays an important role since at least 1950 with the beginning of the cold war. While this is particularly important for subsurface vessels, likewise the acoustic signatures of surface vessels are exploited to identify objects before they reach a visible range, as sound travels much farther and attenuates less severe than in air due to the lower compressibility of the medium. While cavitation noise may be loud, it has an advantage as it is broadband by nature and therefore has the potential to mask information, about driving or driven machinery. On the other hand, periodic noise by liquid displacement due to fluid machinery or tonal noise by the structure directly features information about the propulsor, such as number of units, type of propulsion, number of blades, rotation rate, loading, etc. This can be exploited for reconnaissance or even offensive activities by an opposing party. As one of the main contributors to underwater noise, the propulsion system is therefore required to have the lowest possible acoustic signature, which is typically given as a limit curve obtained from the planned vessel operation profile. Thus, it is crucial to predict the signature of the propulsion machinery before the vessel is built and tested in order to compete for navy applications on the propulsion market. While the methods of the defense industry are mostly kept confidential, it can be assumed that due to technical limitations, the research in this area was historically mostly based on model and full-scale experimental evidence and experience rather than full physics-based simulations. According to anecdotal evidence, the methods implemented in military use are mostly concerned with acoustic radiation of noise, so the acoustic sources themselves may be required as an external input from suppliers. Contemporary methods utilize highly comprehensive simulation approaches including FEM and CFD. In any case, no holistic and monolithic approach that considers hydrodynamic flow, noise generation, and noise propagation is known publicly.

Practical implementation and enforcement of the given limits, either from environmental concerns or from reconnaissance suppression, is not trivial, as there are numerous requirements and external factors influencing full-scale measurements to validate their adherence [18]. Model scale measurements on the other hand may either not be acceptable due to uncertainties in the scaling of the acoustic emission characteristics or unknown measurement quality criteria, such as untracked physical quantities of the medium or measurement geometries, affecting their reproducibility. Full-scale simulations are a possible imaginable remedy as reproducibility is ensured, however, capturing the underlying physical phenomena of turbulent propulsor-vessel flow, noise generation, and propagation are in their current stage not mature enough to be accepted unconditionally. This leads to the pressing necessity to develop and validate holistic simulation methods that are as close to full-scale experiments in both accuracy and meaningfulness as possible.

1.2 State of the art

1.2.1 Experimental investigations of underwater noise

As URN is a topic of high interest to the industry and governing bodies, which is also reflected in the previous availability of funding mechanisms, there are numerous research efforts being conducted in parallel to this study rapidly progressing the technology. Therefore, the state of the art in this section is considered a frozen snapshot at the time of the start of this work, which is around 2018. Additionally a selection of the concurrent research efforts are summarized in the final subsection 1.2.4. In fact, there are different ways to approach the challenge of studying the noise emitted by a marine propulsor: with theoretical considerations and analytical tools, with experimental investigations, and with numerical simulations, which are all used in the field of underwater acoustics. While experimental results are obtained and utilized for validation, the developed methods are purely for a numerical simulation approach, which are primarily discussed in this section. Underwater noise is a complex topic consisting of turbulence, two-phase flow, and acoustics, which are either separately studied or in different possible combinations.

There is an extensive amount of literature about experimental investigations on lifting surface turbulence phenomena, from which trailing vortices and laminar-turbulent transition are of particular interest for studies on hydrofoil and propeller flow. While the topics have been investigated for air flow related applications for a little over a century, which comes with its own challenges, namely supersonics, the area received relatively recent boost of scientific interest in hydrodynamics. Turbulence plays an important role in sound generation, and cavitation, which for contemporary propeller designs occurs as sheet cavitation or trailing vortex cavitation. These are practically the types of cavitation that are of relevance for operation points of interest, as extreme off-design conditions, e.g. emergency stops, rarely receive attention regarding acoustic emissions. With investigations of hydrofoils in water instead of airfoils in air, cavitation phenomena became the primary focus of interest such as in trailing vortex cavitation of a NACA 66_2-415 hydrofoil in a cavitation tunnel investigation by Arndt [19] and unstable sheet cavitation on the suction side of the Delft Twist11 hydrofoil by Foeth [20] and the many experimental and numerical investigations that replicated these experiments in geometry and operation points.

Studying in model scale offers the advantage that, the observation region is easily accessible, and the acoustic sources may be separately studied by adjusting the experiments boundary conditions, however, they suffer from insufficiently known details about the accuracy of scaling methods and possible influence of the test setup. Although, the influence of the test facility is considered in a correction of the results with a transfer function that is obtained from a model test run without the object under investigation, for example the rotating hub without propeller blades, to estimate self-noise of the experimental setup. The final sound amplitudes are then required to exceed the setups self-noise by a certain amount, otherwise the measurements are considered as rejected. According to the ITTC recommendations [21] this amount has to be at least $3dB$ and for a difference of less than $10dB$ between background noise and measured noise, it is suggested to apply corrections. As part of the propeller design process, to avoid excessive erosion by cavitation, observations in cavitation tunnels are industry standard and well-studied. Publicly available results are rare, however, for instance for the PPTC'11 [22], or E779A propeller [23]. Observations are typically documented as cavitation sketches, either given with respect to propeller position, or as single images over one rotation and are obtained from high-speed photography with stroboscope lighting, or high-speed videos. The reason being that in model scale the pressure has to be adjusted to capture the cavitation behavior on each immersion level separately. More advanced methods include tomographic PIV [24] or LDV measurements [25], which may be given in single or multiple planes, or stereometry and advanced velocity-pressure visualization techniques [26]. For cavitation investigations, X-ray densitometry is a possible way to investigate volume void fraction content and thus the mass transfer rate between phases of gas-liquid flows for numerical investigations. [27]

On the hull, pressure pulses are measured with pressure measurement probes located above the propeller or at other locations of interest. With sufficient spatial resolution, a complete 3D-contour of the area of interest is obtained from interpolation between adjacent points, which however are usually limited by number due to economic reasons and thus highly sparse spatial data is created. Further looking at studies with a focus on producing acoustic signatures for hydrofoils and propellers with hydrophones, these are usually either placed inside the test sections in hydrofoil geometries to avoid self-noise or passively outside the test section in small water tanks that are in direct contact with the cavitation tunnel windows. Some representative investigations are the NoiseLES conical NACA0012 axially oscillating hydrofoil with confidential results [28], the Newcastle Propeller Testcase [29], which is investigated in six different facilities independently, or the ProNoVi propellers P1595 and P3193 [30], which are investigated in two different facilities. It is clear that there are still significant shortcomings regarding accuracy and reproducibility of experimental setup and a lack of standardization for the processing of the acoustic raw data signals. Even with the use of transfer functions the reproducibility between facilities is not ensured, which is especially highlighted in the round-robin tests conducted with the Newcastle propeller geometry that all lead to different resulting spectral representations [31]. The ITTC nevertheless provides specifications for pressure pulse [32] and noise measurements in model scale [21], which at least ensure similar procedures between model test facilities and their scaling procedures. Further improvements regarding reproducibility are expected in the near future with the improvement of sensory equipment, to measure water quality criteria, such as nuclei content consisting of dissolved non-condensable gases, or solid particles. However, these measures are not easily implemented as sensor devices are not readily available and thus costly.

Full-scale measurements on the other hand provide the results that are ultimately required for operation of the vessel, i.e. the propulsor-hull noise signature, as they consist of the complete underwater emitted noise. Visual inspection of the propulsor and associated cavitation phenomena are in rare cases possible by installation of transparent observation windows at the aft above or near the propeller or temporarily mounted outboard cameras. Similarly, for some cases pressure probes may be installed at holes in the hull above the propeller or vibration sensors on top of the interior hull plates near the propeller plane. To estimate far-field noise, hydrophone measurements from fixed sea bottom mounted hydrophones, which may be located as an array in a controlled measurement environment [33] or just at the sea floor [34], or hand held devices from measurement boats [35] or automated buoys are used. Except permanently fixed array hydrophones in controlled environments such as military standardized test tracks, all of these suffer from insufficiently accessible data due to test setup constraints such as the resource inflicted restriction to single point observations and environmental influences, e.g. due to signal noise and bathymetry. The complete noise signature for full-scale vessels may include repeatable and environmental components:

- Hydrodynamic noise of the propulsor with its interactions with the vessel wake field from upstream direction, including ESDs or shaft brackets, and steering mechanism utilities in downstream direction, such as rudders or azimuthing propeller shaft lines and housings,
- Noise from induced turbulence and corresponding vortices from the vessel and its appendages,
- Machinery noise by the engine, gears, bearings, etc., which are a significant part of the underwater noise signature due to the tonal emission characteristics and the consequential identification possibilities,
- The contribution of the air-water interface such as the noise created by the vessel wave pattern and the influence on the sound field by reflection due to the Lloyds mirror effect
- The influence by the reflections of the underwater geography, such as the sea floor or slopes especially in shallow water in near coast measurement regions, which are typical for sea trials with its own characteristic controlled by topology and inhomogeneous composition of the ground, whose reflection characteristics depend highly on frequency,
- Third party noise due to the measurement equipment itself, such as the measurement boat, buoys, and cables or third-party vessel traffic or other anthropogenic underwater work, or marine biology sound sources in the vicinity of the measurement,

- Environmental noise, such as from the water or air current, sea waves, or precipitation.

The single point observers are typically non-directional hydrophones with a fixed location passed by the vessel under observation travelling at the operation point of interest. This creates a time-variant test geometry, where the distance changes between observer and interrogation object, raising the necessity for time or geometrical averaging. Most vessels feature non-uniform directional emission characteristics, which means an additional time and frequency dependent variation of the input signal exists over the measurement duration with no valid procedure to remove the influence for a single point observation. Despite these uncertainties, guidelines for the measurement of underwater radiated noise of complete vessels that regard the measurement equipment and different averaging of the time history of the signal are available such as standards [36] [37] or ITTC recommendations for full-scale noise measurements [38]. Typically, the frequency domain signals are evaluated over small time windows while the vessel is passing and the individual spectra are then averaged over time with geometrical corrections for each time window over a valid time range for passing, which depends on the selected standard.

Experimental results are holistic in nature, combining flow field, turbulence, cavitation, structure interaction, and acoustic transmission physics, and as they reflect the real physics they are the only completely valid signals. This poses a difficulty to validate any simulation methods, as the phenomena are so complex that, at the moment, no monolithic solvers, that evaluate the integral problem in a single simulation, are available. Instead, different simulation methods are required for calculating the characteristics of the fluid, acoustics, and structure, which themselves require validation for their individual results, before any hope to achieve a complete picture may be raised. As no investigation of a decomposed element produces the same result as the complete object, no validation material exists to infer full causation.

1.2.2 Simulation of acoustic sources with FVM

Potential flow theory based solvers such as vortex-lattice methods or BEM are utilized in the aerospace, energy, and marine industry for simulations of lifting surfaces, with the best compromise between simulation speed and accuracy attained by the panel method. For propulsion predictions as part of the propeller design process the vessel wake can be considered and the problems are dominated by the pressure field, leading to simple viscous corrections as the decisive unknown. With vortex-lattice based methods even tip-vortex acoustics obtained from empirical data may be included in propeller noise predictions such as in the software Propelements or PROCAL in combination with some empirical models. In simulations for acoustic evaluations, panel methods such as PROPCAV or *pan*MARE are in theory excellent tools in the shipbuilding industry, due to the restrictions of long simulation time, to achieve an accurate estimation of low frequency events and short simulation timesteps in order to resolve high frequency occurrences. In addition, acoustic processing methods often require boundary-based pressure information as they are formally also boundary element methods. Until recently, cavitation is neglected in these simulations, as the dynamic change in cavitation surfaces to consider for the acoustic sources is not trivial, even for the non-errosive cavitation types that are allowed to occur on contemporary propeller designs, i.e. stable suction side sheet cavitation and possibly tip- and hub-vortex cavitation. To this day cavitating tip-vortices, which are considered an important noise source, are not resolved properly in panel methods and require an additional substitute model, in case their acoustic emission is to be analyzed. However, the accuracy over all frequencies of interest for these methods is inadequate for more detailed investigations of the underwater emission characteristics over a wide frequency range.

Accuracy benefits are gained, by resolving flow features with more detail. Especially volume-based turbulence and interactions between solid boundaries that are by definition not resolved with BEMs could play an important part in the overall acoustic emissions, leading to the flow simulation of the complete volume field with FVM as a possible solution, with velocity and pressure as the primary transport variables. At first glance this offers the advantage to evaluate acoustic pressure directly, as both hydrodynamic and acoustic fields are resolved spatially and temporally with high resolution.

However, this comes with two limitations regarding applicability. Firstly, the cells of the finite volume mesh have to be sufficiently fine resolved not only at the noise source but also between the source, on all relevant acoustic paths, and the observer of interest. At the “infinite” boundaries the cell size is required to increase gradually, to numerically dissipate the pressure information, which could also be gained by implementing forcing zones [39]. This often leads to an unfeasible amount of cells for the mesh to be utilized in an industry environment. Secondly, once the far-field distance of a frequency at $r > 3 \cdot \lambda$ is achieved, the wavelike characteristics of propagation show effects that may not be neglected, which are:

- Speed of sound and relative trajectory of the source and observer,
- Reflections at medium interfaces,
- Interference (constructive or destructive).

Incompressibility of water is generally assumed for standard pressure based solvers in the marine industry for FVM, due to the stability of the approach and numerical resource gain. In order to take acoustic effects into account, density based solvers would have to be employed, which is not required by the underlying flow problem. Hybrid methods, where flow and acoustics are solved separately, are the logical next step, for instance based on acoustic analogies [40], which are primarily used for the evaluation of URN from propellers [41].

State of the art for turbulence modelling in the context of resistance, propeller open water, and propulsion simulation is a Reynolds averaging of the high frequency velocity fluctuations (RANS). Two-equation models, which consider the turbulent kinetic energy and dissipation as scalar transport variables in some form are the most utilized. With the k-ω-SST model featuring a wall distance depending blending function as the most popular representative, high accuracy in the free-stream (k-ϵ) and near wall (k-ω) regions are achieved regarding the resolution of low frequency and large scale turbulent fluctuations and the average flow field. As the turbulence noise generation is limited to unsteady low frequency oscillating sources by definition, DES and LES methods that resolve also medium and high frequency turbulent length scales may be required. Until now, however, these methods have usually been employed in an academic context for simple test cases or in the industry to investigate flow fields around propulsors in detail, rather than the influence of high frequency turbulent fluctuations on noise emissions.

As unsteady cavitation phenomena are considered to be a primary contributor to broadband propulsor noise, although there have been reports of attenuation by geometrically steady gaseous structures such as cavitation, additional solution algorithms are required. Considering that cavitation is a heterogeneous two-phase flow occurrence, it is necessary in this context to resolve at minimum the two-phases of water and vapor within the hydrodynamic flow simulation. In FVM, the phases may be simulated in separate solution algorithms such as Euler-Lagrange, where dispersed particles are considered in a Lagrangian gridless method and interpolated onto the FVM solution as a scalar transport variable, or Eulerian two fluid approaches, where both solutions interact at the interface, which both lead to high computational cost. A simplified approach is given by only simulating a homogeneous single flow field and tracking the interface between the phases, such as in the level set method or the VOF method. Even though accuracy benefits, especially for higher acoustic frequencies may be gained by resolving single bubbles with Euler-Lagrange methods [42], for this study VOF is selected as the two-phase flow approach, which comes with the restriction, that only continuous regions of vapor that are larger than one cell size of the FVM mesh are captured for visualization purposes.

The single spherical bubble treatment in an infinite incompressible liquid described by the Rayleigh-Plesset equation is an engineering approach to model phase transition and the basis for many cavitation models. In the literature, several options have been proposed and investigated in detail such as the Merkle, Kunz, Zwart-Gebert and Schnerr-Sauer model. As most models have some empirical tuning coefficients, in recent years the Schnerr-Sauer model has been gaining popularity due to its reliance on only two parameters, namely the nuclei density and the initial bubble radius. With this cavitation model

accurate cavitation predictions have been made for propellers based on both FVM and BEM flow solutions.

1.2.3 Methods for far-field noise evaluation

Besides the option to simulate compressible flow on microscopic levels directly, there are several options for the simulation of sound propagation such as acoustic analogies, Lattice-Boltzmann methods, Ray tracing, or FVM/FEM with use of explicit solution algorithms. Most of these are unfeasible with numerical resources typically available in the industry. Incompressible flow FVM solvers are able to predict acoustic pressure in the near-field as described above, however, once acoustic effects become relevant, hybrid methods need to be applied.

As a decoupled BEM for the propagation of sound generated by an underlying hydrodynamic solver, acoustic analogies are preferred, which were first proposed by Lighthill [40] for sound sources in infinite media at rest. This original formulation was extended in several steps to include:

- Solid boundary effects (Curle)
- Uniform convection effects (Ffowcs-Williams Hawkings [43])
- Non-uniform flow (Howe, Doak, Möhring, Campo)
- Non-uniform flow with vorticity (Philips, Goldstein, Lilley)

For many BEM or FVM methods, the FWH method is implemented in the integral formulation of Farassat [44] and practically applied to rotating machinery. Validation efforts for this approach either compare the near-field pressure obtained from the hydrodynamic method with the pressure at the identical FWH method observer or an analytical solution in the far-field [45]. To avoid more complex mathematics of the advanced acoustic analogies and thus save simulation effort, the permeable surface FWH method in the Farassat 1A formulation, which only considers boundary surfaces in the flow, utilizes a closed passive control surface spanning the complete acoustically relevant part of the hydrodynamic simulation and the pressure on this surface assumes the role of the new acoustic source pressure [46]. The application in FVM for marine problems sparked a discussion on the ideal placement and extent of this passive control surface around the propulsor [47] [48] as spurious noise is detected in many of the simulations acoustic results with unknown origin.

Comparing simulation approaches with experiments, the numerical setups formally do not create self-noise, and thus, no corrections such as transfer functions are necessary. However, numerical inaccuracies, caused by the discretizations, and interpolation or transport schemes of the underlying hydrodynamic FVM are a different source of errors that has to be considered, as well as the interpolation between the FVM mesh pressure and the control surface source for the acoustic analogy.

1.2.4 Parallel research efforts

Due to the high market demand of URN simulations and availability of public funding, there have been multiple research projects and associated groups at various facilities in parallel over the duration of this study. The Newcastle propeller test case research efforts [31] have resulted in a large amount of experimental data and simulation results. Cavitation and underwater noise are studied using panel methods by Göttsche [49] and Kim [50]. The hydrodynamic behavior of propellers in behind ship condition is investigated by other researchers by applying FVM for example with LES and additional acoustic investigations with FWH method by Cianferra [47]. Yilmaz is also developing methods for acoustic analysis of propellers with incompressible FVM in combination with an adaptive mesh refinement technology [51], as is Shin [52]. Both deal with the problem of obstacles in the propeller slipstream and inclined flow, coming to the conclusion that a trailing vortex mesh refinement is required, if the interactions are to be resolved. On the basis of the Newcastle propeller test case, Sezen conducted an identical study to the one in this work in Chapter 5 with their respective methods [53]. Bensow has continued their long term investigations with turbulence resolved simulations with LES in combination with the objective of quantifying acoustic emissions, for example from propellers. However, over the course of this research they went back to more fundamental acoustic test cases such as oscillating cylinders [54]. While the objects under investigation differ from the current study, it has to be noted that

the methods are identical to the current work with implicit LES turbulence modelling and decoupled permeable surface FWH method. While the flow simulation methods are identical, the implementation of the permeable surface FWH method in this work is conducted completely independent from the one from Bensow. Besides, there have been investigations at MARIN on acoustic modelling of propellers [55] and the collaboration of VTT Technical Research Centre of Finland and Aalto University Finland, who studied propeller cavitation with the subsequent goal of acoustic emissions with their proprietary solver, which includes an energy equation reducing some of the assumptions typically associated with the cavitation modelling. [56] Posa has conducted their own LES investigations of a seven-bladed submarine propeller with extremely detailed meshes, which allowed them to better identify the physical mechanisms of acoustic sources of turbulence [57].

All the listed investigations are not suitable for the needs of the industry, where fast and reliable information on the most relevant spectral acoustic emission characteristics of a propulsion system in behind hull condition in full-scale is required in early design stage. The methods selected by the above mentioned researchers are either not resolving the flow field or spectrum sufficiently, such as the panel methods, or are numerically too expensive for repeated investigations of propulsor-hull combinations, so that only open water propellers can be studied once in a feasible manner.

1.3 Aim of the research

The identified open research questions from previous scientific works are: demanding propeller testcases for studying of scaling mechanics of cavitation and acoustics, proper calibration of the mass transfer model, the extent of the permeable surface, reflections at solid boundaries, propeller-rudder or propeller-shaft interaction in the case of a rudderpropeller, tip vortex modelling and its influence on noise generation, interaction of sheet and tip vortex cavitation and finally a well defined procedure for the comparison of cavitation characteristics. In addition, internal requirements by the industry arising from the analysis of the engineering processes and market research, revealed the necessity for efficient and intuitive visualization and exchange formats of pressure pulse information on the hull and URN information emitted into the fluid.

From these requirements, the objectives of this research project are defined as:

- Combination and enhancement of simulation methods for the far-field prediction of underwater noise,
- Conceptualization of best practices for the simulation of acoustic behavior of propulsors operating behind ship hull,
- Development of noise evaluation methods resulting in technical interfaces for exchange of acoustic pressure information and far-field signatures.

The considered method should be able to resolve hydrodynamic flow with high accuracy and yield a validated approach for acoustic predictions of propulsor-hull combinations that can be used in a research environment, or for commercial purposes, such as detailed acoustic predictions in the design stage of a vessel, or investigation of noise emission of existing vessel, with the long term goal of qualifications of ships with respect to acoustic limits imposed by classification or environmental standards. This approach should be able to capture scale effects regarding acoustic emission of propulsors in order to significantly improve upon the state of the art of model scale testing. The developed methods are not intended to replace tools utilized in the propeller design stage, but should be appropriate for recurring problem statements, and thus aim for simulation times in the order of days on medium scale HPC clusters. A large amount of simulations is necessary to create best practices, beginning from simple geometries for validation of integral values and turbulence and cavitation physics and ending with full-scale vessel-propulsor combinations with acoustic emissions.

1.4 Solution approach

Analytical descriptions of turbulence, two-phase flow and acoustics for complex applications are currently impossible. From Section 1.2 it is clear that both potential theory and volume-based methods

offer their individual advantages in the modelling of hydrodynamics, however, this study is restricted to FVM methods in order to obtain an improved insight into the noise sources by capturing more flow details. The approach to apply high-fidelity CFD methods in combination with two-phase flow under consideration of phase-change phenomena for acoustic investigations of ship-propeller combinations in model and full-scale is selected. For this purpose, the results of a high number of CFD-simulations are compared to model scale and full-scale experimentally obtained data sets from the literature, research partners and from own projects. Data is collected from a project conducted within the frameworks of the MarTERA joint EU research project ProNoVi funded by the European Commission as part of Horizon 2020, as well as the national joint research project Red-Emi funded by the Federal Ministry for Economic Affairs and Climate Action and the NATO Science & Technology Organization Applied Vehicle Technology Panel 320 as well as additional research suggested by Technical University Hamburg. Test cases that have been investigated are a NACA0012 half-wing hydrofoil, $NACA66_2$-015 hydrofoil, Delft Twist 11 Hydrofoil, PPTC'11, Newcastle Propeller test case, P3193, E779A, P1595 and the vessel-propulsor configurations from ProNoVi and Red-Emi among others.

The limitation of the applied method in this work arises from the assumption that hydrodynamic noise can be determined with a pressure-based solver, which means that density changes caused by acoustic effects or cavitation physics are neglected. Similarly, the energy equation of state for the flow field is not considered in the computations, i.e. thermal effects of cavitation, which could be physically possible at the investigated operating points, are ignored. Single bubble contributions and bubble deformations from a spherical shape, as well as shear between the phases, are not considered, due to the selected two-phase flow solution method and the cavitation model applied. The consideration of rotation in the computational mesh is realized with either MRF, with added centrifugal and Coriolis forces in the steady rotating region, or AMI, i.e. there is a surface based weighted interpolation between the stationary and rotating regions of the simulation domain. In addition, acoustic reflections of the sound propagation are neglected, which means constructive or destructive interference effects of the sound are not included, acoustic pressure reflections at the simulation domain boundaries of the hydrodynamic solution have an effect on the instantaneous sound pressure field. For the case of propulsor-vessel combinations in full scale, a steady state wave pattern can be considered as the simulation domain boundary at free water surface. Besides acoustically relevant reflections, unphysical numerical reflections may be part of the flow solution.

The most relevant challenge also identified by parallel research efforts is the resolution of the propeller slipstream and specifically the cavitating trailing vortices. The trailing vortices have to be resolved with very fine meshes in an FVM approach in order to capture vortex cavitation. This is not trivial as the length scales between the vessel, the propeller, and the trailing vortices are vastly different. In an open water condition with straight inflow as MRF or AMI rotation, this is realizable by refining the steady tip and hub vortex trajectory in the rotating mesh region, with an axis coinciding with both the free stream flow and the propeller rotational axis. The limitations of this FVM approach for propulsors that also require transient treatment of the simulation are:

1. Inclined flow,
2. Slipstream interactions with obstacles,
3. Upstream wake fueling slipstream distortions.

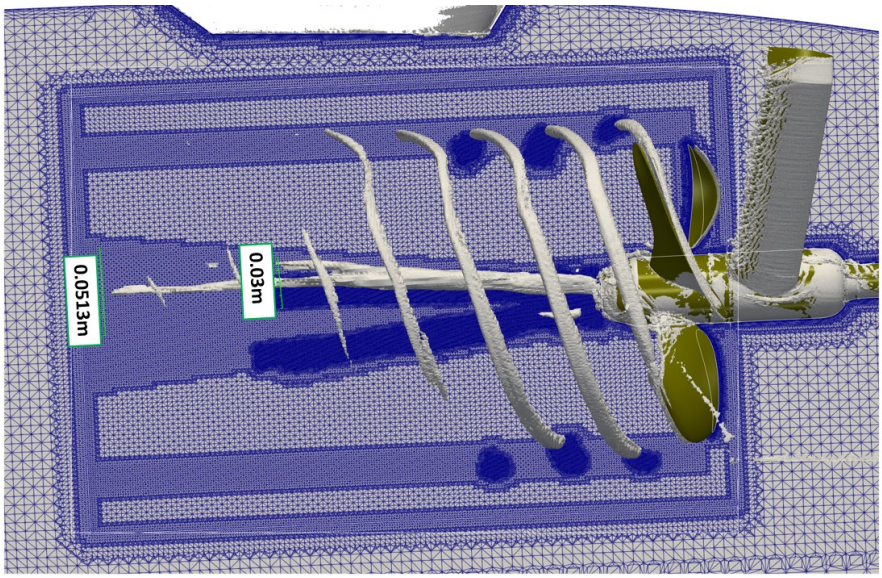

Fig. 2: Restriction by inclined flow

The first problem is posed by inclined inflow conditions, which consistently occur for twin-screw vessels with inclined shaft lines and occasionally for single-screw high-speed vessels. An inclined propeller plane means the trailing vortices are deformed in direction of the free stream flow and do not follow the propeller fixed coordinate system. Resolving all possible trajectories over one propeller revolution would lead to very high cell counts, as the trailing vortex would need to be resolved sufficiently at all angular positions in order for it to wander around in a refined mesh region with a larger diameter than the tip vortex itself. A resulting refined mesh for this approach with an inclined shaft line of 2.75° is indicated in Fig. 2 with the instantaneous tip and hub vortex and the free stream flow coming from the right.

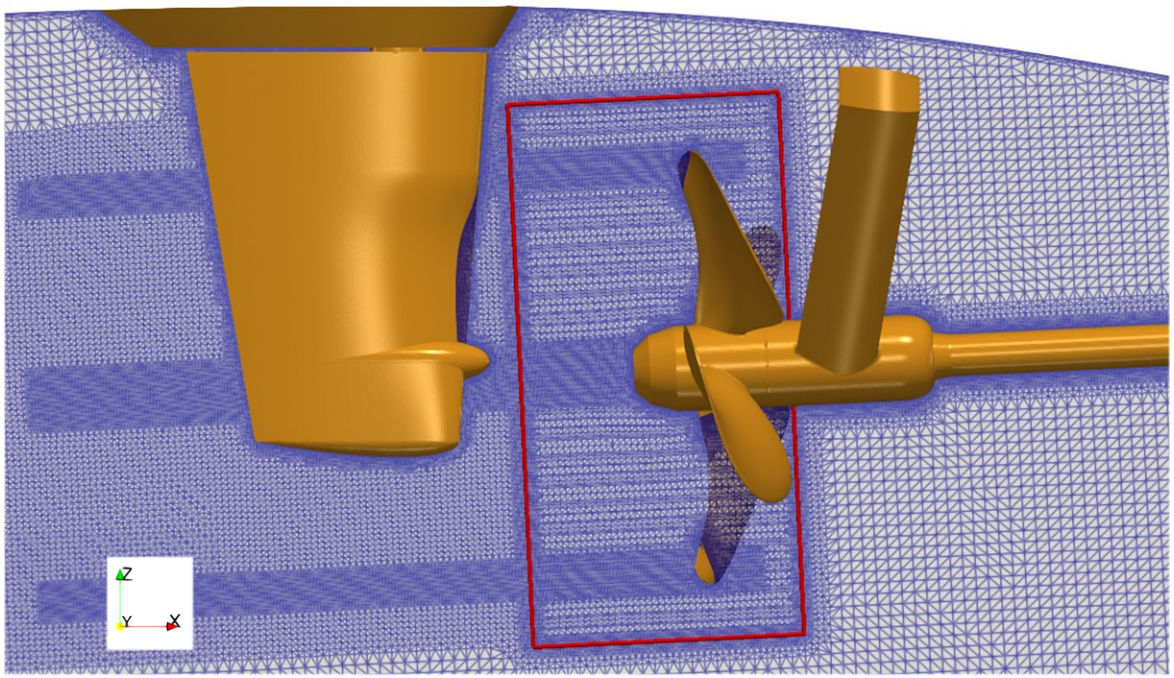

Fig. 3: Restriction of rotating mesh region

The second problem is very common as most propulsion systems have obstacles downstream as part of the steering mechanism, which produces a larger lifting force in the accelerated flow of the propeller slip stream, such as rudders or vertical shafts of azimuthing thruster. A fixed static mesh refinement region in a rotating mesh domain at the location of the tip vortex is not possible in case of non-

axisymmetrical solid boundaries behind the propeller plane. Any possible trajectorial refinements have to end at the downstream section parallel to the propeller plane, where the geometry loses axisymmetric properties. This is indicated by the red line around the rotating mesh region in Fig. 3. The restriction could be circumvented by an overset grid method, where the refined rotating tip vortex region intersects the solid geometry and cells inside the obstacle geometry are deactivated. However, this only works in straight inflow as is described above. In addition, the solid boundaries distort the vortices by stretching them along their leading edge, which in turn requires new refinements with dynamic location that are potentially necessary.

With very sharp wakes upstream of the propeller, such as behind a NACA airfoil in Fig. 4 the tip vortex receives a periodic distortion that is not static with respect to a propeller-fixed coordinate system, as it appears at the inertially fixed intersection of the wake caused velocity deficit of the foil with the tip vortex trajectory. To resolve this issue similar measures as for problem 2. would have to be undertaken.

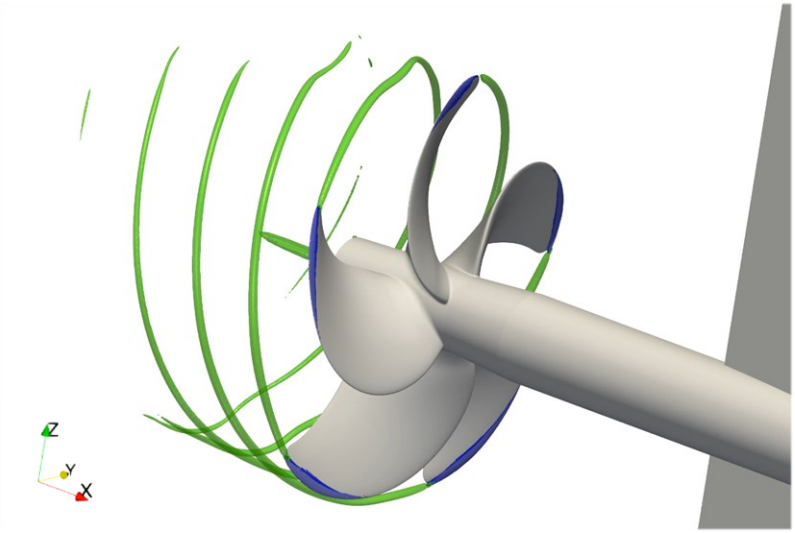

Fig. 4: Restriction by wake fueled vortex distortion

The second and third problem cannot be solved by a static overset grid, therefore the only feasible way to tackle all of the above mentioned limitations is the utilizing of an automatic run-time adaptive mesh refinement, with refinement criteria given by values of available transport variables. This in turn leads to higher calculation times, as the mesh is dynamically adjusted every timestep by splitting and merging cells.

Scientifically, the starting point for this research are single elements of simulation approaches that are fully functional and partly validated, but have never been combined in a holistic approach. These elements are for instance CFD simulations of propellers, or propeller-hull combinations with RANS, cavitation simulations of propellers with potential flow assumption such as with the vortex-lattice method or the panel methods, and acoustic calculations based on empirical data. On a technical side specifically, an existing FVM method with the VOF method and a Schnerr-Sauer based cavitation solver exist and are used with only minor modifications. The classic FWH-method is already implemented in the solver structure as well, however, the KFWH-method is not available as an algorithm in the code applied and only exists as the original concept derived analytically and adjusted for numerical simulation needs [46]. The single methods are not validated for the described purpose and have never been combined and validated in combination with respect to acoustic emissions.

1.5 Structure of Thesis

Due to the complexity and comprehensiveness of the research the results are kept concise and summarized and in most cases only a selection of the large number of simulations conducted as part of this research is shown. The structure of the presentation of the result follows the traditional approach to

exposit the motivation, the theory and the applied methods, followed by a presentation of results and their discussion.

The external factors constituting the necessity for the pertinent approach of simulating marine propulsors with FVM in order to determine far-field noise radiation are explained in the first chapter of the thesis. An accurate approach for simulating acoustic emissions that considers the radiated noise from the base acoustic flow, including its generation and propagation is not trivial and requires three main theoretical aspects which are flow and multiphase physics, description of acoustic sources and a method for the transport of acoustic waves. While each topic itself is its own area of research, the second chapter aims to present a summary of the fundamental mechanisms commensurate to the selected methodology of solving the issue. A comprehensive analysis of the methods for each of the considered steps is then given in the third chapter. Due to the number of conducted investigations, a number of possible variations in the simulation setups are considered. Simulations that are targeting the investigation of the hydrodynamic flow field with a focus on the turbulence modelling and analyzing the two-phase flow phenomena directly in order to study the effects of different numerical settings to prepare for the subsequent acoustic simulations are presented in chapter 4. In chapter 5 the validation of the selected methods is presented, the details of the underlying physics are investigated and a deeper understanding of the mechanisms of flow noise generation is achieved. Each subsection is followed by a summary pertaining to best practices for the simulation of URN with CFD methods. For the URN investigations, the developed numerical methods from chapter 3 are put to the test with simple acoustic validation cases and subsequently use cases from the industry with increasing complexity in chapter 6. This proves the approach as meaningful and applicable within an industry environment for typical tasks that might arise in the field of marine vessel URN engineering. Summarizing the results and the knowledge gained from the validation cases as well as the complete work is chapter 7, which additionally describes the further steps identified for future research efforts.

2 Physical Mechanisms Underlying Far-field Underwater Noise

The continuum physics describing the phenomenon of underwater sound are comprising of different fields of knowledge which each in its own would exceed the framework of this thesis by far. Therefore, the most important aspects of turbulence, cavitation and acoustics are selected for the declared integral objective of simulating a full propulsion unit in the vessels wake. The vortex phenomena subsection focuses on vortex formation and propagation occurring for lifting surfaces. The topic of cavitation is addressing single bubble cavitation dynamics with its fundamental physics, as well as sheet cavitation on lifting surfaces and vortex cavitation. For the acoustic fundamentals, the basic theory of generation of sound by volumetric change of a fluid medium is addressed together with its propagation mechanisms and possible interaction with structures. The implementation of these methods in the selected simulation approach is then explained in chapter 3.

2.1 Trailing Vortex Phenomena

While vortices are the fundamental building blocks of any turbulent structures, such as in boundary layers, they have another engineering significance in the form of macroscopic vortices created at solid structures. A solid body motion relative to a fluid generates a separated vortex layer downstream with a bound vortex around the body, indicated by the derived quantity of circulation $d\Gamma = \vec{u} \cdot dl$ of the fluid around the body. At the bodies free ends the flow rolls up into trailing vortices with the rotation direction governed by the pressure distribution on the body. While the starting vortex at the end of the trailing vortex sheet is at infinite distance from the body according to the second Helmholtz theorem, or more physically, dissipates at sufficient distance from the separation of the body, the two axial streamwise vortices are stable due to their maintained angular momentum for their trajectory downstream far beyond the separation from the lifting surface tips. This can occur for lifting surfaces such as half-wing air- [58] or hydrofoils [19], which have a distinct suction und pressure side dictating the roll-up direction. As each propeller blade acts similar to a hydrofoil, two trailing vortices at the blade tip and the blade foot are created. While the hub near vortices of all blades of the propeller practically immediately interact with each other forming a single hub vortex, the tip vortices are separately only interacting by velocity fields with the corresponding hub vortex [59]. Besides the loading distribution of a propeller blade, given by the chordlength, pitch, and camber distribution, the skew of the foil has significant impact on the tip vortex roll up and its cavitation. [60]

The angular velocity distribution in the vortex can be described for the assumption of a circular cross section with the analytical Rankine model which splits the vortex velocity distribution into the linear solid body rotation in the core with radius a

$$u_\Theta(r) = \frac{\Gamma}{2\pi a^2} r \qquad | \, r \leq a, \tag{1}$$

and the outer region

$$u_\Theta(r) = \frac{\Gamma}{2\pi r} \qquad | \, r > a. \tag{2}$$

The location of a is defined as the radius with maximum azimuthal velocity and the circulation is related to the rotation rate ω with $\Gamma = 2\pi a^2 \omega$. With the more realistic Burgers model

$$u_\Theta(r) = \frac{\Gamma}{2\pi r}\left(1 - e^{-1.256\frac{r^2}{a^2}}\right), \tag{3}$$

derived from the Lamb-Oseen vortex model, a smooth transition between core and outer regions is realized. Differences in the velocity and associated pressure distribution of the two models are given in Fig. 5, where the velocity is non-dimensionalized with $\Gamma_0 = \Gamma/2\pi a$, the radius by a and the pressure by $\rho(\Gamma/2\pi a)^2$.

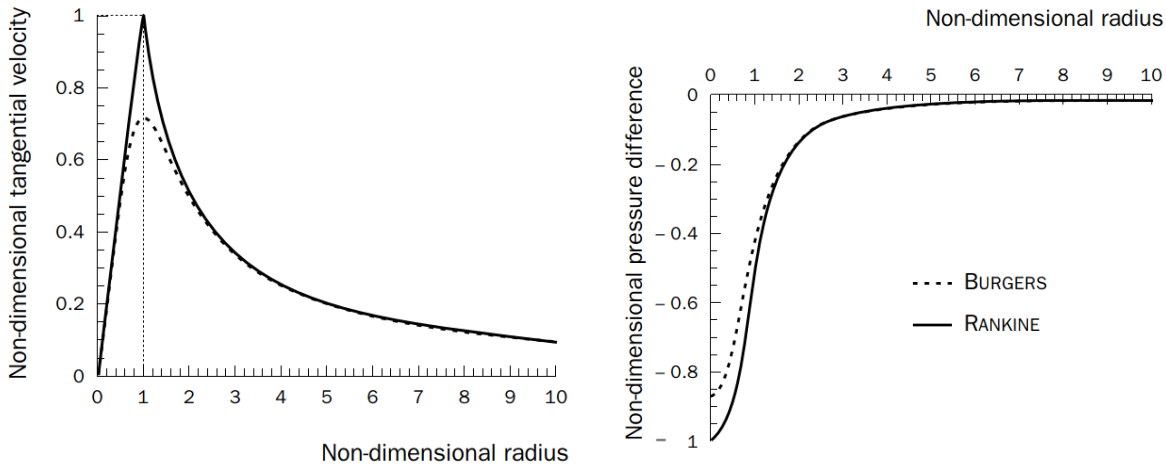

(a) Velocity (b) Pressure

Fig. 5: Analytical vortex models [61]

The vorticity $\omega = \nabla \times \vec{u}$ describes the local rotation of a fluid and may be used to quantify the strength of a vortex, where fluid elements are spinning with an angular velocity relative to a central location, which is called the vortex core. Analytical physical descriptions of streamwise trailing vortices, include the solutions of Rankine, Burgers, or Proctor, which all have the notion in common that the vortex axial cross section consists of an outer region which shows large angular velocity gradients, and an inner viscous region, that experiences solid body rotation behavior with respect to angular velocity. Together with the lower angular velocity in the core, there is also an axial velocity deficit, which can potentially lead to a relaminarization of the vortex core. Conversely, the pressure is also reduced around the core, which can lead to the onset of cavitation in trailing vortices even though the surrounding flow is not at risk of cavitating. Through the Lamb vector $\omega \times u$ shearing and compression in a fluid are connected [62], thus creating the physical foundation of relating sound generation with vortices. The pressure perturbation is proportional to the rate of change of the vortex stretching by the fluid with the intensity at maximum in the plane orthogonal to the Lamb vector. [63]

In this work, the Q-criterion is used to visualize vortices as the positive second invariant of the velocity gradient tensor ∇u with the additional requirement of being below ambient pressure. The gradient may be decomposed into an antisymmetric tensor, the rotation rate Ω_{ij}, and a symmetric tensor, the strain rate S_{ij}, from which the quantity

$$Q = \frac{1}{2}\left(\Omega_{ij}\Omega_{ij} - S_{ij}S_{ij}\right) \quad (4)$$

is obtained, meaning that in local regions of $Q > 0$ vorticity dominates over the strain rate, indicating vortices. For the tip vortex of a propeller the Q-criterion is concentrated around the vortex core with a sharp jump at a certain radius from the core, leading to an excellent trailing vortex visualization method. In Fig. 6 the diameter of the Q-value around the vortex core of the PPTC'11 propeller varies only marginally, with increasing variation for locations further downstream due to numerical dissipation in the underlying RANS simulation.

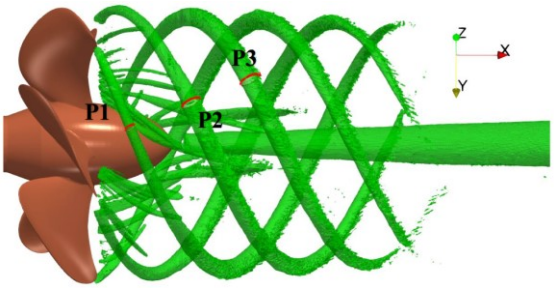

(a) Isosurface $Q = 5{,}000s^{-2}$

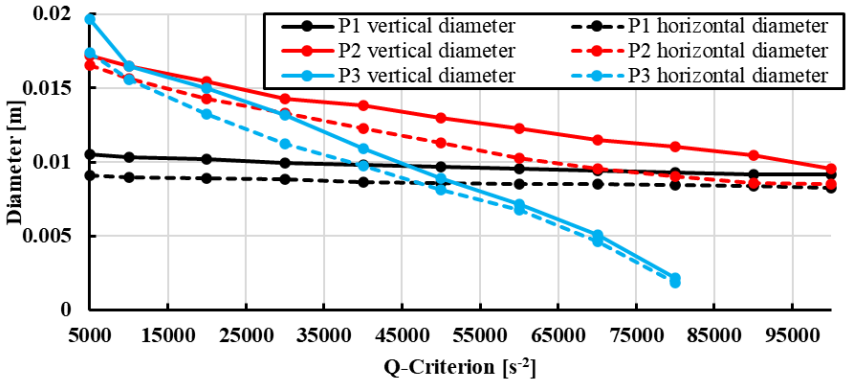

(b) Isosurface radial extent

Fig. 6: Vorticity helical cross section concentration [64]

2.2 Cavitation

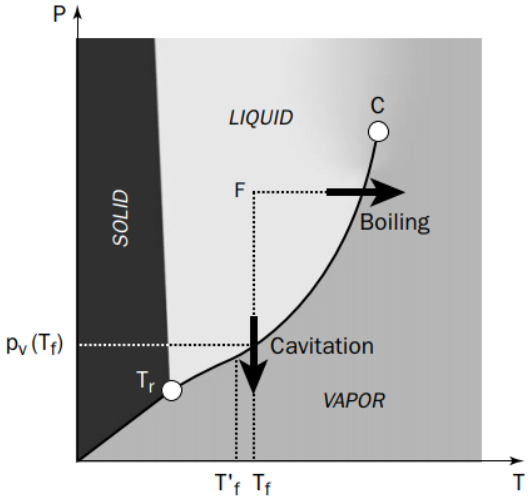

Fig. 7: Cavitation in phase diagram [61]

Macroscopically isothermal liquid-vapor phase change activated by pressure gradients due to local velocity is called cavitation. In the water phase diagram in Fig. 7 the process forms an isotherm, however, the transition line between liquid and vapor or the vapor saturation pressure depends on the initial liquid temperature. On a microscopic level the mechanisms of cavitation are relying on thermodynamic effects as the latent heat for initial vaporization is extracted from the liquid, which would create a thermal delay $T_f - T_f{}'$ in the phase diagram. However, in the context of marine propulsion and the associated scales of time, geometric dimensions, and heat transfer, the temperature change is negligible, fitting with the assumptions mentioned in Chapter 1.

Cavitation structures in real flows are not spherical as a result of pressure gradients, shear forces, and the vicinity of solid surfaces or other vapor structures. Nevertheless, it is worthwhile to examine the physical processes that determine microscopic single bubble growth and rebound and under the right

environmental conditions collapse, because they are the foundation for the mentioned cavitation models. A single spherical microbubble kinematic with radius R in infinite incompressible fluid is described by the Rayleigh-Plesset equation [65]

$$R\ddot{R} + \frac{3}{2}\dot{R}^2 = \frac{1}{\rho}(p_B - p(\vec{x}) - \frac{2\sigma_{st}}{R} - \frac{4\mu}{R}\dot{R}), \quad (5)$$

where the pressure at the interface p_B depends only on the instantaneous local pressure p, the surface tension σ_{st}, and the liquid dynamic viscosity μ, with the partial pressure of non-condensable gases included in p_B and describable by polytropic behavior. The bubble growth is activated by the pressure difference, while the surface tension is the primary mechanism that acts against it. For bubble collapse, the surface tension term is insignificant. In water, the slowdown of collapse or growth due to the viscous forces is also negligible, as the process of cavitation is primarily inertia driven.

To form macroscopic cavitation bubbles, a homogeneous or heterogeneous nucleation process is required. The differentiation depends on if there are nuclei available in the medium as particles or bubbles or on a boundary as a result of the surface roughness. The cavitation process is then either vaporous, if the liquid rapidly changes into vapor when the pressure falls below the vapor pressure of the liquid, or gaseous as a diffusion process driven by the pressure of the liquid being below the saturation pressure of a dissolved non-condensable gas. In marine applications, nucleation sites are practically always available either at solid surfaces or as suspended micro-particles or dissolved gas bubbles in water and thus the cavitation process is vaporous. Although particles or gas is always present, the volume fraction is small, so it does not change the macroscopic properties of water such as density. When a single bubble forms heterogeneously at the propeller blade surface, it is transported away and assumes a hemispherical shape with a thin liquid layer below it. In the free stream a velocity field with a certain acceleration forces a single bubble to lose its spherical shape, if a certain radius is exceeded [61], which for the studied flows is always the case. Once there is sufficient pressure differential between two sides of the bubble, a re-entrant jet forms, which is a liquid jet that enters the bubble and deforms it. This is considered to be a major factor in the mechanisms of bubble collapse near walls and cavitation erosion. On a macroscopic scale re-entrant jets form at the downstream end of cavity sheets on lifting surfaces creating a liquid layer between the solid boundary and the bubble surface.

Once the pressure outside the bubble increases above the vapor pressure, a rapid collapse is initiated, which occurs in such small timescales that there is a discussion among researchers if thermodynamic and compression effects may not be neglected in the final stages of bubble collapse to improve modelling accuracy with respect to acoustic emissions. In the present study, no further investigations are conducted on the importance of thermodynamics and compressibility. However, the induced pressure wave by the bubble or cavity structure collapse, becomes relevant as the source of the cavitation noise. If the collapse occurs near the major influencing boundary, the bubble assumes an elongated spheroidal shape due to the formation of a jet normal to the boundary. The shape is distorted and expands towards the boundary, in the form that the near bubble surface is fixed with respect to the boundary and the far bubble surface distorts towards it. The collapse time is not influenced significantly by the distance to the boundary, which means the Rayleigh collapse time may be used as a fundamental way to estimate the time scales of cavitation induced noise for propellers. A stop or regrowth of a collapsing bubble is possible, which can lead to oscillations in the bubble volume induced by the surrounding pressure, possibly creating its own acoustic emission characteristics. However, single bubbles are not covered by the selected methods within this work.

A state of operation with its cavitation tendency in the propulsion industry is formally only depending on the pressure difference between the local static pressure $p(\vec{x})$ and the saturation vapor pressure p_v, and described similar to the pressure coefficient as ratio against the kinetic energy per volume

$$\sigma_u = \frac{p(\vec{x}) - p_v}{\frac{\rho}{2}|\vec{u}|^2}, \quad (6)$$

$$\sigma_n = \frac{p(\vec{x}) - p_v}{\frac{\rho}{2}(nD)^2}, \quad (7)$$

where $\vec{u}$ is the free stream velocity and can be replaced by a characteristic velocity of the propeller by relating it to the rotation rate n and the diameter D. Undesired side effects of cavitation in the context of propellers are efficiency loss, due to thrust breakdown, additional vibration as a result of vapor volume oscillation, noise generated by the periodic volume displacement and the violent collapse of cavitation bubbles and structures, and erosion, if this collapse occurs near surfaces.

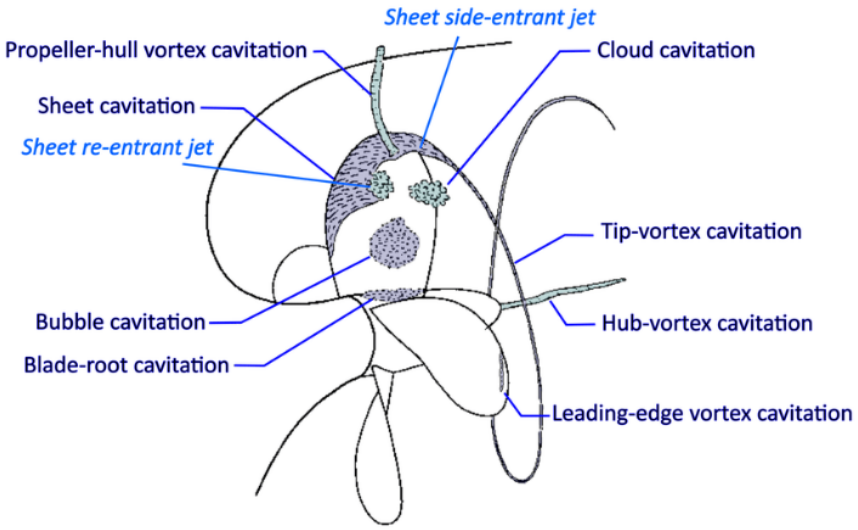

Fig. 8: Cavitation types occurring at a propeller [66]

The cavitation types that occur for marine propulsion systems can be categorized into different types, as shown in Fig. 8. As the least complex form of cavitation, bubble cavitation means there is no interaction between different bubbles as they follow a streamline and follow the description given by Eq. (5). High density accumulations of bubbles near the minimum pressure at a solid surface interact with the boundary layer and combine to a separated region of smooth interface vapor structure, which is called sheet cavitation. Typically sheet cavities form near the suction side leading edge for a propeller and re-entrant jets, thin layers of water between the cavity and the blade surface, are forming shortly downstream, as part of the boundary layer interaction. This phenomenon is easily detectable in CFD simulation results, however, in the visual interpretation of experiments it can be difficult to judge if the cavity is detached from the adjacent surface, which is why research was not focused on this phenomenon until relatively recently. Often these continuous cavitation regions, which are attached to the surface at their initial formation, are extended downstream, where the interface becomes unstable and highly dynamic even in steady state flows. In these regions of higher pressure the cavity collapse or dispersion into single bubbles is initiated, with a high degree of interaction between the locally separate collapse processes due to pressure wave interactions. In fluctuating sheet cavitation, for example excited by the angularly depending disturbance of the propeller inflow in the vessel wake, the cavity extent dynamically changes with time and shedding of cloud like structures from the downstream end of the cavity occurs with its own dynamics. For the termination region of suction side sheet cavitation, single bubbles and shed cloud cavities are transported away from the surface, reducing the risk of harmful cavitation erosion, while pressure side shed cavities are usually transported towards the blade surface. Therefore, suction side cavitation is typically accepted for contemporary propeller design points, while pressure side cavitation is not. When the sheet cavity terminates before the trailing edge of a propeller it is called partial cavitation on the radius section, once the cavitation extends along the complete chord length, it is called super-cavitation.

For propeller designs, cavitation and efficiency are opposing design criteria, which have to be weighed against each other depending on the provided design specifications. A simple example would be that a low area ratio increases efficiency, and at the same time increases cavitation. As most of the market is cost driven, efficiency always plays the most important role, however, a design typically is required to have non-erosive cavitation only. During the propeller design the margin against suction and pressure

side sheet cavitation, as well as tip vortex cavitation must be known, in order to obtain the design fulfilling the specifications best, with respect to the design point of advance ratio and cavitation number. Another requirement is the vibration and noise emission, which are closely connected to the cavitation characteristics.

In the tip or hub vortex of a propeller, nucleation may be initiated due to the low pressure. Once a sufficient number of bubbles are accumulated at the center vortex, cavitation structures in the vortex core begin to form. Typically, the tip vortex consists of several smaller vortices separating at the trailing edge at the blade tip, which assemble beyond the blade to form a single tip vortex. This so called mixing zone features a higher pressure than the vortex core, which means vortex cavitation inception occurs slightly downstream of the blade outside the mixing zone. Depending on the propeller design, the tip of the blade may also feature sheet cavitation in some form, often leading to a continuous cavity combining with the tip vortex and ignoring mixing zone phenomena, once the cavitation number is low enough. With the cavitation inception the cross section of the vortex core changes in area and for the assumption of a circular vortex the ratio of the vapor core diameter to the non-cavitating liquid core is [61]

$$\frac{d_l}{d_v} = \sqrt{\frac{\rho_v}{\rho_l}}, \tag{8}$$

which is around $58 \cdot 10^3$ for water. This leads to extreme displacements of the liquid phase for comparatively little material phase change. The formation of a gaseous vortex core thus fundamentally changes the physics of the trailing vortex turbulence and flow field, as the vapor phase occupies the center of the axial cross section of the vortex. The stretching of the liquid vortex that naturally occurs in the slipstream leads to an increased rotation rate. While the angular momentum needs to be identical between wetted and cavitating condition, the inertia is changed due to the large difference in density and the original relation between elongation and rotation rate is void. With constant ambient pressure, a stretching of the vortex induces an increase in vapor core radius in addition to the increased rotation rate which also occurs in the liquid case. An increase in external pressure on the other hand, reduces the vapor core radius and by reducing the volume of the low density vapor phase increases the rate of rotation. [61] Under the influence of secondary pressure waves, induced by adjacent cavities such as the hub vortex, sheet cavities or other tip vortex cavities, natural oscillations could appear. Both of these effects have significant consequences on the cavitating vortex evolution, however, the flow field of a propeller is extremely complex making the study of these theoretical effects difficult if not impossible in practice. In experimental observations a relative translational motion of the cavitating vortex with respect to the bulk liquid flow is reported, when the cavity undergoes volume variations, which may be attributed to a virtual mass effect. [61]

Velocity distributions are drastically changed with the solid body rotation tangential velocity in the liquid starting at the vapor interface, leading to a reduced radial extent, before the large gradients typically of the angular velocity distribution start. Overall the radii with the maximum radial velocity are larger. Inside the core, the pressure assumes a constant vapor pressure while outside the typical behavior of vortex pressure is assumed. An analytical model to describe the azimuthal velocity of a cavitating trailing vortex with a circular cross section depending on the radius around the core r is the Proctor-Vortex model [67]

$$u_\Theta(r) = \frac{\Gamma}{2\pi r}\left(1 - e^{-\beta\left(\frac{r}{B}\right)^{0.75}}\right), \tag{9}$$

where Γ is the trailing vortex circulation, B is the wing span of the hydrofoil or propeller blade, and β is an empirical vortex roll-up parameter which is assumed to be around 15 in the reference for a stationary wing. The reasoning for relating the velocity field with the wing geometry is that the circulation of the trailing vortices is strongly related to the bound circulation by the lifting surface, which in turn is depending on their geometry. The radial velocity is several orders of magnitude lower and is driven by the mass transfer at the interface, which can be analytically given by a modified Rayleigh-Plesset equation.

The non-cavitating form at the downstream end of a vortex is triggered by radial modes, as the vortex weakens in real flows due to viscous dissipation, whereas the vapor core is infinite for potential flow assumptions. A harmonic oscillation of the tip vortex cavity in different modes is believed to exist, which may be naturally occurring due to the turbulence-cavitation interaction for a specific propeller design or as a result of dynamic excitation of the tip vortex in the interaction with a vessel wake and associated periodic variations of propeller load. In Fig. 9 the first three modes $n = [1, \dots, 3]$ for a columnar vortex with hollow core is illustrated, described by the cavitation radius $\eta(\vec{x}, t) = r_0 + \hat{\eta} \cdot e^{[i(k\psi + n\varphi - \omega t)]}$ in the local cylindrical coordinate system (ξ, φ, ψ) with the axial wavenumber k and the angular frequency ω.

(a) Breathing mode (b) Bending mode (c) Double helix mode

Fig. 9: Postulated first vibration modes of vortex core [68]

Both re-entrant jets for sheet cavitation and trailing vortex cavitation are an example of the close interconnectedness between turbulence and cavitation and give credence to the notion that these phenomena cannot be analyzed separately or with current analytical models. It is important to note that real fluid motions involve viscous effects, surface roughness, variation in nucleation physics, and these all modify the probability of cavitation inception and collapse, and consequently the spectral content of cavitation noise.

2.3 Acoustic Source Generation

2.3.1 Propeller Blades

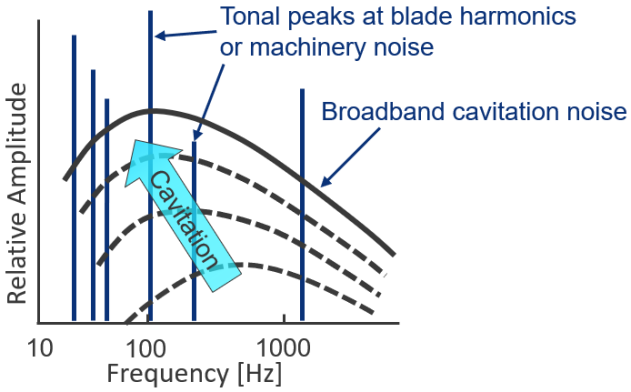

Fig. 10: Illustration of spectrum of radiated noise by a ship-propulsor combination

Sound is generated whenever there is relative motion in a fluid or between a fluid and solid surface. In full-scale measurements, the noise of a propulsor-hull configuration consists of hydrodynamic and mechanical noises, which are caused by machinery, such as generators, engines, pumps and other aggregates, and excitation of structures, e.g. gears, bearings, and hull by drivers or by hydrodynamic forces. Typically, the mechanical noise sources are strongly tonal, meaning they only emit at one frequency, for example the gear mesh frequency or the engine ignition frequency. The hydrodynamic noise on the other hand features both tonal and broadband noise emissions, by periodic events on the one hand and stochastically dominated events in space and time on the other hand, which are cavitation and to a lesser degree turbulence. The noise spectrum of a propulsor-hull configuration is illustrated in Fig. 10, with tonal peaks caused by machinery or propeller blades and the broadband cavitation noise hump. The broadband cavitation increases in amplitude and the maximum moves to lower frequencies,

with increasing occurrence and severity of the cavitation, i.e. lower cavitation numbers. In case of high cavitation noise, tonal emitters can be masked as illustrated in the figure, which means an acoustic observer is not capable to detect these sources in the received signal.

Mechanisms controlling the hydrodynamic noise generated by a propeller, by influencing the pressure field in the vicinity of the propulsor are [69]

- Periodic displacement of liquid by the propeller blades,
- Periodic change of the pressure field due to lifting forces of the propeller working within the vessel wake field,
- The wake field induced periodic volume adjustment and possibly bursting of the sheet cavity on the propeller blade and oscillation of the tip or hub vortex cavitation in the propeller slipstream,
- The broadband noise inducing collapse of the trailing bubbles of larger bodies of cavitation,
- Turbulence caused by the propeller and the vessel and its induced surface waves.

While turbulence plays an important part in the spectral characteristics of the vessel at non-cavitating operation points, for example below cavitation inception speed for some propeller designs of a ship-propeller system [41], it may readily be ignored, once broadband cavitation noise occurs due to masking of the much lower amplitudes.

Assuming the propeller blades rotate with constant rotational speed n, the volume variation is considered a monopole type acoustic source, as it periodically displaces the fluid at a fixed location in space. This creates a tonal emission with the frequency of $f = i \cdot n \cdot z$, where z is the number of blades, if the blades are of identical shape. The event occurring at the frequency corresponding to $i = 1$ is called the blade passing frequency of the propeller or first harmonic frequency with higher numbers of i being the i-th harmonic frequency or the i-th order harmonic, which are also emitting tonal noise. Every blade passing frequency also induces higher order harmonics or overtones as every event occurring x_i times per rotation may as well be perceived as an event occurring $x_i/2$ times per half rotation. With these contributions, the spectrum of a non-cavitating propeller is already filled with high amplitude tonal noise at the propeller harmonics. This type of noise generation is for example in the methodology of acoustic analogies often called thickness contribution, as it is associated with the thickness of the blade.

In addition to the displacement, there is secondary mechanism of noise generation with non-cavitating lifting surfaces, which is turbulence noise caused by the lifting mechanisms and its influence on flow and pressure distribution associated with the single blades as illustrated in Fig. 11. From these types, the main sources in the context of a propeller are believed to be the trailing vortices and the shear layer and to a lesser degree the turbulent boundary layer. Depending on propeller design and operation point leading edge or trailing edge separation may create noise. Adding to these effects can be a turbulent inflow to the profiles of the blades imposed by the vessel wake, which leads to a periodic excitation of these chaotic small-scale structures. It is a common sentiment to assume wake fields are steady state, as they are given as time mean over the measurement period in experiments or simulations, however, in many cases the wake field shows low and medium frequency fluctuations that may be further adding to the non-periodic excitation of turbulent noise. The frequencies of the turbulence noise are connected to the size of the generated eddies, which vary strongly by definition, leading to a wide frequency broadband noise. A special case of tonal noise caused by turbulence is propeller singing, which is created from periodic trailing edge separation similar to a Karman vortex street in combination with the blade structure excitation.

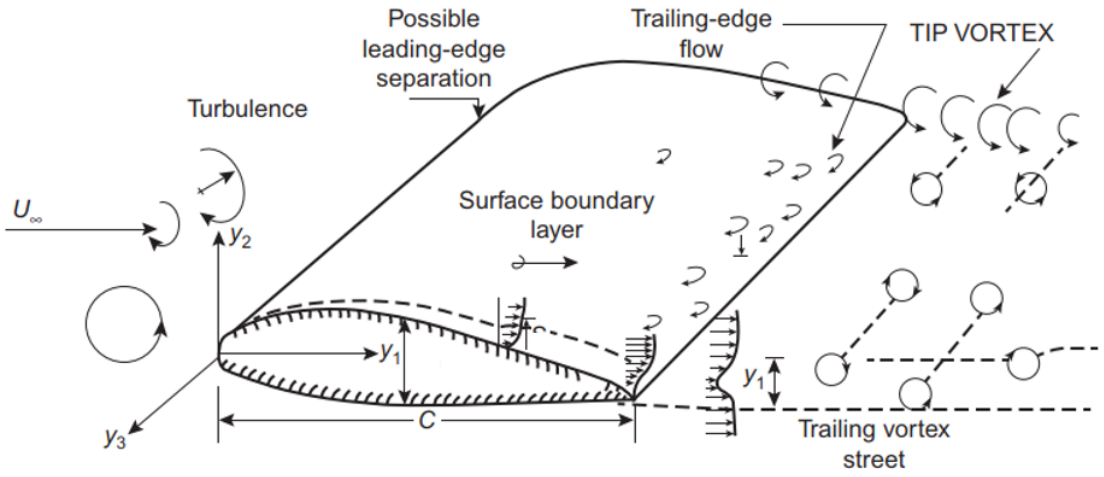

Fig. 11: Turbulence noise sources for a lifting surface [66]

2.3.2 Cavitation Volume

The main contributor to broadband noise is the propeller cavitation, which may have a steady base volume, and moreover generally varies greatly in volume depending on angular position of the propeller with respect to the wake field. Approximately constant cavitation volumes can be theoretically achieved as a steady suction side sheet cavitation starting at the propeller leading edge. That can take place under open water propeller conditions or behind hulls with very low wake gradients. Regarding sound generation these steady cavities operate similar to the blades and periodically displace water, creating theoretically only tonal spectral components. In fact, this may reduce noise by reducing turbulent boundary layer effects as the boundary layer is forming not at the propeller surface, but at the phase interface, which may have reduced wall shear forces. Further noise reduction effects may occur, due to the compressibility and thus dampening of other acoustic waves at the vapor phase and the reduced acoustic transmission quality of the vapor phase. The speed of sound in water vapor is reduced and the attenuation increased compared to the liquid. More realistically, for operation behind a vessel, is the stable variation in thickness and extent of the cavitation volume over the angular positions, triggered by the wake gradients of the vessel, creating emissions at higher order harmonics. Due to this perturbation a fluctuating cavity volume is triggered, which has an oscillating downstream extent on the blade as incoherent collapse, shedding and cavity separation into smaller volumes occur as stochastic processes. The resulting noise is broadband in nature, which is superimposed onto the tonal aspects caused by the remaining base cavity volume. Similar to the propeller, the rudder may also feature stable sheet cavitation, which would not emit any sound. More realistically, a rudder cavity fluctuates periodically with the passing of the blades in front of it and possibly other low frequency disturbances in the wake of the vessel, creating noise emissions due to displacement.

Single bubbles that appear either free floating or downstream from dissolving cavities are another source of noise, by either collapsing or oscillating in volume or location. The imposed pressure field by the blade and the cavitation structures, as well as pressure waves by collapsing bubbles in the vicinity have a considerable contribution to the total radiated sound level. Sound is fundamentally controlled by the volume history of the bubble and thus the deviation from a sphere by a single bubble can be neglected in favor of the applicability of the Rayleigh-Plesset model, as the wave length of the main frequency is attributed to radius and only higher order acoustic multipoles are affected by the actual shape. For the case of bubble collapse, the wall normal acceleration is large during the final collapse stage, so it is reasonable to assume that this motion contributes heavily to the sound production [63]. With the Rayleigh-Plesset description of bubble dynamics, the velocity of the collapsing bubble becomes unlimited for $R \to 0$, however, in reality the velocity in the final stages of collapse is limited by the compressibility of the liquid phase. The exact processes are still the subject of ongoing research as the details of collapse are not easily observed due to the varying time-scales of the phenomena starting from

nearly sonic velocity and ending in motionless state. Another possible physical limit of the collapse velocity is given by the compression of entrapped non-condensable gases, which leads to oscillating bubbles radii with different lower amplitude sound emission characteristics. These rebound dynamics include deviation from the spherical bubble geometry and are strongly influenced by thermal effects such as conduction and radiation and depend on the adiabatic or non-adiabatic heat capacity ratio of the gas. As the implosion of a bubble is just a singular Dirac impulse in time, it creates no spectrum by itself, rather as a result of the large number of microscopic bubbles that are collapsing, a broadband spectrum is created. The emission characteristics of bubbles as a whole are then determined by the radius of the individual bubbles and the temporal spacing between different implosion events. Similar to stable sheet cavities, bubble swarms may lead to reduced sound levels as they possess good attenuation properties [63]. Similar effects are utilized by injecting air into the propulsor inflow, to improve overall compressibility and attenuate the pressure waves in addition to creating nuclei for gaseous cavitation. These contributions to the broadband spectrum, that are not considered in this study's methods, may be required to increase the accuracy of the acoustic predictions. During collapse isolated bubbles emit noise with high frequencies because of the spherical shape and generally weak damping. Partial cavities collapsing are a significant noise source with medium and low frequencies from the sources at the downstream ends, where different connected and shed vapor structures form and dissipation by turbulence is high. Another source of noise is the impact or interaction of the phase interface with the solid walls, which is broadband in nature.

A stable oscillating tip vortex cavity is another source of noise, which is considered to be mostly tonal around frequencies of $600 - 1200Hz$. This oscillation is triggered by the wake field or inclined flow and the associated periodic change in loading of blades and especially outer radii sections. Different modes of tip vortex cavity oscillations are postulated including breathing, bending, and double helix modes. [66] [68] In open water condition in straight inflow these oscillations, cannot be recreated in experiments [67] or in numerical simulations [59]. However, with a wake screen these oscillations are appearing in the experiments. Similar to sheet cavities the tip vortex cavitation sheds smaller cavities and single bubbles, which are again sources of broadband noise emissions. If a cavitating tip vortex is not oscillating and generates neither shed cavities nor bubbles, it is theoretically possible that the noise is dampened due to the additional compressibility in the propeller slipstream and increased sound attenuation by the vapor phase.

2.3.3 Structure Interaction

Two different types of hydrodynamic structure interaction have to be differentiated in the context of underwater noise emissions of a propulsion system. The first is vessel wake upstream, which influences the homogeneity of the inflow and is the source of perturbations on the propeller radii sections angle of attacks and associated loading. The second is the possible downstream interactions of the propeller slipstream with a steering device such as a rudder or an azimuthing propulsions vertical shaft. The first is partly described in the chapters above, while the downstream effects are indicated here.

Downstream of the propulsor the interaction with an obstacle leads to noise by redirecting the accelerated flow, which creates a larger velocity gradient than the case in the free stream flow. This means the obstacle features boundary layers with a higher degree of turbulence and thus is a noise source with higher spectral amplitudes. This acceleration of the flow might lead to such low pressures, that sheet cavities can appear, which generate broadband noise by default, as described in the previous sub-section. The interaction of the wetted or cavitating trailing vortices with obstacles, however, is considered a more severe possible source of sound. Often the rudder profile is located on the extension of the propeller shaft line axis centrally behind the propeller meaning the hub vortex is directly impinging onto the rudder leading edge and split up onto both rudder sides dynamically while rotating, which in itself could create noise as the rather stable angular momentum driven structure of the vortex is ripped apart. When the hub vortex is cavitating, the cavities are split up and collide directly with the rudder boundary layer, which is considered as source of noise and leads to erosion of the rudder material.

The bursting of the tip vortex including the initial stretching along the leading edge of the rudder or shaft is another source of noise, which is intensified if the tip vortex is cavitating, leading to additional erosion of the rudder at the location of the outer radii sections of the propeller. The initial stretching outwards at the leading edge might lead to an interaction with the gap between the rudder structure and the rudder head box, which might create additional noise and is at high risk of erosion.

Another form of structure interaction is the excitation of the structure by dynamic hydrodynamic forces and the subsequent vibrations of the structure. The vibration of the surface is then another noise source in the fluid by volume variation and periodic displacement due to oscillating modes. This effect occurs for azimuthing propulsors, rudders, and the propeller blades themselves. The phenomenon of propeller singing is a result of this type of interaction at the outer blade radii sections near the trailing edge. This phenomenon is not considered in the selected methods of this project, however.

Finally, structural noise from the machinery also induces vibrations on the surrounding hull plates or on rudders and azimuthing propulsors. Typically, only loud tonal contributions are relevant such as the engine, or for an azimuthing propulsor the powertrain inside the underwater housing, where the main contributors are bearings and gears. For podded propulsion, with electric drives at the propeller shaft, the electrical noise of the e-motor is another loud tonal noise. While in most academic cases either the flow or the structural noise dominates, the complete contributions from both aspects have to be taken into account for the case of a propulsor-hull combination over a sufficiently large frequency range.

2.4 Acoustic Propagation

2.4.1 Mechanisms of Acoustic Propagation in a Fluid

Acoustic sources are dynamic elements in the fluid that change the density of the distribution of fluid particles in the immediate vicinity around it with small speed relative to the speed of sound $u \ll Ma = 1$. If the density changes with a high speed $u > Ma = 1$ the variation would result in a shock wave. A dynamic disturbance of the density in space is transported isotropically in the medium beginning at this source. However, sufficiently far away from the source, the propagation mechanisms can macroscopically be described by compression wave characteristics, consisting of regions of compression and rarefaction that are propagated longitudinally in the three-dimensional space, while the transporting particles vibrate around their equilibrium position in the bulk flow. Due to this nature, the compressibility of the medium is the material property that determines the adiabatic speed of sound as the rate of change of pressure p with density ρ at constant entropy [63]

$$c^2 = \left(\frac{\partial p}{\partial \rho}\right). \quad (10)$$

When the velocities are much smaller than the speed of sound, the assumption of adiabatic expansion is valid and is called the linear acoustic approximation, which is always the case for the URN of a propulsor-vessel combination. Besides the requirement that all flow velocities are small in comparison to the sound velocity, the assumption of completely incompressible flow is only valid for wavelike disturbances in the field with frequency f, if the disturbance extent is significantly larger than a characteristic length L of the problem under investigation. With the propeller radius R as a characteristic length [70], the maximum frequency, where this assumption maintains validity is between $500 < f < 5000Hz$, [71] however, this restriction is neglected in most studies as well as this work.

For dispersive waves the linear relation between the phase velocity and frequency is $v_p = \omega/k$, with the frequency $f = \omega/2\pi$ and wave number $k = 2\pi/\lambda$ of the wave. For a non-dispersive wave, the phase velocity is set equal to the speed of sound in the medium $v_P = c$ for all frequencies, which means the phase velocity and the group velocity of the wave are identical. This is a valid approximation for water sound waves, as the material property changes along a waves path in water are minor. However, as part of the wave characteristic the phenomena of reflection and scattering at boundaries and interfaces, absorption, and refraction by variation of fluid properties and thus speed of sound can be considered for increased accuracy of the propagation. The acoustic impedance Z, which describes the resistance R of a medium against acoustic flow is given by the relation

$$Z(\omega) = \mathcal{F}[R](\omega) = \frac{\mathcal{F}[p\prime](\omega)}{\mathcal{F}[Q](\omega)}, \quad (11)$$

where p' is the acoustic pressure, Q is the acoustic flow rate, and $\mathcal{F}$ is the Fourier transform operator. The absolute value of the characteristic specific acoustic impedance may be obtained with $Z_0 = \rho c$, leading to values of about $1.5 \cdot 10^6 Kg/m^2 s$ for water.

Different source types change the absorption characteristics of the wave as high frequency signals have high attenuation and thus do not emit far into the fluid, while low frequency signals may travel large distances. [69] The overall attenuation depends not only on frequency, but also on the viscosity of the medium, which however leads to very low attenuation for water compared to air. As the density is then the main property of the medium transmitting the acoustic waves, the local change of density in water would need to be taken into account by considering temperature, salinity, as well as, for extreme locations in deep water, the pressure. Variations of propagation characteristics of water as transport media, i.e. density or temperature variations depending on depth or region are neglected in both the FVM and the acoustic models in this work.

Sound absorption can also occur at the sea floor when the waves penetrate the sediment to varying degree as a result of layering and gradients with lower frequencies being more averse to absorption. For the near-field propagation, the compressibility of water may be neglected, however, for far-field noise depending on frequency with $r \geq 3 \cdot \lambda$ these effects have to be considered. For reference, in water a wavelength of $\lambda = 1m$ equals a frequency of about $f = 1.5kHz$. While a smooth water-air interface acts as a perfect reflector with a phase shift of 180° between the incident and the outgoing wave, due to the high acoustic characteristic impedance ratio of about $Z_{water} / Z_{air} \approx 3600$, a rough interface due to the sea environment state, entrained bubbles, or fish, lead to scattering.

2.4.2 Acoustic Analogies

Starting from the compressible Navier-Stokes equations for an inviscid Euler fluid the non-linear acoustic wave differential equation formulated by Lighthill is obtained as

$$c^2 \square \rho = \frac{\partial^2 T_{ij}}{\partial x_i \partial x_j}, \quad (12)$$

where $\square = \frac{1}{c^2}\left(\frac{\partial}{\partial t} + u_i \cdot \nabla\right)^2 - \frac{\partial^2}{\partial x_i^2}$ is the differential wave operator, which reduces to $\square = \frac{1}{c^2}\frac{\partial^2}{\partial t^2} - \frac{\partial^2}{\partial x_i^2}$ as the quabla or d'Alembert operator for an acoustic wave in an inviscid, homogeneous, quiescent medium and T_{ij} is the Lighthill stress tensor. In this case, the Lighthill stress tensor assumes the role of the boundary between wave and continuum physics. For this inhomogeneous wave equation, by using the Lighthill stress tensor, there are three different acoustic sources considered in three different right hand side terms

$$c^2 \square \rho = \underbrace{\frac{\partial}{\partial t} \oint_S \left[\rho u_j\right]_{ret} \frac{dS_j(y)}{4\pi r}}_{\text{Monopole}} + \underbrace{- \oint_S \left[\rho u_i u_j + p'_{ij}\right]_{ret} \frac{dS_j(y)}{4\pi r}}_{\text{Dipole}} + \underbrace{\frac{\partial^2}{\partial x_i \partial x_j} \int_V \left[T_{ij}\right]_{ret} \frac{d^3 y}{4\pi r}}_{\text{Quadrupole}}, \quad (13)$$

where y is the source location, x the observer location, and r the distance in space. The terms on the right-hand side are associated with these sources

- Monopole: This omnidirectional source is caused by volumetric expansion or contraction and generates symmetric spherical waves with respect to the source. The amplitude depends only on the distance variable r. A physical interpretation of the sound power of the monopole source is the proportionality to the mean time rate of change of the mass flow rate. In practice, monopoles are associated with translational or oscillational movement of solid body surfaces, such as propeller blades, or phase interfaces, such as stable sheet or trailing vortex cavitation.
- Dipole: This source consists of two monopoles with equal strength but reversed phase that are separated by a distance $r \ll \lambda$. It emits waves directionally along their axis with two maxima that are 180° out of phase and cancel perpendicular to the axis. The amplitude of the dipole depends on the distance r and the location or angle with respect to the origin Θ. The sound

power of the dipole is proportional to the time rate of change of a directional force on the fluid. Dipoles represent, for practical applications, the influence of fluctuations such as the propeller load and growth and collapse of cavity regions or single bubbles.

- Quadrupole: The Lighthill stress tensor itself is formally a quadrupole source. A lateral quadrupole source consists of two dipole sources with equal strength and opposite phase separated by a small distance between their parallel respective axes. A longitudinal quadrupole consists of two dipoles that are adjacent located with their axes collinear, but opposite alignment of the poles. The lateral quadrupole source emits waves with a clover-leaf pattern in the directions of the four monopoles that it consists of, leading to two maxima and minima in the emission directivity. For the longitudinal quadrupole a clover leaf structure is assumed in the near-field and a dipole like field in the far-field. The amplitude of the quadrupole depends on the distance r and the location or two angles with respect to the origin Θ, Ψ. The sound power of the lateral quadrupoles $T_{ij} \mid i \neq j$ can be described with the time rate of change of the shear forces on a fluid volume, while the longitudinal quadrupoles T_{ii}, T_{jj}, and T_{kk} are equivalent to the time rate of change of the stretching and compressive forces on the volume. Quadrupole sources may in practice originate in flow turbulence and volume cavitation phenomena.

A contour illustration snapshot of the amplitude strength and directivity of the different sources are shown in Fig. 12, with the lateral quadrupole shown in (c).

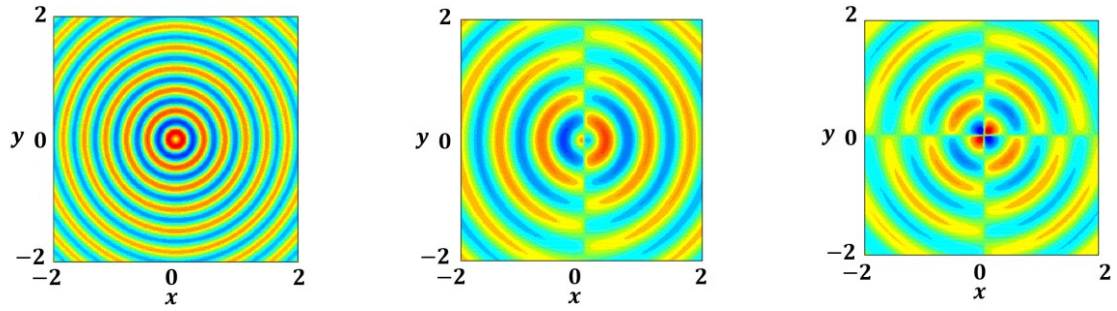

(a) Monopole (b) Dipole (c) Quadrupole

Fig. 12: Wave representation of the propagation characteristics of sound depending on source type [72]

The interface for hybrid solutions between the flow solution and the acoustic analogies are typically applied to boundaries that exist in both domains, where Eq. (13) is integrated along the closed, smooth surface for the monopole and dipole contributions and the flow volume around the boundary for the quadrupole contributions. As most aero- or hydrodynamic flow simulation methods march forward in time, the most used acoustic analogies are time-domain differential formulations of the FWH equation for the acoustic pressure p' applied to a free space f

$$\square^2 p'(x,t) = \frac{\partial}{\partial \mathrm{t}}\{[\rho_0 v_n + \rho(u_n - v_n)]\delta(f)\} - \frac{\partial}{\partial x_i}\{[\Delta P_{ij} n_j + \rho u_i (u_n - v_n)]\delta(f)\} + \frac{\partial^2}{\partial x_i \partial x_j}[T_{ij} H(f)], \quad (14)$$

with P_{ij} as the fluid compressive stress tensor, u_n the local fluid velocity component orthogonal to the boundary with normal vector n_i and v_n is the local normal velocity of the boundary. The right side again consists of the three source contributions, with the Dirac functions indicating singular application of the term at the boundary surface and the Heaviside function $H(f)$ indicating that quadrupole volume sources are outside of the boundary surface.

Applying this to a marine propulsor, the propeller noise due to thickness and loading of the blades is considered as mostly deterministic monopole or dipole noise, while the volume acoustic sources in the propulsor slipstream are generally deemed as non-linear stochastically dominated quadrupoles. As described in 2.3, the volume noise sources are a considerable part of the broadband spectrum of URN for the propeller-hull combination. Thus, it is essential to consider them in some form, which is

expensive with this classic acoustic analogy approach. Acoustic analogies are initially designed as a line-of-sight methods, however, they can be modified to include reflections at modelled boundaries.

2.5 Summary

The main subject of investigation, when considering acoustic emissions of propulsion systems is the hydrodynamic noise. In this chapter it is addressed that turbulence is a fundamental property of fluid flow and creates the phenomena of boundary layers and trailing vortices in connection with propeller blades, which both create sound by themselves. Furthermore, it is established that cavitation is the most significant noise contributor as rapid collapse of cavities and bubbles causes pressure waves. Combined, the interaction of turbulence and cavitation drives the noise emission of a marine propulsion system with suction side sheet cavitation and tip and hub vortex cavitation as the most relevant occurrences. In addition, the interaction with obstacles in the slipstream contributes by deforming or bursting trailing vortices. On a macroscopic scale the acoustic emissions can be modelled with wave physics, meaning they are subject to typical properties of waves such as reflection, absorption, scattering, and refraction. Acoustic sources are separated by their emission characteristic into monopoles, dipoles or quadrupoles. In practice acoustic sources, described by the Lighthill stress tensor, and their emission to an observer by wave transmission can be calculated by utilizing acoustic analogies. With this short insight into the turbulence and cavitation phenomena and how they pertain to acoustic emissions, the question of which methods are implemented to capture these physics and obtain valid acoustic results is answered in the next chapter.

3 Numerical Modelling

The physics described in the previous chapter have to be simulated with feasible numerical resource requirements and be used in problem statements that recur frequently in the marine propulsion industry. For that purpose, a fully functioning publicly available FVM software is selected and adjusted to fit the investigated problem, regarding solver settings, as well as turbulence and cavitation setup. This investigation focuses on the numerical simulation of the underwater radiated noise of propulsor-hull combinations by resolving medium and large scale turbulent fluctuations with LES. By utilizing an implicit subgrid-scale modelling, the simulation times may reach similar orders of magnitude as typical eddy viscosity based turbulence approaches. In addition, the permeable surface FWH acoustic analogy is implemented as a hybrid solution in order to obtain far-field noise information with minimal additional resource demand in the context of a typical problem statement.

3.1 Turbulence Modelling

3.1.1 RANS

Once fluid particles move with relation to a reference frame and there are streamwise velocity gradients in the flow, different layers of fluid particles with a velocity difference start to create shear. In laminar flow the layers are sliding along each other, until a critical difference is reached, where irregular particle exchange between layers is triggered. This is initiating the transition from laminar to turbulent flow, which depends on velocity distribution, body geometry, and viscosity of the fluid. In an engineering context the state of turbulence may be identified by the Reynolds number for a specific geometry. Turbulence itself is difficult to define, however, there are three typical flow characteristics that are always attributed to turbulence [73], which are:

1. The flow is required to be chaotic in the sense that deterministic equations are not able to predict the flow field on a microscopic level,
2. The structures are three-dimensional, as much of turbulence generation is attributed to the formation of microscopic vortices that are stretched and compressed in the bulk flow leading to directional dependence of microscopic structures or macroscopically to the feature of anisotropy of turbulence,
3. And finally turbulent behavior requires by definition multiple coexisting scales of vortical structures in space and time, as a key feature of turbulence is the scalewise mostly downwards cascading nature of energy transfer from large eddies that transmit their velocity to smaller whirls down to viscous dissipation. [74]

Other properties that arise from these primary characteristics are that the temporal evolution of turbulent flows are always unsteady and irreversible, and any particle inside experiences high mixing behavior, in the sense that the single particles path may not be predicted, whereas bulk packages of fluids trajectories are possible to predict. For these reasons, the description of turbulent flows is closely connected to stochastic descriptions of fluid flows [75], which is based on the Reynolds decomposition of the velocity of the flows

$$u(\vec{x},t) = \overline{u}(\vec{x}) + u'(\vec{x},t), \qquad (15)$$

where u is the instantaneous local fluid velocity and barred quantities are the averages of the velocity following spatial ergodicity and prime means the local fluctuation with respect to the temporal dimension.

The adhesion at solid surfaces with the shear stress $\tau = \mu(\partial\vec{u}/\partial\vec{x})$ creates the velocity gradients for boundary layers, which, depending on the characteristic length of interaction of the stream path along the surface, transitions from laminar to turbulent, while increasing the wall distance to the undisturbed flow. In laminar flow, interaction between particles is weak due to low shear stress τ, so adjacent layers can slide along another with different velocities and there is only molecular mixing between different layers with normal direction perpendicular to the wall. Fundamentally different is the turbulent flow regime, where fluid is mixing macroscopically in all directions as a result of turbulent eddies creating an increased boundary layer thickness, containing higher energy and increased shear stress. This

phenomenon is called turbulent diffusion and can be described formally identical to molecular diffusion on a macroscopic scale. For a vessel hull, or a propeller in full scale, transition effects are irrelevant, as the scale imposes fully turbulent regimes, however, in model scale significant sections of the propeller blades or hydrofoils could operate in laminar regime, which creates its own difficulties regarding scaling of the measured quantities.

For the Reynolds averaged flow solution the Reynolds decomposed time-averaged Navier-Stokes equations with incompressible and isothermal assumption in a Newtonian fluid are in Cartesian coordinates $i = [x;\ y;\ z]$

$$\begin{gathered} \frac{\partial \rho_m}{\partial t} + \frac{\partial}{\partial x_j}\left(\rho_m u_j\right) = 0, \\ \frac{\partial}{\partial t}\left(\rho_m u_i\right) + \frac{\partial}{\partial x_j}\left(\rho_m u_i u_j\right) - \frac{\partial}{\partial x_j}\left[(\mu + \mu_t)\left(\frac{\partial u_i}{\partial x_j} + \frac{\partial u_j}{\partial x_i}\right)\right] + \frac{\partial p}{\partial x_i} + F_S = 0, \end{gathered} \tag{16}$$

where the Reynolds stress tensor $\rho\overline{u_i' u_j'}$ is approximated by an eddy viscosity model with μ_t. F_S includes external forces such as the surface tension in two-phase flows and is only active near the interface depending on α. This approximation constrains the flow to isotropic turbulence, which means the off-diagonal components of the full Reynolds stress tensor are identical to zero, while in reality they are proportional to the square of the mean shear, which is a contribution that has to be considered missing in the overall sum of the acoustic source for RANS. As there is two-phase flow in a homogeneous mixture m, with varying volume fractions, the density information $\rho_m = \alpha(\rho_1 - \rho_2) + \rho_2$ from the two species water and vapor is maintained. The calculation of μ_t is carried out using the k-ω-SST model for a fully turbulent flow assumption or the γ-$Re_{\Theta,\mathrm{t}}$ model for flow regimes that experience laminar, turbulent, and transitional flows, such as model scale propellers.

For the first, the closure of the Reynolds stresses is obtained based on the Boussinesq hypothesis

$$\rho\overline{u_i' u_j'} = \mu_t\left(\frac{\partial u_i}{\partial x_j} + \frac{\partial u_j}{\partial x_i}\right) - \frac{2}{3}\rho k \delta_{ij}, \tag{17}$$

as a two-equation model with two additional transport equations, based on semi-empirical constants. According to the Boussinesq hypothesis, linear dependency between Reynolds shear stress and strain rate and coincident orientations between them creating an isotropic turbulence model can be assumed. The transport equations for the turbulent kinetic energy

$$k = \frac{1}{2}(\overline{u_x'^{\,2}} + \overline{u_y'^{\,2}} + \overline{u_z'^{\,2}}), \tag{18}$$

and the specific dissipation rate

$$\omega = \frac{\epsilon}{k}, \tag{19}$$

feature a production and dissipation source term. The main approach of the SST-turbulence model is based on the combination of the advantages in accuracy of the $k - \epsilon$ model in the free stream and $k - \omega$ model in near wall regions by switching between them with two blending functions depending on wall distance: F_1 for the specific dissipation rate and the empirical constants, and F_2 for the viscosity limiter. Due to wall functions implemented in the models, the wall mesh resolution may be either for low Reynolds ($y^+ < 1$) or high Reynolds ($y^+ > 30$) treatment.

The second case, the γ-$Re_{\Theta,\mathrm{t}}$ model, is a four transport equation correlation based model with two transport equations with modified production and dissipation terms for the variables k and ω from Eq. (18) and Eq. (19). The two additional transport variables are the intermittency γ, which gives a percentage of time that turbulent fluctuations are locally present in the boundary layer with its own production and dissipation terms, and the local momentum thickness boundary layer Reynolds number $Re_{\Theta,\mathrm{t}}$. As a transport variable $Re_{\Theta,\mathrm{t}}$ is solved everywhere in the flow field, however, it keeps its freestream value initialized at the inlet from an empirical turbulent intensity and diffuses towards the walls with a blending function. This model supports only $y^+ < 1$. As in most cases LES is conducted

subsequently to the RANS simulation on the same mesh the respective low Reynolds wall distance is aimed for, making the meshes suitable for the γ-$Re_{\Theta,t}$ model. A supporting simulation is conducted with the k-k_l-ω RANS model, which is not the focus of this work.

3.1.2 Large Eddy Simulation

As turbulence in rotational flows is a key aspect in studying the noise from propellers, the assumption of fully isotropic Reynolds stresses may hinder the accuracy of the results. While Reynolds stress turbulence models offer anisotropic turbulence by modelling the full Reynolds stress tensor, they are found to feature insufficient stability for dynamic propeller open water simulations. DES on the other hand offers the qualities of resolving the turbulence far from boundaries and instead model the turbulence near the wall with RANS, to strike a good balance between flow detail and computational effort. While technically feasible, the research project ProNoVi establishes that there are some differences in the results between DES and LES, not only near the walls, but also in the propeller slipstream, most notably the interaction of consecutive trailing vortices is missing. Furthermore, the acoustic results are differing slightly between the approaches, which is expected. For the simulations in this work LES is utilized with different subgridscale modelling approaches.

The LES turbulence modelling functions fundamentally different from RANS, in that it attempts to resolve turbulent length scales of the flow in space and time limited by the respective discretization of the simulation. As it is computationally too expensive to resolve the complete turbulent energy spectrum down to the dissipative Kolmogorov length scale or even the Taylor scales and, in addition, these frequencies contribute little to the overall energy, only the medium and large length scales are respected. For this reason, the quantities are filtered in time, by the simulation timestep, and space, be the mesh discretization with a filter kernel $G = G(\vec{x}, \overline{\Delta})$. Practically, only energy scales with twice the length of the filter may be resolved by the simulation, due to the Nyquist theorem. For the case that the physical space filter length $\overline{\Delta}$ is identical to the cell size Δ of the mesh, the resolved quantities that are larger than a single cell with 2Δ are resolved, as illustrated in Fig. 13 (a). In this case the filter yields a sharp cutoff frequency in the turbulent energy spectrum in (b) at $k_c = \pi/\overline{\Delta}$, however, other filters in space and time exist to create a smoother transition between resolved and filtered scales. As indicated in the diagram, the aim is to resolve around 80% of the turbulent kinetic energy of the spectrum. The remaining 20% may either be modelled by a subgrid scale model or in the case of implicit LES are caused by the mesh filtering. Due to the nature of the direct simulation of turbulent fluctuations the y^+ value loses its original meaning, but may still be seen as good indication of the mesh refinement necessary to resolve the wall turbulent boundary layer.

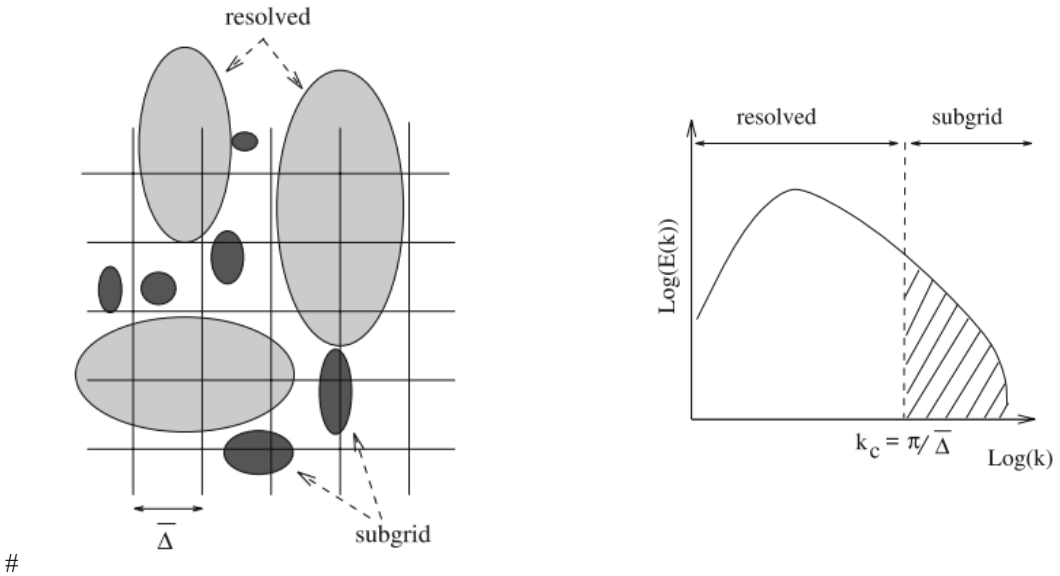

#

(a) Filtering by the mesh (b) Filter location in turbulent energy spectrum

Fig. 13: Illustration of filtering process of LES [76]

The general transport equations of the LES approach are

$$\frac{\partial \rho_m}{\partial t} + \frac{\partial (\rho_m \overline{u}_i)}{\partial x_i} = 0, \quad (20)$$

for mass transport of a mixture m with the low pass filtered velocity $\overline{u} = u - u'$, with the residual component u'. For the momentum transport with the low pass filtered pressure $\overline{p}$ and viscous stress tensor $\overline{S}_{ij}$ and the subgrid stress tensor B_{ij} the transport equation is

$$\frac{\partial (\rho_m \overline{u}_i)}{\partial t} + \frac{\partial (\rho_m \overline{u}_i \overline{u}_j)}{\partial x_i} = -\frac{\partial \overline{p}}{\partial x_i} + \frac{\partial}{\partial x_j}\left(\overline{S}_{ij} - B_{ij}\right) + \rho_m g_i. \quad (21)$$

The viscous stress tensor is obtained from the strain rate tensor $S_{ij} = 2\mu D_{ij}$ with the strain rate

$$D = \frac{1}{2} \cdot \left(\frac{\partial u_i}{\partial x_j} + \frac{\partial u_j}{\partial x_i}\right). \quad (22)$$

The unresolved transport term B_{ij} is obtained from

$$B_{ij} = -\rho(\overline{u_i u_j} - \overline{u_i}\,\overline{u_j} + \tilde{B}), \quad (23)$$

where $\tilde{B}$ indicates the remaining unknown quantity of the subgridscale influence onto the resolved turbulent structures. Different models exist such as Smagorinsky, Lilly and WALE, however, in this work primarily implicit subgridscale modelling and to a small extent the Smagrinsky model is utilized. In the case of implicit LES the subgridscale influence of the unresolved scales is assumed to equal the numerical dissipation caused by the spatial discretization of the mesh and the error of the respective convective scheme fluxes similar to Fig. 13. Implicit LES is activated by changing the turbulence model settings to laminar and reducing the timestep accordingly.

For the temporal resolution of the LES not only the temporal filter regarding turbulent structures, but also the restriction of $CFL \approx 1$ has to be considered. Due to the fine mesh resolution required to resolve 80% of the turbulent energy, the timestep is reduced accordingly. In the approach in this work, the meshes for RANS and LES are identical, however, RANS turbulence modeling in combination with the utilized two-phase flow solver family is able to deal with CFL numbers of order $O(10^2)$ within the stability limits.

While the timestep is about $1 \cdot 10^{-1}$ times smaller than for RANS in order to fulfill the CFL requirement (and for stability), no additional transport equation is solved for the ILES modelling. This boosts the computational speed significantly per solver iteration compared to the RANS with at least two additional scalar transport equations. Depending on the selected timesteps and their associated stability in this framework a computational speed higher than for RANS modelling can be achieved, as shown for the PPTC'11 open water simulation in Table 1. Besides the corresponding CFL number range the effect on the trailing vortex flow, visualized by Q-criterion is shown. In the mesh the maximum CFL number given is only reached in a single cell with the mean number over all cells much closer to the lower limit. The rotating mesh region ends downstream near the end of the image region at $2.5 \cdot D$, which coincides with a reduction of mesh resolution leading to the dissipation of all vortices. Lower timesteps do not benefit the capturing of trailing vortices for the RANS and ILES achieves the best performance at intermediate timesteps of $t = 0.1°$ as most details are visible in the vortex structure. This is particularly apparent for the level of detail in the hub vortex as a result of the indentation caused by the interaction with the corresponding tip vortices. For a large timestep of $t = 1.0°$ the hub vortex dissolves before reaching the downstream sliding mesh interface, where the tip vortex dissolves. For a small timestep of $t = 0.01°$ the level of detail in the hub vortex indentation fades away, possibly as a result of the reduced numerical error responsible for the subgrid scale influence in the case of implicit modelling. In the case of RANS neither trailing vortex type reaches the end of the rotating mesh region. It is assumed that with ILES and the applied mesh resolution the tip vortex could be maintained for a distance much larger than $2.5 \cdot D$ and is only limited by the available resources. As established before, the slipstream is in practice not resolved further downstream as the influence on the acoustic emissions is considered low.

Table 1: Simulation type and timestep with required computational effort for PPTC'11 [59]

Type	Step [°]	Q-isovalue of $Q = 5 \cdot 10^4 s^{-2}$ with axial velocity	CFL [-]	Effort (2rot/ 100 CPUs) [d]
RANS	10		1.38-550.49	0.1
RANS	1	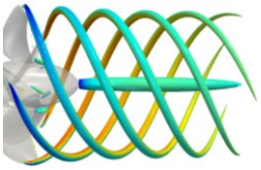	0.13-72.38	0.32
RANS	0.1	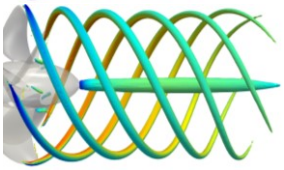	0.01-7.33	3.4
ILES	1	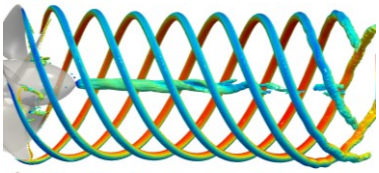	0.13 - 66.20	0.4
ILES	0.1	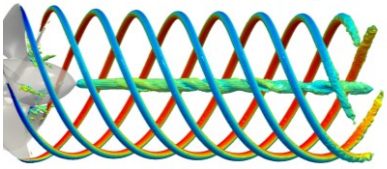	0.01 - 6.95	3.0
ILES	0.01	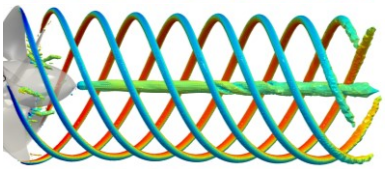	0.001 - 0.66	28.0

The Smagorinsky model [77] offers another option to include the influences of the subgridscale turbulence on the larger scale flow and is also utilized in this work. With an additional transport equation, the model assumes that the subgridscale kinetic energy is in local equilibrium and the production and dissipation of kinetic energy is equal.

3.1.3 Solver

A cell-centered collocated FVM for hexahedral based spatial discretization with unrestricted parallelization capabilities is applied. It uses the integral mass conservation and Navier-Stokes momentum conservation equations to solve for two incompressible, isothermal immiscible fluids as an Eulerian homogeneous mixture with a VOF interface capturing method. As a result, only one additional scalar transport variable, the water volume phase fraction α, is required, which makes this approach desirable for industry applications due to computational speed. To ignore the energy equation in this fluid problem is also reasonable as the thermal energy is highly decoupled from mechanical energy, except in the final stages of cavitation bubble collapse. However, neither single bubbles are resolved nor the timescale for these processes and the complete cavitation dynamics are modelled. By employing the OpenFOAM Schnerr-Sauer cavitation model, a source term in the mass conservation equation is fueled based on the pressure difference between the local static pressure and the water vapor saturation pressure. Turbulence is completely modelled with RANS in combination with a turbulence model or resolved for large and medium length scales of the turbulent energy spectrum with LES.

The main solver used is the OpenFOAM *interPhaseChangeDyMFoam*, a transient solver with the ability to realize the dynamic propeller rotation with either MRF as a stationary mesh with a function object for realizing the rotational movement or a dynamic rotating mesh with AMI. In the MRF approach centrifugal and Coriolis forces are added as source terms to the equations in the active region, while the mesh region inside the AMI rotates with time and transport variables are interpolated with their fluxes between rotating and stationary part at the sliding interface with the functionality *dynamicMotionSolverFVMesh*. Besides the single phase coupled solvers *tdiCoupled* and *helyxCoupled* are used for some supporting investigations.

The simulations are typically run until convergence and all acoustic investigations are completed in the following order, with the stages and the timesteps aimed for in the case of propulsor-hull simulations given by feasibility and stability criteria:

1. RANS with stationary mesh ($\Delta t > 10°$), in other words, the time step corresponds to the time needed by the propeller to turn more than 10°.
2. RANS with dynamic mesh motion ($\Delta t = 1°$)
3. RANS with dynamic mesh motion with activated cavitation ($\Delta t = 1°$)
4. LES with dynamic mesh motion with activated cavitation ($\Delta t = 0.1°$)
5. LES with dynamic mesh motion with activated cavitation and AMR ($\Delta t = 0.1°$)

Each stage uses the final solution of the volume field obtained in the previous stage as their respective initialization. Between stage 2 and 3 is the most unstable situation with the vapor phase building up the cavitation regions. When the hull is involved, the solution of stage 1 is critical, as the wake field is required to converge fully before, the transient propeller rotation begins. As a rough estimate the duration of the bulk flow passing the hull at least once is applied to find the duration of this stage. In simulations without hull, stage 1 may be skipped. All stages and their applicability are illustrated in Fig. 14.

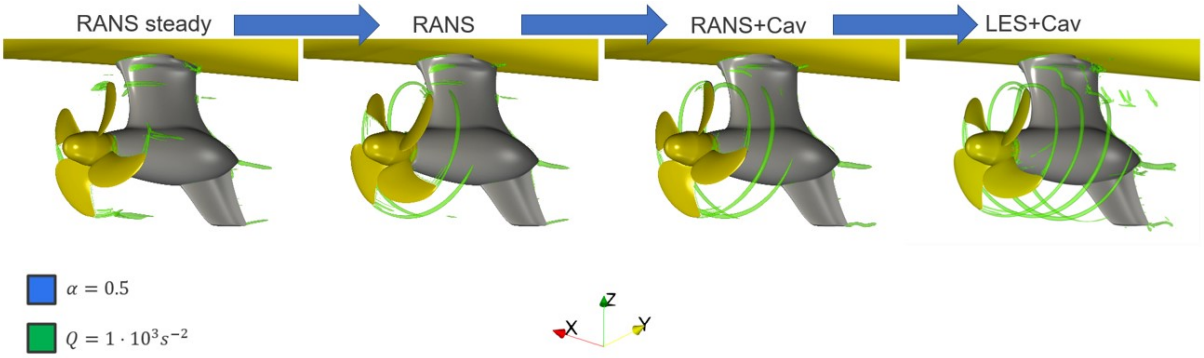

Fig. 14: Simulation stages

All simulated problems are solved using a combination of a velocity inlet and a pressure outlet boundary condition, while the outer walls of the simulation domains are either no-slip walls in the case of simulating a cavitation tunnel or extend either inlet or outlet for quasi-infinite simulation setups, such as for full-scale problems. The velocity inlets use a fixed normal velocity value as a Dirichlet boundary condition, which equals the velocity difference between the object under investigation and the free-stream, and a fixed flux pressure for the pressure Neumann boundary condition. This setup of the pressure boundary condition achieves comparatively high stability and ensures physical pressure reflections in a cavitation tunnel are considered. In full-scale a symmetry boundary condition is used for the wave pattern, which is evaluated in a precursor resistance simulation with free surface without propulsor at the achieved velocity. This approach is followed to reduce the computational effort. As a result, in full-scale the wave pattern velocity is fixed and there might be a force imbalance between vessel and propulsor. In model scale simulations of the open water condition the inlet velocity used in the experiments is applied, however, for propulsion simulations the measured thrust k_T of the propeller is considered to achieve the correct operation point. With this approach the correct operation point for the propeller is ensured, as the inlet velocity is not measured accurately in the experiments and the restriction of the cavitation tunnel cross section accelerates the flow significantly around the hull as demonstrated with Fig. 15. This requires iterative calculations

with varying inlet velocity with interpolation along the calculated k_T value for convergence acceleration in model scale. For full-scale simulations the k_Q value is used to determine the simulation point, instead of the measured vessel velocity as there might be inaccuracies with the speed in water values.

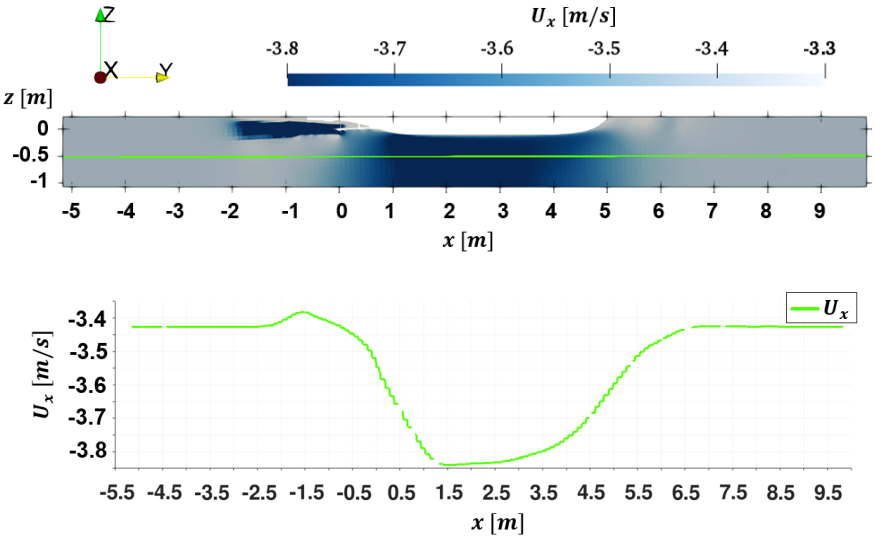

Fig. 15: Axial velocity distribution for propulsion in cavitation tunnel

The hull and the appendages, as well as the rotating propeller, are modelled as walls, which is specified with a fixed velocity value of $\vec{U} = (0,0,0)$ in the rotating region, the rotational velocity of the respective faces is added to this velocity. A fixed flux pressure boundary condition for the pressure is employed at the cavitation tank walls, which sets the pressure gradient to the value required by the flux of the velocity at that location

$$\nabla p = -\nabla\rho(\vec{g} \cdot \vec{x}). \qquad (24)$$

This is similar to a zero gradient boundary condition adjusted for the static pressure with gravity and thus ensures pressure reflection occurs at the walls for all boundaries including the cavitation tunnel. If reflections are not desired, such as in a quasi-infinite domain, the mesh is designed to numerically dissipate pressure information towards the walls, by applying coarse cells in the outer regions.

The solution algorithm for the discretized equations is a three cycle PIMPLE loop with three inner pressure equation corrector loops, which is found as minimal number of iterations to achieve convergence for acoustic pressure test observers in the domain far-field representatively placed next to the pressure outlet, although the number of correctors is increased, if the simulation becomes unstable such as at the start of the cavitation stage. First and second order time discretizations are employed, however, it is found that in most simulations with two-phases only the less accurate first order approximation produces consistently stable simulation runs. Transport equation relaxation factors are utilized at the start of the cavitation stages to strengthen to diagonally dominant structure of the respective solution matrices. While the vapor saturation pressure is slowly increased to the physical value. In addition, the number of α-equation sub-cycles and correctors is slowly reduced to a number of 3 each, and an extremely low timestep of typically $\Delta t = 0.01°$ for example in propeller based simulations, is slowly increased to the intended simulation timestep given above. Typically, the convective fluxes are mostly using a cell limited second order least square scheme, however, $\vec{u}$ and α, employ a second order Gaussian integration. Diffusive fluxes are either modelled with up to second order bounded or unbounded schemes, with $\nabla \cdot (\rho\vec{U}\alpha)$ being simulated with a Gaussian upwind scheme.

In Table 2 representative simulation times are given for the different stages for 100 cores with around $3GHz$ in days, with the manual cavitation ramp-up of stage 3 neglected until convergence is achieved and for the acoustic evaluation in brackets. Of course the actual times vary greatly depending on the initial mesh sizes, which are targeted between $20 - 35 \cdot 10^6$ cells depending on propeller and hull

geometry. The RANS simulation is comparatively long, as the fluid is required to pass the complete vessel hull at least once, in order to produce a converged wake field. Once the AMR refinement is active the simulation time increases significantly as the target mesh sizes are then $\leq 65 \cdot 10^6$ cells. Of course the simulation times can be greatly accelerated by utilizing more cores. For instance, stage 5 acoustic simulations are conducted only with ≥ 200 cores for relatively low number mesh sizes and stable simulations, as it is otherwise unfeasible.

Table 2: Representative 100 core CPU times for the simulation stages

Stage	Openwater [d]	Propulsion [d]
1	-	1
2	2(1)	4(1)
3	3(5)	4(6)
4	3(14)	3(15)
5	14(70)	14(70)

3.2 Cavitation Modelling

3.2.1 Volume of Fluid Method

The VOF method uses the scalar volume phase fraction information α in its own transport equation to track the interface between the two-phases

$$\frac{\partial \alpha}{\partial t} + \nabla \cdot (\alpha \vec{u}) + \nabla \cdot [u_c \alpha (1-\alpha)] = S_\alpha, \qquad (25)$$

with the additional source term S_α for phase transfer, which is described in detail section 3.2.2. The VOF method does not define an interface sharply, but rather it is transported across the domain and gradually changes over the volume cells. The equations natural numerical diffusivity has to be reduced with an anti-diffusive flux achieved by the interface compression term, which is the third term besides the temporal change and convective flux term. It relies on the compression velocity $u_c = C_\alpha \, |\vec{u}| \nabla\alpha/|\nabla\alpha|$, which ensures a counter gradient with the velocity in interface normal direction according to the curvature $\nabla\alpha/|\nabla\alpha|$ and a velocity in the order of the local velocity $\vec{u}$ and the empirical constant $C_\alpha = 1$. The explicit parameter α is used here to indicate the liquid phase, while the vapor phase fraction may be calculated by $(1-\alpha)$.

Selecting appropriate α-transport divergence schemes such as an interface compression scheme are aiding in countering the diffusivity. Alternatively, strictly bounded schemes such as the van Leer scheme may be used to ensure the stability of the solver, when phase change is activated. In some simulations standard first order bounded upwind or central differencing schemes are applied. A symmetric Gauss Seidel algorithm is used for α with appropriate number of correctors and subcycles.

To obtain the wave pattern for the simulation of the wave system induced by a vessel in full scale, the same base solver is utilized, but phase transition or dynamic mesh functionality features are deactivated. The difference is that these simulations are quasi-steady with CFL-number controlled large timesteps and thus do not feature the stages mentioned above in section 3.1.3. However, mesh generation for these cases is not trivial as the diffusivity of the α-transport variable has to be considered by special treatment of the interphase region with fine cell sizes. For that reason, an initial block mesh with a refined water surface is generated beforehand and Kelvin wake refinements around the vessel hull are specified.

3.2.2 Cavitation Model

In the two-phase solver with phase transition a submodel, the OpenFOAM Schnerr-Sauer cavitation model, is applied to consider the phase change between the two species water and vapor. The implemented model differs from the originally published Schnerr-Sauer model [78], in that the number of nuclei is a constant so the number of activated nuclei is not reducing the available nuclei content. This is in agreement with the investigated flows as it can be assumed that sufficient number of nuclei are practically always present. The number of nuclei per discrete volume element consisting of vapor and liquid $V_v + V_l$ is constant at the initially calculated value of $\alpha = V_v/(V_v + V_l)$ with

$$\alpha_{Nuc} = \frac{V_{Nuc}}{1+V_{Nuc}}, \quad (26)$$

by applying the initial nuclei volume from the spherical bubble assumption

$$V_{Nuc} = \frac{\pi n_0 {d_{Nuc}}^3}{6}. \quad (27)$$

The empirical parameters for the nuclei density n_0 and the initial nuclei diameter d_{Nuc} have to be obtained from direct measurements, which are rarely available, or parameter studies, where the cavitation observation is compared between simulation and experiment. As the number of nuclei is constant the value of the volume phase fraction of the vapor phase may be obtained with

$$\alpha_{\mathrm{v}} = min\big((1-\alpha)+\alpha_{Nuc}, 1\big), \quad (28)$$

which is used in the further equations. The nucleation site radius is then obtained from the nuclei volume phase fraction α_{Nuc} and the local water volume phase fraction α in Eq. (26)

$$r_{Rb} = \sqrt[3]{\frac{3(1+\alpha_{Nuc}-\alpha)}{4\pi n_0 \alpha}}. \quad (29)$$

The phase change from liquid into vapor is given by the mass transfer rate, which is not explicitly calculated by the solver,

$$\dot{m}^+ = C_V(1+\alpha_{Nuc}-\alpha)\cdot p_{Coeff}\cdot \min\,(p-p_{Sat}, 0), \quad (30)$$

and vice versa with

$$\dot{m}^- = C_c\alpha\cdot p_{Coeff}\cdot \max\,(p-p_{Sat}, 0), \quad (31)$$

where C_c and C_v are the condensation and vaporization coefficient, which are set to unity, as in the original Schnerr-Sauer model, except at the initial simulation time of stage 3 simulations, where it is gradually increased to ensure stability during the emergence of the vapor phase. The mass transfer rate is not available by default in the public solver family, however, to increase analysis insight, it is implemented in the solver loop. Here the quantity p_{Coeff} is an auxiliary variable

$$p_{Coeff} = 3\rho_l\rho_v\sqrt{\frac{2}{3\rho_l}}r_{Rb}\alpha\cdot\frac{1}{\sqrt{|p-p_{Sat}|+0.01\cdot p_{Sat}}}, \quad (32)$$

with the constant liquid and vapor densities ρ_l and ρ_v and the constant saturation vapor pressure p_{Sat} of fluid at the respective temperature. To avoid singularities, a dimensionless non-physical margin of $0.01\cdot p_{Sat}$ is introduced. The mixture density for further use in the Navier-Stokes equations results as

$$\rho_m = \alpha\rho_l + \alpha_V\rho_V. \quad (33)$$

The final source term S_α in Eq. (25) consists of an evaporation term and a condensation term and is based on the equivalent volume transfer rate corresponding to Eq. (30) and (31) with

$$S_\alpha = \alpha\cdot\dot{V}^+ + (1-\alpha)\cdot\dot{V}^-, \quad (34)$$

which can be separated into an implicit term, $S_p\alpha = \left[\dot{V}^+ - \dot{V}^-\right]\alpha$, and an explicit term, $S_U = \dot{V}^-$ for the solver.

Determining the mass transfer rate $\dot{m}^\pm$ according to Eq. (30) and (31) from the simulations is implemented in the source code in order to extract the information about regions of condensation and vaporization. This implementation is validated with a simple cavitating bullet case in Fig. 16 (a) and (b), where the quantity initial state of the simulation and a converged timestep is shown respectively, which is then applied to a simple propeller case in (c) for the volume flow rate $\dot{V}$. In both cases the $\alpha = 0.5$ isosurface and thus the approximate extent of the cavity is visualized in green and in case of the bullet the quantity $\dot{m}$ is shown on the centerline intersection in the streamwise plane. Regions of mass transfer appear only near the isosurface proving the plausibility of the implementation. Vaporization regions with $\dot{m} < 0$ appear just downstream of the leading spherical section of the bullet and in the low-pressure recirculation region behind the bullet, which appears physical. For the propeller case in (c) the

vaporization clearly occurs at the upstream chord coordinate, and the condensation region downstream beyond the trailing edge, substantiating the implementation.

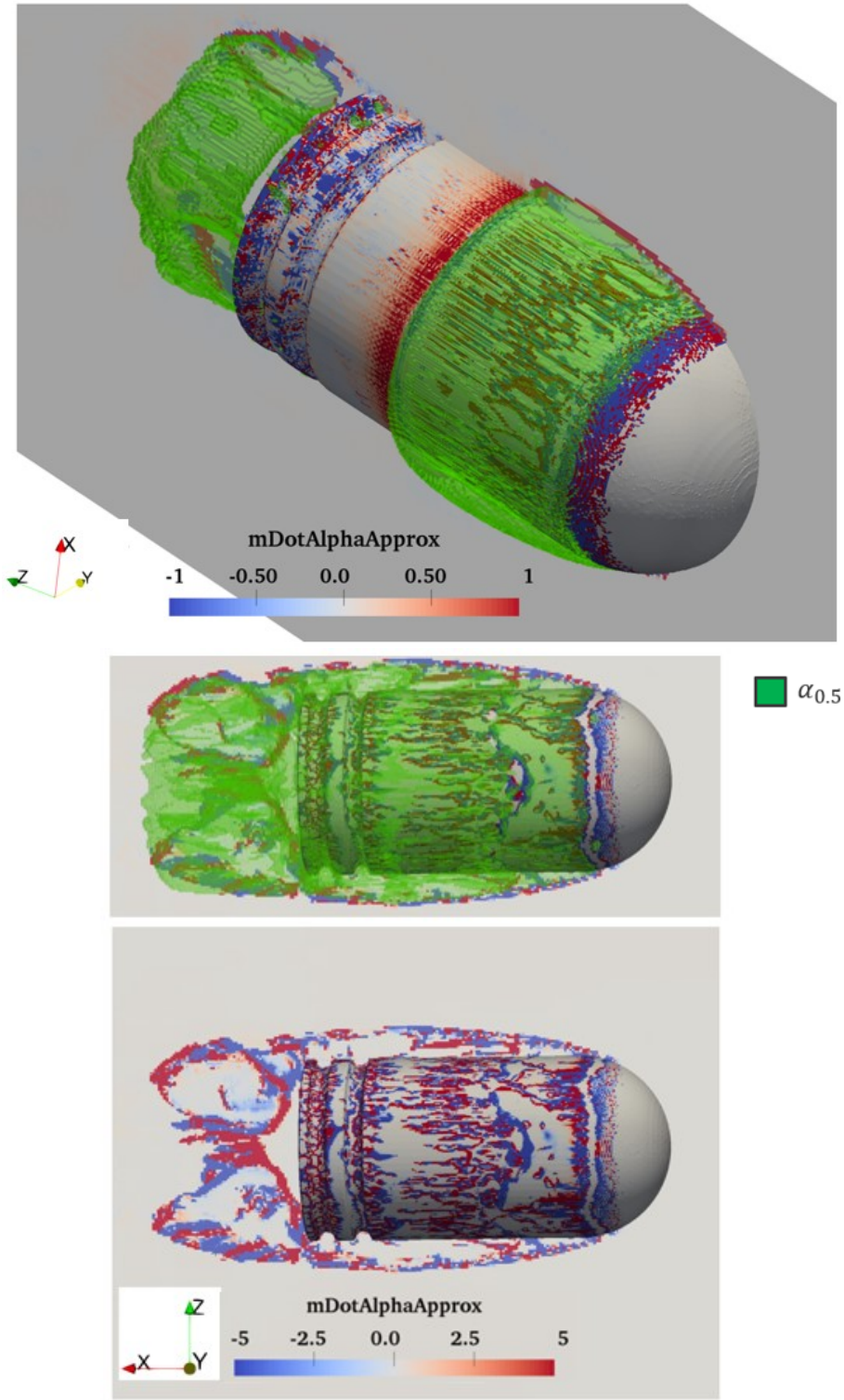

(a) Cavitating bullet Initial

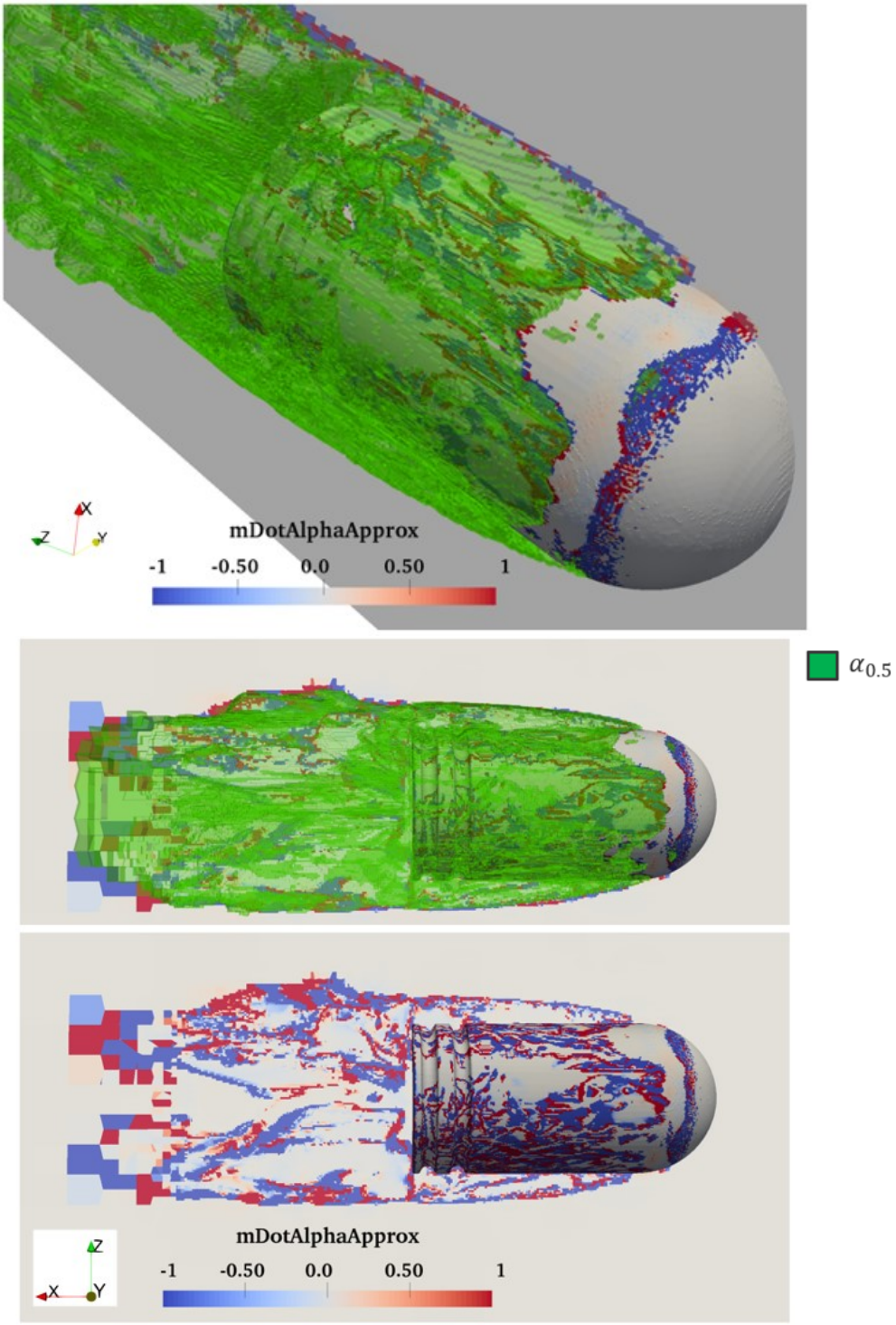

(b) Cavitating bullet at later timestep

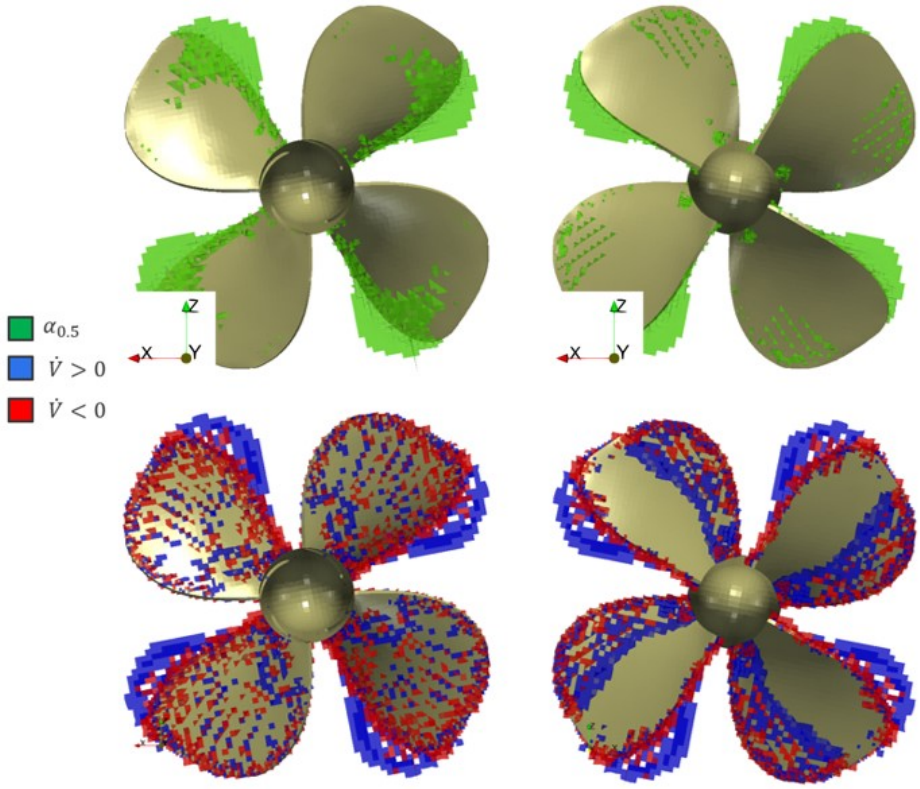

(c) Applied to propeller

Fig. 16: Mass transfer rate implementation

To investigate further, the streamwise normal plane integral mass transfer rate evolution is examined in Fig. 17 with a corresponding illustration of the planes. The bullet is located between $-0.005 < z < 0.015$ and rotationally symmetric along its axis, which means that the mass transfer should be rotationally symmetric and thus a suitable representation of the overall axial cavitation distribution. However, in the intersection planes it seems that there is high angular asymmetry in the in-plane distribution of mass transfer. Nevertheless, it appears that in the integral values there is vaporization at the leading end of the body and condensation downstream, which is in accordance with the physical phenomenon, giving further confirmation of the correct implementation.

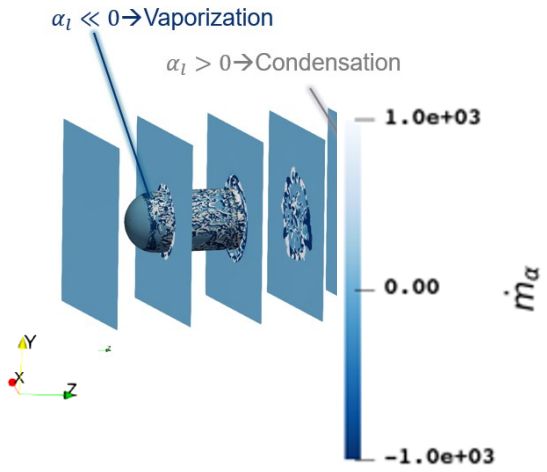

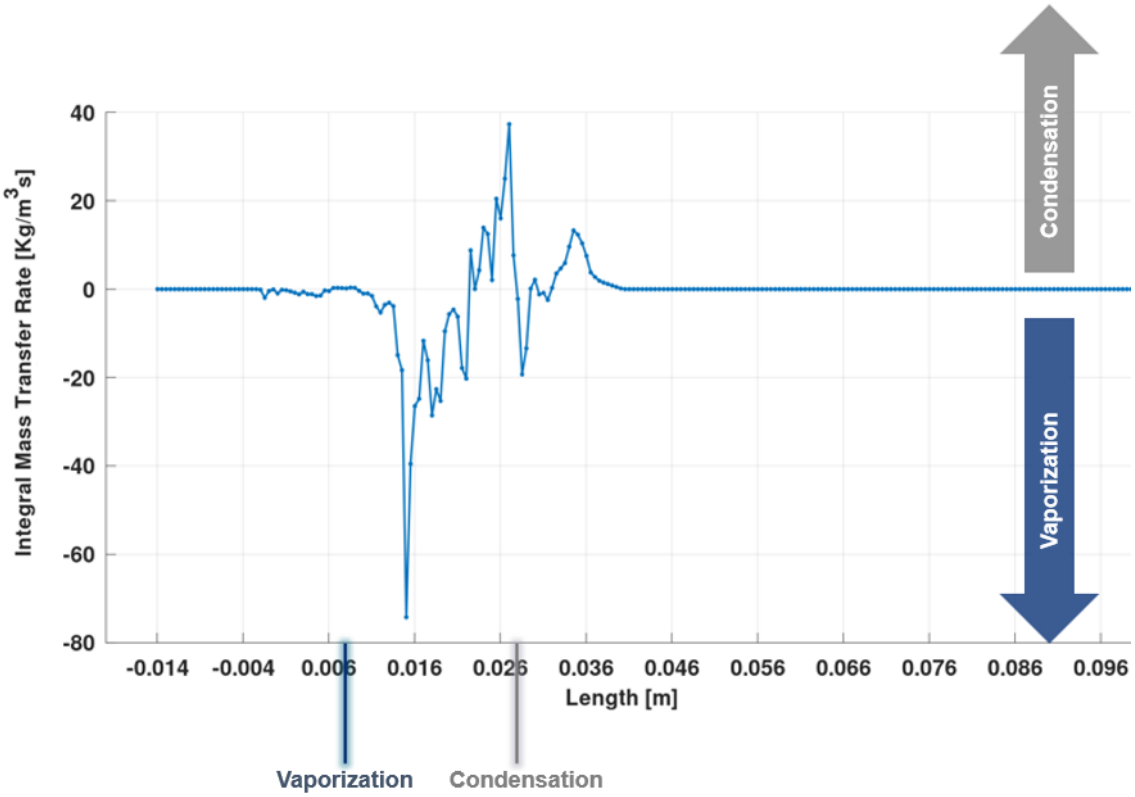

Fig. 17: Cavitating bullet axial mass transfer

3.3 Acoustic Modelling

3.3.1 Acoustic Sources

As described in 2.4.1 sound information is transmitted via transversal waves in solids and longitudinal waves of rarefaction and compression in fluids, while the transmitting particles or molecules themselves are moving about their initial position. Thus, sound is fundamentally a compressible problem, meaning compressibility must also be considered for the limit $Ma \rightarrow 0$. The speed of sound increases with the density of the medium and therefore water has a much higher speed of sound and less attenuation than air. In air, all reflections are reverberant, meaning the density of the material the reflection occurs on is higher than air, which implies the phase of the wave is consistent over the reflection. In water the reflection at the free surface on the other hand is a soft reflection, creating a phase shift of 180°. However, the reflections are only considered in the hydrodynamic analysis, not in the acoustic analogy and as a result the phase shift at the water-air interface is not considered in this work. It is also important to realize that underwater noise cannot be compared to airborne noise as the quantities are measured differently by experimental equipment and biological perception. Human hearing evolved to perceive airborne noise, so many of the evaluation procedures of sound used to describe noise do not necessarily create good basis for treatment of underwater noise. Nevertheless, they are used as a result of the reliance on analysis methods adopted from airborne noise, which are not always practical in this context.

The hydrodynamic pressure is composed of the static pressure at the respective depth and the dynamic pressure induced by the mean velocity flow field. It is not related to acoustic pressure, as acoustic sources are phenomena that are inherently connected to timescales, and may be defined as the instantaneous deviation of the total pressure from the mean local pressure

$$p'(\vec{x},t) = p(\vec{x},t) - \overline{p}(\vec{x}). \qquad (35)$$

A location with high p' and thus high amplitude of its sinusoidal decomposed signals is considered a loud noise source, while the evolution of the deviation over time or the synthesized sine signals determines the spectral content of the source. The source of the pressure time evolution may be a change in dynamic pressure on small timescales, e.g. a lifting surface moving relative to the fluid medium, or a

change in the local volume occupied by the fluid caused by oscillating other material pockets inside, e.g. an oscillating solid boundary or a gaseous cavity. As described in 2.4 the periodic volume variation of displaced fluid by the propeller blade rotation or the cavity on the blades has the acoustic characteristics of a monopole source and is called thickness p'_T in acoustic analogies. A dynamic pressure field induced by the thrust generation of the blade and the influence of the cavity on the limiting streamlines has the source characteristic of a dipole and is called lift p'_L in acoustic analogies. Quadrupole sources p'_Q are non-linear terms in acoustic analogies and are attributed to cavitation-turbulence interaction sources in the fluid volume, such as (cavitating) trailing vortices, shed cavities or structure influence on the flow. As the vorticity and cavitation phenomena in the volume are highly dynamic they are considered a relevant noise source. The types of sources that the signal is composed of are combined as

$$p'(\vec{x}, t^*) = p'_T(\vec{x}, t^*) + p'_L(\vec{x}, t^*) + p'_Q(\vec{x}, t^*). \quad (36)$$

In Fig. 18 a local single point observer signal near the acoustic sources of a propeller-hull combination is translated from time to frequency domain to propeller blade harmonic frequency information for four different simulation approaches with increasing level of detail of the physical modelling from *RANS* to *RANS+Cav* to *ILES+Cav* to *ILES+CavQRef*. The acoustic pressure is evaluated in (a) by subtracting low frequency long term trends and shifting the pressure variations to a mean zero value. For RANS turbulence modelling, a periodic low frequency sine curve is achieved where the wavelength corresponds to the propeller blade harmonics, while the active cavitation in *RANS+Cav* skews the time domain wave oscillations in the direction of higher times and increases the amplitude slightly. Once turbulence is resolved in ILES it causes high frequency fluctuations visible atop the maxima of the elemental sine wave, due to high frequency fluctuations and trailing vortices. With the highest level of physical modelling in *ILES+CavQRef*, the trailing vortices are spatially resolved by the mesh refinement strategies explained in 3.4.2 so that the trailing vortex cavities are part of the simulation, which increases the low frequency amplitudes, and smoothens the low frequency fluctuations. The increasing amplitudes with improved modelling at the propeller blade frequency are compared in the Fourier-transformed discrete spectral data in (b) with the first four propeller blade harmonic frequencies marked with dashed vertical lines. In (c) the post-processed pressure pulses are given for this source at these harmonics.

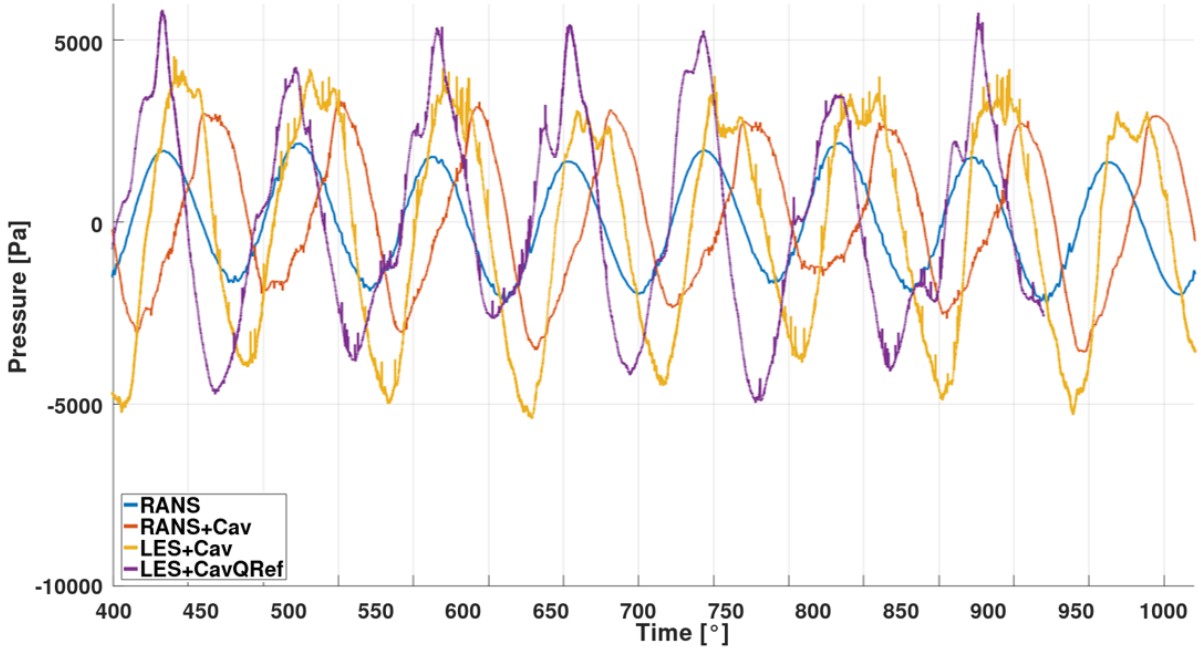

(a) Time domain

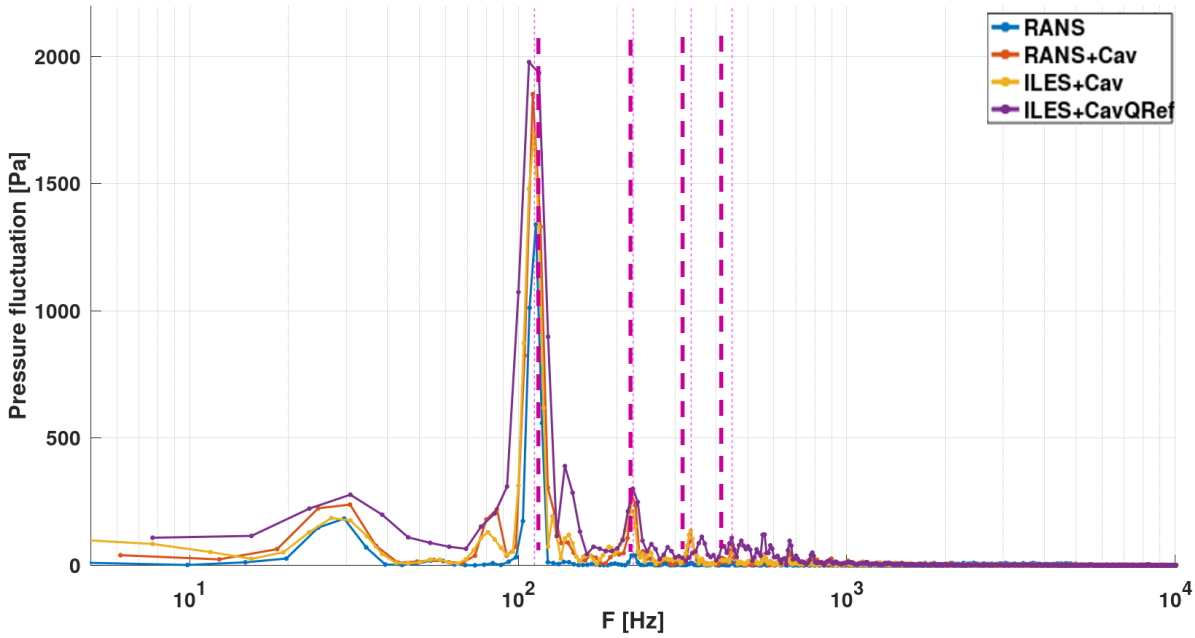

(b) Discrete spectrum

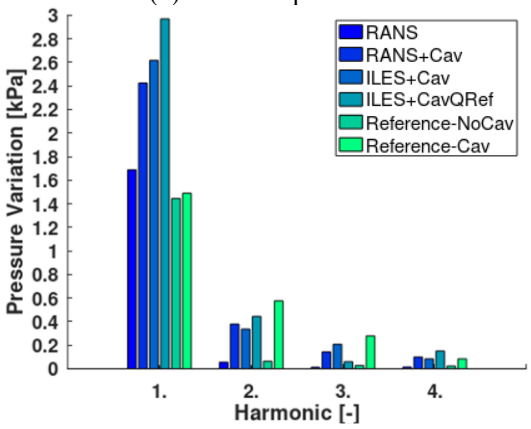

(c) Propeller harmonics

Fig. 18: Acoustic signal example with individual acoustic processing steps

For far-field analysis with a distance of $r \geq 3 \cdot \lambda$, modelling a pure incompressible treatment is not adequate as the traveling time between the origin, at which the noise is generated (t^*) and the time at the observer location (t) has to be considered.

The distance affects the travel time of the acoustic wave between source location $\vec{x}$ and observer location $\vec{y}$ depending on the speed of sound

$$t_{ret} = t^* - \frac{||\vec{x}(t^*) - \vec{y}(t)||}{c}. \quad (37)$$

The retardation allows for phase effects to appear as a result of the multipole nature of complex sound source regions. Besides the compressibility, the other wave characteristics mentioned in 2.4.1 are not considered in the approach, however, this is a matter of insufficient data, for example regarding the sea floor material properties.

3.3.2 Permeable Ffowcs-Williams-Hawkings Method

With the classical Ffowcs-Williams-Hawkings method only solid surfaces or boundaries of the fluid domain are considered. As described, much of the sound generation occurs not directly at boundaries, but in the volume downstream of a solid body, such as turbulence and cavitation. In the Farassat 1A formulation based on Eq. (14), these contributions are considered as volume integrals, which is numerically expensive to solve. If it is assumed that near the acoustic source the instantaneous pressure field on an arbitrary closed passive control surface contains the surface as well as the volume

contributions of the acoustic field within, this surface may be used as a new acoustic emitter replacing all sources inside, without knowledge of the exact phenomena and their origin. This approach is called the permeable surface FWH method and respects also the sound sources in the volume outside of the surface to infinity. The permeable surface FWH method is also known as Kirchhoff FWH method, as it is based on the first Kirchhoff-FWH equation. Following the publication by Francescantonio [46] the permeable surface FWH yields the acoustic or perturbation pressure at the receiver applied to a control volume in integral form as

$$4\pi p'(x,t) = \frac{\partial}{\partial t}\int \left[\rho_0 u_n + \frac{(\rho-\rho_0)(u_n-v_n)}{r|1-M_r|}\right]_{ret} dS + \frac{1}{c}\frac{\partial}{\partial t}\int \left[\frac{P'_{nr}+\rho u_r(u_n-v_n)}{r|1-M_r|}\right]_{ret} dS + \int \left[\frac{P'_{nr}+\rho u_r(u_n-v_n)}{r^2|1-M_r|}\right]_{ret} dS + \frac{1}{c^2}\frac{\partial^2}{\partial t^2}\int \left[\frac{T_{rr}}{r|1-M_r|}\right]_{ret} dV + \frac{1}{c}\frac{\partial}{\partial t}\int \left[\frac{3T_{rr}-T_{ii}}{r^2|1-M_r|}\right]_{ret} dV + \int \left[\frac{3T_{rr}-T_{ii}}{r^3|1-M_r|}\right]_{ret} dV, \quad (38)$$

which extends the Farassat 1A formulation for permeable surfaces. The t^* notation is dropped and instead the ret subscript is introduced to indicate that the respective terms are evaluated at a previous timestep depending on the distance travelled by the soundwave, which is more suitable for numerical codes. For the integrals the surface S of the permeable FWH control surface and V, the fluid volume outside of the surface, have to be considered. The velocity consists of the control surface velocity $\vec{v}$ and the flow velocity $\vec{u}$ with the components v_n and u_n normal to the control surface and u_r in receiver direction, ρ_0 is the reference density, and M_r is the Mach number of the permeable surface in the vectorial direction from the surface element to the receiver

$$M_r = \frac{v_r}{c}, \quad (39)$$

with v_r as the source-receiver component of $\vec{v}$. For the Lighthill stress tensor T

$$T_{ij} = P'_{ij} + \rho u_i u_j + c^2(\rho-\rho_0)\delta_{ij}, \quad (40)$$

there are two magnitudes, the directional magnitude

$$T_{rr} = T_{ij} r_i r_j, \quad (41)$$

and the trace of the tensor

$$T_{ii} = tr(T). \quad (42)$$

The first term of Eq. (40) is the perturbation stress tensor

$$P'_{ij} = P_{ij} - \overline{p}\delta_{ij}, \quad (43)$$

which itself consists of the reference pressure taken as the time mean local pressure and the fluid compressive stress tensor

$$P_{ij} = p\delta_{ij} - (\mu+\mu_t)\left(\frac{\partial u_i}{\partial x_j} + \frac{\partial u_j}{\partial x_i}\right), \quad (44)$$

consisting of the instantaneous local pressure, the velocity gradient and the molecular and turbulent viscosities. For the LES simulation approach μ_t is set to zero as the turbulence influence is included as fluctuations in the instantaneous velocity u. Regarding the influence on the acoustic field in Eq. (38), the terms with r in the denominator are far-field terms, and the terms with r^2 near-field terms, while r^3 terms are influencing the sound field only in the immediate distance to the source.

In the analyses with the permeable surface FWH method the two following simplifications are generally established for Eq. (38):

- Except for some test cases, the volume terms or the quadrupole contributions outside of S are neglected, completely removing the last three terms, as the integration of the complete outside volume increases the simulation time significantly,
- The surface S is stationary with respect to the hydrodynamic simulation, which removes all terms containing any component of the surface velocity $\vec{v}$ (v_n, M_r),

leading to the simplified version with components that are similar to the thickness and loading of the original FWH formulation, however, since they are attributed to the complete region inside the control surface are termed pseudo-thickness

$$p'_T(\vec{x},t) = \frac{1}{4\pi}\int_S \left[\frac{\rho_0(\dot{v}_n+\dot{v}_{\dot{n}})}{r(1-M_r)^2}\right]_{ret} dS + \frac{1}{4\pi}\int_S \left[\frac{\rho_0 v_n(r\dot{M}_r+cM_r-cM^2)}{r^2|1-M_r|^3}\right]_{ret} dS, \quad (45)$$

and pseudo-loading

$$p'_L(\vec{x},t) = \frac{1}{4\pi c}\int_S \left[\frac{\dot{l}_r}{r(1-M_r)^2}\right]_{ret} dS + \frac{1}{4\pi}\int_S \left[\frac{l_r-l_M}{r^2(1-M_r)^2}\right]_{ret} dS + \frac{1}{4\pi c}\int_S \left[\frac{l_r(r\dot{M}_r+cM_r-cM^2)}{r^2|1-M_r|^3}\right]_{ret} dS. \quad (46)$$

Here $\vec{l}$ is the pressure force at the permeable surface consisting of static pressure and the dynamic pressure created by the flow through the surface

$$\vec{l} = p\vec{n} + \rho\vec{U}(u_n - v_n), \quad (47)$$

with $v_n = 0$ for the second simplification above.

For FVM hydrodynamic simulations the extent of the boundary surface is not only limited by the near-field requirements, but primarily by the cell size and density, which is usually high in the vicinity of the propeller and gets coarser the further the distance from the object of interest. For many propulsor configurations the geometrical dimensions are given, as there are solid structures near the region of interest, such as rudders, shaft brackets, azimuthing propulsor vertical shafts or similar. In almost all cases of propeller-based propulsion there is a shaft line transmitting thrust and torque between the vessel and the propeller, which connects stationary and rotating boundaries and has to be necessarily intersected by the FWH permeable surface. As the surface has to be closed to solve the integral, the sources from the surface area which is enclosed by the shaft line are subtracted from the received acoustic pressure. In theory it is possible to extend this approach to arbitrary geometries such as rudders or parts of the hull, however, it is not tested in this work.

There are several limitations of the current implementation regarding placement and extent (discussed in Section 3.3.4), removable surface intersections, and propagation. Specifically, only one surface intersection with simple shapes of a cylinder or box can be removed from the source surface at the moment and reflections at boundaries are not respected. Another constraint lies in the setup of the simulation, which determines the interpolation of surface S once before time is started, meaning the surface is required to be located outside of all dynamic mesh regions, i.e. rotating, deforming, or refining.

3.3.3 Acoustic Propagation

The received signals are compared in the frequency domain by applying a Fourier transformation convoluted with a Hanning window H with length of the data set to reduce spectral leakage

$$\widetilde{p'}(f) = a_1 \cdot a_2 \cdot \left|\sum_{t=1}^{n} H(n) * p'(t) e^{\frac{-2\pi i}{n}}\right|, \quad (48)$$

where $a_1 = 2$ is the conversion factor for single sided spectra, taking into account only the first half of the values in f in accordance with the Nyquist criterion, and $a_2 = 1.633$ is the energy correction factor for the Hanning window to preserve the energy content of the amplitudes. The corresponding frequencies f are obtained from the sampling frequency f_s and the number of data points n, and the phase angle θ is obtained from the transformation from the complex number of the form $z_c = |z_c| \cdot e^{i\Theta}$. In the following the tilde sign is dropped, which indicates a frequency domain transformed acoustic pressure in Eq. (48). As peaks are usually not resolved well unless the simulation time is very long and the timestep is very short in order to increase the number of data points in the time series, the engineering solution of estimating the peak value from the adjacent points around the frequency of interest is implemented with the approximation

$$p'_{peak,i} = \sqrt{{p'}^2_{peak,i-1} + {p'}^2_{peak,i} + {p'}^2_{peak,i+1}}. \quad (49)$$

For the acoustic processing and analysis of the results, there are classification guidelines, and standardization documents from ISO and ITTC. In this work the near-field sound in full-scale is given directly, or scaled to full-scale for model scale simulations with

$$p_S = p_m \cdot \frac{\rho_S n_S^2 D_S^2}{\rho_m n_m^2 D_m^2}, \quad (50)$$

while the model scale frequencies are transformed with

$$f_S = f_m \frac{n_S}{n_m} \sqrt{\frac{\sigma_S}{\sigma_m}}, \quad (51)$$

following ITTC procedures [21], where σ_S is the full scale cavitation number and σ_m the model scale cavitation number according Eq. (7).

For the evaluation of underwater noise as signatures, there are different types of conventions, which all have in common that they are given as levels in dB, as the range of the order of magnitude of event amplitudes of acoustic phenomena is large. Octave or one third octave spectra sum frequency contributions into large bands, a procedure derived from musical acoustics and human hearing which makes only moderate sense in the setting of underwater noise. However, they are popular, as many corrections for acoustic measurements are created for airborne-noise and then applied to underwater noise, due to a lack of suitable regulations. Narrowband spectra on the other hand give equidistant discrete data points, which requires a bandwidth information in order to relate them to each other.

To compare URN signatures the sound pressure level

$$SPL = 10 \log \left(\frac{p'}{p_{ref}} \right)^2, \quad (52)$$

is used by relating the acoustic pressure to the reference pressure for URN measurements of $p_{ref} = 1 \cdot 10^{-6}\ Pa$. To take into account the distance to the observer and relate the results to standardized distance of $r_{ref} = 1m$, a frequency independent distance correction to source level (SL) or radiated noise level (RNL) is applied

$$SL = SPL + 10 \log_{10} \left(\frac{r}{r_{ref}} \right)^2. \quad (53)$$

If a frequency dependent correction is applied, the results are called monopole source level (MSL), however, this approach is not used within this work. To correct the one third octave bands with $1Hz$ sampling frequency the levels are adjusted depending on the center band frequency f_0 of the individual bands with

$$SL_{1Hz} = \mathrm{SL}_{1/3\ octave} - 10 \cdot \log_{10}(0.23 f_0). \quad (54)$$

For the evaluation of the cavitation tunnel results, the interference with standing waves in the tunnel domain by pressure waves, which occur for surface waves in resistance calculations is analyzed with the frequency of a standing wave with the water speed of sound as the phase velocity c

$$f = c \cdot \frac{n}{2 \cdot L} \text{ with } n = 1,2,3, \dots . \quad (55)$$

With the characteristic length L set to the dimensions of the cavitation tunnel, frequencies between $f \approx 500 - 800Hz$ are estimated, which is checked when evaluating the simulation results. However, no interference is detected for the setups.

3.3.4 Validation

The analytical solution of the acoustic pressure of a stationary acoustic monopole source in a quiescent fluid is given at distance r by [79]

$$p' = \frac{\rho}{4\pi \cdot r} \frac{\partial Q(t)}{\partial t}\Big|_{ret}, \quad (56)$$

with the acoustic pressure generated by a variable volume flow rate $Q(t)$ and the typical monopole behavior with distance $1/r$. For the case of a relative velocity Ma between source and receiver the acoustic pressure is

$$p' = \frac{-c\,Ma\cdot\cos(\theta_0)}{4\pi\cdot r^2\left(1-\left(Ma\,sin(\theta_0)\right)^2\right)^{\frac{3}{2}}}\,\rho Q(t)|_{ret} + \frac{1}{4\pi\cdot r(1-Ma^2)\cdot(1-Ma^2\sin(\theta_0)^2)^{0.5}}\cdot \frac{1-Ma\cos(\theta_0)}{(1-Ma^2\sin(\theta_0)^2)^{0.5}}\cdot\frac{\partial Q}{\partial t}|_{ret}, \tag{57}$$

which collapses to Eq. (56) for $Ma = 0$. The directivity of the noise is given by the angle Θ_0 and similar to the FWH method, the near- and far-field terms may be differentiated by r^2 and r in the denominator, respectively. For different velocities the obtained directivity of the signal is given in Fig. 19, where the Doppler effect is visible when the velocity is near the speed of sound $c = 1462m/s$.

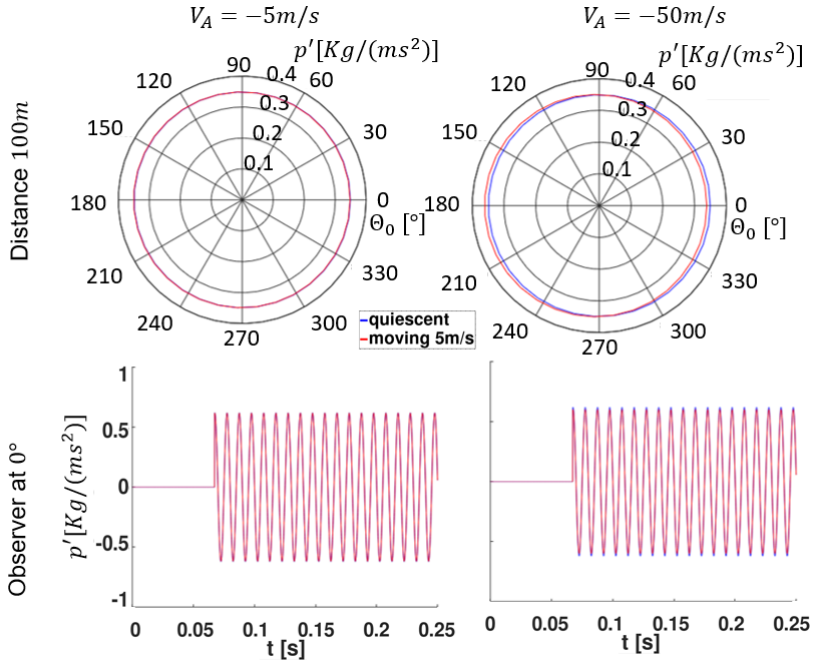

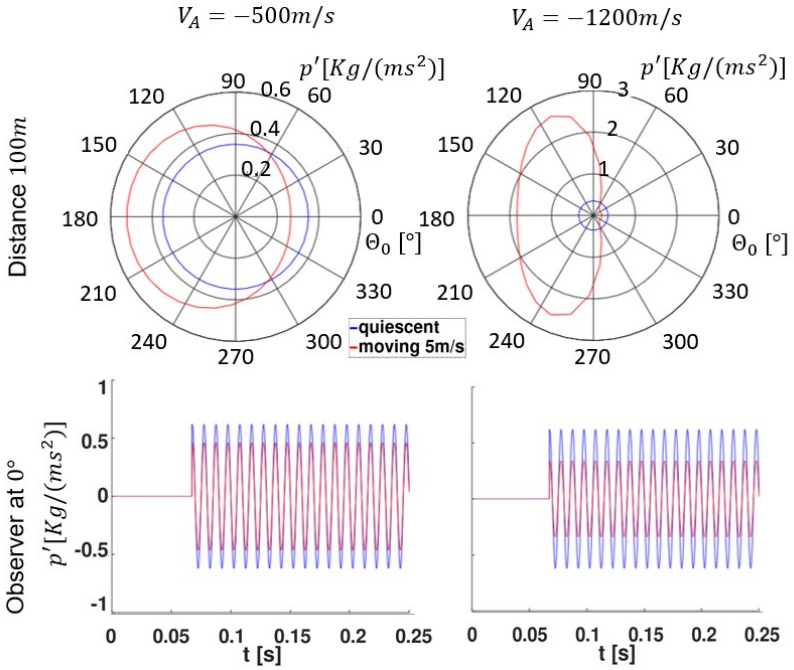

Fig. 19: Analytical solutions for monopole source at different relative velocities for observer distance of $6.7476 \cdot \lambda$

In the FVM a stationary sphere with radius $r_S = 0.01m$ in Fig. 20 (a) with a sinusoidal oscillating flow rate inlet in a quasi-infinite domain is modelled with $f = 100Hz$. Relative acoustic pressure results are compared for different FWH results and the analytical solution in (b) at a far-field distance of $r = 40 \cdot r_S$ in the point symmetric acoustic field. The analytical solution is taken from Eq. (56), the *PressureProbes* result is directly interpolated from cell centers of the FVM solution at the observer and for the KFWH method different control surfaces with radii of $r = 1.5 \cdot r_S$ labelled *KFWH-Small* and $r = 2 \cdot r_S$ as *KFWH-Medium* shown in blue and red in (a) are used as the sources, as well as the sphere surface itself labelled *OnTop*. For the small and medium spheres the quadrupole contributions outside the control surface are in the comparison in (b) with the addition *Quad*. All three KFWH control surfaces produce the same result as the FVM, so the implementation can be considered validated for simple monopole sources. With the quadrupole contributions the FVM results are overpredicted, but independent of the radius of the surface, possibly meaning that some spurious noise is created in the FVM in the outer regions of the quasi-infinite domain. The analytical solution is the baseline result and overpredicts the FVM by around 20%, as a result of non-existent attenuation by the medium.

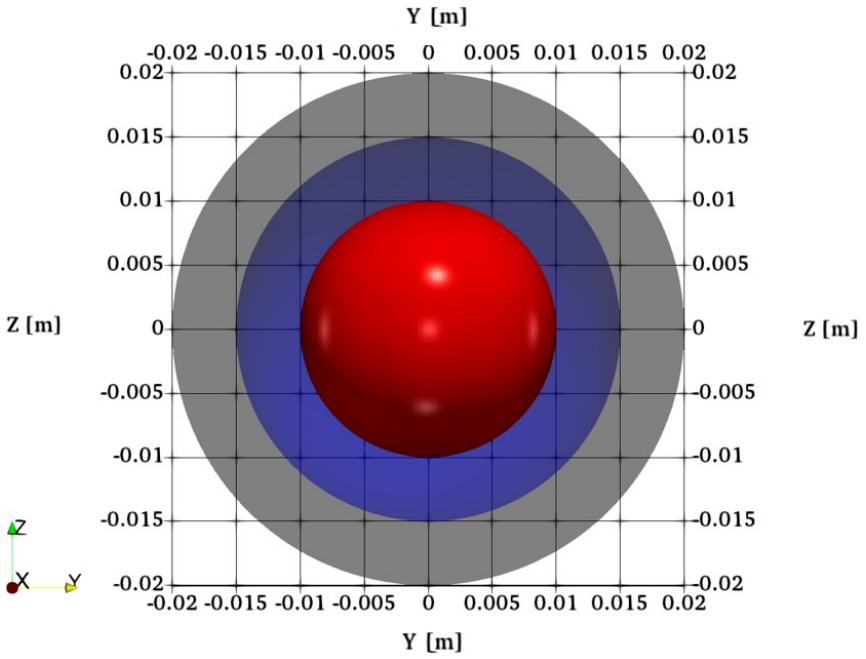

(a) Sphere (red) and FWH surfaces (blue, black)

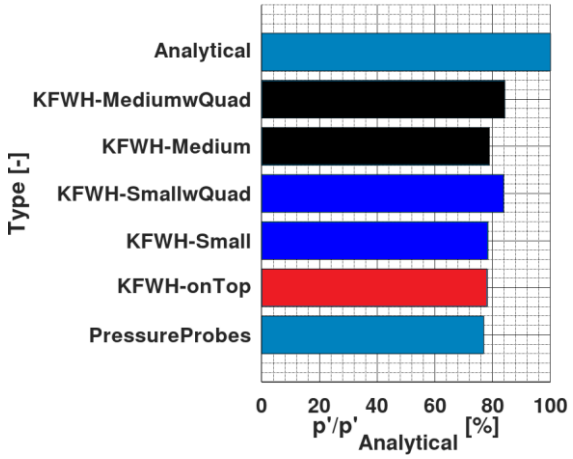

(b) Comparison of acoustic pressure at $f = 100Hz$

Fig. 20: Comparison of acoustic pressure between analytical solution, hydrodynamic simulation and FWH methods [80]

Next, the same spherical sinusoidal volume flow rate inlet is compared for stationary and moving flow situations with a velocity of $5m/s$, which is realized in different ways in order to evaluate the FWH methods susceptibility to flow noise and increase of relative distance between source and observer. In Fig. 21 the first setup is a stationary mesh with a sphere in a quiescent fluid (a), the second is a stationary mesh and sphere in an imposed fluid flow (b), the third is a moving sphere in quiescent fluid, whereby the constant translation speed is realized by mesh deformation with the sphere at the center (c), and the final test is a constant speed mesh translation in a fixed coordinate system with rigid mesh and imposed inflow (d). While the difference between (a) and (b) is caused by the additional turbulent flow around the sphere, the acoustics of (c) and (d) involve a relative motion between sound source and observer. As the sphere is changing the location in space for setup (c) and (d) and the FWH control surface requires to be stationary, a cylinder with its axis in direction of the movement is the source for the FWH method, which is not completely correct for case (c) as the mesh deformation, changes the interpolation of cells on the control surface. However, this effect is considered minor over the short duration of simulation time. The resulting velocity field is shown on the right of each image, where it seems that only (a) and (b) produce the intended result for the flow field of a stationary and a moving sphere in a fluid, and the

resulting discrete spectra are given in Fig. 22 and compared to the analytical solution from Eq. (57) at $0m/s$ and $5m/s$ for far-field observer locations that are to the side of the direction of travel (a) or closing or increasing distance. For the analytical solution the velocity of the sphere is negligible compared to the speed of sound $v \ll Ma$ resulting in identical spectra, however, both solutions with an inlet velocity (b) and (d) create a frequency shift, which must stem from the velocity field instead of the distance between sphere and observer as case (c) does not show a different dominant frequency and case (a) and (c) yield the same amplitude. The difference between the FWH contributions is given in Fig. 23 showing that outside the control surface or non-linear quadrupole contributions generate the most significant part of the spectral amplitude, which explains the higher values of the cases with active inflow velocity, while the pseudo-loading seems to be negligible in this case, as the only acoustic source is a monopole. Overall, this test case can be considered as ineffective for the evaluation of the acoustic effects of the FWH method by the source-observer distance, especially due to the restrictions of the control surface. However, this test demonstrates that a FVM simulation with a moving vessel with respect to the coordinate system is not feasible with the current implementation, thus frequency shifts as a result of moving sources cannot be considered.

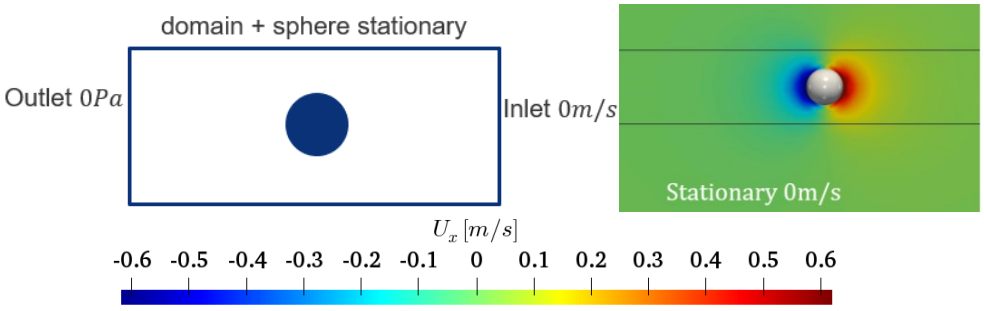

(a) Stationary $0m/s$

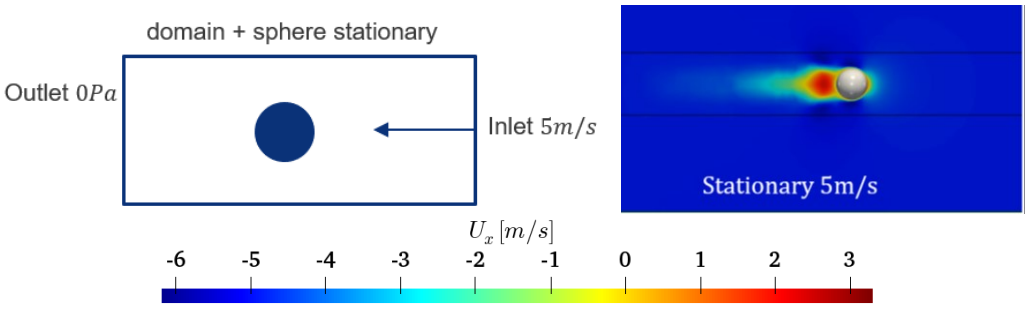

(b) Stationary $5m/s$

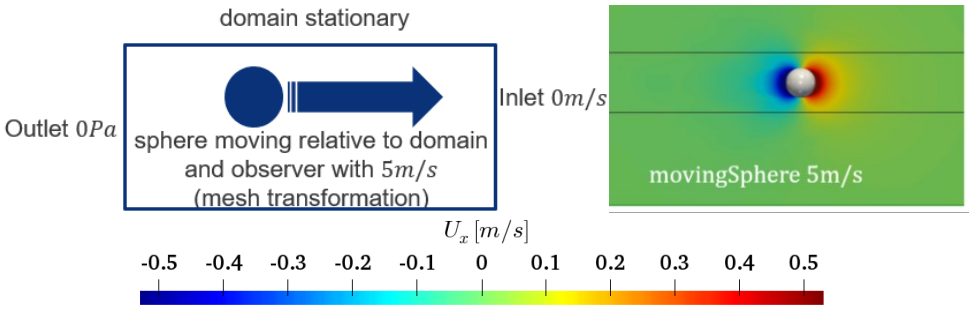

(c) moving Sphere $5m/s$

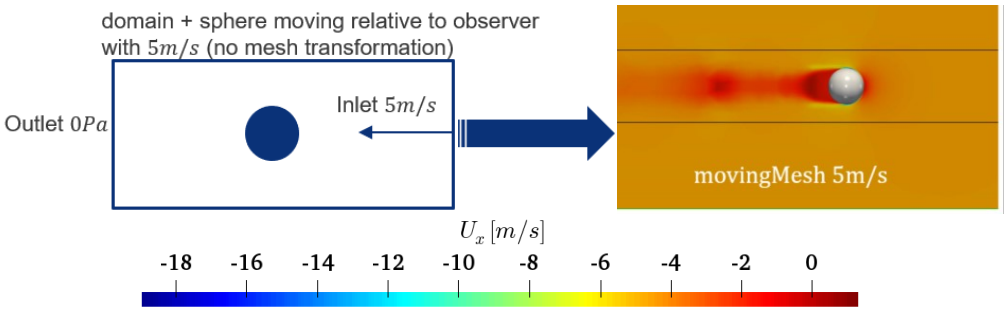

(d) moving Mesh 5m/s

Fig. 21: FVM setups for comparison of stationary and moving sphere

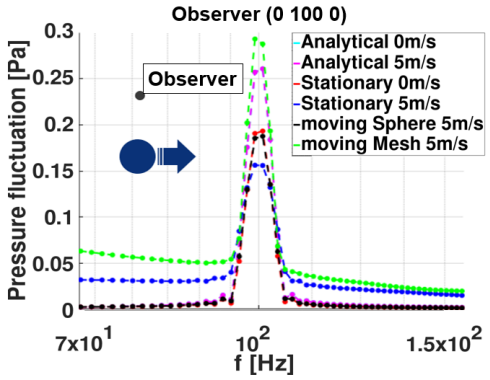

(a) Observer Side

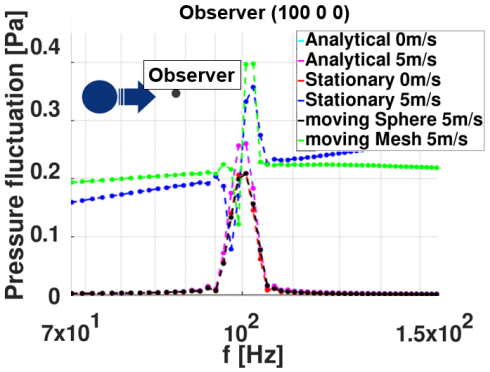

(b) Observer Upstream

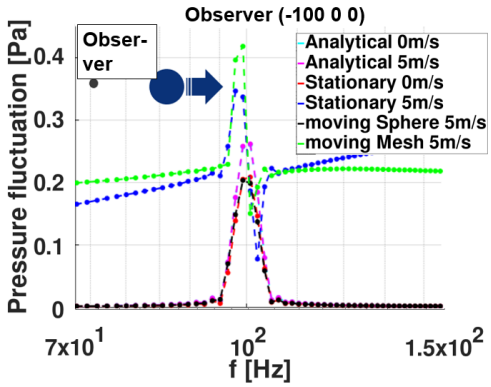

(c) Observer Downstream

Fig. 22: FWH results for different far-field observer locations

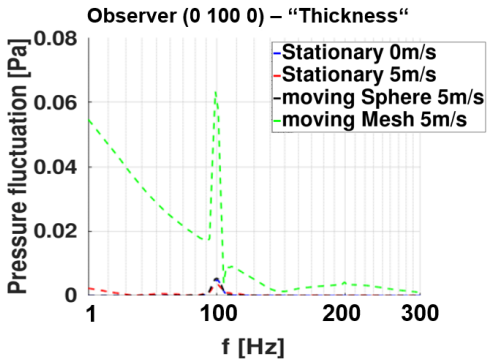

(a) Thickness contribution

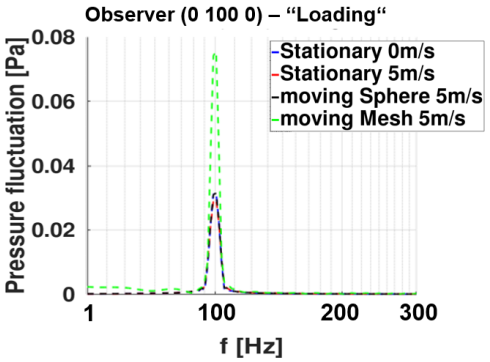

(b) Loading contribution

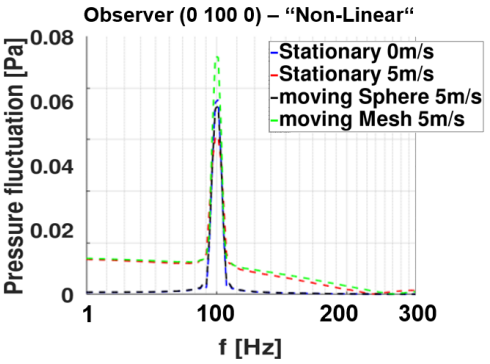

(c) Non-Linear contribution

Fig. 23: Single contributions of FWH acoustic pressure

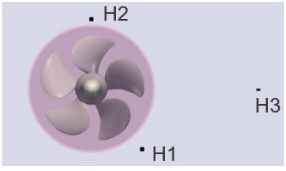

Fig. 24: Front view of PPTC'11 setup with AMI, *Inner* KFWH surface, and observer locations

For an open water propeller simulation with the PPTC'11 test case with a propeller diameter of $D_P = 0.25m$ with the center at $\vec{x} = (0,0,0)$, the radial extent of a cylindrical FWH control surface and its relation to the rotating mesh interface is investigated at three observer locations in Fig. 24 at $\vec{x} = (0.0545, -0.393, 0)$, (0.0495, 0, 0.163), and (0.1255, -0.12, -0.142) as well as observers far from the source. A hydrodynamic solution is solved with RANS k-ω-SST turbulence modelling in quasi-infinite domain without cavitation, with an initial cylindrical sliding mesh interface based on AMI interpolation at $r = 0.15m$ around the axis of rotation shown in red. Cylinders with different radii are placed around the cylindrical AMI containing the propeller and the refined regions of the mesh in the tip and hub vortex to study the influence of the position of the control surface. The infinite domain cylindrical mesh section

is in Fig. 25 (a) with the near-field acoustic observers as black squares and the investigated cylindrical control surfaces are illustrated in (b) with *Outer4* also shown in (a) as a reference. The exact dimensions of the five cylinders with rotational axis coinciding with the mesh x-axis are listed in Table 3, while the AMI reaches $\Delta x = 0.100m$ upstream of the propeller plane, $\Delta x = 0.500m$ downstream and has a radial extent of $r = 0.150m$.

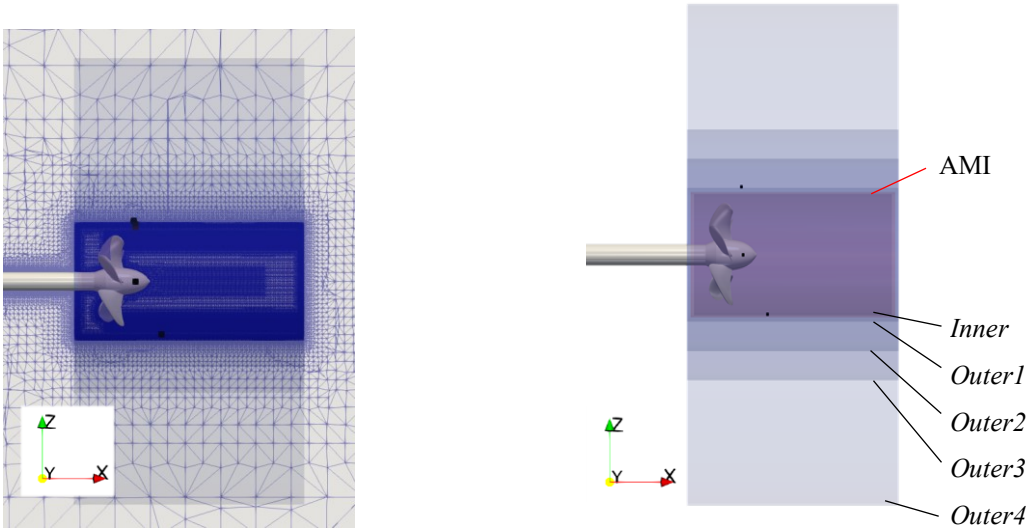

(a) Mesh (b) Control surfaces

Fig. 25: Mesh and locations of AMI and control surfaces

Table 3: Geometries of permeable surface FWH method control surfaces with respect to the propeller plane and axis in initial investigation

Parameters [m]	***Inner***	***Outer1***	***Outer2***	***Outer3***	***Outer4***
r	0.145	0.160	0.230	0.300	0.600
$l_{upstream}$	0.090	0.110	0.110	0.110	0.110
$l_{downstream}$	0.490	0.510	0.510	0.510	0.510

The time domain signals for the near-field observer H2 in Fig. 26 (a) and a far-field observer at $\vec{x} = (0, 100, 0)$ in (b) are split into the single contributions of the FWH terms, obtained from the control surface *Outer1*. Note that within the scope of this study all quadrupole contributions are deactivated. While the near-field observer yields low frequency oscillations with the blade passing frequency, the far-field observer receives highly blurred oscillations as both components are experiencing high frequency fluctuations, with only the thickness term mirroring the blade passing frequency to a degree. The high frequency fluctuations are more severe in the loading term.

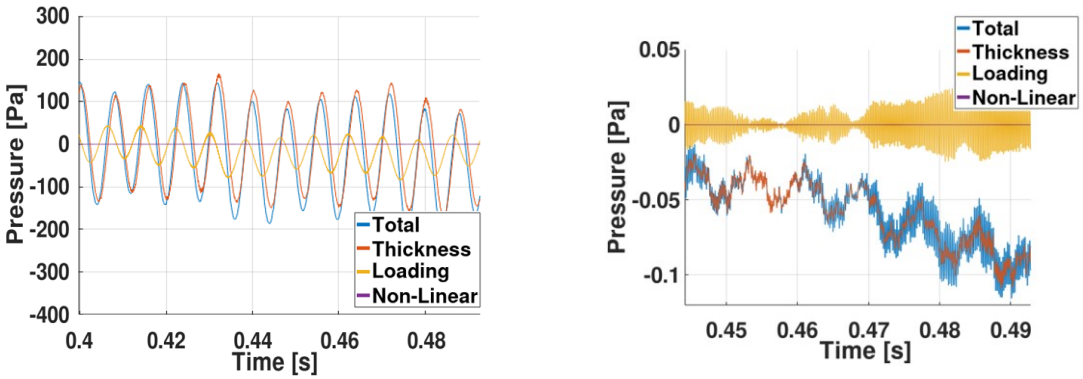

(a) Observer H2 (b) Observer at $\vec{x} = (0\ 100\ 0)$

Fig. 26: Single term contributions of the permeable surface FWH method for two observer locations

The total sound pressure from all thickness and loading terms of different control surfaces outside the AMI, are compared in the near-field at H2 in Fig. 27 (a) with the hydrodynamic calculation dynamic pressure and the standard Farassat 1A formulation FWH method only considering blade, shaft and the quasi –infinite domain far-field walls. As the observer H2 is close to the source and in a moderately well refined mesh region, the pressure probe information is considered as the base value. It is evident that the radius of the control surface has a major influence on the received pressure amplitudes, as the differ by a factor of around 5. Similarly, the frequencies show completely different behavior depending on the control surface radius. For the geometries *Outer3* and *Outer4* this can be attributed to the inability of the method to correctly calculate sound propagation inside the control surfaces, as it is based on FVM only, and on the other hand the course mesh in the regions of the surface for interpolation coupling the two methods. The values obtained from the *Inner* control surface, located inside the rotating part of the mesh, are several magnitudes higher and not displayed. These values can be considered unphysical, as the interpolation of the FWH control surface is determined beforehand and the mesh rotation is not considered. Furthermore, a general issue with the underlying FVM leads to differences of the pressure, as it is treated differently inside the rotating region, as shown in Fig. 27 (b) for two adjacent pressure observers monitored inside and outside of the rotating region, with $\Delta d = 1mm$ radial distance to the interface on each side, where practically the same result is expected.

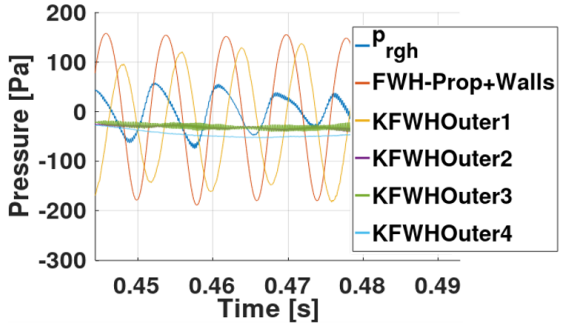

(a) Comparison of different control surface radii

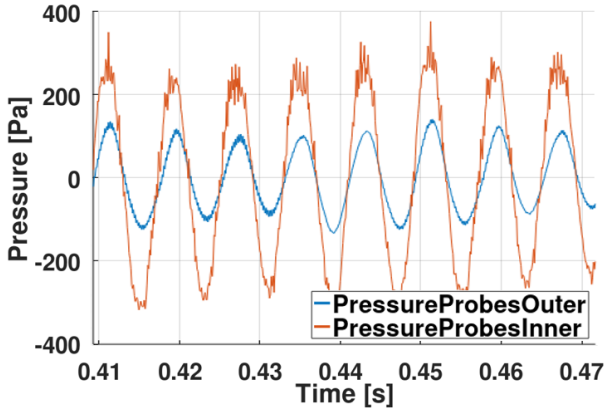

(b) Pressure observer results for adjacent points to AMI

Fig. 27: Pressure signals depending on method and location

Due to the detected issues, the only viable position of the control surface at the moment is immediately outside the AMI, where the mesh is still refined and the pressure is correct, which excludes studies of observers located within the rotating region with the permeable surface FWH method. To further study the effects of the position of the control surface, minor variations in radial extent, within the refined region of the mesh, immediately outside of the rotating region interface, are evaluated for the near-field observer H2 in the time domain in Fig. 28 (a) and in (b) for the frequency domain. The exact extent of the surfaces with respect to the propeller plane is listed in Table 4, with the *OnTop* surface being identical to the interface. It is evident that small changes in the radial extent have a significant influence on the acoustic pressure amplitude independent of the mesh, as all control surfaces are placed in a similarly

refined radial section. While it is expected that a control surface close to the interface produces the most accurate results, the *OnTop* surface yields identical results compared to the *Close* surface and both are overestimating the actual pressure at the location of the observer by a factor of about 3. The most accurate result seems to come from the *Outer11* surface, with a moderate radial distance to the interface of $\Delta r = 0.02m$, which corresponds to $\Delta r = 13\% \cdot r_{AMI}$ in terms of the rotating region or $\Delta r = 8\% \cdot D_p$ in propeller diameters. However, the generalization of this result is questionable until further studies are available.

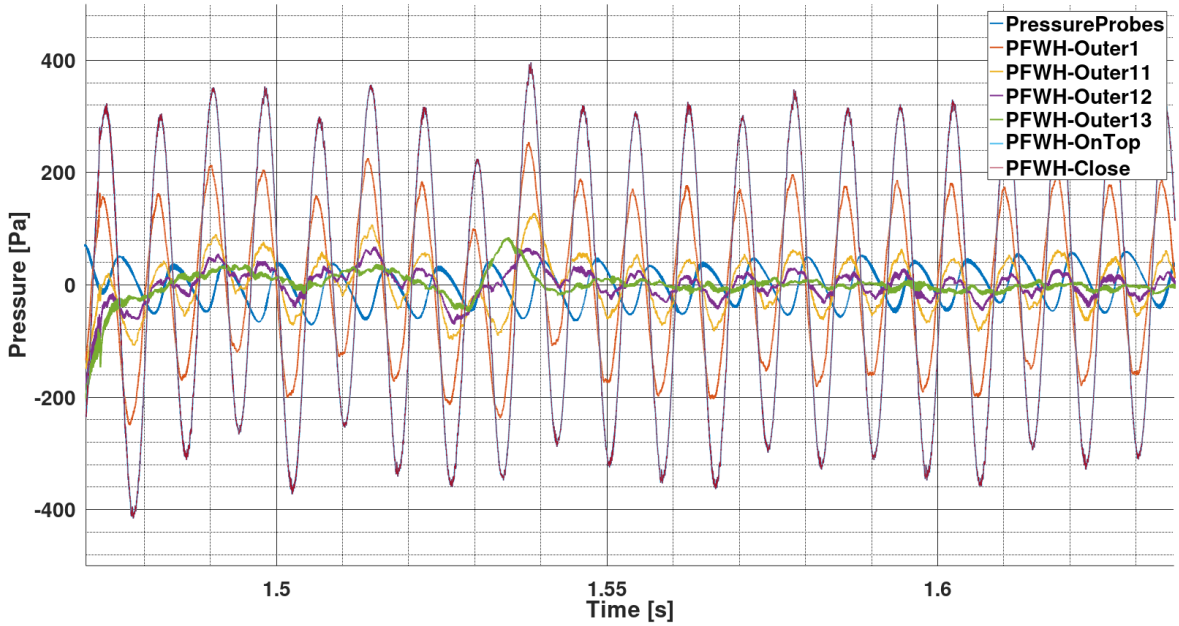

(a) Time domain

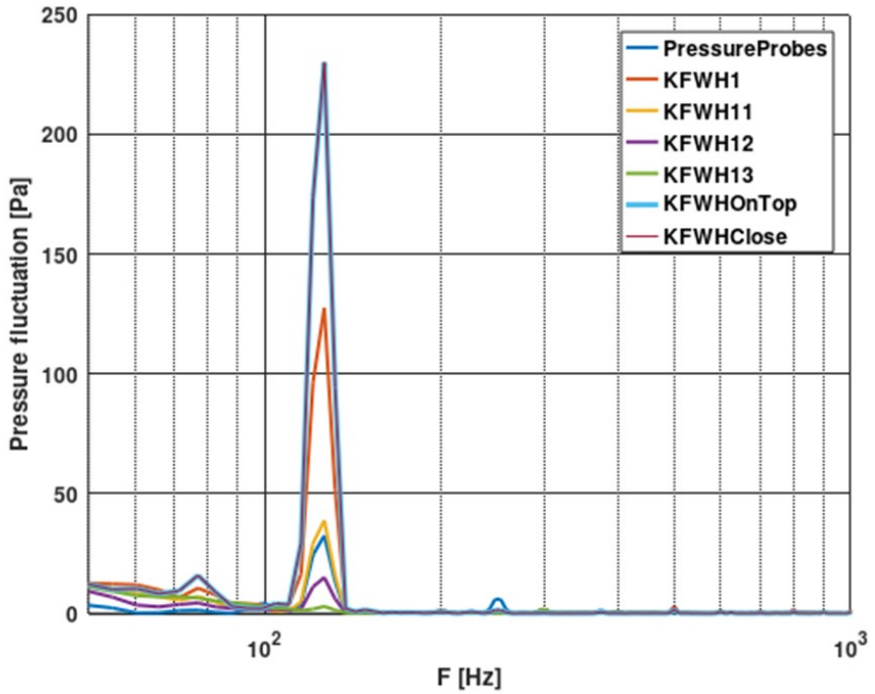

(b) Frequency domain

Fig. 28: Pressure and acoustic signals depending on source geometry

Table 4: Geometries of permeable surface FWH method control surfaces, with respect to the propeller plane and axis for the investigation near the rotating mesh interface

Parameters [m]	*Outer1*	*Outer11*	*Outer12*	*Outer13*	*OnTop*	*Close*
r	0.160	0.170	0.180	0.190	0.150	0.151
$l_{upstream}$	0.110	0.110	0.110	0.110	0.100	0.101
$l_{downstream}$	0.510	0.510	0.510	0.510	0.500	0.501

On the other hand increasing the radial extent of the AMI significantly is not desirable as the cell count increases with $\propto r^2$, if the cell refinement sizes at the interface are fixed, which is recommended to avoid interpolation issues. Additionally, the timestep reduces considerably, if the sliding mesh interface CFL number is to remain identical over all calculations, which is required as otherwise the simulation turns unstable. An example of this behavior is shown by the unphysical pressure developing at the interface in Fig. 29. Since the above investigations show, that a control surface inside the rotating region produces wrong results, an increase of the radius of the AMI is not recommended, if observers near the propeller are also of interest. The studied interface radii are summarized in Table 5, with the resulting cells that are passed at the interface radius in one timestep, which can be considered as a sliding mesh interface CFL number. A refinement of the mesh leads to reduced cell lengths at the interface, which is investigated for the $r_{AMI} = 0.65$ case, however, this increases the number of passed cells per timestep and thus the interface CFL number, which in turn would require reduced timesteps leading to unfeasible calculation times of the setups. If the whole domain with radial extent of $r = 25m$, is to rotate, there are no timestep or interface interpolation issues, however a useable control surface cannot be positioned.

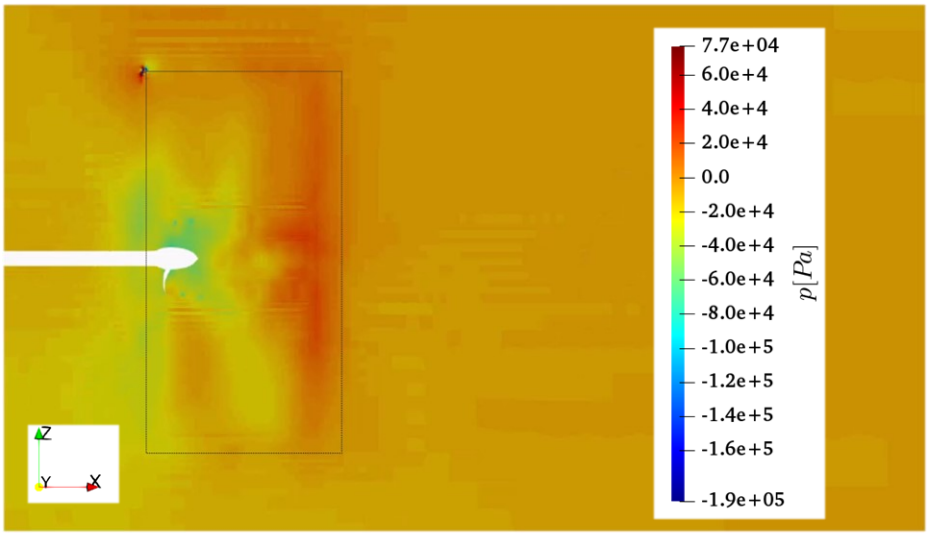

Fig. 29: Midplane pressure with $r_{AMI} = 0.65m$ as black dashed line and refined interface resulting in unphysical pressure at interface due to high interface CFL number

Table 5: Rotating region radial extent effect on interface CFL number.

AMI radius	Rotational speed	Mean cell length	Number of cells passed per timestep
[m]	[m/s]	[m]	[cells]
0.15	23.562	0.0015	1.745
0.65	102.102	0.0030	3.782
0.65	102.102	0.0015	7.563
25	3926.991	-	0

3.4 Simulation Accuracy

3.4.1 Mesh and Simulation Quality Criteria

For the meshing a standard unstructured hexahedral based algorithm with extrusion for layer addition is used and standard quality criteria are applied. Negative cell volumes are not allowed, the face area and cell volume magnitudes are checked, as well as the mesh non-orthogonality and severely non-orthogonal faces, face pyramids and skewness are confirmed to be in an acceptable range. Depending on the simulation case between 5 and 20 layers are implemented on the boundaries with one layer on the sliding mesh interface on each side as it is found to help with the smoothness of the surface of the interface boundaries, which is a key quality criterion that is examined visually before starting the simulation. Kinks in the sliding mesh interface create highly unstable interpolation and lead to unphysical pressure jumps combined with an associated numerical noise in the acoustic solution. A layer coverage of 99% is targeted for all surfaces, however, for the hull it is not achieved in most cases due to the large extent and the difference in surrounding cell levels. For RANS simulations, wall functions are used, that automatically switch between modelling and resolving the turbulence properties, however, many of the created meshes aim for low y^+ values in order to be able to resolve the wall flow and be used appropriately in the LES simulation stage. For the final propulsion setup the y^+ distribution on the hull is given in Fig. 15 (a) for a converged stage 2 simulation, which mostly shows the adherence to the low Reynolds criterion, except upstream of the onset of the stern angle of the vessel. A jump in wall treatment is visible at this location marked by the short streamwise $2 < y^+ < 30$ region appearing in red and the $y^+ > 250$ region in bow direction, which is confirmed to cause no adverse effects in the velocity flow field. For the propeller a target $y^+ < 1$ is achieved, even for the stage 3 simulation with sheet cavitation at the blade leading edge in (b).

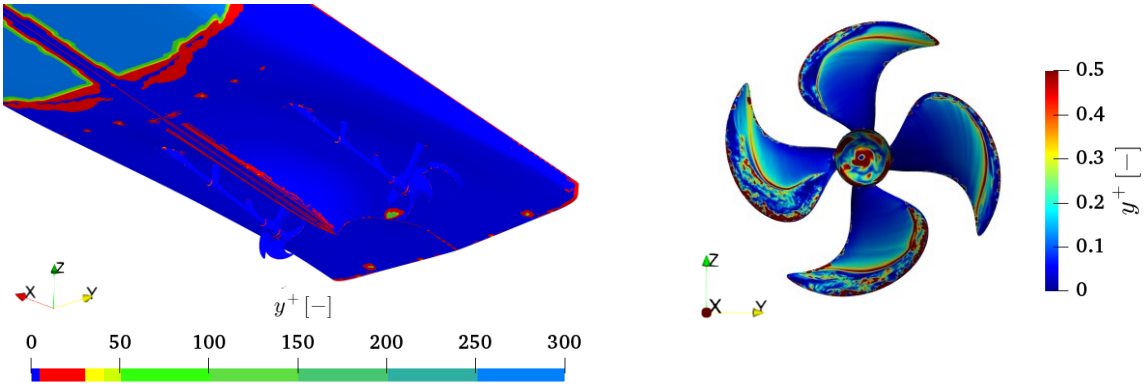

(a) Hull (b) Detail cavitating propeller suction side

Fig. 30: y^+ distribution for the propulsion simulation with the ProNoVi target case

For determining convergence of the flow solution, the following criteria are checked that are listed with increasing order of simulation time to achieve convergence:

1. Residua of transport variables
2. Propeller forces and moments
3. Topology and shape of the phase-locked Q-criterion trailing vortices
4. Topology and shape of the phase-locked α isosurfaces (if applicable)
5. Periodic pressure time history of the outlet acoustic observers (if applicable)

In fact only criterion 3.-5. are meaningful, as non-converging residua would lead to a simulation crash and forces are converged long before the vortices in the propeller slipstream reach periodic behaviour. For acoustic simulations the relevant criterion to start the recording of the signal for acoustic evaluation is 5., as the pressure information at the outlet is usually last to show periodic behavior.

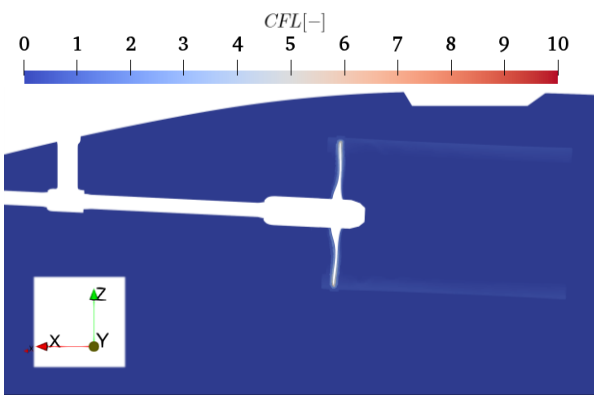

(a) CFL

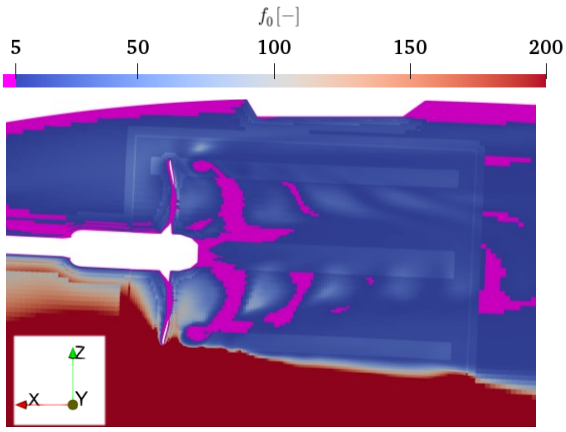

(b) f_{int}

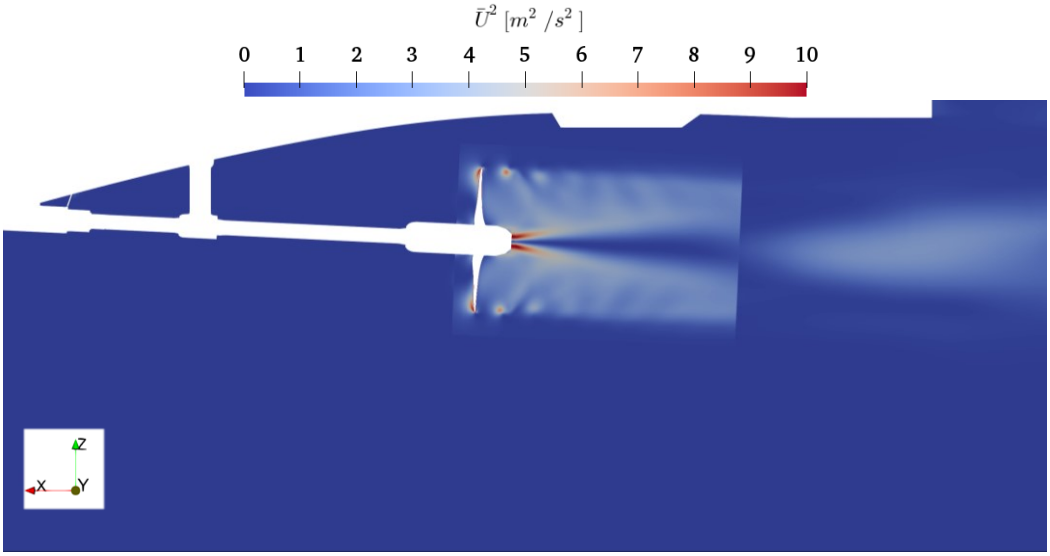

(c) $\overline{U'}^2$

Fig. 31: LES quality criteria

It is crucial to ensure that the mesh and simulation quality criteria of CFL number, resolved turbulence, and second order statistical moments of velocity are sufficient for implicit LES. In Fig. 31 the three additional quality criteria are given on a midplane for the ProNoVi target case. The maximum CFL number for LES in the mesh is set around 1-5 even though the average is at least two orders of magnitude smaller and the spatial distribution is visualized on the midplane in (a), where most regions are $CFL \leq 5$ with only the propeller tip boundary layer reaching values of up to $CFL \leq 10$. In the tip vortex region the CFL number is generally higher due to the initial cylindrical cell refinements around the radius $r/R = 1.0$. For the LES the target resolved turbulence for the mesh is 80%, for which a precursor RANS simulation is evaluated, in order to avoid a long repetitive process of starting up several LES simulations with different mesh refinements. With the value f_{int} calculated from [81]

$$f_{int} = \frac{l_0}{\Delta} = \frac{k^{\frac{1}{2}}}{C_\mu \omega \cdot \Delta}, \tag{58}$$

the cell size Δ determined from the cubic root of the cell volume is related to a value representing the integral length scale l_0. In a RANS simulation this may be obtained from the modelled parameter of the turbulent kinetic energy k and ω and the model coefficient for turbulent viscosity C_μ. Considering the restriction of

$$\Delta = \frac{l_0}{5}, \tag{59}$$

80% of the turbulence is resolved when the value $f_{int} > 5$, which is given in (b) and marked in magenta for regions below 5. The validity of this approach is tested by comparing the implicit LES resolved turbulent kinetic energy obtained from the second order moments of the velocity as the trace of the Reynolds stress tensor $k_{res} = 0.5 \cdot (\overline{u'u'} + \overline{v'v'} + \overline{w'w'})$ and subtracting it from the direct evaluation of the transport variable k in RANS in Fig. 32 for a simulation of the PPTC'11 with active cavitation. Besides the regions in the tip vortex near the propeller blades and the hub vortex, which are also the regions occupied by the gas phases, the agreement is very good. Some spurious turbulence exists in the ILES at the downstream end of the rotating region, which is unphysical and appears as a difference here.

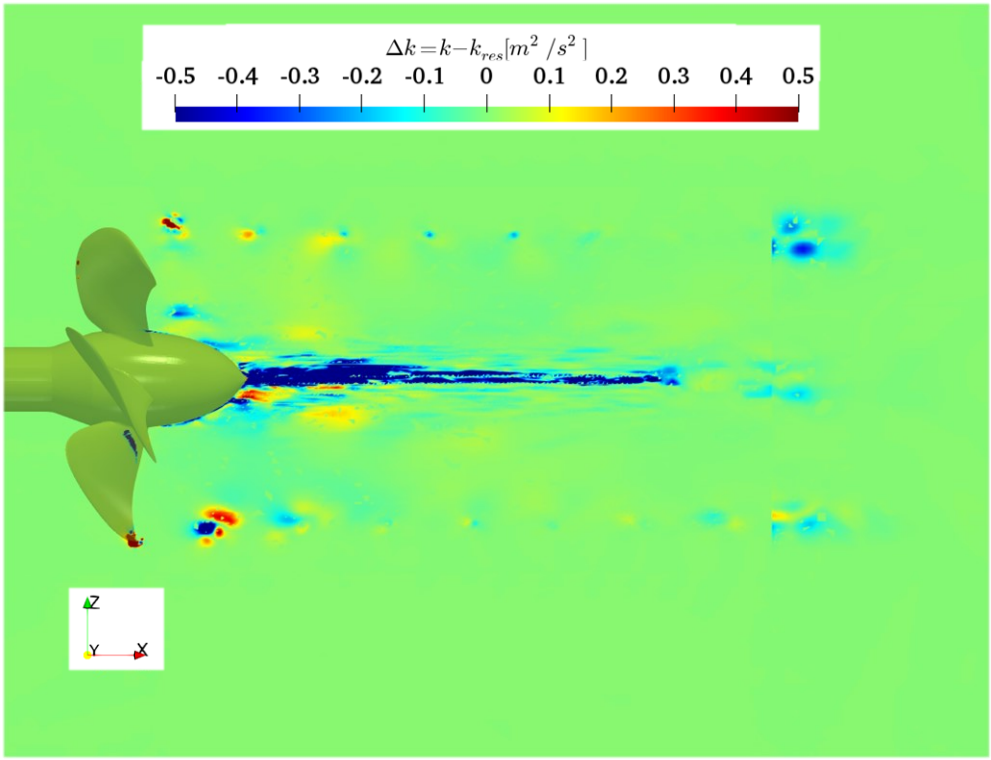

Fig. 32: Modelled TKE in RANS vs. resolved TKE in LES

In Fig. 31 (b) a very good accordance with Eq. (59) is shown for the complete midplane, except the tip vortex and its corresponding shear layer connecting it to the hub vortex. Achieving higher mesh resolution with a typical cylindrical mesh refinement in order to fulfill the requirements would result in unfeasible mesh sizes. Thus, a priori or runtime adaptive mesh refinements of the tip vortex helical shape are necessary, which are discussed in the next subsection. Another deficiency aspect of the mesh is revealed at the downstream end of the rotating region, where spurious turbulence is also detected in Fig. 32. An insufficiently fine mesh resolution is predicted, however, this is an inherent issue with the approach resulting from the sliding mesh interpolation, rather than the underlying mesh size and smaller cells lead to even more spurious turbulence generation at the sliding mesh interface. It is also clear from the image in (b) that the turbulent boundary layer on the hull is resolved insufficiently fine for the implicit LES in this case, however, this is adjusted for further simulations. The second order statistical moments of the time-history of the velocity $\overline{U'}^2$ are checked in (c) for the LES as the resulting representation is time-invariant and may thus be used to find numerical issues, such as the sliding mesh interface interpolation.

Another way to check the resolved turbulence in the LES is by generating a turbulent spectrum for single point observers in space, which can be achieved by evaluating the velocity fluctuations around a time mean velocity value at the respective position. The turbulent spectrum then is required to show similar behavior to a standard normalized turbulent spectrum [73] as shown in Fig. 13 (b), which may be tested with the average gradient of k in the plot. To change the spectrum from frequency to wave number with space dimensions the Taylor frozen flow turbulence hypothesis [82] may be used, which can be utilized

to generate spatial information from a fixed location observation for a fluid with free stream velocity by assuming that the average particle velocity is equal to the bulk fluid velocity with $\delta x = U \cdot \delta t$ to obtain the wave number k

$$k = \frac{1}{U} \cdot f, \qquad (60)$$

where f is the turbulent kinetic energy frequency. The assumption is that the flow is statistically stationary and the bulk flow velocity is larger than the velocity fluctuations, which is the case for hydrofoil and propeller simulations, except in the propeller slipstream. In Fig. 33 (a) three fixed point observers around a hydrofoil are indicated, with one being upstream, one downstream near the shear layer and one located in the tip vortex. In (b) the turbulent energy for the observers is given over the frequency of the velocity fluctuations obtained with an FFT of the time history around the mean velocity. It seems that only the observer located in the tip vortex shows significant values of energy and achieves a gradient of around $\delta k/\delta f = -6/2\ m^2/s$. By applying the Taylor frozen flow hypothesis the turbulent energy is given depending on the wave number in (c), which is a linear operation and results in a shift of the abscissa only.

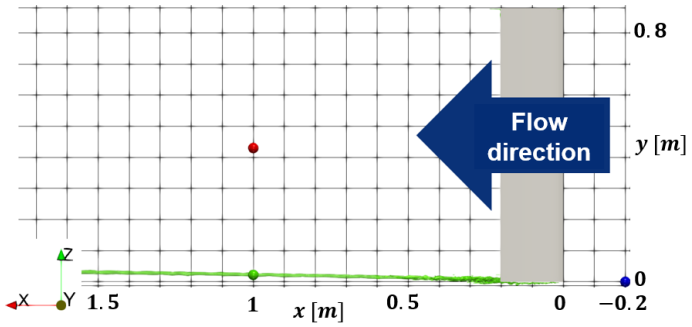

(a) Setup with hydrofoil and velocity observers

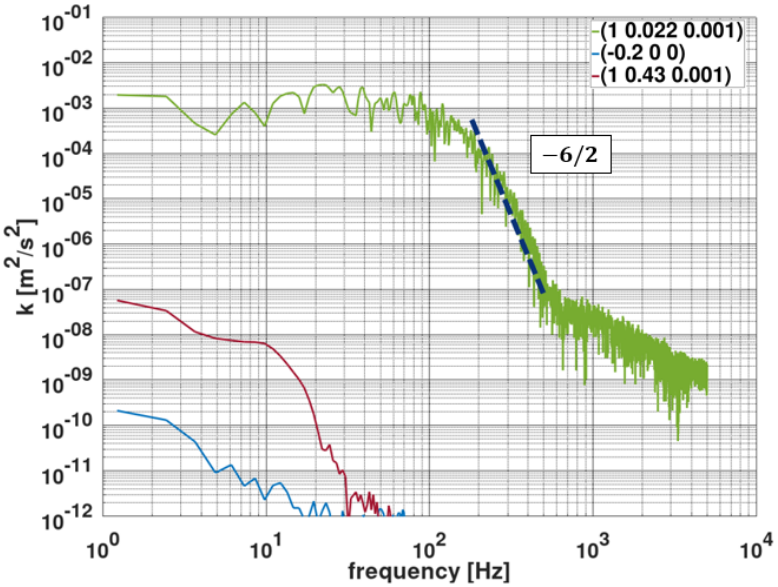

(b) Turbulent frequency spectrum

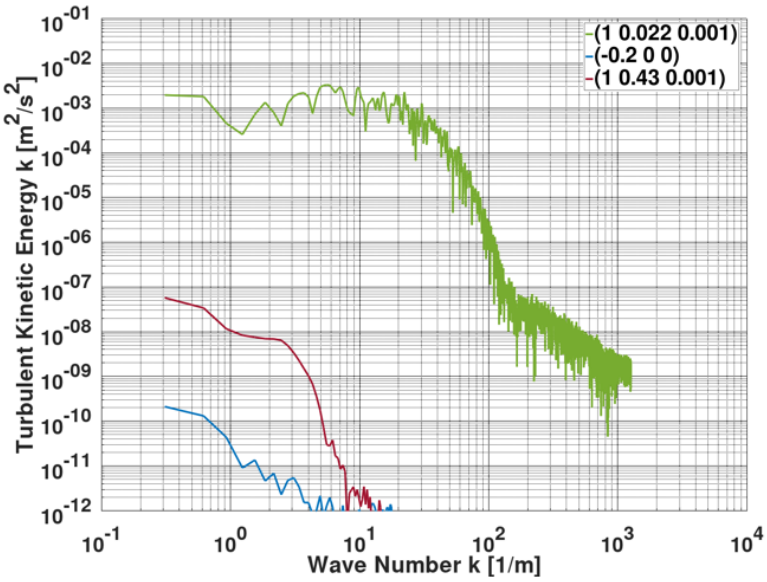

(c) Turbulent wave number spectrum

Fig. 33: Evaluation of turbulent spectra for hydrofoil in cavitation tunnel

Similar evaluations are conducted for the propulsion case in Fig. 34 (a) and (b) for a free stream observer and an observer upstream of the propeller plane to obtain the energy in the vessel wake field, leading to similar gradients in the relevant frequencies of the energy spectrum.

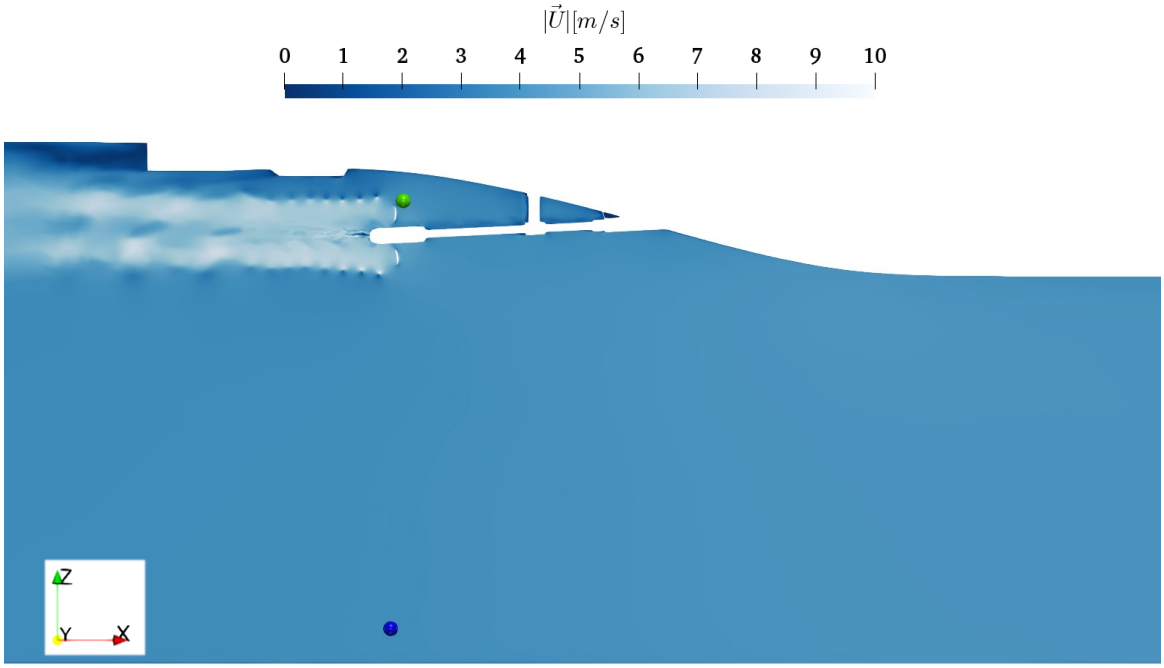

(a) Setup with hydrofoil and velocity observers

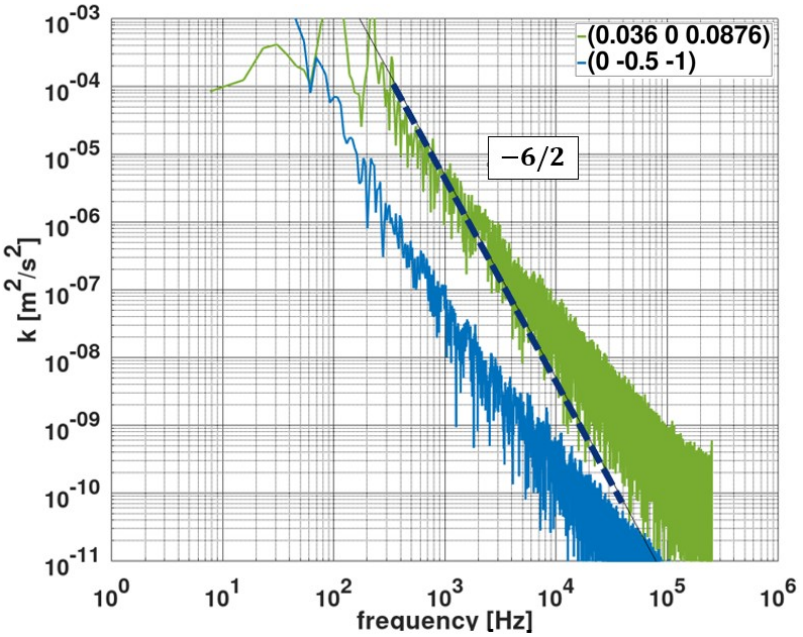

(b) Turbulent frequency spectrum

Fig. 34: Evaluation of turbulent spectra for ProNoVi reference target case in cavitation tunnel

3.4.2 Mesh refinements

Two types of adaptive mesh refinements are utilized for increasing the mesh resolution of the trailing vortex regions of a propeller identified as featuring insufficient CFL and f_{int} values in the previous subsection. While one issue is resolving 80% of the turbulence in LES the more strict requirement may be capturing the cavitating tip vortex, which requires at least 30 cells across the vortex core in order to achieve the correct core pressure.

Several suggestions for the edge length or the cells across the vortex core exist in the literature [83]. For globally unstable flow the cell size Δ_{Max} depends on the characteristic diameter of the problem d_{Ref}, which can be taken as the propeller diameter D,

$$\Delta_{\mathrm{Max}} \leq (0.05 \ldots 0.1) \cdot d_{Ref}, \tag{61}$$

while the size for locally unstable flow is given by

$$\Delta_{\mathrm{Max}} \leq R_L \cdot \tau \cdot k^{\frac{1}{2}}, \tag{62}$$

with the time scale τ and turbulent kinetic energy k and the ratio R_L suggested as 0.1. [84] Besides these empirical suggestions, a physical derivation gives the inertial subrange length of

$$\lambda_T = \left(10 \cdot k \cdot \frac{\nu}{\epsilon}\right)^{\frac{1}{2}}. \tag{63}$$

From empirical observations [85] of cavitating flow the minimum bubble radius generated by a propeller is related to the diameter with

$$r_b = 0.1\% \cdot D. \tag{64}$$

The result from Eq. (64) are achieving a good resolution of the cavitating tip vortex and determine the cell sizes in this work. For standard meshes with $20 - 35 \cdot 10^6$ initial cells this results in an increase of the tip vortex core cell size by at least 5 leading to around double the initial cell size by number of cells, depending on the streamwise length of the tip vortex refinement.

A general a priori mesh refinement of the helix shape of the tip vortex may be employed before the initial simulation stage, however, the exact topology and shape of the tip vortex is usually unknown and cannot be obtained from the pitch of the outer radii sections of the propeller alone. Therefore, after the RANS and LES stages of the simulation are finalized, stage 5 is prepared, by extracting an appropriate

Q-isosurface from the converged solution and using it as the source of a distance refinement, as shown in Fig. 35 (a) together with the resulting mesh midplane, with the appropriate cell size from Eq. (64) as shown in (b) with values below 5 in magenta. In this case the complete remeshing leads to a suitable mesh for resolving the turbulence and cavitation for acoustic evaluation, except far downstream from the propeller. However, due to resource restrictions a cutoff of the slipstream is always required and it can be assumed that far downstream the noise sources are small compared to the propeller surface and cavitation caused noise due to physical (and numerical) dissipation. In this case the consideration of the contribution of the shear layer connecting tip and hub vortex to the noise is neglected, so further refinement in the radii sections between is not required, which would additionally exceed the feasibility limits of the number of cells for the simulations.

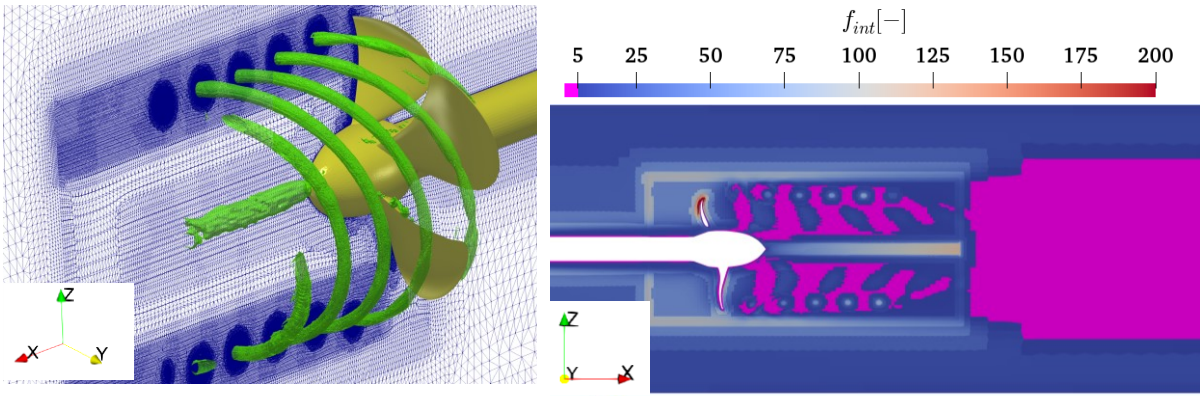

(a) Refinement source (b) Resulting f_{int}

Fig. 35: A priori AMR and effects on resolved turbulence

In Fig. 36 a velocity distribution at a downstream plane parallel to the propeller plane at a location of tip vortex intersection is illustrated, where the black circle sectors are the radii sections of the propeller projected area of $r/R = 0.97$ and $r/R = 1.0$. Between the initial mesh (a) and the mesh after the AMR (b) the velocity reaches higher maximum values and moves further inward towards lower radii sections, while the overall extent is similar. In magenta the elliptical cross section of the $\alpha = 0.5$ phase interface is marked in (b) which appears in this case as a result of the larger number of cells across the vortex core.

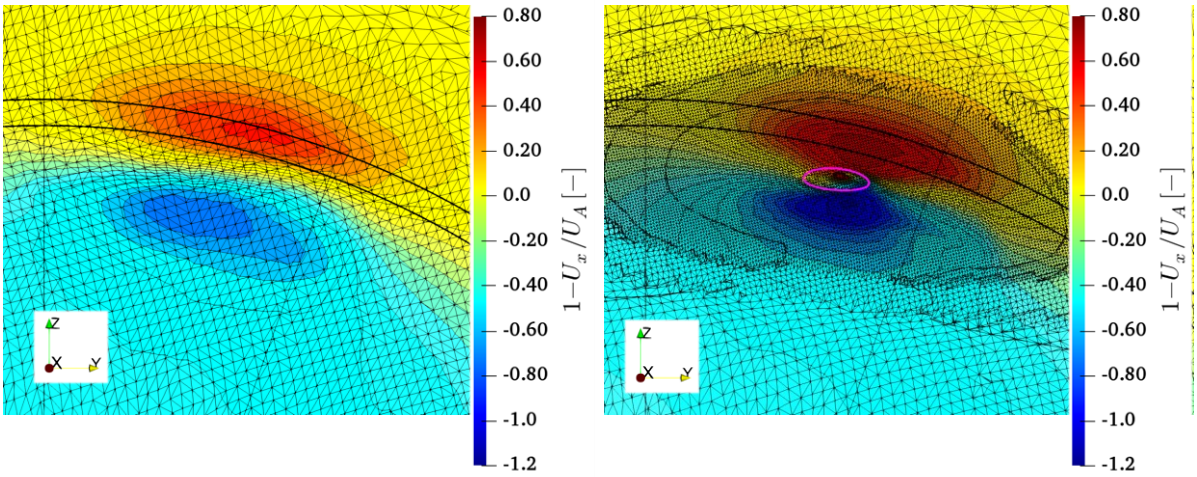

(a) Initial (b) After a priori AMR

Fig. 36: Velocity and mesh at tip vortex $x/D = -0.2$ on radii sections $r/R = 0.97 - 1.00$

As explained in section 1.4 the a priori AMR approach works well for propellers in the case of straight inflow. This allows the turbulence to be sufficiently resolved, which is essential for calculating the low pressure in the vortex core of the tip vortex to predict cavitation. For oblique flow, the main problem is that the rotational axis is not parallel to the flow direction. For this the approach can be adapted, by

rotating the source Q-isosurface for the tip and hub vortex in ways that all mesh regions are refined that are intersected by the trailing vortices over a complete propeller rotation, which is demonstrated in Fig. 37. The downside is that this leads to a very high cell count, with most of the cells unnecessary over a large portion of the propeller rotation.

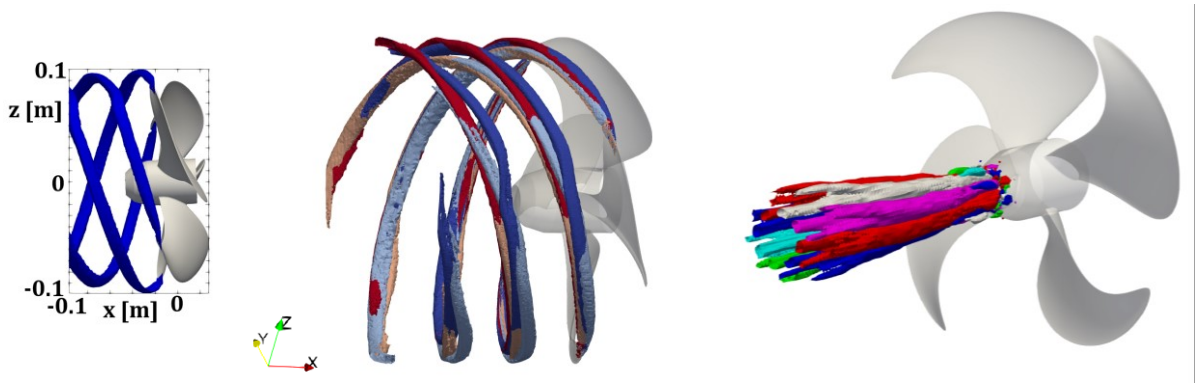

(a) Extracted vorticity (b) Tip vortex rotated $4 \times 90°$ (c) Hub vortex rotated $8 \times 45°$

Fig. 37: A priori mesh refinement for oblique flow

However, the variations with obstacles in the slipstream or strong slipstream distortions fueled by an upstream wake, a priori refinements are not possible, and an adaptive and automated refinement algorithm is required. Due to the high cell count achieved with the a prior meshing in oblique flow, the resulting simulation time on the grid with high resolution has to be compared to the additional calculation time for an automated dynamic refinement of cells according to the instantaneous Q-criterion and $\alpha = 0.5$ isovalue. With the implemented gradient-based automated AMR for hexahedral cells, the upper and lower refinement value for both criteria is set. The cells falling inside the limits are split and refined by using an octree data structure storing cell connectivity and size hierarchically and increases the cell count by eight for each split as indicated in Fig. 38, with an implementation of local one-irregularity constraint to keep mesh gradients smooth. The condition is checked for each refinement and unrefinement step, where in the first case neighboring cells are also refined and in the latter the cell stays refined.

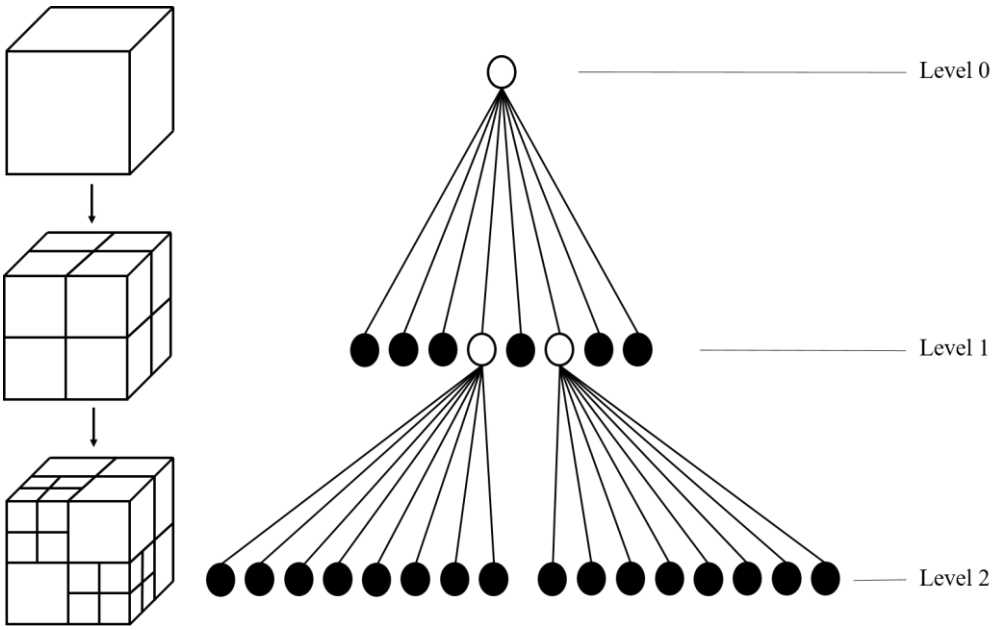

Fig. 38: Illustration of octree cell refinement procedure [64]

For each cell adaptation the cell-centered volume fields are mapped on the new mesh by adopting the same value for refinement and assuming the average of the consisting eight cells for unrefinement.

Fluxes are mapped directly for faces that are coincident with source faces or interpolated for internal faces from the arithmetic mean of the four corresponding master faces with possible sign adjustment depending on surface field face normal orientation. The initial mesh is decomposed into equal load processor subdomains, which is altered by the refinement steps, leading to imbalance during runtime. If the imbalance

$$\Delta_{CPU} = \max\left\{\frac{nCells_i - \frac{\sum_{i=1}^{n} nCells_i}{n}}{\frac{\sum_{i=1}^{n} nCells_i}{n}}\right\},\ 1 \leq i \leq n, \qquad (65)$$

with $nCells_i$ as the number of cells in each subdomain n, exceeds a specified amount, the automated dynamic balancing is initiated. While originally an unstructured domain decomposition algorithm is selected, stability and performance issues demand a structured hierarchical decomposition, which yields good rebalancing results for straight inflow open water propeller cases, but may be less optimized for inclined flow conditions with vessel.[1] There is an issue with the dynamic balancing for boundary fields as a mapping algorithm is not provided for boundary conditions, requiring to exempt all solid boundaries from the algorithm. For this purpose, protected cells are specified around solid surfaces, at the AMI and in the boundary layers, which prevent the algorithm from refining these cells. If the region near a solid boundary is required to be very fine to resolve a cavitating tip vortex, these refinements need to be implemented a priori, as in the case of rudder – tip vortex interactions. The protection functionality is also used to exclude the region of the shear layer between the tip and the hub vortex from the refinement, in order to keep the number of cells at a feasible amount. An example for the protection zones are illustrated in Fig. 39 (a) for the shear layer and far downstream of the propeller plane and in (b) for the simulation boundaries, such as the solid surfaces and sliding mesh interface at the AMI. In (a) the necessary disk mesh refinements at the sliding interface at the location of tip and hub vortex intersection are visible to ensure fine cells in the protected regions and reduce information loss at the interface.

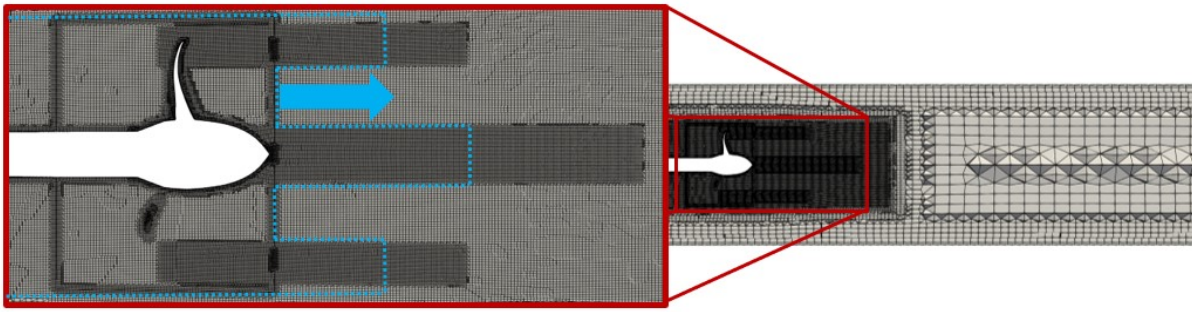

(a) Blue dotted line indicates protected zones (protected direction according to arrow)

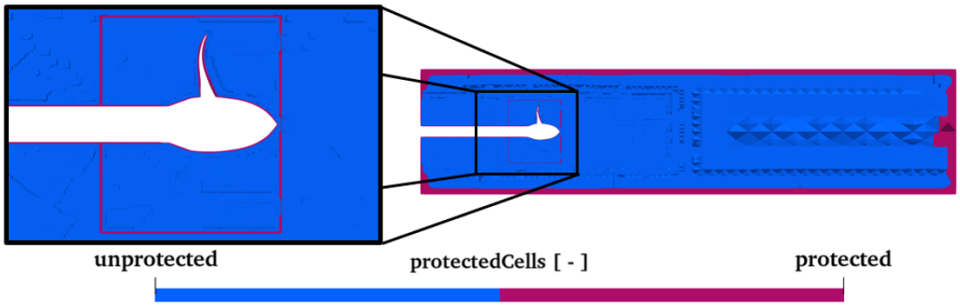

(b) Protected boundary layer and AMI cells

Fig. 39: Protected cells [64]

[1] In the available software this functionality is not supported and manual rebalancing is required until the issue is resolved in future releases.

The complete process of refining, executed at prescribed refine intervals, which are coinciding with $\Delta t = 1°$ timesteps for propeller simulations, is given in the flowchart in Fig. 40.

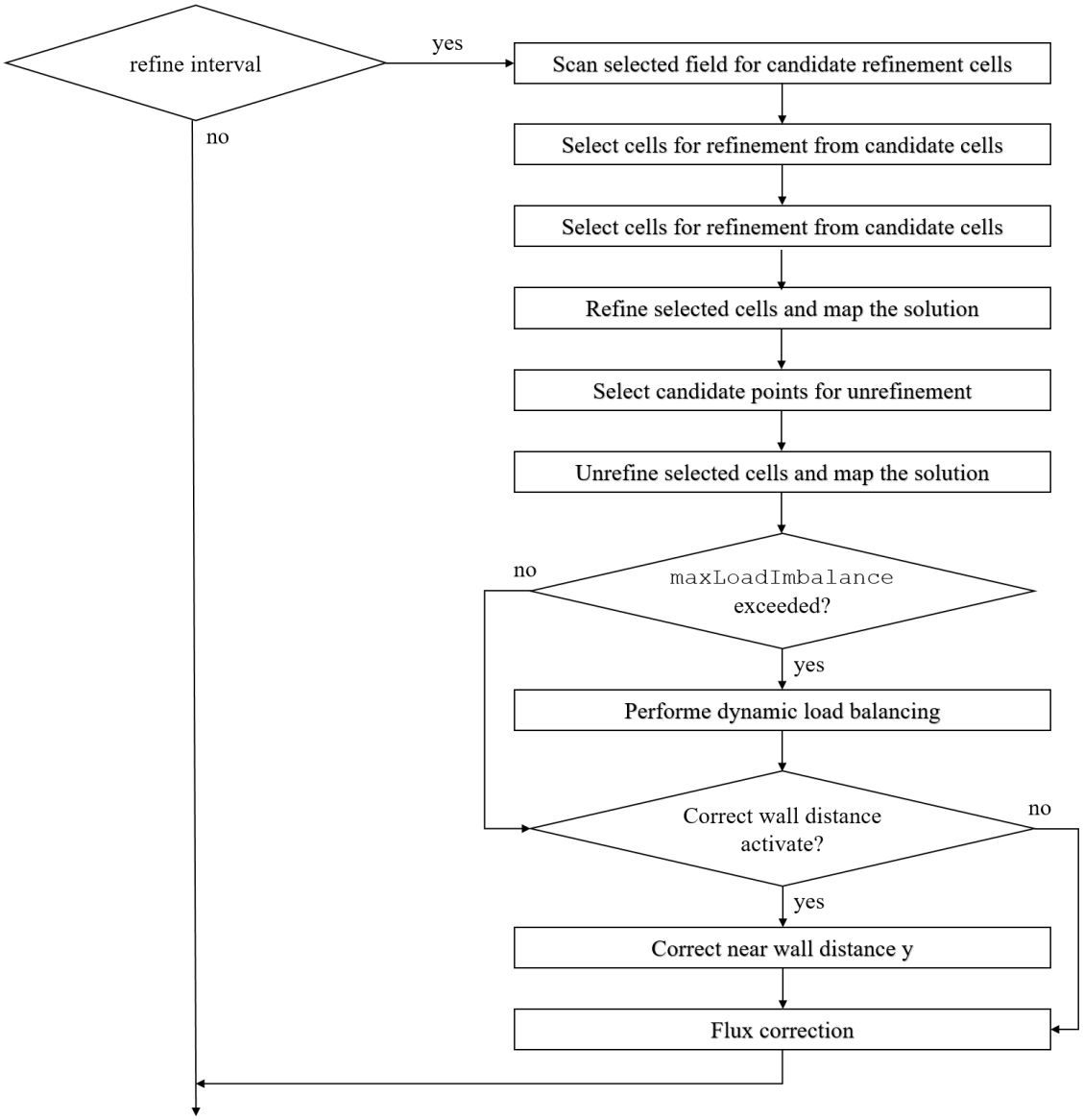

Fig. 40: Flow chart of refinement process [64]

3.5 Summary

Now the methods of this study and their applicability to the problem of propulsor-hull configuration underwater radiated noise are outlined. With the general solution approach by the FVM, the modelling or resolving of turbulence with RANS or LES and the two-phase flow VOF and phase transition cavitation physics with the OpenFOAM Schnerr-Sauer cavitation model the required hydrodynamic flow solution can be achieved. Additionally, the permeable surface FWH acoustic analogy implemented in combination with the hydrodynamic flow solver and how the methods are coupled is described and validated. With these mathematical models, the numerical simulation setups to investigate acoustic sources are described in the next chapter, followed by the investigation of the flow solution and the sound emissions thereafter with a summary of the results.

4 Test Case Simulations

In this chapter the simulation test cases for the validation of the methods and the investigation of underlying physics are described in preparation for the next chapters, where the best practices are developed. Beginning with simple test cases of lifting surfaces such as hydrofoils, continuing with more complex model scale propellers in cavitation tunnels in push and pull configuration with increasing complexity, and finishing with propulsor-hull configurations the developed methods are put to the test.

Different meshing strategies, such as classic disk-shaped refinements at the radii sections of the propeller tip, a priori helix shaped refinements at the trajectory of the tip vortex or automated mesh refinements are used depending on the case. To reduce the complexity and possibly additional numerical errors of the sliding mesh interface, the hydrofoil test cases are investigated prior to the open water propeller test cases, which consist of academic test geometries and propeller geometries utilized on vessels in the field. Finally, the three primarily investigated propulsor-hull configurations are described and how the respective validation simulations are constructed.

4.1 Hydrofoils

4.1.1 NACA 0012 Hydrofoil

In this test case the tip vortex of a non-cavitating rectangular NACA 0012 hydrofoil is analyzed using different turbulence models inside a cavitation tunnel. The half-hydrofoil profile has a chord length of $c = 0.203m$ and a half wing span of $s = 0.879m$. The coordinate system origin is placed at the tip of the leading edge. The angle of attack is $\alpha_{OA} = 5°$ in positive y-direction. The generated tip vortex is refined initially with an $r = 0.1 \cdot s$ inclined cylindrical refinement beginning at the origin with a streamwise length of $\Delta x = 10 \cdot c$ as shown in Fig. 41 (a). Downstream is another straight cylindrical refinement with the same diameter and a lower refinement level. Once the radial extent and the trajectory is known from an initial simulation, the Q-criterion isosurface is utilized to create an a priori distance refinement with very high resolution up to $\Delta x = 10 \cdot c$ downstream by one-time manual remeshing. The cavitation tunnel domain has a streamwise length of $\Delta x = 36 \cdot c$, with the inlet located at $x \approx 4.9 \cdot c$ and a square cross section with a length of $\approx 2.1 \cdot s$.

The flat tip of the foil featuring $293 \cdot 10^3$ faces in Fig. 41 (b) is highly refined in order to create the most accurate flow around it with a 100% layer coverage, while the total layer coverage of the mesh is 98.3%. There are 10 layers on the cavitation tunnel walls and 15 layers on the foil, to resolve the laminar-turbulent transition. Initially the total number of cells is $24.8 \cdot 10^6$ and after the Q-criterion refinement in Fig. 41 (c) reaches $93.1 \cdot 10^6$ cells, while the number of faces of the foil is unchanged.

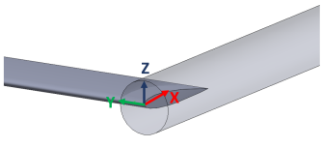

(a) Geometry and refinement cylinder

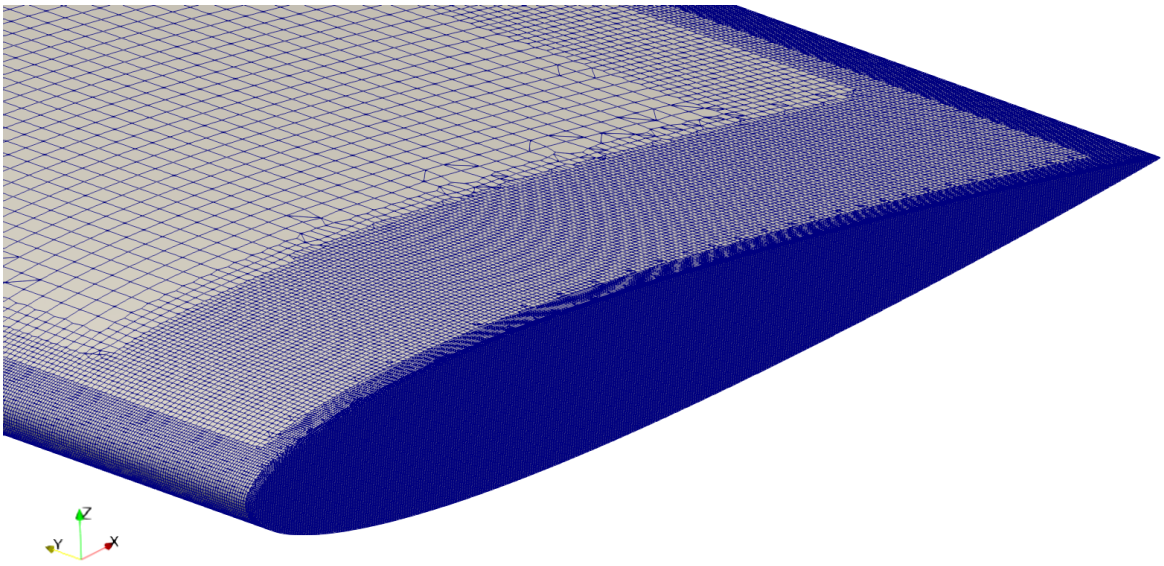

(b) Tip surface mesh

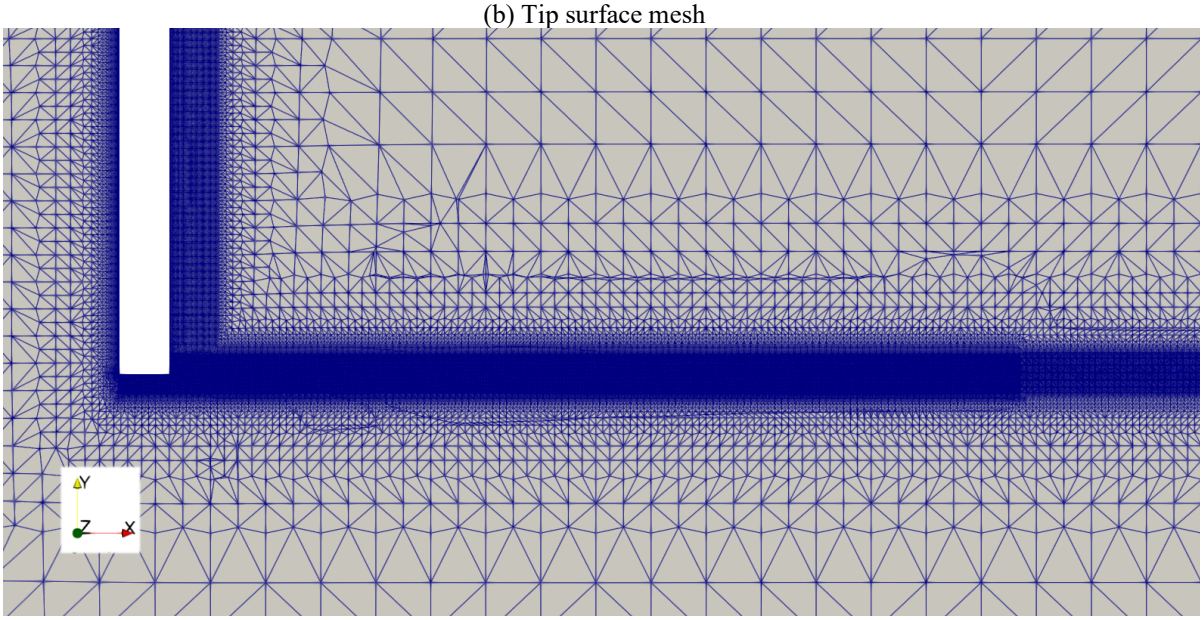

(c) Top view mesh intersection

Fig. 41: NACA 0012 Refinements

This test case is simulated without cavitation only with a RANS γ-$Re_{\Theta,t}$ transition model, a LES with a Smagorinsky subgridscale model with van Driest damping coefficients and the panel method *pan*MARE. The achieved lift forces for $Re = 530 \cdot 10^3$ are given in Table 6. As this test case does not have experimental measurements, only simulation values of FVM, *pan*MARE and a simulation reference are given. The test case is reconstructed from Devenports experiments [58] with a flat tip and is additionally simulated with a round tip according to the investigations by Chow [86]. For the evaluation of the tip vortex there are 21 stations placed along the downstream trajectory given in Table 7.

Table 6: Lift forces of the NACA 0012 foil with $\alpha_{OA} = 5°$

C_l [−]	RANS-fine	LES-fine	LES-superfine	*pan*MARE Tunnel	*pan*MARE free	Feder 2018 [87]	Chow 1997 [86]
Flat Tip (Devenport)	0.439	0.425	0.410	0.441	0.346	0.41-0.47	
Round Tip (Chow)	0.434	0.423	-	-	-	-	0.51

Table 7: Stations along the tip vortex

Pos.	S1	S2	S3	S4	S5	S6	S7	S8	S9	S10	S11	S12	S13	S14	S15	S16	S17	S18	S19	S20	S21
$[\cdot c]$	0	0.25	0.5	0.75	1	1.25	1.5	1.75	2	2.5	3	3.5	4	4.5	5	5.5	6	7	8	9	10

4.1.2 NACA 66_2-415 Hydrofoil

To study a non-cavitating and cavitating tip vortex, the NACA 66_2-415 elliptical hydrofoil test case is analyzed with a root chord length of $c = 0.1256m$ and a half wing span of $s = 0.15m$ and an angle of attack of $\alpha_{OA} = 9.0°$. At the center of the root chord of the hydrofoil is the coordinate origin with the x-axis pointing in downstream direction. For the cavitation tunnel a $2 \cdot s$ rectangular cross section domain is modelled with a length of $14 \cdot c$ with the inlet $4 \cdot c$ upstream of the origin.

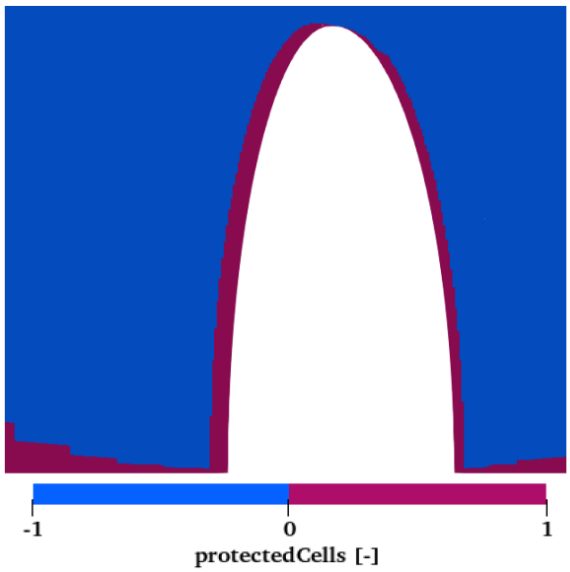

Fig. 42: Protected cells with value 1 on midplane

It is simulated for a root chord length Reynolds number of $Re = 8.1 \cdot 10^6$ for three different inflow cavitation numbers $\sigma = 0.58$, 1.2, 2.6, and 4.2, as well as non-cavitating condition with RANS k-ω-SST and implicit LES. This case is also used to determine the Schnerr-Sauer coefficient for the initial nuclei density for the subsequent propeller simulations and simulated with $n_0 = 1 \cdot 10^6\ 1/m^3$ and $n_0 = 1 \cdot 10^{12}\ 1/m^3$.

An initial mesh in Fig. 43 (a) is generated with $6.6 \cdot 10^6$ cells with $550 \cdot 10^3$ faces on the hydrofoil with a layer coverage of around 99.8% and 5 layers, whereas the cavitation tunnel wall has $60 \cdot 10^3$ faces with an average of 3 layers and a coverage of 95.1%. Once converged with RANS without cavitation, an automatic local run-time AMR is applied based for instance on the Q-criterion of $Q_{min} = 5 \cdot 10^4 s^{-2}$ to $Q_{max} = 1 \cdot 10^5 s^{-2}$ leading to a final mesh with a cell count of $104.6 \cdot 10^6$. Other refinement criteria such as the pressure gradient in the streamwise normal planes is also considered, however, due to impractical adoption for propeller cases not pursued further. This final converged mesh is used statically for the cavitation simulations to ensure stability. For the AMR, protected zones are implemented around the hydrofoil boundary layer and the cavitation tunnel walls as seen in Fig. 42, to avoid the refinement of the complete tunnel walls and issues with the non-hexahedral cells created by cell splitting near the surfaces. Both initial and final mesh are shown in Fig. 43 with the protected zones near the wall clearly visible in (b). For the LES simulations an a priori refinement is employed yielding a mesh with up to $13.5 \cdot 10^6$ cells and 10 layers on the foil and 100% layer coverage.

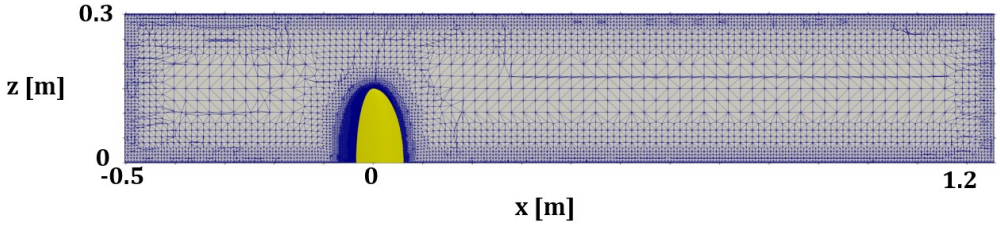

(a) Initial

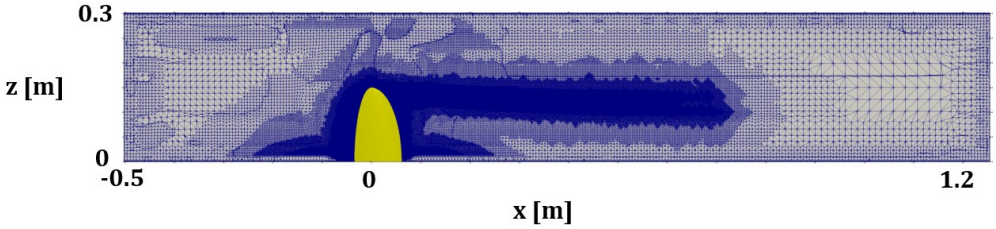

(b) After AMR

Fig. 43: NACA 66_2-415 hydrofoil mesh

The complete AMR is conducted in RANS only leading to insignificant change in the forces on the hydrofoil. In the experiment the reported lift coefficient is $C_L = 0.67$ while the drag coefficient is not reported, which yields an error of the simulation of $\Delta C_L = 2.7\%$ in the forces and the drag coefficient converges to $C_D = 0.61$ with a continuous fluctuation of around 4.5%.

4.1.3 Delft Twist11 Hydrofoil

The Delft Twist11 symmetrical NACA 0009 hydrofoil is a test case with an unstable sheet cavity created by a spanwise varying angle of attack between $\alpha_{OA} = -2°$ at the outer sides to $\alpha_{OA} = 9°$ at the center. The foil has a chord length of $c = 0.15m$ and a span of $s = 0.3m$. This case is simulated with RANS k-ω-SST and LES with a Smagorinsky subgridscale model with van Driest damping coefficients in cavitating condition at an inflow cavitation number of $\sigma = 1.07$ and a chord Reynolds number of $Re = 6.9 \cdot 10^5$. With a coordinate origin at the chord center at the outer hydrofoil side, the domain has a length of $\Delta x = 7 \cdot c$ with the inlet located at $2.5 \cdot c$ upstream and a rectangular cross section with a width of $\Delta y = s/2$ and a height of $1 \cdot s$ according to the simulation references [20], [88].

The static mesh in Fig. 44 (a) with a half-wing model, realized with a symmetry boundary condition at the center, features $32.8 \cdot 10^6$ cells with $1.6 \cdot 10^6$ faces in order to resolve the fluctuating cavity with LES and a layer coverage of 100% with 15 layers. An additional distance refinement at the main cavity region is projected from $+z$-direction onto the suction side of the foil given in Fig. 44 (b) with a normal extent of up to $0.05 \cdot c$ in two refinement level steps. In Fig. 44 (c) the $\alpha = 0.5$ isosurface of an arbitrary timestep is shown with the underlying volume mesh, indicating that the further downstream transported large cavities are leaving the refinement zone. However, due to the resource requirements imposed by low timesteps and high number of α correctors as a result of the highly unstable cavity and subsequent numerical instability of the simulation, further refinement is not pursued.

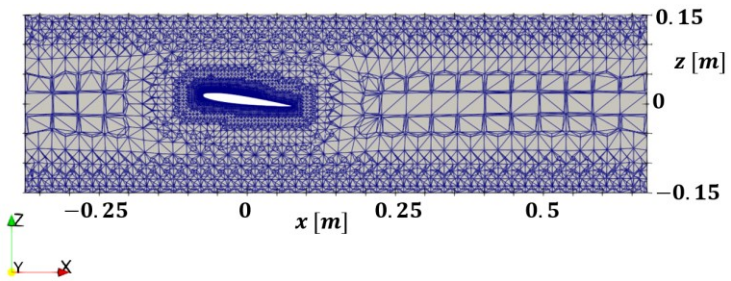

(a) Volume mesh midplane intersection

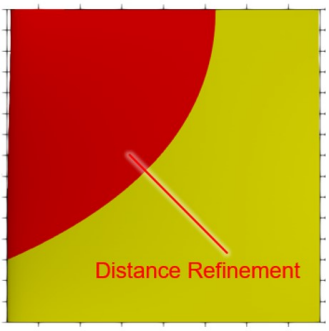

(b) Refinement region

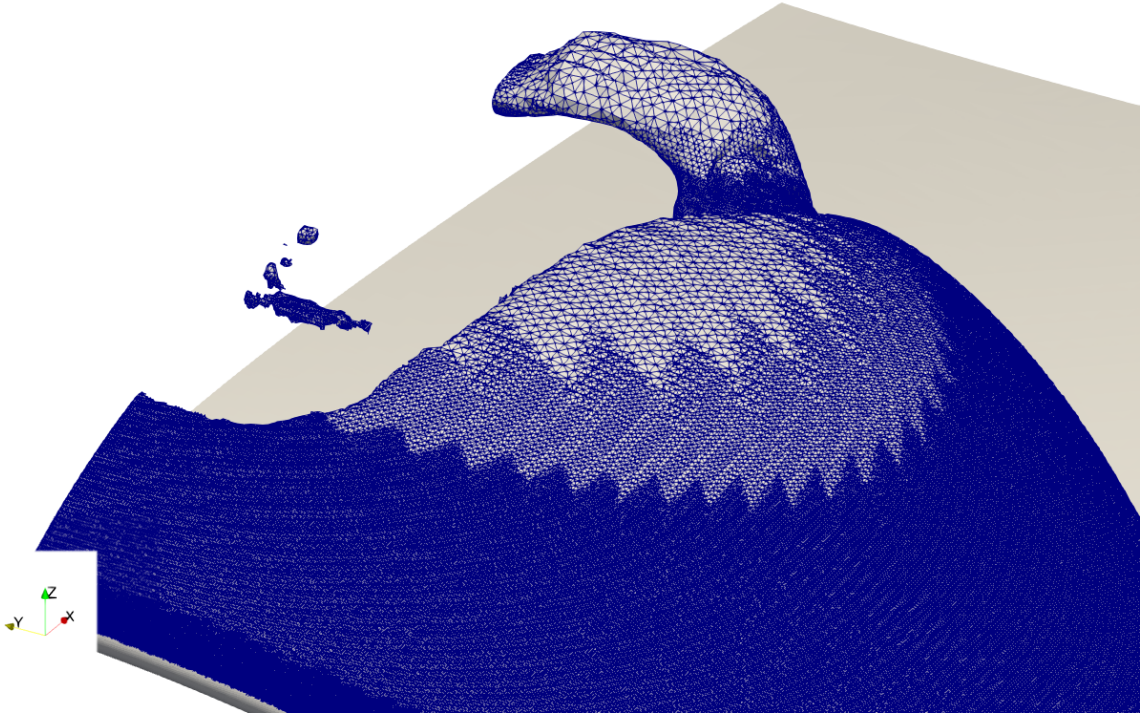

(c) Cavitation isosurface with corresponding mesh

Fig. 44: Delft Twist11 foil mesh

The time evolution of the forces on the hydrofoil over six shedding periods are given with an average of $C_L = 0.51$ for the non-fluctuating RANS and $C_L = 0.56$ for the LES, which is equivalent to an error of $\Delta\, C_L = -4.3\%$ and $\Delta\, C_L = 4.8\%$. The shedding frequency is determined to be $f_{FO} = 27Hz$ with a standard deviation of $\sigma^2 = 3.9$, which is significantly slower than the experiment with $f_{FO} = 32.55Hz$.

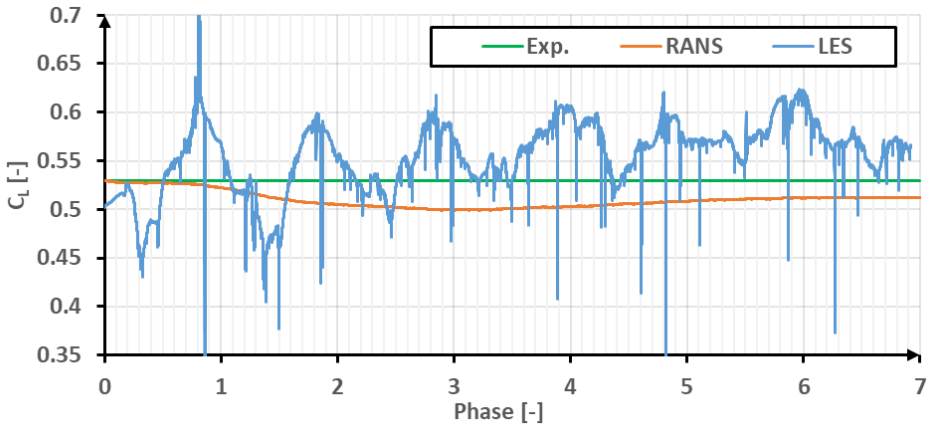

Fig. 45: Lift forces on the foil

4.2 Propeller Open Water

4.2.1 PPTC‘11

The PPTC’11 is a straight flow open water 5-bladed propeller test case with a stable leading edge suction side sheet cavity and a connected stable tip vortex cavity with distinctive nodes and anti-nodes in diameter along the trajectory. With a special converging hub cap design, a large cavitating hub vortex is generated with distinct interaction with the cavitating tip vortex. At higher advance ratios blade root cavitation occurs on the suction side blade fillet. The propeller main parameters are summarized in Table 8 together with the other propellers analyzed in this work. For all open water propeller cases the origin is set at the intersection of the rotational axis and the propeller plane with the x-axis pointing upstream. The cavitation tunnel has a $l = 2.4 \cdot D_P$ rectangular cross section with rounded edges and a length of $\Delta x = 12 \cdot D_P$ and the inlet $\Delta x = 2.8 \cdot D_P$ upstream. In the model, the gap between shaft line and propeller hub is neglected.

Table 8: Main propeller parameters for the open water test cases

Parameter	Unit	PPTC’11 (VP1304)	Newcastle	P1595	P3193	E779A
Configuration	-	Push	Pull	Push	Pull	Push + Rudder
Diameter	$[m]$	0.250	0.220	0.204	0.204	0.227
Pitch ratio	$[-]$	1.635	0.861	1.188	1.061	1.115
Area ratio	$[-]$	0.78	1.02	0.63	0.85	0.68
Skew	[°]	18.39	18.96	42.00	42.00	4.48
Number of blades	$[-]$	5	5	4	5	4

This case is the main test case in this work for developing the simulation approach and the investigation of cavitation on a propeller. The case is simulated as a full model with RANS k-ω-SST, RANS γ-$Re_{\Theta,t}$, implicit LES, and LES with Smagorinsky subgridscale model with MRF and AMI rotation realization, as well as with and without AMR. The investigations include two advance coefficients $J = 1.019$ and $J = 1.262$ with cavitating conditions for $\sigma_n = 2.0$ and $\sigma_n = 1.5$ respectively. Experiments and simulations are conducted with a rotation rate of $n = 25Hz$ and $n = 15Hz$ for the respective advance coefficients. There are propeller wake field velocity measurements, cavitation sketches and high speed videos available from the experiments, albeit wake field measurements and high speed videos for the higher advance coefficient are for a slightly different advance ratio of $J = 1.269$ (video) and $J = 1.253$ (wake field).

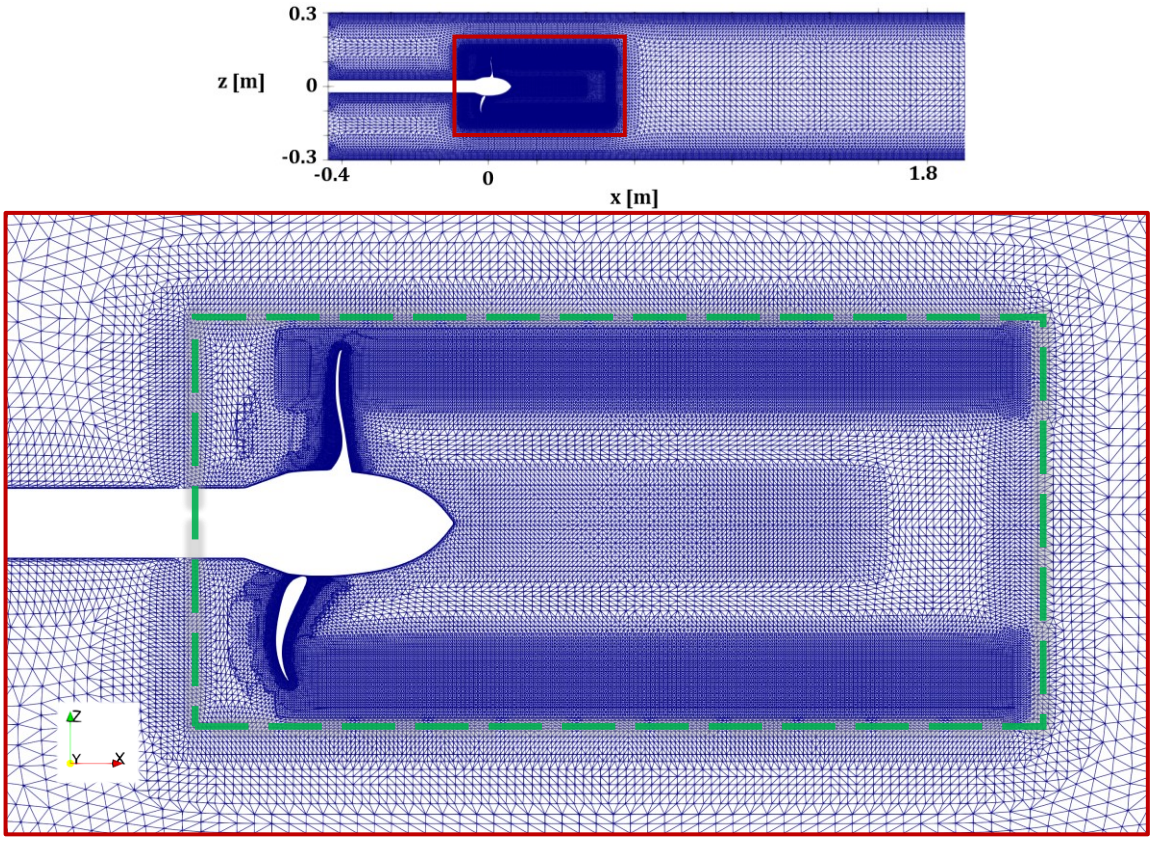

Fig. 46: PPTC'11 typical mesh

After a grid independence study regarding layers and slipstream resolution, a typical base mesh in Fig. 46 features $11 \cdot 10^6$ cells with $297 \cdot 10^3$ propeller faces, while a final mesh after AMR has for instance $34.7 \cdot 10^6$ cells for a $Q > 20 \cdot 10^3\ s^{-2}$ criterion. The cylindrical rotating region for AMI or the MRF region is required to be sufficiently long downstream with $\Delta x = 2.0 \cdot D_P$ as indicated by the green dashed line, which is also indicating the KFWH permeable surface with $1 \cdot 10^{-3} m$ offset to the outside as described in 3.3.4. On the initial mesh a disk refinement is placed in the tip vortex region from $r/R = 0.7$ to $r/R = 1.1$ up to the downstream end of the rotating region and a hub vortex refinement with lower resolution is placed up to $r/R = 0.32$. The layers on the propeller are between $5 - 20$, depending on the simulation and the cavitation tunnel features 5 layers. Time mean forces for some of the modelling approaches for $J = 1.019$ are given in Table 9 and for $J = 1.262$ in Table 10.

Table 9: Integral values for PPTC'11 at $J = 1.019$

Investigation	Solver	Cav	k_T [-]	Δk_T [%]	$10k_Q$	Δk_Q [%]
Experiment	-	Off	0.381	-	0.976	-
Experiment	-	On	0.374	-	0.970	-
RANS k-ω-SST*awt*	*tdiCoupled*	Off	0.381	0.1	1.008	3.3
RANS k-ω-SST	*helyxCoupled*	Off	0.389	2.2	1.025	5.0
RANS k-ω-SST	*helyxCoupled*	On	0.372	-0.5	1.116	15.1
RANS k-ω-SSTLM	*helyxCoupled*	Off	0.391	2.6	1.027	5.2
RANS k-ω-SSTLM	*helyxCoupled*	On	0.377	0.9	1.121	15.6
RANS k-k_l-ω	*helyxCoupled*	Off	0.398	4.4	1.036	6.1
ILES	*pimpleDyMFoam*	Off	0.396	4.1	0.995	1.9
LES Smagorinsky	*interPhaseChangeDyMFoam*	Off	0.383	0.4	1.027	5.2
ILES	*interPhaseChangeDyMFoam*	On	0.429	14.9	0.995	2.6
IDDES k-ω-SST	*interPhaseChangeDyMFoam*	Off	0.390	2.3	1.002	-2.7

Table 10: Integral values for PPTC'11 at $J = 1.262$

Investigation	Solver	Cav	k_T [-]	Δk_T [%]	$10k_Q$	Δk_Q [%]
Experiment	-	Off	0.249	-	0.719	-
Experiment	-	On	0.206	-	0.631	-
RANS k-ω-SST*awt*	*tdiCoupled*	Off	0.252	1.4	0.709	-1.4
RANS k-ω-SST	*helyxCoupled*	Off	0.255	2.5	0.755	5.0
RANS k-ω-SST	*helyxCoupled* MRF	Off	0.261	1.5	0.748	4.0
RANS γ-$Re_{\Theta,t}$	*helyxCoupled*	Off	0.254	2.2	0.754	4.8
RANS k-k_l-ω	*helyxCoupled*	Off	0.267	7.3	0.761	5.9
LES Smagorinsky	*interPhaseChangeDyMFoam*	Off	0.246	-1.1	0.756	5.1
ILES	*interPhaseChangeDyMFoam* MRF	Off	0.266	6.6	0.746	3.7
ILES	*interPhaseChangeDyMFoam* GRF	Off	0.187	-24.8	0.690	-4.0
ILES	*interPhaseChangeDyMFoam* MRF	On	0.206	8.5	0.631	-23.7
IDDES k-ω-SST	*interPhaseChangeDyMFoam*	Off	0.254	2.0	0.754	4.9

4.2.2 Newcastle Propeller

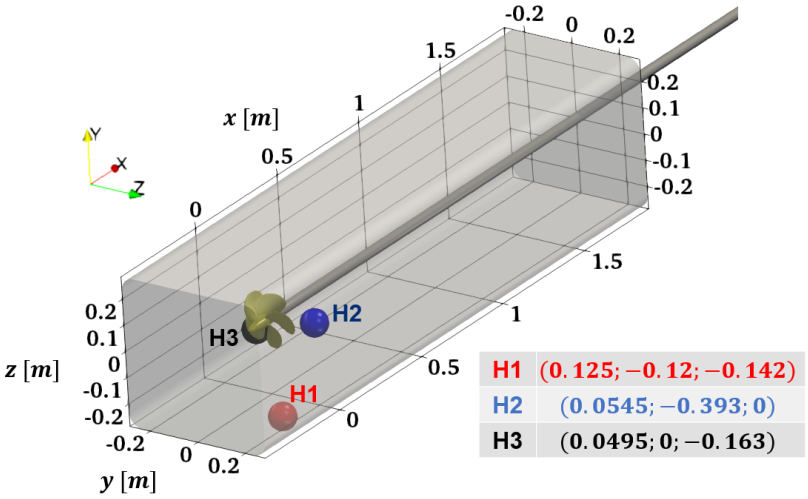

Fig. 47: Newcastle domain and acoustic observer

The Newcastle propeller is a 5-bladed propeller. The test case is conducted for parallel inflow open water test condition and the main parameters are summarized in Table 8. A suction side leading edge sheet cavity is generated and depending on the operation conditions a tip cavity with nodes and anti-nodes along the trajectory or cavity filaments and bubbles can be observed. Far downstream, vortex grouping, and subsequent merging and bursting instigated by tip-hub vortex instability interactions occur. Investigated operation points are summarized in Table 11 with the resulting propeller integral forces summarized in Table 12. Experimental data for the case is available as cavitation photographs and acoustic signatures from 6 different facilities. The case is simulated with RANS with k-ω-SST, and LES with implicit subgridscale modelling in non-cavitating and cavitating conditions, in order to prove the simulation approach developed with the PPTC'11 case for a larger variety of propellers and operation points, as well as to validate the acoustic approach outlined in the methods in chapter 3.3. The cavitation tunnel rectangular cross section with rounded corners and a width of $l = 2.3 \cdot D_P$ is indicated in Fig. 47 and the length is $\Delta x = 10.6 \cdot D_P$ and the inlet $\Delta x = 2.05 \cdot D_P$ upstream. This cavitation tunnel geometry as well as the three acoustic observers locations H1-H3 are modelled according to the University of Genoa setup reported in the reference [29].

In Fig. 48 is a typical mesh with the rotating region indicated by the green dashed line with around $22.3 \cdot 10^3$ cells and $242 \cdot 10^3$ faces on the propeller with a layer coverage of 100% with 10 layers, while the shaft line behind the propeller and the cavitation tunnel walls have 5 layers. The tip vortex region is refined at the same radii sections and downstream length as the PPTC'11 case, however, an additional

disk refinement is placed around the blade tips between $0.78 < r/R < 1.005$ downstream for $0.18 \cdot D_P$. To refine the tip vortex regions sufficiently for capturing cavities, an a priori AMR with a $Q = 5 \cdot 10^5 s^{-2}$ criterion over a distance of $r = 0.015 \cdot D_P$ is implemented once the LES simulations are converged, before the start of the acoustic evaluation.

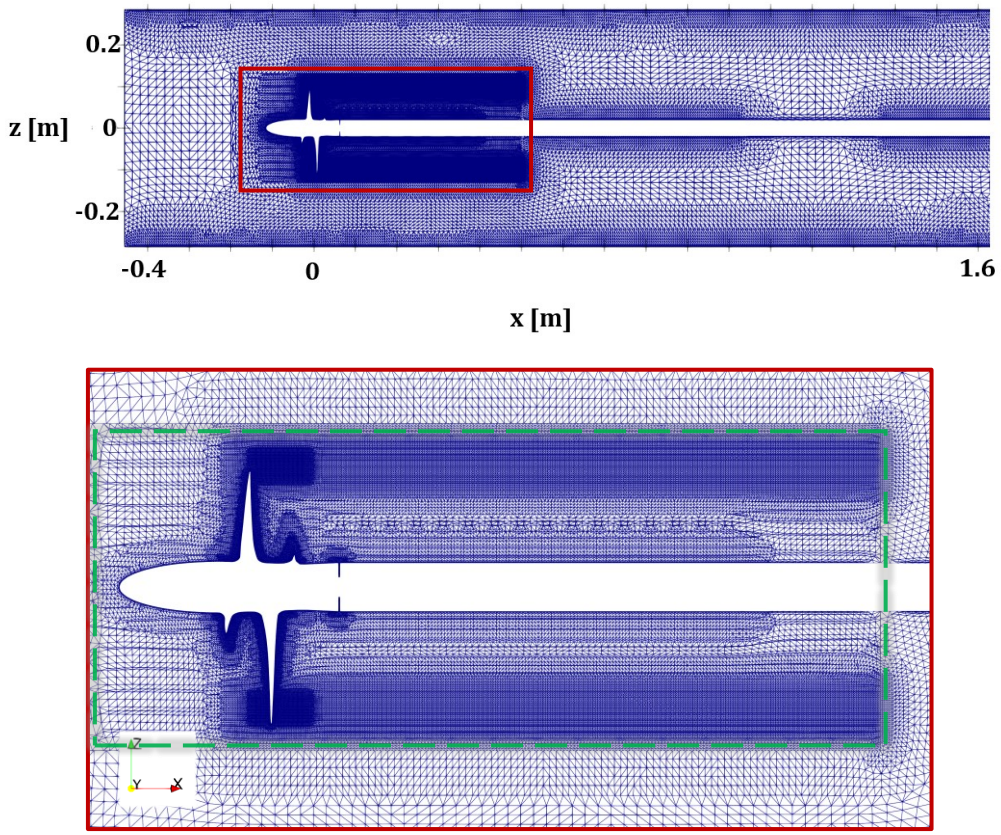

Fig. 48: Newcastle typical initial cavitation tunnel mesh

Table 11: Analyzed operation points for the Newcastle propeller test case

Condition	C1	C2	C3	C6
J [−]	0.4	0.4	0.4	0.5
σ_n [−]	2.22	1.3	0.72	1.13
n [Hz]	35	35	35	35

Table 12: Integral values at $J = 0.4$ and $J = 0.5$, Newcastle propeller test case.

Investigation	Solver	Cav	k_T [-]	Δ [%]	$10k_Q$	Δ [%]
$J = 0.4$ - condition: C1, C2, C3						
Experiment	-	?	0.242	-	0.341	-
RANS k-ω-SST	*sdiCoupled* (steady)	Off	0.243	-0.6	0.340	0.3
ILES	*interPhaseChangeDyMFoam*	On	0.231	4.6	0.358	0.9
$J = 0.5$ - condition: C6						
Experiment	-		0.190	-	0.284	-
RANS k-k_l-ω	*interPhaseChangeDyMFoam*	Off	0.182	-4.1	0.271	-4.5
ILES	*interPhaseChangeDyMFoam*	On	0.204	7.2	0.318	11.9

4.2.3 P1595

The P1595 is an unoptimized 4-bladed propeller for the ProNoVi reference target case vessel with the main data given in Table 8. It produces a thin stable sheet cavity with increasing pattern area towards

outer radii and a prominent thin cavitating tip vortex with a cavitating hub vortex depending on the hub cap geometry, which is executed as converging or diverging. This parallel inflow case is investigated with transition turbulence model to quantify the influence on noise and is together with the P3193 the main propeller investigated in behind hull condition and in addition generate the base acoustic signature of the propeller as comparative data to the case in behind hull condition. A quasi-infinite cylindrical domain contains the propeller in push configuration, which is simulated in non-cavitating and cavitating condition with RANS k-ω-SST and RANS γ-$Re_{\Theta,t}$. An advance coefficient of $J = 0.6$ is examined with a cavitation number of $\sigma_n = 1.5$ with $n = 20Hz$ and $n = 30Hz$ yielding the results in Table 13. In cavitating conditions there are no torque measurements available, so the reference for the simulations is the non-cavitating torque coefficient. The mesh and the rotating region in green is presented in Fig. 49 with around $15 \cdot 10^6$ cells and $407 \cdot 10^3$ propeller faces with 20 layers and no AMR treatment is applied. As the inlet is $\Delta x = 17 \cdot D_P$ upstream, the shaft is trimmed to reduce cell count.

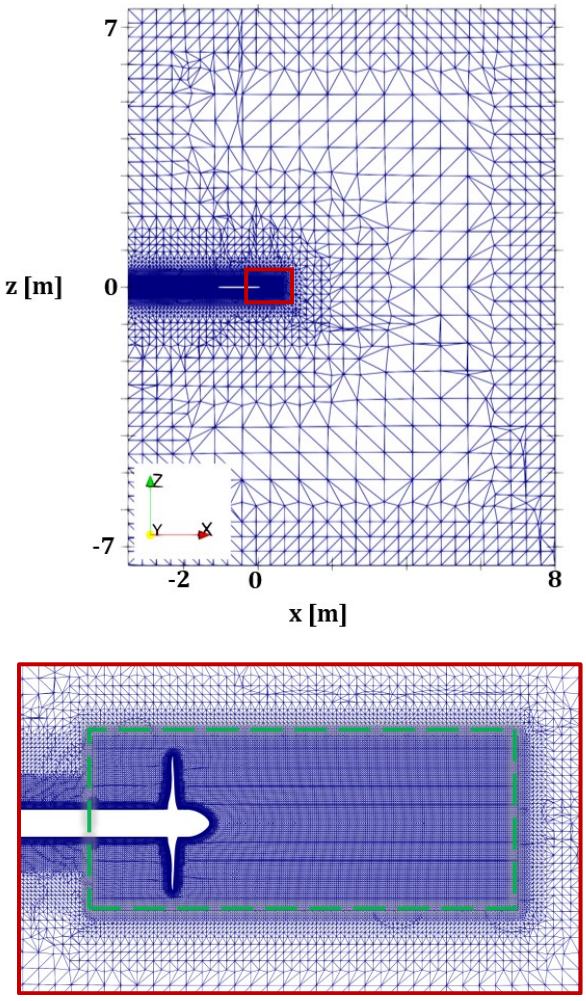

Fig. 49: P1595 propeller typical open water quasi-infinite domain mesh

Table 13: Integral values for P1595 at $J = 0.6$

Investigation	Cav	k_T [-]	Δk_T [%]	$10k_Q$	Δk_Q [%]
Experiment	Off	0.305	-	0.536	-
Experiment	On	0.302	-	NA	-
RANS k-ω-SST	Off	0.306	0.4	0.528	-1.6
RANS γ-$Re_{\Theta,t}$	Off	0.306	0.2	0.524	-2.3
RANS k-ω-SST	On	0.301	-0.3	0.554	3.4
RANS γ-$Re_{\Theta,t}$	On	0.296	-2.1	0.559	4.2

4.2.4 P3193

The P3193 propeller is an acoustically optimized 5-bladed propeller for the ProNoVi reference target case vessel with the main parameters indicated in Table 8. It is the only propeller geometry within this work that has its data not public. The design generates features of several weak vortices at the trailing edge at the outer radii sections that are forming a tip vortex sheet rather than a central tip vortex, which dissipates quickly, due to a design with tip unloading and high tip rake. The test case is a straight flow $r = 6.4 \cdot D_P$ large cylindrical domain pull configuration, that is simulated with RANS k-ω-SST and implicit LES for $J = 0.74$ in non-cavitating conditions with a rotation rate of $n = 20.5Hz$ achieving a thrust of $k_T \approx 0.20$, similarly to the behind hull case. With this case, the applicability of the approach to capture the tip vortex for open water propeller simulations is tested by extending it to cases with very weak tip vortices. The propeller origin is located $\Delta x = 4 \cdot D_P$ downstream of the inlet with a total domain length of $17.6 \cdot D_P$. Similar refinement regions to the previous cases are placed in the tip vortex region from $r/R = 0.68$ to $r/R = 1.1$ with an axial extent of $\Delta x = 2.45 \cdot D_P$ and additionally a more refined ring at the blade tip with an axial extent of $\Delta x = 0.3 \cdot D_P$ inside the rotating region of the mesh indicated with the dashed green line in Fig. 50. AMR is not employed in the open water case resulting in a mesh with $14.4 \cdot 10^6$ cells and $235 \cdot 10^3$ faces on the propeller.

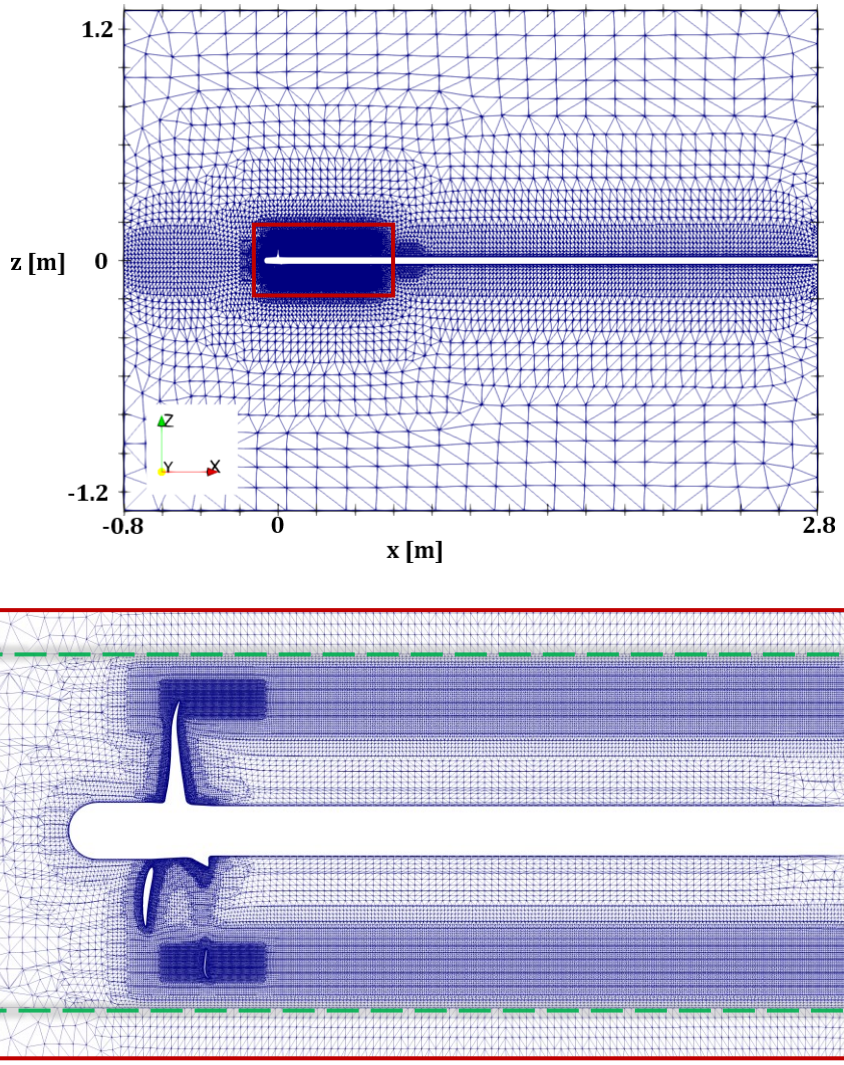

Fig. 50: P3193 propeller open water mesh

4.2.5 E779A

The E779A propeller is a historic camberless propeller design for a ferry vessel, investigated in 4-bladed straight flow open water configuration with a NACA 0020 rudder and a converging hub cap. At $J =$

0.88 and $\sigma_n = 1.2$ it produces a stable leading edge sheet cavity and a relatively large diameter stable cavitating tip vortex with a cavitating hup vortex, depending on the hub cap geometry. In model tests, it generates tip vortex grouping and merging at a certain distance downstream depending on the number of blades and advance ratio. [89] Besides the applicability of the approach to propeller-rudder combinations, the feasibility of the implemented AMR for the interaction of the cavitating tip vortex with obstacles in the slipstream and the suitability for acoustic prognoses is tested with RANS k-ω-SST for this case in non-cavitating and cavitating conditions with and without rudder. However, only the simulations in non-cavitating conditions are producing physical results with $k_T = 0.157$ without rudder and $k_T = 0.162$ with rudder compared to the experimental value of $k_T = 0.145$ without rudder.

It is modelled in a $l = 2.64 \cdot D_P$ square cross section cavitation tunnel geometry with a length $\Delta x = 11.5 \cdot D_P$ and the inlet $\Delta x = 5.4 \cdot D_P$ upstream. The hub cap is converging and the centrally located rudder at $x = D_P/2$ runs vertically through the complete cavitation tunnel. AMR is employed at a converged stage in the simulation with an initial mesh with $30.6 \cdot 10^6$ cells and $178 \cdot 10^3$ faces on the propeller with a distance refined tip and $737 \cdot 10^3$ faces on the rudder, which features a pre-refined boundary layer and highly refined leading and trailing edges as a result of the restrictions of AMR in the vicinity of surfaces. In Fig. 51 the mesh is illustrated with the rotating region marked with a green dashed line and the refinement zone confinement indicated by the blue dashed line. An additional tip and hub vortex disk and cylindrical refinement are included with protected cell zones in between, in order to reduce the number of cells during runtime, as well as a refinement between the radii of the tip vortex intersection with the downstream end of the AMI. With a $Q > 5 \cdot 10^3 s^{-2}$ refinement criterion a numerically stable AMR is achieved for some refinement levels, however, higher refinement levels lead to instabilities.

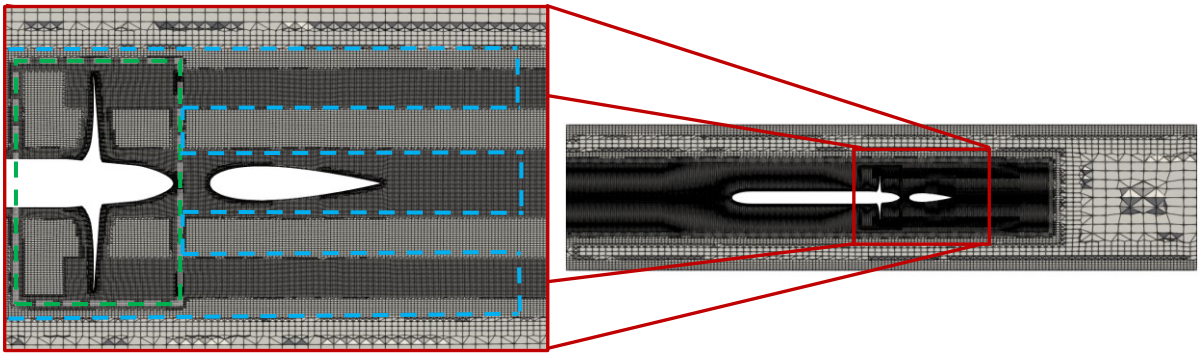

Fig. 51: E779A propeller open water cavitation tunnel mesh

4.3 Propulsor-Hull Configurations

4.3.1 ProNoVi Reference Target Case

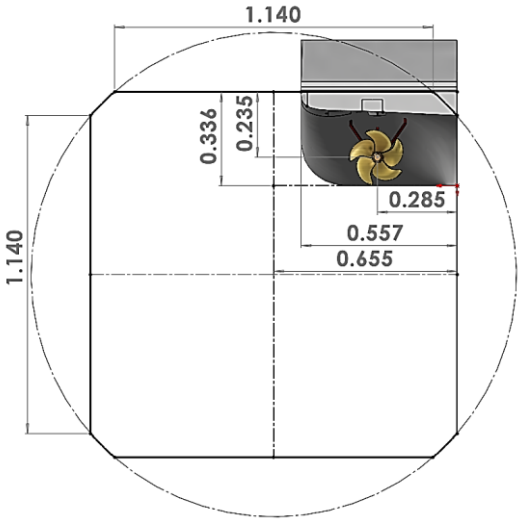

Fig. 52: ProNoVi reference target case cavitation tunnel [80]

A $L_S = 130m$ twin-screw mega yacht in model scale $\lambda = 21.08$ and full-scale is the main investigated case with two conventional shaft lines with rotation direction inwards over the top, which are installed with a $\Delta z = 0.31 \cdot D_P$ tip clearance. There is one shaft bracket far upstream and two immediately in front of the propeller implemented with shaft fairings on the 2.75° inclined shaft line. For this vessel the P1595 and P3193 propellers given in Table 8 are examined as an acoustically unoptimized and an optimized solution, with the first one without and with rudder in the cavitation tunnel experimental setup and the latter with rudder in the cavitation tunnel setup and a quasi-infinite domain. Depending on the propeller a converging (P1595) or a converging-diverging (P3193) propeller hub cap is installed and a twisted rudder is located centrally on the shaft axis downstream of the propeller. For these cases experimental data exists in model and full scale, which is used to analyze the feasibility of the proposed simulation approach as well as its limits and the quality of the cavitation and noise prediction methods. The investigations give an insight into the influence of the domain size, the propeller design and in combination with the open water simulations the effects of the hull, as well as a quantification of noise scaling. All cases are simulated with RANS k-ω-SST and subsequently implicit LES.

The cavitation tunnel setup cross section is given in Fig. 52 with the inlet at $\Delta x = 48 \cdot D_P$, while the quasi-infinite domain extends $\Delta x = 490 \cdot D_P$ upstream. Both are simulated with a solid wall at the centerline to replicate the acoustics of the cavitation tunnel measurements, however, the quasi-infinite domain has symmetry boundaries at the remaining sides. Due to the shaft line inclination the meshing setup is tilted around the y-axis in order to create a sliding mesh interface aligned with the initial block mesh, which avoids anisotropic snapping of the faces and thus reduces the risk of flux interpolation issues during runtime. In Fig. 53 (a) the size difference of the quasi-infinite domain (grey) and the cavitation tunnel setup (red) is illustrated with the complete cavitation tunnel mesh and an identically sized section of the quasi-infinite domain mesh, which is increasingly coarser with distance from the propeller as the walls are located in the far distance. This leads to the advantage that there are no high frequency pressure reflections at the quasi-infinite domain walls, as most of the low wavelength information is dissipated before reaching the walls. The cell count of the initial meshes are between $19 - 25 \cdot 10^6$ cells with around $\approx 0.8 \cdot 10^6$ faces on the propeller with $> 95\%$ layer coverage and around 10 layers. In (b) the circular sliding mesh interface as a green dashed line for the P3193 case with rudder is located around the propeller with axial restrictions imposed by the shaft brackets upstream and the rudder downstream, which leads to information loss before the slipstream reaches the rudder. In the case without rudder displayed in (c), with the rudder location indicated in transparent black, the line labelled *AMI-NoRudder* indicates the extent of the sliding mesh interface, which leads to improved

information conservation on the mesh in the slipstream and thus higher resolution of trailing vortices. Also visible are the initial ring and circular refinements around the axis of rotation up to $r/R = 0.15$ and between $0.84 < r/R < 1.03$. All cases feature initial refinements in the hub and tip vortex region as cylinders and disks respectively. In the case without rudder a one-time manual a prior AMR is employed after convergence of the implicit LES by rotating the $Q = 1 \cdot 10^5 s^{-2}$ criterion isosurface as described in 3.4.2 and illustrated in Fig. 37. For the full-scale setups the water-air interface is imported from precursor two-phase simulations, where the wave pattern is generated to achieve correct reflections in the hydrodynamic solution and the water depth is $\Delta z = 40m$, with the inlet located at $\Delta x \approx 70 \cdot D_P$ upstream.

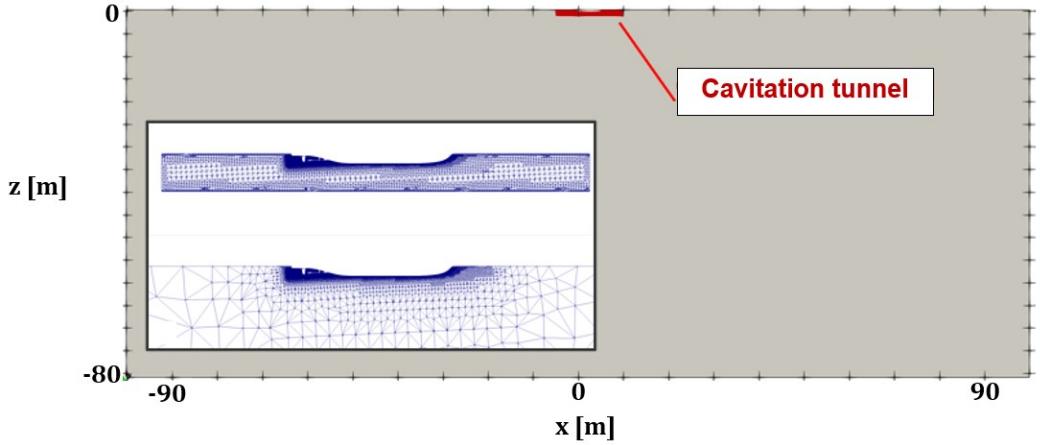

(a) P3193 cavitation tunnel and quasi-infinite domain

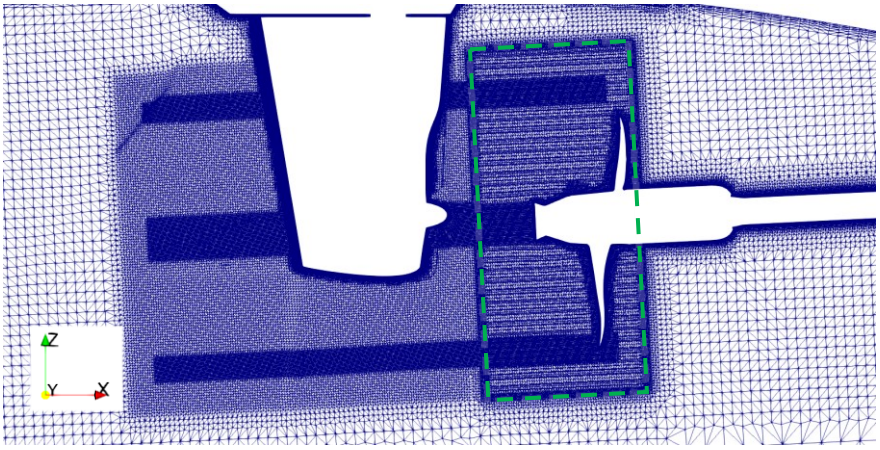

(b) P3193 propeller region

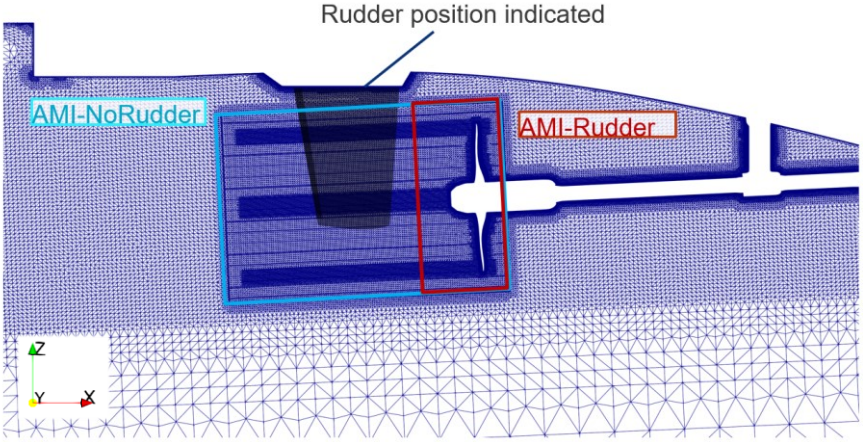

(c) P1595 without rudder propeller region [80]

Fig. 53: ProNoVi reference target case mesh

Table 14: Investigated operation points for the ProNoVi reference target case

Setup	$k_T[-]$	$\sigma_n[-]$	$n\ [Hz]$	$J\ [-]$
P1595 C1	0.302	2.00	28.0	0.63
P3193 C2	0.274	1.20	32.0	0.64
Full scale	0.236	1.57	3.1	0.80
Full scale	-	1.20	3.1	0.64

Achieved thrust in the simulations for the investigated operation points in model scale and in full-scale are summarized in Table 14. As mentioned in Chapter 3 the thrust is the control quantity to set the operation point for these cases, as neither torque nor relative water velocity measurements are available for some of the experiments. The iterative nature of the approach yields a final error in k_T of $+0.3\%$ (P1595) and $+2.9\%$ (P3193) respectively. For the quasi-infinite domain a different inflow speed of $J = 0.71$ is set to achieve the cavitation tunnel k_T with an error of 2% in the case of the P3193-C2 simulation due to the missing obstruction effects by the vessel hull in the cavitation tunnel illustrated by the velocity field in Fig. 15. A simulation matrix for the model scale operation points is given in Table 15. All cases have been investigated with the standard approach described in Chapter 3 with RANS, RANS with cavitation, and LES with cavitation.

Table 15: Investigated cases ProNoVi reference target case

Type	Propeller	Rudder	AMR	Domain
Experiment	P1595	0/1		Cavitation tunnel
Experiment	P3193	0/1		Cavitation tunnel
Simulation	P1595	0	X	Cavitation tunnel
Simulation	P1595	1		Cavitation tunnel
Simulation	P3193	1		Cavitation tunnel
Simulation	P3193	1		Quasi-infinite
Full-scale Experiment	P3193	1		Water Surface+Ground
Full-scale Simulation	P3193	1		Water Surface+Ground

For the acoustic evaluation there are 16 pressure sensors located above the propeller in the hull for the experiment, which are also placed in the simulation in model and full-scale as mapped in Fig. 54 (a). Since the pressure is known at all volume cells and at the boundary surface faces, the complete area indicated in (b) may be monitored over the acoustic simulation, to evaluate blade harmonic pressure distribution on the hull with a higher spatial resolution. To evaluate the directivity of the noise emissions, a passive control surface that reports the pressure over the simulation runtime, similar to the KFWH surface is placed around the propeller for instance as sphere shown in (c) and the complete vessel as a rectangular box. While the KFWH surface is a cylindrical surface around the sliding mesh interface, the directivity interrogation surface around the propeller is a sphere to be able to normalize all directions equally to a monopole source located at the propeller center.

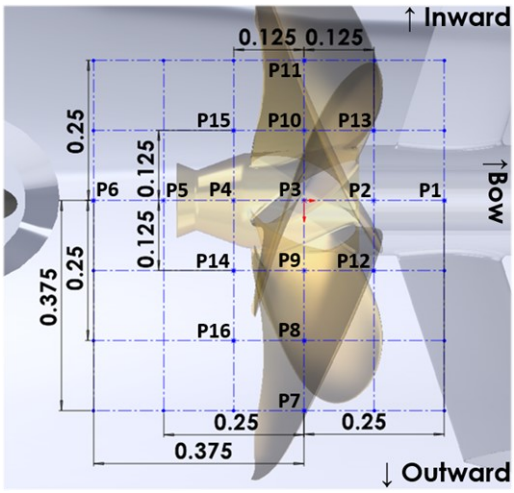

(a) Pressure pick ups [90]

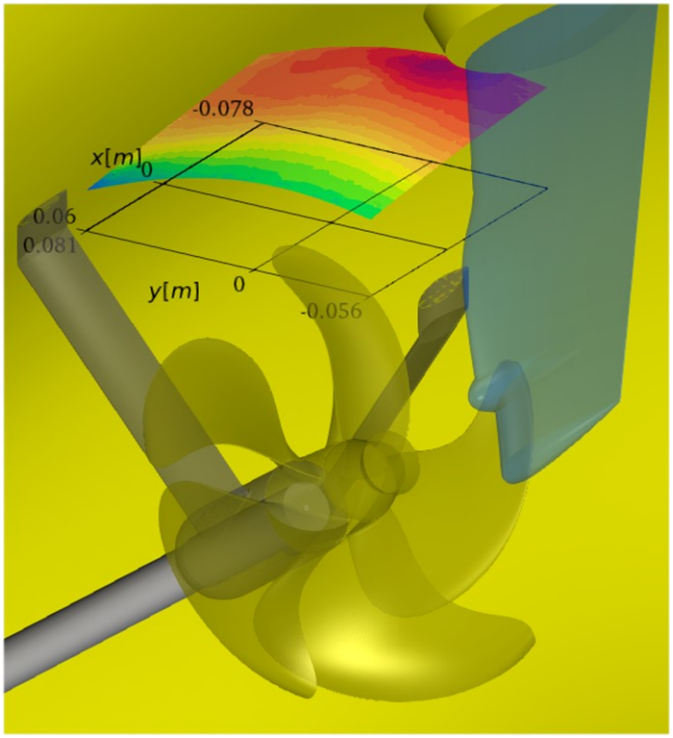

(b) Boundary surface patch [91]

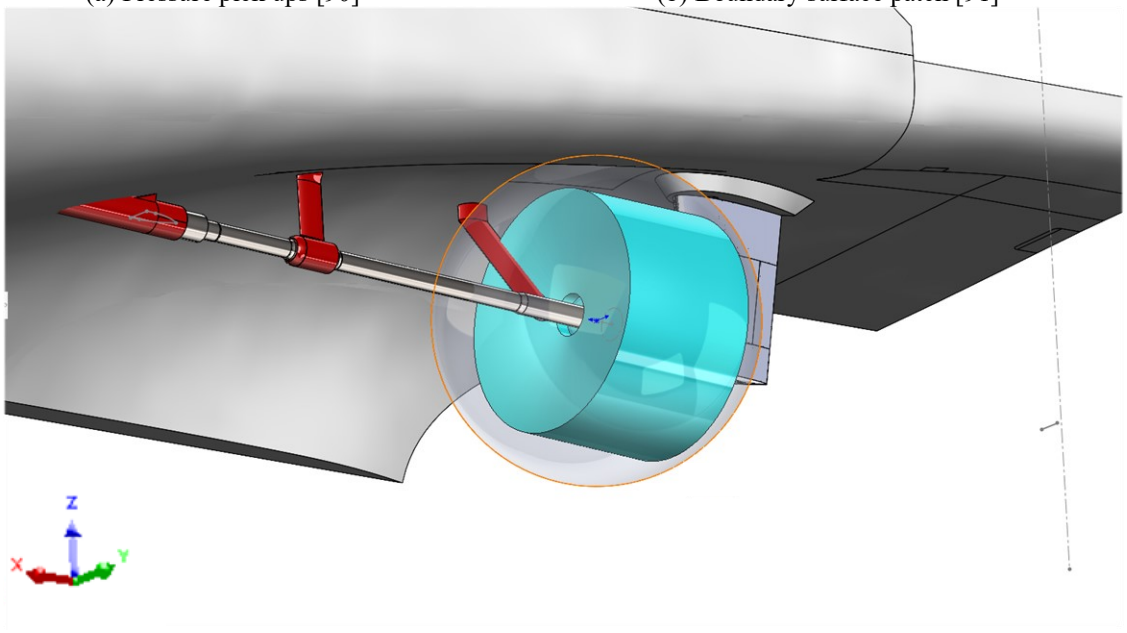

(c) Directivity interrogation surface [91]

Fig. 54: ProNoVi reference target case acoustic monitoring

4.3.2 ProNoVi SCHOTTEL Target Case

A $L_S = 145m$ single screw generic container feeder vessel with a $D_P = 5.8m$ conventional propeller on a horizontal shaft line is simulated in full-scale at $J = 0.89$ with $n = 1.85Hz$ and $\sigma_n = 1.87$ at $r/R = 0.7$. It features a straight rudder with a bulb immediately downstream of a circular hub cap and has a propeller tip clearance of $0.25 \cdot D_P$. There is periodic suction side leading edge cavitation at the outer radii sections with strong reentrant jets that detaches completely from the suction side after passing the 12 o'clock position. This case applies the developed methods to a further use case, with the objective of quantifying pressure pulse prediction methods by comparing them to available scaled model test measurements. The wave pattern is extracted from a precursor two-phase flow simulation at the same velocity. Due to the centerline screw a full hull geometry has to be simulated, leading to a mesh in Fig.

55 (a) with around $20 \cdot 10^6$ cells and $1.44 \cdot 10^6$ propeller faces. There is a conical refinement between $r/R = 0.89$ to 0.91 and up to $r/R = 1.01$ for $\Delta x = 1.12 \cdot D_P$ just downstream of the rudder as shown in (b) together with the sliding mesh interface in green. For this case the pressure is monitored at hull locations specified by the experiment with FVM and KFWH pressure probes. All 17 pressure monitoring locations are given in (c) with the shaft bulb and the rudder, as well as an indication of the propeller, with P10 located directly above the propeller.

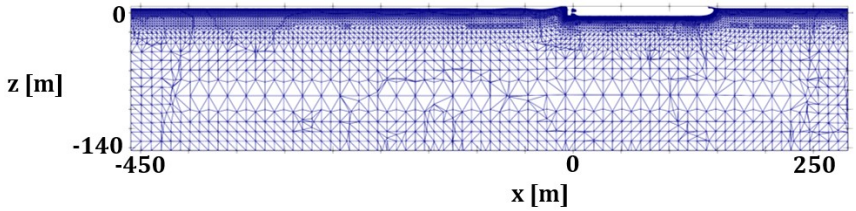

(a) Domain with water surface and ground

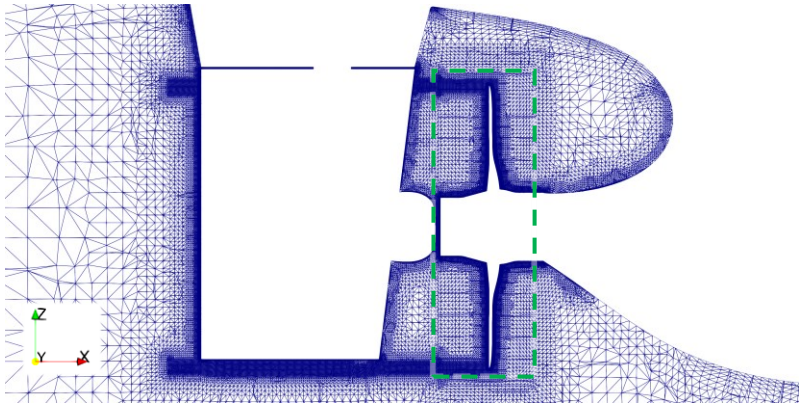

(b) Mesh at propeller with sliding interface/KFWH surface

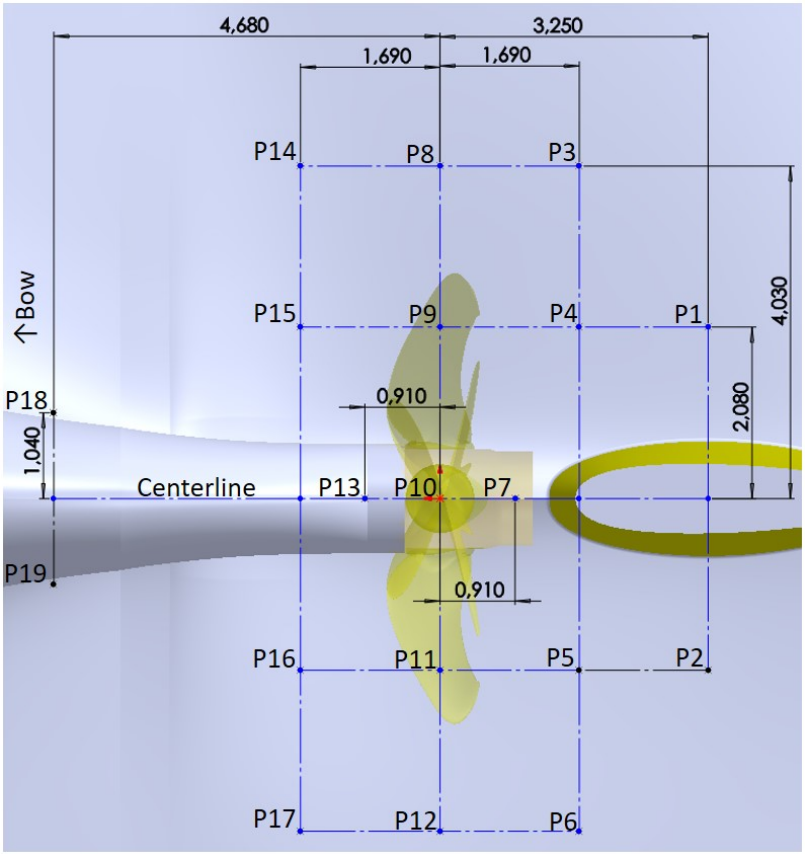

(c) Pressure pick ups

Fig. 55: ProNoVi SCHOTTEL target case [92]

4.3.3 Red-Emi SCHOTTEL Target Case

On this $L_S = 130.3m$ double ended ferry a 5° inclined SCHOTTEL SRE490 azimuthing propulsor in pull configuration is installed on the centerline at each end with both units at 0° steering angle and the front unit propellers in free sailing condition. The 3D-model with a refinement box around the unit and a disk refinement region at the propeller tip vortex is pictured in Fig. 56 (a). It has a controllable-pitch propeller diameter of $D_P = 3.1m$ with an immersion of $1.3 \cdot D_P$ and an operation point of $J_S = 0.85$ and a full-scale propeller speed of $n = 2.81Hz$. This test case extends the applicability to complete propulsion units and is used to further validate the approach with full-scale URN measurements conducted at this operation point in deep water. The wave pattern established in a two-phase precursor simulation is visualized in Fig. 56 (b), which is boundary for the full-scale mesh with cells.

The investigated operation point is summarized in Table 16 and is evaluated from mean values across the acoustic measurement window for the full-scale experiment. In the simulation the azimuth angle, propeller pitch, rotation rate and vessel speed are imposed, thus only the power remains to evaluate the simulation accuracy. However, the power measured on the vessel is the generator power and not the power at the propeller, which means, it can only be interpreted as an upper limit for the operation point. The achieved power in the simulation at the propeller is $P = ■■■■kW$, which is by assumption of 3% mechanical losses still 12% below the measured value. This seems plausible as there must be additional losses in the connection, converter, and e-motor, which are estimated to be in the order of magnitude of 10%.

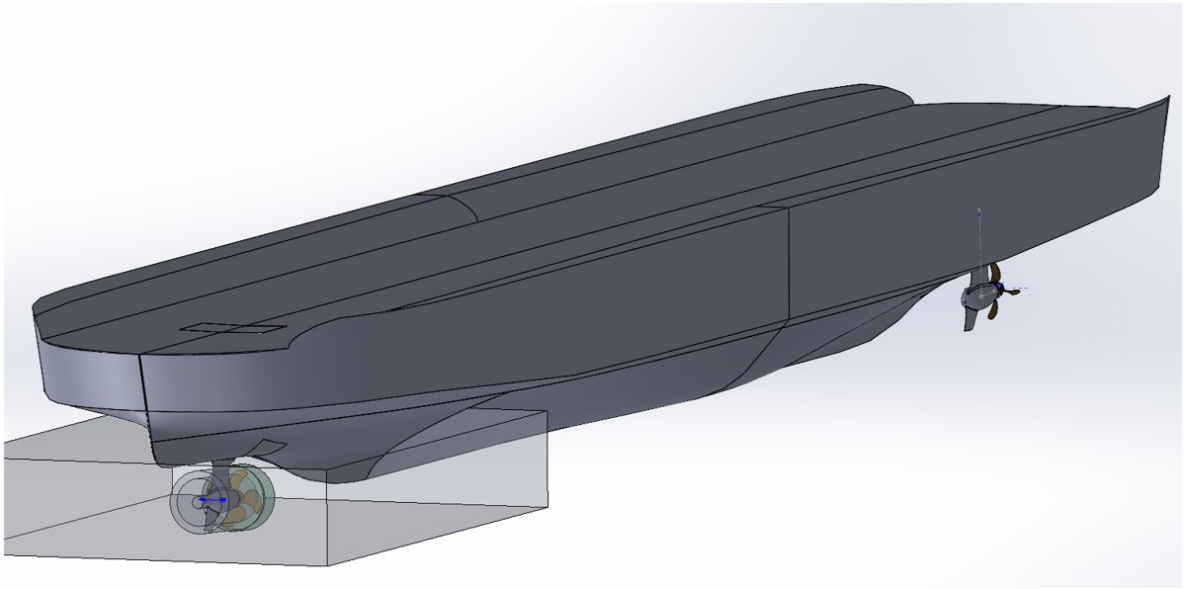

(a) Vessel and Propulsor with refinement box

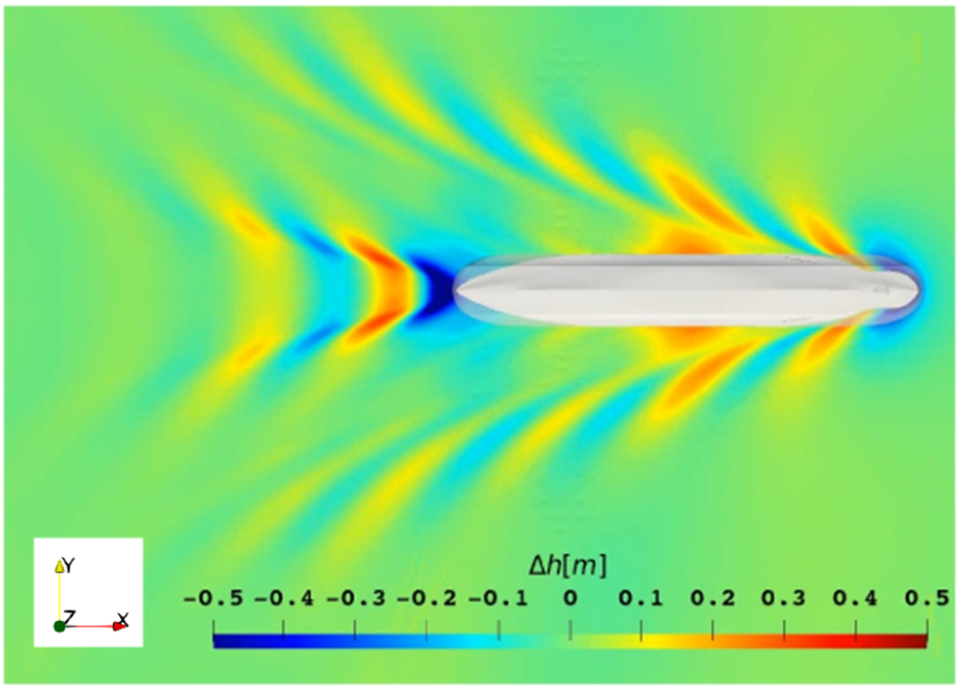

(b) Wave pattern for domain top

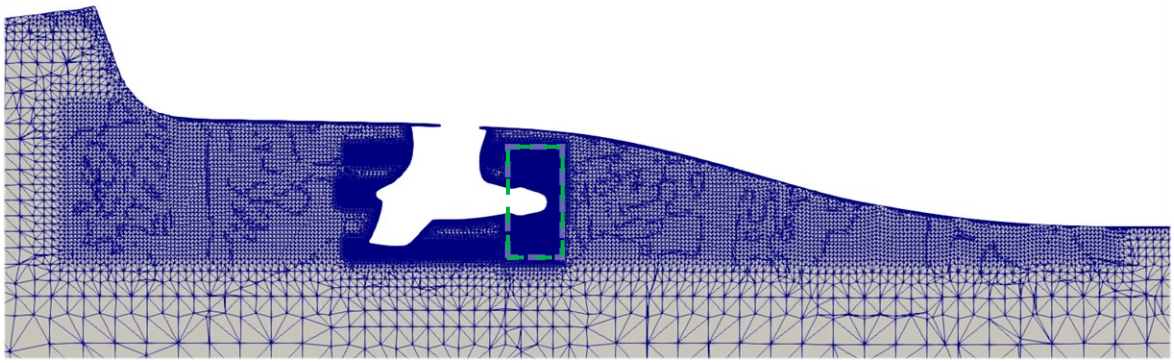

(c) Mesh at propeller with sliding interface/KFWH surface

Fig. 56: Red-Emi SCHOTTEL Target Case

Table 16: Investigated operation point for the Red-Emi reference target case

Azimuth	Input Speed	Pitch	Pitch $r/R = 0.7$	Measured Power	Vessel Speed
[°]	$[rpm]$	[%]	[°]	$[kW]$	$[kn]$
180.8	169.5	34.1	27.52	[redacted]	14.4

4.4 Summary

In this chapter the test cases investigated as part of this work are presented with their geometrical discretization for the numerical realization of the simulations. The complexity is increased stepwise with non-cavitating and cavitating hydrofoils, propellers in straight flow open water condition and propulsion units with vessels in a multitude of configurations. The hydrodynamic solution typically agrees well with the experiments with both RANS and LES turbulence modelling according to the integral forces and moments on the propeller, which is expected. However, some difficulties in measurement procedures lead to slight deviations. With the results from these test cases readily available the open research questions posed in the Introduction in 1.3 may be answered in the following chapters.

5 Investigation on Influence Factors of Ship Radiated Noise

In this chapter relevant influences that are believed to affect the simulation of noise emissions are investigated using the methods described in Chapter 3. The physical phenomena pertaining to the objective of understanding underwater noise generation for propulsion systems are investigated and interpreted by analysis of the results of the test cases described in Chapter 4. Most important identified factors that influence ship radiated noise are:

- Turbulence, specifically the interacting boundary layer and vortices,
- Cavitation,
- Turbulence cavitation interaction phenomena,
- Influence of structures around the propeller,
- Geometric scale of the simulation.

Following the evaluation of these isolated effects, conclusions regarding the numerical capturing of the related physical phenomena with these methods and the underlying physics of the phenomena themselves are drawn in order to provide best practice approaches. The sections are centered around the single contributors to noise with the trailing vortices, cavitation and in the final section, the interaction of turbulence-cavitation with secondary structures such as a rudder shape in the propeller slipstream or a vessel wake upstream of the propeller. As final investigation the influence of the scale on the flow field results and the subsequent noise emissions is presented.

5.1 Turbulence

5.1.1 Numerics

Turbulence is the main source of volumetric noise without cavitation and is thus under special consideration in the proposed approach. For propellers and ship hulls the time and length scales for the simulations are vastly different, thus the capabilities of LES to resolve the turbulence at all time and length scales that typically occur in propeller-hull combinations are investigated. For this purpose velocity probes are positioned upstream, downstream near the shear layer and in the tip-vortex of the NACA 0012 hydrofoil experiment setup, as well as in the wake field of the ProNoVi reference target case vessel in model scale just before the propeller. The location of the velocity observers and the corresponding results in the turbulent frequency spectra for the hydrofoil are given in Fig. 33 and Fig. 34 respectively. Due to the similarity of the slopes between $10^2 Hz < f < 10^4 Hz$ to the turbulent frequency spectra in the inertial subrange, LES may be used to resolve the turbulence in this case. For the larger time and length scales of complete vessels, the accuracy is also adequate as can be seen by the comparison of the full-scale effective wake field with RANS and LES for the ProNoVi reference target case in Fig. 57 and the ProNoVi SCHOTTEL target case in Fig. 58. RANS simulation is used in this comparison for the baseline data, as it is known that the hull flow is well resolved in this case. At $\Delta x = -0.25 \cdot D_P$ the effective wake field is averaged over 6 rotations with a sampling frequency of $f_s = 1°$ for both cases, with the propeller area with the radii sections $r/R = 0.3 - 1.0$ indicated with the circles. In (a) the difference for the Cartesian velocity components is shown, whereas (b) shows the local difference of the time series fluctuations. For the ProNoVi reference target case this comparison only yields little deviation with maximum values around $\Delta V_x/V_A < 10\%$ between the hull of the vessel and the propeller radius $r/R = 1.0$ and high values between the shaft brackets on the inward side. Near the hull the insufficient resolution of the boundary layer is indicated with high deviations in x-direction. Overall, mean values of less than $\Delta V_i/V_A < 2\%$ are achieved. For the fluctuations given as standard deviation, the outstanding feature is the large area of difference between the shaft brackets, which is naturally resolved better time scale wise for the LES case leading to larger discrepancies than the surrounding regions.

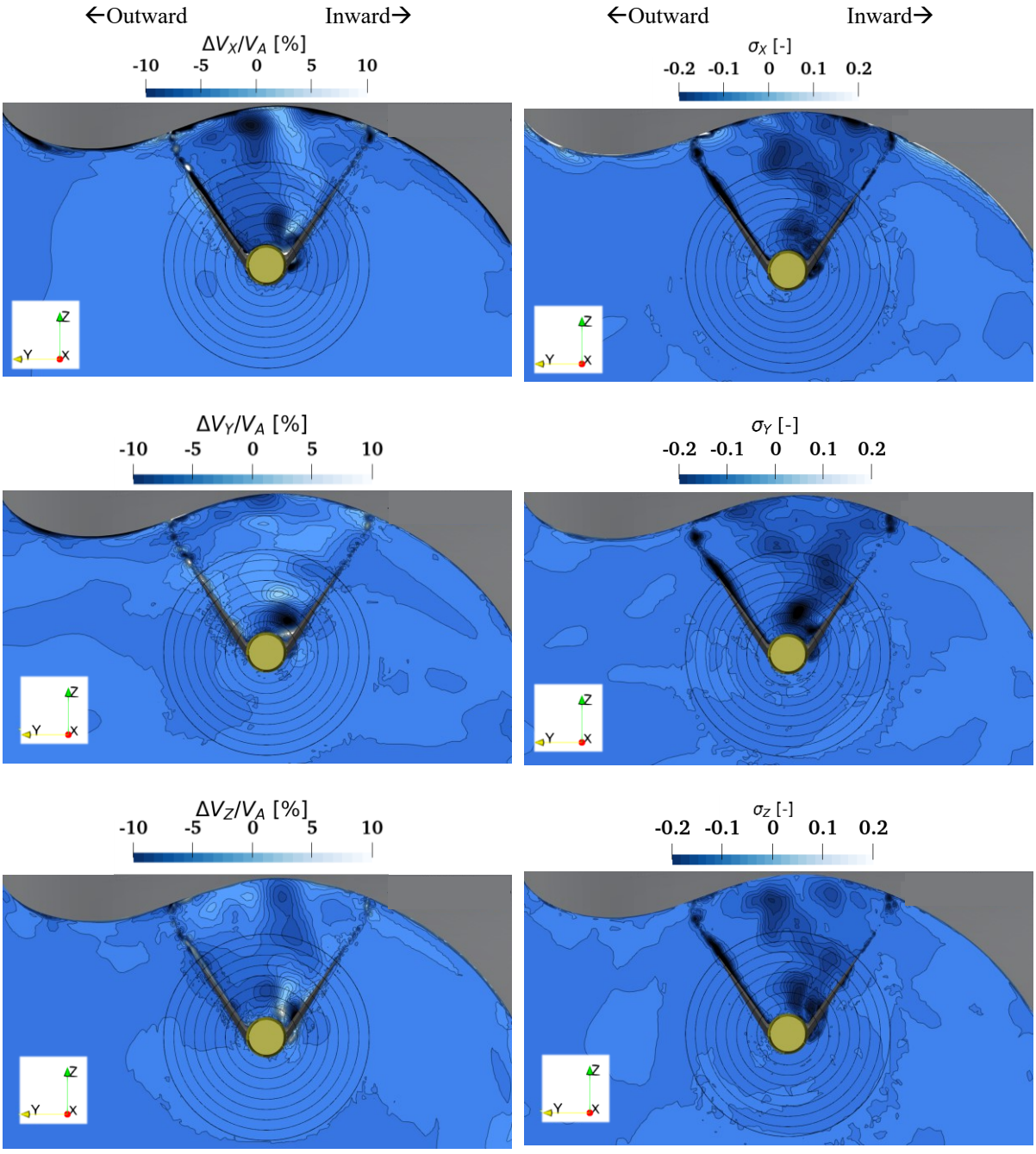

(a) Velocity difference (b) Velocity standard deviation difference

Fig. 57: ProNoVi reference target case wake field comparison RANS-LES [92]

For the ProNoVi SCHOTTEL Target Case the difference between the turbulence resolving strategies of RANS and LES is generally lower, as there are no strong fluctuations in the inflow to the propeller for this single screw vessel. As mentioned before, the highest discrepancy occurs in x-direction, with the mean in the propeller plane and values of less than $\Delta V_x/V_A < 2\%$. Due to the limited amount of fluctuations in the wake field, the standard deviation in (b) shows similar results for the turbulence resolution with RANS and LES. Both wake field comparisons for single screw and twin screw vessels in model and full-scale respectively confirm that the approach may be utilized to resolve large scale turbulence for marine vessels.

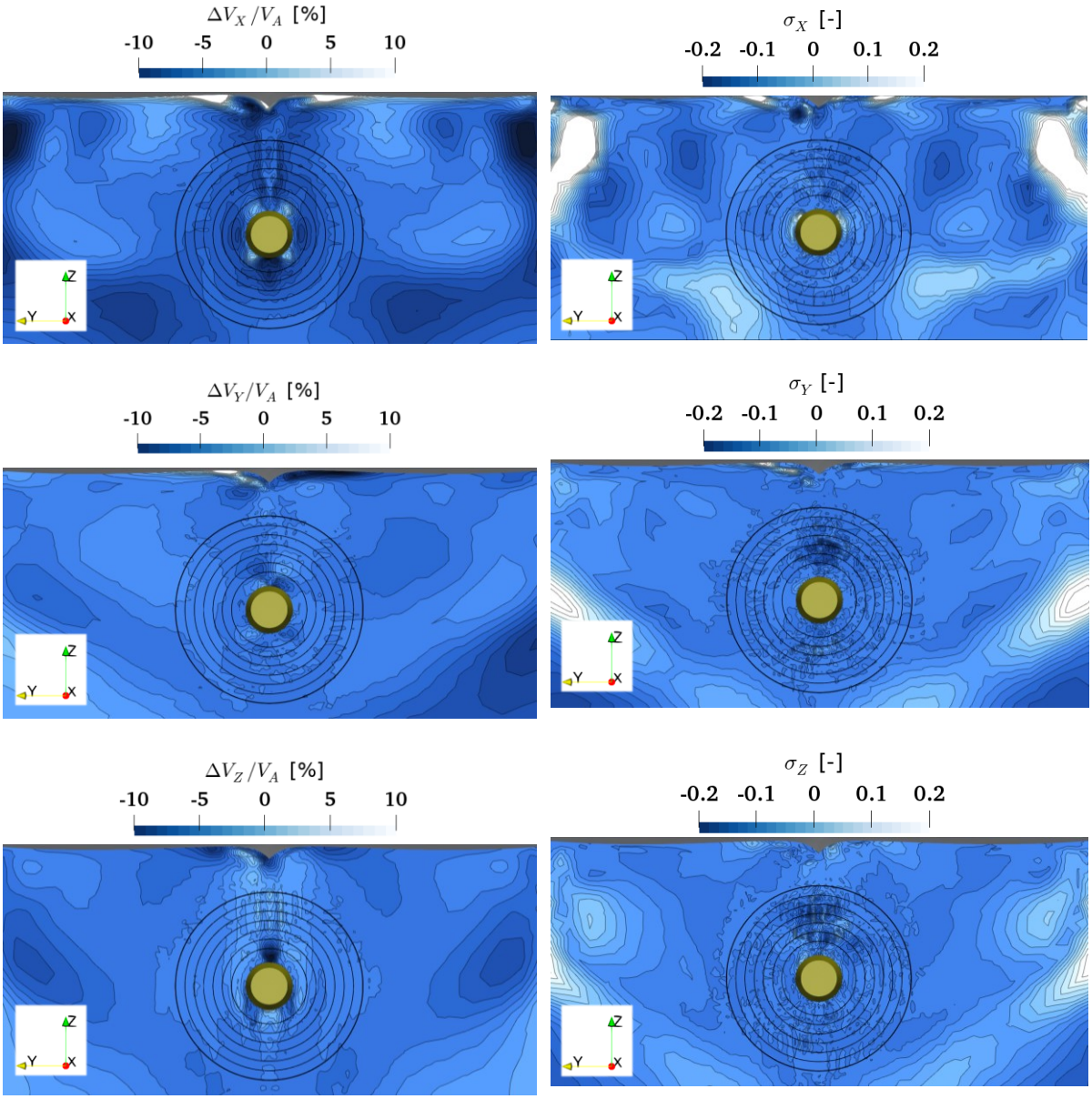

(a) Velocity difference (b) Velocity standard deviation difference

Fig. 58: ProNoVi SCHOTTEL target case wake field comparison RANS-LES [92]

In order to be able to validate the propeller slipstream acoustic sources the derived flow quantity of circulation Γ is compared between experiment and simulation. Beforehand to validate the evaluation method for CFD, the slipstream streamwise normal plane for the PPTC'11 at $x/D_P = 0.094$ is compared between the experiment and the k-ω-SST simulation for similar operation points, which are $J = 1.019$ and $J = 1.262$ in the simulation and $J = 1.253$ in the wake measurement. On this plane a tip vortex intersection location is identified, and the circulation is obtained from a closed loop integration along a circle with three different center definitions. The report velocity data is brought into a viable form from raw data in Fig. 59 (a) to processed data in (b) to be able to undergo similar evaluation procedures as a simulation result.

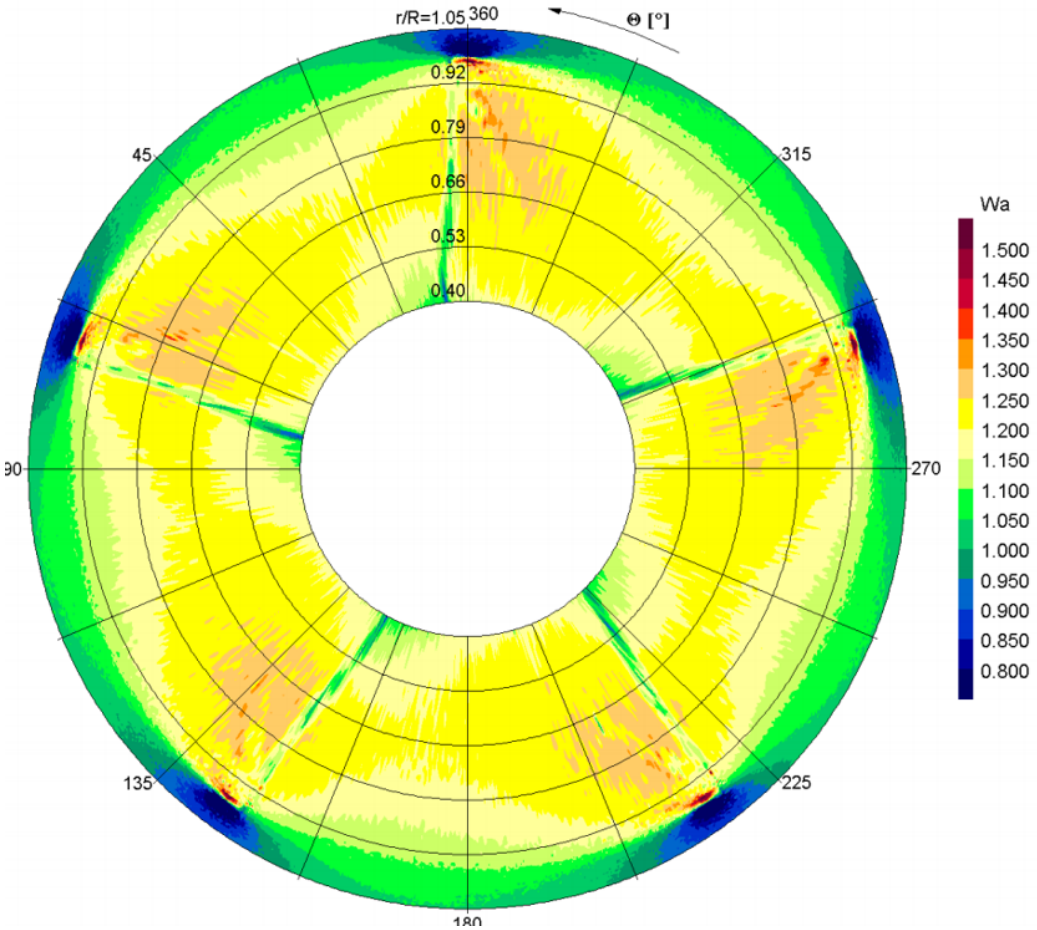

(a) SVA-Report [22]

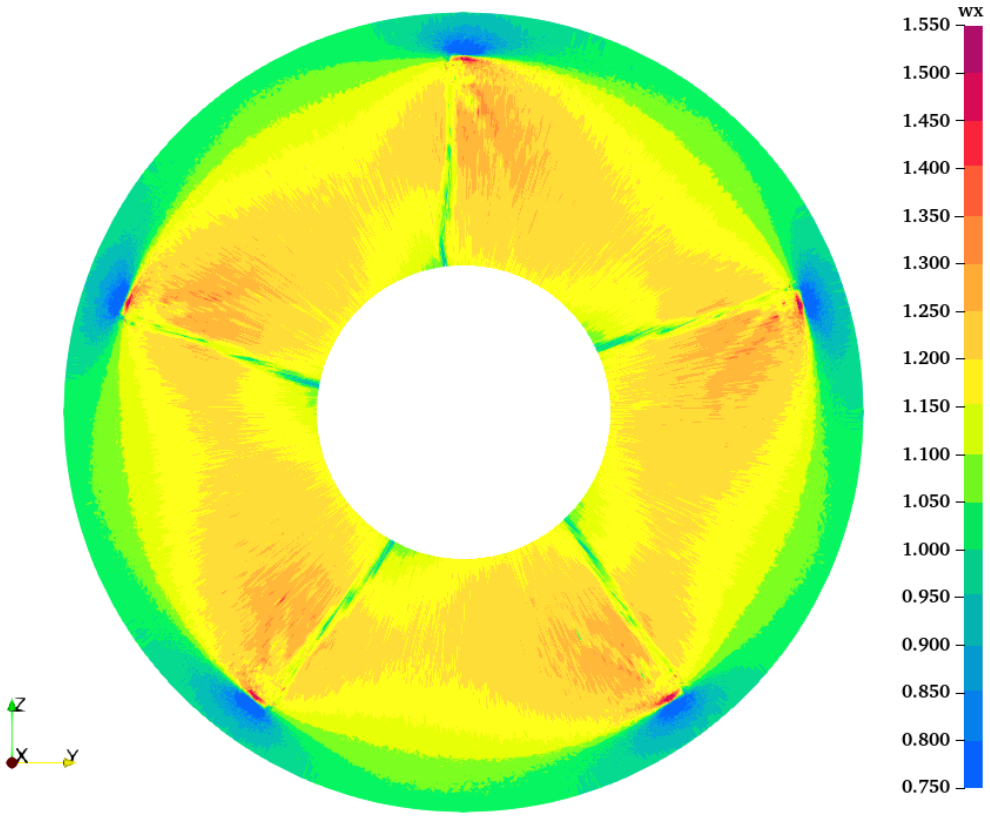

(b) Processed report data

Fig. 59: Reading algorithm of wake field data

With this data and the simulation results, different circular integration loop center locations are applied in Fig. 60 for the non-cavitating k-ω-SST simulation with $J = 1.019$. In (a) the minimum velocity indicated by the magenta sphere is the center of this circle, in (b) the minimum pressure obtained by the Bernoulli relation from the velocity field is used and in (c) the helix coordinate obtained by the trajectory established by the pitch of the propeller at the radii section $r/R = 1.0$ is the center. The closed loop integral is indicated by the magenta circle with an arbitrarily selected radius of $r = 0.0048 \cdot D_P$ for both simulation and experiment.

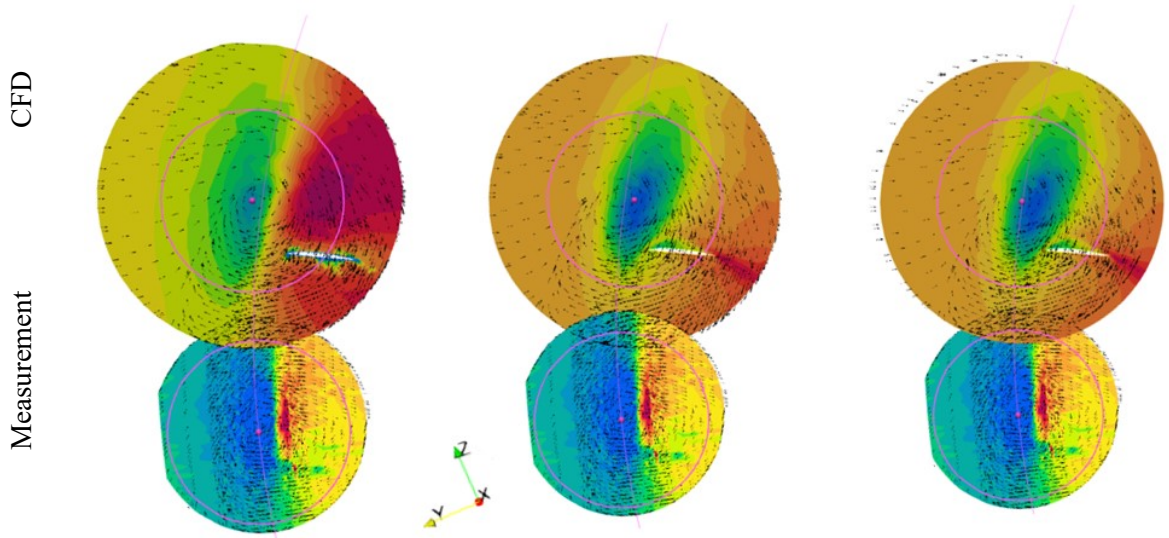

(a) $min(|\vec{U}|)$ (b) $min(p)$ (c) $x(f_h)$

Fig. 60: Comparing tip vortex velocity CFD vs. Experiment

A comparison of the circulation results is summarized in Table 17, with the difference between the measurement and the closest simulation advance ratio of $J = 1.262$ and the difference between the two simulated advance ratios. While the difference between the simulation results for the two advance ratios is quite significant, the difference between the similar advance ratios with a distance of 0.8% in J is rather low with a deviation of around 6%. Therefore, the evaluation of circulation from the simulations can be assumed as validated.

Table 17: Circulation at $x/D = 0.94$ for the PPTC'11 $J = 1.019$ case

Evaluation type	CFD $J = 1.262$ $[m^2/s]$	CFD $J = 1.019$ $[m^2/s]$	Exp. $J = 1.253$ $[m^2/s]$	$J = 1.019$ (CFD) vs $J = 1.262$ (CFD) [%]	$J = 1.262$ (CFD) vs $J = 1.253$ (Exp.) [%]
$\Gamma(min(p))$	0.01761	0.02862	0.01902	62.5	7.41
$\Gamma(min(\vec{U}))$	0.01709	0.02559	0.01835	49.7	6.87
$\Gamma(x(f_h))$	0.01709	0.02741	0.01828	60.3	6.51

An important aspect for the noise of the blades and the slipstream evolution of turbulence is the accurate boundary layer modelling. The boundary layer on the propeller blade is directly connected to the thickness and loading noise of the propeller by viscous interaction with the fluid medium. For the boundary layer the LES may either be wall modelled or resolved, while the resolved case is preferred it creates more numerical effort. Thus the capturing of the near wall velocity gradients is analyzed with a numerically feasible mesh. For different outer radii sections, the boundary layer wall-parallel velocity is given for $c = 25\%$, 50% and 75% in Fig. 61 for the PPTC'11 $J = 1.019$ case for RANS with a modelled and a resolved near wall and with implicit LES. As RANS is assuming a fully turbulent boundary layers inherently as a result of the turbulence model, the laminar turbulent transition is not

captured. In the turbulent region at $c = 75\%$ all simulation agree well. At $r/R = 0.7$ the difference of the normal velocity gradient at the chord length 25% and 50% is significant, however, this means that the LES may resolve the tendency of the less disturbed flow near the wall as a result of lower amount of turbulent fluctuations. Overall the number of cells in the boundary layer may be insufficient for the LES, which equals a y^+ of about $5 - 15$ in this particular case. For the simulations with the other open water propellers and the propeller-hull configurations the value is reduced to $y^+ < 1$, as a result.

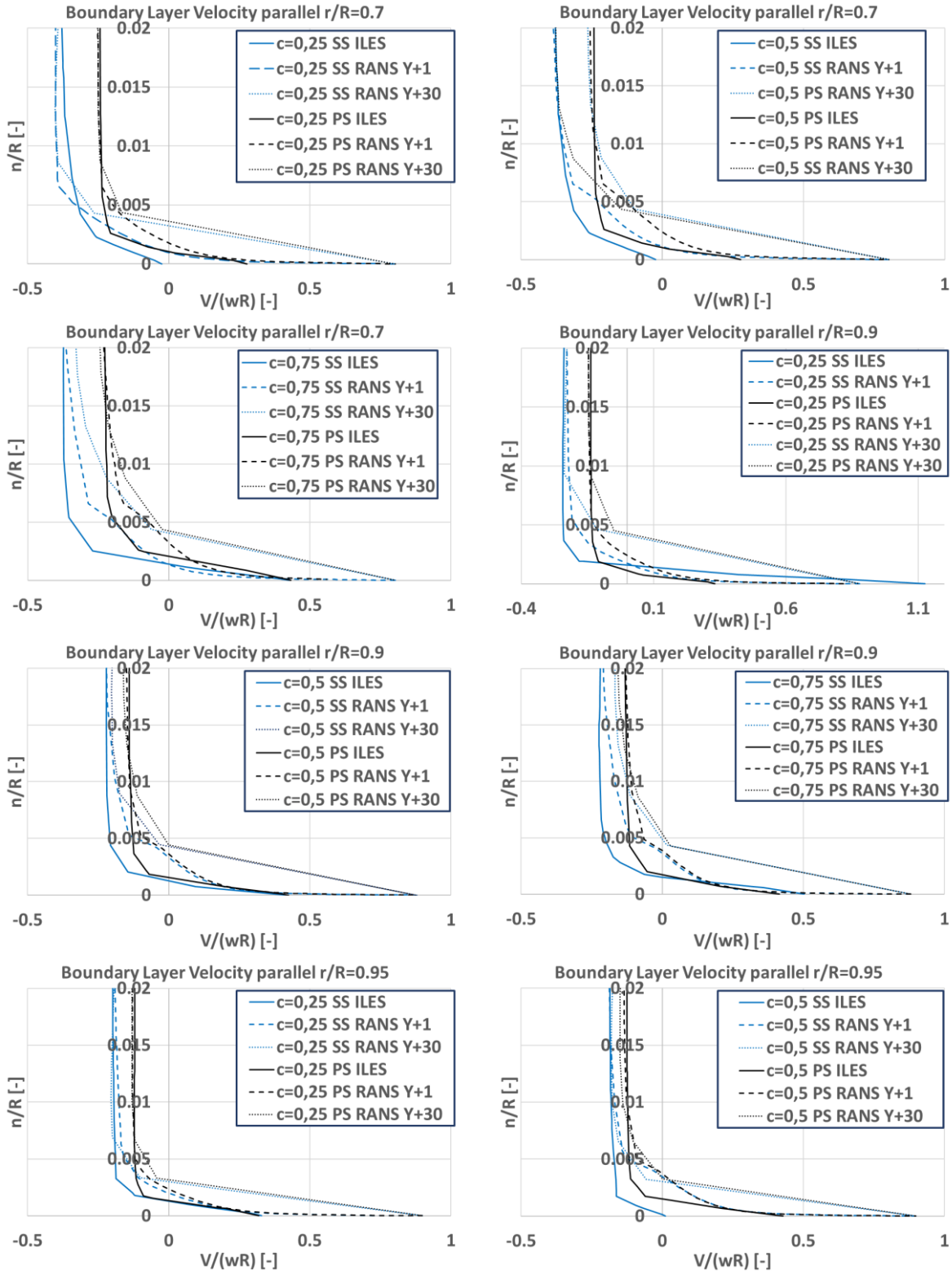

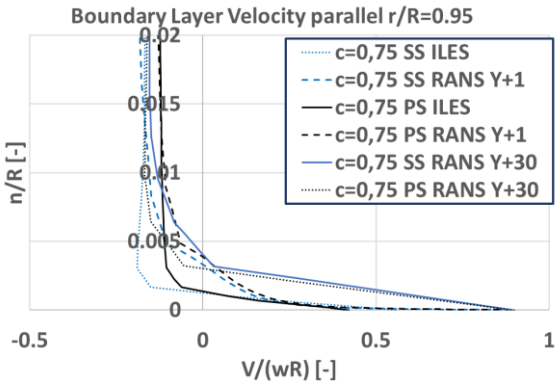

Fig. 61: Boundary layer velocity profiles, PPTC'11

In the propeller slipstream the LES approach is required to resolve the tip vortex with high accuracy in order to capture the turbulence-cavitation interaction of the cavitating tip vortex, which is considered to be a dominant source of radiated noise. The region between the two black circle sections indicating $r/R = 0.95$ and $r/R = 1.00$ in Fig. 62 contains the tip vortex intersection at $x/D_P = 0.2$ for the PPTC'11 $J = 1.019$ case. The axial velocity distribution gives an indication of the tip vortex extent and the resolution. With k-ω-SST the most dissipated resolution of the tip vortex is achieved, followed closely by the k-k_l-ω model, the transition model achieves a higher velocity and the LES achieves the least dissipated result. Comparing the time discretization schemes in (d) and (e) the second order backward scheme experiences, as expected, less dissipation.

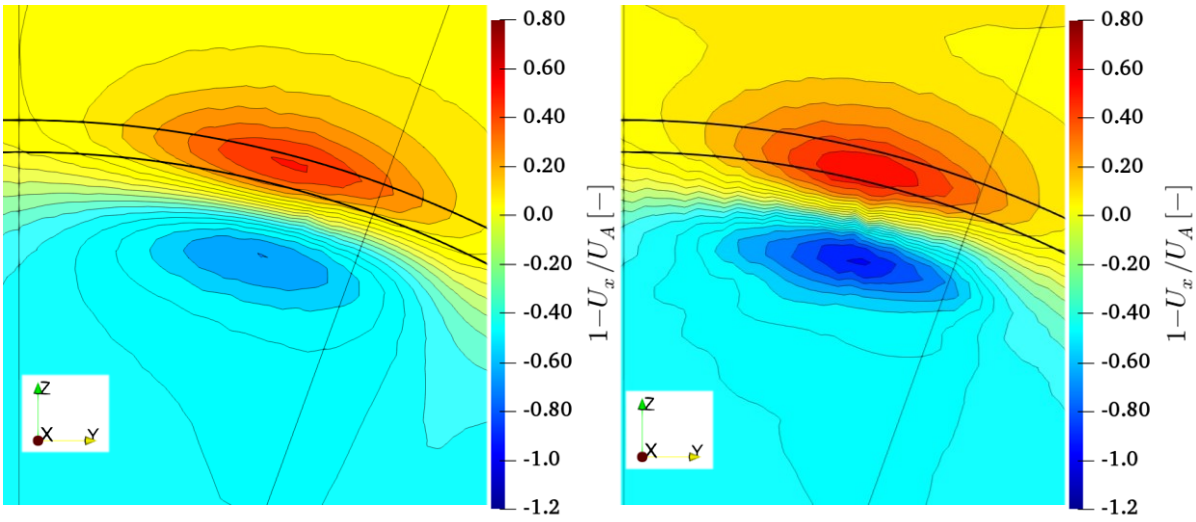

(a) RANS k-ω-SST

(b) RANS γ-Re$_\theta$

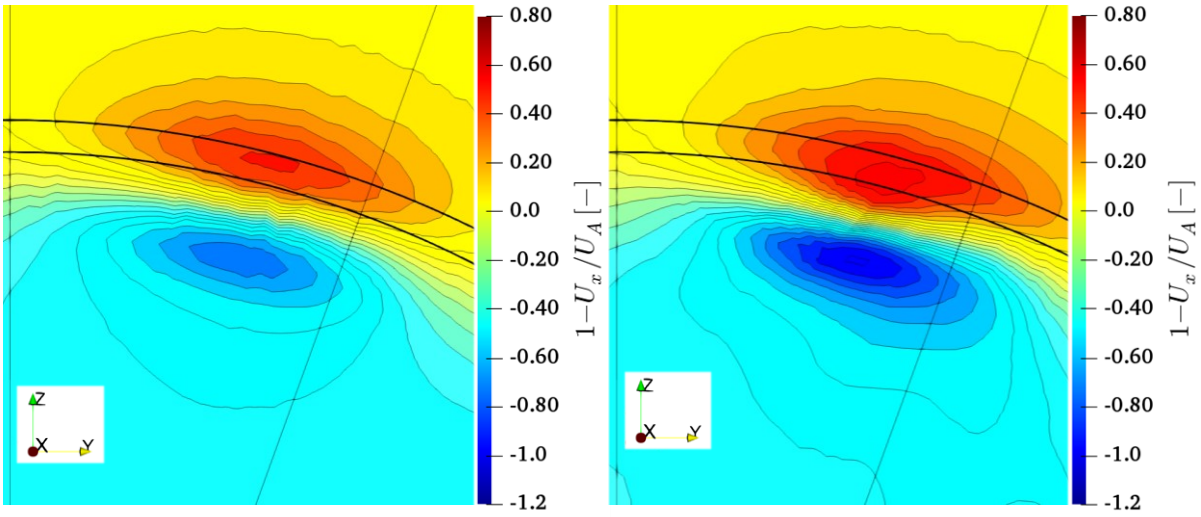

(c) RANS k-k_l-ω

(d) ILES Euler

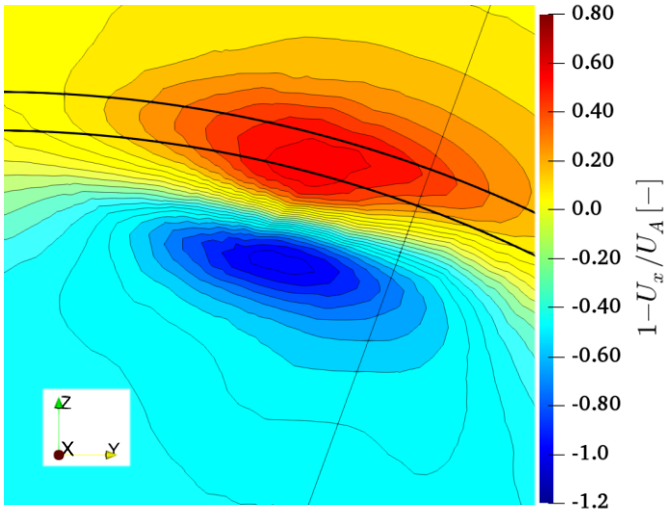

(e) ILES backward

Fig. 62: Effect of turbulence model on slipstream

On the same mesh the accuracy in the slipstream and extent of the numerical capturing of the tip vortex may be severely improved by changing from RANS to LES modelling, which is shown for the PPTC'11 test case, the Newcastle $J = 0.4$ case and the P3193 case in Fig. 63. The rotating mesh region is indicated with the dashed green line with the tip vortex and the corresponding velocity magnitude indicated by the Q-criterion. For the PPTC'11 the tip vortex is extended by 250%, although this is only limited by the extent of the refined mesh region in this case. Downstream of the rotating mesh region, the resolution of the mesh is reduced and the sliding mesh interface introduces additional loss of information. It is expected, that the resolved tip vortex length may be extended much further, if the mesh refinement level is kept at the same level for a longer downstream extent, however, this is not feasible due to numerical limitations imposed by the number of cells and thus available resources. This challenge has to be considered when evaluating noise emissions as well. There is much discussion over the placement of the permeable FWH surface in the literature, however, the downstream end of such a surface is not the decisive factor in this, but instead the numerical resources for resolving the propeller slipstream sufficiently far downstream. The resulting tip vortex length for each case is summarized in Table 18, where the length of the tip vortex L_Q is based on the value of $Q = 5 \cdot 10^4\ s^{-2}$.

PPTC‘11

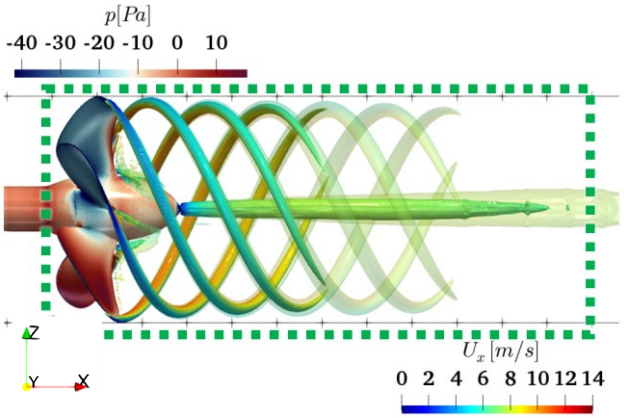

Newcastle

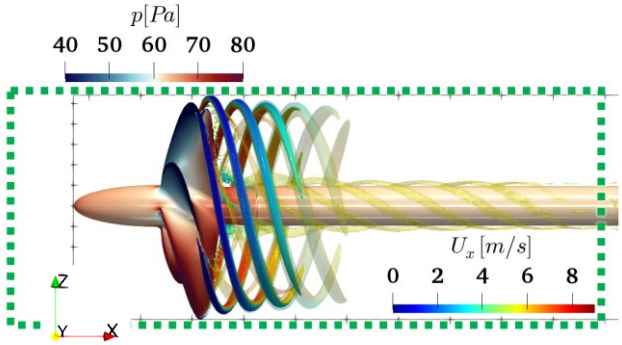

P3193

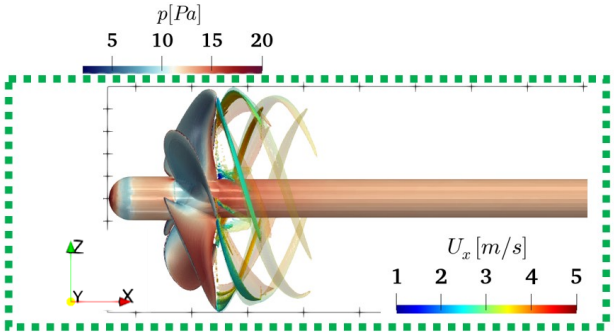

(a) RANS

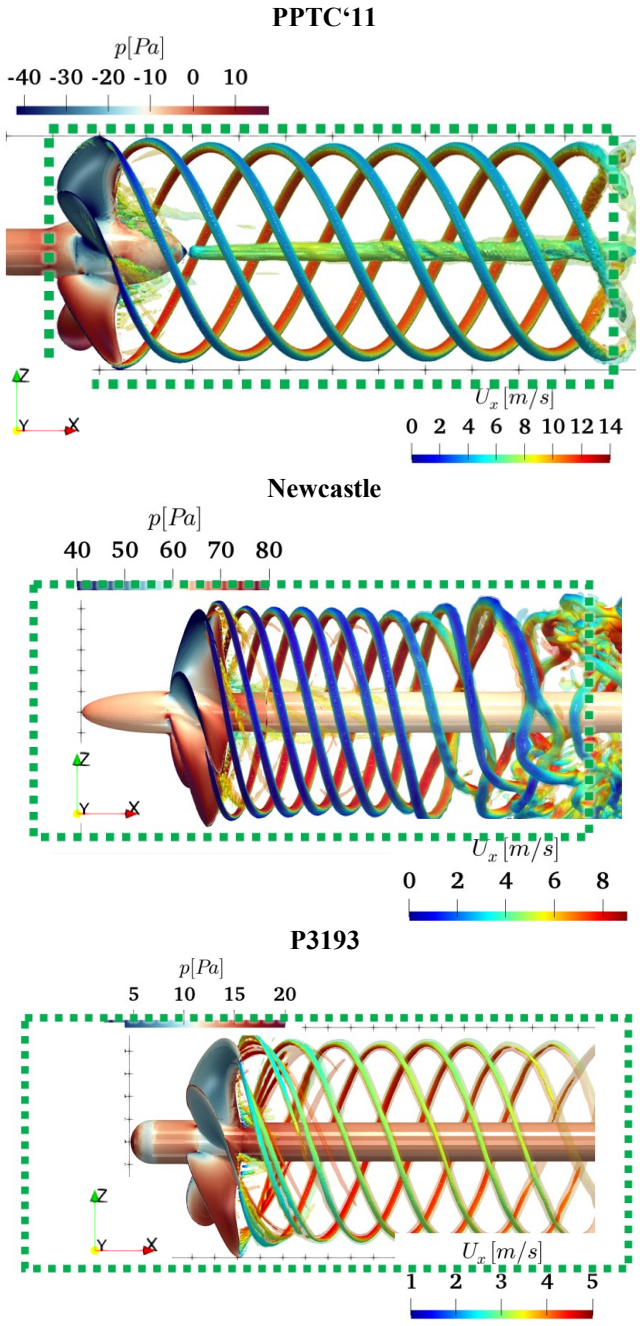

(b) LES

Fig. 63: Comparison of iso-surfaces $Q = 1 \cdot 10^4 s^{-2}$ (semitransparent) and $Q = 5 \cdot 10^4 s^{-2}$ (opaque)

Table 18: Length of tip vortices for propeller open water cases

Propeller	**Operation Point**	$L_Q/2\pi r$ [-]	
	J [-]	**RANS**	**LES**
PPTC’11	1.019	0.67	1.68 (end of refined mesh and rotating region)
Newcastle	0.400	0.43	1.06 (bursting of tip vortex)
P3193	0.740	0.13	0.93

For the Newcastle case the tip vortex is slightly weaker as seen by the shorter axial extent of the tip vortex indicated by the same Q-values for RANS. In case of the LES, the extent of the rotating mesh region and thus the refined mesh is not the limiting factor, instead the interaction between consecutive tip vortices leads to a swirling of these vortices around each other with subsequent merging, which even

extends to three vortices later on. Once the vortices are merged they are highly susceptible to turbulent flow instabilities, which in turn lead to the bursting of these vortices as visible on the right of the image in (b). This transient effect is investigated in more detail in the time evolution series in Fig. 64 for one rotation indicated as ΔT. Here the trailing vortices are visualized as the same Q-criterion values on the left and the axial velocity field on the right. For the right image the tip vortices are additionally highlighted in black for $Q = 5 \cdot 10^4 s^{-2}$. The interactions start appearing after a distance of $\Delta x > 1.0 \cdot D_P$ downstream of the propeller plane.

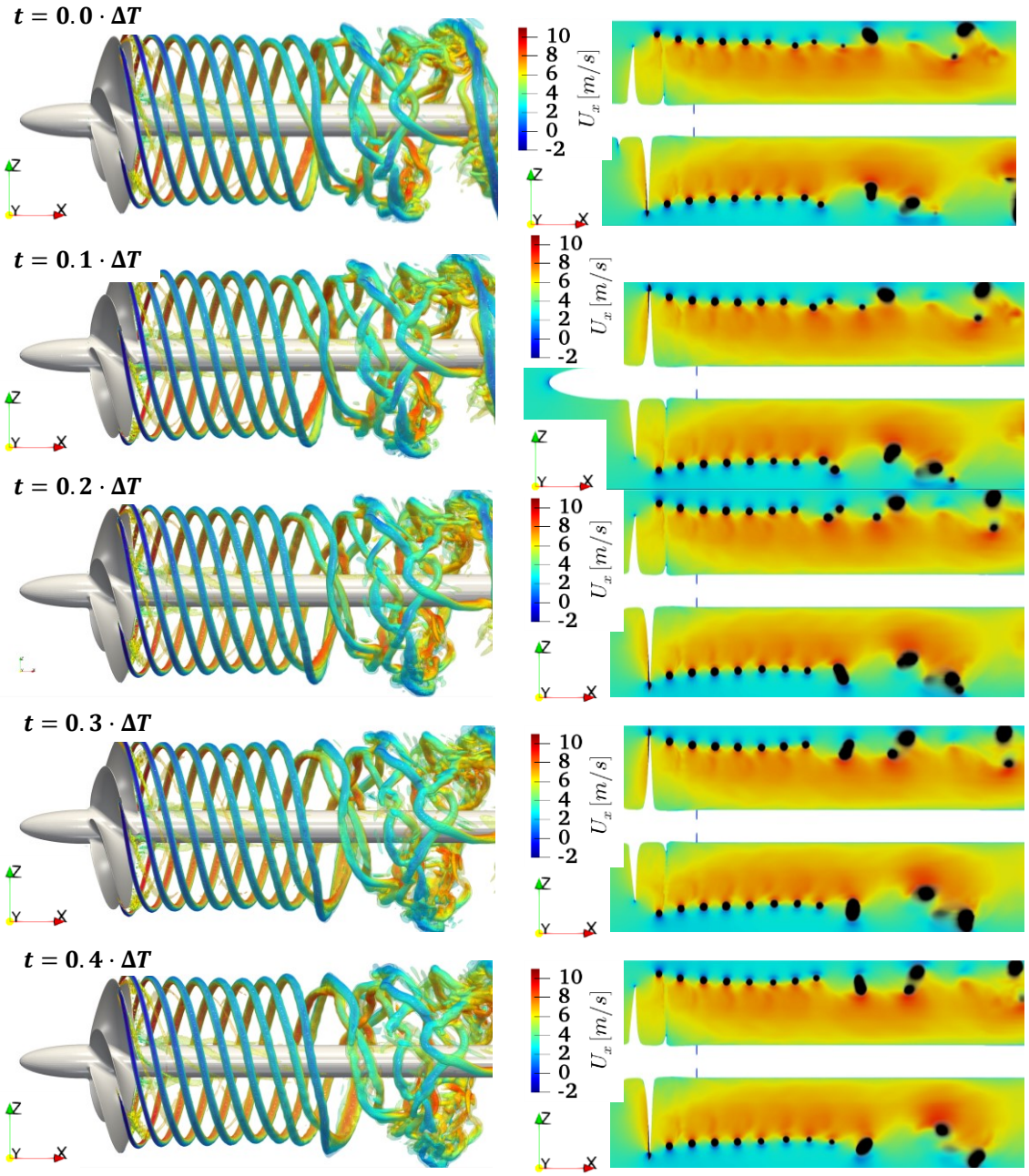

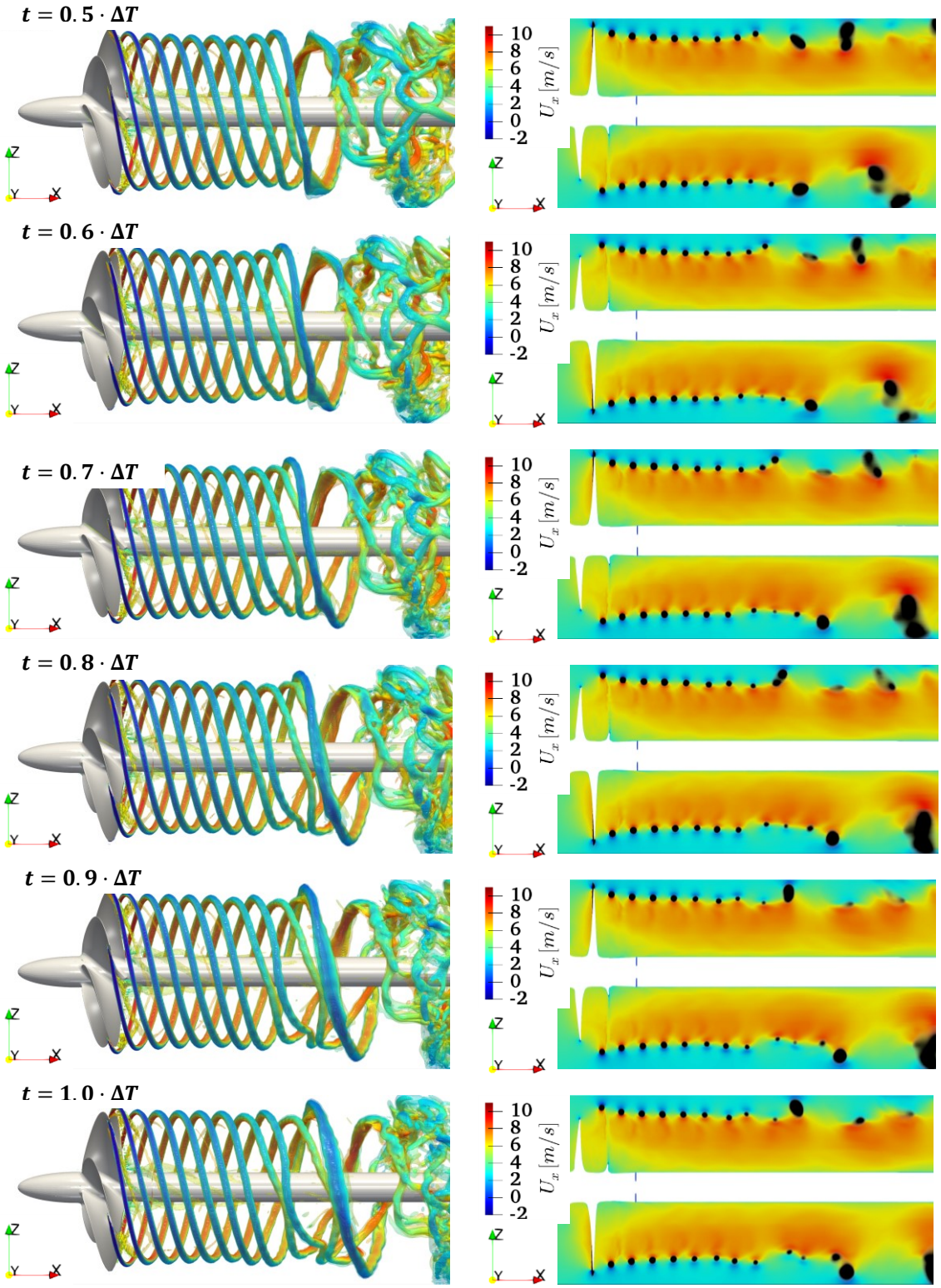

(a) Q-criterion (b) Velocity field and vortex cores

Fig. 64: Tip vortex interaction time series, Newcastle propeller test case [90]

For the LES a timestep convergence check of the Q-criterion isosurface is given in Table 19, which is one of the basic properties to check for convergence before engaging an acoustic evaluation of the case as explained in 3.4.1. The result is that a decrease of the simulation timestep by one third does not invoke any change of the tip vortex structure, thus timestep convergence is considered as achieved. A similar comparison is shown in Table 1 for the PPTC'11 case. While technically the CFL number should remain below 1 for LES it has to be noted that the maximum CFL number given in the table is only achieved in

very few cells and as long as stability of the simulation is ensured, the impact on the overall flow field may be ignored. In addition, a speed up of the calculation time by 260% is achieved by increasing the timestep from $\Delta t = 0.1°$ to $1/3°$ without any loss of accuracy in the flow field and sufficient stability.

Table 19: Timestep convergence and computational effort for Newcastle propeller [59]

Step [°]	**Q-isovalue of $Q = 5 \cdot 10^4 s^{-2}$ with axial velocity**	**CFL [-]**	**Effort (2rot/ 100 CPUs) [d]**
0.33	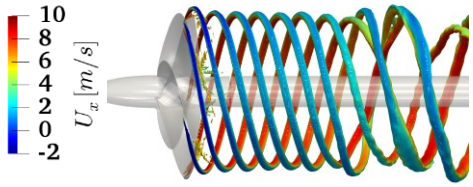	0.03 - 11.51	0.72
0.1	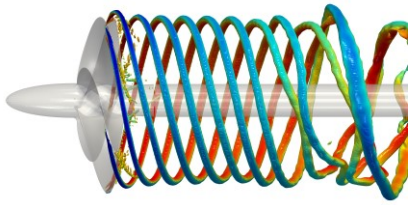	0.00 - 3.44	1.87

For an elliptical hydrofoil the influence of AMR on the resolution of vortices and calculation time is investigated. A balance is required to capture the relevant noise sources on the one hand and create feasible simulation approaches for industry application on the other. The Q-criterion shape at the trailing edge for the NACA 66_2-415 Hydrofoil is shown in Fig. 65, for the initial mesh from Fig. 43 (a) and the refined mesh by means of AMR from Fig. 43 (b). Not only is the downstream extent increased by 786%, but also the level of detail and especially the interaction with the secondary vortex sheet is captured by the simulation. These details and the interaction between vortices are one of the sources of turbulent noise generation and thus are required to be resolved in the simulation.

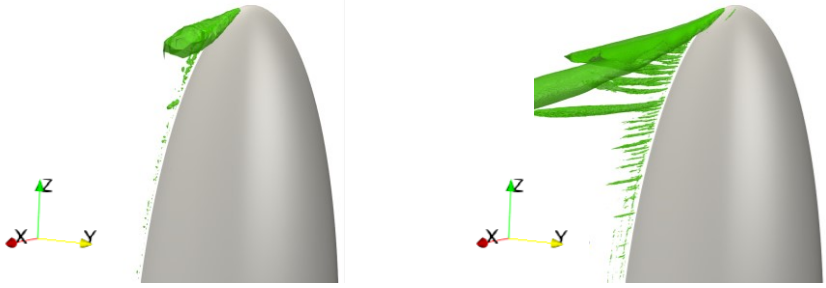

(a) Initial mesh (b) Final mesh

Fig. 65: Vorticity information by $Q = 50 \cdot 10^3 s^{-2}$ isosurface

A streamwise normal plane axial velocity distribution at $x/c = 0.5$ is given in Fig. 66 with the corresponding mesh. In (a) the overall mesh is shown with the refined secondary vortex sheet and the intermediate regions between refinement levels. The refinements of secondary vortices in the vortex sheet on the left of image (a) are required to be resolved by the mesh, as they would not appear otherwise and even influence the trajectory of the primary tip vortex. In (b) the detail of the vortex core is shown with $0.02 \cdot c$, which leads to large scale differences between the largest and smallest cells.

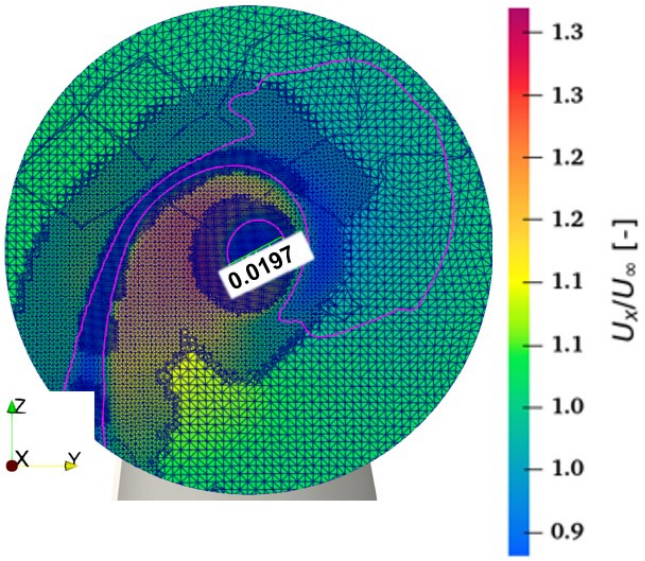

(a) Magenta line defined by axial velocity deficit

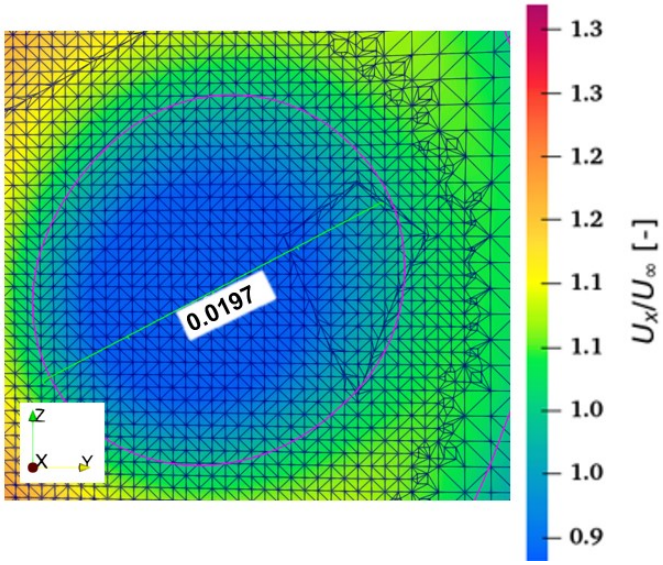

(b) ~30 cells across core

Fig. 66: NACA 66_2-415 hydrofoil mesh details

The cost of the increase in accuracy with a cell number growth by 775% is of course a simulation time increase. This depends strongly on the load imbalance between the processor cores, which dynamically changes with each refinement step. A good load balancing algorithm is therefore crucial for the automated application of AMR, especially with propeller-hull combinations. In this specific case, the load balancing is conducted manually by pausing the simulation and recomposing the mesh into equal processor loads. The AMR process itself takes about $t = 20s$ per PIMPLE loop, which amounts to $t = 60s$ per timestep on 100 cores. In the case of this hydrofoil, the cost may be neglected as the refinement is carried out only 40 times. However, in a dynamic mesh scenario such as a propeller this is a significant increase of simulation time, if the remeshing is required for instance every 1°. Thus the algorithm is adjusted to only be executed in the first loop, which means the refinement is based on the previous time step Q-criterion values. In fact, this is not an issue in the hydrofoil case, however, in the propeller case this leads to the effect of the tip vortex partly leaving the refinement region depending on the time step. [64]

From these investigations, the best practices for turbulence capturing required for acoustic investigation of ship radiated noise are concluded, considering the requirement for a numerically feasible way in an industry environment with contemporary typical hardware. With the selected approach of LES, the turbulence in the freestream, as well as behind vessels may be resolved on relevant time and length

scales with sufficiently high mesh resolution. The turbulent phenomena near walls and in the shear flow can be captured as well with LES. The approach is able to resolve both the boundary layer of the propeller blade, and the tip vortex of a lifting surface with sufficiently high accuracy with LES and specifically with implicit subgridscale modelling, which further speeds up the simulation time as a result of the missing requirement for additional transport equations for any turbulent quantities. A second order time discretization scheme is beneficial for resolving the trailing vortices, however, it may be changed to first order as it leads to higher instability and calculation times. The simulations also show that the refinement of the mesh for the resolution of vortices is crucial, however, this increases numerical effort significantly. If possible the sliding mesh interface should be placed far downstream to avoid further loss of information. In addition it is found, that an evaluation of the derived quantity of circulation from velocity fields is accurate within the simulation accuracy, which can be exploited for validation purposes.

5.1.2 Physics

For accurately capturing the volumetric noise sources around the propeller, flow properties induced by lifting surfaces are investigated first. To verify if the circulation in the volume around a hydrofoil is appropriately resolved with the methods, the NACA 0012 hydrofoil test case is analyzed regarding the near-field flow around the foil in Fig. 67. By evaluating the spanwise circulation distribution

$$\Gamma = \oint_C \vec{u} \cdot d\vec{s} \tag{66}$$

for a hydrofoil at a variety of distances from the foil chord center point the independence of the radius can be proven, with the velocity field u and the finite line element s. Naturally the hydrofoil has to be evaluated for different closed loops at sections of similar circulation, meaning a spanwise normal plane is the dimension of comparison. In (a) the different circles for evaluation are illustrated in the velocity flow field on an intersection plane and the spanwise similarity is given in (b). It is essential to use a hydrofoil case here, as for a propeller the influence of neighboring blades and the bulk flow velocity distorts the results significantly as shown in the next section, meaning that the circulation distribution is not independent of the radius. Furthermore, this result is only valid for the bound circulation of a lifting surface, as the next paragraphs demonstrate.

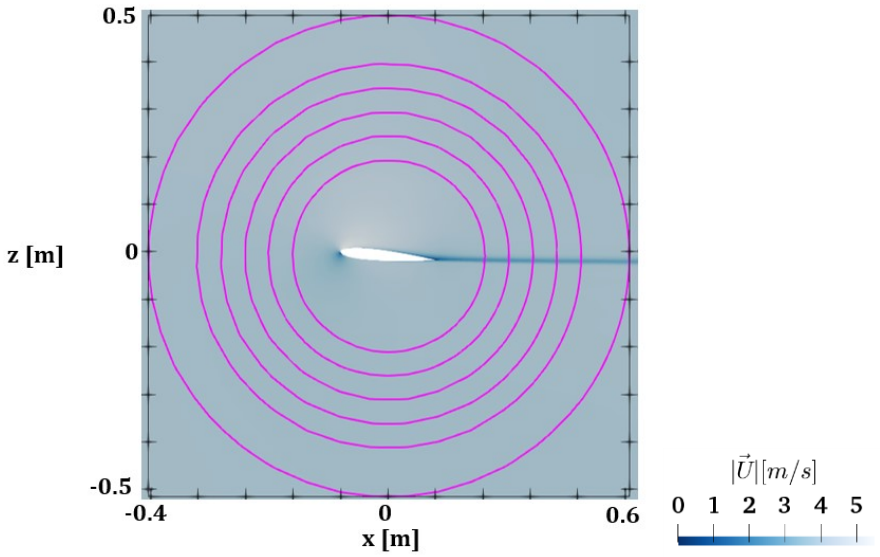

(a) Radii illustration

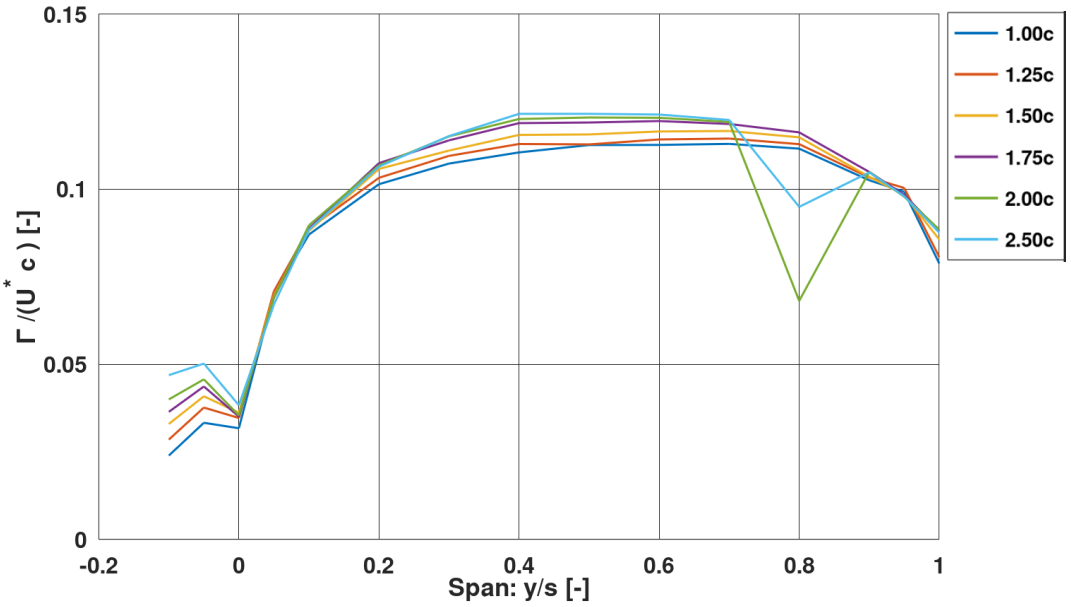

(b) Spanwise circulation

Fig. 67: NACA 0012 Hydrofoil bound circulation, dependence on radius

For RANS and LES with different tip executions the spanwise circulation distribution is compared in Fig. 68, leading to similar conclusions. It is interesting to note that the tip execution has a strong influence on the circulation detected with Eq. (66) beyond the blade for $y < 0$. An additional wall refinement causes the near wall difference between the variation flat tip with LES-superfine (*Flat LES-superfine)* and the remaining simulations.

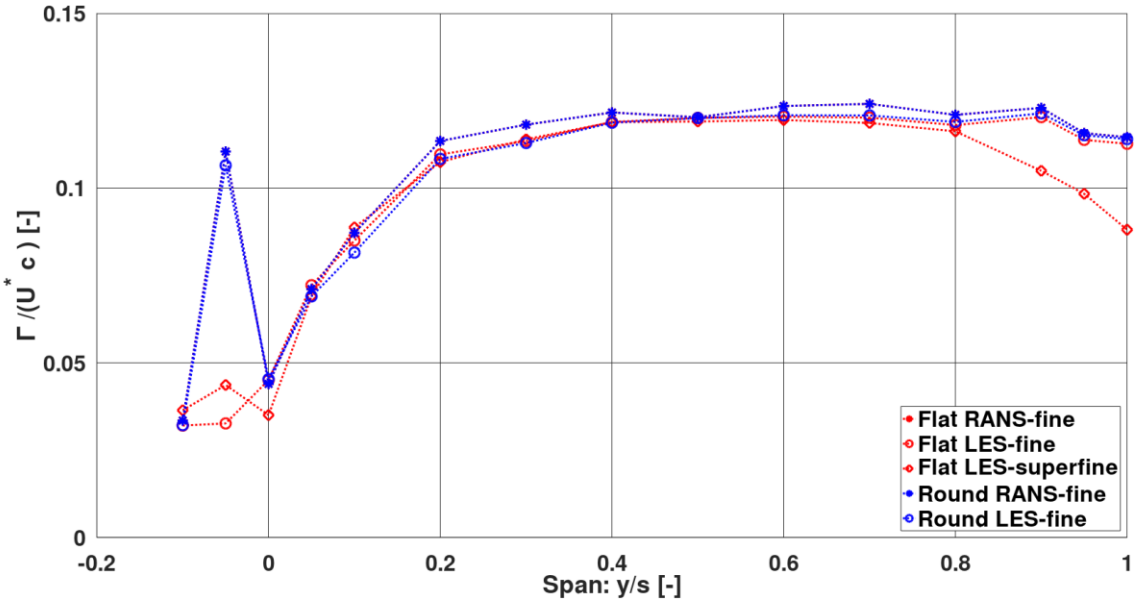

Fig. 68: Hydrofoil bound circulation, dependence on tip execution and turbulence model

Since the flow properties induced by a lifting surface are successfully proven, the circulation induced in the volume by the tip vortex is analyzed next. For the NACA 0012 hydrofoil the circulation obtained from circles of varying radii are evaluated in Fig. 69 with the center around a fixed coordinate with respect to the streamwise normal plane in (a) or around the core pressure center in (b). While the absolute values between (a) and (b) are in good agreement, in accordance with the theory that any closed loop integral around the region of interest may be selected, the evolution far downstream, which is dominated by numerical dissipation is deviating, with the vortex pressure core centered circles yielding more accurate results. With increasing radius of the circle closed loop, the curves collapse on each other, meaning there is a radial convergence for $r > 0.3 \cdot s$.

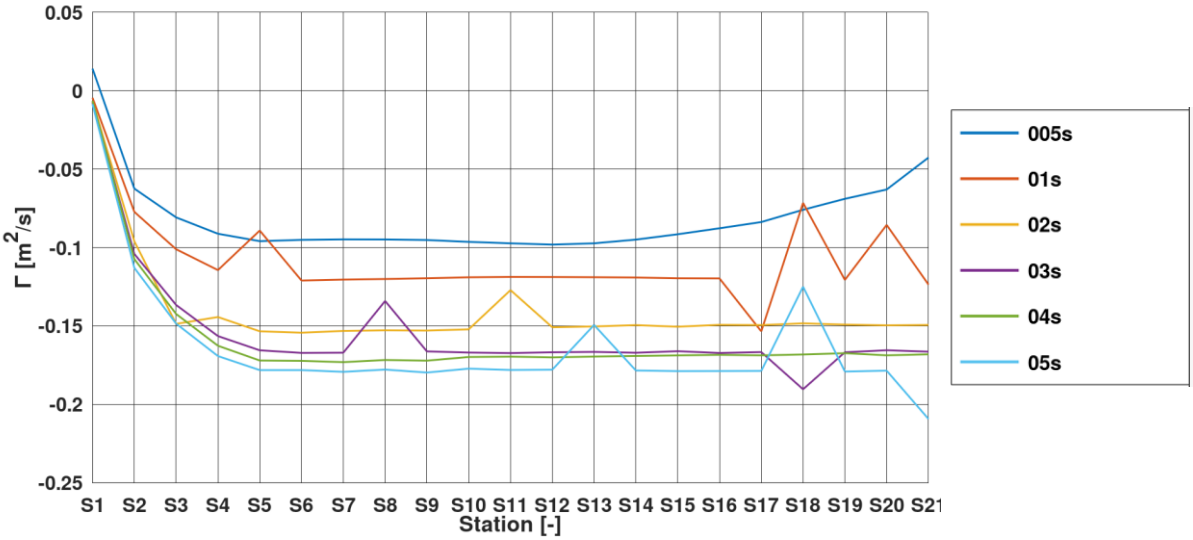

(a) Center at $y = 0, z = 0$

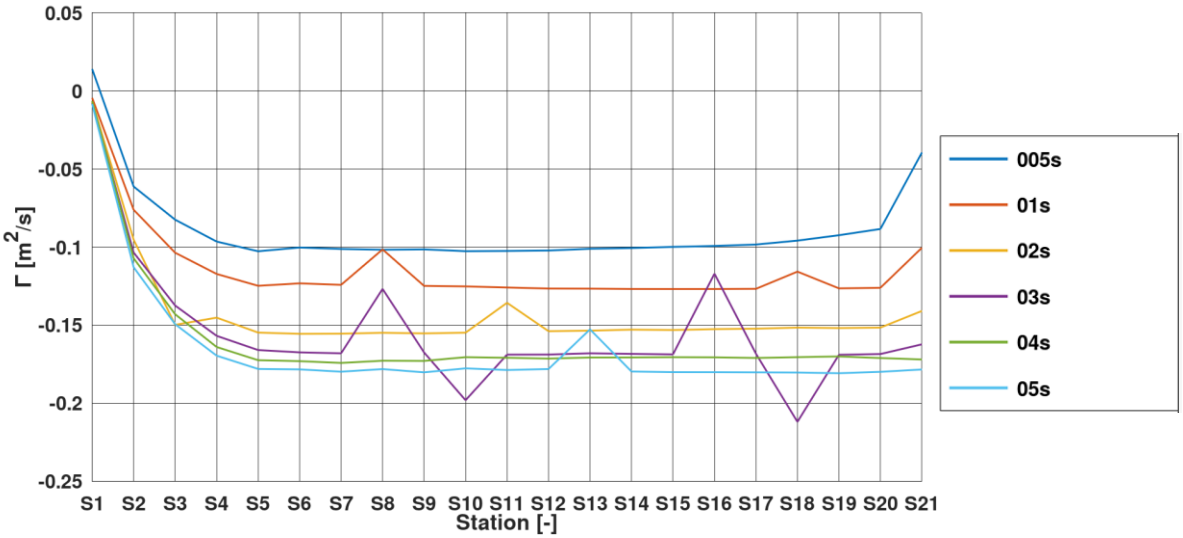

(b) Center at vortex core (c_P)

Fig. 69: Hydrofoil tip-vortex circulation, dependence on radius center

In streamwise direction the circulation converges at station S5, which is identical to the hydrofoil trailing edge, so the circulation in the tip vortex assumes its final value immediately beyond the foil, which is disputing the findings in [93], where it is stated that for a propeller blade the tip vortex roll-up causes circulation variations for some distance downstream of the tip. Similar results are obtained for the comparison of the turbulence models in Fig. 70, where a transition model (a) is compared to the LES simulation (b) with a finer tip vortex mesh resolution with the closed loop radii around the vortex pressure core. Again the radial convergence with the evaluation loop is found as well, however, the absolute values of the circulation of the two approaches differ by about 50%, which may be a result of either the mesh resolution or the turbulence model.

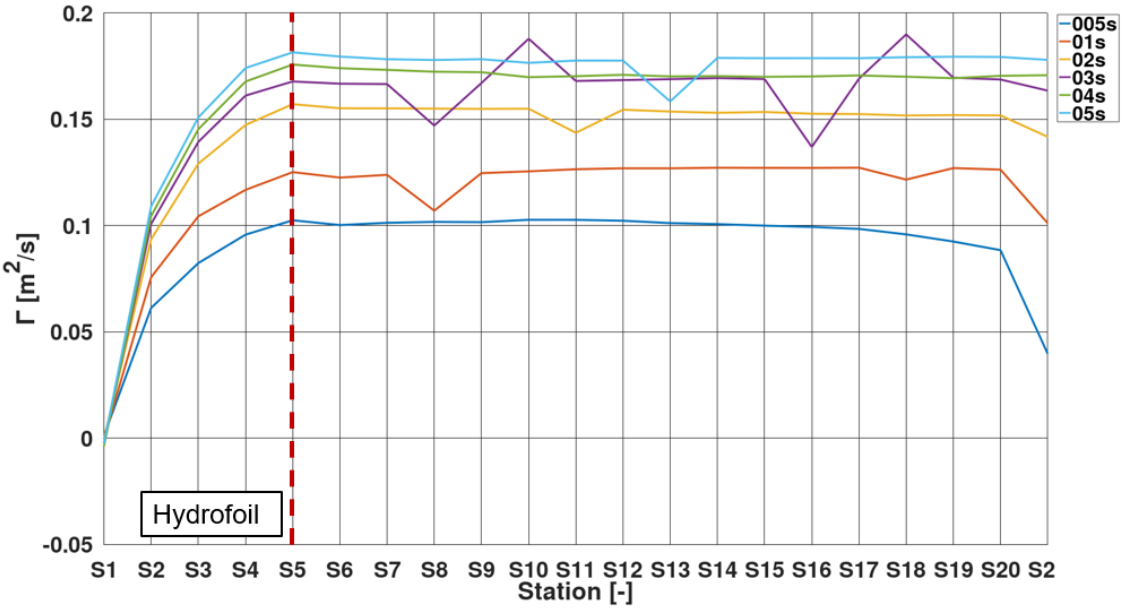

(a) *RANS* $\gamma - Re_\theta$

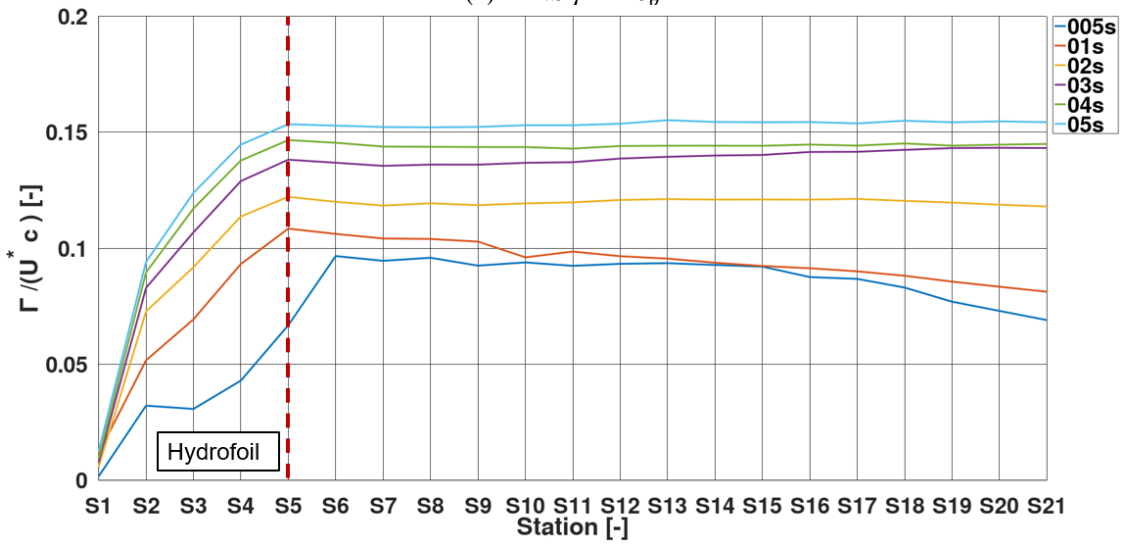

(b) *LES-Smagorinsky-Superfine*

Fig. 70: Hydrofoil tip vortex circulation, dependence on turbulence modelling

Reduced circulation for LES turbulence modelling is also found in [87], which is compared to the achieved angular mean circulation through the vortex in streamwise normal planes near the foil and at some distance beyond the foil. RANS and LES, as well as the numerical reference are found in Fig. 71. Here the reference *Feder2018 w/o* is comparable to an implicit LES simulation result. With the utilized approach of Smagorinsky in this work, the circulation is reduced at both intersection planes by about 50% independent of radius, which is an effect not experienced in the reference but shows a similar trend.

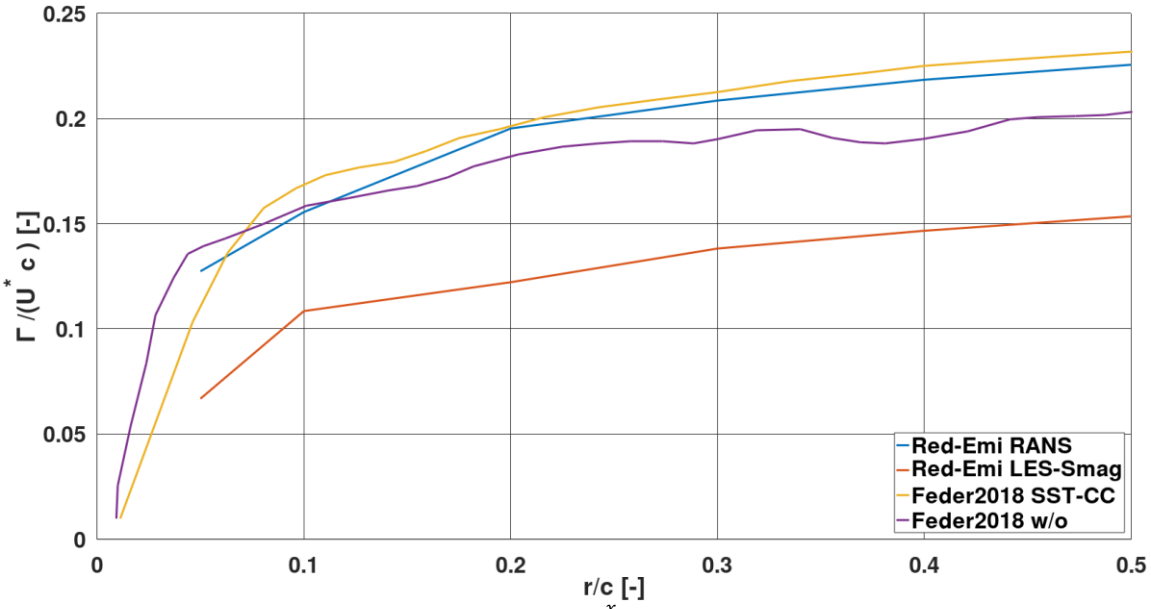

(a) $1 \cdot \frac{x}{c}$

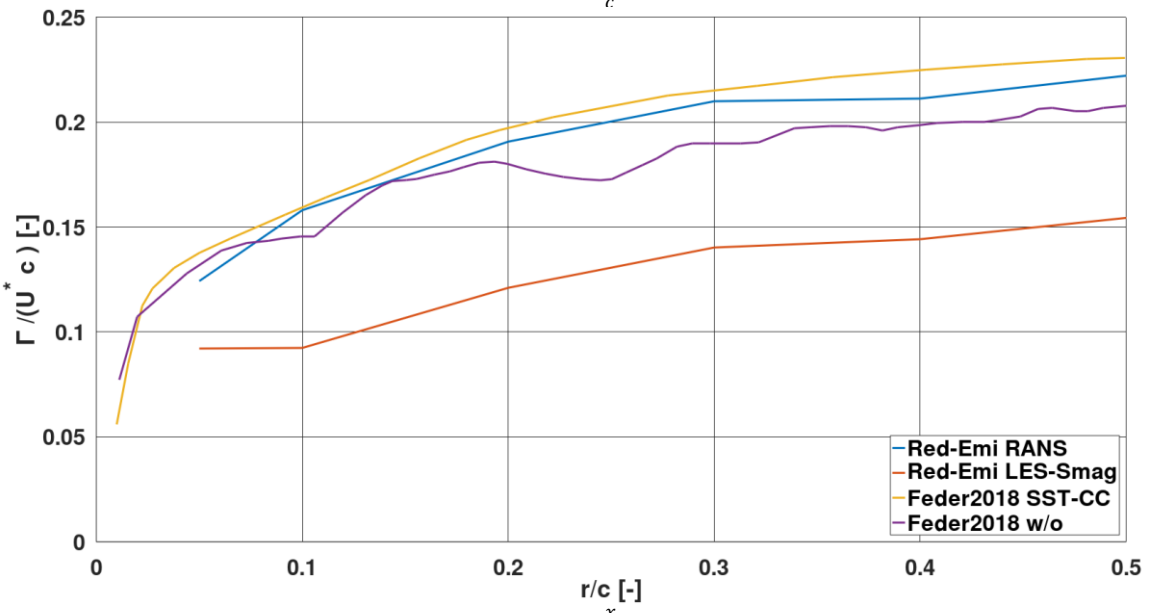

(b) $5 \cdot \frac{x}{c}$

Fig. 71: Hydrofoil tip-vortex circulation, comparison with literature

The streamwise (x-direction) evolution of the physical properties of the core for the NACA 0012 hydrofoil is given in Fig. 72, where the magenta lines indicate the position of the hydrofoil. In (a) the pressure immediately assumes the minimum at the leading edge and then progressively increases with increasing distance from the trailing edge depending mostly on dissipation of the core. In (b) the mean axial velocity in the core is given, which is a velocity deficit of about $4 - 6\%$ between $x = 0.25 - 1.7m$. A temporal snapshot of the geometry of the vortex is given in (c) and (d), meaning the vortex is moving inwards behind the foil into the shear layer and slightly upwards in the direction the foil leading edge, which is angled by 5°.

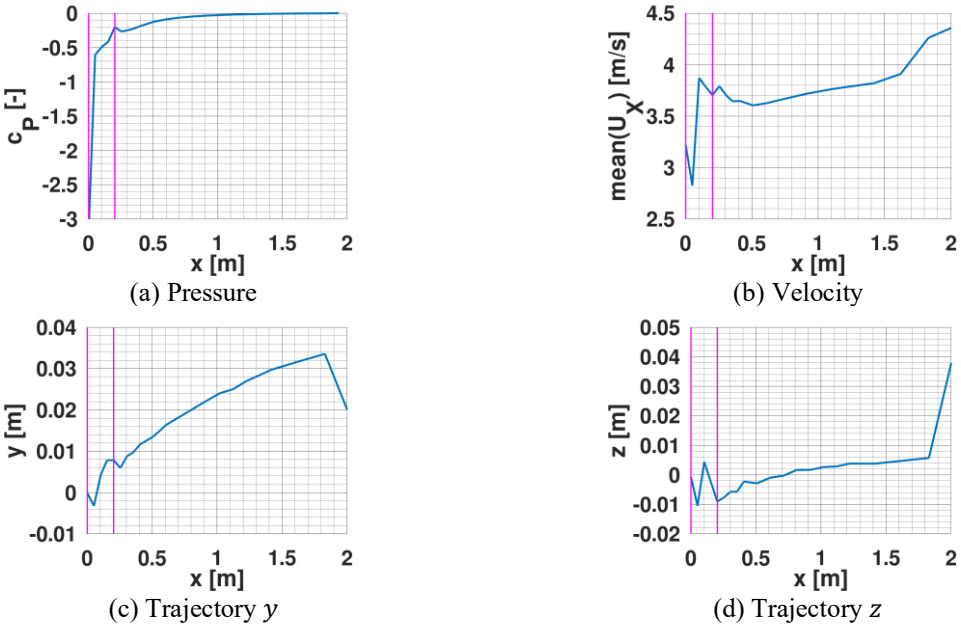

(a) Pressure (b) Velocity

(c) Trajectory y (d) Trajectory z

Fig. 72: Core spatial evolution

A main aspect of trailing vortex flow is the low pressure in the core and the proposed relaminarization thereof. From the information in (b) together with the streamwise normal plane time snapshot evaluation in Fig. 73, with the streamwise velocity distribution in (a) and the in-plane velocity in (b), there is no turbulent motion in the core and it is reasonable to assume the core is laminar and any velocity fluctuations are inactive motions as the core is buffeted by the turbulence from the surrounding wake spiral as described in [58], for the same hydrofoil test case.

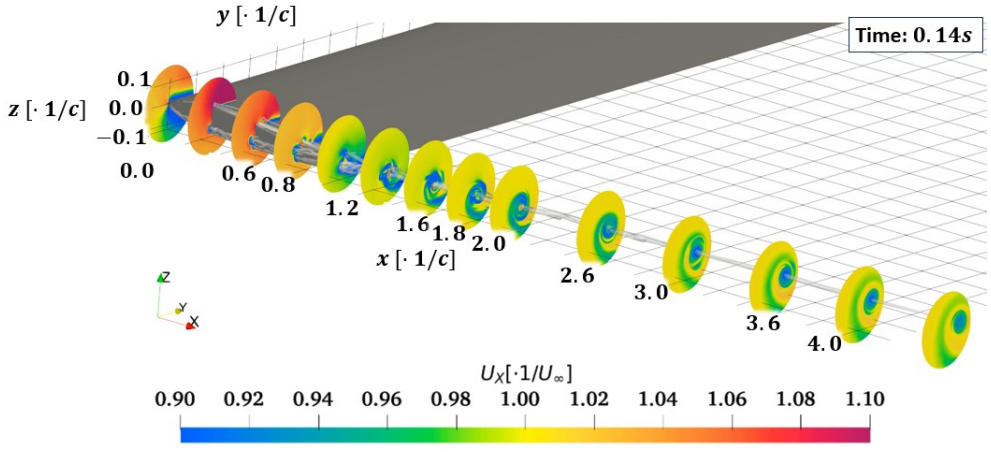

(a) Axial velocity

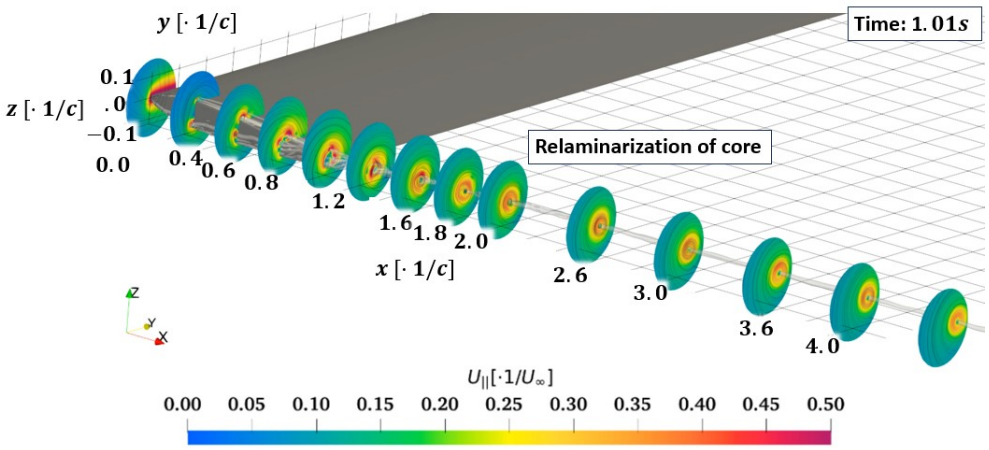

(b) In-plane velocity

Fig. 73: Core velocity distribution

Best practices can be obtained for the capturing of the physics of turbulence that are attributed to the underlying phenomena for noise generation in the volume and prediction of derived quantities. The flow around a lifting surface is appropriately resolved by RANS and LES in the volume to achieve circulation convergence with respect to the closed line integral. Furthermore, an accurate detection of the free circulation of a trailing vortex is depending on the distance of the closed loop integral, but not on the streamwise position for sufficiently refined meshes with low numerical dissipation. A streamwise convergence of circulation for each radius is detected. A vortex core relaminarization can be predicted by the simulation approach when the vortex core mesh resolution is very high. Achieving a similarly well resolved tip vortex for a dynamic case such as a propeller is a challenge, which may only be solved with AMR.

5.2 Cavitation

5.2.1 Numerics

Similarly to the wetted flow, the cell resolution in the core is the most important aspect to capture the low pressure and thus the cavitation forming at the core center, which is attributed to be the primary noise source in the propeller slipstream in cavitating condition. For the different steps of the simulation approach, the saturation pressure isosurface is given in magenta in Fig. 74 for the PPTC'11 $J = 1.019$ case on the same initial mesh. While the RANS solution in (a), as expected from the previous investigations, achieves an insufficiently low pressure region in the tip vortex core, the LES in (b) yields a tip vortex core, that continues beyond the trailing edge for about 1/5 of a rotation and the hub vortex maintains a low enough pressure for cavitation to potentially occur for a downstream extent of up to $1.6 \cdot D_P$. Once the cavitation model is activated in (c), the cavitation region is slightly longer and disappears completely while passing the mixing zone, where the single weaker vortices are merging into the tip vortex that assumes the pressure core with sufficiently low pressure to invoke cavitation. Besides, a more dynamic albeit slightly shorter hub vortex cavity region is visible in (c) as a result of the pressure interaction with the tip vortices. By increasing the number of cells in the tip vortex according to Eq. (64) the cavity length can be increased significantly to $3/5$ of a rotation and a high level of detail of the cavity morphology is created as shown in the comparison in Fig. 75, where a photograph from the experiment is given as reference. This results in around 30 cells across the cavitating core of the tip vortex.

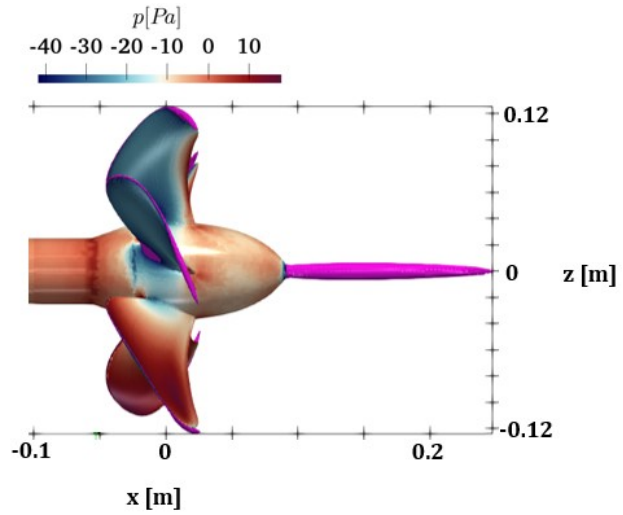

(a) RANS

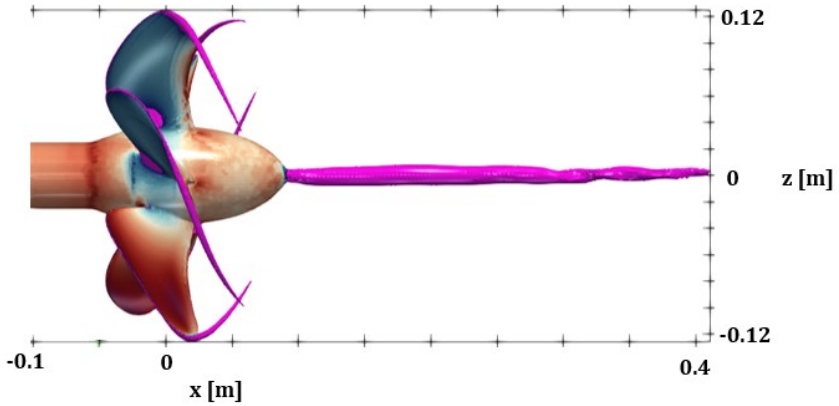

(b) LES - No cavitation model

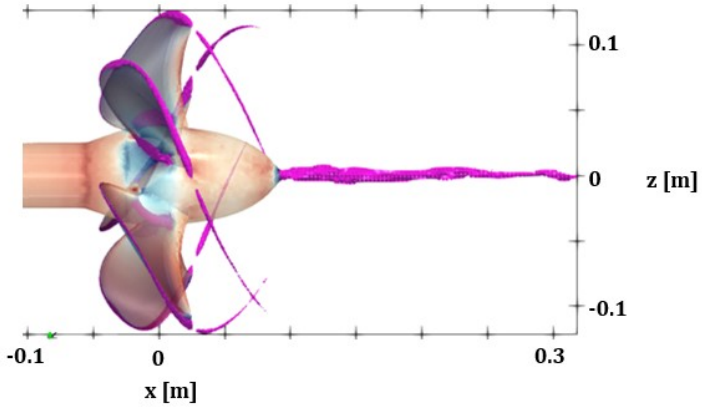

(c) LES - OpenFOAM Schnerr-Sauer cavitation model

Fig. 74: Saturation pressure isosurface [90]

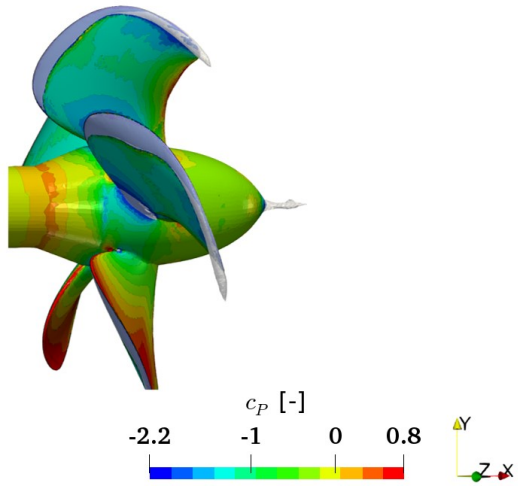

(a) Initial mesh [90]

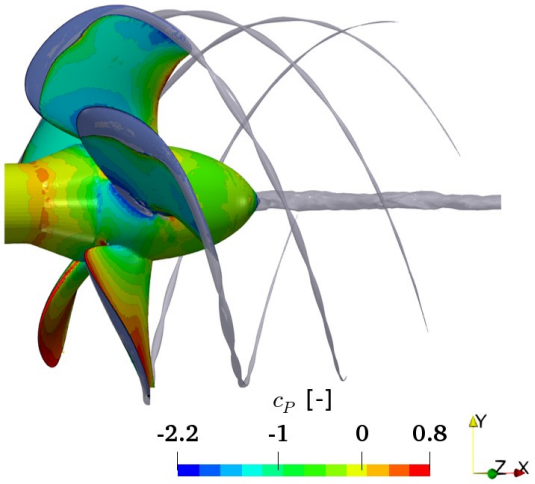

(b) Final mesh [90]

(c) Experiment [22]

Fig. 75: Comparison of cavity for tip vortex mesh size, PPTC'11

For the PPTC'11 case with the stations defined by Fig. 80 the helix normal plane intersection pressure distributions at the tip vortex are given in Fig. 76 for two stations in the tip vortex in (a) and (b) and for a streamwise normal cross section plane for the hub vortex in (c). With the magenta line the intersection of the cavity with the plane is indicated. The station t_3 is a node and the station t_4 an anti-node of the tip vortex diameter variation. This highlights one of the challenges in resolving the cavitating tip vortex appropriately, as in both cases a minimum of 30 cells across the diameter has to be ensured, however, the meshing algorithm does not take into account any information regarding the morphological evolution

along the tip vortex helix and thus node or anti-node structure. While in (a) only the major axis of the ellipse created by the cavity intersection fulfills the requirement, at the more circular shape of the anti-node in (b) it is fulfilled with directional independence. For the hub vortex there is a much larger number of cells across the cavity as the limiting factor is here the result of Eq. (64) leading to around 60 cells across the diameter.

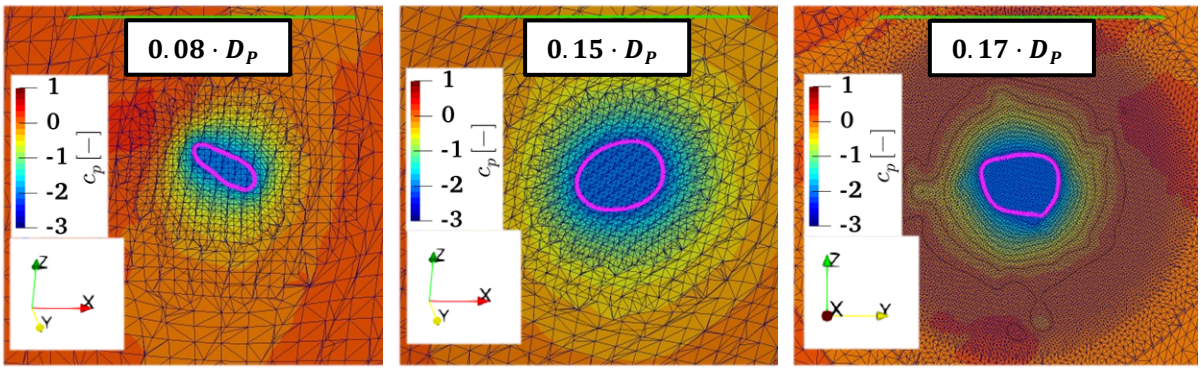

(a) t_3 (b) t_4 (c) $x = 0.4 \cdot D_P$

Fig. 76: Mesh resolution in tip and hub vortex [59]

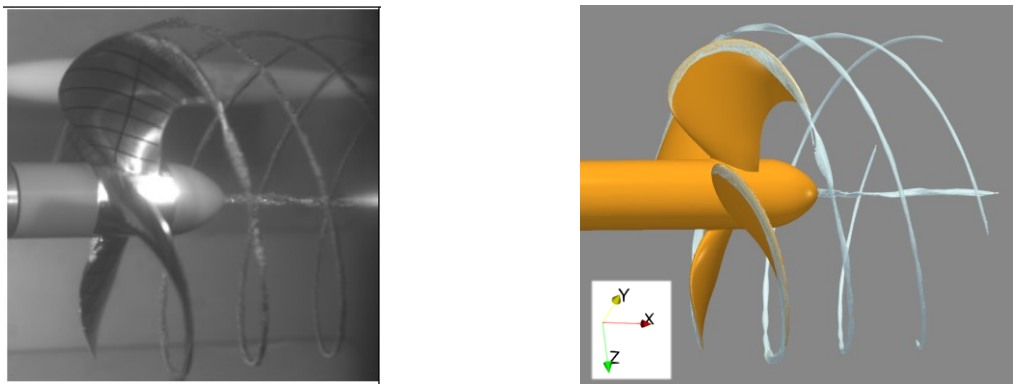

(a) Suction side view

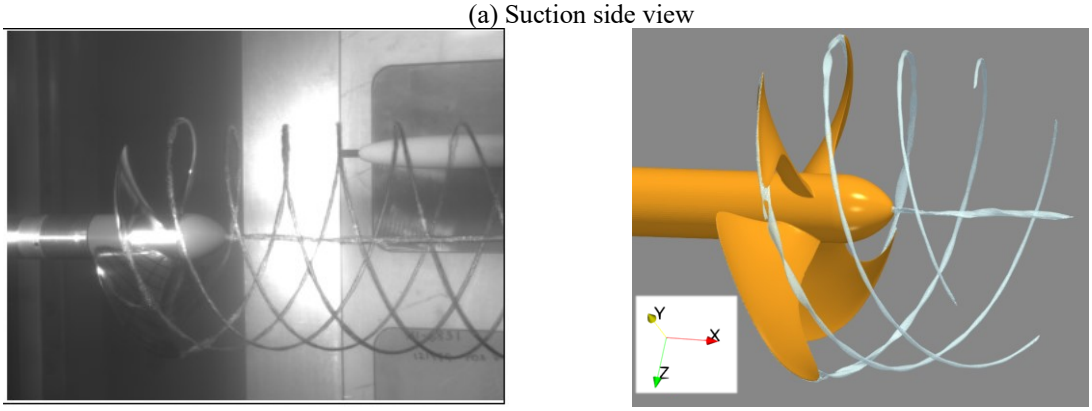

(b) Pressure side view

Fig. 77: P1595 cavitation observation

For the P1595 in Fig. 77 and the Newcastle propeller in Fig. 132 with the same mesh criteria, a similar well resolved cavitating tip vortex is achieved. The cavity morphology is evaluated to qualify the influence of the developed automatic AMR approach. For the tip vortex a slightly longer axial extent is visible in the comparison in Fig. 78 between a priori and runtime AMR with the same target refinement level. For the hub vortex on the other hand the opposite occurs with an overall deviation in morphology that seems to be closer to the experimental photographic observations. In addition, the suction side blade root cavity appears more detailed and dynamic in the runtime AMR case.

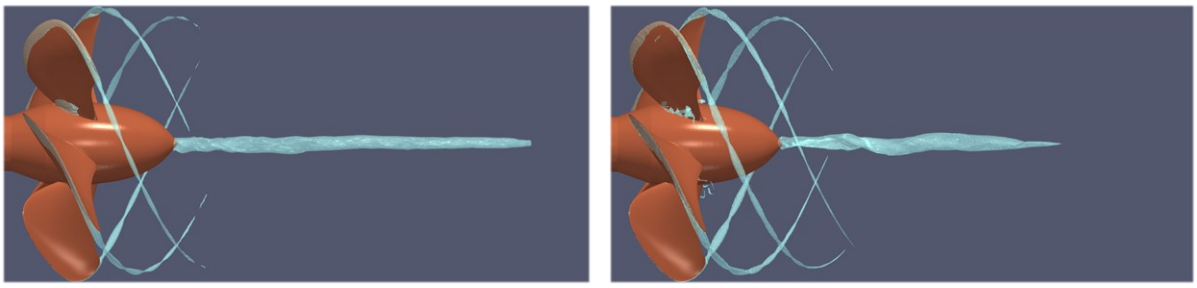

(a) A priori AMR (b) Runtime AMR

Fig. 78: Comparison of the resulting cavity between refinement techniques

The numerical challenges in the resolution of cavitation as an acoustic source in the volume pertain mostly to the meshing strategy. While near wall meshes are easily targeted for refinement, the volumetric meshes require advanced methods to address geometrically in a feasible way. However, a sufficiently fine cell resolution in the tip-vortex is required to resolve cavitating tip vortices, which then can lead to a very accurate prediction of a cavitating tip vortex. Purely from comparing results for a simple open water propeller test case, the automatic runtime AMR is not strictly required, as with similar refinement levels, the extent of the resolved cavity is identical between manual a priori and automatic runtime adaptive mesh refinement. Only the runtime automated refinement leads to more dynamic cavities at lower propeller radii sections along the complete slipstream, which hardly justifies the additional resource cost. However, as explained in the introduction, the point of automatic AMR is a future use in combination with the limiting cases of high wake field velocity gradients or inclined flow.

5.2.2 Physics

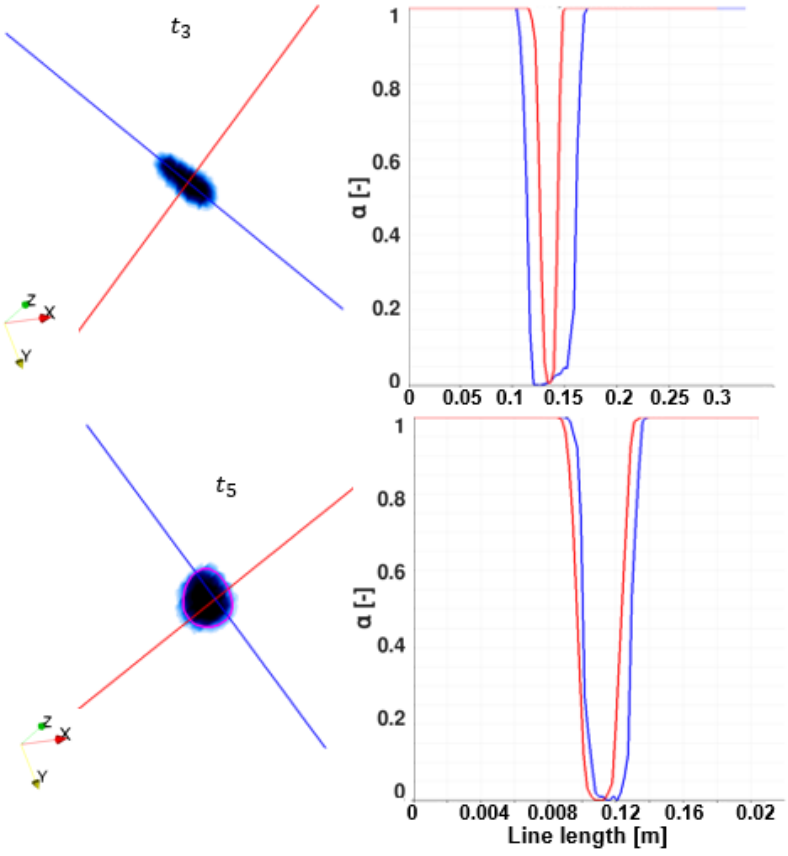

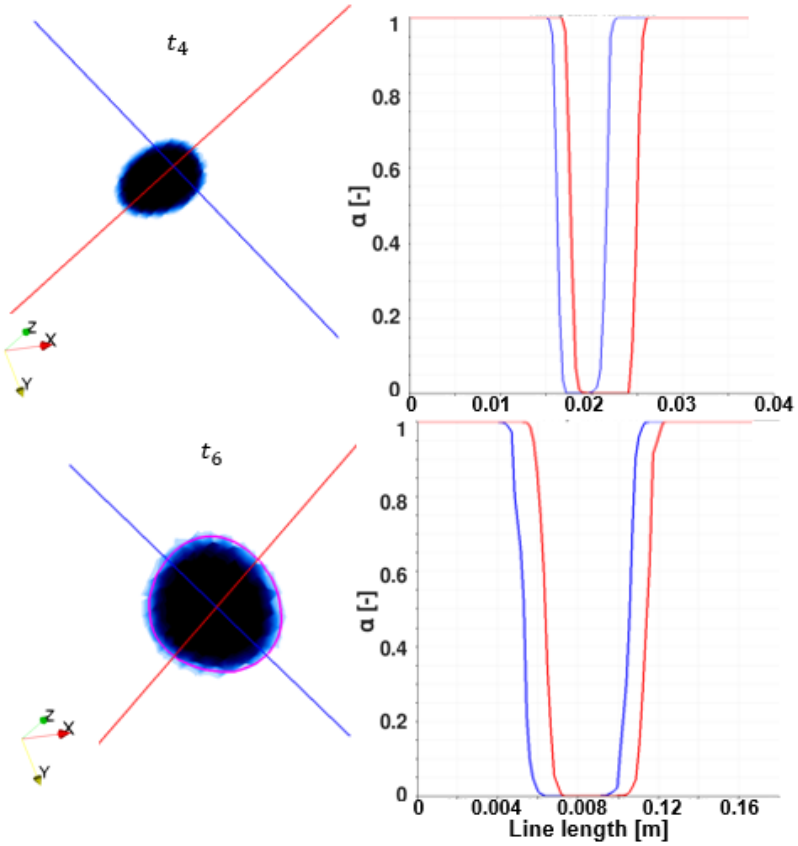

Fig. 79: α distribution across tip-vortex core

As cavitation is the most important source of noise, the validation of the prediction is conducted by the use of cavity visualization. With VOF a primary question is the capturing of the interface and the associated isovalue for morphological, topological and dynamics analysis. To highlight the interface of the trailing vortex cavitation the visualization of the phase interface with the value α is utilized, for which an appropriate choice of $0 < \alpha < 1$ is required. For the magenta colored intersections of the cavity with helix normal planes from Fig. 80 at the stations t_3 to t_6 of the PPTC'11 tip vortex the α value is given as a contour and plotted in Fig. 79 along the major and minor axes of the elliptical cavity intersection shapes indicated by the blue and red line. The value is changing rapidly, creating a sharp gradient at the interface and either assumes the value of 0 inside the cavity or 1 outside, which means that the exact choice of α is in this case irrelevant, thus $\alpha = 0.5$ may be used for the identification of the phase interface and is from this point forward assumed when the quantity α is mentioned. For station t_5 and t_6 the interpolated $\alpha = 0.5$ value, which is used to create the isosurfaces is given as a magenta line in Fig. 79 and for all major stations in Fig. 80.

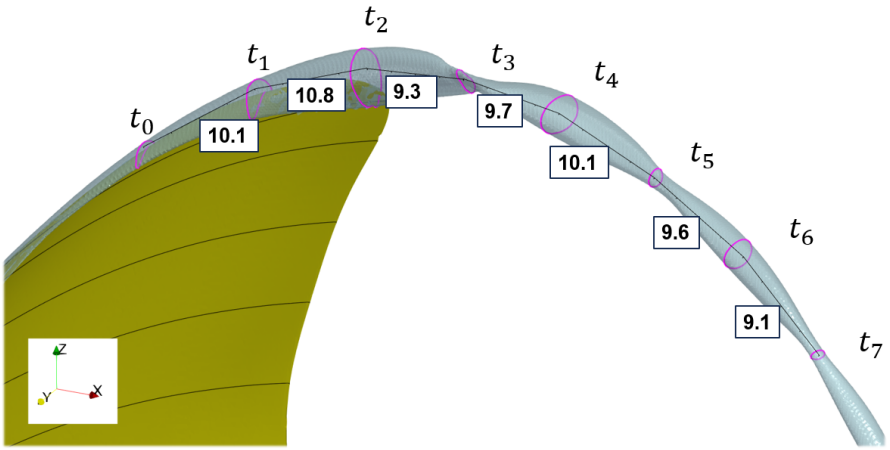

Fig. 80: Major stations in tip vortex for PPTC'11 [59]

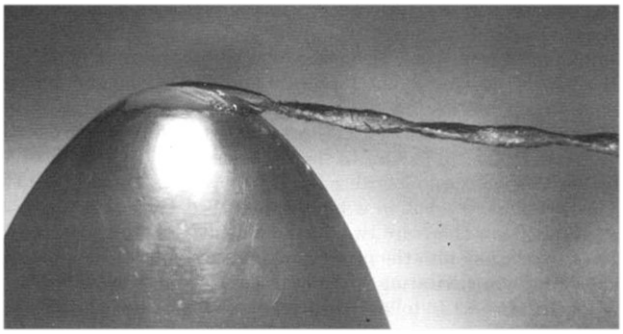

(a) Experiment

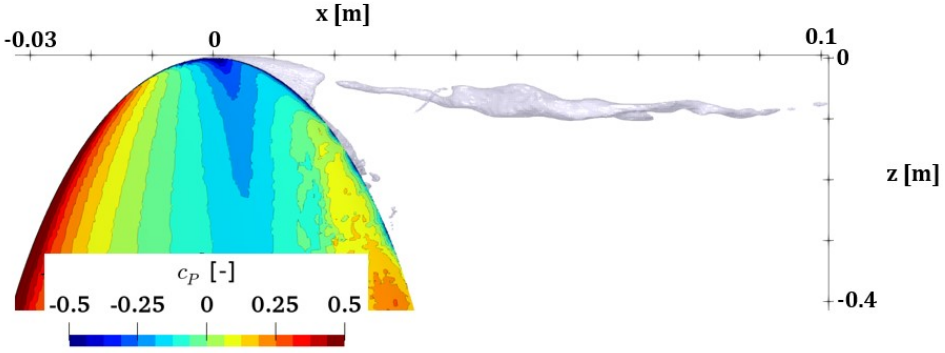

(b) $n_0 = 1 \cdot 10^{12} 1/m^3$

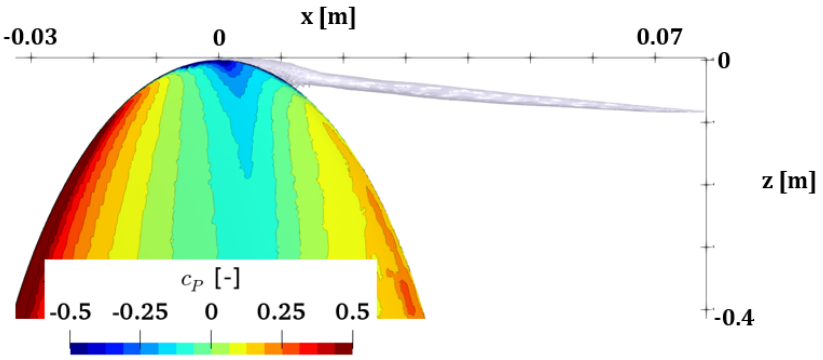

(c) $n_0 = 1 \cdot 10^{6} 1/m^3$

Fig. 81: Cavitating vortex at foil tip, view from pressure side, $\alpha_{0.5}$ isosurface [90]

Often there is no information about the exact nuclei content in model tests, as this quantity is rarely measured during the experiment. However, it is known to affect the cavity extent and dynamics significantly and thus may also alter the noise emissions. Thus the influence of the model parameter

nuclei density on the cavitating structure and the simulation stability is determined for two values. For the NACA 66_2-415 hydrofoil case the cavity is shown for two nuclei densities in Fig. 81 and compared with the experimental observations [19]. With the higher nuclei density in (b) the cavity is remarkably dynamic and experiences highly detailed morphology such as secondary vortices and small cavity filaments within the secondary vortex sheet. For the low nuclei density in (c) the cavity is static and shows no morphological details and a rather simple topology. While both simulations do not achieve the axially varying cavity diameter observed in the experiment, there is an undeniable large influence on the solution depending on the nuclei density model parameter. It has to be noted, that the dynamic cavity naturally also leads to higher instability in the solution of the transport equations, so a larger number of corrector loops for the α-equation is required to ensure the simulation is able to continue with this setting. For the sake of achieving an accurate cavity for the highest level of detail of the sound source capturing, the higher nuclei density is selected for subsequent simulations with the final Schnerr-Sauer parameters given in Table 20.

Table 20: Empirical parameters of the OpenFOAM Schnerr-Sauer cavitation model

Parameter	n_0	d_{Nuc}	C_c	C_v
Unit	$1/m^3$	m	$-$	$-$
Value	$1 \cdot 10^{12}$	$1 \cdot 10^{-4}$	1	1

The turbulence cavitation interaction is the driver for the formation and dynamics of the cavities in the propeller slipstream such as the cavitating tip vortex. Therefore, it is imperative that the turbulent length scales are captured that are responsible for the phenomenon. For the Delft Twist11 Hydrofoil this effect is particularly prominent, as there is no fluctuation of the cavity extent in RANS, however, once LES is activated the dynamic periodic behavior observed in the model test is revealed as illustrated in Fig. 82. Five stages are identified for each period by observation:

I. Separation,
II. Downwash,
III. Dissolving,
IV. Growth,
V. Collapse.

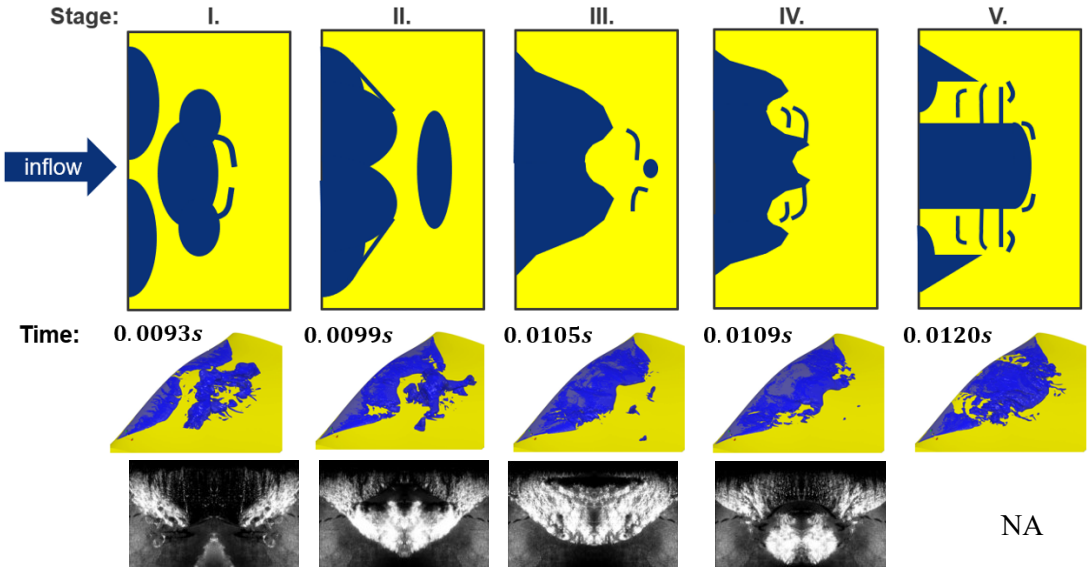

Fig. 82: Stages of cavity collapse

In Fig. 83 the same point in time of the period at stage V. is given for 6 consecutive periods in the same simulation, which all show slightly different behavior. Even though the FVM is based on deterministic

equations it seems that the stochastic elements of non-exact periodicity, which is expected in nature, is somehow ensured in the simulations, which must be a result of the turbulence modelling by LES.

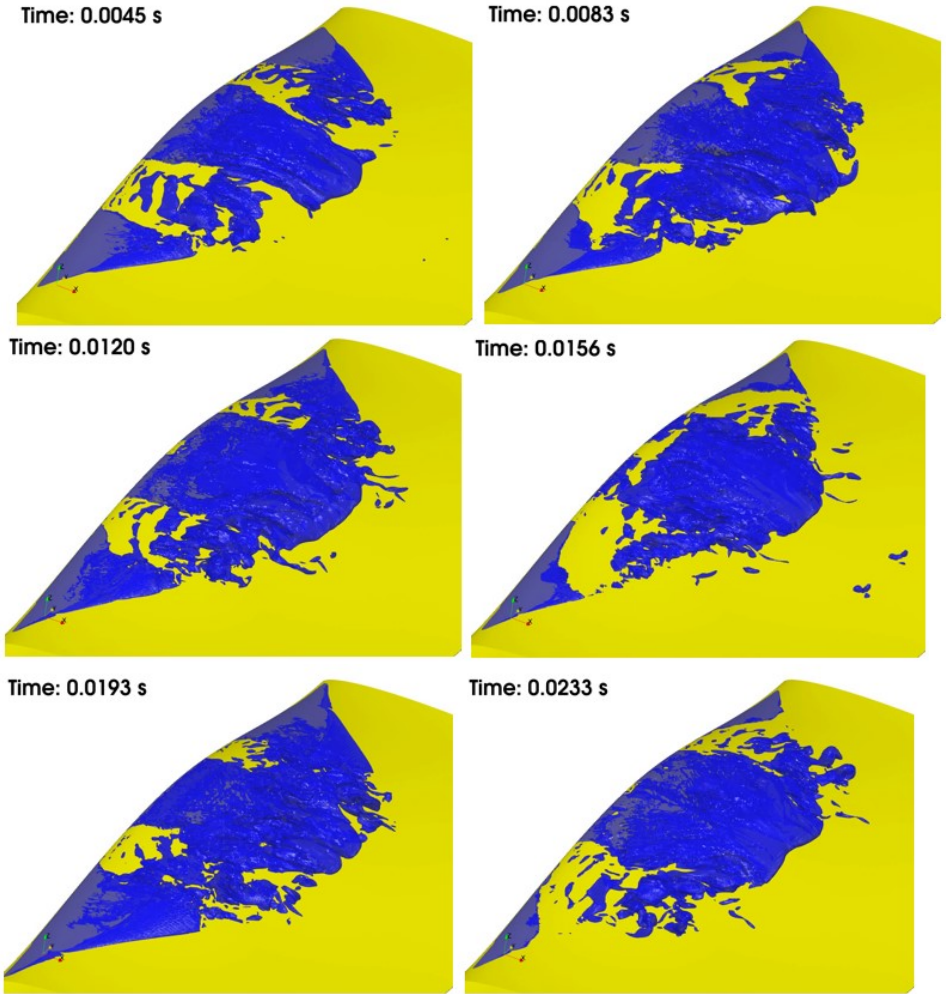

Fig. 83: Periodicity of cavity collapse

For the case of a propeller, the turbulence interacts with the cavities in numerous ways as indicated in Fig. 84 by the green $Q = 50 \cdot 10^3 s^{-2}$ isosurface weaving around the blue cavity, which might be correlating with the cavity diameter variation along the helical running length of the tip vortex. These secondary vortices are, however, typically not as pronounced as in this case and might be difficult to resolve on the FVM meshes.

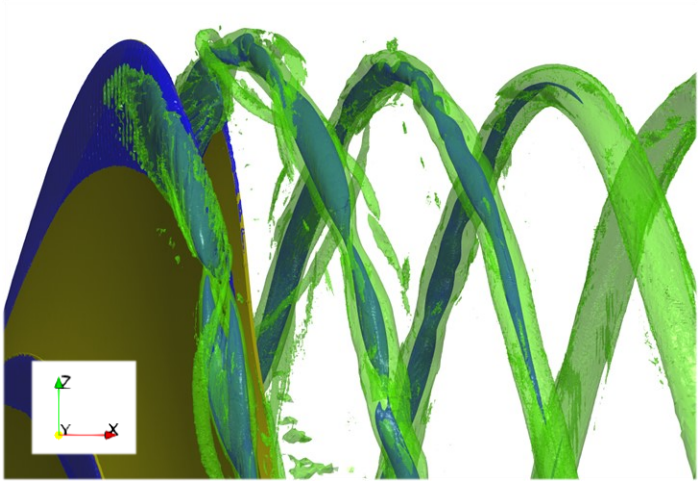

Fig. 84: Newcastle C2 cavitation turbulence interaction [59]

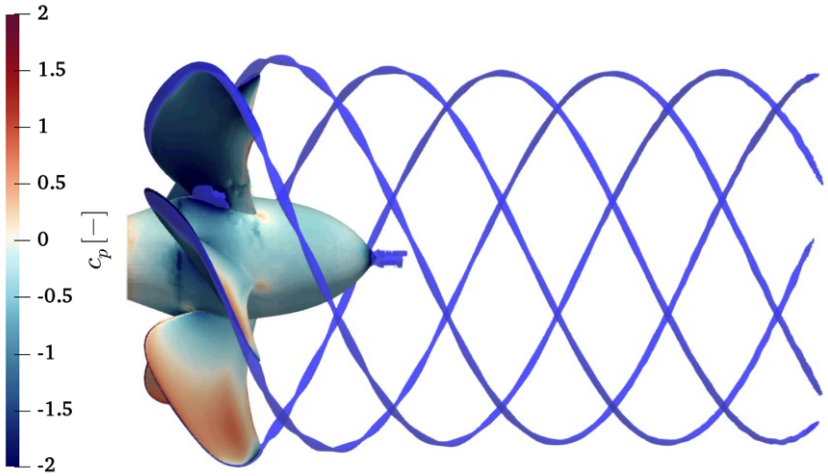

(a) Only tip vortex refined

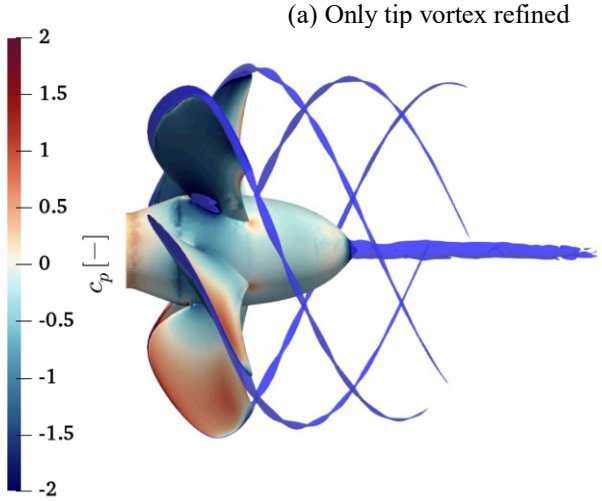

(b) Tip and hub vortex refined

Fig. 85: Interaction between tip and hub vortex mesh resolution

The interaction of cavitating tip and hub vortex by vortex-vortex interaction may change in cavitating condition with an additional interaction caused by the pressure distribution. This effect can be enforced in the simulation by numerically dissipating the hub vortex. For the PPTC'11 $J = 1.019$ case, the cavitating trailing vortices are resolved on two meshes in Fig. 85, with the one from subfigure (a) only resolving the tip vortex and in subfigure (b) with tip and hub vortex equally resolved according Eq. (64). For the first case a rather static cavitating tip vortex propagates up to $x = 1.4 \cdot D_P$ downstream in the

case of a numerically suppressed hub vortex only ending with the subsiding of the refined mesh regions in the tip vortex. In the second case in (b), the tip vortex refinement also reaches to the same downstream distance, however, the emergence of the dynamic cavitating hub vortex has some pressure interaction with the tip vortex reducing its length. This appears as a somewhat dynamic behavior, with the tip vortex length varying slightly around $\Delta x \approx 0.1 \cdot D_P$. This could indicate that the shortening of the extent is either caused by the dynamic behavior of the hub vortex, which prevents a stable tip vortex cavity to form, or alternatively means that in general the pressure field is affected around the cavitating hub vortex to lead to reduced negative pressure difference in its surroundings. It has to be noted that this numerical setup is in a constricted cavitation tunnel volume, which means axial pressure variations occur. However, the length of the tip vortex does not have any influence on the morphology upstream, which is an identical geometry for both cases.

One of the most important factors in the noise generation in the slipstream is the spatial evolution of the tip and hub vortex cavity. For this purpose a detailed analysis of the cavity in the slipstream for the open water propeller test cases follows, where the cavity extent and spatial evolution is investigated, as well as the temporal evolution, in order to examine possible cavity volume variation modes.

For the stations t_1 to t_7 along the helix normal planes shown in Fig. 80 the cavity shape is given in magenta together with the pressure distribution and the in plane velocity components in Fig. 86 for the PPTC'11 $J = 1.019$ case. The nodes with a constricted shape are t_3, t_5 and t_7 and the anti-nodes with the largest cross section are t_4 and t_6. For the emerging tip vortex on the leading edge of the blade in t_1 to t_2, the reentrant jet like structure is visible as the cavity shape separates from the blade surface. As expected there is a significant rotational component starting from the pressure difference at the blade tip well into the fluid at the downstream trajectory.

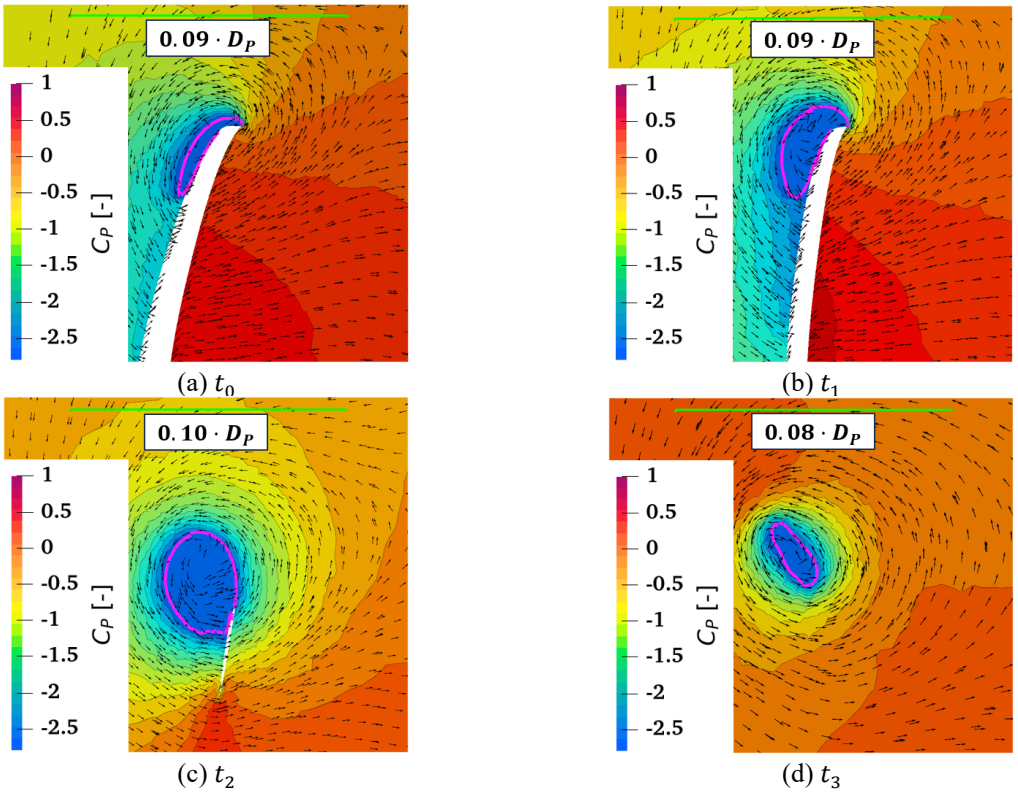

(a) t_0 (b) t_1

(c) t_2 (d) t_3

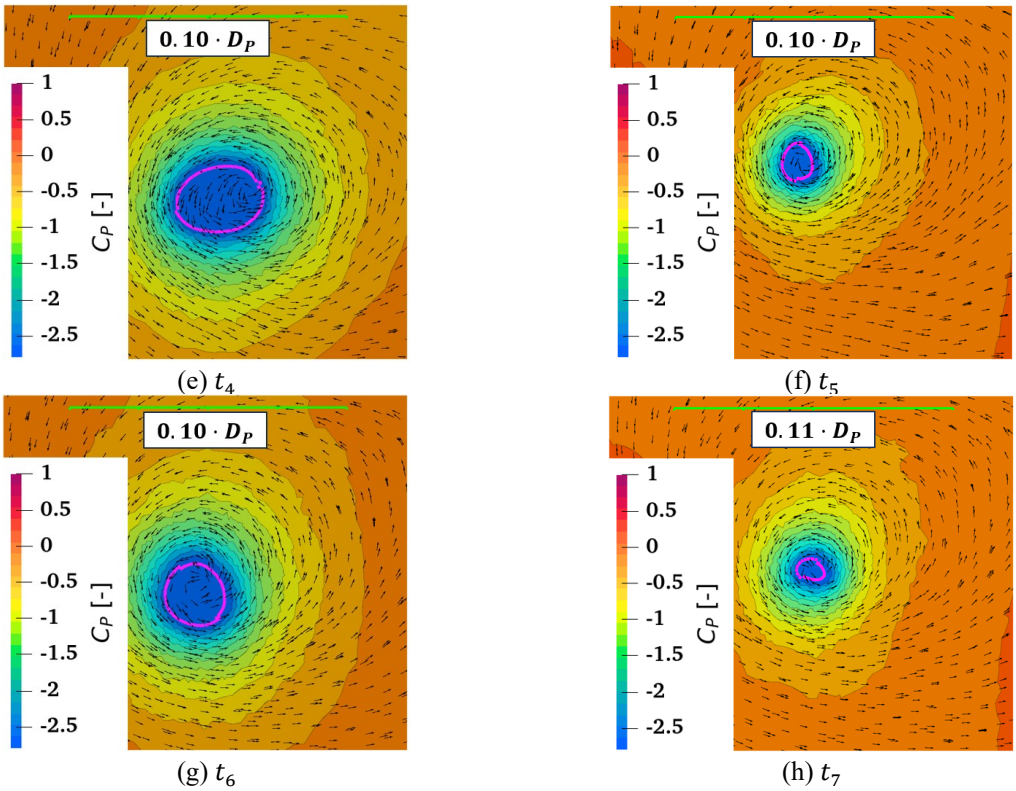

(e) t_4 (f) t_5

(g) t_6 (h) t_7

Fig. 86: Velocity distribution across core at major stations [59]

This shape evolution is shown in more detail for highly resolved helix plane intersections with the plane normal velocity distribution in Fig. 87 (a) with the plane intersections numbered. For the Newcastle C2 and C6 case the same illustration is given in (b) and (c), which are the only Newcastle operation points with a stable connected tip vortex cavity where such an analysis is viable. While the in-plane velocities around the cavity are relatively consistent along the trajectory the normal velocity inside the cavity is fluctuating strongly with the helix trajectory coordinate and radius from the cavity center. Inside the center there is an upstream velocity component of about 2.5 times the downstream component at the edges at the anti-nodes. In the nodes however, there is only a downstream component along the trajectory of the tip vortex. This phenomenon starts at the leading edge and proceeds over the complete cavity, however, dissipating in strength, further down the trajectory.

The flow properties in the cavitating tip vortex region are particularly influencing the shape variations of the cavity, which is expected to influence sound emissions. To describe the trajectorial variation, the axial volume flow rate and mass flow rate $\dot{m} = \rho_m \cdot u \cdot A$ is estimated in Fig. 88 in the upper plots, which are obtained with the mean mixture density $\rho_m = \alpha_l \cdot \rho_l + (1 - \alpha_l) \cdot \rho_v$ inside the automatically detected cavity borders. In the lower plots the shape evolution along these planes is plotted for the three open water cases (a)-(c) with a stable tip vortex cavity as perimeter and area on the left and their relation as the quantity compactness on the right, which is defined as

$$c = \frac{4\pi \cdot A}{P}, \qquad (67)$$

with the perimeter P and the cross-sectional area A of the cavity shape intersection. While in the upper plots the visually identified nodes and anti-nodes are indicated in magenta, the separation from blade is given as a black indicator in the lower plots. For the geometry the wave behavior of the relationship is visible, which correlates with the smaller node and the large area anti-node morphology. In addition, from the compactness parameter it is clear that the anti-nodes appear almost perfectly circular, while the nodes feature more elliptical appearance in cross-section. The sharp fall off at the nodes is a numerical issue and should be ignored.

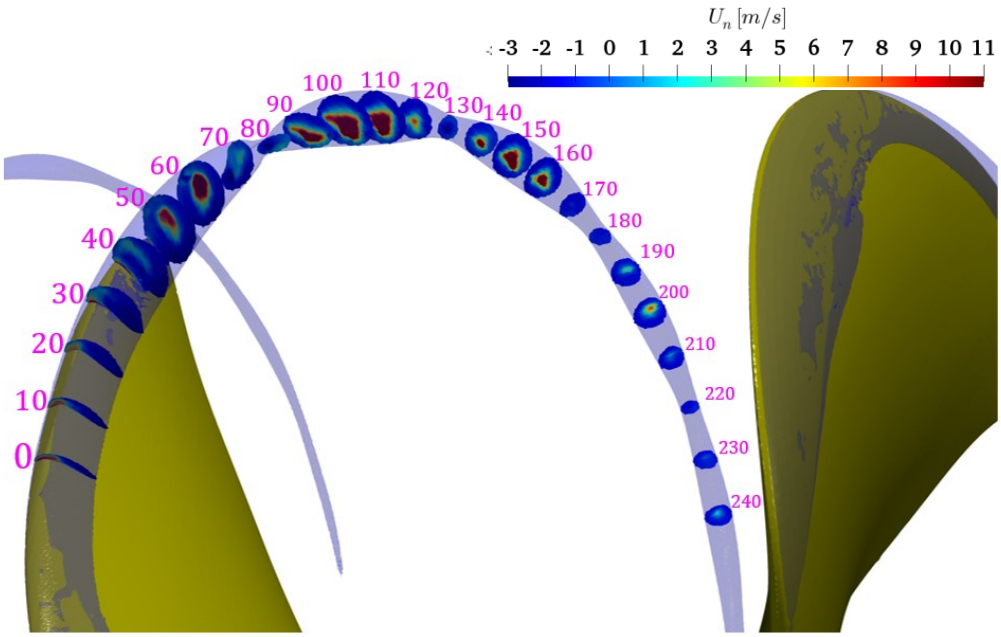

(a) PPTC'11 $J = 1.019$

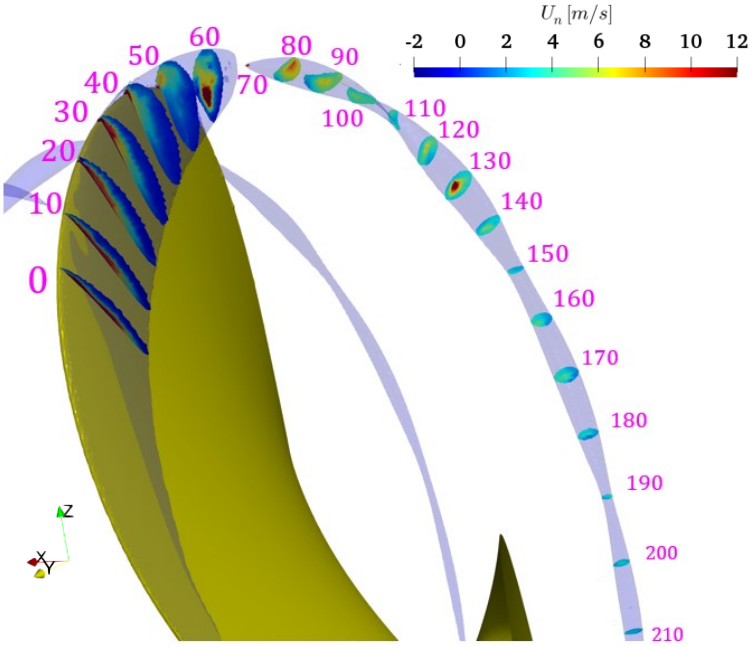

(b) Newcastle C2

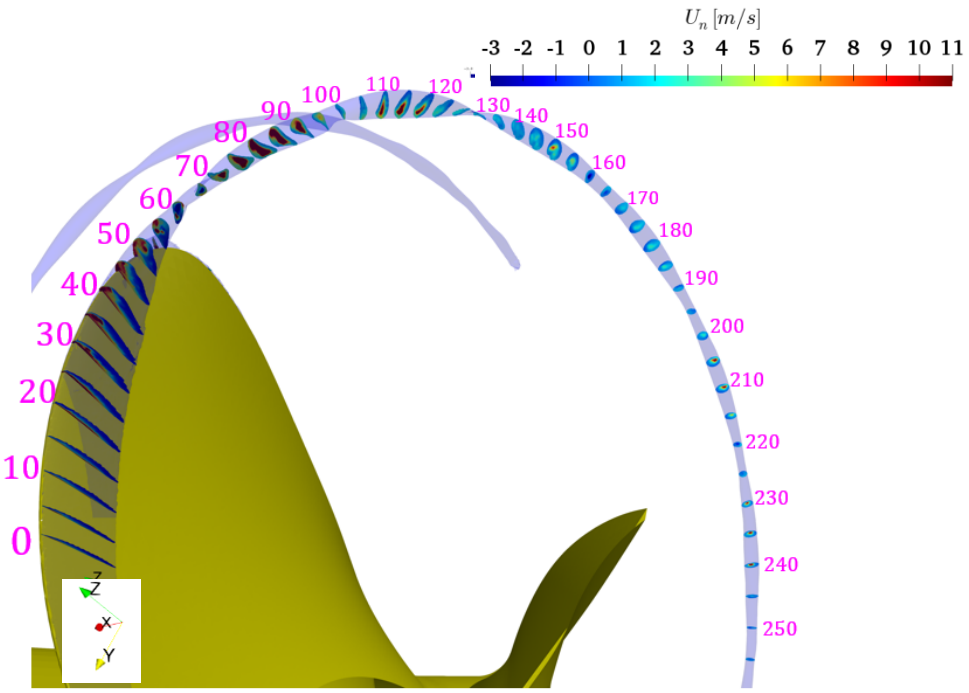

(c) Newcastle C6

Fig. 87: Highly resolved trajectory stations for tip vortex analysis

An explanation for preference of a vortex cavity to assume a circular shape is the lower pressure in the vortex core. An equilibrium between the centrifugal force and the under pressure of the cavity [94] creates the rotational form of a circle, thus in an infinite quiescent medium a cavity assumes the shape of a sphere. However, in the case of a tip vortex there are external factors such as the secondary vortices and the strong rotational components, as well as the vapor phase internal velocities seen in Fig. 87 that prevent the circular form and lead to the spatial waveform varying between elliptical and circular shapes.

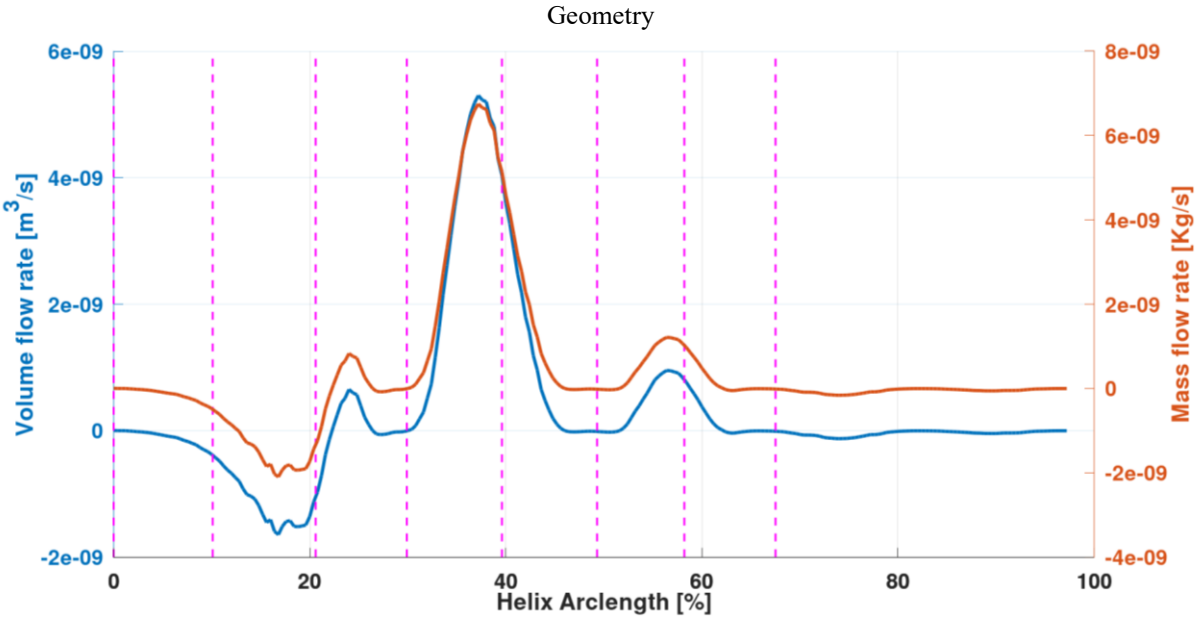

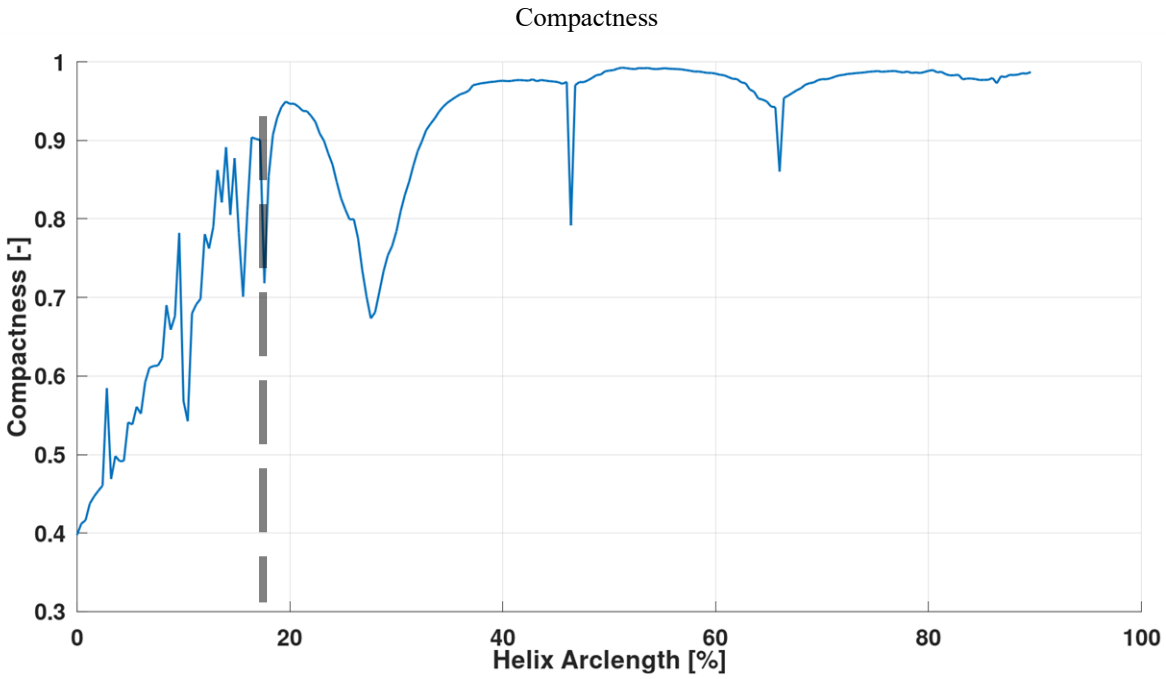

(a) PPTC'11 $J = 1.019$

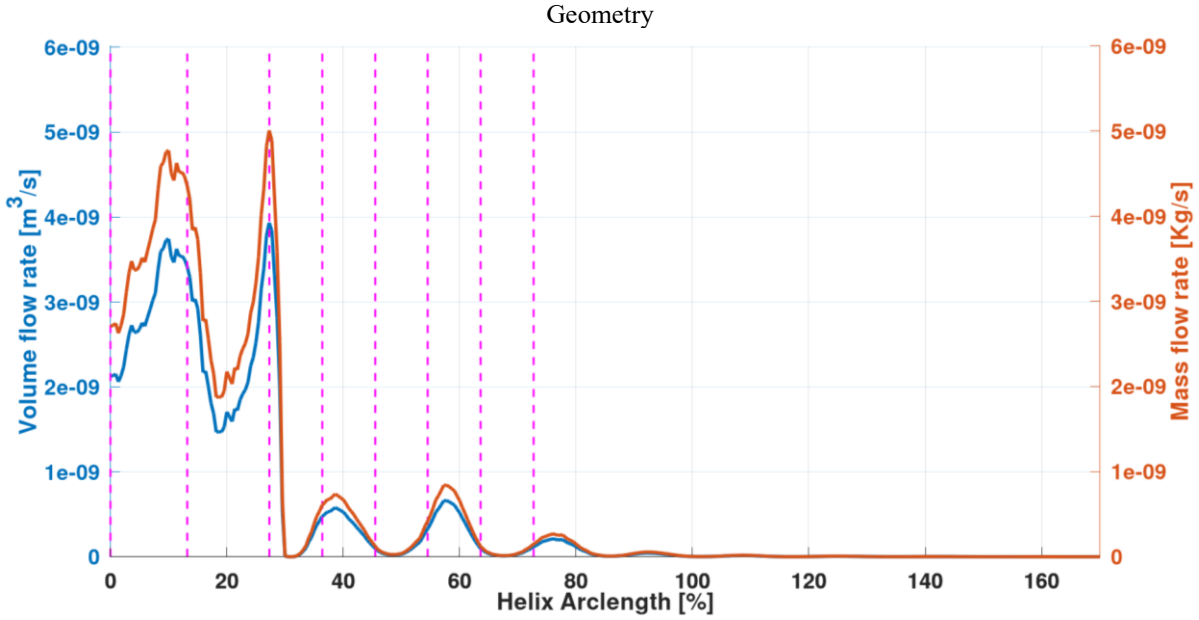

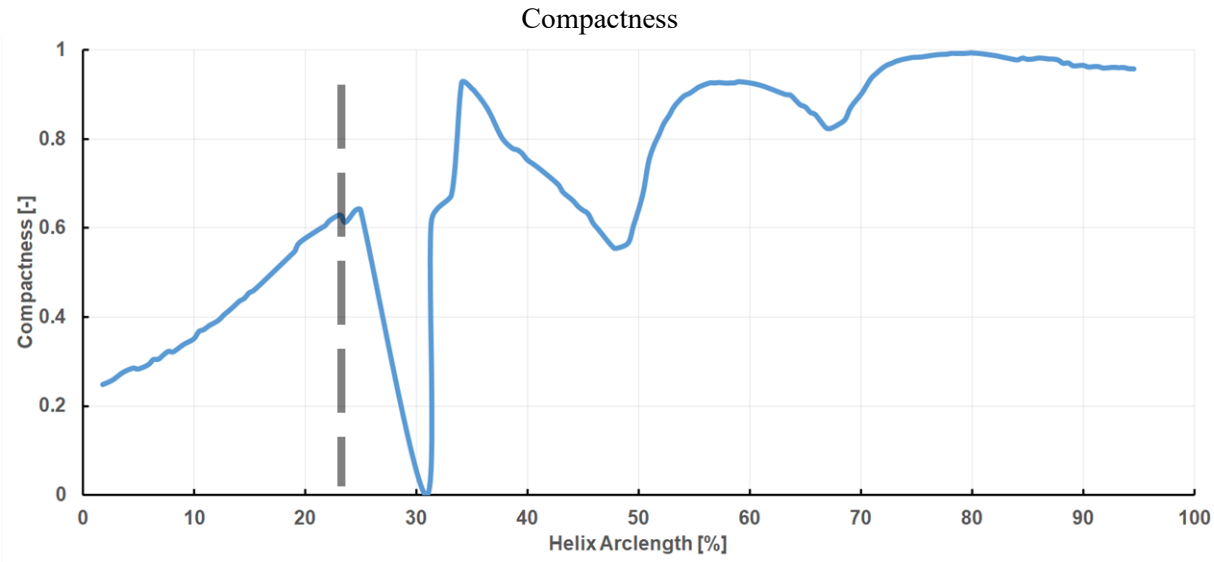

(b) Newcastle C2

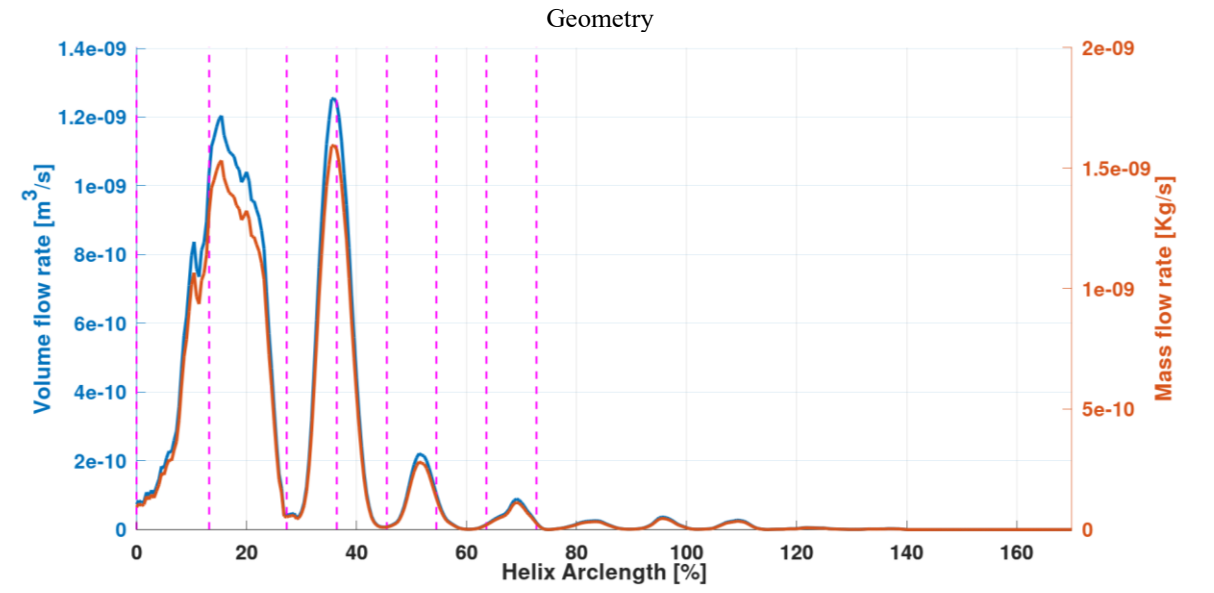

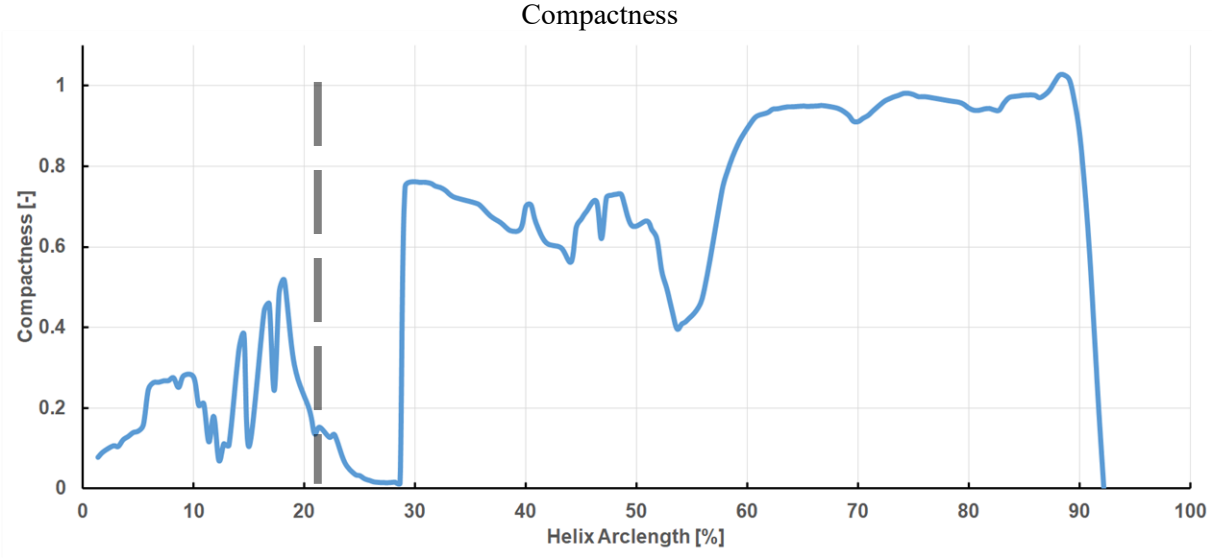

(c) Newcastle C6

Fig. 88: Shape parameters of tip-vortex cavity [59]

A detailed view of the intersection planes with the normal velocities of the four regions is given in Fig. 89 for the PPTC'11 case showing the leading edge in (a), the mixing zone in (b) and one node and anti-node in (c) and (d) respectively. Here it is particularly apparent that the upstream flow only occurs in the larger cross sectional areas of the anti-nodes. As a small overlay picture in the figures, the region shown is highlighted.

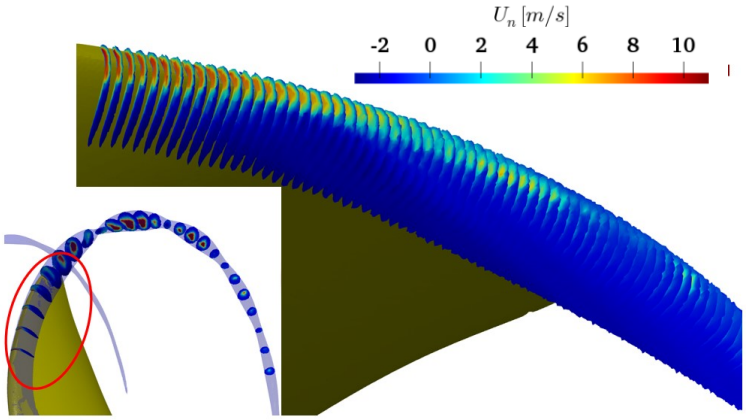

(a) Leading edge

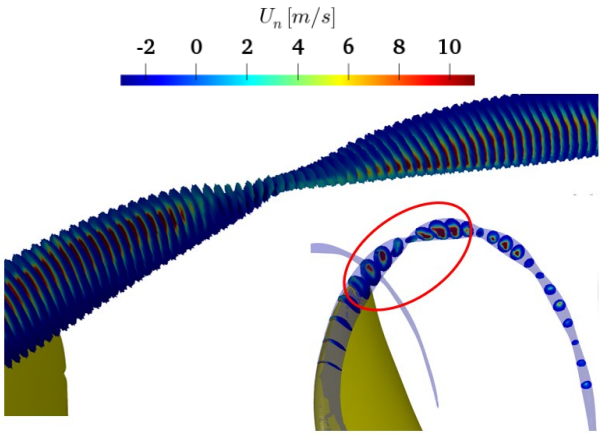

(b) Mixing zone

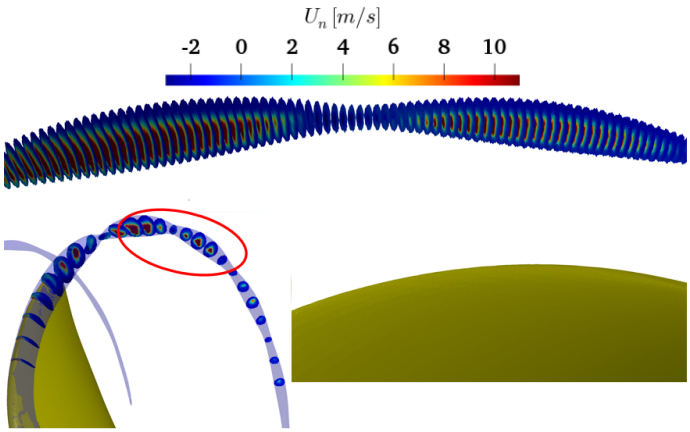

(c) 1. node

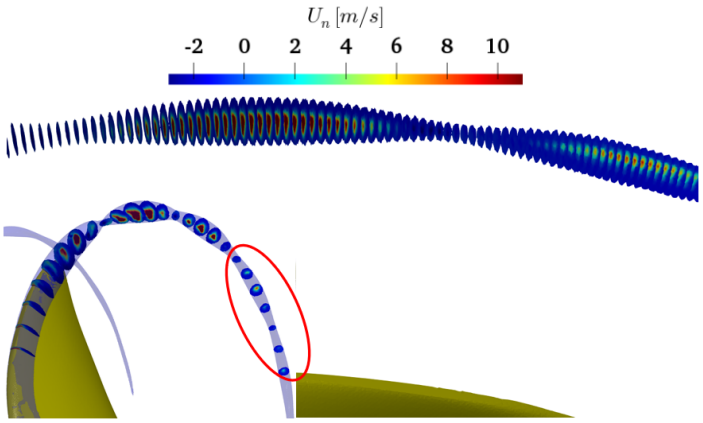

(d) 3. Anti-Node

Fig. 89: Details of tip vortex flow

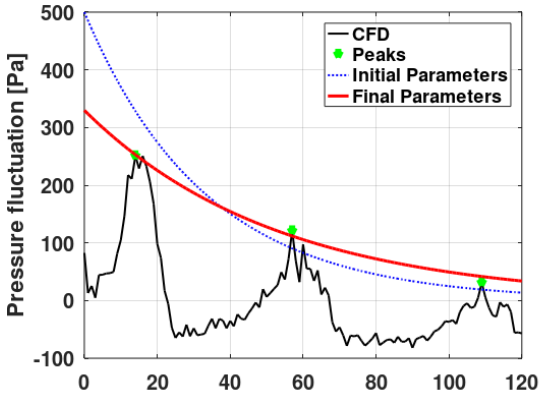

Helix slice number [-]

Fig. 90: Logarithmic decrement of area of cavity intersection

From the minimal pressure variations inside the vapor cavity the damping is calculated with the mean pressure period of $0.04325 \cdot D_P$ in m. The damping coefficients obtained from an exponential curve fit through the local maxima of pressure are summarized in Table 21 for a fit through all geometric data points describing a maximum or a mean of consecutive data points only. From this the damping of the nodes and anti-nodes follows the form of $f(\xi) = C \cdot e^{-\delta\xi}$ very well, where ξ is the longitudinal coordinate in the helix. The fitting of the function is shown in Fig. 90 with the peaks used for the fitting for the initial and final timestep of the converged MRF simulation. In addition, the MRF approach results are given for the case of applying all geometric data points to the fit as a comparison in the table and it achieves a mean period of $0.0463 \cdot D_P$.

Table 21: Axial pressure damping in vapor phase

Parameter	Average logarithmic decrement	Lehr damping factor	Damping constant
Equation	$\Lambda = \frac{1}{n}\ln\left(\frac{A_1}{A_n}\right)$	$\zeta = \frac{1}{\sqrt{1+\left(\frac{2\pi}{\delta}\right)^2}}$	$\delta = \frac{\Lambda}{T_D}$
Consecutive maxima only	0.46	0.073	–
All maxima	0.41	0.065	9.5
MRF	0.64	0.091	13.8

The cross-sectionally averaged resolved turbulent kinetic energy k_{res} in the vapor phase is plotted in Fig. 91. This quantity is highest in the mixing zone, where the formation of the primary tip vortex takes

place. This region corresponds to a node of the shape for example by comparing Fig. 89 (b) with a close view of the mixing zone. In this context it has to be noted that for other propeller cases the cavity is not formed in the mixing zone, but slightly downstream and thus cannot appear in this processed representation. The next peak of k_{res} is at the 1. node after the mixing zone, however, with a large decrease of the value and a similar trend followed by the 2. node. Thus, the mean turbulent kinetic energy is highest inside the nodes with small cross sections. The large downstream axial velocities and lowest turbulent kinetic energy take place at the anti-nodes, although there are velocity components in up- and downstream direction present.

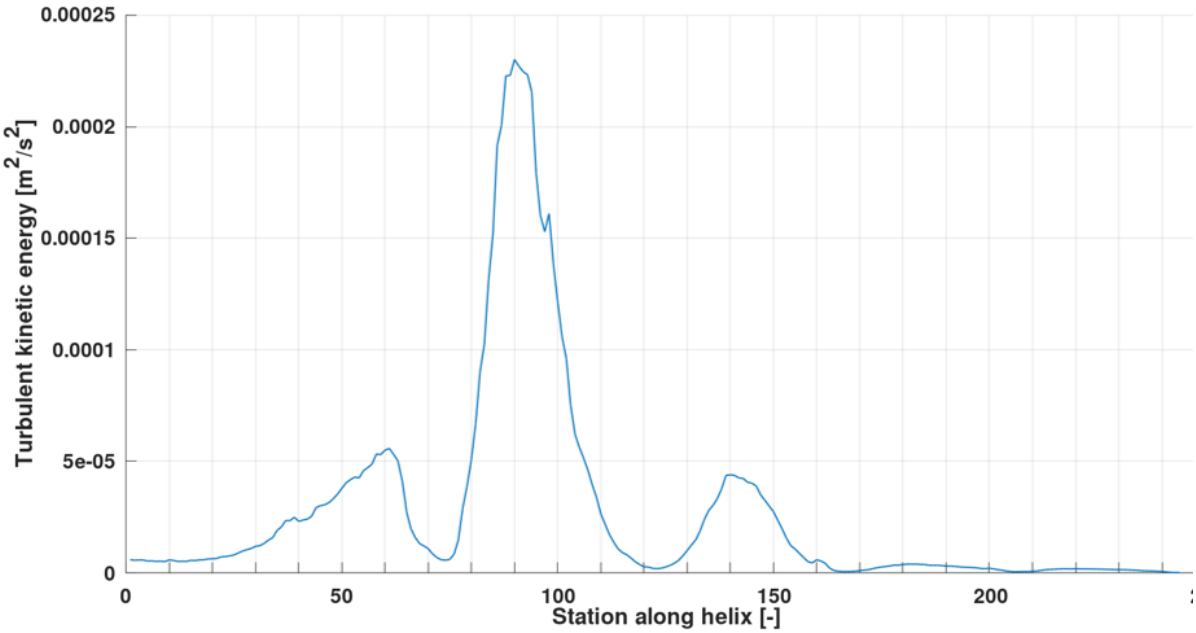

Fig. 91: Averaged resolved turbulent kinetic energy

An intersection along the minor and major axes through the tip vortex cavity at the node station t_3 and the anti-node station t_4 is shown at the top of Fig. 92 with the relative plane normal velocity for the non-cavitating case on the left and the cavitating case on the right. Below is a plot of the plane normal relative velocity along these lines leading to the typical characteristics of a rotationally symmetric vortex at least for the node station. However, at the anti-node station the modified velocity distribution due to cavitation and the flow inside the cavity is clearly visible. The location of the maxima are almost unchanged by the appearance of cavitation. In addition, an asymmetry due to the vortex roll up is visible, where one maximum is significantly higher than the other one, which is also well visible in the velocity contours above the plots. For reference the core center symmetrical Rankine and Burgers analytical solutions Eqs. (1) - (3) are given, where the viscosity is taken from water and the strain rate is used as a fitting parameter for the maximum of the Burgers vortex. At the nodes, the analytical solutions fit very well with the non-cavitating case and still resemble the shapes outside the vapor core for the cavitating case.

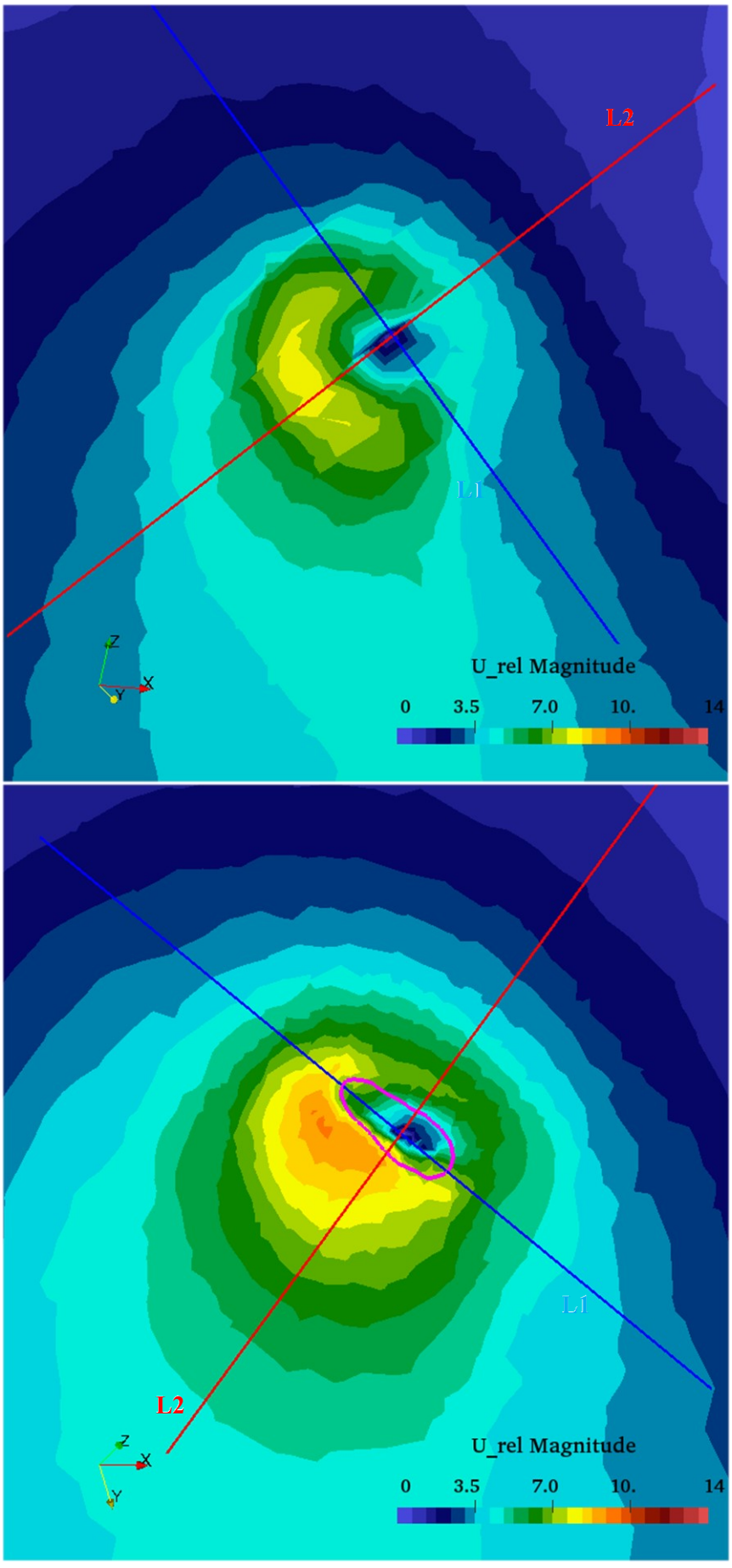
L2
L1
U_rel Magnitude
0
3.5
7.0
10.
14
L1
L2
U_rel Magnitude
0
3.5
7.0
10.
14

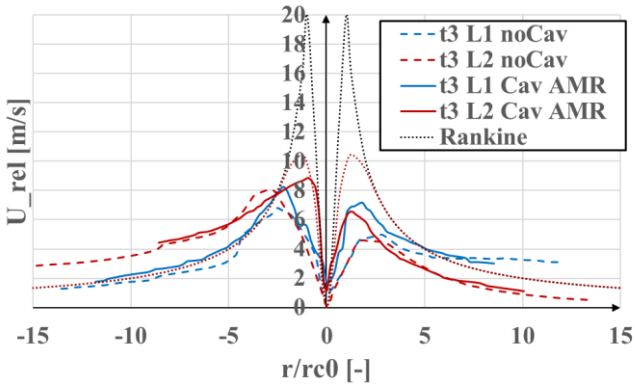
t3 L1 noCav
t3 L2 noCav
t3 L1 Cav AMR
t3 L2 Cav AMR
Rankine
U_rel [m/s]
r/rc0 [-]
20
18
16
14
12
10
8
6
4
2
0
-15
-10
-5
0
5
10
15

(a) t_3

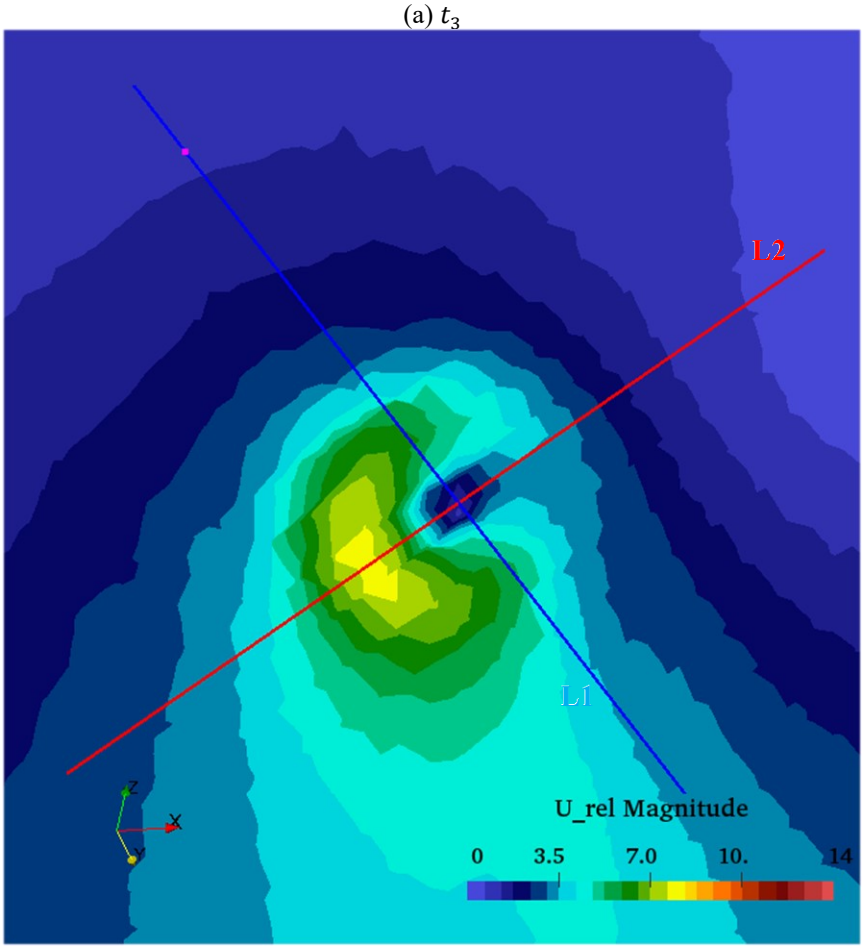
L2
L1
U_rel Magnitude
0
3.5
7.0
10.
14

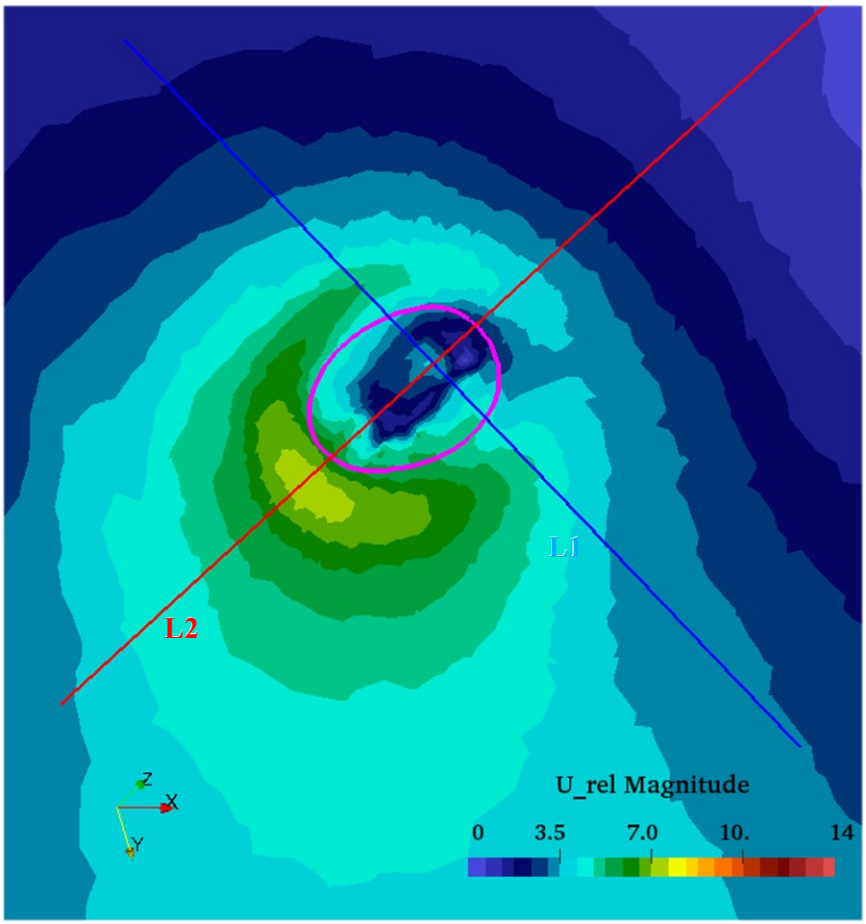

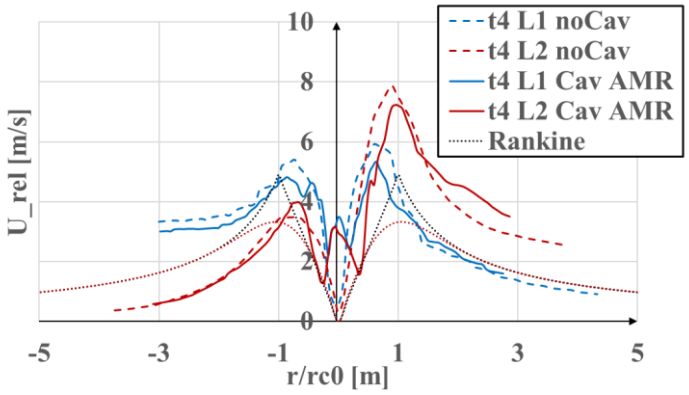

(b) t_4

Fig. 92: Azimuthal in plane velocity [59]

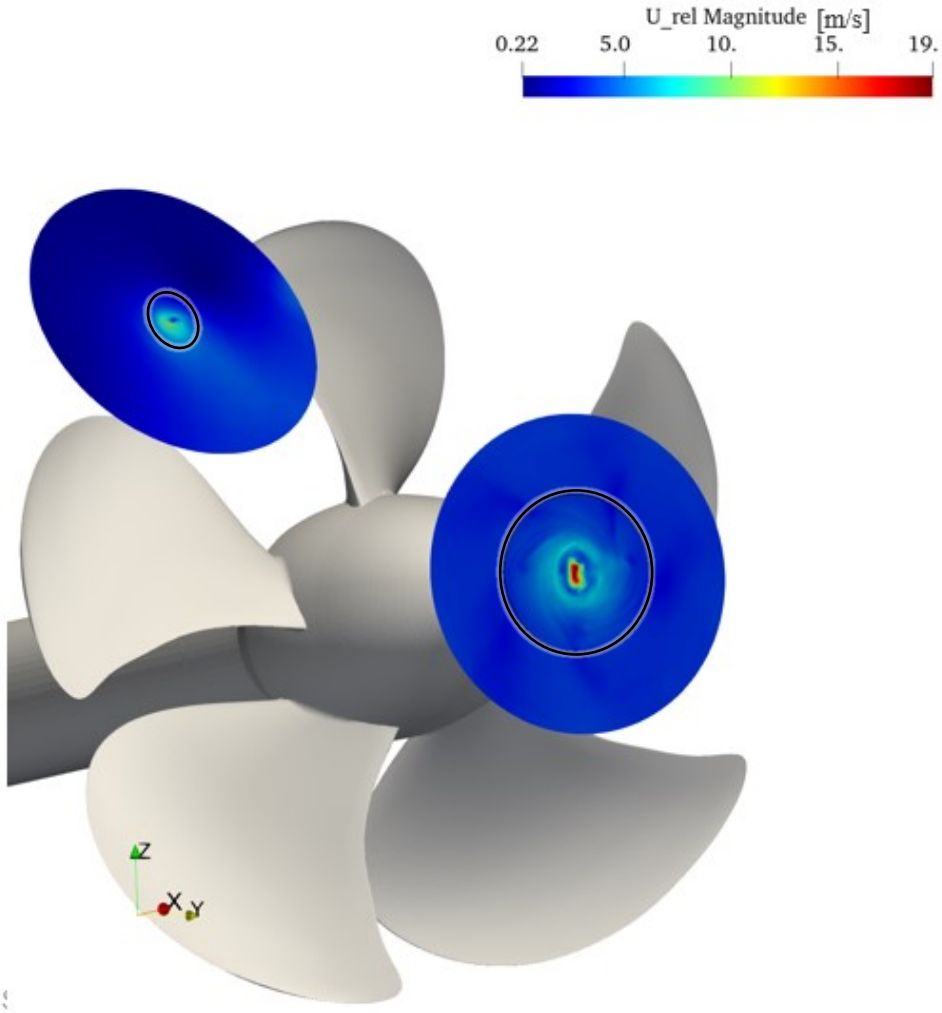

Fig. 93: Circulation radii

To characterize the vortex flow, the circulation is evaluated around a tip vortex and the hub vortex for the PPTC'11 $J = 1.019$ case as indicated by the black circles on the plane sections in Fig. 93. For this purpose appropriate integration centers and circles are required similar to the NACA 0012 hydrofoil from 5.1.2, as the circulation for a propeller is more sensitive to the location due to the complex bulk flow around the vortex.

While the selection of the integration circle for the cavitation hub vortex is trivial in the case of a propeller with straight inflow by placing the center on the rotational axis and using a flow normal plane as the dimension for integration, different options for the tip vortex are explored. The most obvious one would be to use the helix trajectory coordinate on helix normal planes, however, after the 2. anti-node the helix trajectory departs from the actual tip vortex trajectory in a non-negligible way as a result of propeller slipstream flow contraction. In Fig. 94 at station t_3 the center of area, the normal velocity maximum and the maximum vorticity inside the vapor phase are given, which are decidedly different for this node in the mixing zone. Whereas a deviation is visible between the point of maximum velocity and the center of area in the figure, they correlate well with each other at the anti-nodes. The Q-criterion shows an unclear distribution for this highly elliptical shape in (c), which is why it is excluded in the further analysis.

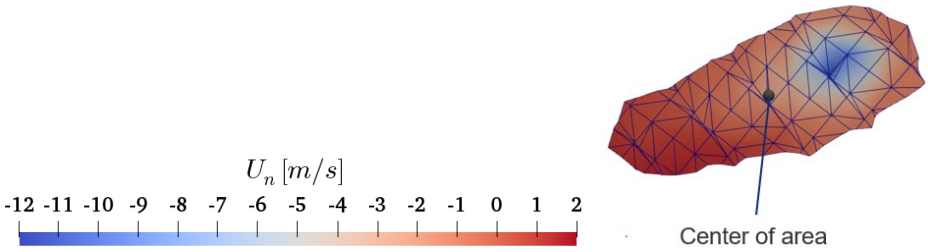

(a) Center of area

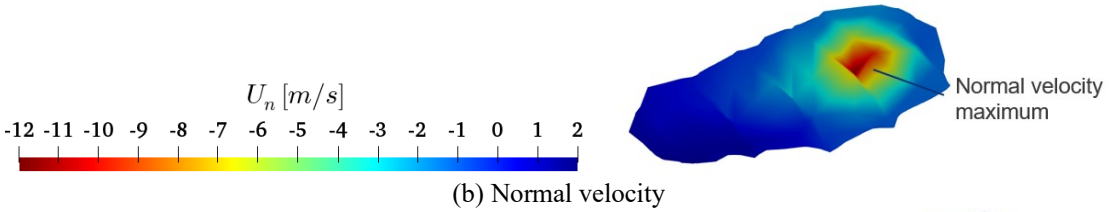

(b) Normal velocity

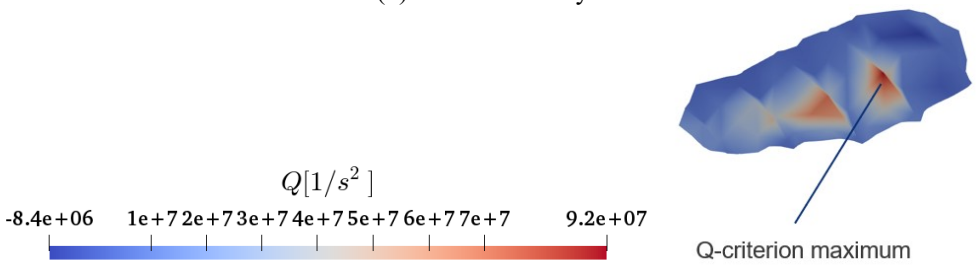

(c) Q-Criterion

Fig. 94: Determining the cavity center

Pressure on the other hand is very similar inside the complete cavity at the value of the vapor saturation pressure and shows only little local variation. The minimum pressure is thus not necessarily centered inside the cavity at most slices and additionally varies strongly between consecutive slices. In Fig. 95 (a) circular slices along the helix trajectory with the center at the trajectory intersection are shown, while in (b) the respective pressure center is used for circular slices with the same radius. This proves that there is a strong trajectorial variation and thus the circles are misaligned with respect to each other. In (c) the minimum pressure for a random slice is illustrated with the magenta point, which shows the location might deviate strongly from the actual center of the cavity.

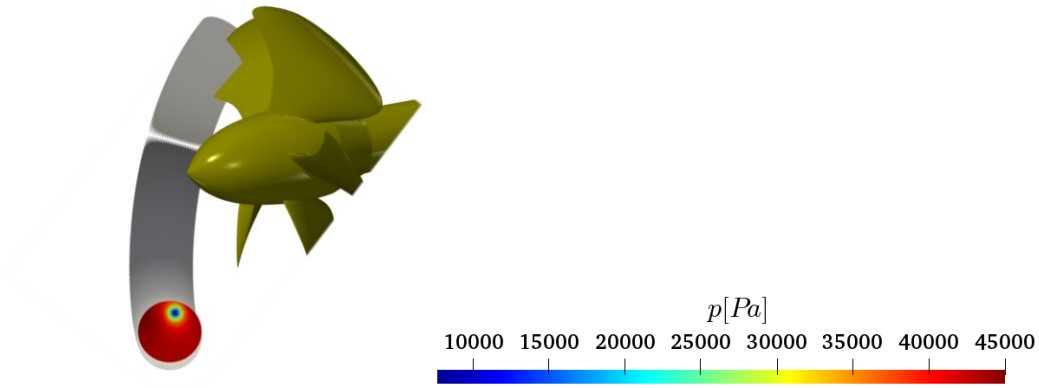

(a) Helix coordinate slices

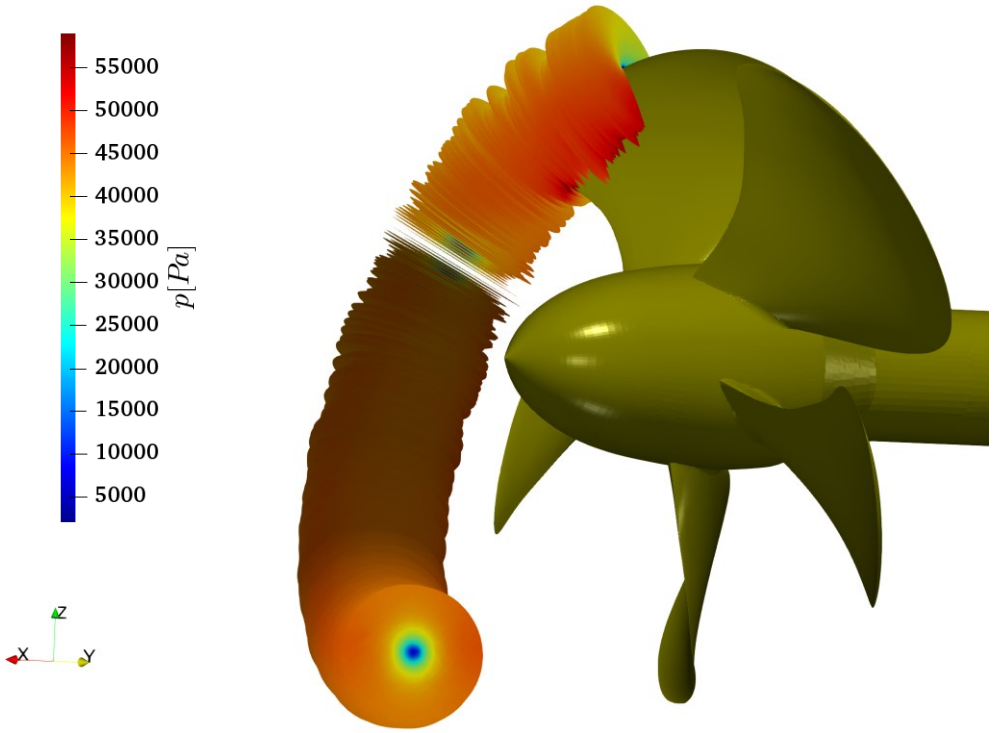

(b) Pressure center coordinates

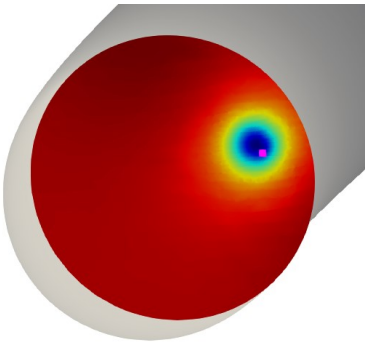

(c) Minimum pressure

Fig. 95: Determining the integration loop center

The resulting circulation along the cavitating tip vortex for three integral center options is summarized in Fig. 96. Even though it is the easiest evaluation to set-up, the effect of the tip vortex leaving the helix trajectory due to jet contraction in the propeller slipstream is illustrated by the falloff of the circulation value after the 2. anti-node around slice 170 in (a). The resulting circulation relative to the pressure centers as circulation integration center is given in (b), which leads to an overall well converged cavitation along the vortex trajectory, however, there are large fluctuations between adjacent planes and this form of automated evaluation is only possible, if there is a clear pressure minimum, which is for instance not given in vicinity of rudders or other appendages that the tip vortex may interact with. In (c) the circulation around the center of area of the cavity cross section in the planes leads to a well converged circulation similar to a hydrofoil, with the only disadvantage that it requires an active cavity to evaluate. So in summary while the first two options may be evaluated in non-cavitating conditions, the best result for the circulation in terms of a converged tip vortex circulation is achieved with the center of area of the cavity intersection.

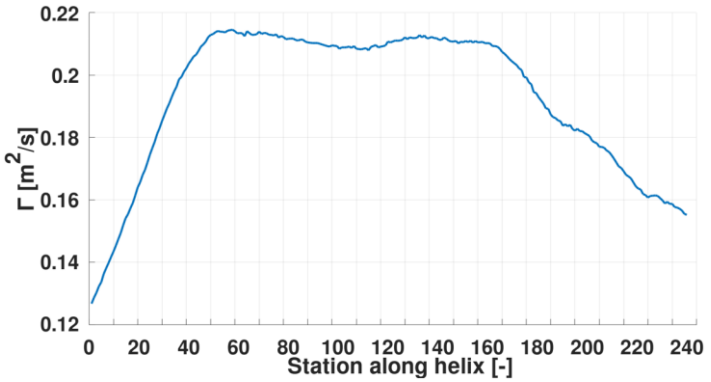

(a) Helix Coordinate

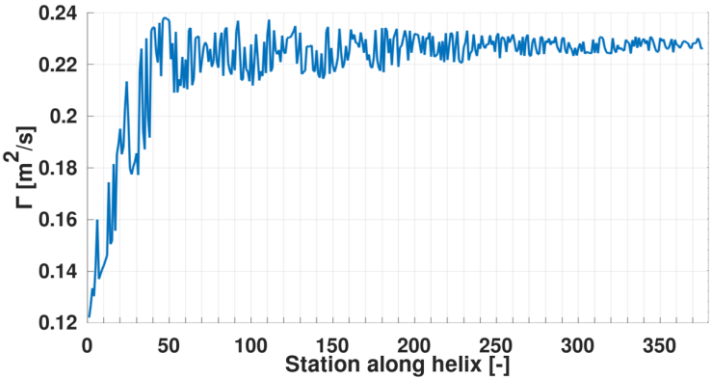

(b) Minimum pressure

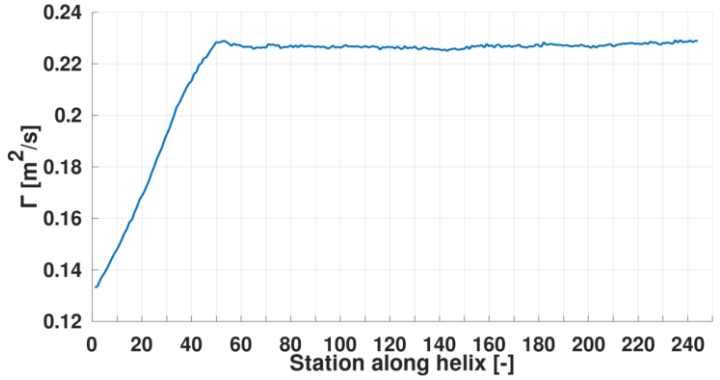

(c) $\alpha_{0.5}$ slice area center

Fig. 96: Circulation along streamwise cavitating tip vortex trajectory

For the Newcastle cases similar results are achieved with a circle of radius $r = 0.068 \cdot D_P$ in Fig. 97 for the two options along the helix coordinates and the center of area of the cavity intersection. For both cases the blade ends around plane 60 as seen in Fig. 87 (b) and (c) respectively. There is an issue indicated in red with the automated evaluation for the case C2 around the center of area coordinate, which lies in the fact that in the mixing zone the cavity disappears, so the data point for evaluation cannot be found. Otherwise, the cases are consistent and show a jump in the circulation value in the mixing zone, just when the cavity leaves the blade, and remain at a constant value over most of the trajectory, which slowly dissipates downstream. For the case of C2 evaluated with the helix coordinates, a peak appears at the 2. anti-node, however, it can be expected that this is caused by the slipstream contraction and thus incorrect circulation evaluation rather than the physical phenomenon.

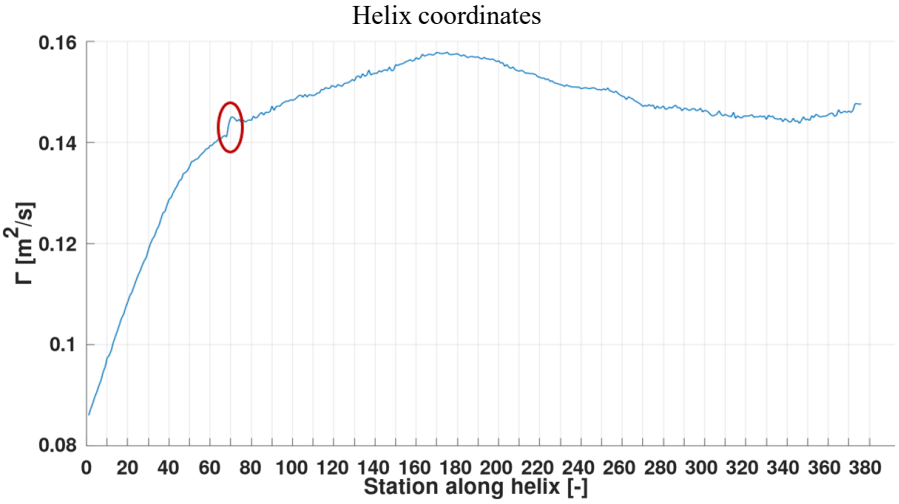

Center of area of α

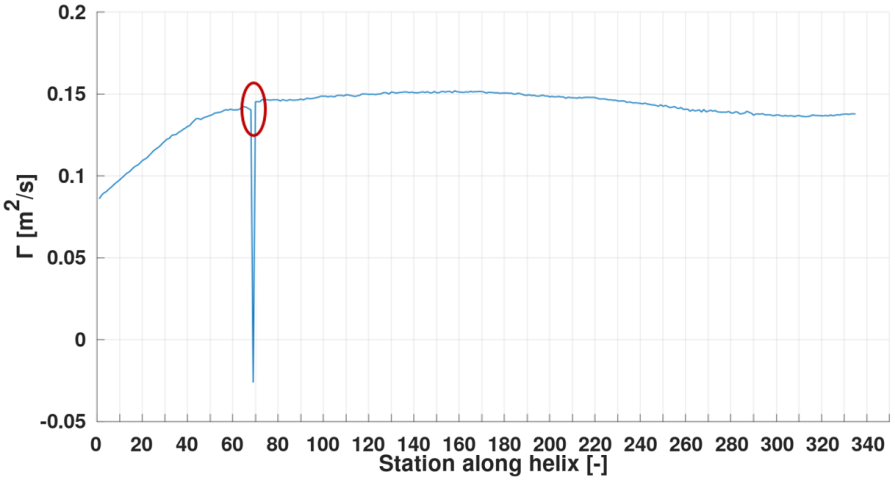

(a) C2

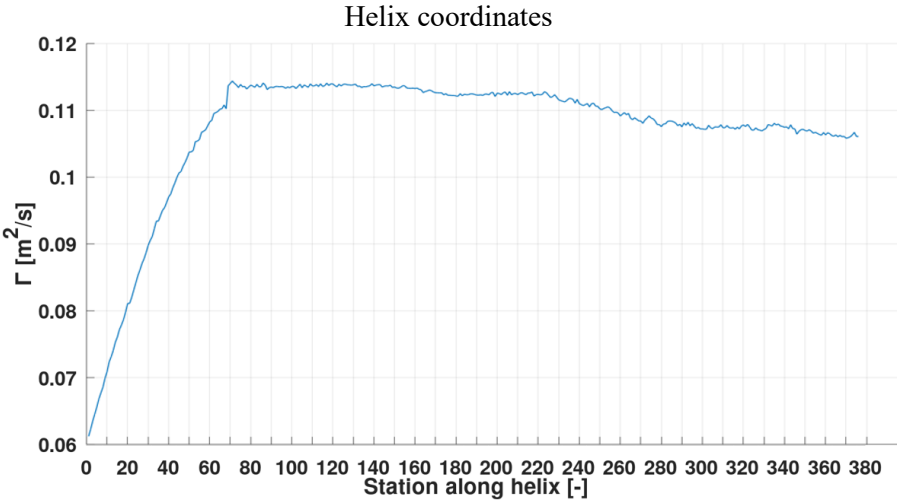

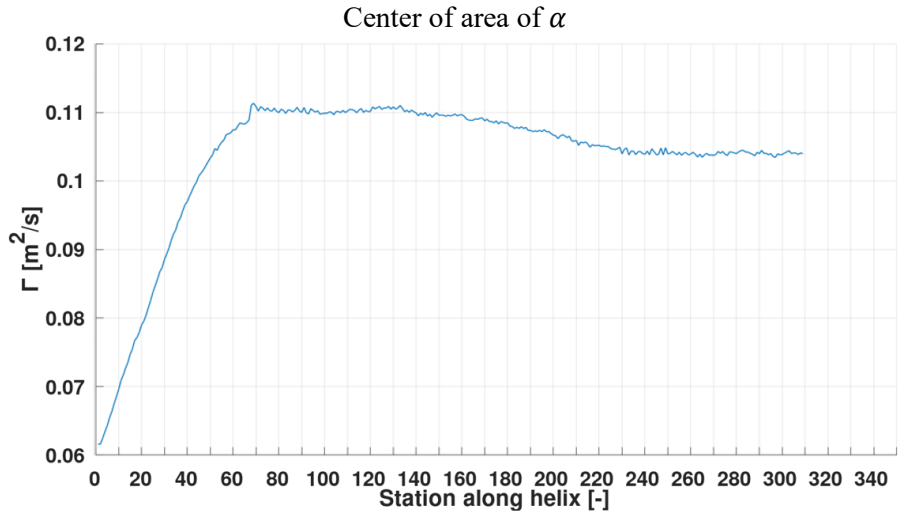

(b) C6

Fig. 97: Circulation along different vortex trajectory definitions

A comparison of the circulation of the tip and hub vortex for the PPTC'11 $J = 1.019$ case and the relation between the two trailing vortex quantities is given in Table 22. Since the hub vortex originates from the combination of the root vortices from the five propeller blades, it is expected that the circulation in the hub vortex is similar to the circulation of the 5 blade tip vortices. This would be true for a hydrofoil with constant loading along the span, for this propeller, however, it seems that the tip vortices combined hold about 2.7 times the amount of circulation contained in the hub vortex. This should be an effect of the high tip loading of the PPTC'11, which is intentionally created to produce stable cavitating tip vortices.

Table 22: Circulation relations

Location	**Γ [m^2/s]**
Γ_{Tip}	0.222
$\Gamma_{Tip} \times 5$	1.110
Γ_{Hub}	0.412
$\Gamma_{Tip} \times 5$ / Γ_{Hub} [%]	269

Next the temporal evolution of the tip vortex cavity in uniform inflow is analyzed. The cavity oscillating modes are believed to be one of the primary additional noise sources from a stable tip vortex cavity [68], besides the dissolving of the cavity downstream. Fig. 98 shows the time evolution of the length of the perimeter of the cavity cross section on the helical trajectory for the PPTC'11 $J = 1.019$ case at the node t_3 and the anti-node t_4. Overall, these shape variations can be considered minor in size and with frequencies of about 1 per rotation or $f = 25Hz$, which is too low to be considered vortex oscillating modes. These variations could instead stem from numerical issues due to their appearance once during rotation.

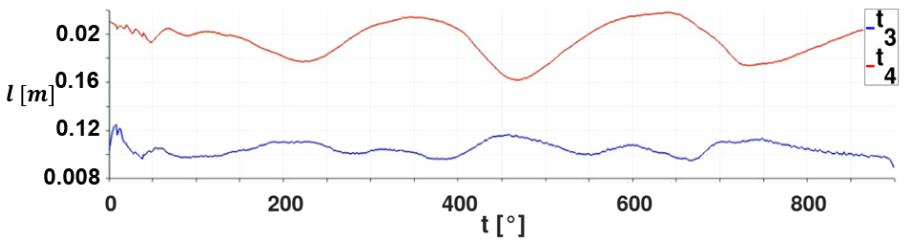

Fig. 98: Time evolution of cavity diameter t_3 and t_4

In Fig. 99 (a) the domain pressure at three observers with one directly located at the sliding mesh interface and two further away at $r/R = 2.0$ as indicated in the overlay image are showing different fluctuations. While the far observers experience the same trend, with a very low frequency caused possibly by domain pressure fluctuations between inlet and outlet with $f = 0.25Hz$, the pressure observer at the sliding interface correlates with the propeller rotation rate as expected. The cavity surface area in (b) respectively shows again a low frequency fluctuation period with a peak at $f = 35 - 40Hz$ as given in the Fourier transformation of the cavity surface in (c), which is about 1.4 times the propeller rotation frequency $f = 25Hz$ and about ≈ 0.28 times the propeller blade frequency of $f = 125Hz$. Additionally, there is a post-processing issue visible in (b) with a time wise irregular drop to an extreme local minimum, which should be ignored.

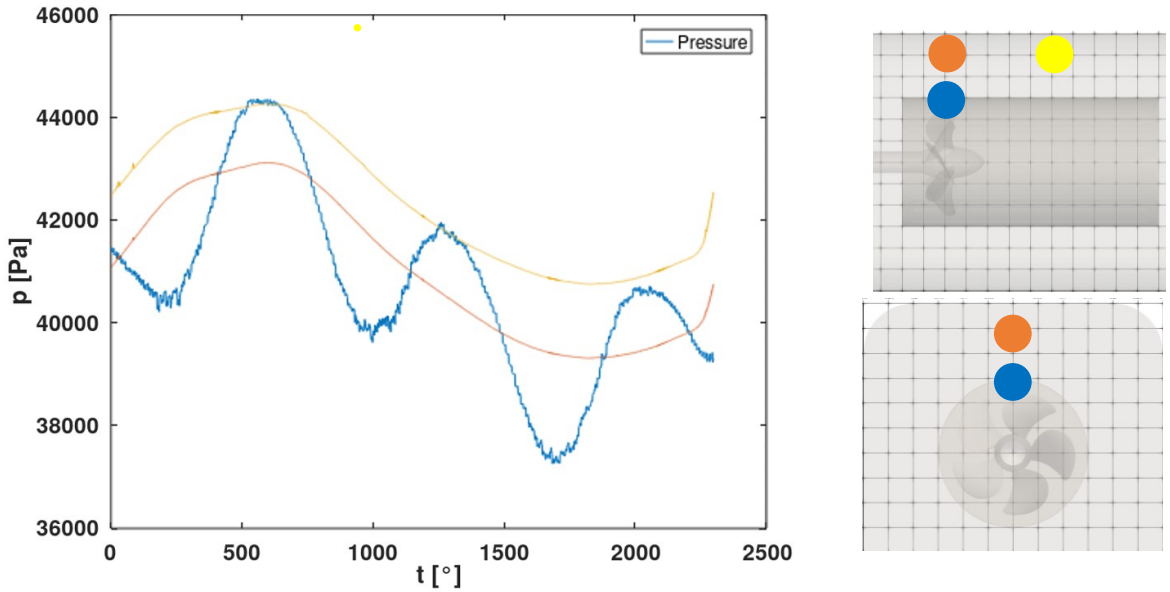

(a) Pressure over one rotation at all observers

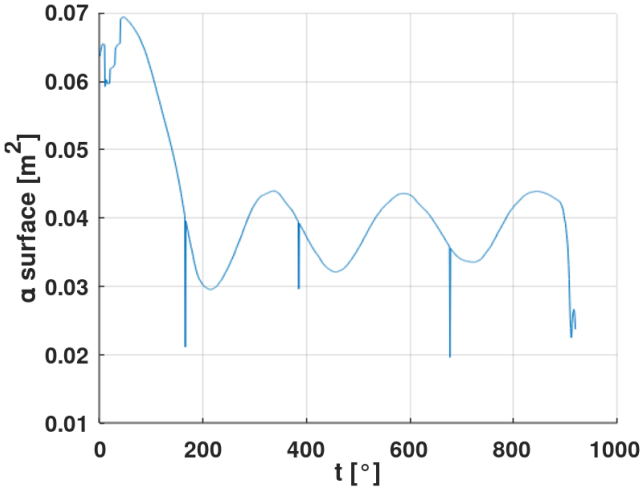

(b) α surface area

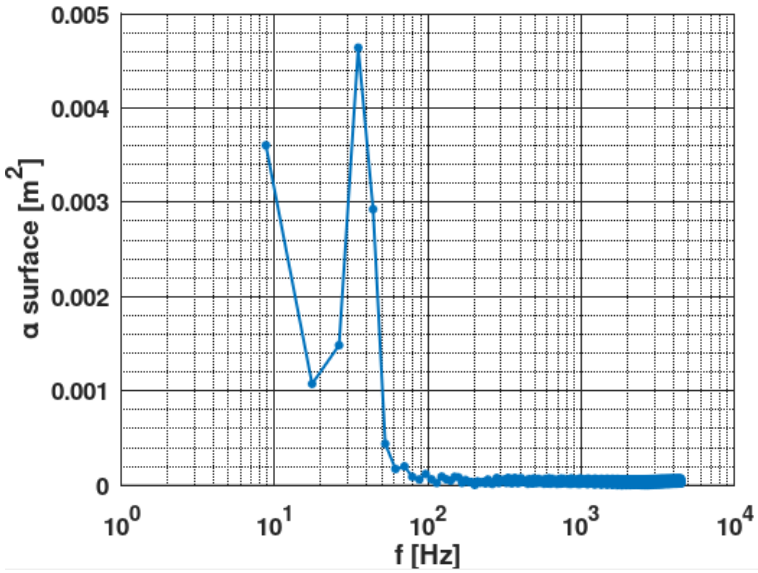

(c) α surface area FFT

Fig. 99: Cavity surface temporal development, PPTC'11 $J = 1.019$

A similar evaluation is conducted for the Newcastle C2 case in Fig. 100. In (a) the pressure temporal development at the observers defined in Fig. 47 is plotted together with the cavity surface size over time. There is a slight correlation between the quantities as expected, however, the cavity surface area time development Fourier transform in (b) leads to a peak frequency of $f = 45 - 50Hz$, which is again 1.4 times the rotation frequency of the propeller $f = 35Hz$ and 0.28 times the blade passing frequency $f = 175Hz$. Thus, it seems the cavity modes are not captured by these simulation setups, which is confirmed to stem from the missing wake field excitation of the cavity. [93]

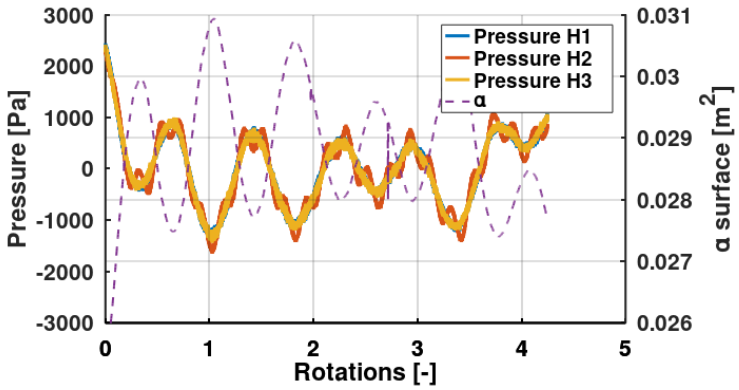

(a) Pressure at the observer locations with α isosurface area

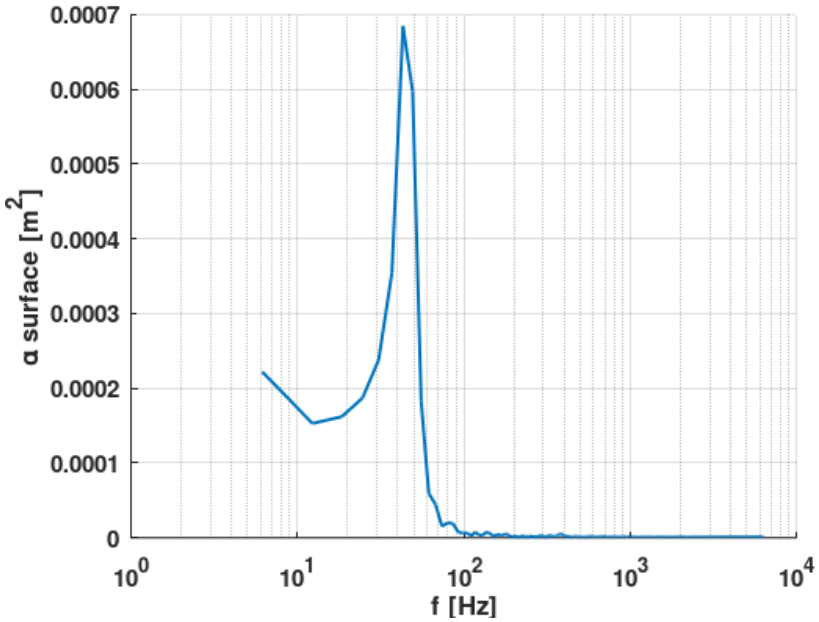

(b) Spectral α surface area

Fig. 100: Cavity surface temporal development, Newcastle C2

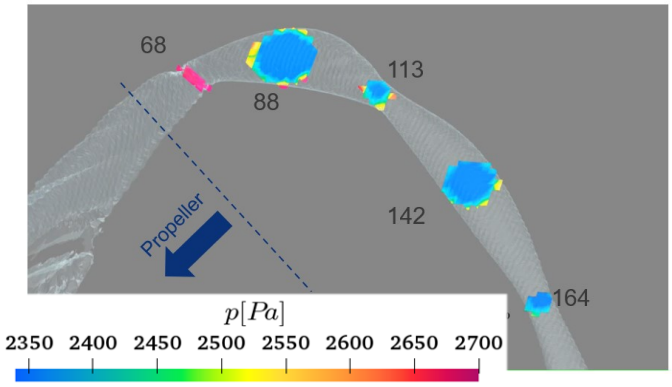

Fig. 101: Sample evaluation slices in helix normal plane

Nevertheless, to exclude any issues with the dynamic evaluation as the tip vortices are moving with each time step, the time evolution of the cavity fluctuations is investigated further with a simpler approach. The PPTC'11 $J = 1.262$ case is simulated with MRF, in order to have fixed cavity locations in the simulation domain and facilitate the time dependent evaluation of the geometry and flow characteristics with time invariant positions in space. With identical slice definitions along the vortex helix trajectory as in the $J = 1.019$ case, the α isosurface with plane locations is indicated in Fig. 101. The time history of several flow variables is given in Fig. 102 in the mixing zone for plane 68 and the first two nodes in plane 113 and 164 and anti-nodes in plane 88 and 142 as indicated in Fig. 101 over one fifth of a rotation or $\Delta t = 72°$ with a time resolution of $\Delta t = 0.1°$. The cavity area mean mixture density ρ_m in (a) gives an indication of the relation of water to vapor content inside the detected cavity at the respective trajectory intersection plane, which correlates also with the cross-sectional area of the cavity. The smaller the area the larger the density, as there are less cells and thus a more blurred interface. From the development of the quantity over time it can be concluded, however, that the mean density at anti-nodes is time-invariant, while the nodes experience high fluctuation decreasing in amplitude with increasing distance from the propeller blade. This is in accordance with the damping along the node found for the pressure in the AMI analysis. Accordingly, the cavity helix trajectory cross-sectional area mean volume flow rate $\dot{V}$ normal to the intersection, or in other words the material flow along the vortex, varies

similarly over time in (b). While all intersection planes experience slight fluctuations in area and velocity, it is the anti-nodes that experience the largest amplitudes, together with the mixing zone. Along the vortex the time mean flow rate is consistent, however, the last anti-node or plane 142 shows a two times larger volume flow rate over the complete duration, although the nodes before and after this plane feature identical lower flow rates. This implies that the volume flow rate along the vortex is increased and reduced over the passage between two nodes, which must mean that the amount of vapor mass changes in-between. The cross-sectional mean mass flow rate $\dot{m}$ in normal direction along the vortex is evaluated in (c), showing similar trends regarding the amplitude of the fluctuations over time, with the node experiencing almost no fluctuations, while the mixing zone and the anti-nodes show large fluctuations that are decreased in downstream direction along the vortex. Within the second node, the fluctuations are almost attenuated, although the mass flow is consistently higher over the complete duration. A closer look at the time mean values reveals, that up to the second node the flow rate increases, with the largest rate of positive change between the anti-nodes and nodes, which is accompanied by a reduction of the cross section, meaning the velocity within the vapor phase has to increase significantly and possibly new vapor mass has to be generated in-between. The subfigure (d) indicates the mass exchange rate $\dot{m}_\alpha$ parallel to the cross-sectional plane from vapor to water, which varies strongly over time without clear correlation with the normal flow rates in (b) and (c). Generally, the nodes experience lower fluctuations over time, while the mixing zone and anti-nodes show larger variations, which unlike the other quantities are not periodic. There is a tendency of the rate of change from water to vapor (negative values) reaching a peak about half a period before the downstream plane experiences a peak of axial flow rate.

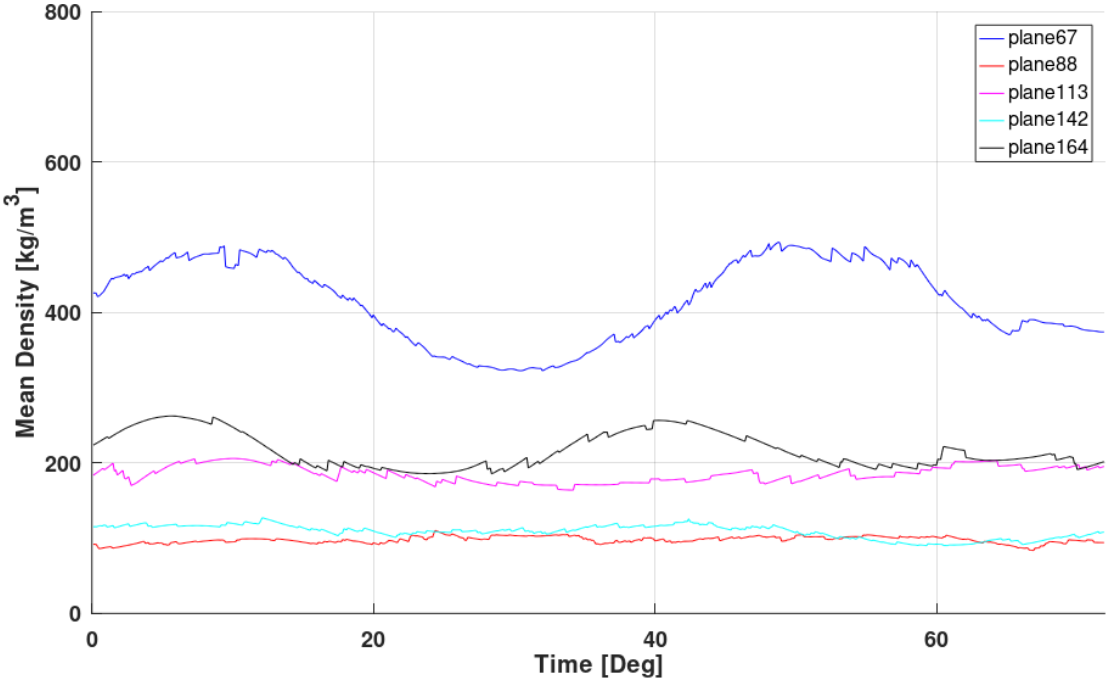

(a) Density

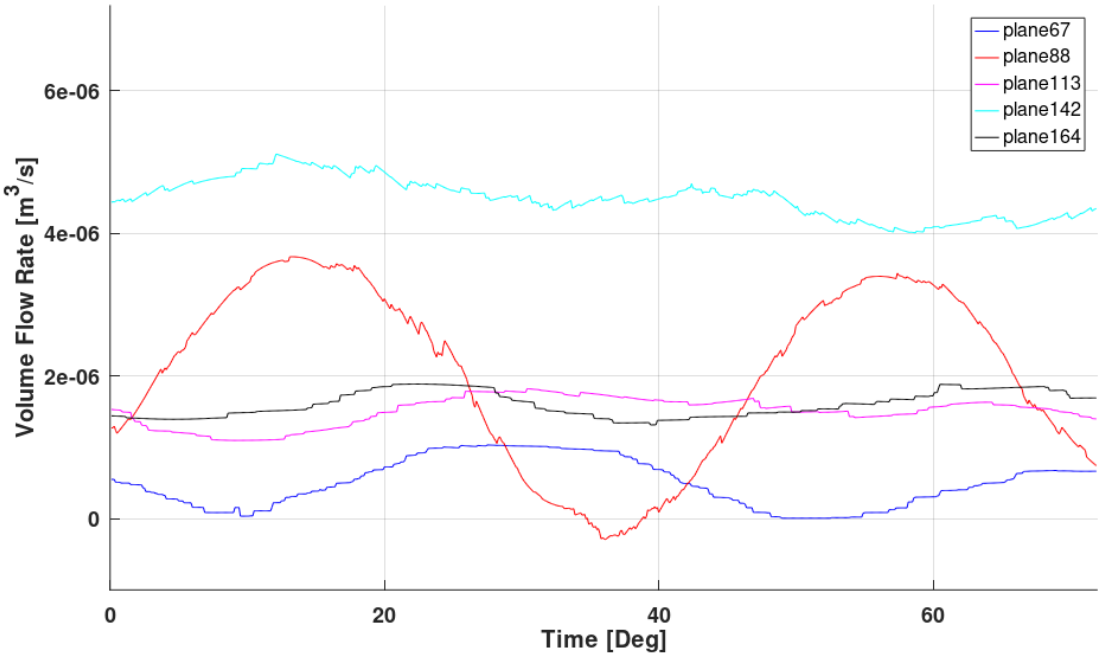

(b) Volume flow rate along vortex inside of vortex

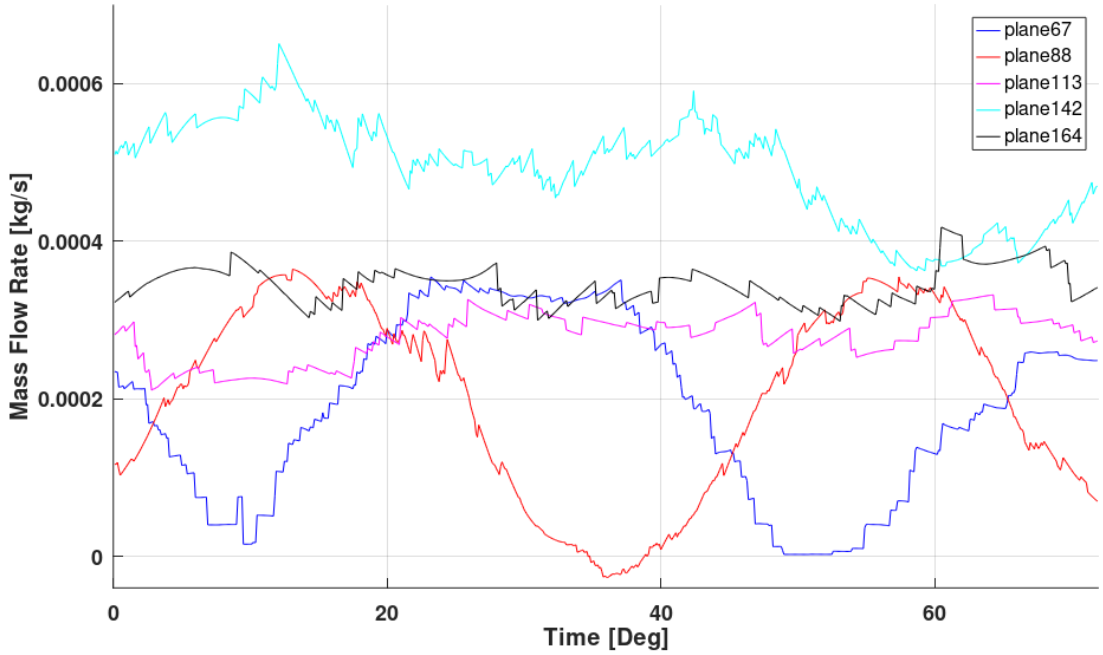

(c) Mass flow rate along helix

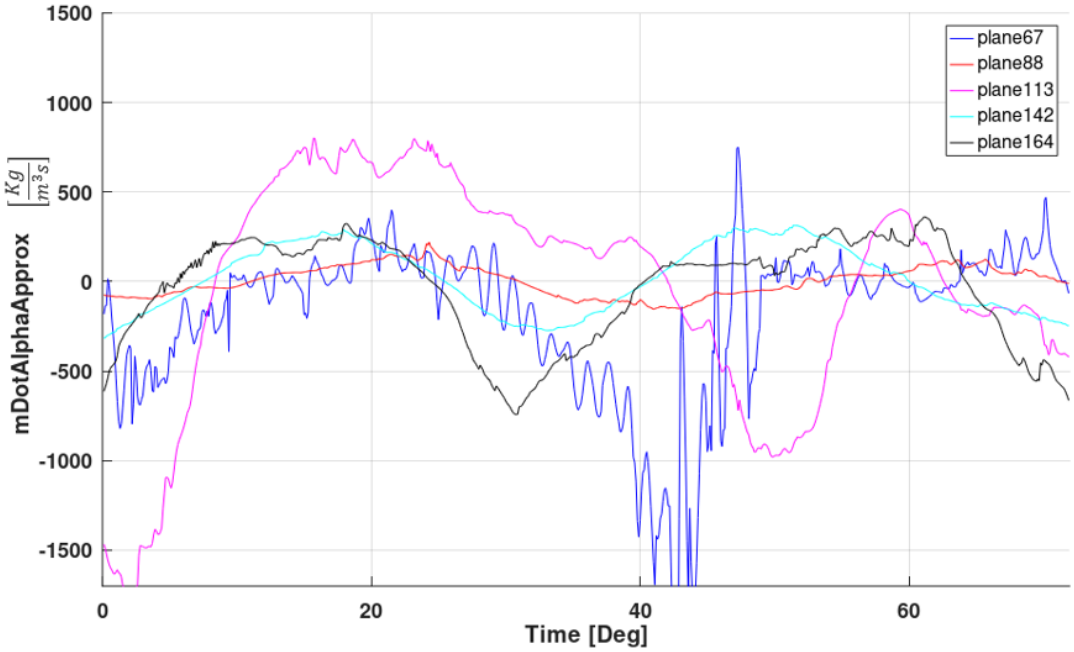

(d) Integral mass transfer rate

Fig. 102: Flow variables in cavity at planes over time

In conclusion, at nodes the fluctuations are lower than at anti-nodes, which means vapor has to condensate in between over time. The mass transfer rate from vapor to liquid seems to fluctuate more at nodes. The question remains, if there is an increase in vapor mass in-between those stations, which triggers these periodic oscillations of the flow rate. For this reason, the gradient between the values of the neighboring stations from Fig. 101 with intermediate stations is calculated in Fig. 103 and given in relation to time. Firstly, in (a) the mass transfer rate sorted by the four regions of increasing and decreasing cross-sectional area appears to experience similar trends independent of location along the vortex with sign changes happening at the same point in time. It can be said that the mass transfer is almost zero in the regions of increasing diameter of the cavity and high in regions of decreasing diameter and the temporal fluctuations are generally higher in the nodes than the anti-nodes. This means the primary driver of mass transfer lies between the anti-node and node locations with decreasing diameter. In (b) and (c) the flow rate is positive, meaning that the bulk flow is traveling downstream along the vortex at all locations. In the first anti-node the volume flow rate, however, reaches almost zero twice over the evaluation period, which coincides with upstream mass exchange from vapor to liquid and with the upstream velocities in the vapor core seen in Fig. 89 for the other operation point $J = 1.019$. Overall, the nodes have a low fluctuation in the volume flow rate, while the anti-nodes experience some fluctuations over time. The dissipation of these fluctuations is very high in the first two spatial oscillation periods of the cavity along the trajectory, which could be numerical. Although time variations can be observed in this simulation, they are relatively small and in combination with the findings of reference [93], it is clear that for the open water test condition, the cavity does not achieve sufficient excitation by an upstream disturbance such as a wake field to generate the cavity deformation modes postulated in the literature.

The subfigures (d) and (e) show the time dependent gradient determined from the quantities between the neighboring stations. A strong anti-correlation between the regions of increasing and decreasing cross sectional area of the cavity can be identified. It appears that the difference of the flow rate between the anti-nodes and nodes correlates somewhat with the mass transfer from vapor to liquid at the respective upstream anti-node.

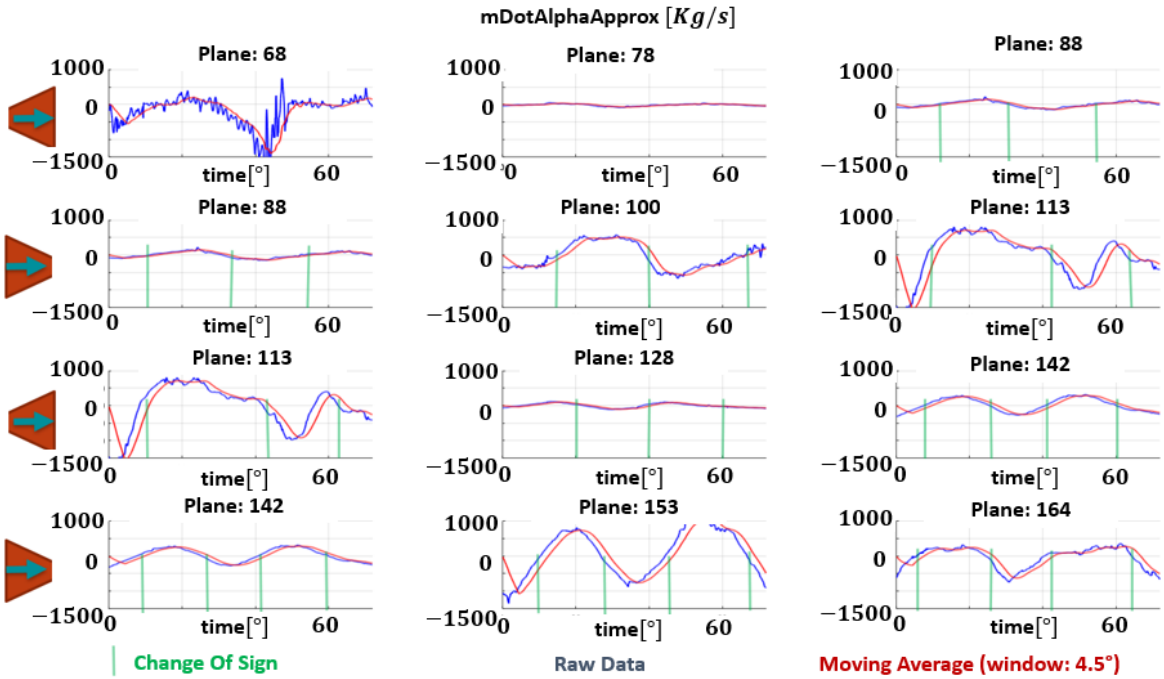

(a) Mass transfer from vapor to liquid

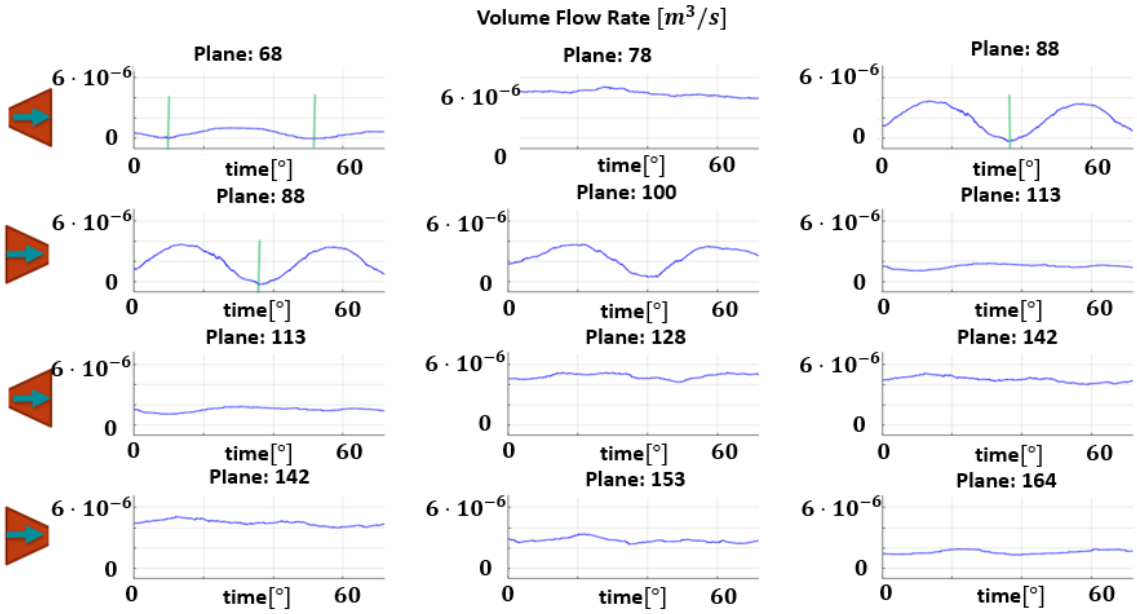

(b) Volume flow rate along helix

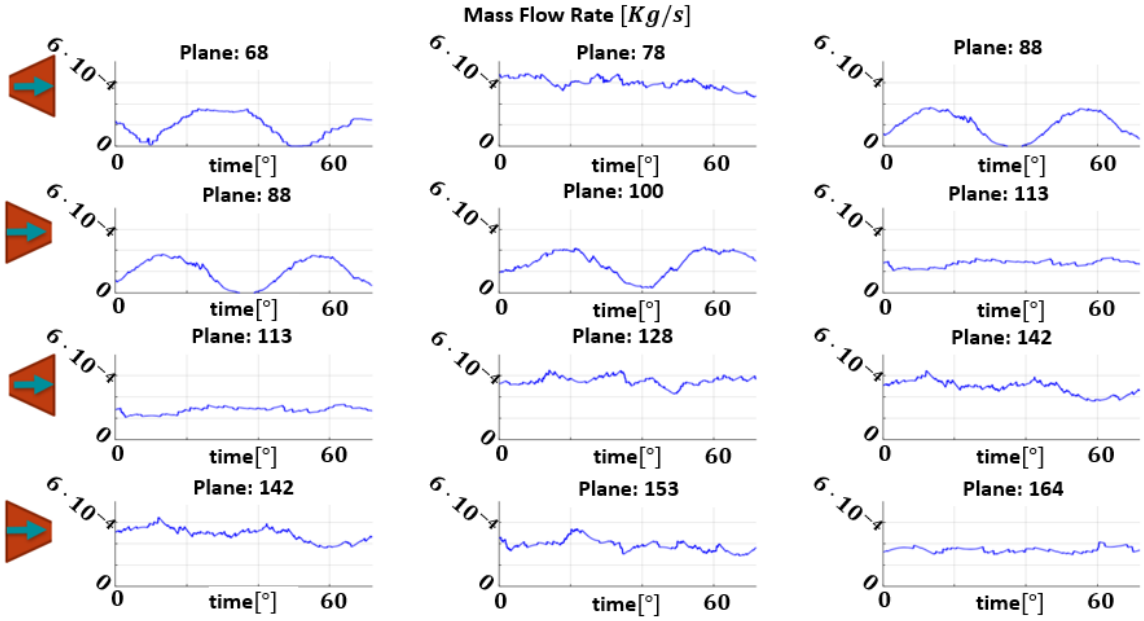

(c) Mass flow rate along helix

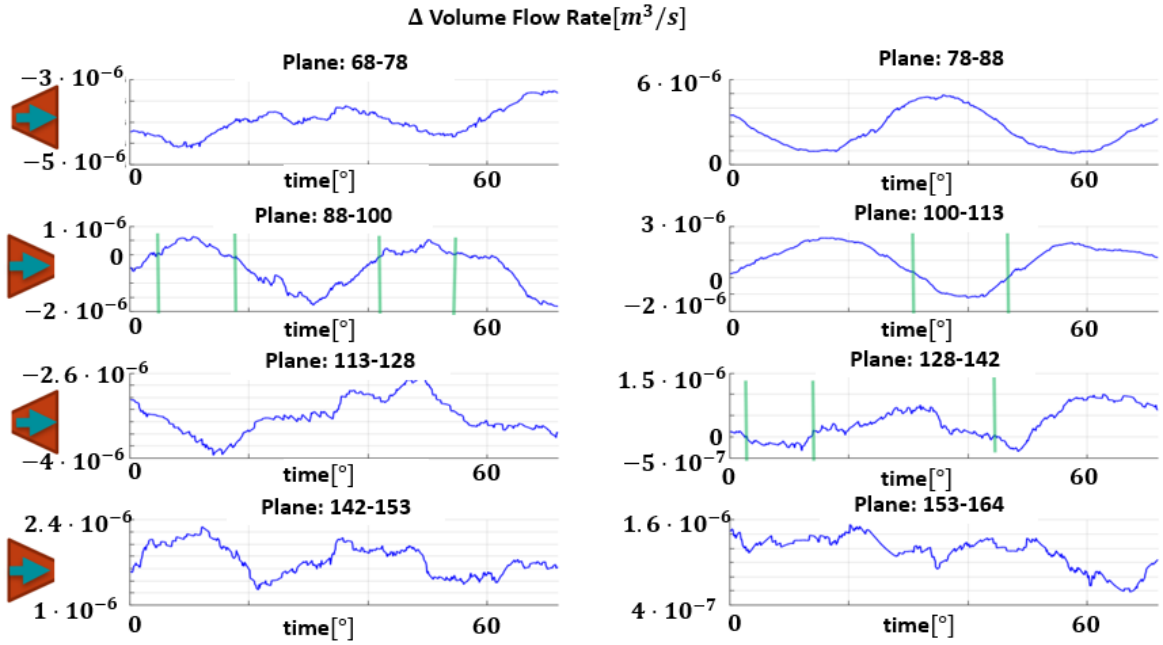

(d) $\Delta\dot{V}_l$ between planes

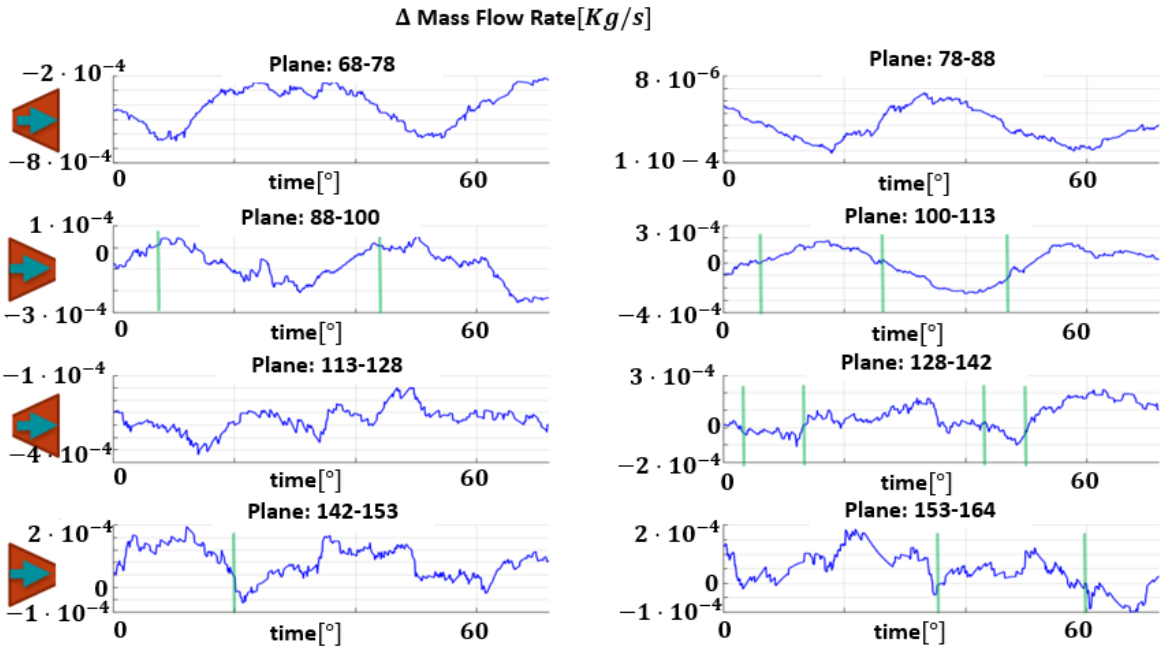

(e) $\Delta\dot{m}_l$ between planes (calculated with mean density)

Fig. 103: Gradient at nodes over time

The results from the subfigures (d) and (e) are summarized in Table 23 with the arithmetic mean values over the 720 timesteps, where a negative value means the increase of mass flow with downstream direction and vice versa. For normalization of each value the upstream plane is used leading to a percentage value of change over time with respect to the upstream plane of the respective trajectory section. It results, that the relative spatial rate of change of volume and mass flow rate along the vortex is considerable over the complete investigated period and changes strongly in both the regions of increasing and decreasing diameter of the cavity. Opposed to the instantaneous observations above, it seems that the time mean values lead to larger changes in the regions of increasing cavity area. However, it is consistent regarding the dissipation of the excitation with increasing trajectory length downstream.

Table 23: Mass transfer volume flow rate gradient between planes

Type	Planes	Change in $\dot{V}$ [%]	Change in $\dot{m}$ [%]
Mixing zone to anti-node 1	68-78	-799.73	-214.07
Increasing area	78-88	-54.00	66.10
Anti-node 1 to node 1	88-100	-20.69	-39.29
Decreasing area	100-113	39.41	0.93
Node 1 to anti-node 2	113-128	-219.93	-99.35
Increasing area	128-142	6.74	11.42
Anti-node 2 to node 2	142-153	38.73	21.03
Decreasing area	153-164	41.81	11.22

Next the mass transfer in the cavitating trailing vortices is analyzed in detail. A visual representation of the instantaneous mass transfer rate in the tip and hub vortex of the PPTC'11 $J = 1.019$ case is presented in Fig. 104 on intersection planes. In (a) the helix intersection planes for the first spatial half-period along the trajectory is given with the mixing zone, the first node and the first anti-node, which are shown in detail in subfigure (b) to (d) together with the cavity isosurface in transparent grey. While the mixing zone shows relatively random angular distribution, possibly driven by the secondary vortices, a preference of regions of condensation and vaporization is visible. At the 1. anti-node four angular regions exist with evaporation and vaporization respectively with a slight point symmetry with respect to the cavity center and more angular directions showing condensation than evaporation at this location.

For the 1. node both transfer directions seem to have an equal angular share around the cavity with only two regions. It seems that the mass transfer along the cavity trajectory assumes directional preference shortly after leaving the mixing zone and is split into lower number, but more distinctive regions of evaporation and condensation directions. The hub vortex midplane is given in (e) and some flow normal intersection planes in (f) showing again a directional preference that is assumed shortly after separating from the hub geometry.

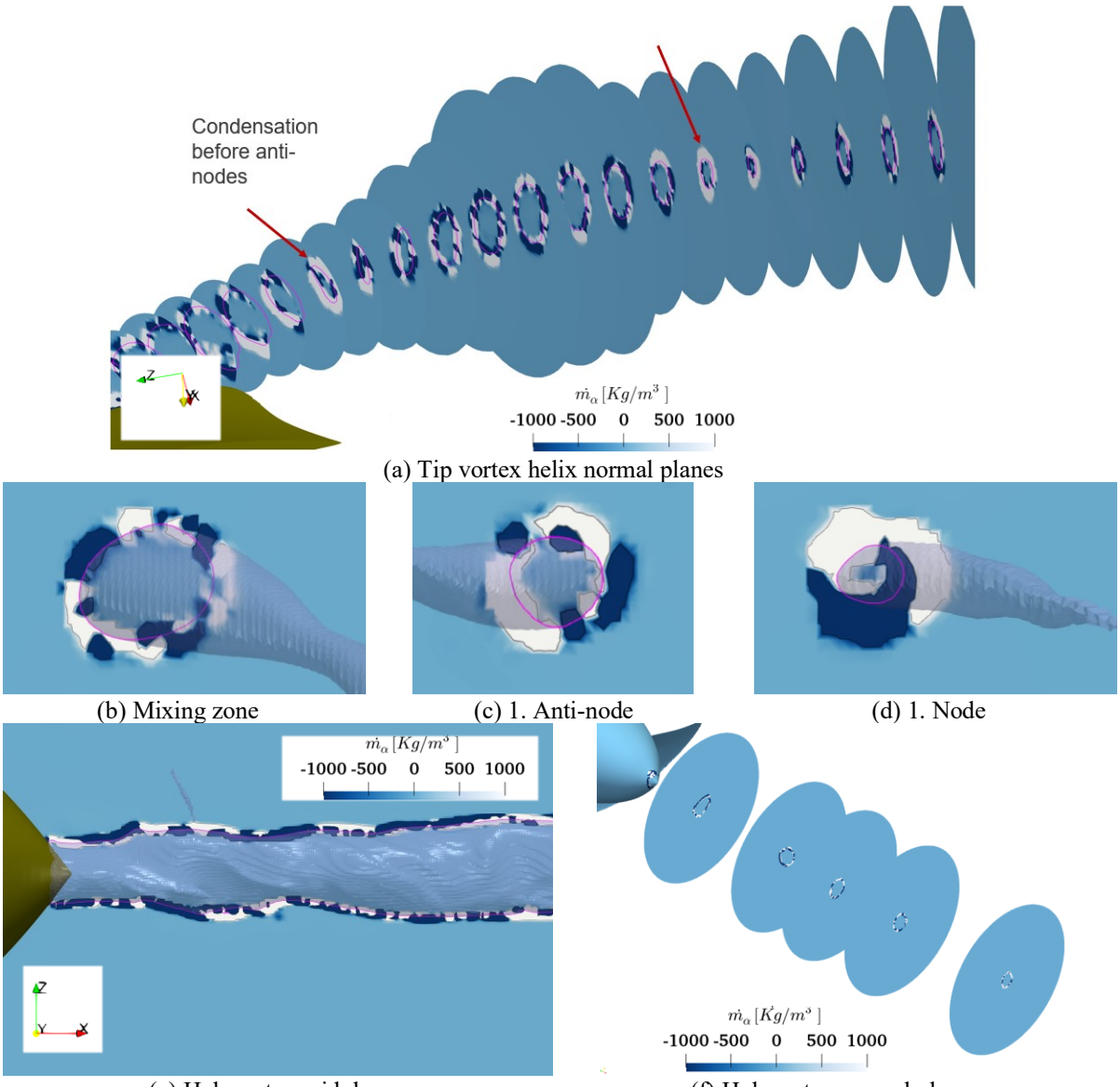

(a) Tip vortex helix normal planes

(b) Mixing zone (c) 1. Anti-node (d) 1. Node

(e) Hub vortex midplane (f) Hub vortex normal planes

Fig. 104: Mass transfer in trailing vortex in $[Kg/s]$

For the tip and hub vortex, the area mean mass transfer rate along flow normal intersection stations along the cavity is shown in Fig. 105, where a moving average with window size 10 is also given for the hub vortex data. It appears that on average there is no correlation between tip and hub vortex mass transfer. While the tip vortex has no clear trend overall, two locations exist with increased fluctuations. The hub vortex on the other hand has clear trends with regions of preferred vaporization and condensation.

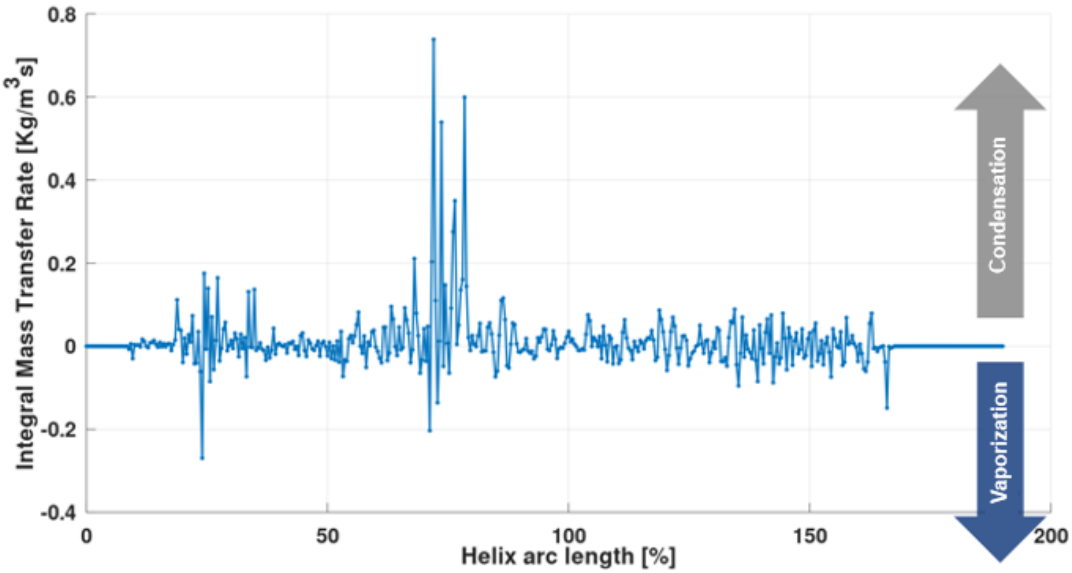

(a) Tip Vortex

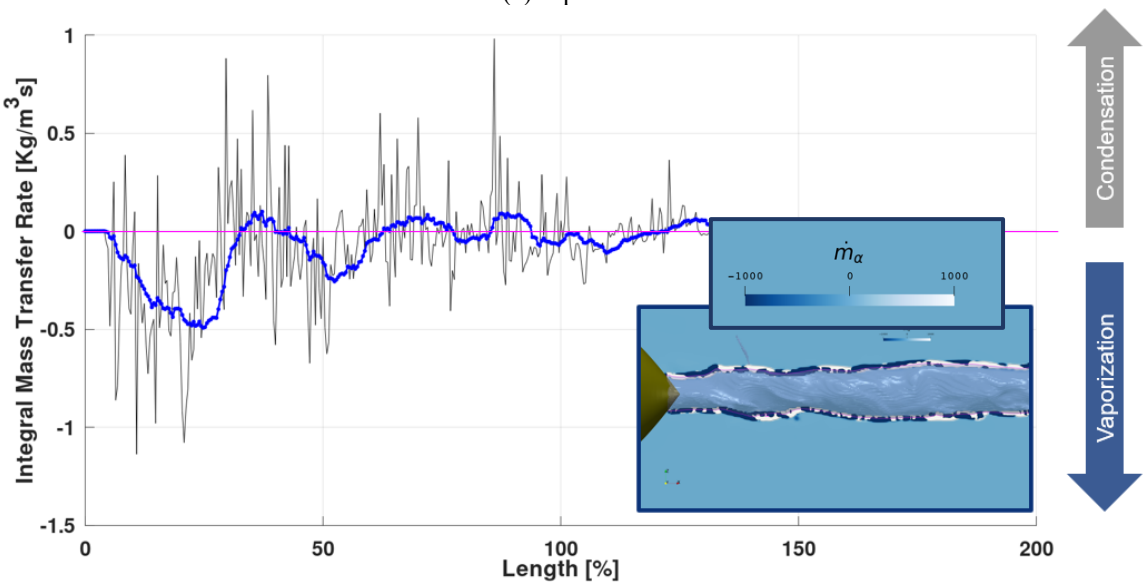

(b) Hub Vortex

Fig. 105: Mass transfer rate evaluation

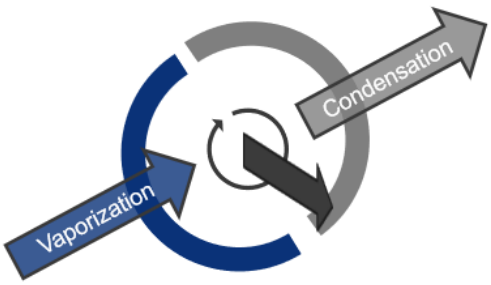

Fig. 106: Postulated mechanism of mass transfer in tip vortex

This leads to the conclusion that there are angular preferences for the mass transfer in the tip vortex, which are possibly rotating along the trajectory axis with increasing downstream distance as indicated in Fig. 106. To investigate this, the mass transfer rate is integrated for angular sections of 5° over all directions at 95 normal slices along the hub vortex with a distance of $\Delta x = 0.02 \cdot D$ and a radial

influence of $r/R = 0.4$. The expectation is that a mass transfer „wave“ travels angularly around the core correlating with the five propeller blades. However, in Fig. 107 where each curve represents a normal slice, no clear directional preference is visible that changes over the streamwise location, although there are three directions at $\Theta = 70°$, 190° and 280° with generally higher mass transfer occurring at several of the planes.

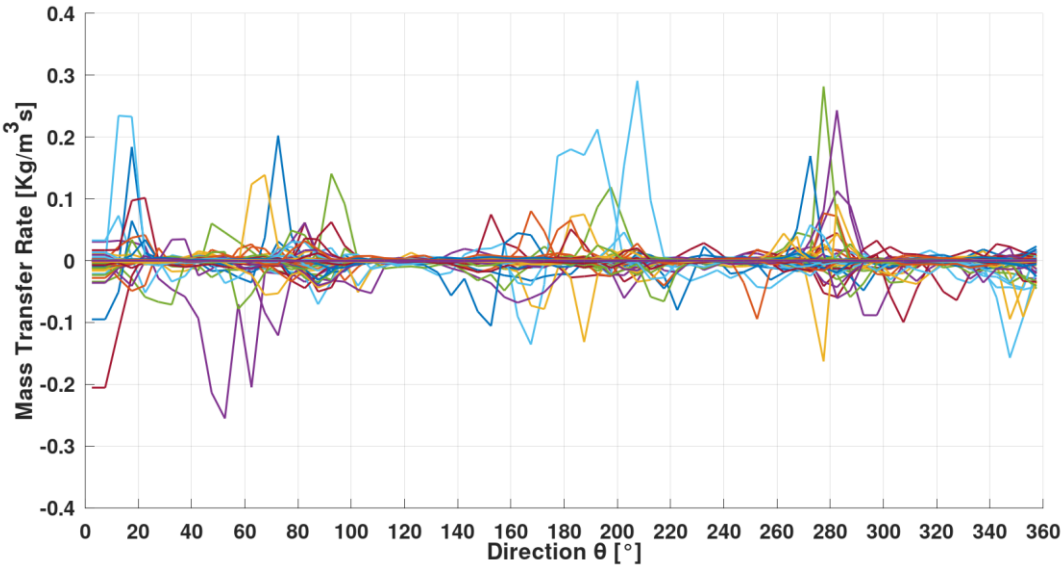

Fig. 107: Slice Mass transfer directional preference

The investigations of physics of the cavitation and particularly the cavitating trailing vortices with respect to the statement of best practices can be summarized as follows. It is clear that with the selected solution approach cavities and in particular trailing vortex cavities experience a sharp interface, which simplifies cavity tracking and discussion. A large influence of the nuclei density of the Schnerr-Sauer model on the cavity extent and dynamics as well as simulation stability is noticeable. Besides, a sufficient range of turbulent length scales are required to be resolved in order to achieve turbulence cavitation interaction phenomena in a numerical simulation. For propellers a strong pressure interaction between the tip and hub vortex, which affects the cavities volume and shape is observed and depending on the propeller tip design the tip vortex experiences different diameter and shape variations along the vortex helix. The internal velocity along the helix axis and the corresponding pressure variation are following the nodes and anti-nodes of the shape evolution with the helix trajectory. In general the cavitating vortex can be described with classic single-phase vortex physics for circular cavity shapes, by analytical vortex descriptions and the derived flow quantity of circulation. Opposed to previous findings the helix trajectory-wise circulation along the tip vortex cavity is constant, similar to the longitudinal circulation along a hydrofoil tip vortex. However, the circulation is difficult to determine in the complex flow of a propeller blade and the most suitable closed loop integral around the center of area of the cavity cross section has to be used to define a circular integral. It is found that the hub vortex circulation is less than the combined tip vortex circulation, however, this might depend on the loading distribution of the propeller design. The shape variations of the tip vortex cross section along the helix can be considered time invariant for open water propeller cases. This is considered to be caused by missing angular varying excitation by the inflow in the straight flow open water condition, which should be considered in future investigations. There is a strong angular dependence of the mass transfer rate in the trailing vortices with the trajectory coordinate. Thus, it appears that the mass transfer is highly non-axisymmetric and can be considered as more of an angularly dependent phenomenon instead of axially dependent as initially assumed. For noise generation the implication is that the trailing vortices are not contributing significantly with volume variation modes in the selected numerical approach, but instead with the termination of the cavity at the downstream end or through dynamics caused by external flow phenomena along the vortices. This behavior is assumed to be specific to individual propeller designs and requires more investigation in the future.

5.3 Interaction with Structure

5.3.1 Vessel wake

With the vessel boundary layer, the wake as an inflow to the propeller and in general the flow field behind the vessel has considerable influence on the propagation of the propeller slipstream and thus the acoustic emissions. In Fig. 108 a midplane through the propeller of the full-scale simulation of the ProNoVi reference target case with $J = 0.8$ is shown with the corresponding wave pattern behind the vessel. Compared to the model scale simulation with a flat top domain, similar to the experimental setup, the wave pattern affects the propagation direction of the propeller jet in a slightly upwards direction. Therefore, the vessel wave pattern is significantly affecting the direction of the far downstream propeller slipstream.

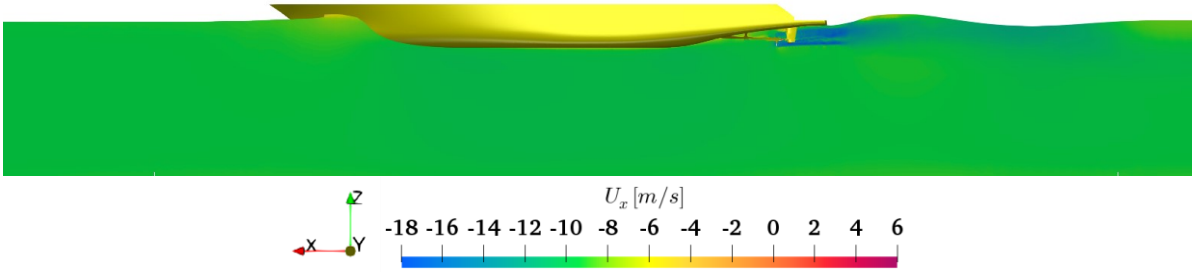

Fig. 108: Section of full-scale domain with wave pattern

In Fig. 109 the propeller tip vortex for the full-scale case for $J = 0.71$ shows a significant dent downstream of the inward located shaft bracket, which develops only two trajectory rotations behind the propeller plane. In addition, it only appears for the LES case, as the tip vortex is dissipating before this location on the same mesh with RANS. Thus, the wake field may not only affect the cavitation behavior, but also have influence far downstream in the propeller slipstream.

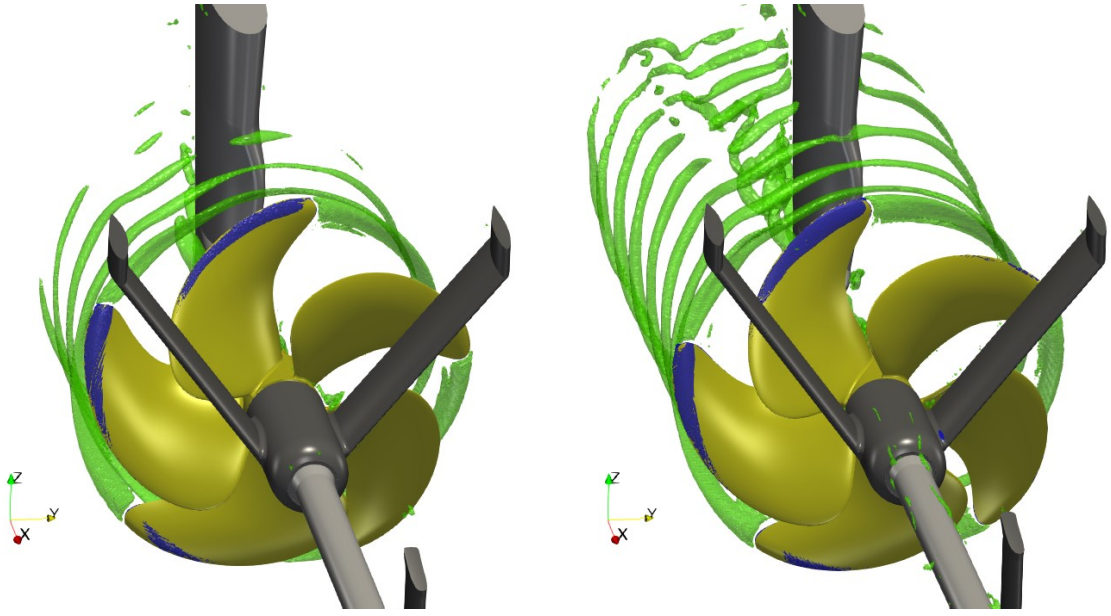

(a) RANS (b) LES

Fig. 109: Influence of shaft brackets on the trailing vortices

As shown in the previous example, the capturing of the trailing vortex interaction with the wake field and obstructions in the propeller slipstream can be achieved by resolving the large and medium turbulent length scales. In Fig. 110 the ProNoVi reference target case in model scale with the P1595 propeller is depicted for the consecutive simulation approaches with RANS (a), LES (b)(c) and LES with AMR (d), where the LES results are also compared for the case with and without rudder. For all cases without rudder, the position of the rudder is indicated with a transparent geometry. While the RANS features no

details in the tip vortex morphology and only propagates half of a rotation downstream, the LES tip vortex reaches over one rotation downstream and features a large amount and highly resolved details such as the inward shaft bracket influence on the far downstream tip vortex and the direction of the overall flow along the ship hull and consecutive wave pattern direction. Here it has to be noted, that the images are rotated by 2.75° in order to align the propeller shaft axis horizontally. The a priori AMR utilized here can only be realized for cases without rudder in the propeller slipstream with a rotating mesh region that extends beyond the rudder, whereas it ends between the propeller plane and the rudder for the case with rudder. The tip vortex dissipates while interacting with the rudder in (c), while in (b) it is maintained even downstream of the rudder, indicating a strong physical dissipating effect of the rudder on the tip vortex. As the AMR in (d) only reaches towards $\Delta x = 0.54 \cdot D_P$ or just upstream of the leading edge of the rudder due to numerical resources, the downstream extent of the vortices is unchanged compared to (b), however, in the region between the propeller plane and the rudder the level of detail in the trailing vortices increases significantly. In addition, a cavitating tip vortex is present in this case, which is not resolved on the initial mesh.

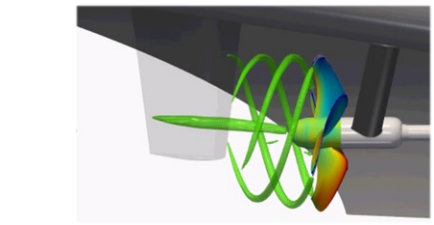

(a) RANS

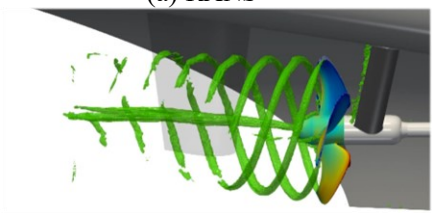

(b) LES

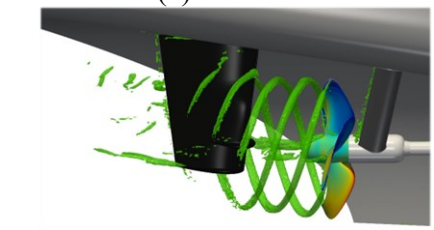

(c) LES with Rudder

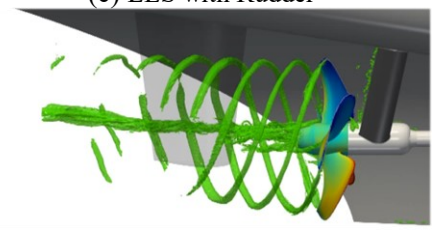

(d) LES+AMR

Fig. 110: Trailing vortices in vessel wake ProNoVi reference target case with P1595 [80]

Similar findings are obtained with the SCHOTTEL target case in Fig. 111, where the tip vortex reaches over the complete extent of the rudder in the case of LES turbulence modelling. Here the effects of the propeller slipstream inclining upwards on the upwards going blade side are visible and vice versa on the side not shown. Resolving the tip vortex sufficiently far downstream is especially important in this case, since there is some interaction with the rudder gap, which is captured well by the simulation.

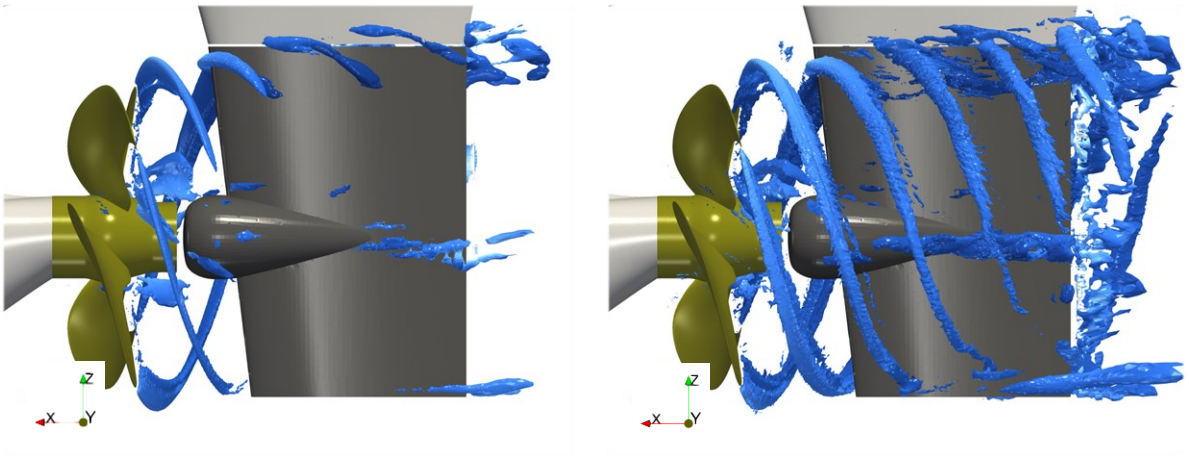

(a) RANS (b) LES

Fig. 111: Trailing vortices in vessel wake, SCHOTTEL Target case [92]

As mentioned, the cavitating tip vortex is only apparent in the case with AMR, which is compared to the experiment in Fig. 112 for the P1595 propeller. For LES, some vortices appear at the blade leading edge, which produce stripe like structures on the blade surface visible at the outer radii which are not appearing for RANS. At the lower radii sections leading edge, the cavitation is overpredicted by the approach, however, over the complete rotation a good agreement with the sketches from the experiment in (a) can be achieved. Comparing with the photographic observation in (d), the cavitating tip vortex is slightly weaker in the simulation, however, shows similar diameter variations with the helix trajectory.

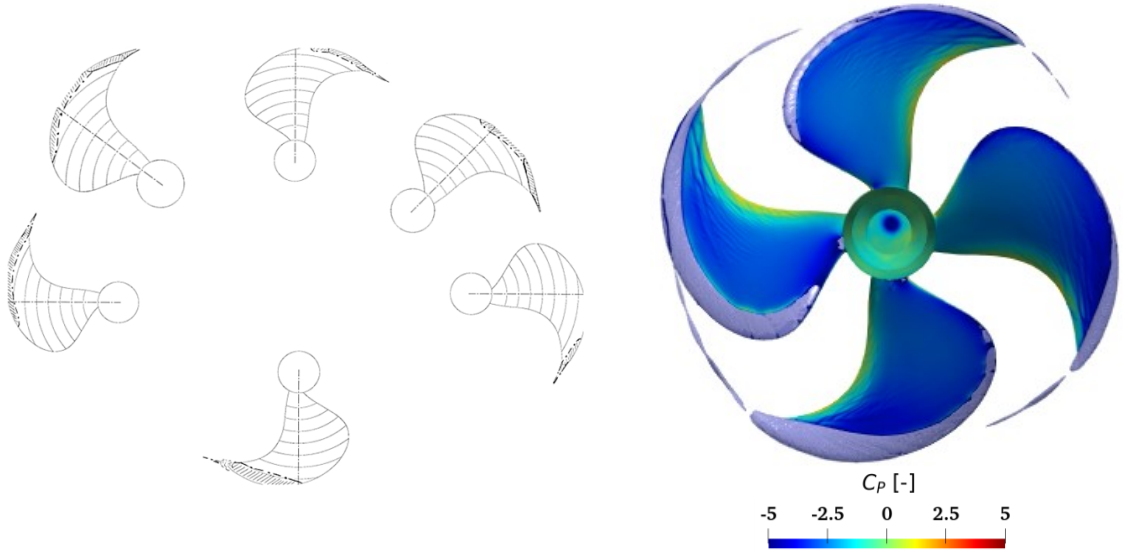

(a) Sketches [95] (b) 0°

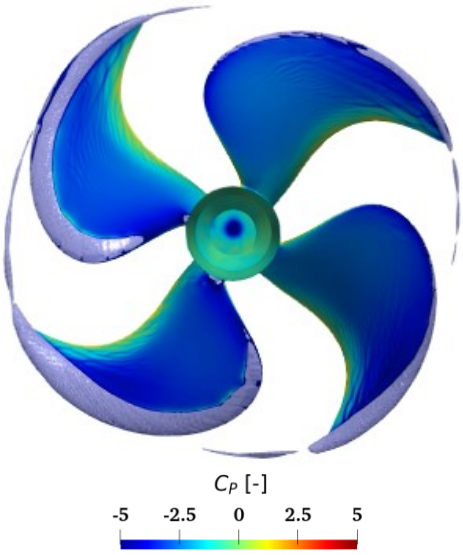

(c) 45°

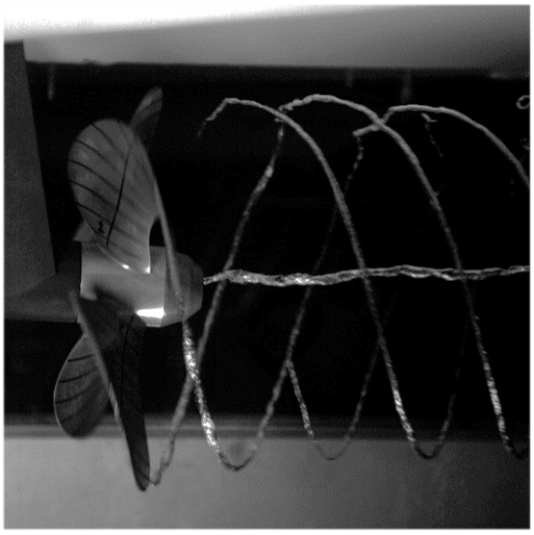

(d) Observation [95]

Fig. 112: Cavitation observation

For the SCHOTTEL Target case the cavity on the blade agrees very well with the experiment in Fig. 113 (a) and (b). Although this case does not feature cavitating trailing vortices, a stable cavity is separating on the blade just after passing the 12 o'clock position as indicated in (c), which can only be captured by the LES, although the reentrant jet under the cavity is also visible in the RANS simulation.

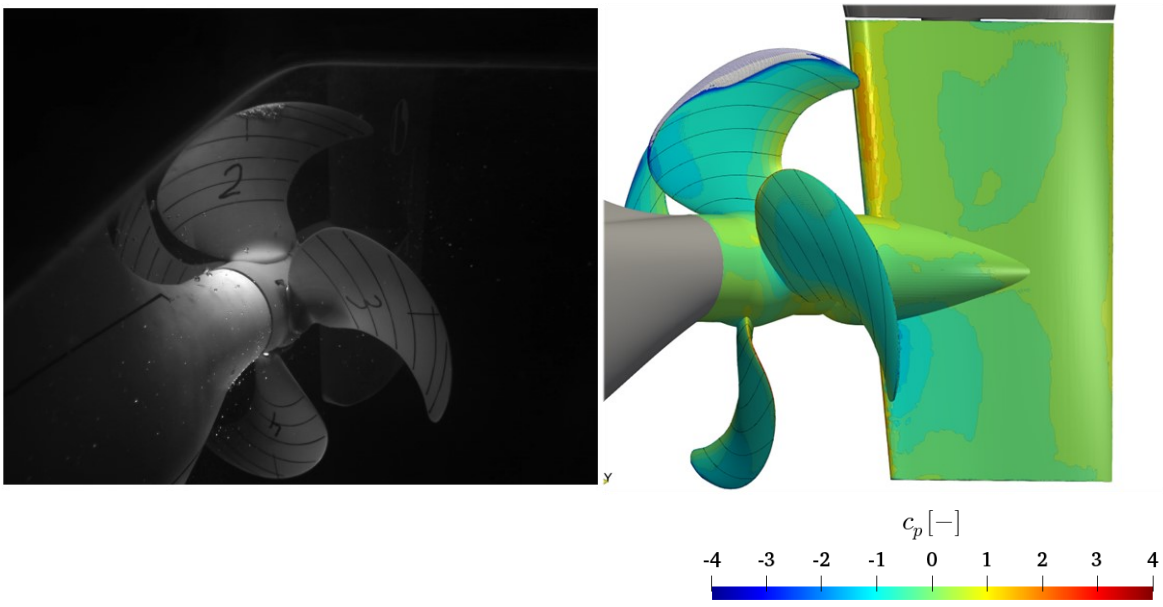

(a) Starboardside view [92]

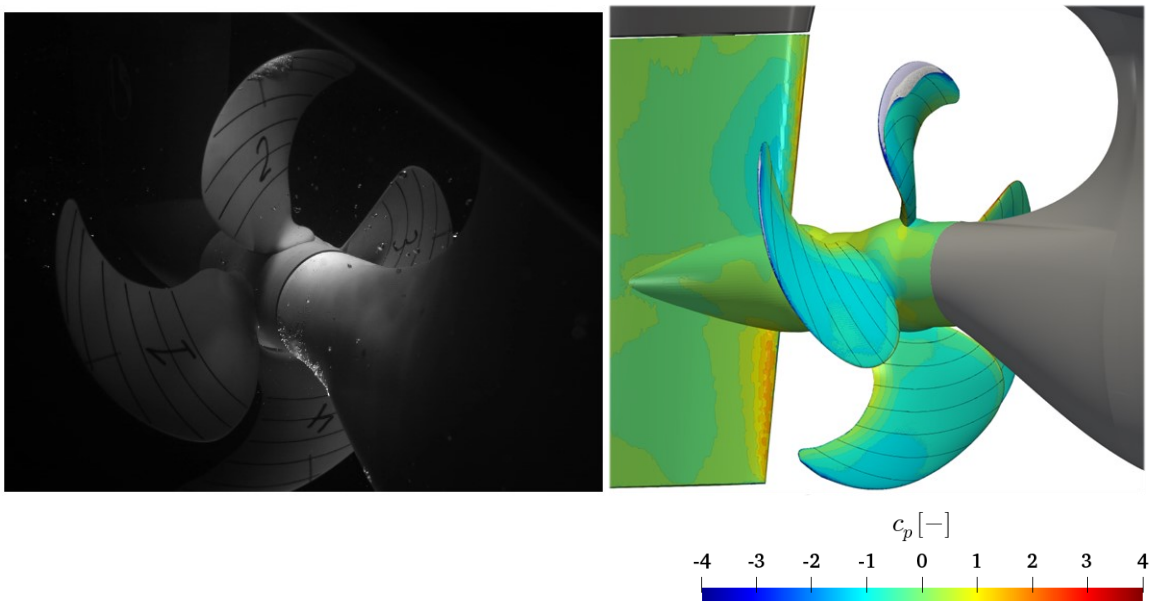

(b) Portside view [92]

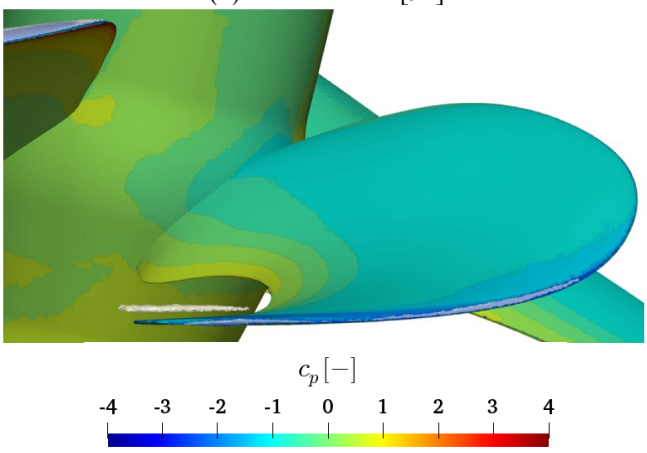

(c) Separated blade cavitation

Fig. 113: SCHOTTEL Reference case cavitation region and surface pressure coefficient

In summary, a vessel wake has significant influence on the general flow field into the propeller, which affects the propeller trailing vortices and the general slipstream behavior, which in turn both are expected to affect the noise generation. For this, resolving the turbulence is required to capture the detailed slipstream deformation caused by the vessel wake propeller interaction. The accurate capturing of flow and cavitation behavior on the propeller blades as well as the detached cavitation and trailing vortex cavitation for propeller-hull combinations requires resolving significant amounts of the turbulent energy.

5.3.2 Rudder

The rudder has an influence on the noise generation, not only by noise of the medium flowing around the structure, but also due to breaking up trailing vortices, which is considered to create a significant sound contributions. For the ProNoVi reference target case at $J = 0.80$ in model scale and the SCHOTTEL target case in full scale, the tip vortex helical trajectory is utilized to evaluate circulation evolution along the streamwise direction in Fig. 114. The integral is evaluated along the indicated black line, which is an in-plane circle with the center at the helical coordinate with a radius of $r/R = 0.74$ for the ProNoVi reference target case and $r/R = 0.81$ for the SCHOTTEL target case. For this purpose, the plane indicated with 0 is located at the midchord section of the outermost profile of the propeller. Whereas for the propeller open water cases the circulation is approximately constant beyond the mixing zone, there is a strong fluctuation apparent between the propeller plane and the rudder, which may be caused by the upstream influence of the rudder and the tip vortex excitation by the vessel wake field. In

both cases the circulation reaches a peak just before the rudder, while between the rudder outer surfaces the automated evaluation should be neglected, as the closed loop integral intersects the rudder geometry. Beyond the rudder the disconnected part of the tip vortex maintains a lower circulation. For the ProNoVi target case the tip vortex trajectory intersects the rudder a second time between plane 95 and 105, leading to a similar phenomenon. On the other hand for the SCHOTTEL target case even downstream of the rudder when the tip vortex reconnects, the effect of the separation of the slipstream into the upwards and downwards rotating region are visible between plane 280 to 310. Here the circulation increases just before the rudder wake is intersected and vice versa on the downwards going side of the rudder. The reduction of the circulation to zero between the two intersections might be caused be the deviation of the tip vortex from the helical evaluation trajectory caused by the rudder intersection. It can be expected that the vortex is stretched on the downwards going side of the propeller and compressed on the upwards going blade side, which leads to the increase and decrease in circulation respectively.

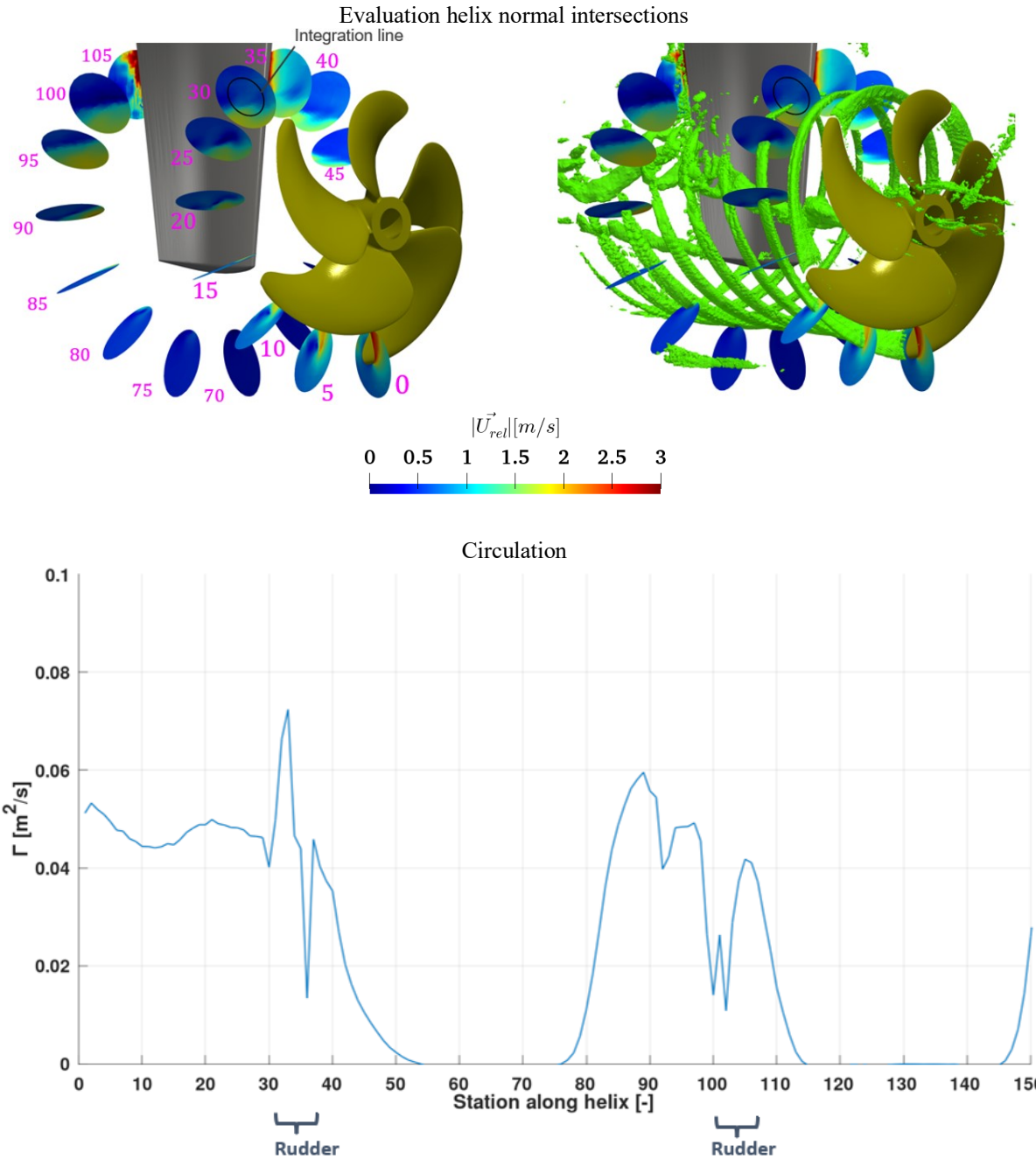

(a) ProNoVi target case

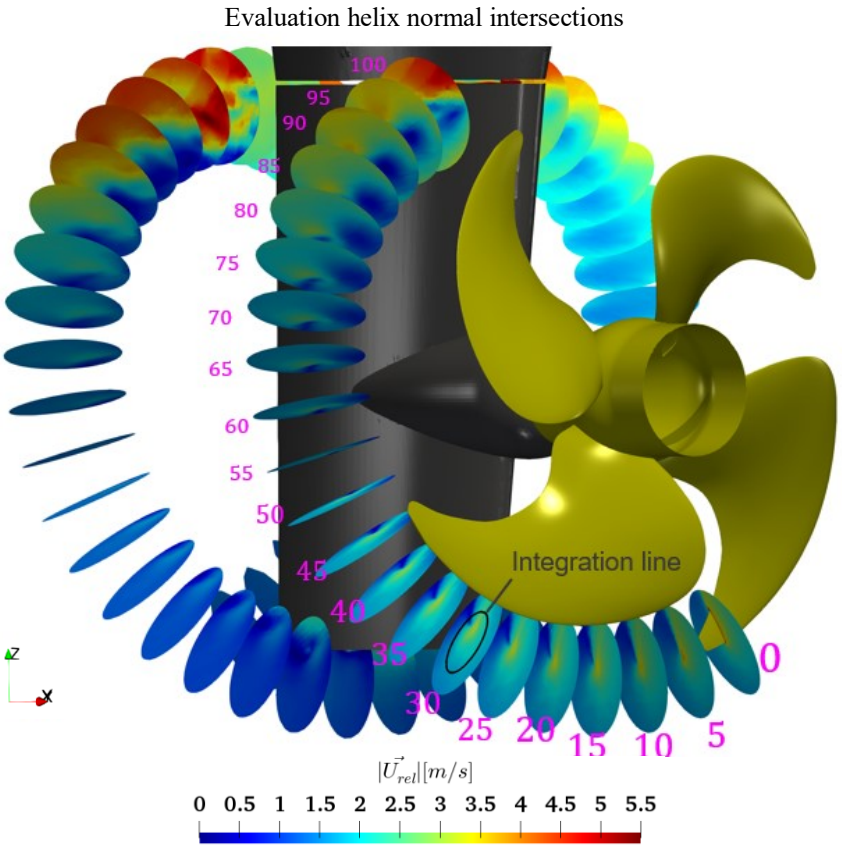

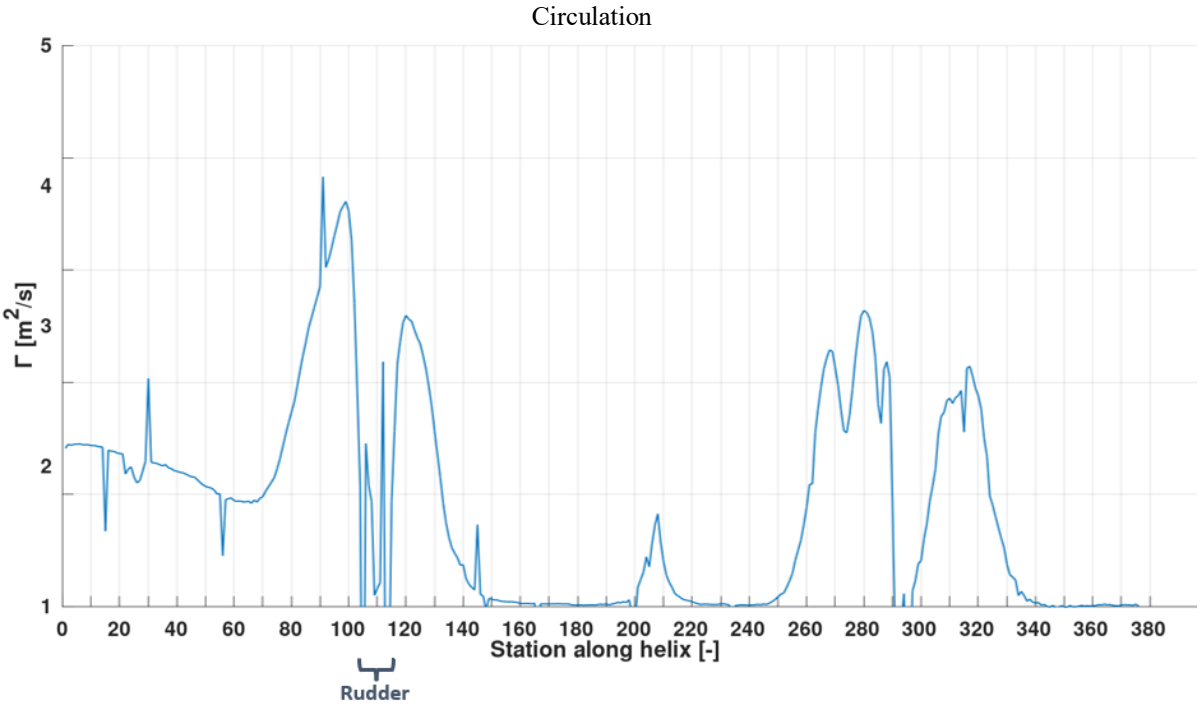

(b) SCHOTTEL target case

Fig. 114: Tip vortex circulation interaction with rudder

For the E779 propeller the automatic runtime AMR is tested with the rudder for two Q-criterion values in Fig. 115, where the selected criterion and a mesh intersection plane through the rudder is visualized. The AMI end base between the propeller hub cap and the rudder leading edge and the borders of the protected zones are indicated in red on the intersection plane. Essentially, only the tip and hub vortex regions down to a distance of $\Delta x = 2 \cdot D_P$ are allowed to be refined. In accordance with the findings from Fig. 6, the Q-criterion is dissipated with increasing downstream distance leading to lower diameter

isosurfaces, which in turn lead to less refined regions. However, the savings in cells are relatively minor with the lower Q-criterion value in (a) only achieving 6% less cells. In order to resolve the necessary flow details for acoustic simulations, the lower Q-criterion isovalue should thus be selected. Regarding the simulation numerical effort, the CPU time is almost identical for both of these cases, however, in a comparison without rudder the PPTC'11 propeller with a priori AMR achieved a simulation time of 1.5 days per revolution on 100 cores with a maximum CFL number of 7, while the runtime AMR achieves the same results with 8.6 days. In its current implementation there are two issues with the simulation time for AMR:

- The mesh update time may take up to $\approx 50\%$ of the iteration time,
- The processor imbalance is fluctuating, leading to high load on single processors while others are idling.

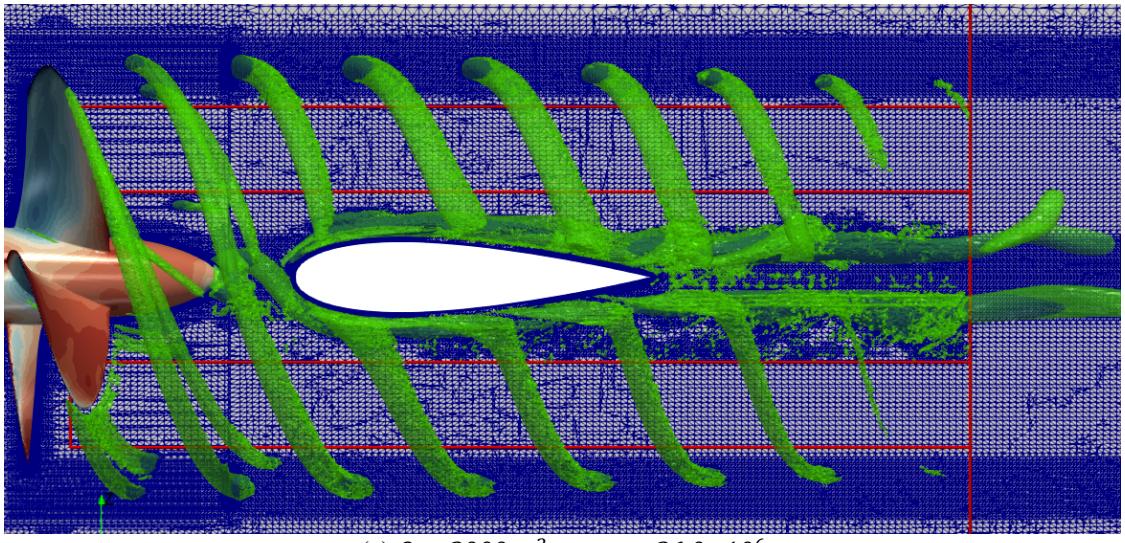

(a) $Q \geq 2000 s^{-2}$, $n_{Cells} \approx 26.0 \cdot 10^6$

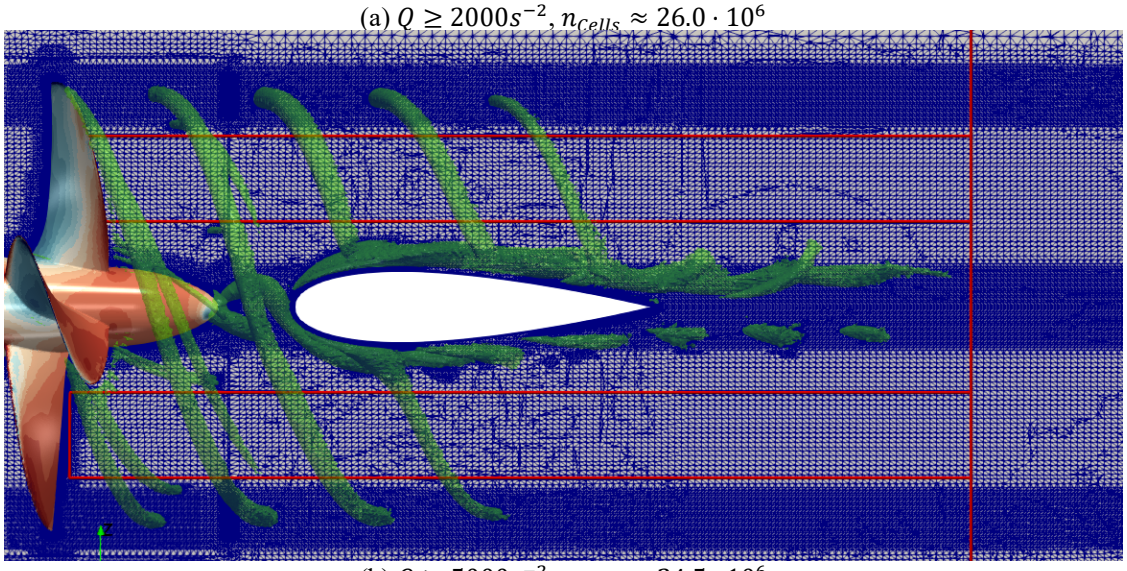

(b) $Q \geq 5000 s^{-2}$, $n_{Cells} \approx 24.5 \cdot 10^6$

Fig. 115: AMR with rudder

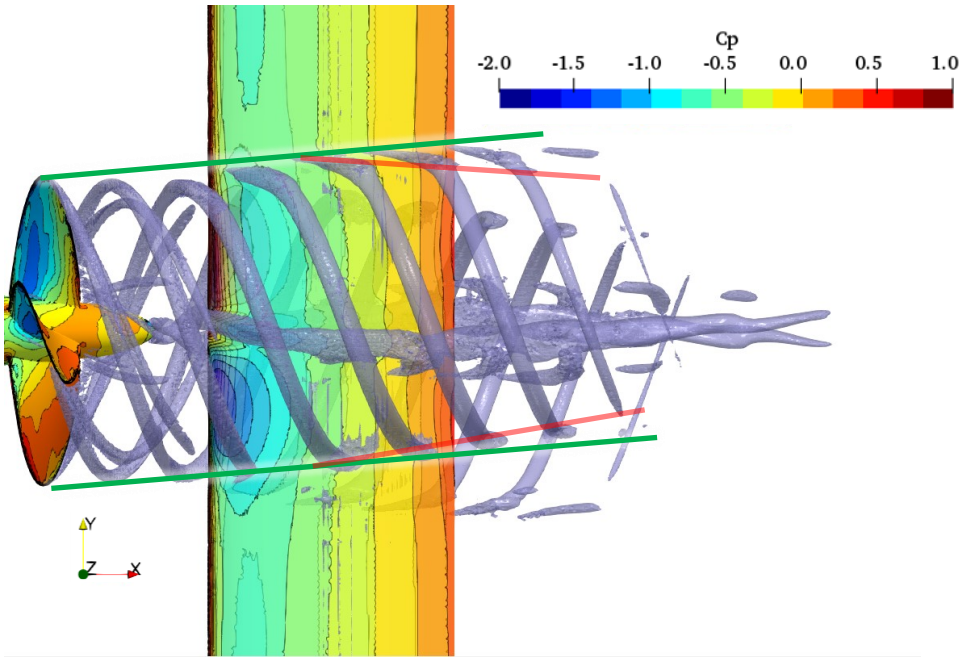

(a) Portside

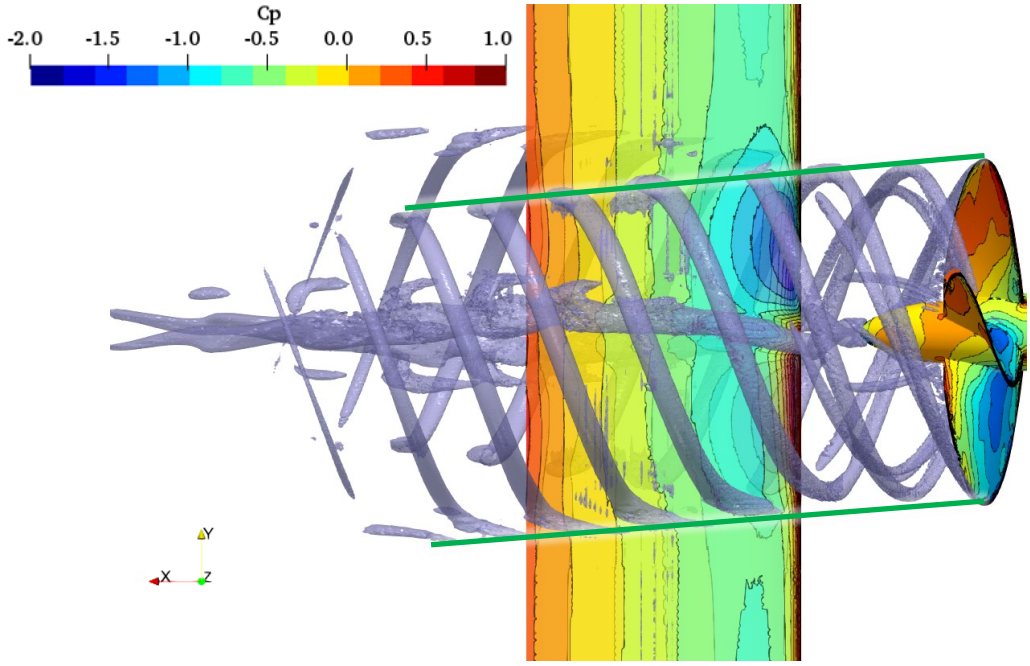

(b) Starboardside

Fig. 116: Vortex propagation direction

The resulting slipstream trailing vortices for the E779 are visualized in Fig. 116, for both sides of the rudder. With the AMR the tip vortex passes the rudder and dissolves in the protected zone downstream, where the mesh is not resolved sufficiently. A secondary tip vortex is resolved immediately beyond the trailing edge as well as the intermittent splitting of the hub vortex. The physical phenomenon of the change of travel direction in rudder spanwise direction is highlighted in green. Similar to the findings in [23], the upwards going blade side leads to the tip vortices travelling upwards along the rudder, while on the downwards going blade side the effect is the opposite. Whereas in the experiment the vortices reconnect downstream of the rudder this effect is not seen in the simulation, which is most likely a result of insufficient mesh resolution. For this particular case a change of direction of propagation vertically inwards along the rudder is found in the experiment at the axial location of the largest thickness in the

rudder profile after which the propeller jet contracts noticeably. This effect, which is indicated in transparent red in (a), cannot be reproduced in the simulation.

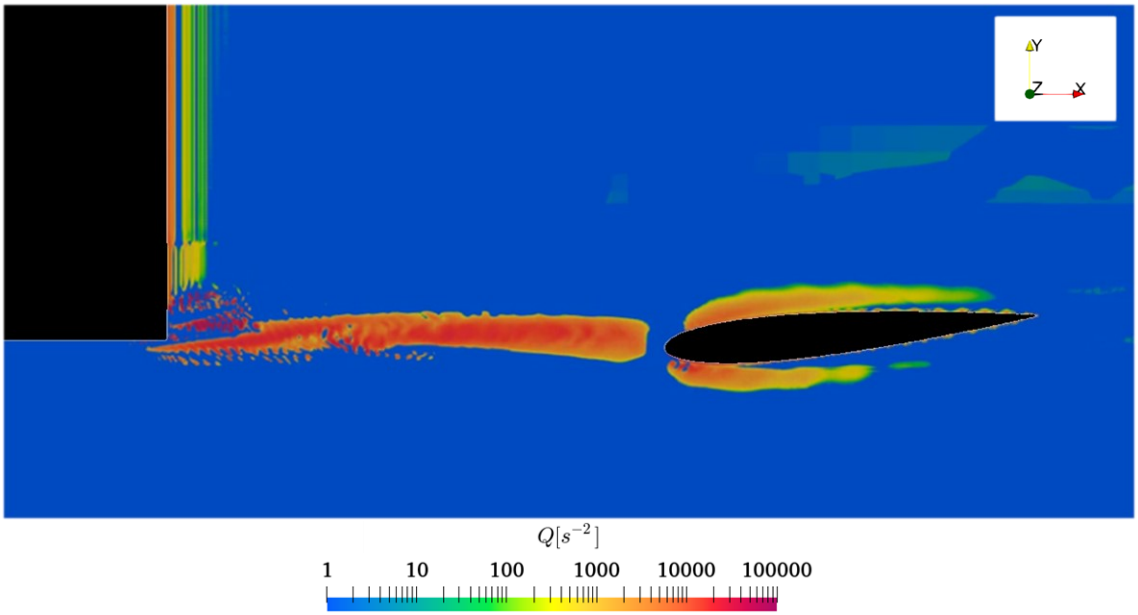

Fig. 117: Q-criterion on NACA 0012 midplane

The presented result cannot be achieved with a priori mesh refinement due to the rudder, thus it is necessary to utilize runtime AMR, however, it cannot be used in the current implementation for acoustic simulations, since the interpolation of the pressure field between the timesteps from different local source refinement levels onto the target refinement levels, leads to unphysical pressure peaks. In addition, with the current solver an unphysical distortion of the velocity flow field occurs downstream of the sliding mesh interface which increases in severity with higher refinement levels, which is noticeable as a slight axial stretching followed by the dissipation of the Q-criterion isosurface. This effect is caused by the refinement algorithm using the previous timestep criterion for the current timestep refinement.

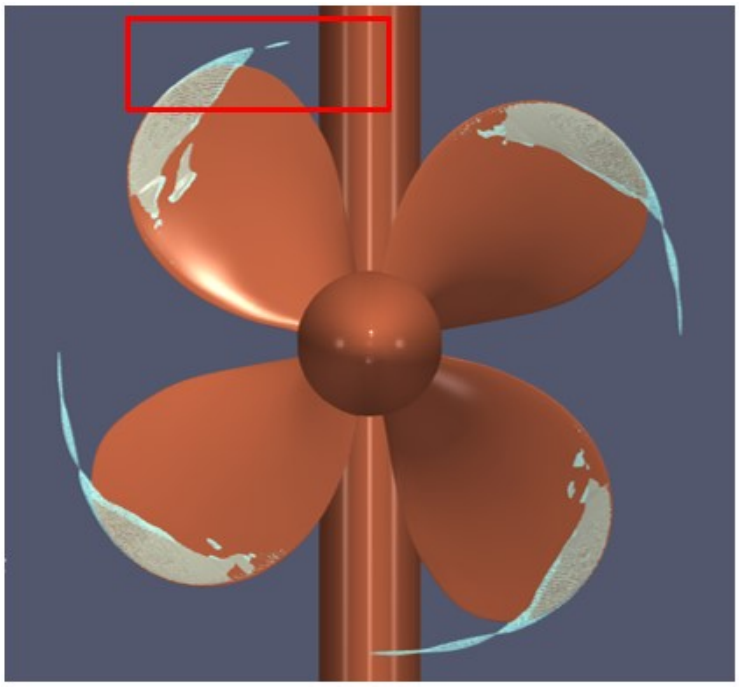

Fig. 118: Cavitation pattern

Another important aspect is the upstream influence of the rudder. For the NACA 0012 hydrofoil test case an upstream influence of a second downstream hydrofoil rotated by 90° on the tip vortex of the first is shown in Fig. 117, with the Q-criterion on an intersection plane. Just before the leading edge of the downstream hydrofoil the Q-criterion disappears completely due to the upstream influence of the leading edge pressure field, while it reappears past the leading edge on the foil.

The same effect is captured in the simulations with AMR for the cavitating tip vortex of the E779 case, which is given as a snapshot of one of the blades just passing the 12 o'clock position in Fig. 118 marked in red. Over the complete revolution the cavitating tip vortex is slowly propagating downstream from the blade, however, once it passes the rudder, the cavity collapses, which is considered to be an effect of the upstream influence of the rudder on the pressure field. Thus, even with AMR the cavity may not expand beyond the rudder, based on this physical effect, which however is not observed in the corresponding experiment.

Concluding, for the interaction of the propeller with rudder downstream several effects are important. A circulation peak is caused by an obstruction in the propeller slipstream in the tip vortex and the circulation continues for the tip vortex section on the side of the rudder in rotation direction. Additionally, an upstream influence of the rudder on the pressure field and thus the streamwise propagation of the trailing vortex cavitation effects is proven. It is shown that AMR is an excellent way to resolve the cavitating trailing vortices passing an obstacle in the propeller slipstream numerically, however, it is not fit for acoustical analysis due to pressure sensitivity in the interpolation between dynamic refinements.

5.4 Geometric Scale

For the comparison of model scale and full-scale results the ProNoVi reference target case with the P3193 propeller is investigated at $J = 0.712$ and $\sigma_n = 1.20$ at the propeller center, which yields slight cavitation at the suction side leading edge and no tip vortex cavitation. The model scale results are from the half-model in the SINTEF Ocean cavitation tunnel domain and the full-scale simulation is a half model with wave pattern and $40m$ water depth similar to the full-scale experiment. The stable cavitation extent is significantly larger with radii down to $r/R = 0.5$ for the model scale simulation in Fig. 119 and to $r/R = 0.7$ for the full-scale results, which may be attributed to the domain extent. In model scale the pressure distribution on the blade is smoother overall and the full-scale pressure experiences lower pressure on the blade at the outer radii above $r/R = 0.7$. There is noticeable blade root cavitation and rudder cavitation in both cases, however, the location for the cavitation on the rudder is dissimilar at the same propeller position as it appears above the rudder bulb for model scale and below for full scale.

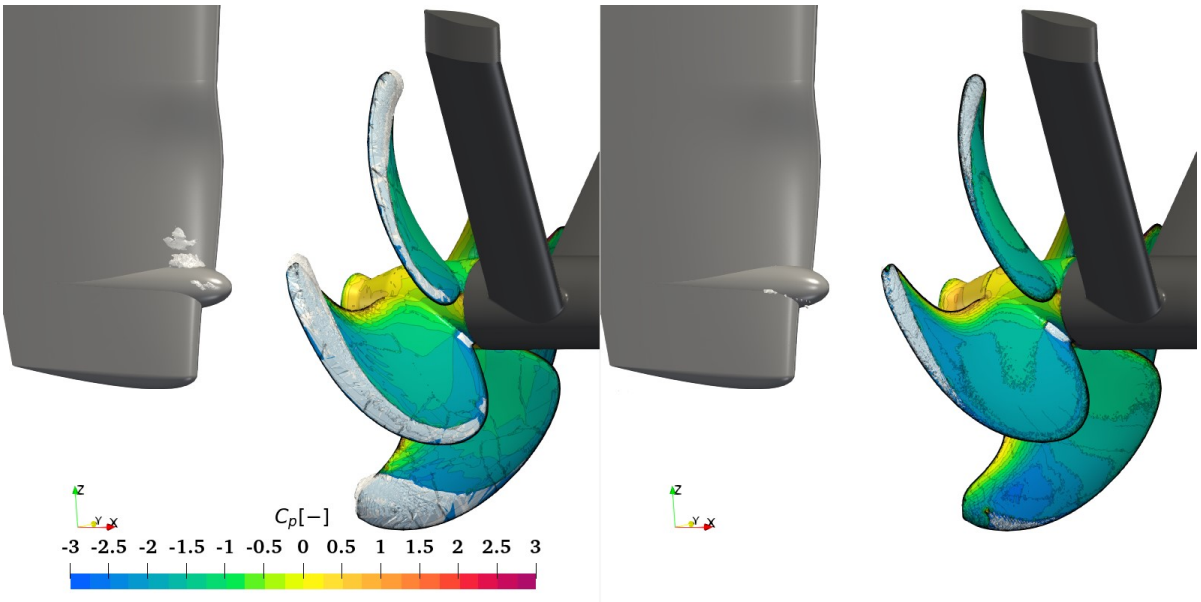

(a) Model scale (b) Full scale

Fig. 119: Pressure distribution on blade suction side and volume cavitation

The pressure fluctuations at the hull above the propeller at P3 are given as a time series over five rotations as raw data and scaled to full-scale as vessel signature for the three simulation stages in Fig. 120. In the RANS pressure time series in (a) there is a difference of about factor 4 in the primary sinusoidal signal and in addition the full-scale pressure experiences some high frequency fluctuation added on top of the signal, whereas the model scale results lead to a smooth sinusoidal graph. In the spectrum this is visible for the full-scale results, which have a deviation of around $\Delta SPL = 8dB$ at the first harmonic, but deviate more beyond the third harmonic with up to $\Delta SPL = 10dB$. For values lower than $f < 10Hz$ the agreement is poor. Similar trends are observed for RANS with cavitation in (b), although the first harmonic is underpredicted severely in model scale. The reason for this cannot be identified, but it might be a numerical issue, as it does not meet the expectations for a comparison with the propeller cavitation pattern. The best agreement is achieved with LES with cavitation in (c) with both results almost identical above $f > 15Hz$, which validates the full-scale correction applied and the developed simulation methods in equal measure. Overall, the full-scale results tend to be lower, which can be attributed to the lower cavitation on the blade for the harmonics and the dissipation effects of the domain for the high frequencies. The latter effect is presented in the comparison of the domain size in 6.2.2. Although the full-scale domain is relatively small due to the water depth, it is comparatively larger than the cavitation tunnel domain.

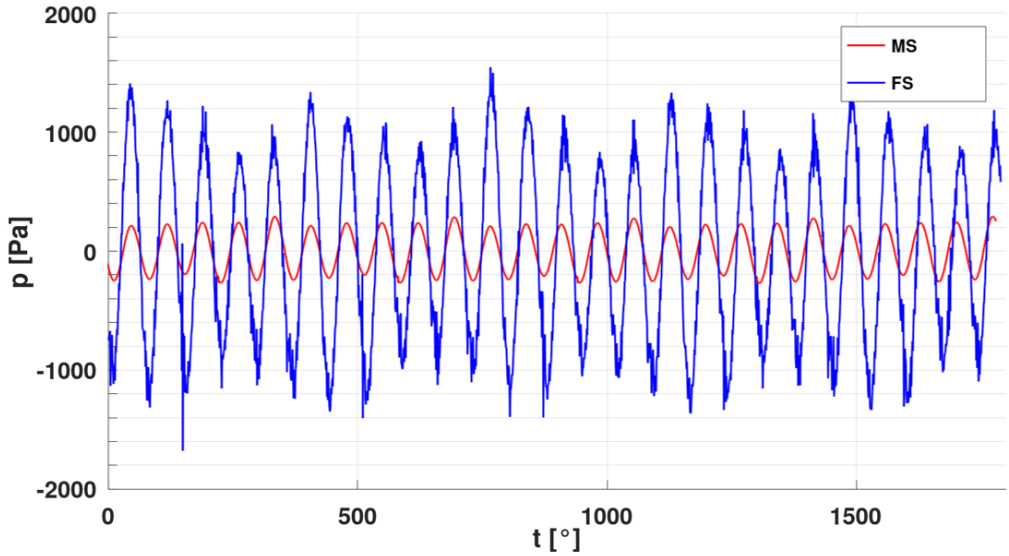

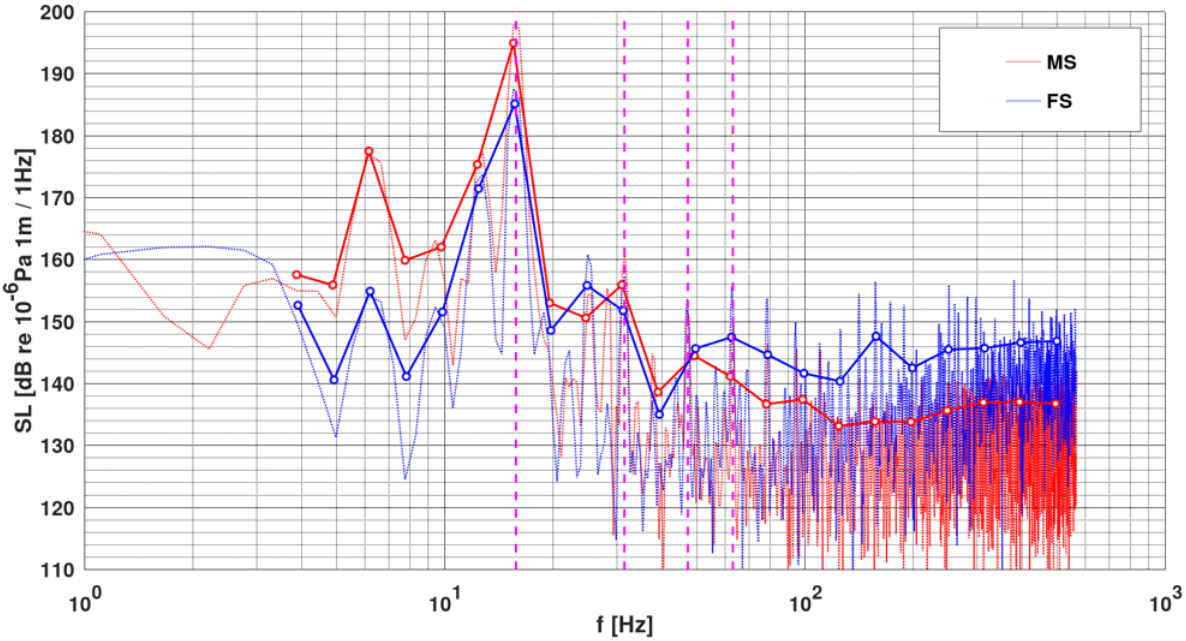

(a) RANS wetted

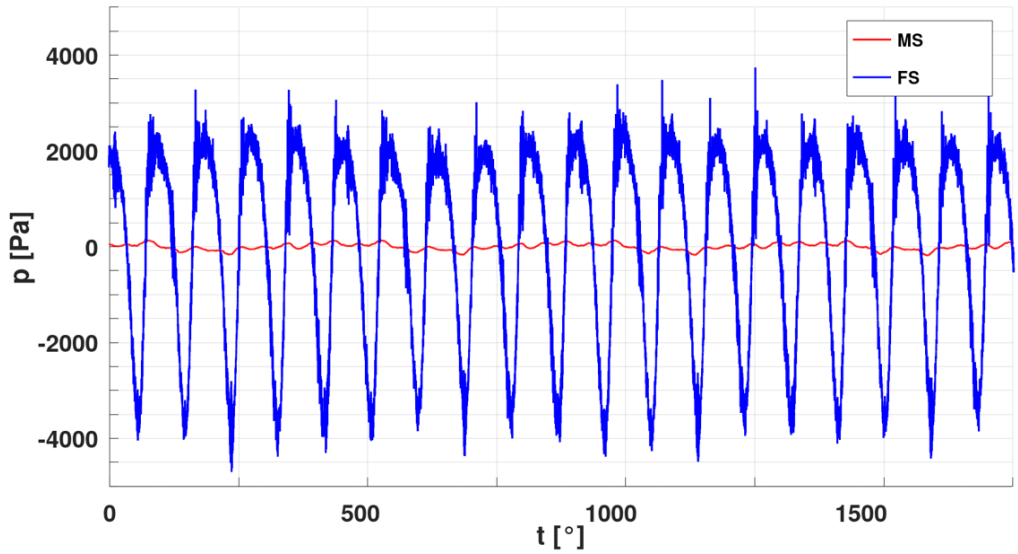

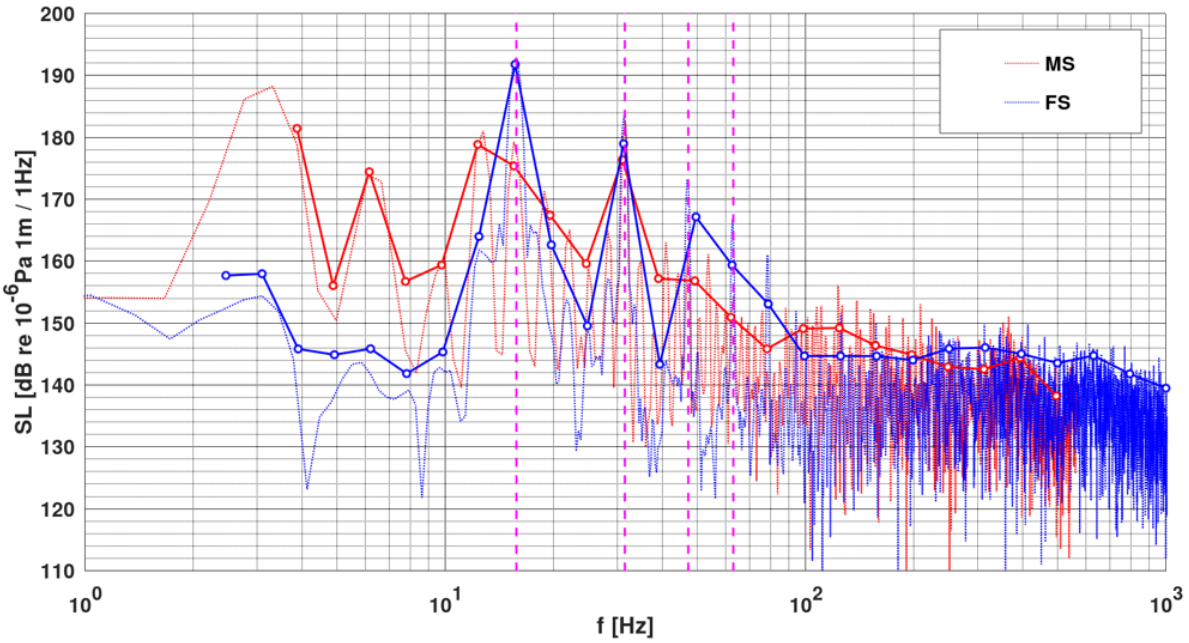

(b) RANS Cavitating

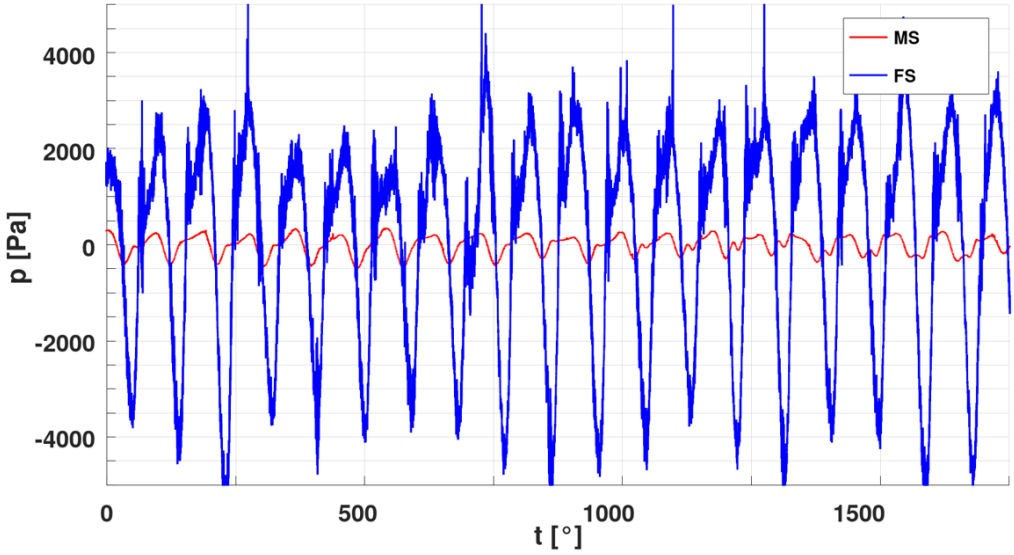

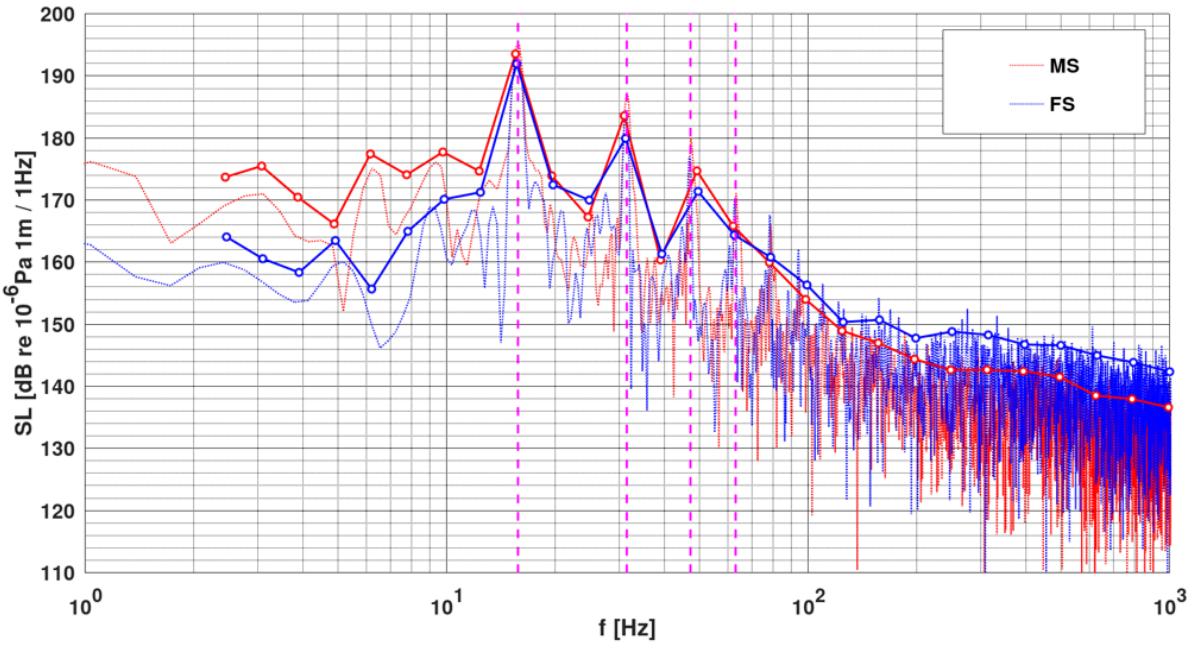

(c) LES Cavitating

Fig. 120: Comparison of model and full-scale simulation on hull

For a the hydrophone observer from the experiment the results are given for LES with cavitation in Fig. 121 together with the experimental results of SINTEF and CNR-INM scaled in to full scale. Similar to the hull observer, the agreement between the results for both simulation scales is excellent above $f > 15Hz$. Compared to the experiments there are some deviations above $f > 80Hz$ for the measurements at SINTEF Ocean cavitation tunnel and below $f < 20Hz$ for the measurements at CNR-INM.

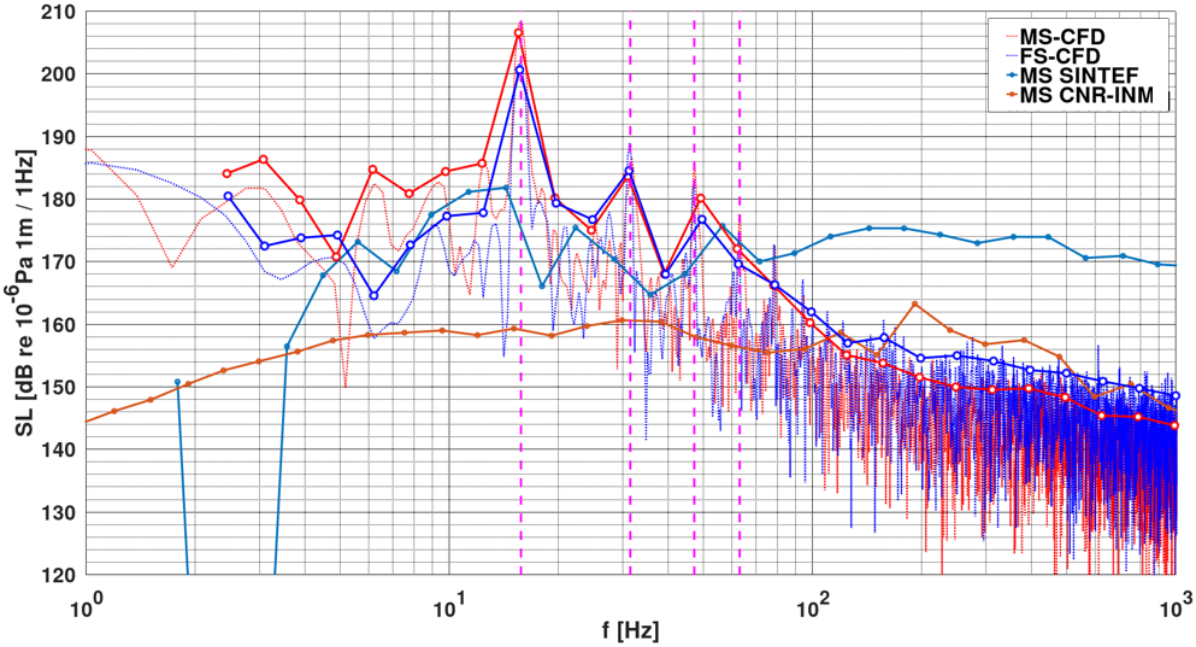

Fig. 121: Comparison of model and full-scale simulation at hydrophone

5.5 Summary

The capabilities of the proposed approach with LES, VOF and OpenFOAM Schnerr-Sauer cavitation model to capture acoustic sources, which are attributed to turbulence, cavitation and their interaction are demonstrated successfully with hydrofoil and propeller test cases, where they resolve sheet cavities and wetted and cavitating trailing vortices limited only by the available numerical resources. Some of the

mechanisms driving cavitating vortices are explored and the interactions with the vessel wake and the rudder are investigated. Scale effects can be captured with the methods and result in a difference of about $8dB$ depending on frequency. With the approach applied a consistently stable and accurate prediction of the hydrodynamic flow field is possible, although automatic runtime AMR cannot be used to overcome the problem of slipstream interactions of trailing vortices as unphysical pressure waves are created by the combined temporal and spatial interpolation between volumes at consecutive mesh refinement steps with the current implementation.

6 Calculation of Underwater Radiated Noise

The hydrodynamic approach proposed and validated in the previous chapter is utilized to estimate underwater radiated sound emissions with either direct pressure observers on the FVM mesh or the permeable surface FWH method in this chapter. In the first section the interaction of the pressure waves with the ship structure is investigated with single pressure observers on the hull similar to experimental setups. This method of evaluation turns out to be non-intuitive and lead to wrong conclusion as only localized variations of pressure are captured. Thus, a more intuitive high spatial density analysis is required that utilizes the complete available information from the underlying FVM method without any additional resources. Following that in the second section underwater noise signatures are obtained for the emissions into the fluid domain in model and full scale.

6.1 Interaction with Structure

6.1.1 Single Point Observers

In the previous chapter the influence of turbulence modelling on the level of detail of the flow field is demonstrated, however, the connection to the acoustic signal is not established. AMR is utilized to achieve a sufficiently low pressure in the core of the trailing vortices to create a vapor phase. In Fig. 122 (a) the pressure time domain signal is provided for the ProNoVi reference target case with the P1595 propeller without rudder for the different simulation stages at observer P11. While the RANS signal is a consistently sinusoidal signal, once cavitation is activated, the sine waves are skewed towards larger time gradients and show low amplitude overlaying fluctuations, especially on top of the peaks. With LES the total amplitudes are severely increased and plateaus appear with more low frequency fluctuations on the high pressure side, while the low pressure side or the region between two blades passing shows no plateau. With AMR the purple curve achieves somewhat different trends, with double peaks at the blade passing and overall higher amplitudes. The Fourier transformed signal in (b) confirms that there are three distinct amplitude levels for wetted, cavitating and AMR simulation approaches. Only with cavitation, signals appear over large frequency ranges, while the wetted simulation generates primarily tonal signals in the blade passing frequency.

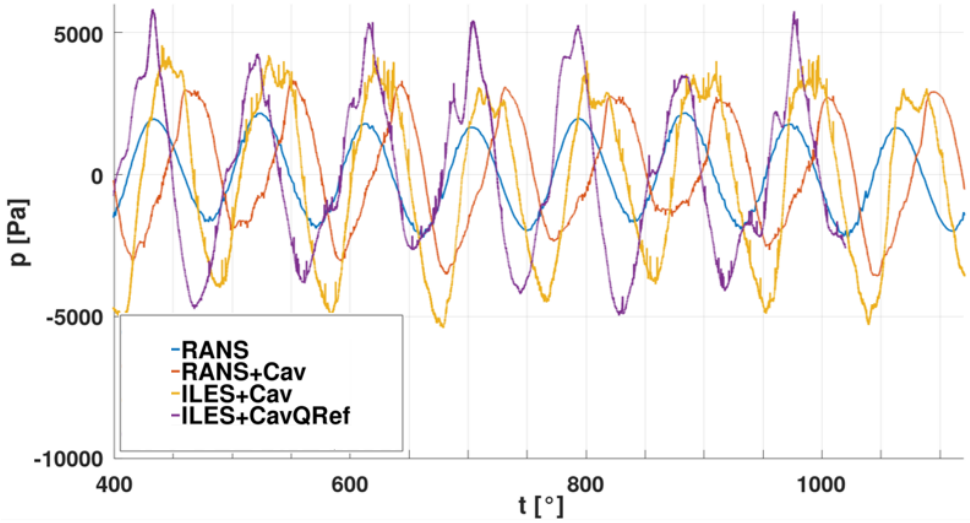

(a) Time domain signal

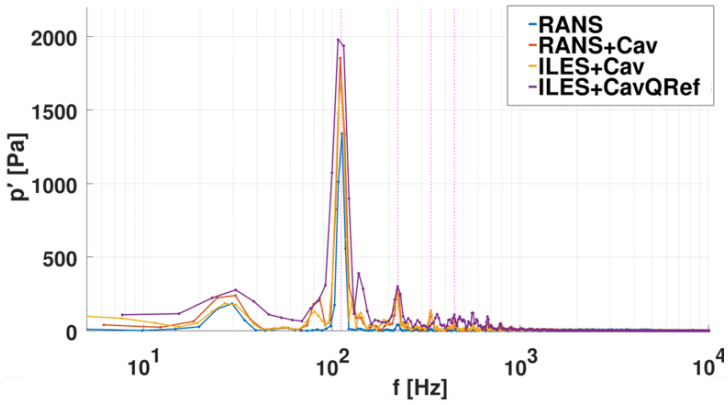

(b) Spectral representation

Fig. 122: Single point incompressible hull pressure

To verify the KFWH method, the same simulation for the ProNoVi reference target case is analyzed with the method regarding the pressure pulses at P8. The single contributions of the KFWH method are compared as a time series signal and as spectrum for wetted and cavitating RANS in Fig. 123. Pseudo thickness has a larger amplitude and is dominated by a low frequency oscillation with a smaller double frequency oscillation added on top, while the pseudo loading on the other hand experiences an almost sinusoidal shape. Both signals show very high frequency oscillations that are added to the signal in the time series, however, these cancel out to insignificant values in the total acoustic pressure in the non-cavitating condition in (a). For the cavitating case in (b) these high frequency oscillations are larger in amplitude, leading to the effect that all terms combined create a larger acoustic pressure, which is particularly visible at the second and third harmonic. Inter-harmonic noise appears for the cavitating case up to frequencies of $f < 1 \cdot 10^3 Hz$.

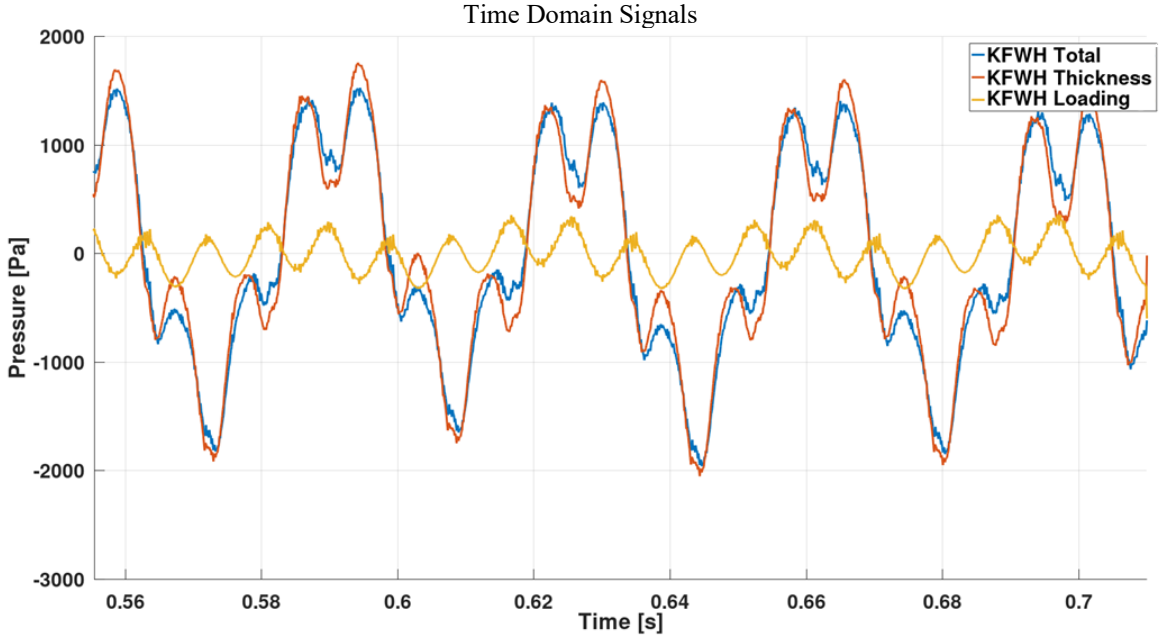

Frequency Domain Signals

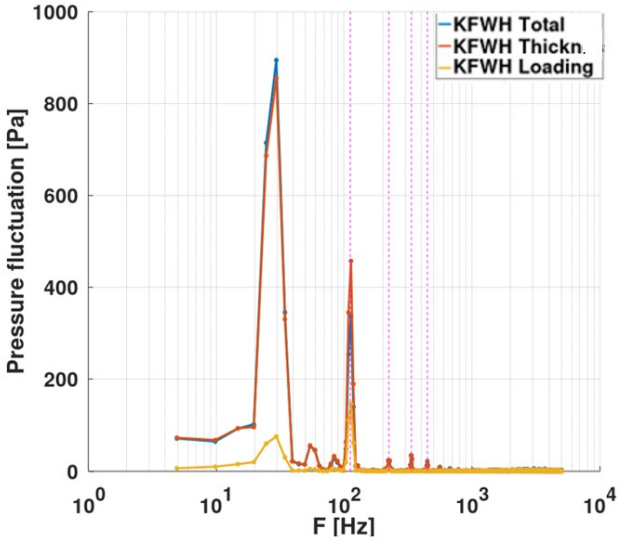

(a) Wetted

Time Domain Signals

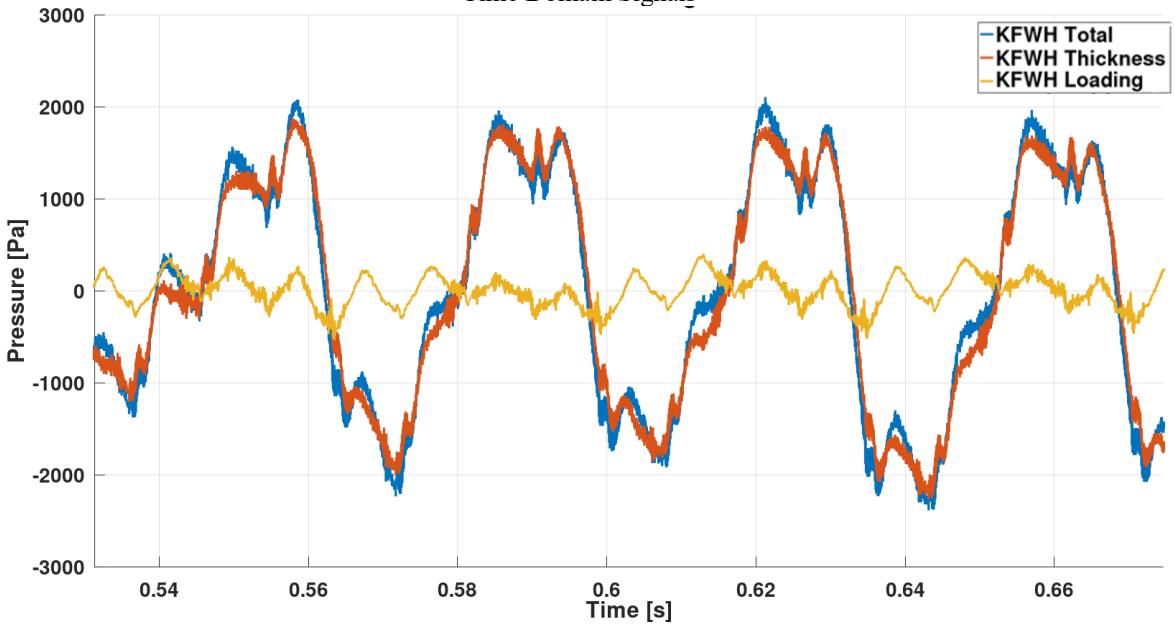

Frequency Domain Signals

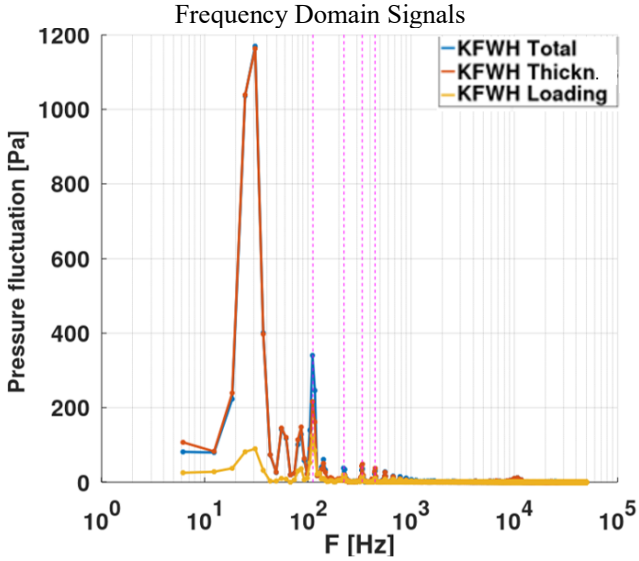

(b) Cavitating

Fig. 123: KFWH term contributions

To ascertain the influence of the hull on the acoustic emissions of the propeller, the propeller emissions without and with hull are compared. For the P3193 a time domain signal excerpt of about one rotation at P10 is plotted as acoustic pressure in Fig. 124. Without hull the amplitudes are about three times smaller than the measurement, while the amplitudes with hull are only slightly lower. However, there is an overlaying low frequency fluctuation in the case with vessel, possibly caused by pressure variations in the wake of the vessel or pressure reflections at the numerical domain boundaries.

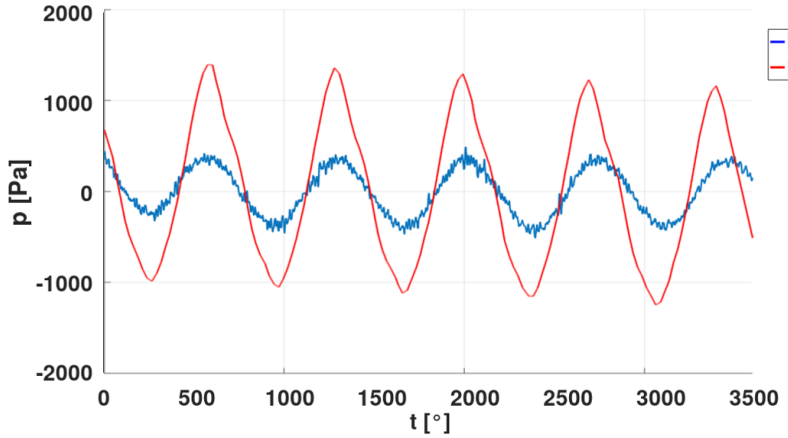

(a) Propeller only

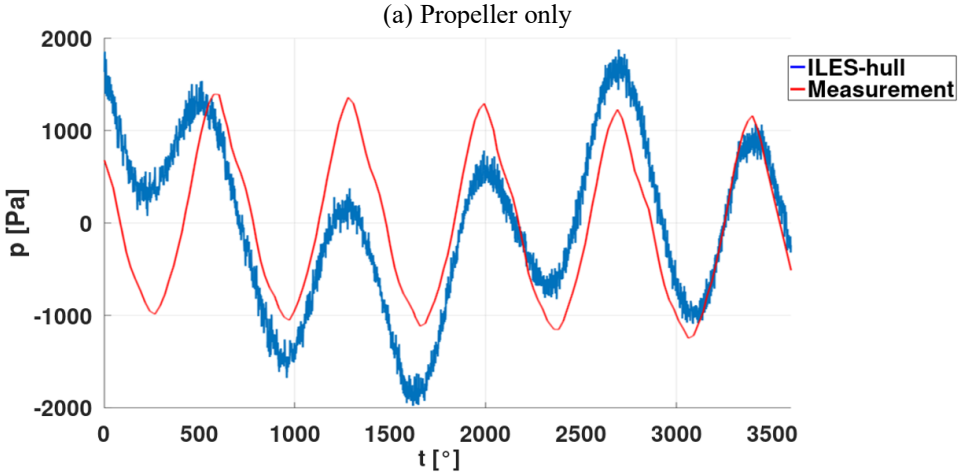

(b) Propeller and vessel

Fig. 124: Incompressible hull pressure at P10 for ProNoVi Target case with P3193 [92]

Comparing the pressure pulse information obtained from a RANS simulation at P10 in Fig. 125, the amplitude at the blade passing frequency is about 10% or less of the results for the case with hull *Hull* in (a) for the first four blade passing harmonics. On the other hand, the case with rudder *HullR* yields lower FVM pressure on the blade passing frequencies than the case without rudder, which must mean that the rudder is attenuating or detuning the emissions into the hull. The same results for different physics and turbulence modelling are given in (b), where good agreement with the experiments is found. Generally, the first harmonic is slightly underpredicted by all methods, the higher harmonics without cavitation show a tendency to be overpredicted by the numerical approach. The more level of detail in the simulation by means of more realistic physics i.e. cavitation and turbulence modelling, the more the pressure pulses increase.

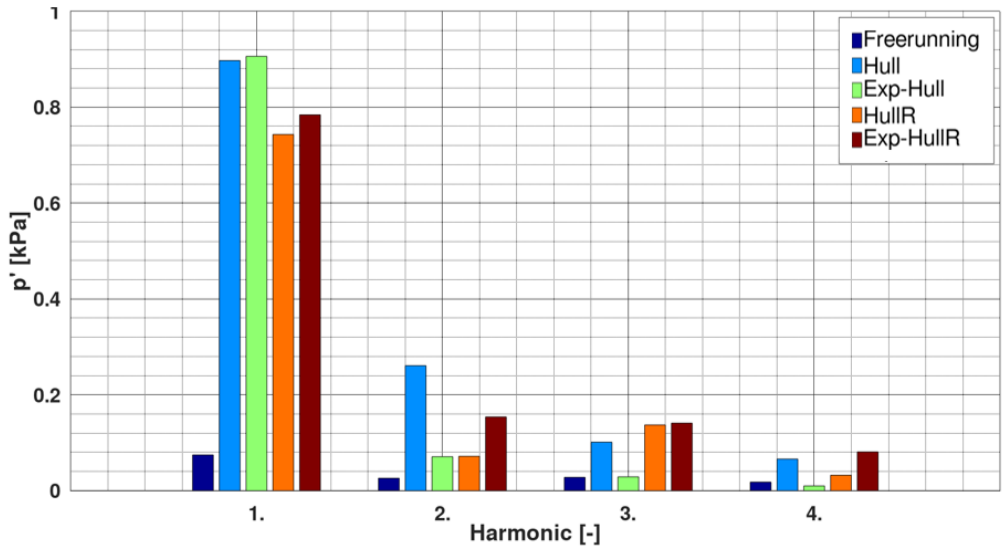

(a) Influence of vessel

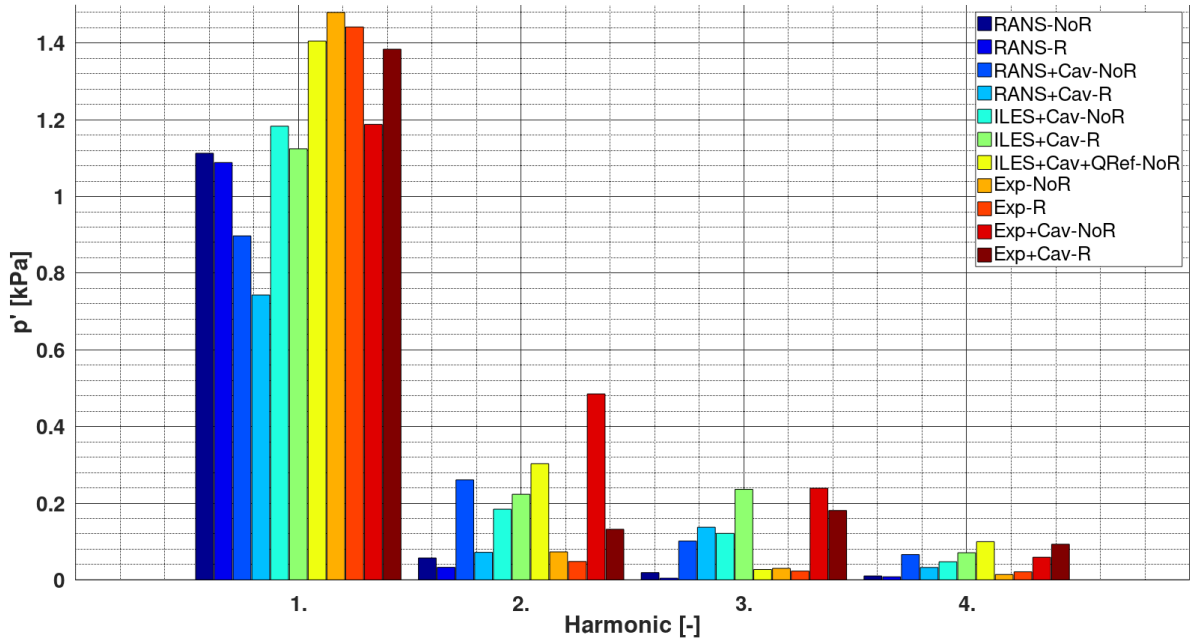

(b) Influence of turbulence model

Fig. 125: Incompressible hull pressure pulses for P10, for ProNoVi Target case with P1595

In the simulation results from the LES with the ProNoVi reference target case with the P1595 propeller in Fig. 126 (a), the acoustic pressure for the first harmonic is plotted along the intersection of the hull surface with the propeller plane and along the projection of the shaft line axis together with the experiments pressure pick-ups. For the cases without rudder *NoR* and with Rudder *R* the FVM pressure yields good agreement with the experiment, which improves upstream of the propeller plane and inwards of the vessel. For the improved resolution of the trailing vortices and the cavitating tip vortex *QRef*, the FVM pressure generally increases, the KFWH loading component is largely unaffected and the thickness component increases severely. For the case with rudder the KFWH thickness components yield unphysical results, which is a result of placing the cylindrical control surface downstream base between propeller and rudder, where the pressure fluctuations are too large. Otherwise for the FVM pressure, the same trends between geometries without and with rudder are confirmed, yielding slightly lower pressure pulses with rudder.

Along shaft axis

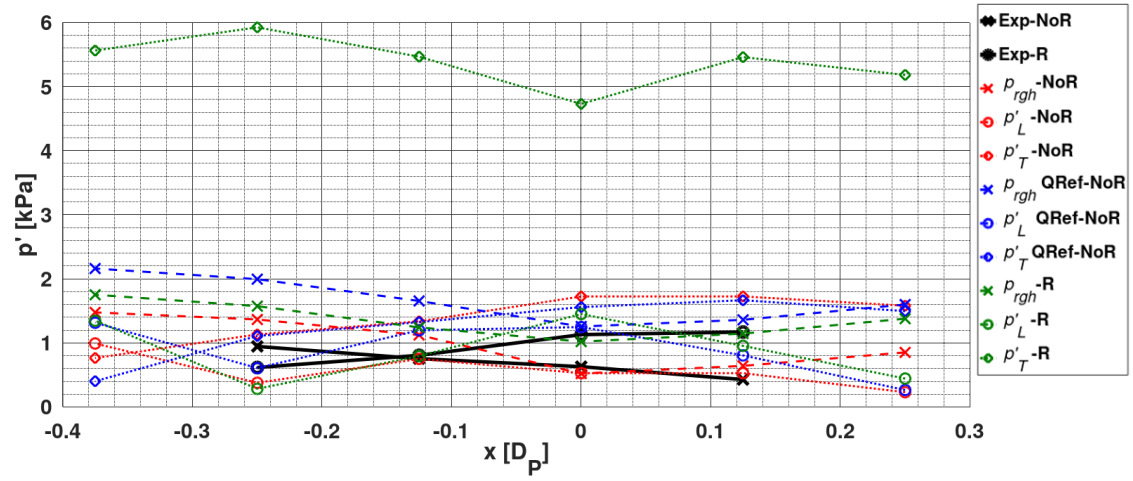

In propeller plane

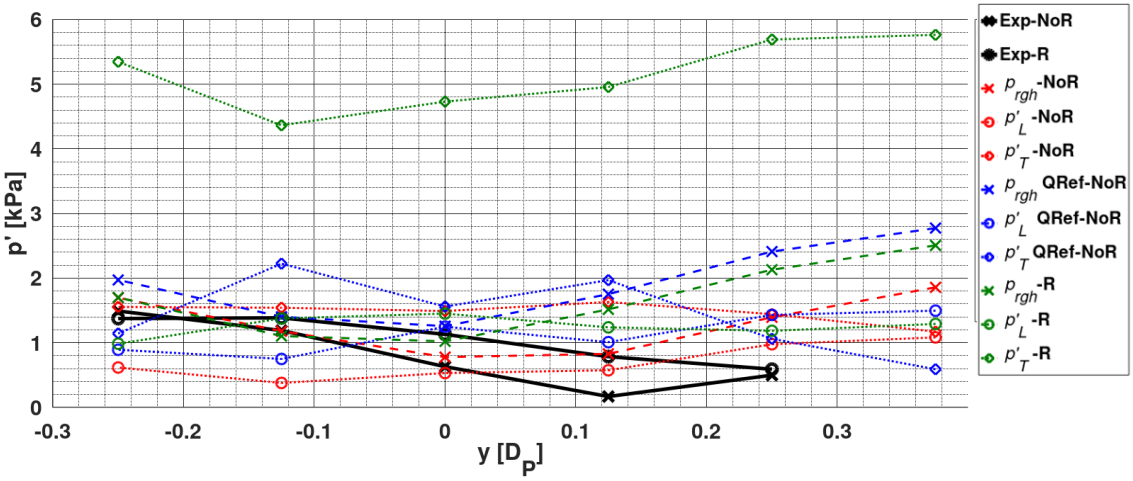

(a) P1595

Along shaft axis

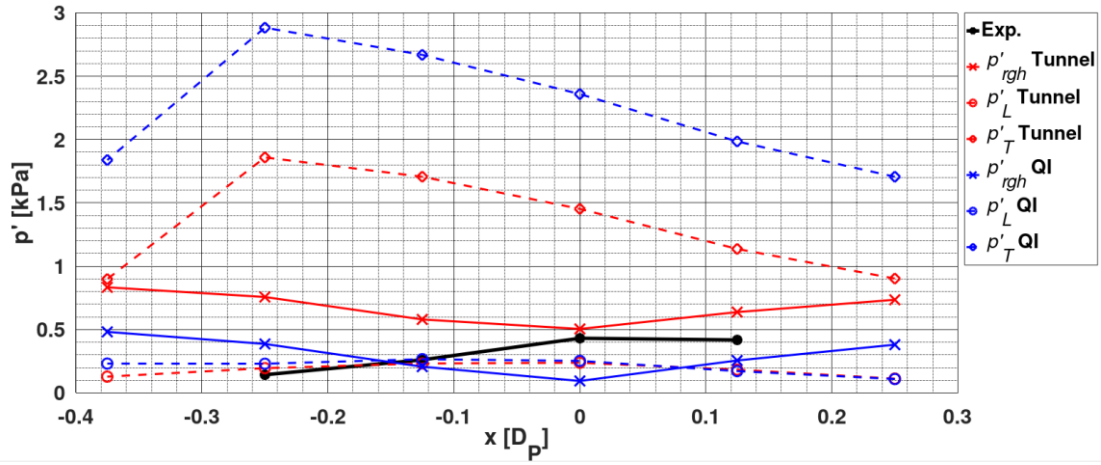

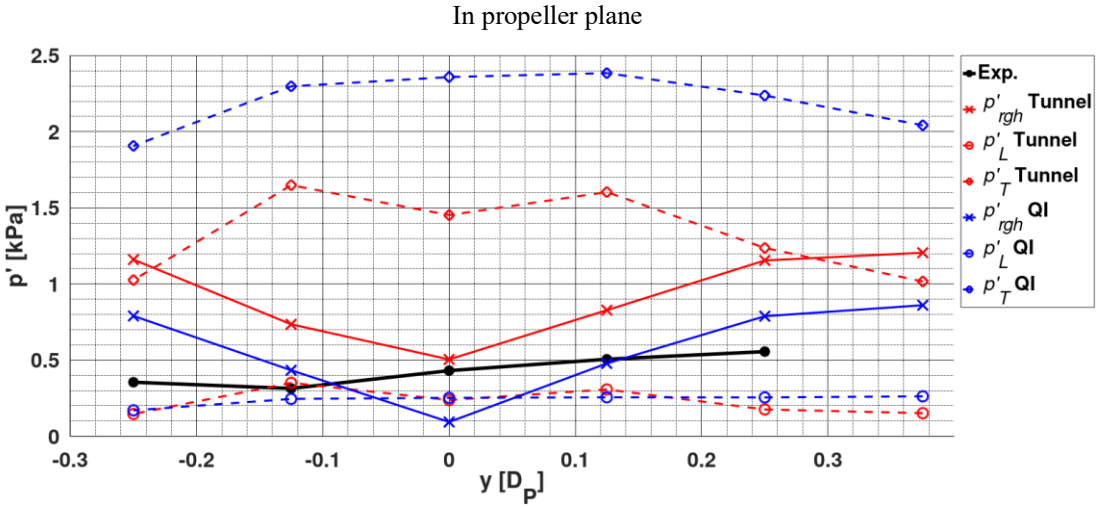

(b) P3193

Fig. 126: Incompressible acoustic hull pressure and KFWH terms with respect to propeller location [80]

In general, it can be said that the local variation of trends of the pressure pulses are predicted with moderate success for any of the approaches in comparison to the experiments. In the propeller plane a minimum is predicted by the simulation methods, which is mirrored along the shaft line axis with respect to the experimental observation. The prediction of the trend along the shaft line axis follows the experiment better, even capturing the reversed incline along the axis caused by the geometry variations, however, a minimum is predicted for this case not seen in the experiment. Although the minimum lies outside the interrogation region of the experimental observation.

The single point observer investigations show, that AMR is necessary to resolve the acoustic details in the pressure time signal for the trailing vortices in the propeller slipstream. A comparison of the pressure and the KFWH method proves that volume cavitation effects can be captured by the method. For the pressure pulses of propeller-hull combinations several effects are observed. The pressure signal overall amplitudes obtained by an open water propeller are a fraction of the amplitude of the case with ship hull and the rudder may detune or attenuate the pressure pulses introduced into the hull for certain propulsor-ship configurations. Switching to the acoustic analogy, the KFWH method overpredicts the thickness component, in some cases severely, while the loading component achieves physically supported acoustic pressure.

6.1.2 High Spatial Density Analysis

For the P1595 ProNoVi reference target case, the pressure distribution of the first four harmonics is given for RANS turbulence modelling in Fig. 127 with the propeller at an arbitrary angle for reference. The case without cavitation in (a) creates a rather intuitive distribution of pressure on the hull, with the first harmonic largely centered in the propeller plane and the second harmonic more centralized at the closest point of the blade tips passing the hull. Next, the third harmonic shows a more axially centered distribution of high pressure along the shaft line and the fourth harmonic a concentration above the propeller slipstream and trailing vortex region, where higher frequency turbulent fluctuations are relevant. On the other hand, the pressure distribution obtained with active cavitation in (b) is not intuitive and requires some explanation. For the first harmonic, the central point above the propeller experiences a pressure pulse minimum while there are two maxima located towards the outer sides, which are caused by the propeller blade leading edge suction side cavities generated on the upwards going blade on the outwards side and imploding on the downwards going side on the inwards side of the vessel. For the second harmonic, the sheet cavitation yields a similar pattern slightly moved downstream and the third harmonic represents the region of the collapsing cavity on the downwards going blade very well. The fourth harmonic maximum upstream of the propeller is mainly caused by the blade cavities emitting in

direction of the suction side, as the emission downstream is blocked by the solid propeller blade surface. These structures may either be not detected by single point observations or lead to wrong conclusions as small scale extrema are missed due to insufficient spacing of the observers. Thus, the local distribution of pressure peaks may not always be intuitive by analyzing single point observers and small-scale pressure structures could lead to difficulties in finding explanations, which is not the case for a high resolution of pressure information on the hull.

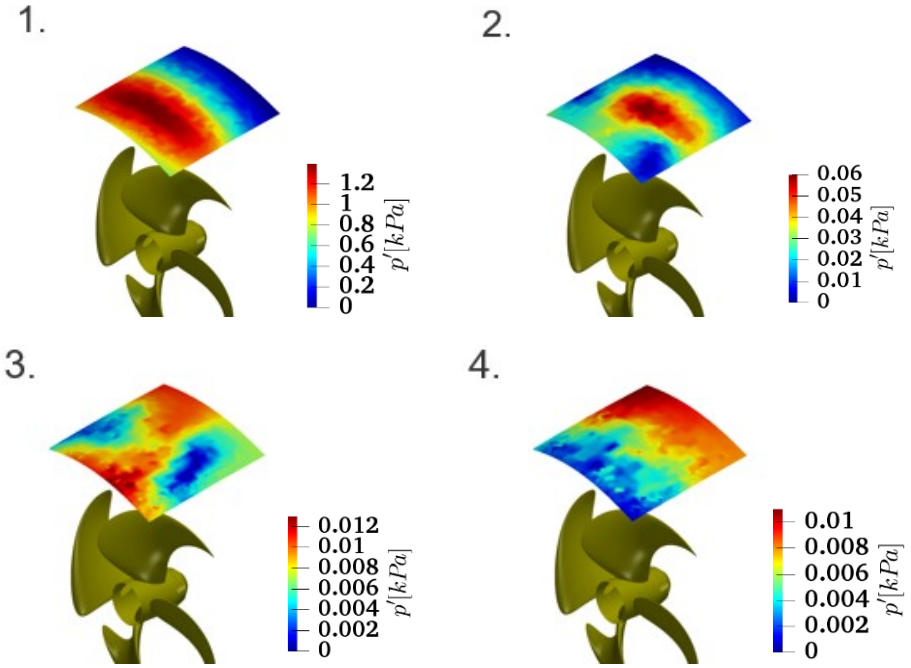

(a) RANS without Cav

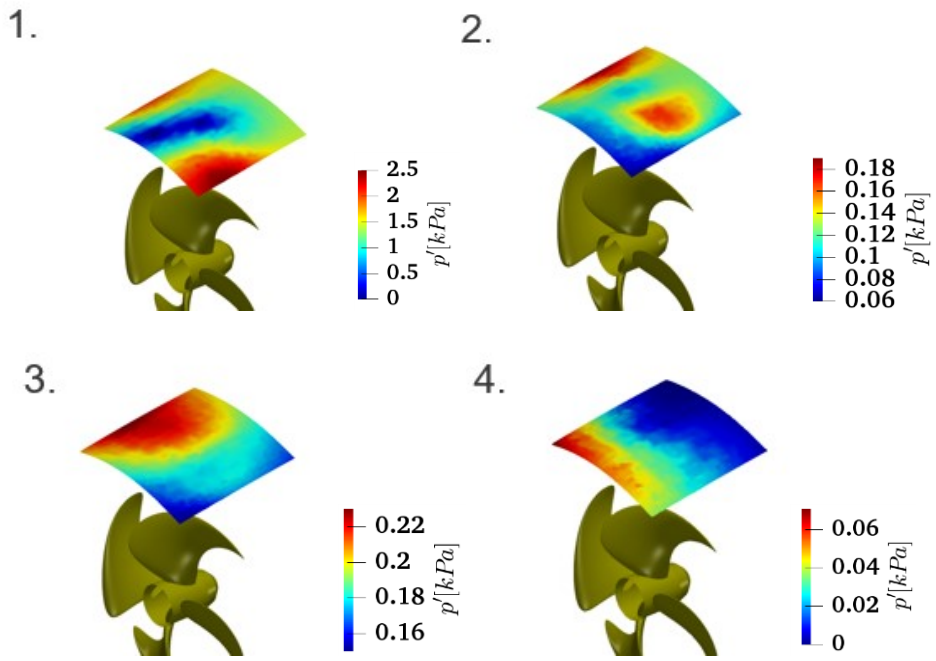

(b) RANS with Cav

Fig. 127: Pressure distribution on the selected hull patch with illustration of propeller

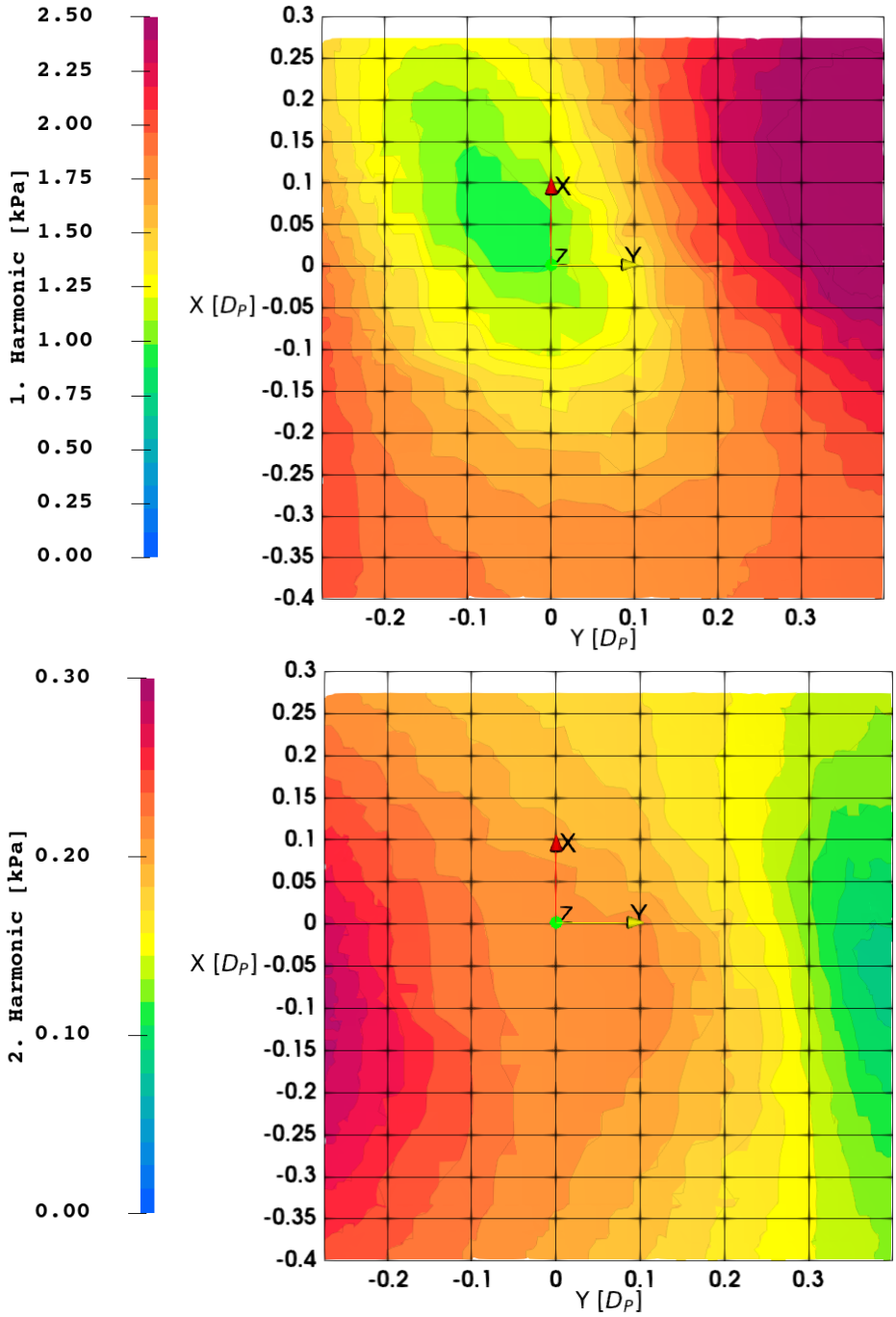
1. Harmonic [kPa]
2.50
2.25
2.00
1.75
1.50
1.25
1.00
0.75
0.50
0.25
0.00
X [D_P]
Y [D_P]
0.3
0.25
0.2
0.15
0.1
0.05
0
-0.05
-0.1
-0.15
-0.2
-0.25
-0.3
-0.35
-0.4
-0.2
-0.1
0
0.1
0.2
0.3
X
Z
Y
2. Harmonic [kPa]
0.30
0.20
0.10
0.00

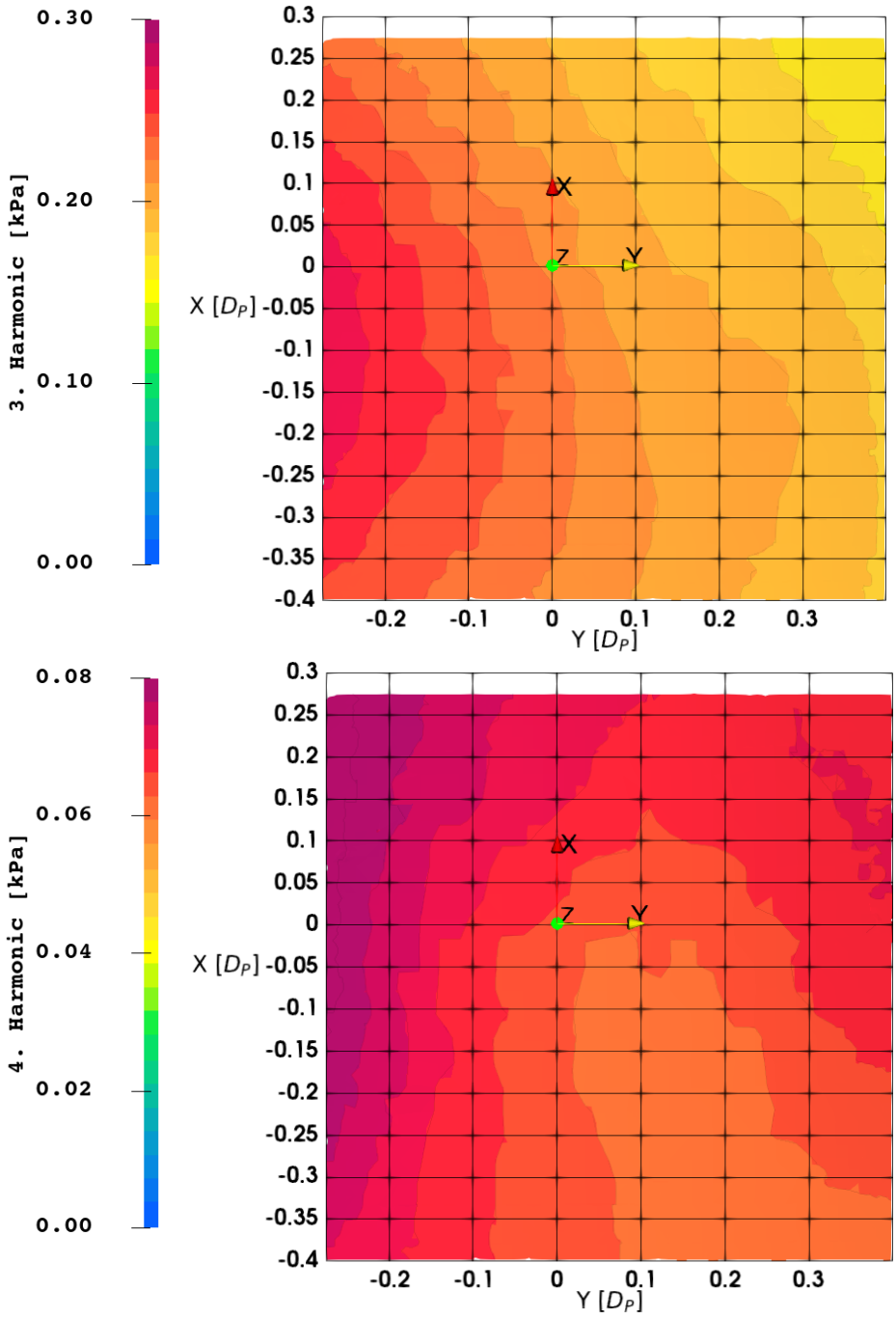
3. Harmonic [kPa]
0.30
0.20
0.10
0.00
X [D_P]
Y [D_P]
4. Harmonic [kPa]
0.08
0.06
0.04
0.02
0.00
X [D_P]
Y [D_P]

(a) P1595

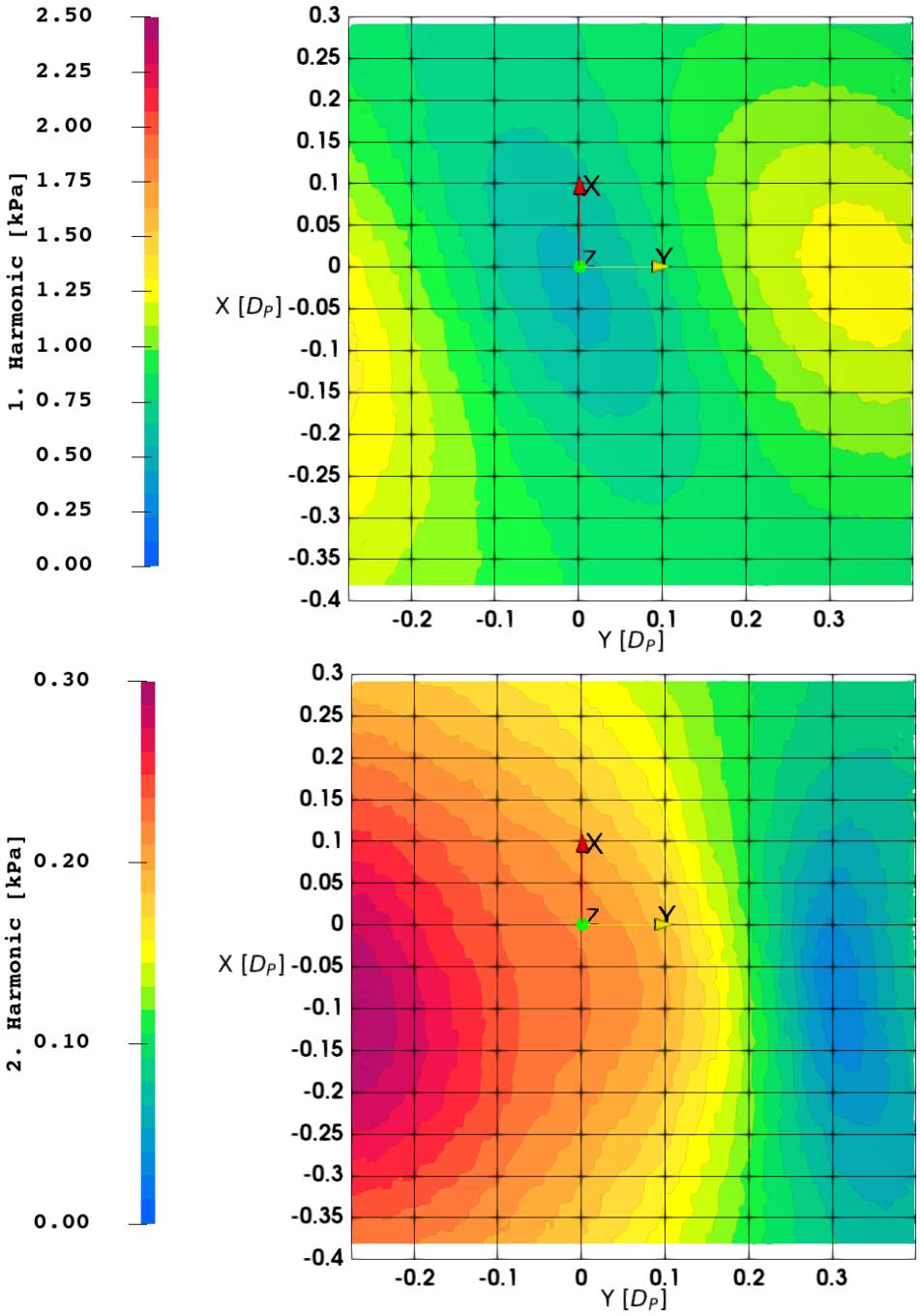
1. Harmonic [kPa]
2.50
2.25
2.00
1.75
1.50
1.25
1.00
0.75
0.50
0.25
0.00
X [D_P]
Y [D_P]
0.3
0.25
0.2
0.15
0.1
0.05
0
-0.05
-0.1
-0.15
-0.2
-0.25
-0.3
-0.35
-0.4
-0.2
-0.1
0
0.1
0.2
0.3
X
Z
Y
2. Harmonic [kPa]
0.30
0.20
0.10
0.00
X [D_P]
Y [D_P]

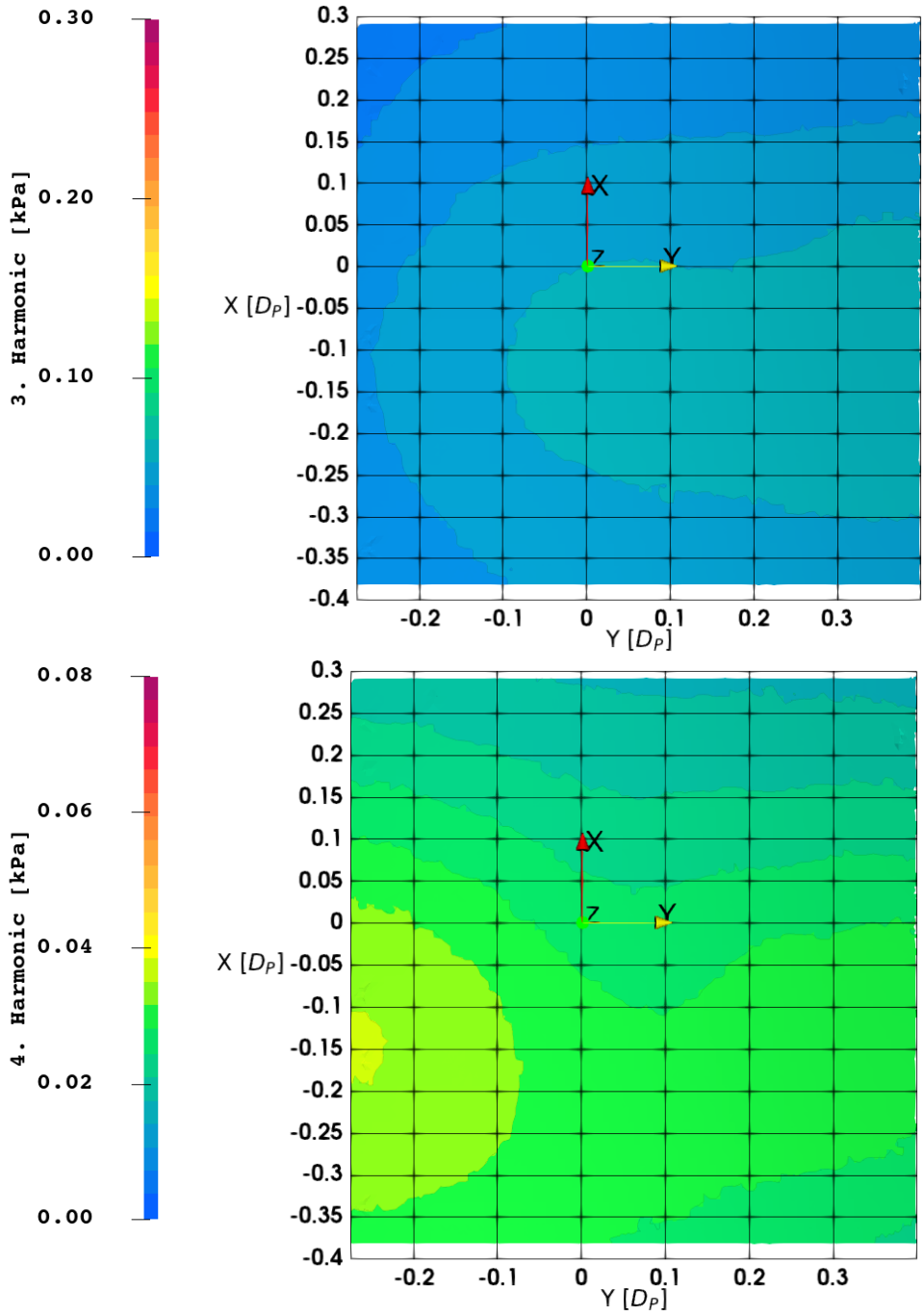

(b) P3193

Fig. 128: Comparison of hull pressure pulses for the propeller designs [80]

Next, the influence of the propeller design on the pressure pulses is investigated. Both propeller variants for the ProNoVi reference target case are compared regarding the hull pressure distribution obtained with LES and active cavitation for the first four harmonics in Fig. 128, where the direction of travel points upwards and the ship inwards direction is left. Similar findings between the propeller designs are obtained regarding the preference of the upwards and downwards going blades for all harmonics. While the first harmonic reaches higher pressure at the upwards going blade at the formation of the cavity, the higher harmonics have larger pressure fluctuations on the downwards going blade along with the cavity collapse. However, the small area of interrogation might cut off higher pressure areas to the left of the region in the first harmonic. To conclude, the difference in level between the two propeller designs for the same hull configuration is undeniable with a reduction of up to $\Delta p \approx 1kPa$ for the optimized propeller design in (b). The main difference between the propeller designs is the complete mitigation of a strong tip vortex, while the cavitation on the blade is unaffected. Thus, the second harmonic is largely

identical in level and distribution, while the higher harmonics do not feature large variations across the surface for the colormap scale selected for both propellers.

In Fig. 126 (b) this case is investigated in the same way as the P1595 propeller before for the P3193 propeller for the first blade harmonic. With the tunnel domain, the FVM pressure at the hull is larger over the complete region, which appears as a constant shift of all values by an amount of about $\Delta p \approx 0.5kPa$ independent of the value. For the KFWH method on the other hand, the loading component is largely unaffected by the domain geometry, while the thickness component experiences a constant shift of about $\Delta p \approx 1kPa$. However, similar to the P1595 case the thickness component is highly inaccurate with an overprediction in the order of three to four times the measurement values, which is attributed to the spurious noise of the propeller slipstream crossing the permeable surface interface just downstream of the propeller. Also similar to the other propeller is the local capturing of the pressure trends along the hull.

In the following Fig. 129, the pressure pulses for the P3193 case are given for all simulation steps for the cavitation tunnel and the quasi-infinite domain as a comprehensive overview. In the figures the direction of travel is to the right and the outwards ship direction is up. The quasi-infinite domain yields consistently a lower overall pressure level for all cases, while the patterns are comparable for each simulation step and the respective harmonic. A difference in the pressure distribution pattern only emerges for the LES simulation third and fourth harmonic, caused by a highly resolved propeller slipstream that may be affected by the dissimilar high frequency pressure reflections in the near-field caused by the cavitation tunnel domain, which are non-existent in the quasi-infinite case. Between the simulation steps a clear distinction between wetted and cavitating flow is identifiable in the first harmonic, where the RANS features a single centrally located pressure peak, whilst the cavitation yields the two peaks caused by the cavity formation and collapse on either side of the propeller axis.

Cavitation Tunnel

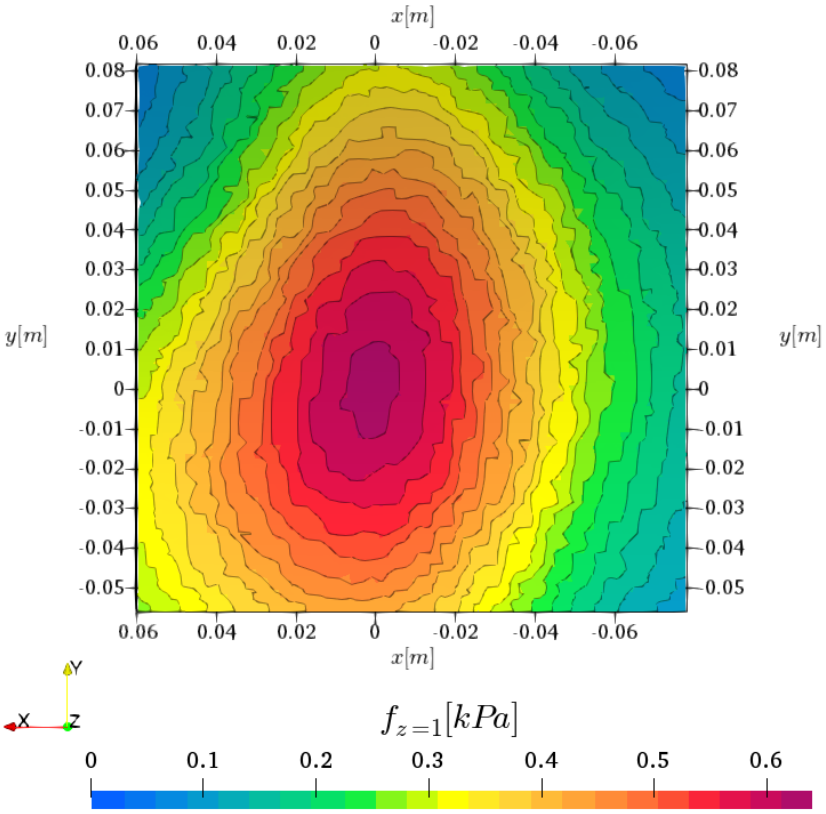

Quasi-Infinite

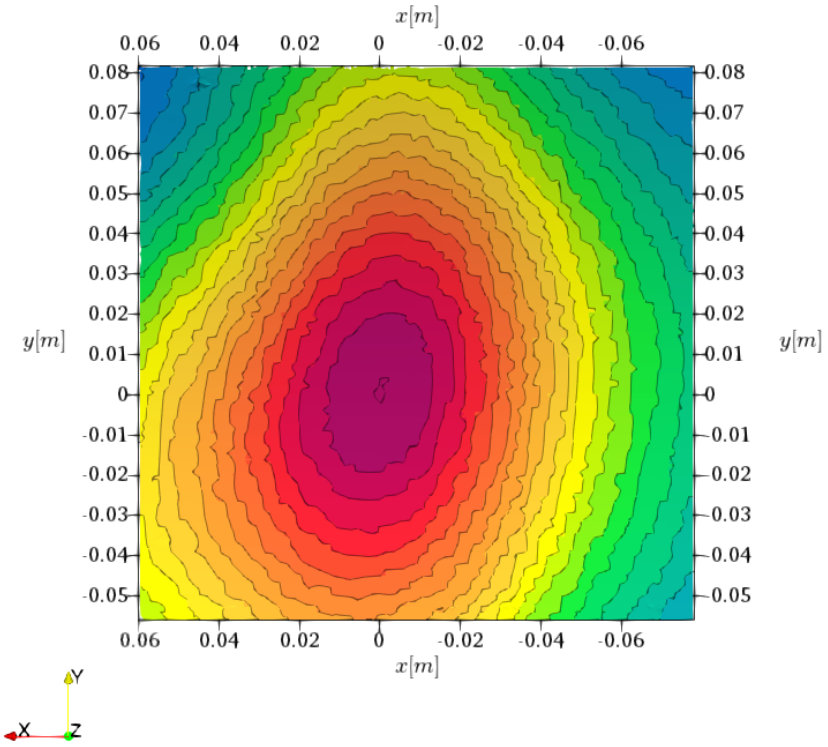

Cavitation Tunnel

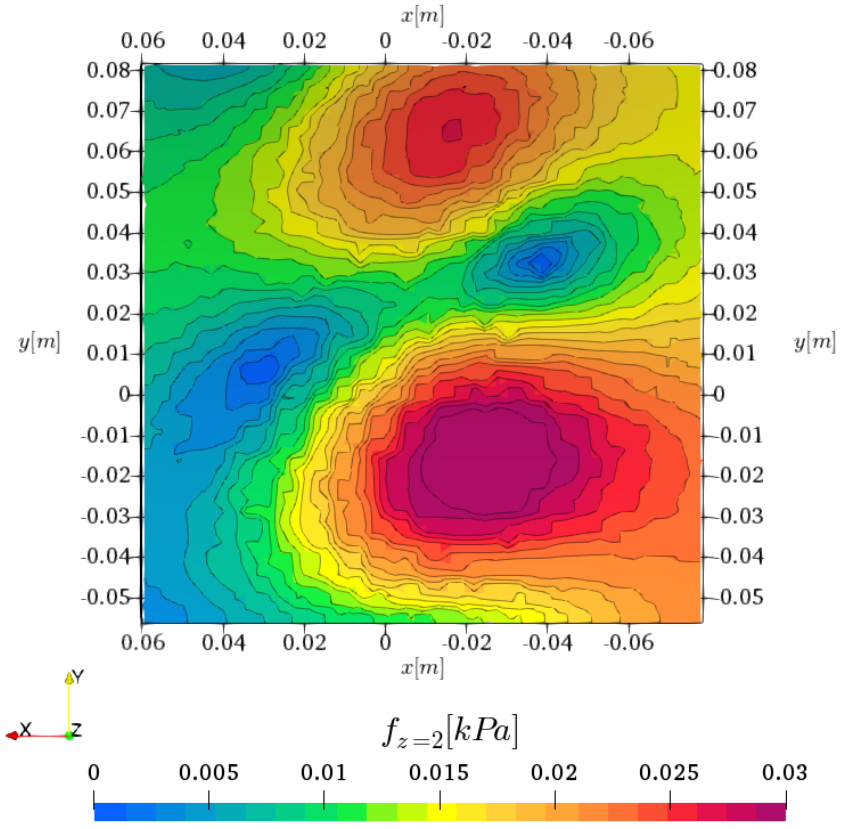

Quasi-Infinite

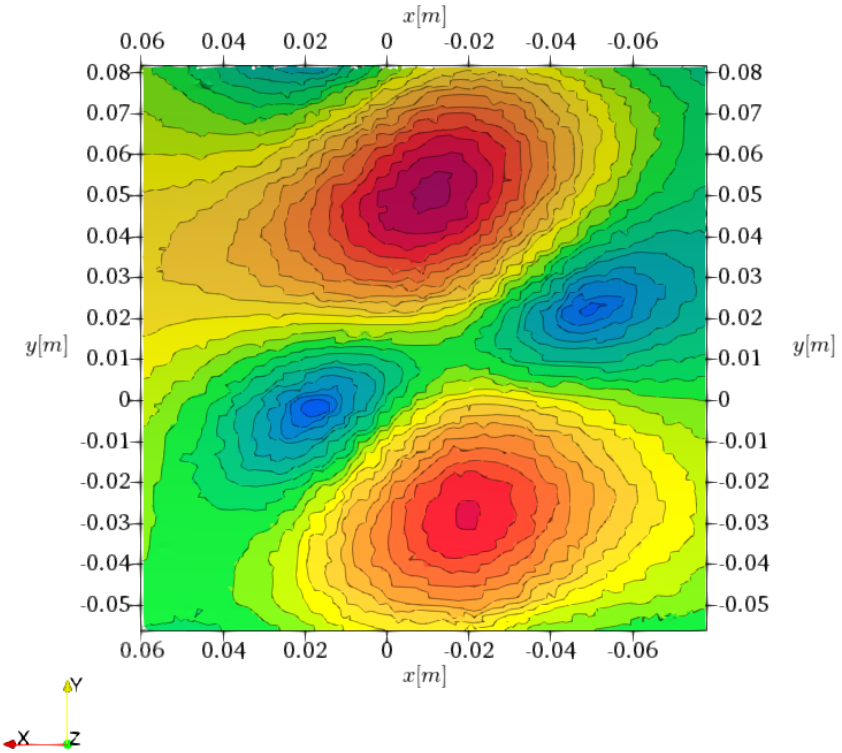

Cavitation Tunnel

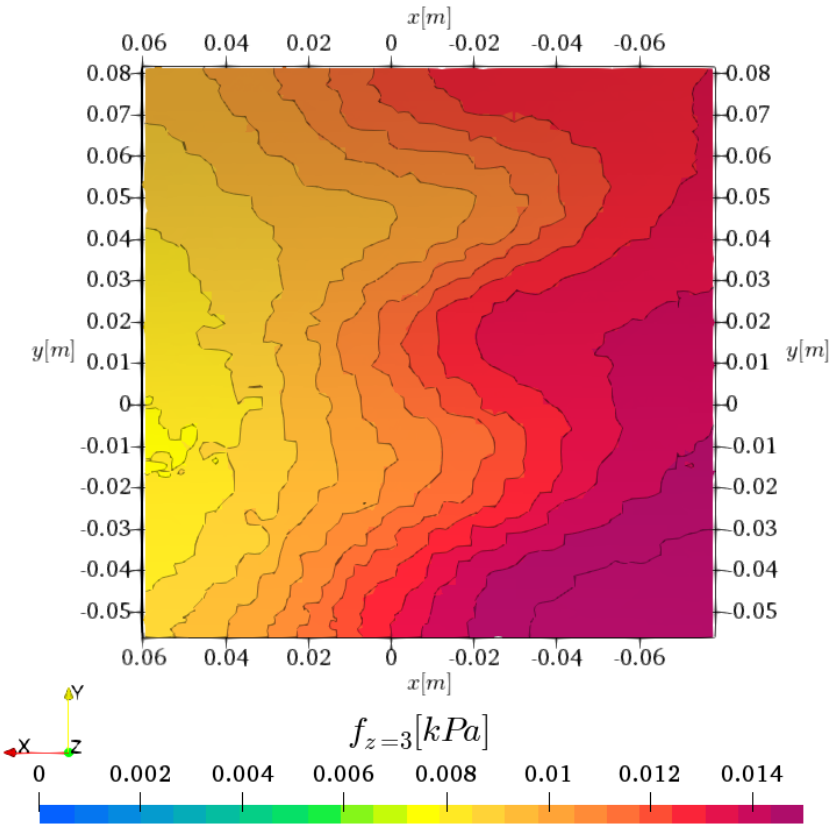

Quasi-Infinite

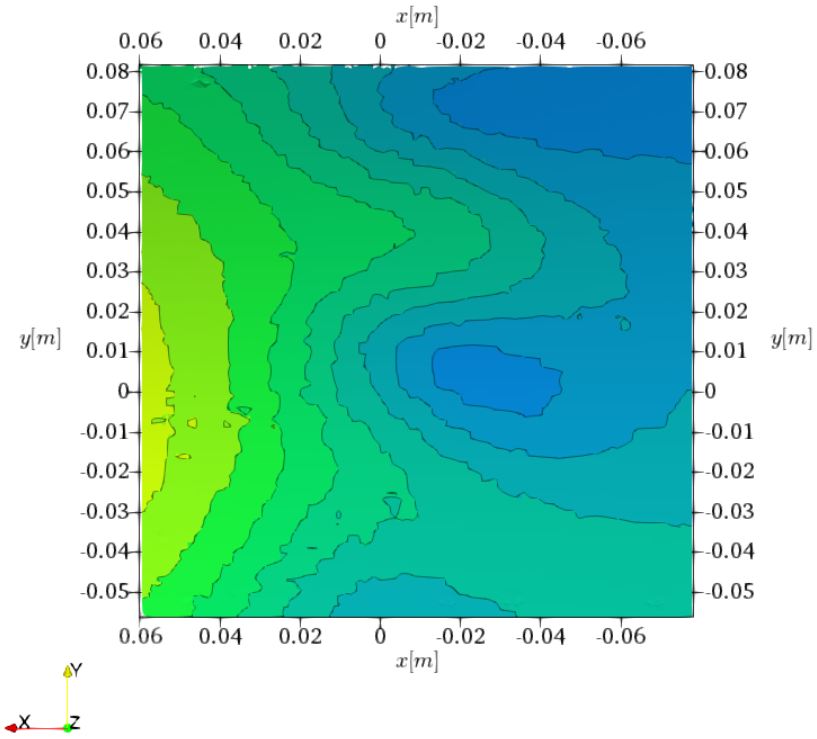

Cavitation Tunnel

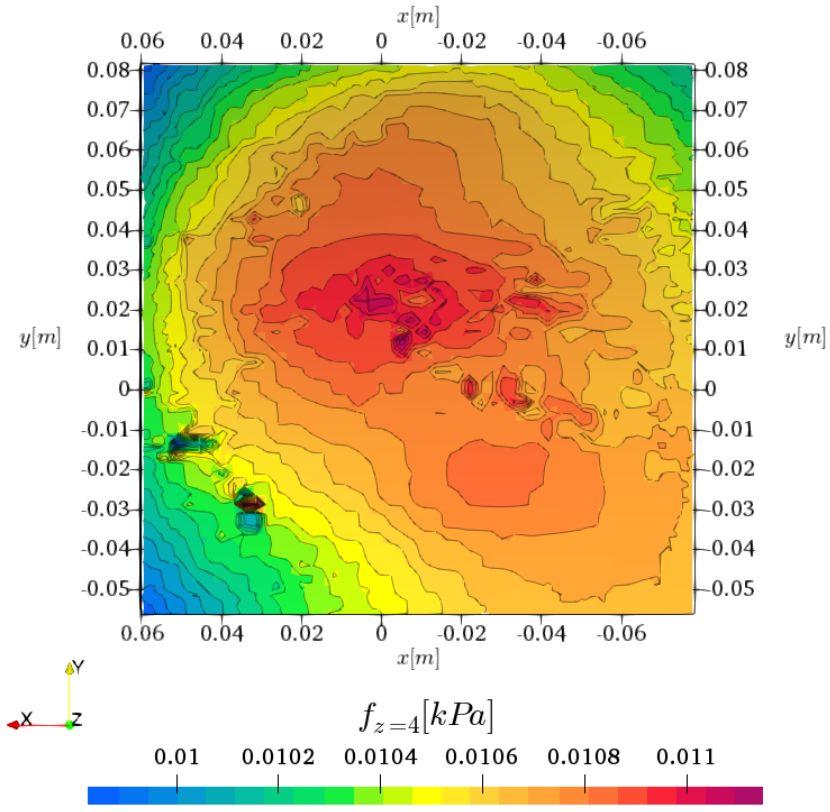

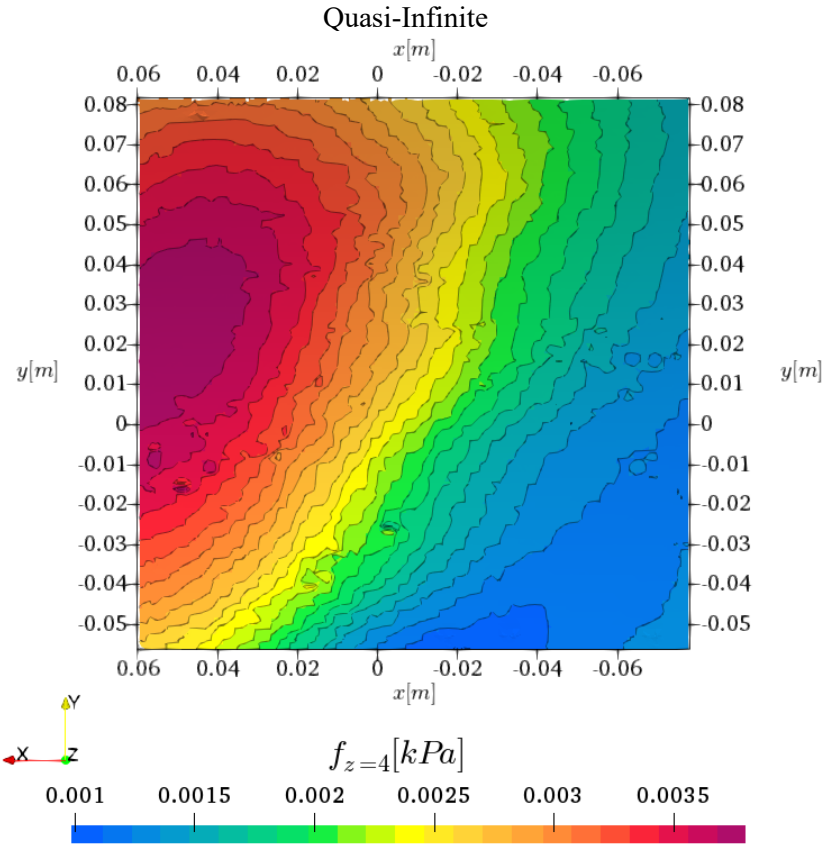

(a) RANS without cavitation

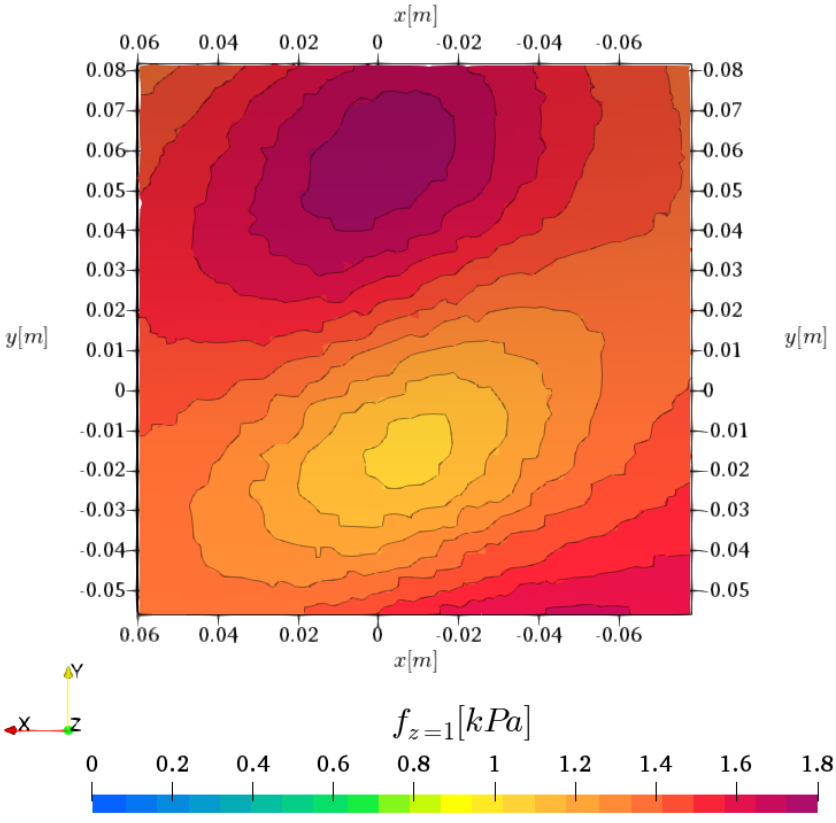

Quasi-Infinite

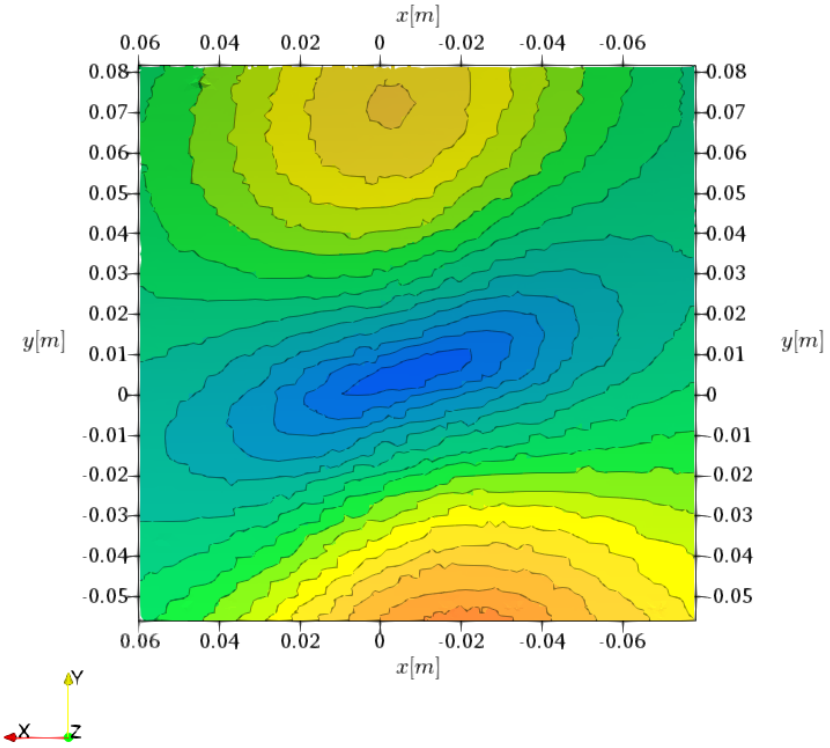

Cavitation Tunnel

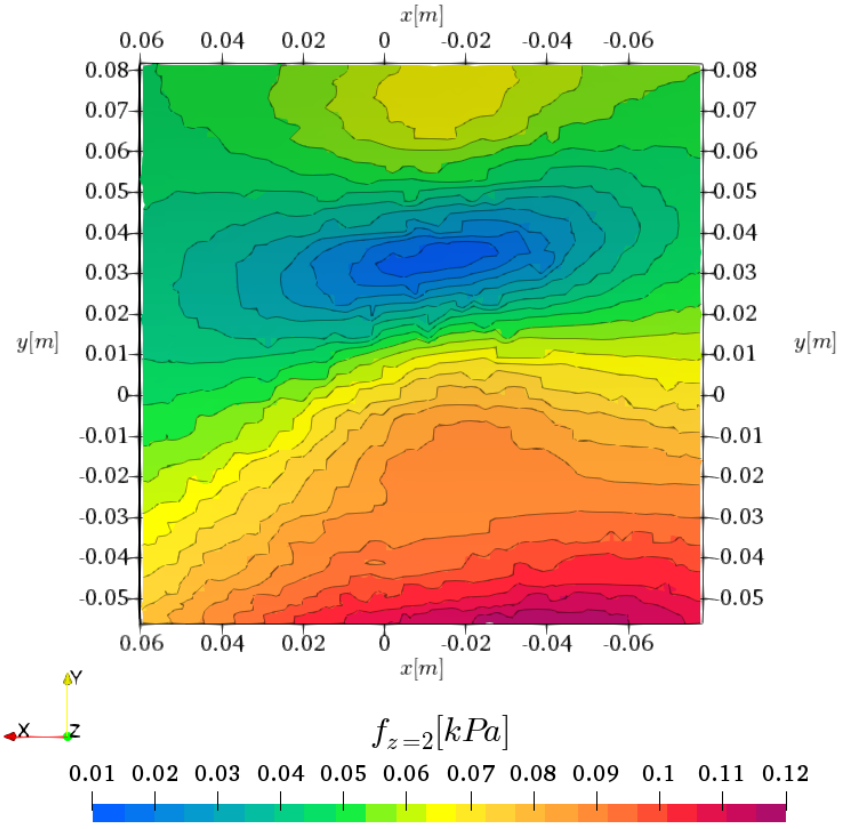

Quasi-Infinite

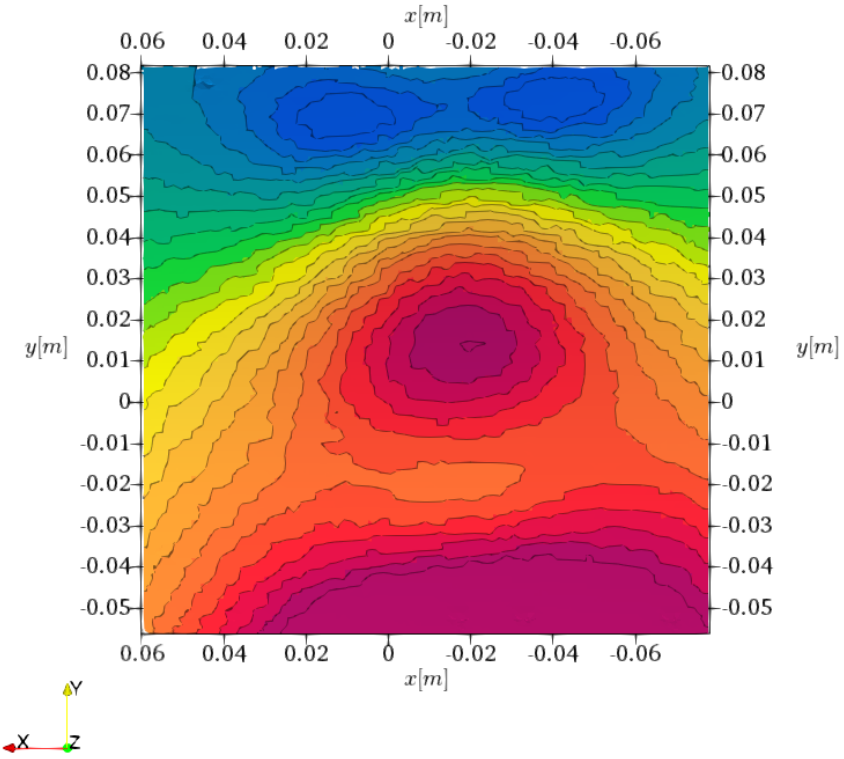

Cavitation Tunnel

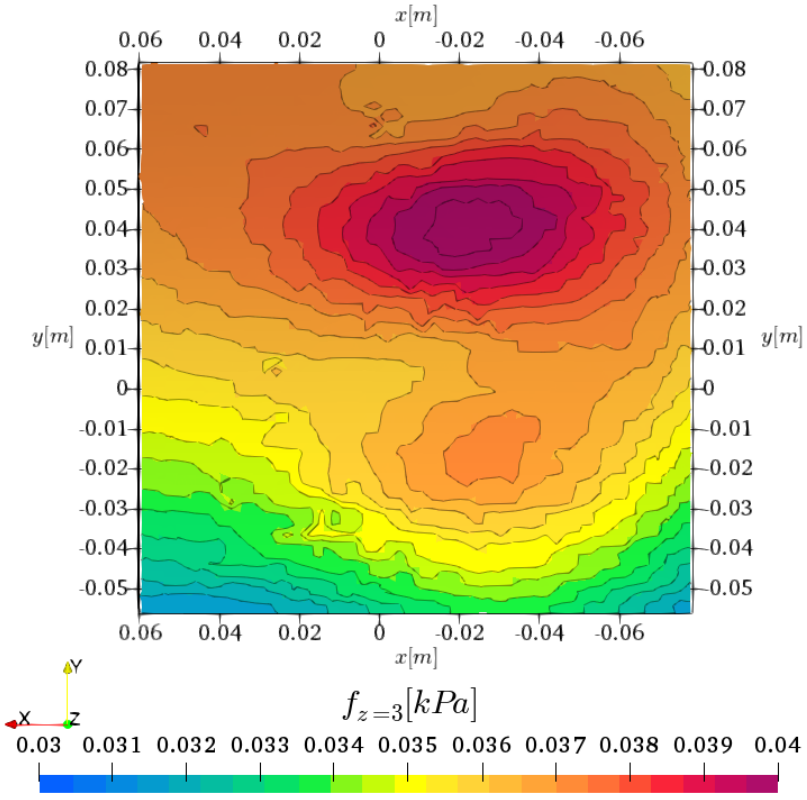

Quasi-Infinite

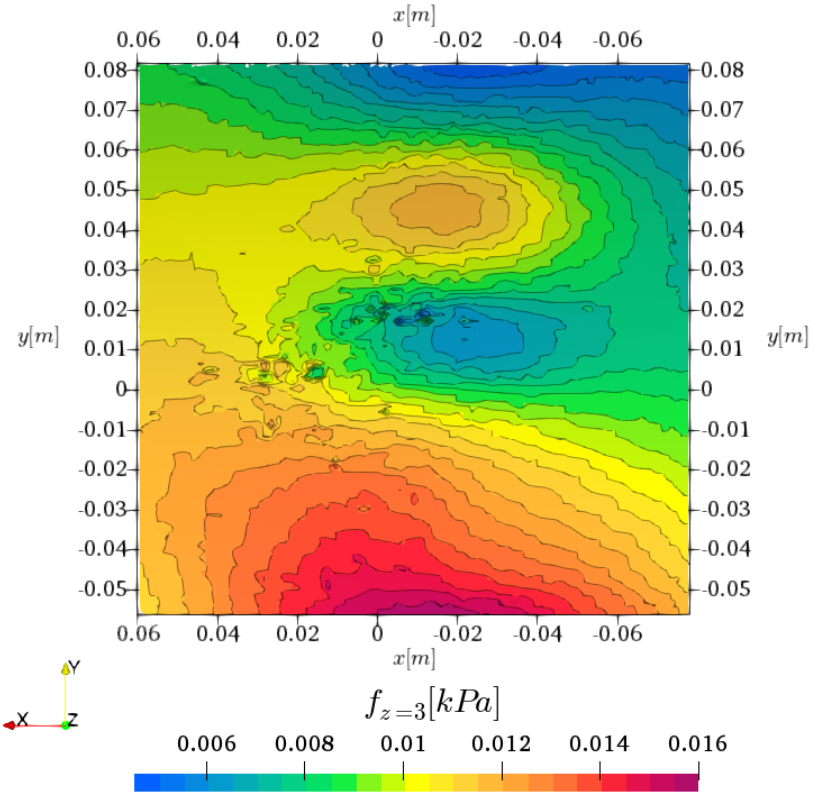

Cavitation Tunnel

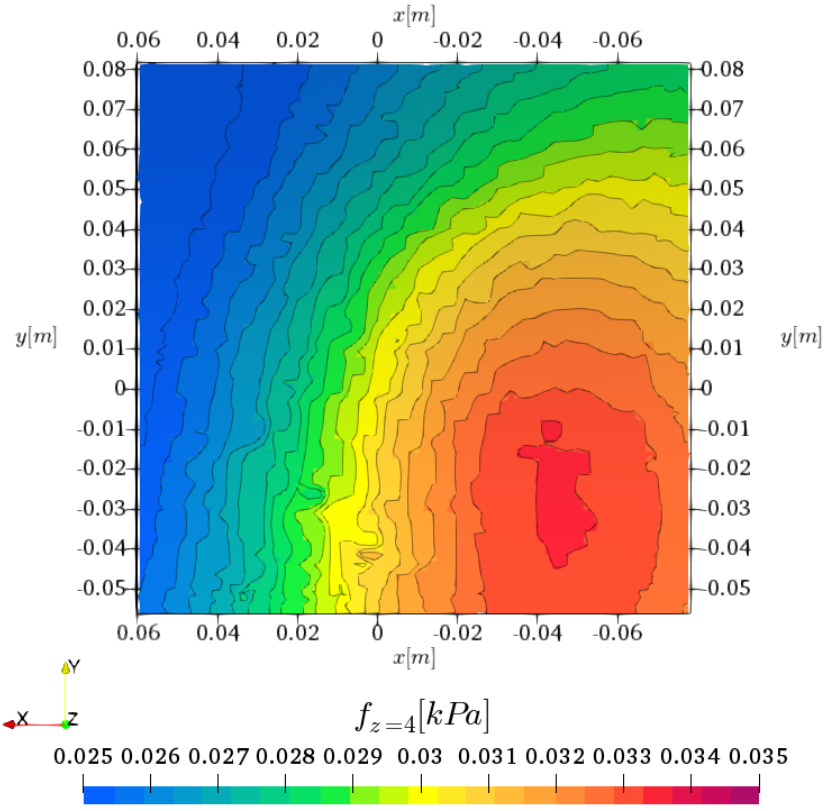

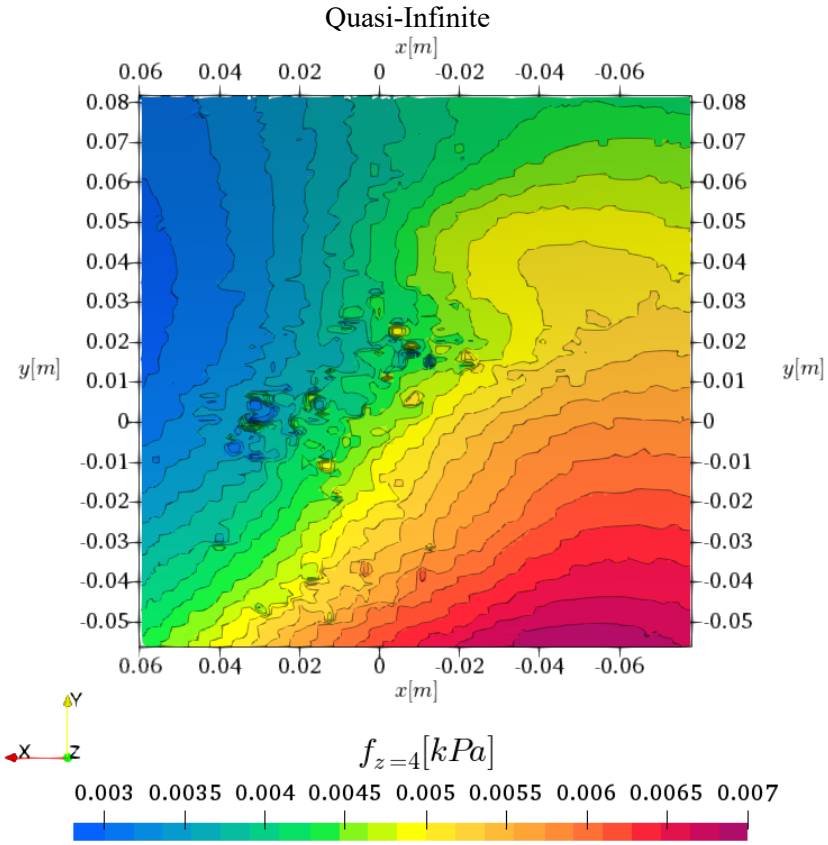

(b) RANS with cavitation

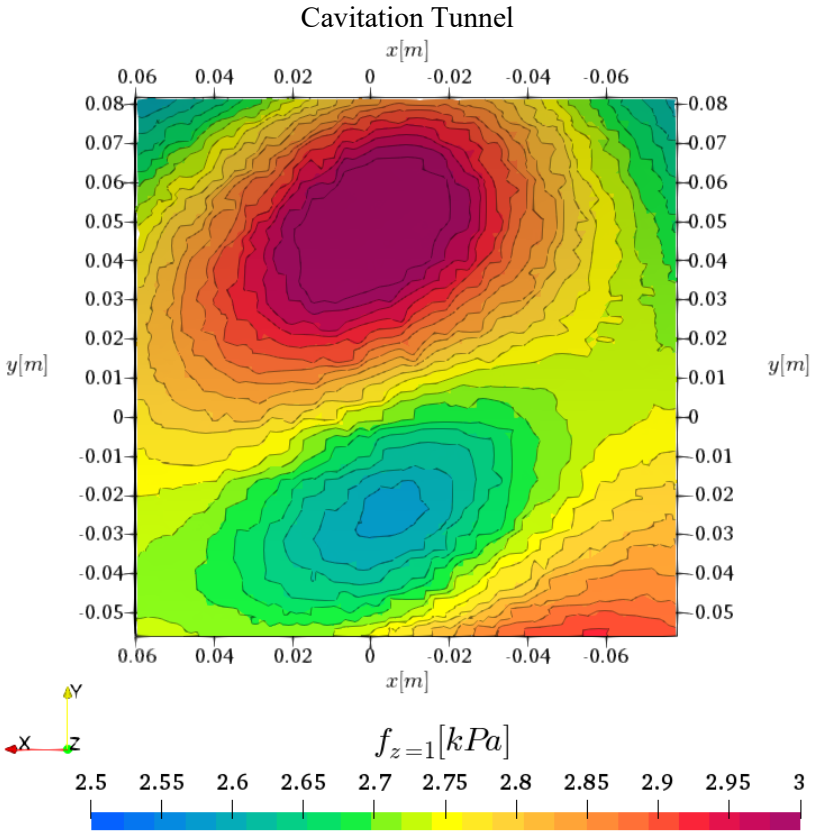

Quasi-Infinite

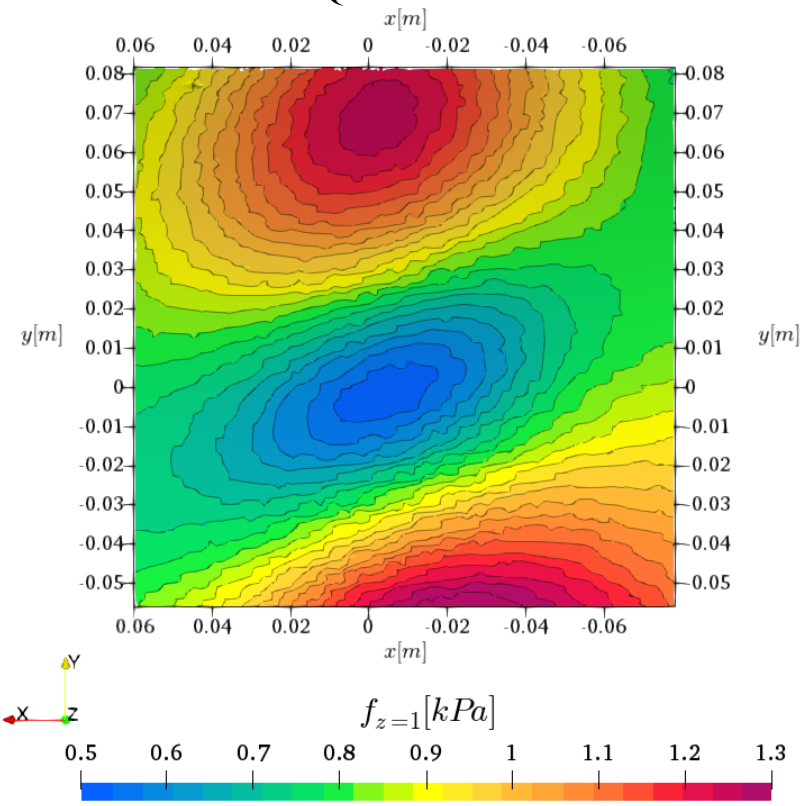

Cavitation Tunnel

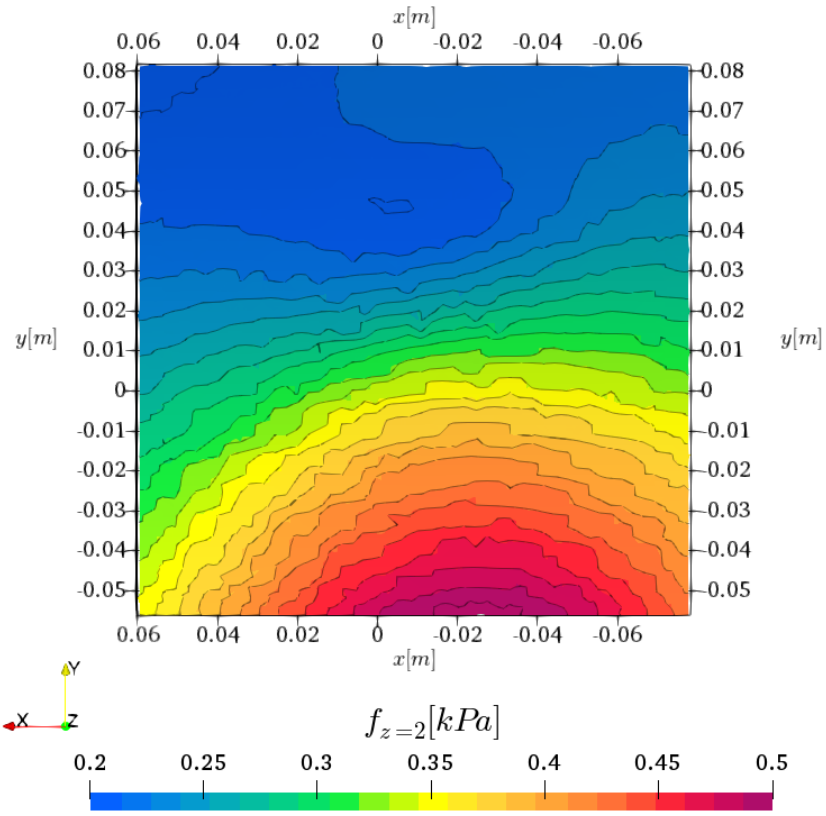

Quasi-Infinite

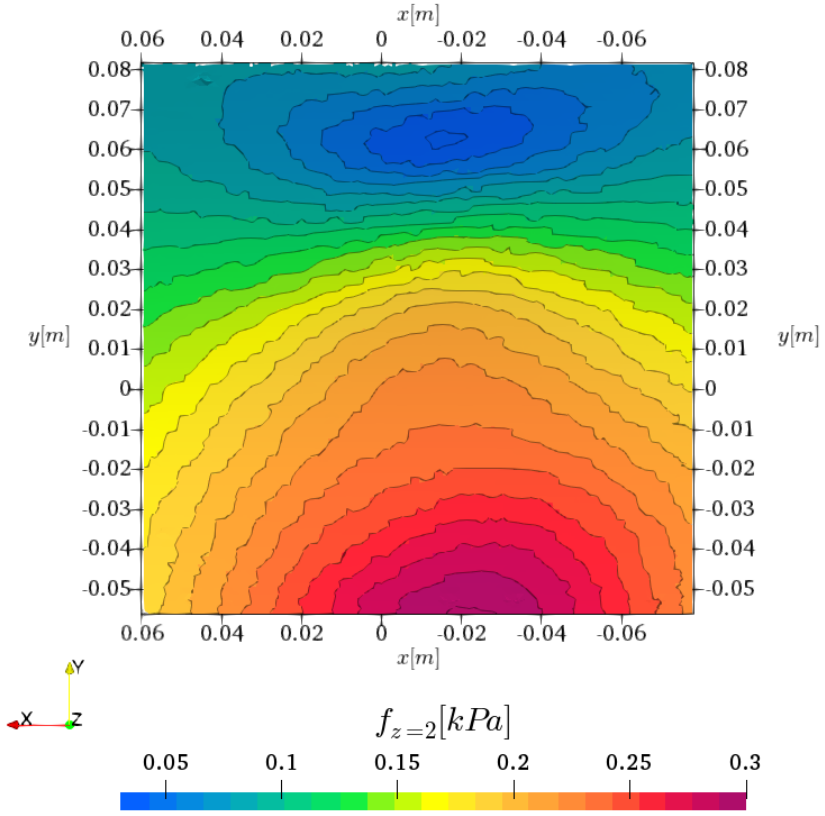

Cavitation Tunnel

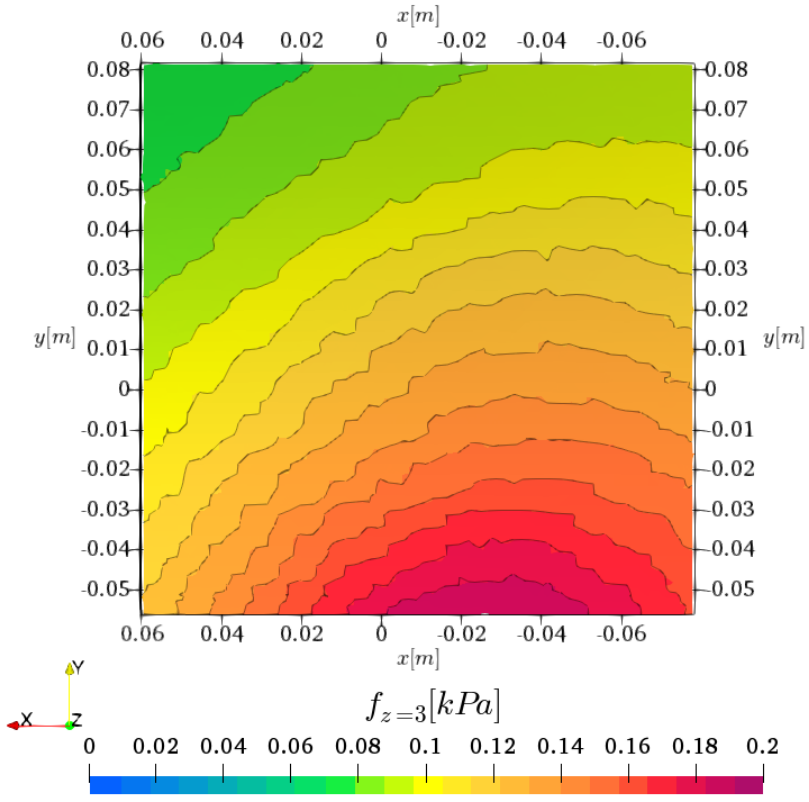

Quasi-Infinite

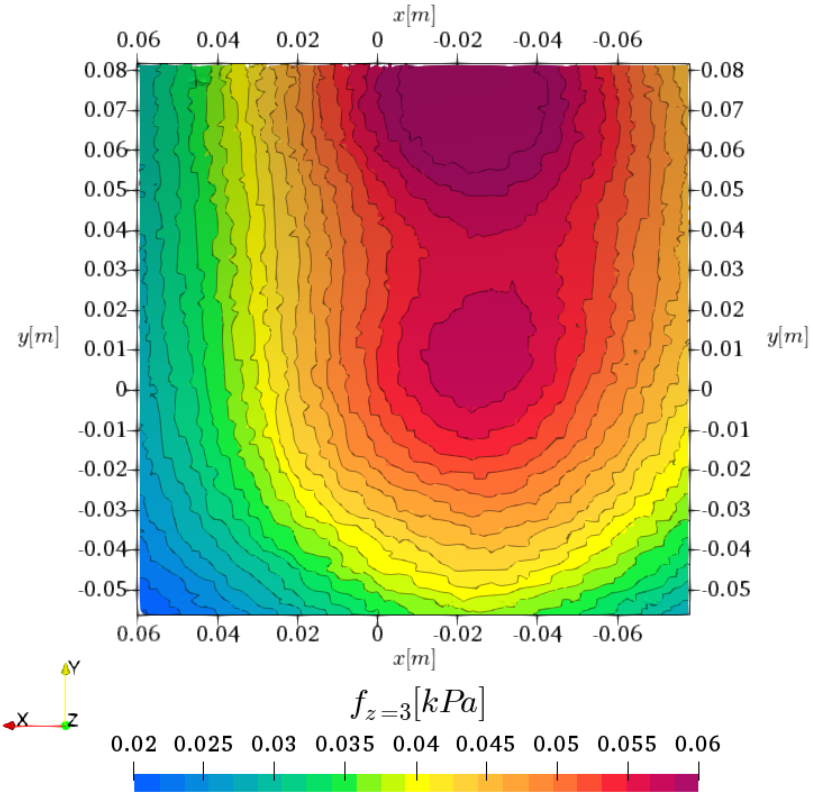

Cavitation Tunnel

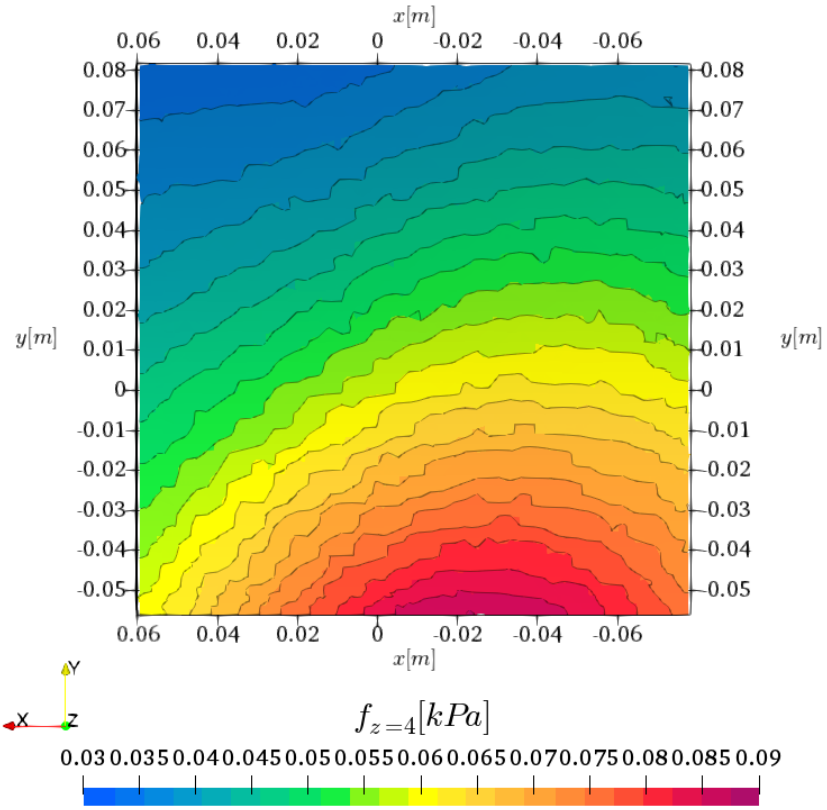

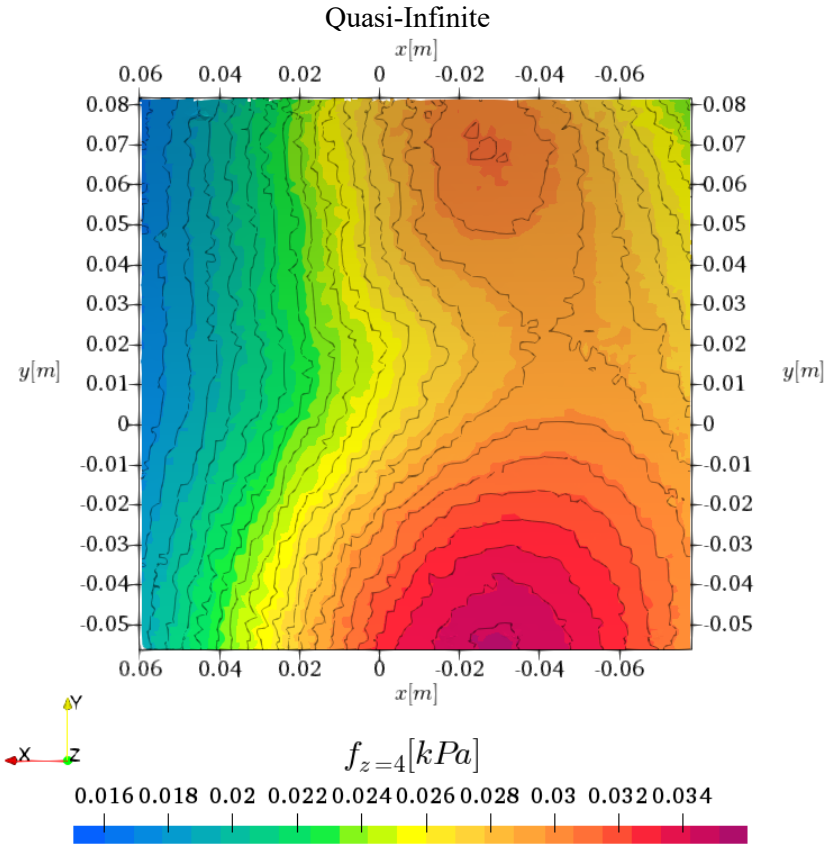

(c) LES with cavitation

Fig. 129: Harmonic frequencies incompressible hull pressure above propeller, comparison of domain extent [91]

Further analysis with POD may be utilized to investigate the hull surface pressure time history data, such as in Fig. 130 for the LES simulation of the ProNoVi reference target case with P3193 in the cavitation tunnel. All modes have been normalized to a value range of $[-1; 1]$ and signs may be reversed arbitrarily. Comparing this with the pressure pulses for the identical case in Fig. 129 (c), reveals that the first and second POD mode are surprisingly similar to the first two harmonics, while the higher POD modes only show a lateral resemblance to the pressure pattern, although the local structural patterns deviate. For this case the POD energy is concentrated in the first mode with a share of $> 95\%$, while the remaining three modes are relatively equal. Comparing this with the spectrum in Fig. 122, where the relationship between the first and the second harmonic is more akin to 15%, the pressure pulses do not share this amplitude relationship even though the pattern of mode 2 is identical to the pressure pattern. A reason for the severe local variations in the higher modes is that the pressure pulses are very low compared to the overall spectrum, thus all frequencies are equally contributing with low values.

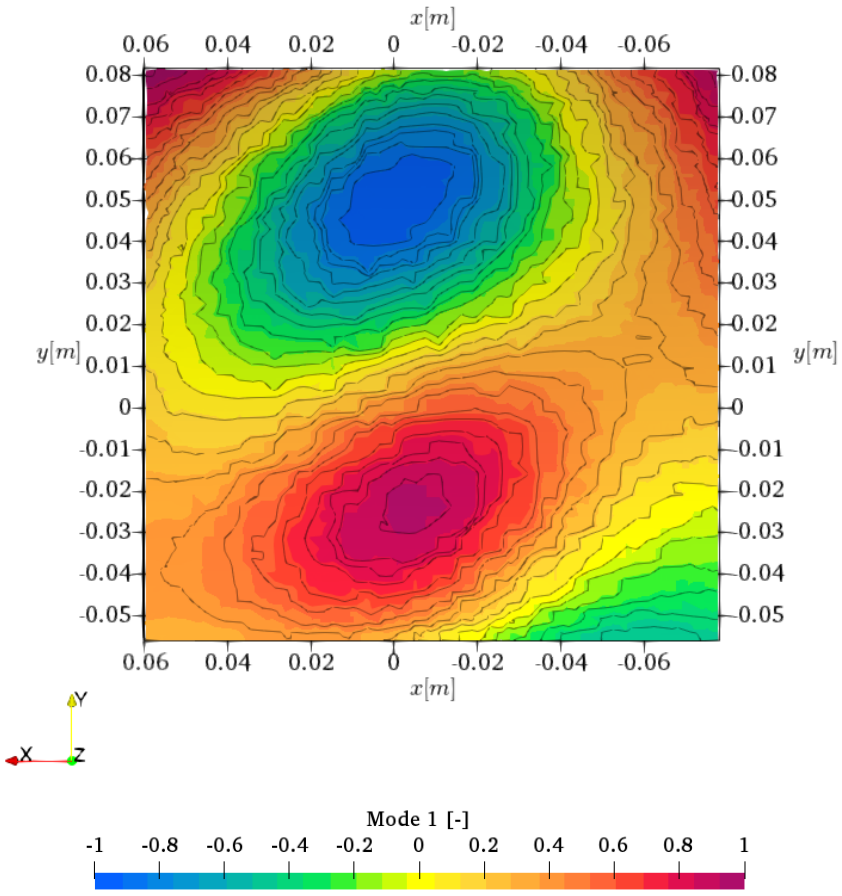
x[m]
0.06 0.04 0.02 0 -0.02 -0.04 -0.06
y[m]
0.08 0.07 0.06 0.05 0.04 0.03 0.02 0.01 0 -0.01 -0.02 -0.03 -0.04 -0.05
Y
X
Z
Mode 1 [-]
-1 -0.8 -0.6 -0.4 -0.2 0 0.2 0.4 0.6 0.8 1

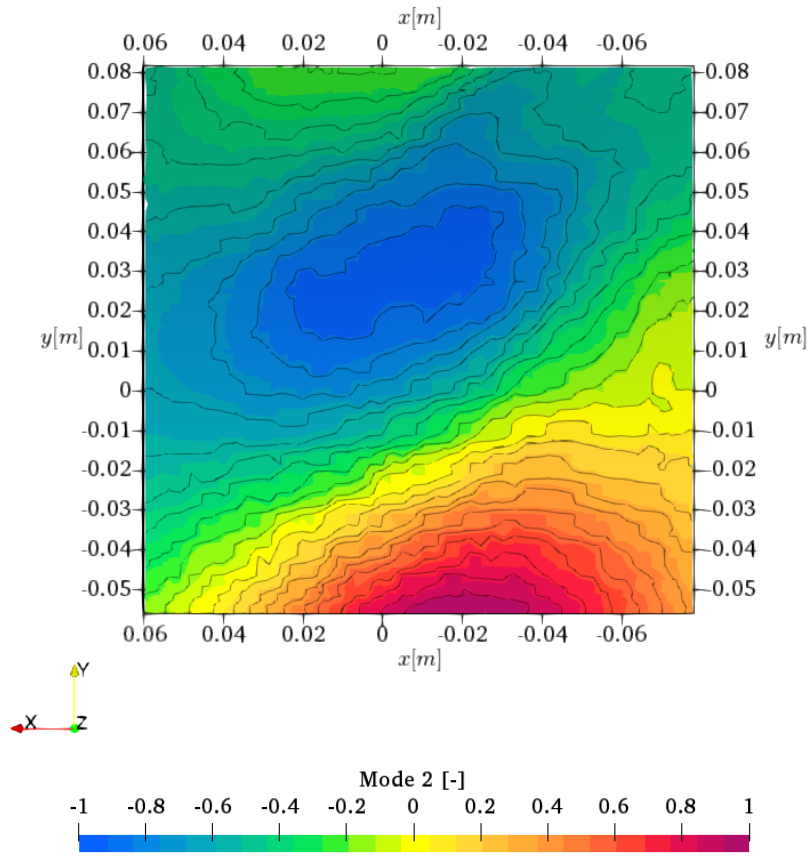
x[m]
0.06 0.04 0.02 0 -0.02 -0.04 -0.06
y[m]
0.08 0.07 0.06 0.05 0.04 0.03 0.02 0.01 0 -0.01 -0.02 -0.03 -0.04 -0.05
Y
X
Z
Mode 2 [-]
-1 -0.8 -0.6 -0.4 -0.2 0 0.2 0.4 0.6 0.8 1

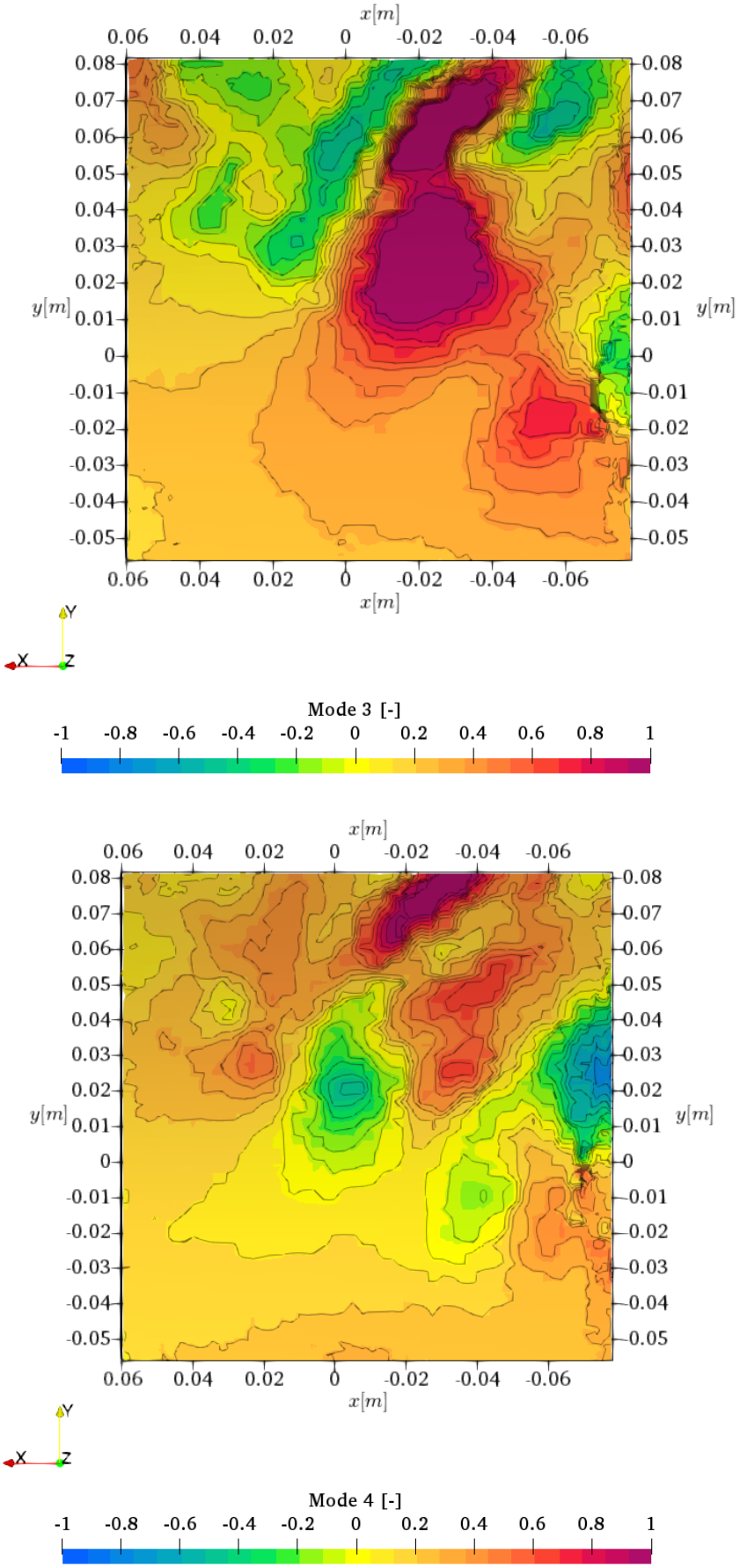

Fig. 130: First four POD modes on hull surface patch [91]

Summarizing, an analysis of the hull surface above the propeller with a very high spatial resolution is necessary to grasp the local distribution of the pressure pulses on the hull, as there may be small localized non-linearities. It is shown, that an acoustically optimized propeller design, such as with tip unloading or tip rake, leads to lower pressure pulses into the hull. Care has to be taken in setting up a domain and in what is to be simulated, as the numerical simulation domain size influences the acoustic pressure considerably. In addition, besides physical quantities, statistical data of the hull may help in identifying acoustic patterns, which is shown here by using the POD.

6.1.3 Full-scale Application

For the SCHOTTEL target case with cavitation and LES, the first four harmonics are listed for all hull observers in Fig. 131. In this case the KFWH consistently yields less acoustic pressure than the FVM pressure probes, however, both agree well with the experiment in the first and third harmonic, whereas the second harmonic is somewhat overpredicted and the fourth harmonic underpredicted. The increase towards the center above the propeller from P7 to P13 with a maximum at P10 is captured very well, as there is less local non-linearities in the cavitation pattern compared to the ProNoVi reference target case. In this case, there is a very good correlation for the spatial variation between FVM and KFWH pressure, with almost identical trends. Thus, for a full-scale simulation very good agreement can be achieved with experimental measurements scaled to full-scale according ITTC.

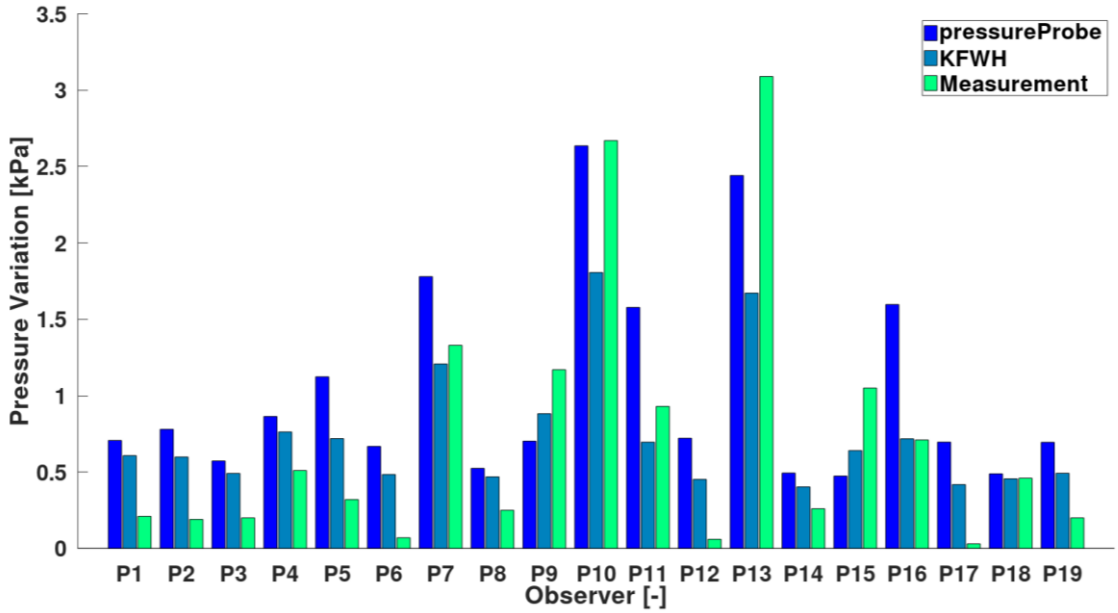

(a) 1. Harmonic

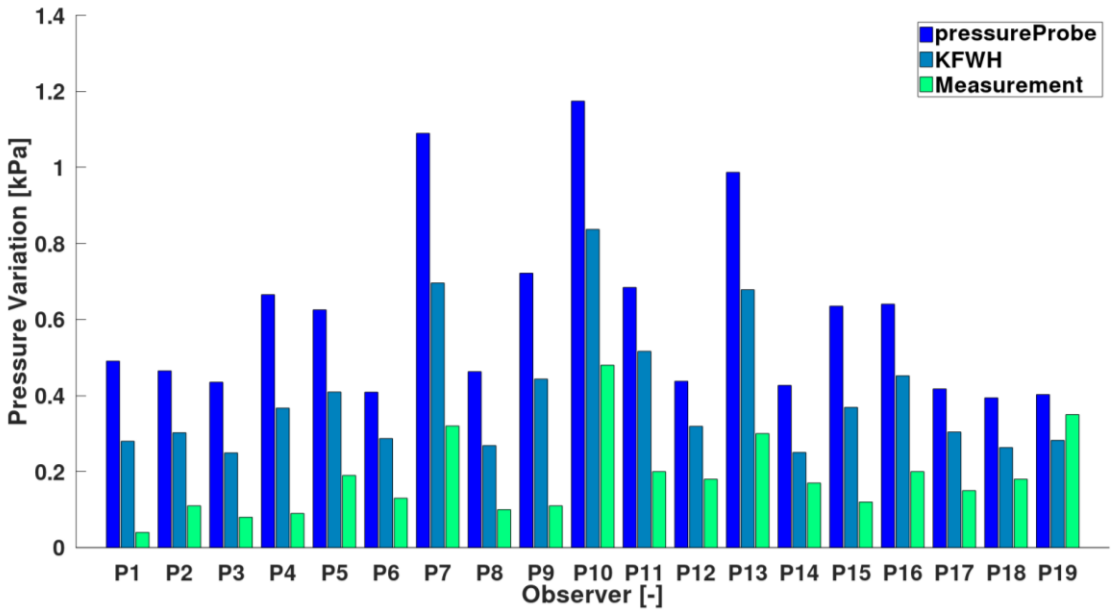

(b) 2. Harmonic

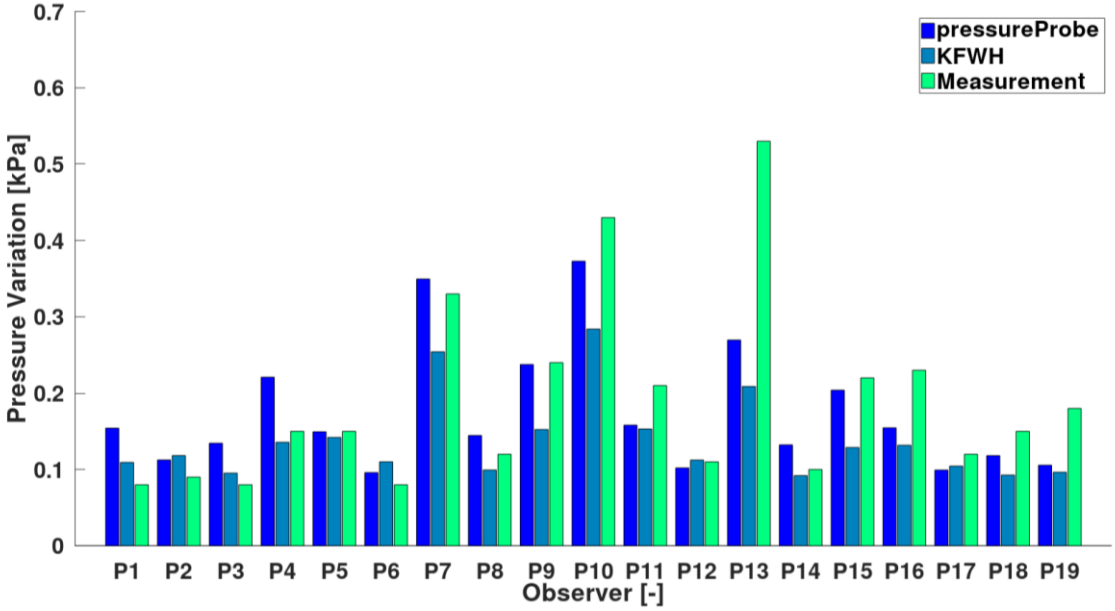

(c) 3. Harmonic

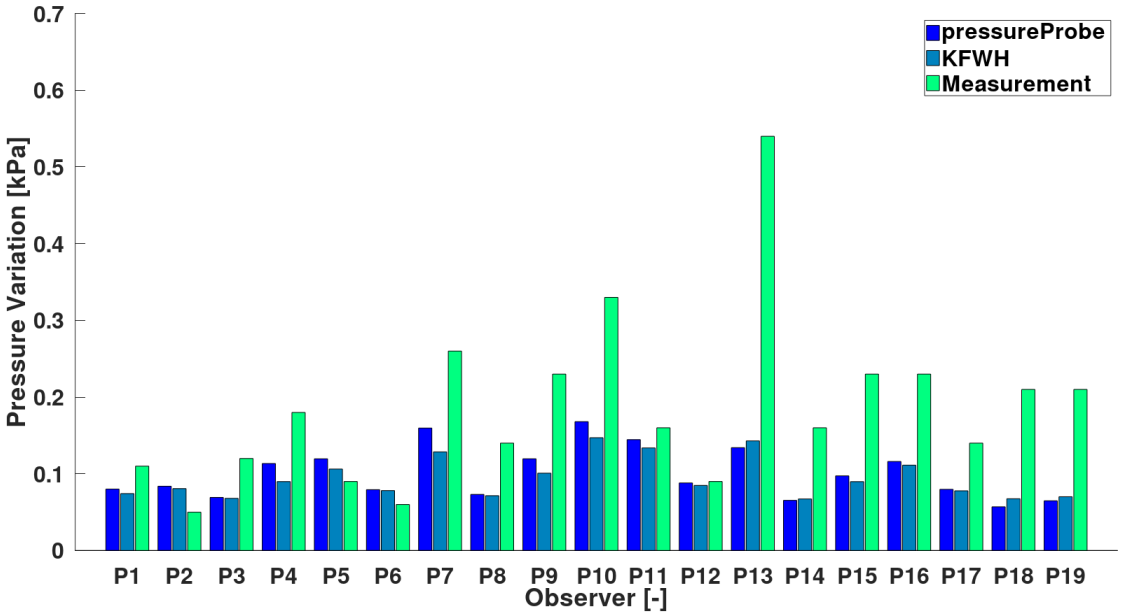

(d) 4. Harmonic

Fig. 131: Comparison of hull pressure with FVM and KFWH to experiment [92]

6.2 Emission into the Fluid Domain

6.2.1 Propeller Open Water

In Fig. 132, the URN signatures for four conditions of the Newcastle propeller test case are given together with the achieved cavitation pattern with the initial mesh and after AMR, as well as a photograph of the cavitation in the model test. With AMR, the case C2 and C6 produce a stable cavitating tip vortex, whereas the cavitating tip vortex diameter is too thin for the selected refinement level of C1, which is one level lower than the other cases. For C3 there are tip vortex cavity filaments and blobs along the helical trajectory, but no connected vortex cavity. In general, there is a very good agreement of the location and morphology of the cavitation regions with the experiment. The URN signature contains the narrowband simulation results from the FVM pressure for the three observers H1-H3 from Fig. 47 as solid colored lines, which are averaged in the references. In addition, the graphs contain the University of Genoa experimental results as a dashed black lines, as the simulation setup is copied from the experimental domain geometry. The acoustic measurements of the exact same case from six different model test facilities are combined in the green area envelope. While this envelope shows rather large differences of up to $20dB$ depending on the frequency, the simulation results are mostly within the limits meaning that the approach is similarly applicable and suitable for the prediction of URN of open water propeller test cases than non-specialized model test facilities with appropriate preparations. Especially at higher frequencies there seems to be a trend in the envelope that is captured well by the simulations. For the propeller blade harmonics on the other hand, only the observer H1 in the simulation, which is furthest away from the propeller blade tip, seems to achieve peak values, which are also visible in the envelope.

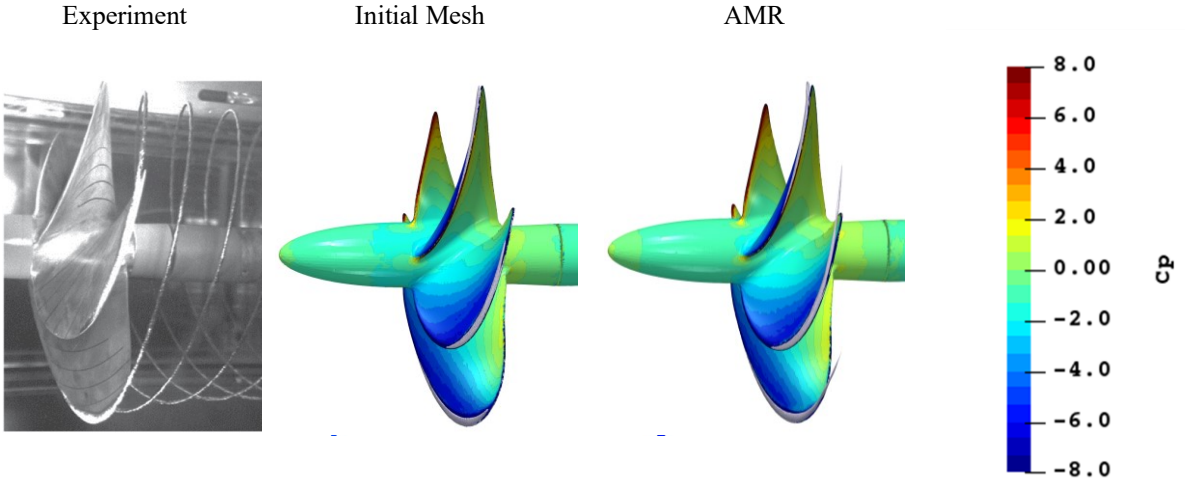

URN Signature

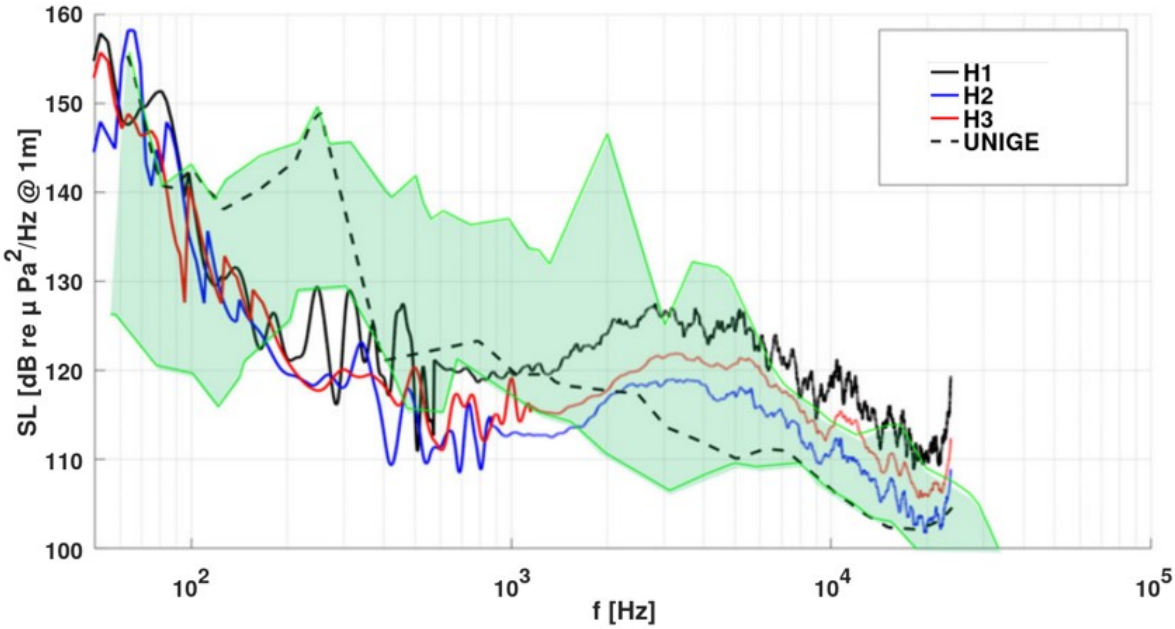

(a) C1

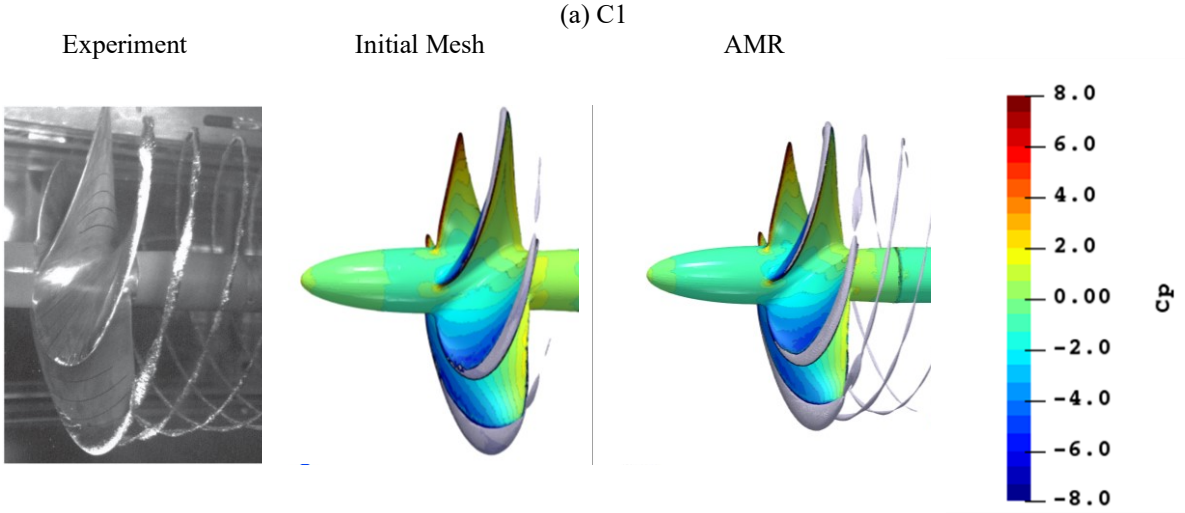

URN Signature

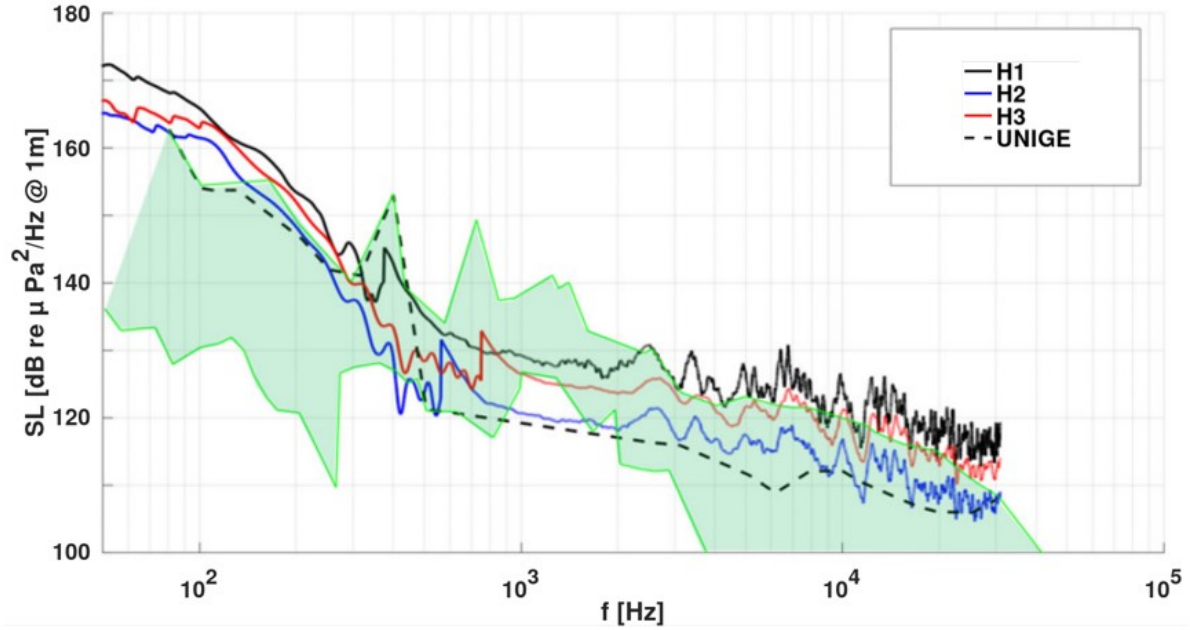

(b) C2

Experiment Initial Mesh AMR

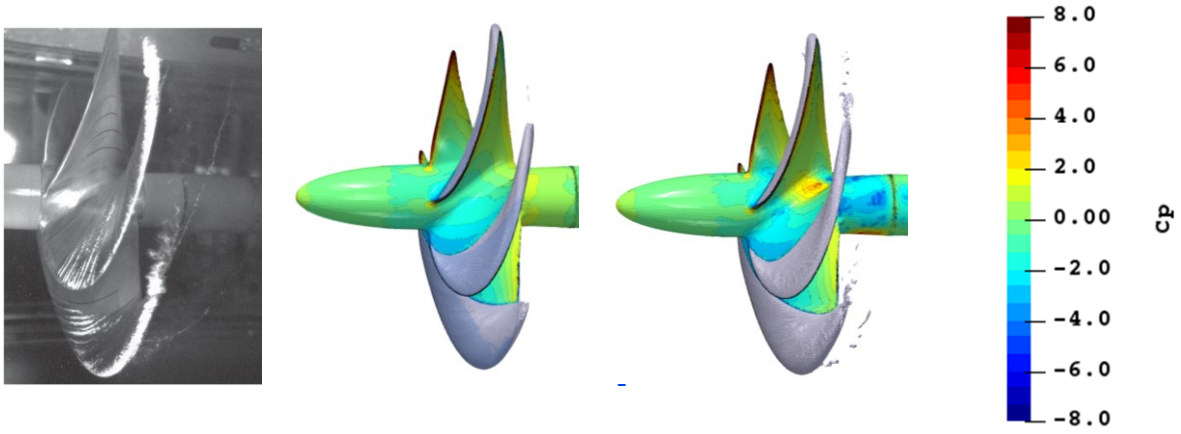

URN Signature

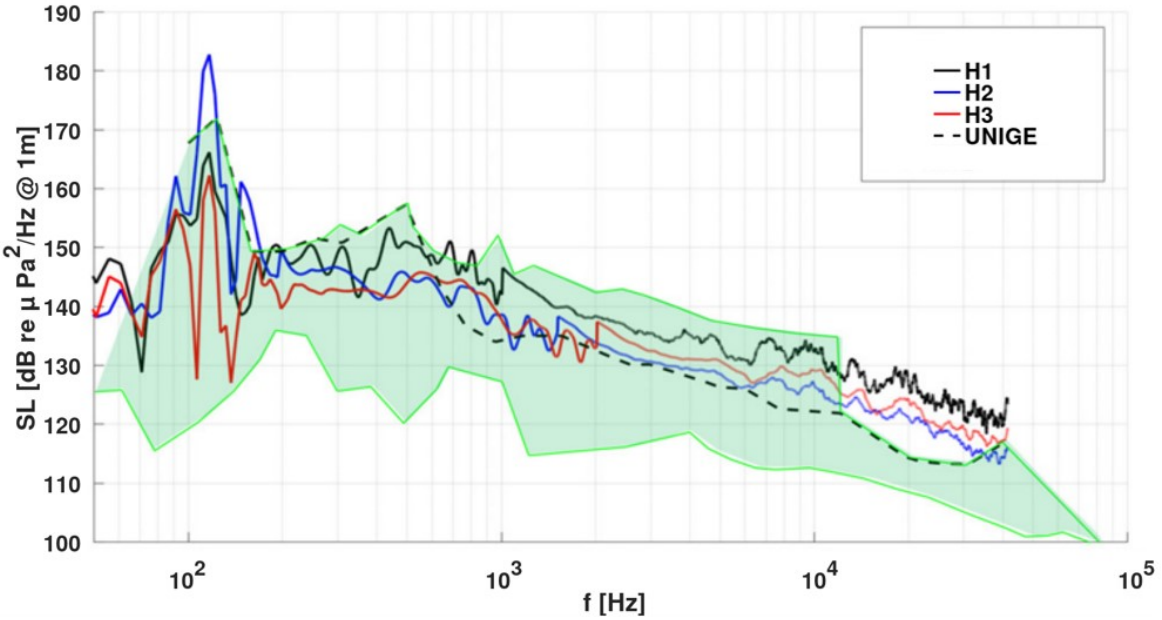

(c) C3

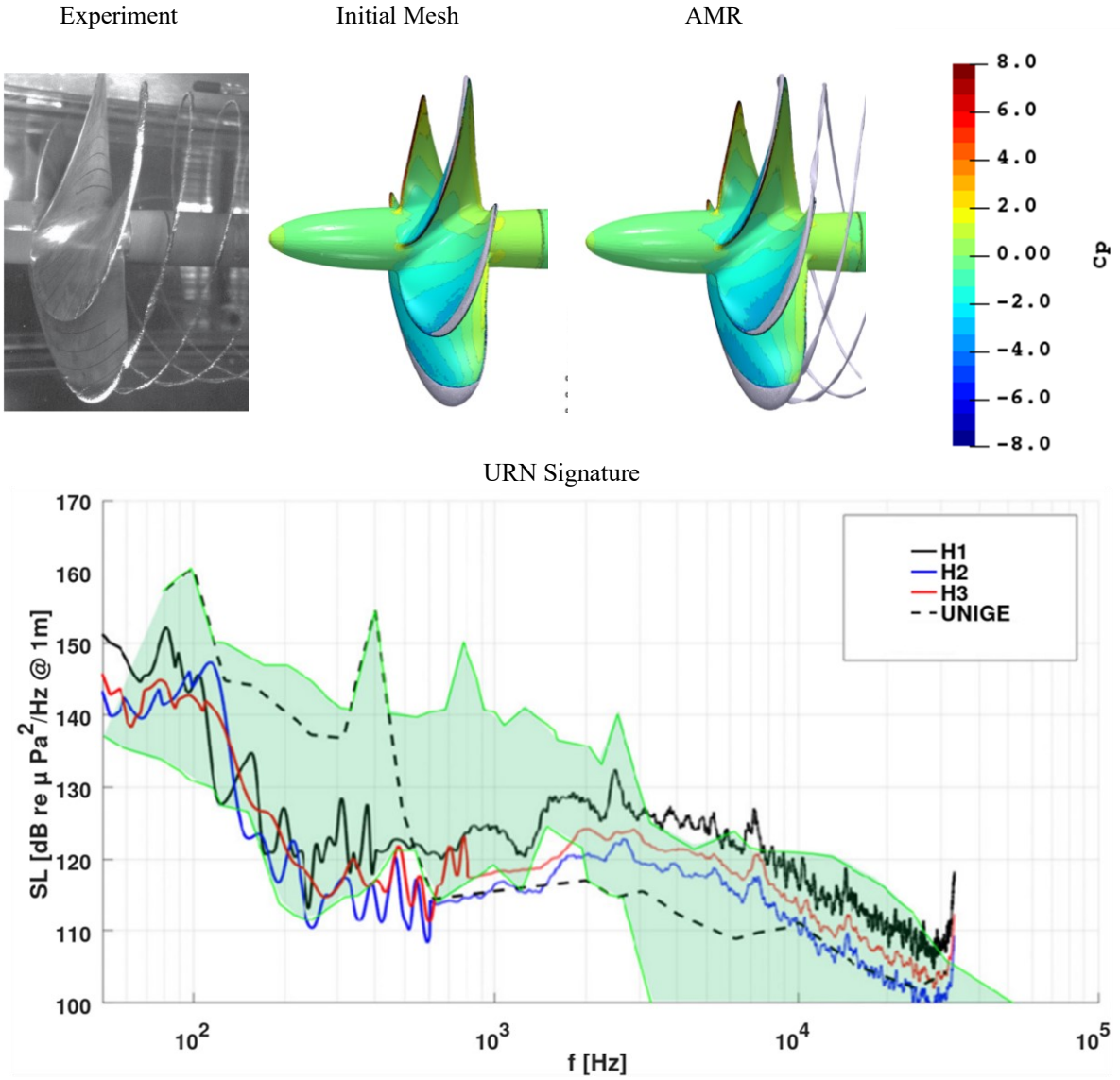

(d) C6

Fig. 132: Comparison experiment with $\alpha_{0.5}$ iso-surface, Newcastle propeller test case [31], [92]

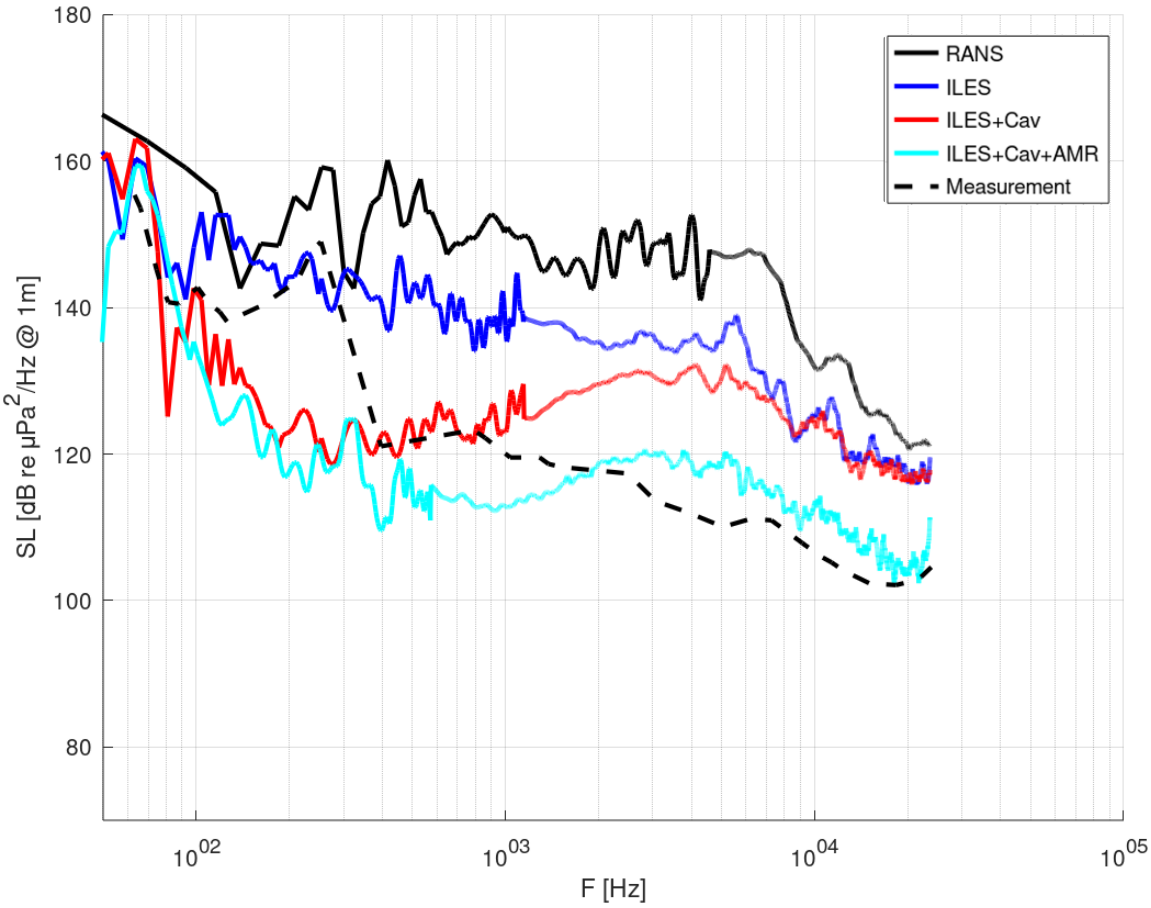

Fig. 133 Comparison of spectral results for applied methods, Newcastle propeller test case C1

Comparing the different simulation stages and thus approaches in physics and turbulence modelling in Fig. 133 for the Newcastle C1 case for the FVM pressure, reveals that there are large differences in the sound levels. Most surprisingly the wetted RANS simulation achieves the highest acoustic pressure closely followed by LES without cavitation with distances of around $20dB$. Once cavitation is activated the sound level is reduced in the mid frequencies, which includes the propeller blade harmonics such as the first harmonic at $f = 175Hz$, while in the high frequency range above $f > 1 \cdot 10^4 Hz$ the activation of cavitation is not affecting the levels. Once the AMR procedure for the tip vortex is activated the high frequency levels drop to the experimentally measured results, which may only be explained by an attenuating effect of the stable cavitating tip vortex, as there is no excitation by upstream variations of the inflow as usually caused by the wake field. However, in the experiment the same levels are reached, where the excitation of the tip vortex may depend on the general tunnel inflow turbulence levels.

For the low frequency range, the KFWH results for the P1595 open water case are given in Fig. 134 for the wetted and cavitating flow with a turbulence modelling and scale resolving approach. Furthermore, the experiment background noise is indicated in black and the experiments measured noise in green. The sound level between experiment and simulation is overall very similar with maximum distance of around $\Delta SL \approx 10dB$, which again strengthens the validity of the approach. However, similar to the Newcastle C1 case the SL of the LES compared to the RANS is lower over a large frequency range above $f > 300Hz$, which is unexpected and may possibly be explained by larger stable cavity regions that dampen the FVM pressure waves that are used to create the KFWH sources on the permeable surface. This explanation is supported by the fact that there is a difference of $\approx 15dB$ between the wetted and cavitating RANS simulation results and almost no change in the SL between these cases for the LES approach. While all simulations capture the first two harmonics, it seems only the LES without cavitation predicts a peak at the third harmonic.

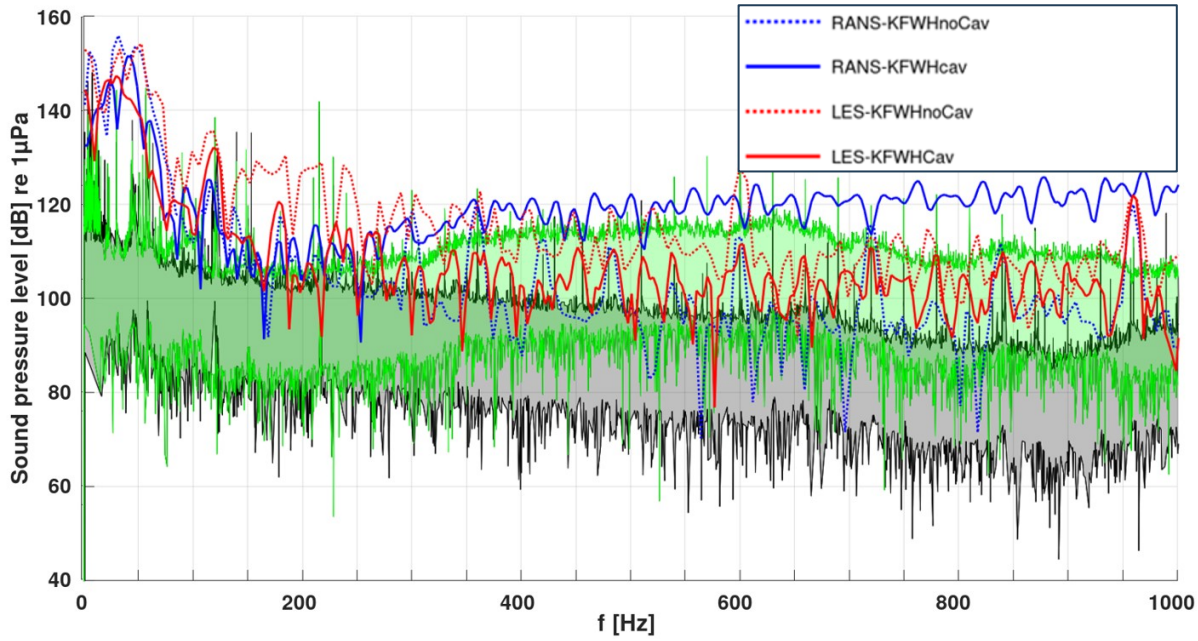

Fig. 134: Comparison of P1595 RANS and LES without and with cavitation [64]

These investigations show that with the established simulation approach the acoustic emissions of an open water propeller test case are captured accurately within the margins of reproducibility of model test acoustic measurements. However, cavitation modelling and resolving the turbulence is required, to achieve a realistic prediction of URN signatures over all frequencies with FVM simulations.

6.2.2 Propulsor-Hull Configurations

The Fig. 135 shows the URN signature obtained with the KFWH method normalized to $1Hz$ for the P1595 propeller in open water and behind hull condition without and with rudder for the same rotation rate of $n = 30Hz$ and with the blade harmonics indicated with vertical dashed lines in magenta. The simulation results with the circular markings are achieved with RANS turbulence modelling and activated cavitation. Above $f > 20Hz$ the simulation and experiment deviate strongly from the experiments being around $30dB$ lower in RNL, which could indicate a strong background noise in the experiments caused by different inflow turbulence. In this case the higher frequencies would not be excited in the simulation due to a lack of high frequency turbulent fluctuations at the propeller. Comparing the different simulation results and experimental results respectively there is surprisingly little difference between the configurations, with maximum deviations of around $RNL < 5dB$. Even though the simulations underpredict the experiments severely, this trend is captured by the simulations very well.

Considering the first harmonic frequency in narrowband (NB), it is clear that between each case is about $\Delta RNL \approx 15dB$ difference with the open water being the least high, followed by the behind hull condition and the case with rudder. Similar trends appear for the higher frequencies, however, the case without rudder achieves higher RNL at the second frequency. Interestingly, the open water case produces higher RNL between the blade passing frequencies and lower values at the higher harmonics than the other cases, which may be explained by better resolution of the propeller slipstream due to larger axial extent of the rotating mesh region.

In Fig. 135 all cases show the blade passing frequencies in narrowband, however, only the case with rudder seems to show characteristic peaks in 1/3 octave frequency bands as for the other cases secondary noise masks these peaks. Only in the narrowband the validity of the simulation results may therefore be approved as the harmonics are consistently apparent for all cases.

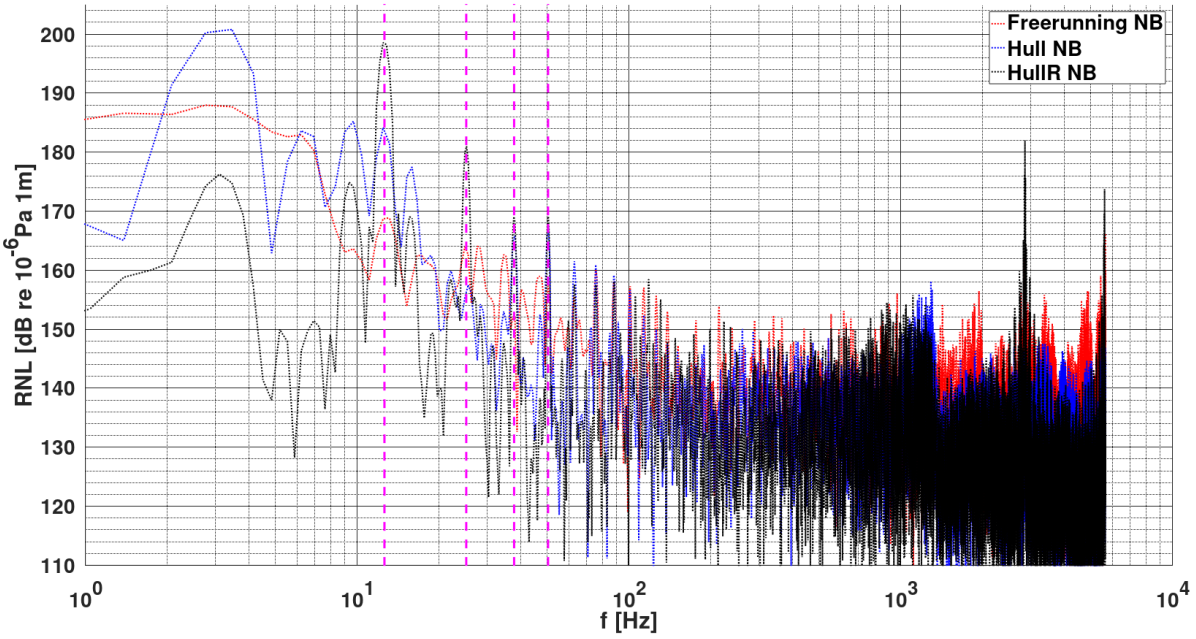

(a) Narrowband representation

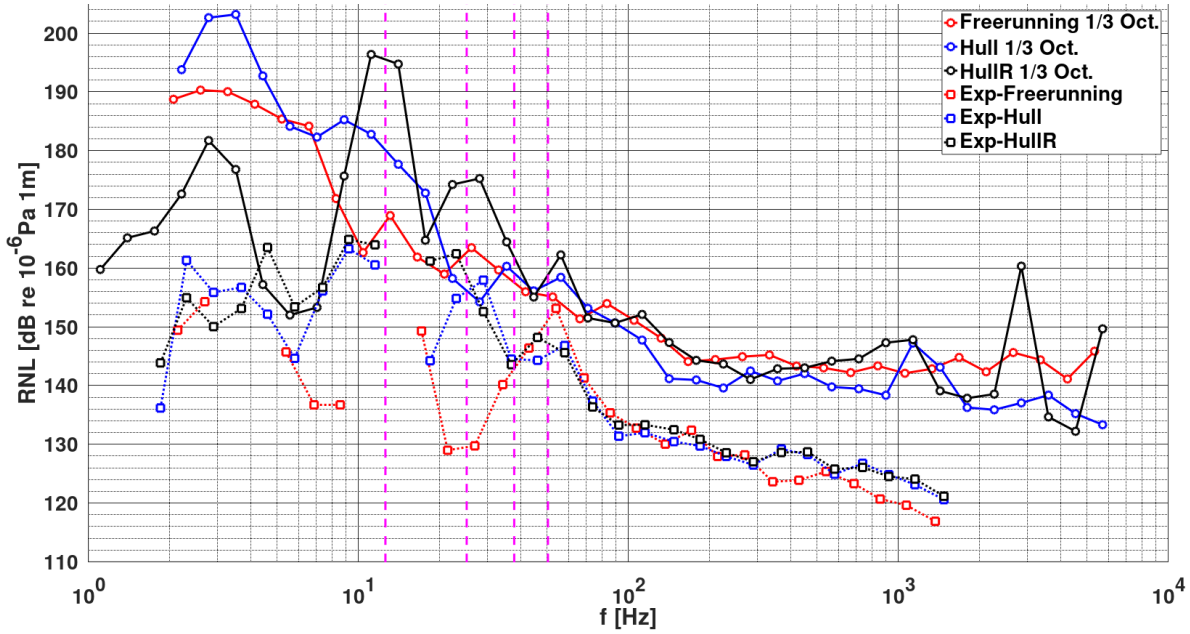

(b) 1/3 Octave band representation

Fig. 135: P1595 open water vs. behind hull [80]

For the P1595 and P3193 propeller in behind hull condition, the difference of the RNL normalized to $1Hz$ in Fig. 136 indicates similar findings than the investigation of the pressure pulses on the hull. The P1595, which is considered to be the unoptimized and louder propeller, creates higher noise levels over the complete frequency range for the simulation including the propeller blade frequencies. This is in agreement with the experimental results up to a frequency of $f \approx 70Hz$ or the fourth blade harmonic after which the trend reverses in the experiment with the P3193 reaching up to $10dB$ higher noise levels. In this case the trends of experiment and simulation between $100Hz < f < 1 \cdot 10^3 Hz$ are also reversed.

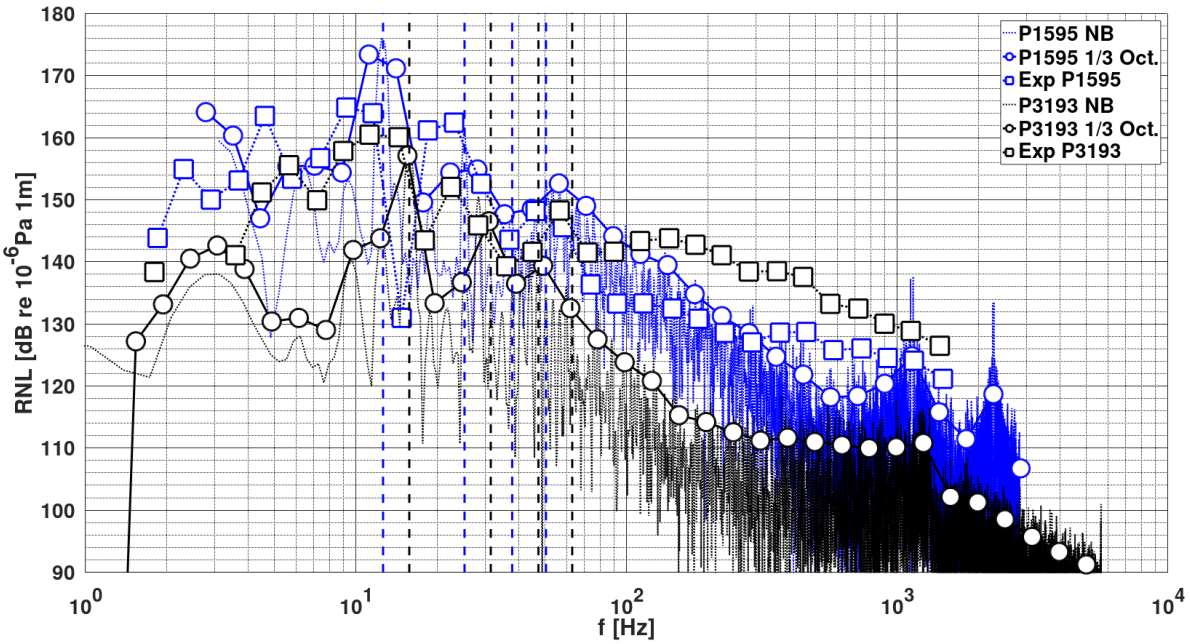

Fig. 136: RNL comparison between propeller designs, respective harmonics indicated by dashed vertical lines [80]

For the cavitation tunnel domain and the quasi-infinite domain from Fig. 53 (a) there appears to be a constant shift of about $\approx 15dB$ in the RNL in Fig. 137. At higher frequencies $f > 800Hz$ the trend flattens for the quasi-infinite domain and the similarity in the frequency distribution is lost. While both simulation results achieve a clear prediction of the blade passing frequency peaks, especially for the narrowband representation, there is a large distance to the experimental results, with unknown source. The implications of these findings are important, as simulation domains are frequently approximated with quasi-infinite extent to avoid pressure reflections at walls or inlet and outlet. However, these effects may be solver specific and can be mitigated by implementation of a numerical beach that dissipates unphysical reflections at inlet and outlet, whereas physical wall reflections appear in the experiment and require more investigations.

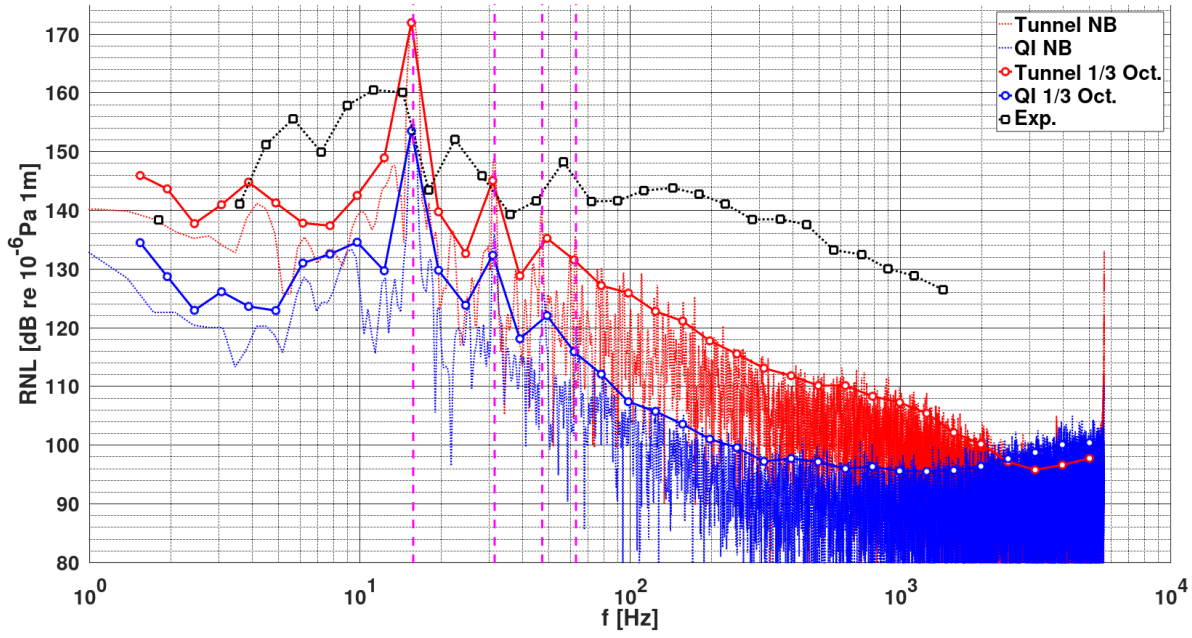

Fig. 137: RNL for P3193 cavitation tunnel vs. quasi-infinite domain [80]

At an arbitrary timestep in the simulation, the pressure distribution is plotted onto the cylindrical surface identical to the stationary KFWH surface in Fig. 138 (a) for the ProNoVi reference target case with rudder. The upstream induced under pressure by the five blades and the over pressure in the inter-blade space is visible on the surface. A magenta intersection line is drawn horizontally along the cylinder, which is used to sample the pressure over the acoustic evaluation period of the simulation time. In (b) the pressure along this line over the simulation time in 1° steps along the angular position is given, where 0° is the direction of travel along the shaft line. Low pressure regions appear upstream of the blades and in the hub vortex at 180°, while the sides between 80°-175° seem to show relatively low pressure fluctuations. Upstream of the blades the passing of the blades is noticeable by the regular high pressure peaks. It is not entirely clear why these pressure peaks seem to vary between inward and outward side over the evaluation period. However, some of these effects may be attributed to low frequency pressure fluctuations caused by the vessel wake, or pressure reflections of the numerical domain. Thus this representation may possibly be utilized to assess acoustic convergence under consideration of all emission directions.

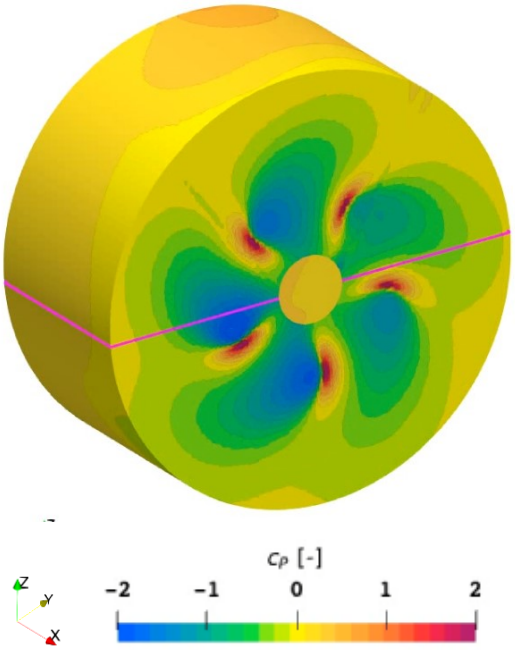

(a) Instantaneous pressure and sampling intersection

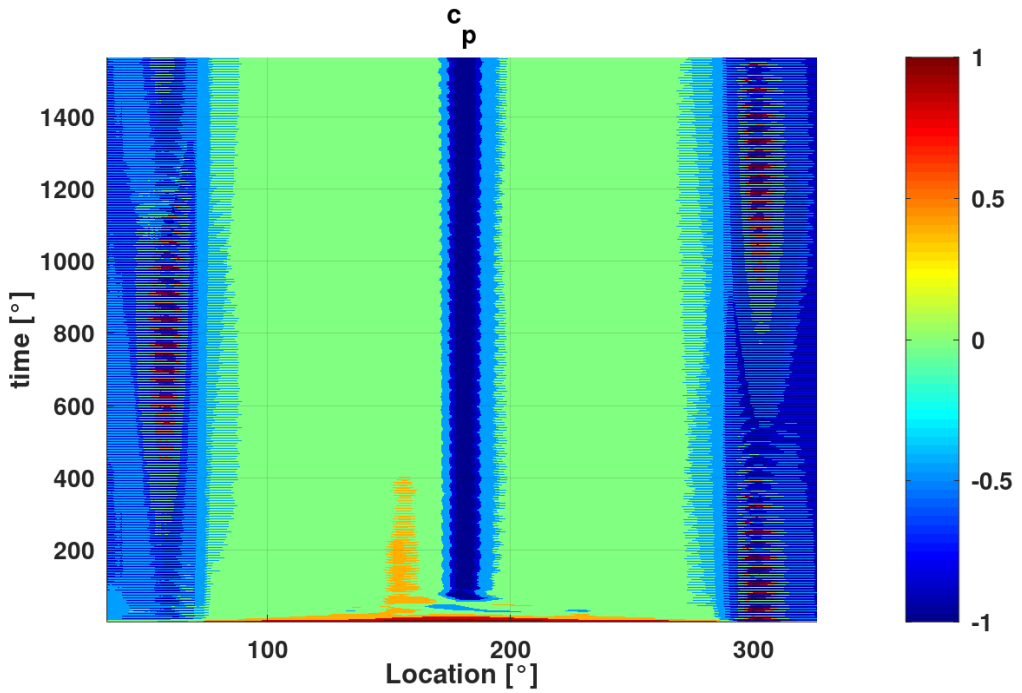

(b) Time evolution of pressure on intersection

Fig. 138: Pressure distribution on KFWH surface

The first three harmonic frequency pressure distributions and the POD modes are illustrated on the same passive surface in Fig. 139, where distinct shapes form. For the harmonics, which are scaled to full scale, large difference in the pressure levels exist, so logarithmic colormaps are used for some illustrations. While the upstream surface of the cylinder is dominated by the induced pressure, there are specific shapes visible, for instance in (a) on the downstream base of the cylinder the pressure at $r/R \approx 1.0$ is larger on the outward direction than on the inward direction, which can be attributed to the upstream wake field generated by the shaft brackets and possibly some upstream influence of the rudder. Another example is the increased pressure towards the top direction and the lateral directions for the second harmonic in (c) on the cylinder outer surface or the influence of single blades at specific positions for the third harmonic in (e) on both the upstream and downstream bases of the cylinder. For the POD modes on the other hand the difference between modes is minute, with only more shapes associated with the rotating propeller showing up with increasing mode number, which, similar to the observation on the hull, means this evaluation method is rather robust.

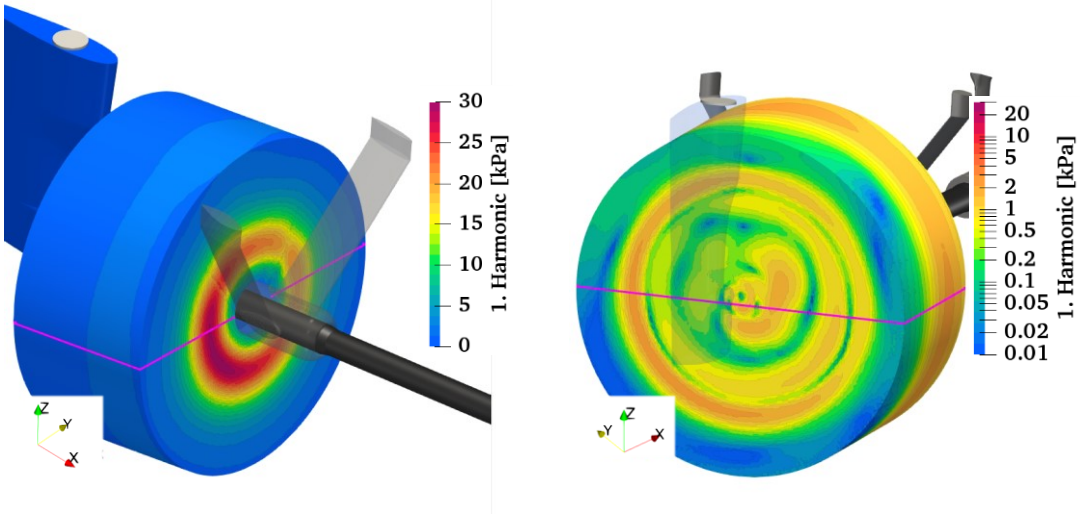

(a) 1. Harmonic on AMI

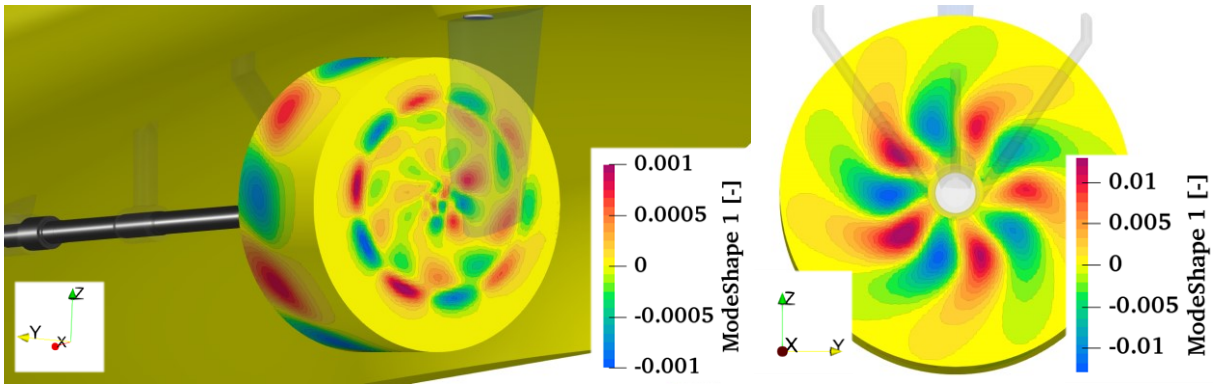

(b) POD mode 1 on AMI

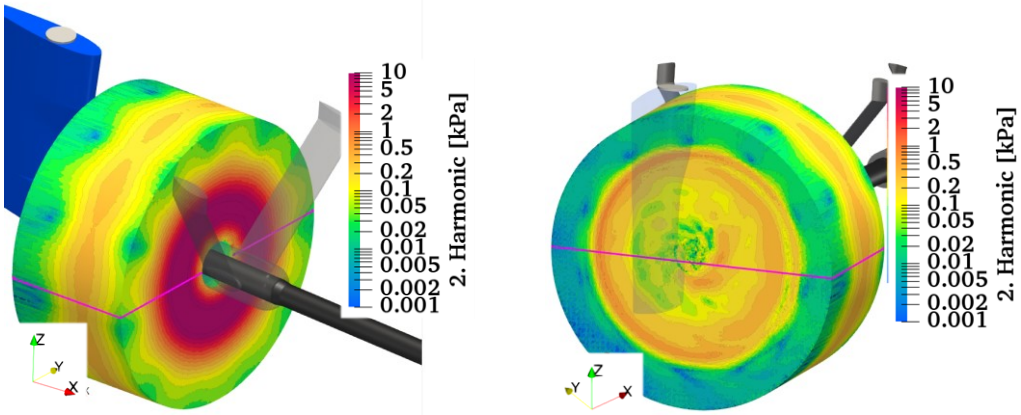

(c) 2. Harmonic on AMI

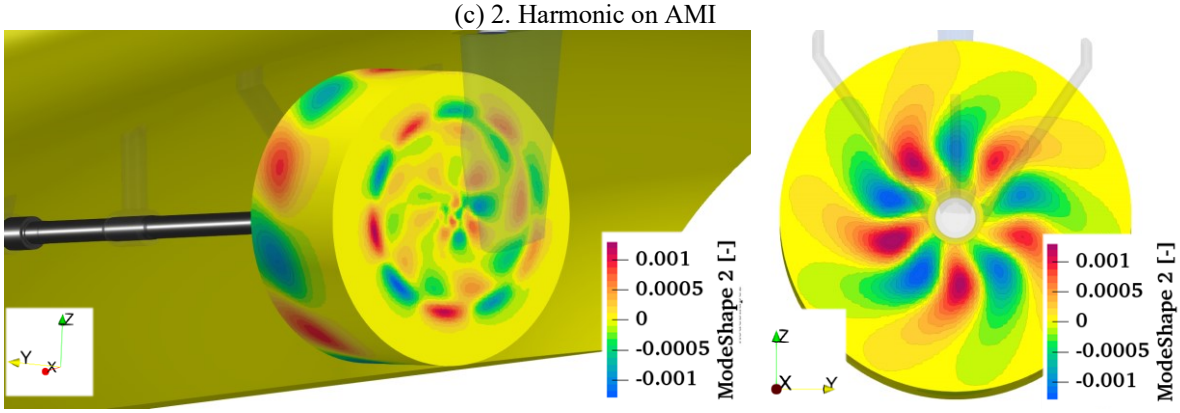

(d) POD mode 2 on AMI

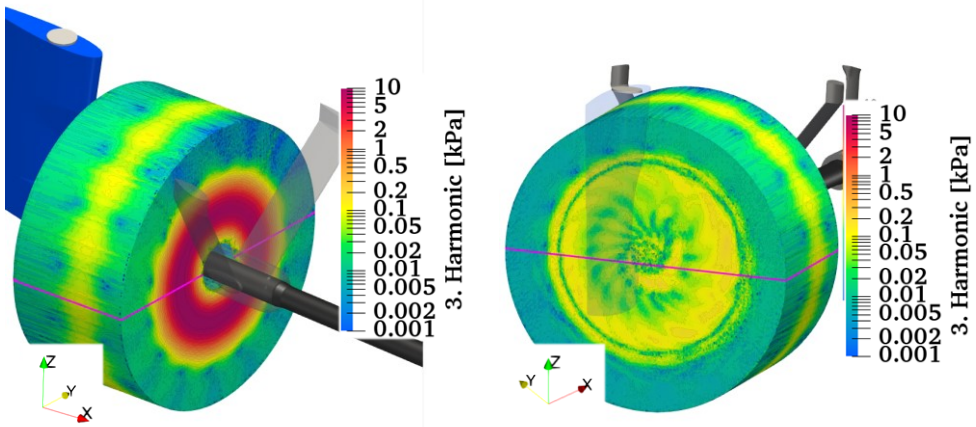

(e) 3. Harmonic on AMI

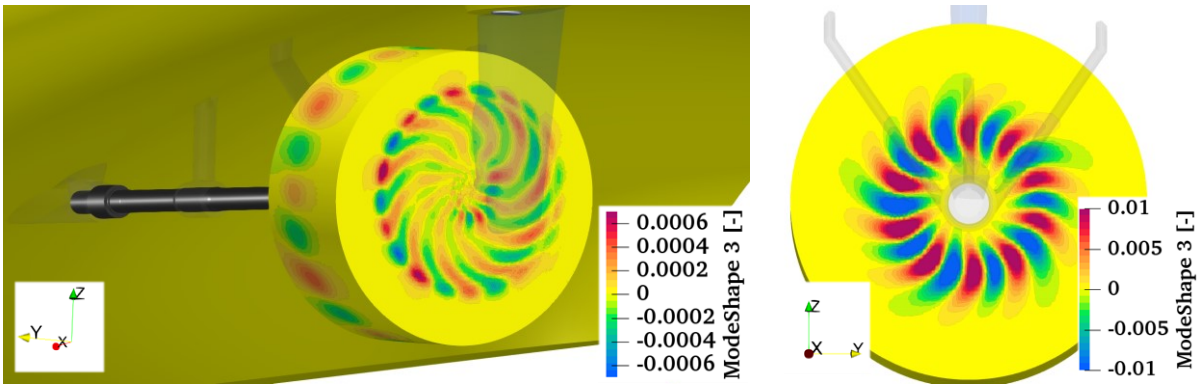

(f) POD mode 3 on AMI

Fig. 139: Pressure and POD modes on the passive KFWH surface

The angular pressure distribution along the horizontal sampling intersection line for the harmonics is given in Fig. 140 (a) and normalized directionally to a reference distance of $r = 1m$ in (b). As the KFWH surface in model scale is generally closer than the reference distance, the harmonic data is reduced in amplitude. The directions close to the passing blades upstream at 60° and 300° specifically feature large pressure fluctuations, as well as the lateral directions, where the blade tips are passing at 90° and 270°. Between 330° and 30° is the shaft line and thus no data available for the intersection. Aft wards between 140 and 220° there are various angular fluctuations caused by the turbulent slipstream, which apparently have an influence on the first three harmonic frequency signals.

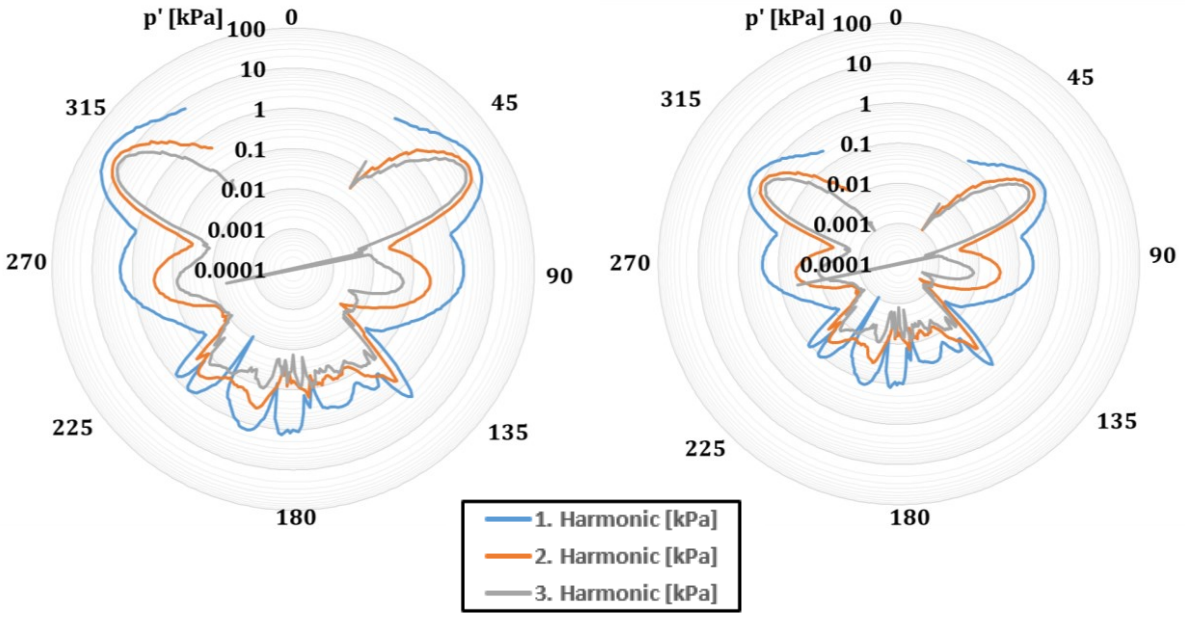

(a) Values on KFWH surface (b) Normalized to $r = 1m$

Fig. 140: Directivity of acoustic emissions at first three blade harmonic frequencies

Of course other intersections of this surface may be selected to obtain information about emissions in any direction such as downwards of the ship and towards the hull as indicated in Fig. 141 (a) and normalized to $r = 1m$ in (b). As the KFWH surface is close to the propeller, the influence of the hull is not very noticeable with the emissions almost symmetrical to the horizontal axis. However, in the propeller slipstream some directivity is evident, which must be caused by the rudder blocking half of the propeller jet vertically and possibly by increased inflow speed into the propeller plane for the lower part of the wake field.

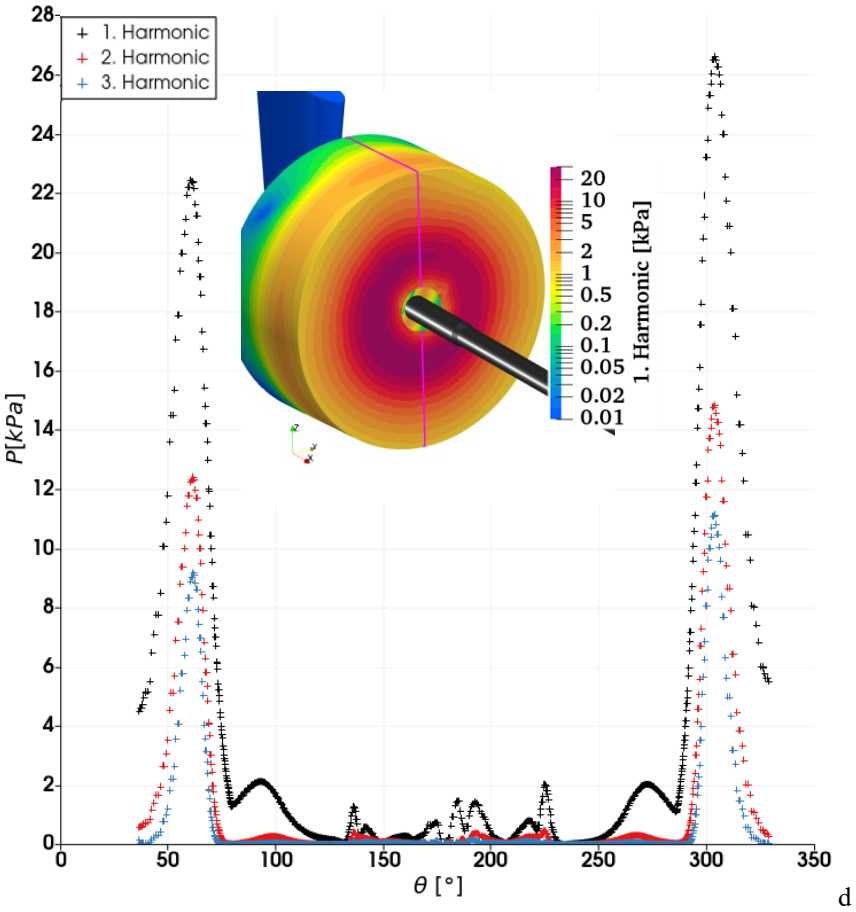

(a) Vertical intersection of control surface

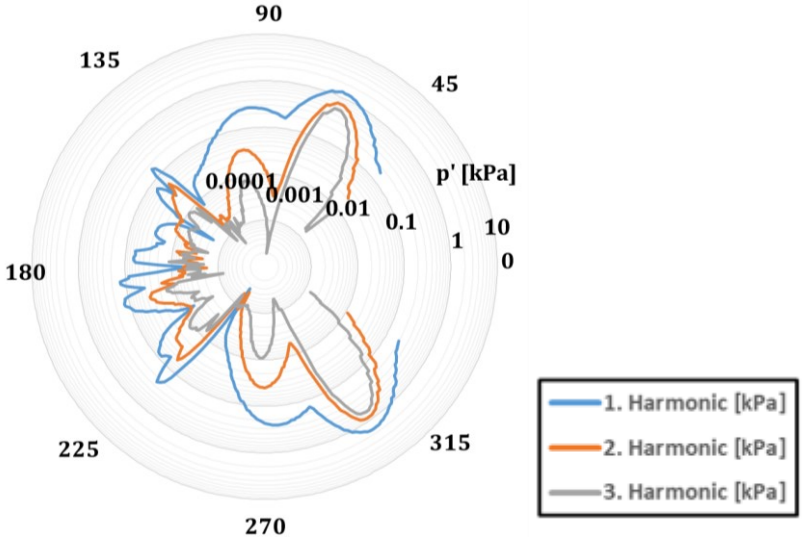

(b) Polar plot

Fig. 141: Pressure fluctuations along the vertical axis

In a more systematic approach, a passive spherical surface, that requires equal normalization in all directions may be used for the propeller and to include the influence of the vessel, a passive box shape spans the complete half-ship in the simulation. Even though a sphere would be advantageous for normalization purposes, this cannot be realized for the vessel, as a sphere with the origin at the propeller and a radius extending up to the bow would in case of the cavitation tunnel intersect the tunnel walls and in the quasi-infinite domain reach extremely coarse regions of the mesh, so that an interpolation onto the surface would be prone to large errors. For this investigation the spherical coordinate system

defined in Fig. 142 with the origin at the intersection of the propeller plane and the rotational axis is applied to the results summarized in Fig. 143.

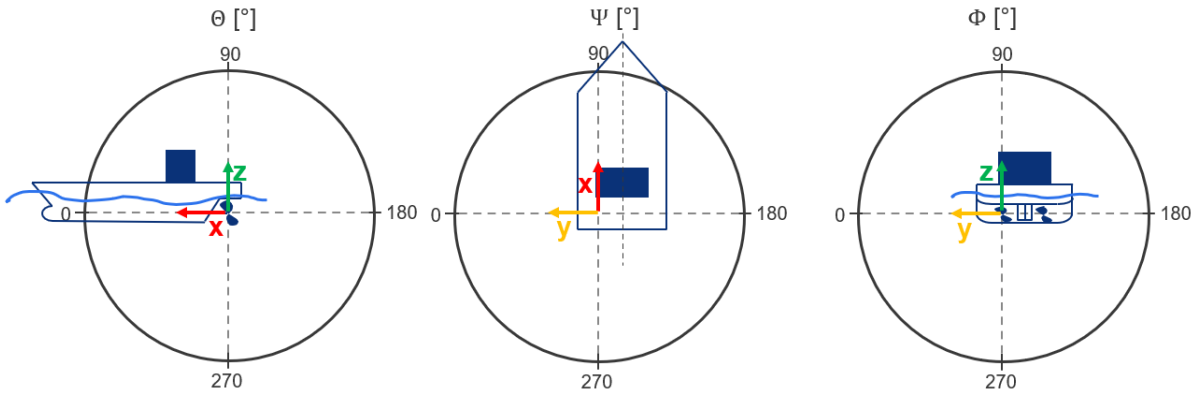

Fig. 142: Definition of the spherical coordinate system for the directivity investigation [91]

In (a) the instantaneous pressure distribution on a sphere at an arbitrary simulation timestep is given with three intersections highlighted in respective colors and plotted along the spherical axes. As mentioned before, there seems to be a lateral difference caused by the downstream rudder or the inflow variation from the shaft brackets. The intersections of the tip vortex at the outer radii and the hub vortex in the center with the sphere are apparent. Overall the pressure is larger downstream of the propeller, which is expected. As this is only a snapshot of the overall pressure, this representation does not indicate the strength of acoustic emissions, which requires a representation of the pressure fluctuations instead. For the box spanning the complete configuration the same results are given in (b). Here the high pressure region just behind the propeller plane especially in downwards direction is striking. Furthermore, the low pressure region behind the transom is noticeable, which is an indication that the wave pattern is required for accurate predictions, as the flat cavitation tunnel top surface causes this unphysical pressure region.

The fluctuations normalized to the reference distance of $r = 1m$ are given for the sphere around the propeller in (c) and the complete configuration in (d). For the case with rudder used for this evaluation the sphere is intersected by the rudder, which explains the large section without data in the downstream direction. Also the sphere intersects the hull, as the radius has to be larger than the largest distance between the origin and the sliding mesh interface, which leads to the empty section above the propeller. For the vertical intersection along Θ dimension, clear preferences of direction are visible for both propeller and the full configuration towards the front, which are also seen in the horizontal or parallel to waterline intersection along Ψ. For the framewise intersection along Φ the directivity of the emission is rather low. For this intersection the case for the full configuration is mirrored, leading to some skewed results, as the origin is not at the ship centerline, but the propeller included in the domain.

A comparison of the emission for the cylindrical surface in Fig. 140 (b) and the emission characteristics in Fig. 143 (c) along the Ψ axis, reveals that the choice of the passive surface has a large influence on the acoustic emissions. For the cylinder, the edges where the bases meet the outer surface are clearly visible in the plot with reduction of the pressure fluctuations due to larger distance, which do not appear for the sphere, where the distance between source and evaluation surface is constant. This effect also affects the emitted sound obtained with the KFWH method. Similar effects are observed for the Θ dimension by comparing with Fig. 141 (b).

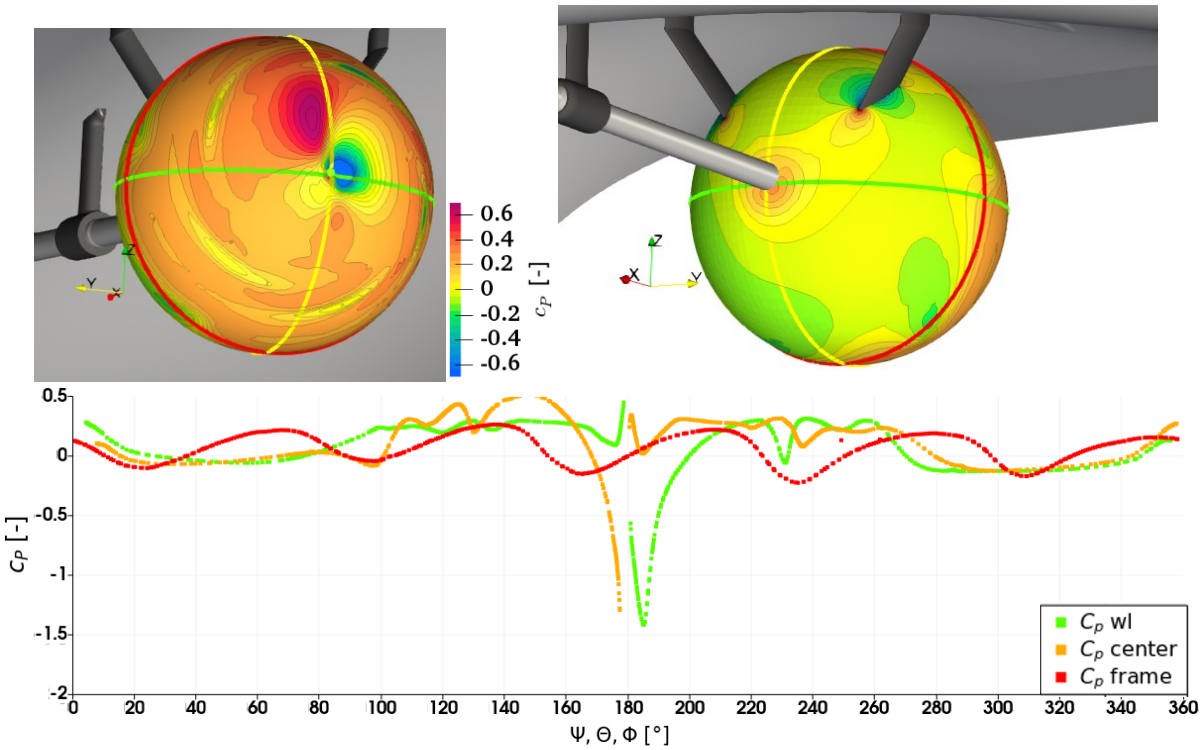

(a) Pressure on passive surface around propeller

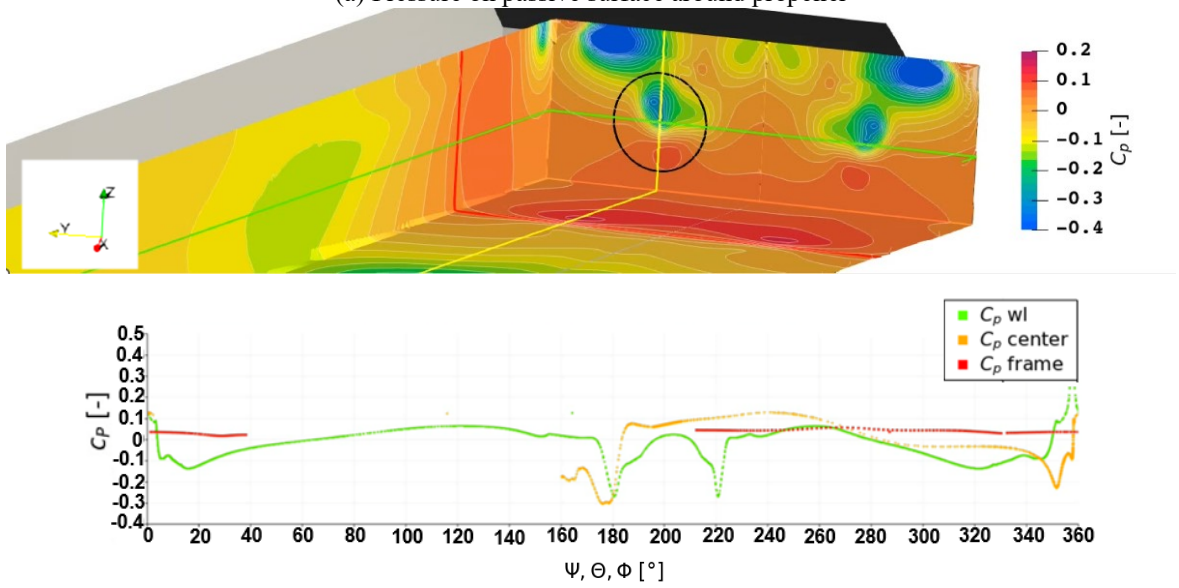

(b) Pressure on passive surface around propeller-hull combination

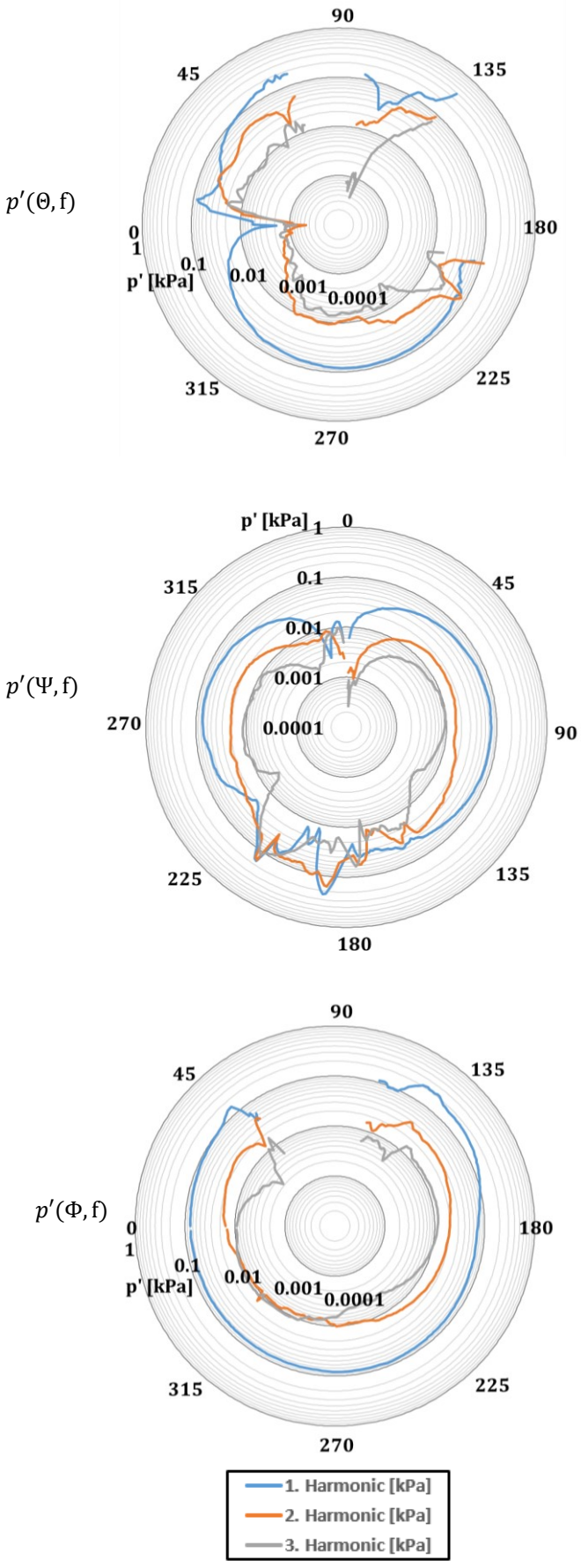

(c) Propeller emission

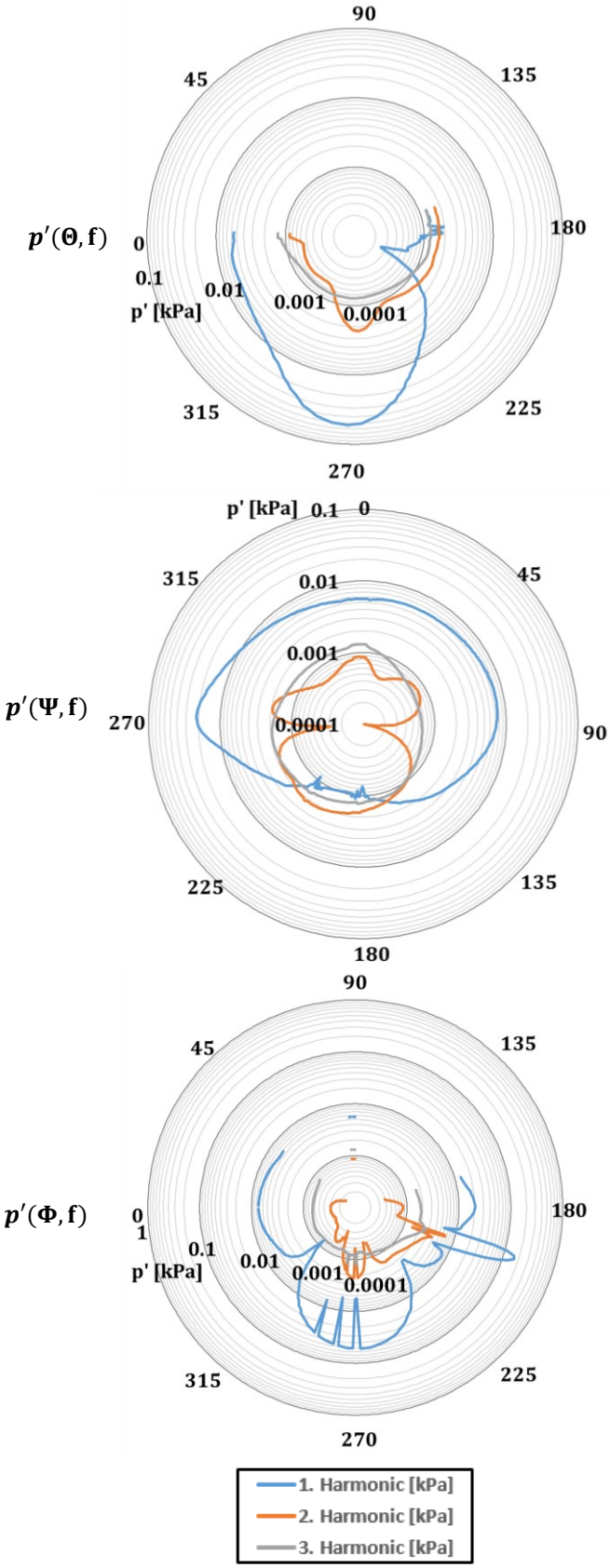

(d) Propeller-hull combination emission

Fig. 143 Directivity of harmonic frequencies on passive surfaces [91]

To conclude the investigations with the propulsor-hull combinations, there is a noticeable difference in the URN signature at the lower frequencies between the open water propeller and the same propeller in

behind hull condition, while the influence in higher frequencies is rather low. It is expected that this behavior is highly dependent on propeller and hull design. In general, a narrowband representation gives an overall better insight into the sound emission for marine propulsion and should be preferred. The developed method achieves good agreement with the experiment for several frequency ranges and the difference between propeller designs may be analyzed intuitively. However, the simulations show that there is a strong dependence of the results on the domain geometry and specifically the dimensions with respect to pressure dissipation. Finally, passive surfaces are an invaluable tool to gain information about the directivity of the emission.

6.2.3 Full-scale

For the ProNoVi reference target case at $J = 0.8$ in full scale, observers for the acoustic pressure from the KFWH method are located at $r = 140m$ to the side of the vessel from the origin, to mirror the full-scale experimental measurements from a hydrophone that is passed by the configuration. At this distance, the received acoustic pressure in the simulation is very low with amplitudes of less than $p' < 2Pa$ at the first and third blade harmonic frequencies and $p' < 4Pa$ for the second and fourth. Over the rest of the frequency spectrum the acoustic pressure fluctuations are generally around $p' \approx 1Pa$. The SPL for this observer at a bandwidth of $0.1Hz$ is given in Fig. 144 (a) together with the full-scale experimental results in (b) with identical representation and respective environmental corrections and the measured background noise.

There is some agreement, especially up to frequencies of $f \approx 40Hz$ after which the measurement experiences a declining linear trend followed by a broadband hump between $100Hz < f < 1500Hz$, possibly caused by cavitation. The simulation on the other hand achieves relatively constant levels up to $f \approx 800Hz$ after which it assumes a linearly decreasing trend with similar slope to the high frequency trend observed in the measurement. It can be assumed that the constant averaged value between $100Hz < f < 800Hz$ for the simulation is also caused by the cavitation, which means the method accurately captures the influence of the cavitation on acoustic emissions regarding range of frequency, however, predicts about $10dB$ shift towards higher SPL in amplitude. It is important to note that quantifying the results may not be generalized, as the cavitation pattern for this case experiences no strong fluctuations with angle and a cavitating tip vortex is not present for this operation point.

In fact, in the measurement the frequency range below $f < 100Hz$ is rejected, as the level is similar to the background noise. There are no visible peaks at the propeller blade harmonics, which on the other hand are very well represented in the simulation, whereas the local minimum in the spectrum at $f \approx 90Hz$ is not captured at all in the simulation.

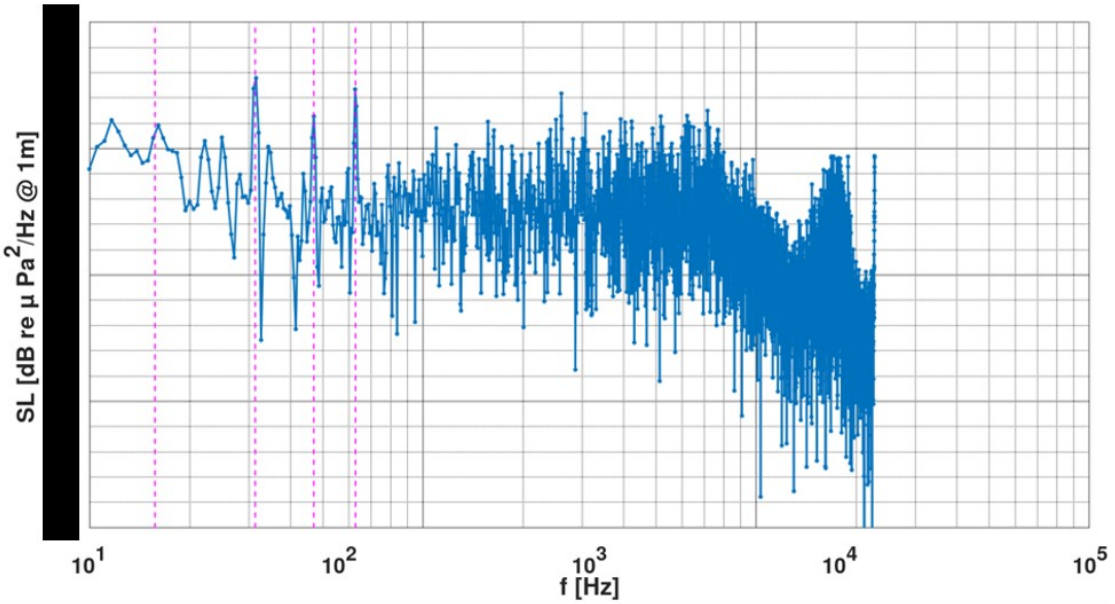

(a) Simulation

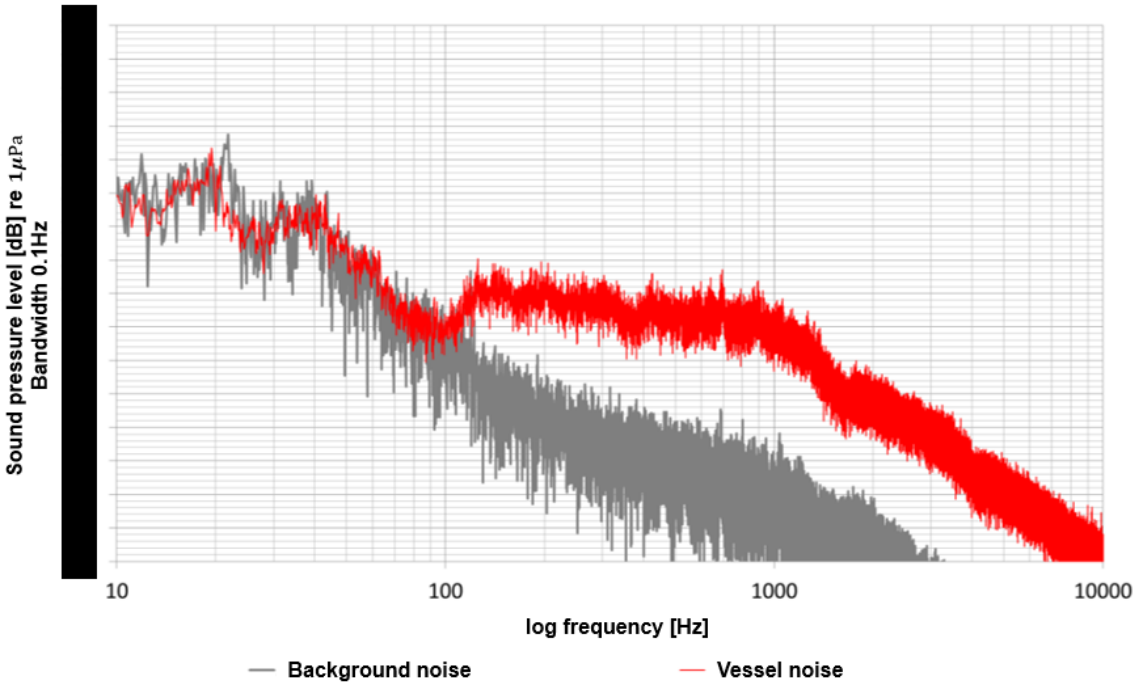

(b) Experiment [96]

Fig. 144: Full-scale acoustic signature comparison

For the 1/3 octave representation in Fig. 145 the differences between simulation and experiment are also apparent with up to $20dB$ higher estimations in the low frequency range and no decreasing linear trend above $600Hz$, which is very prominent in the measurement. For this case, the loss of information by applying the 1/3 octave representation is also visible for the simulation, as only the second and fourth blade harmonic appear as distinct peaks in the synthesized plot, while all are visible in narrowband.

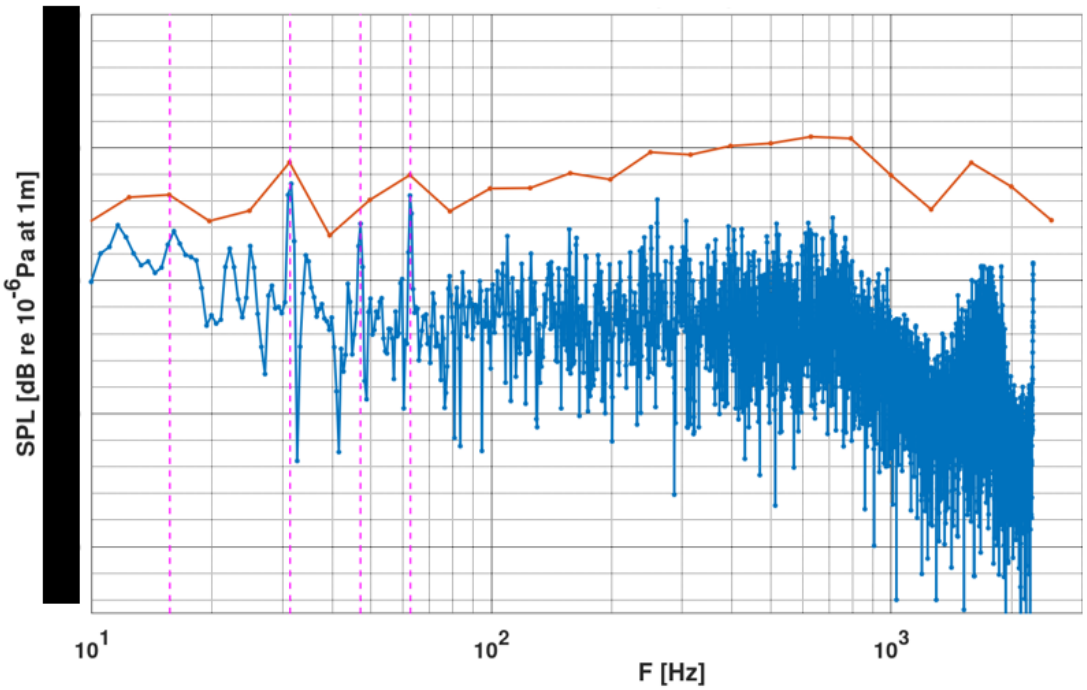

(a) Simulation narrowband and 1/3 octave

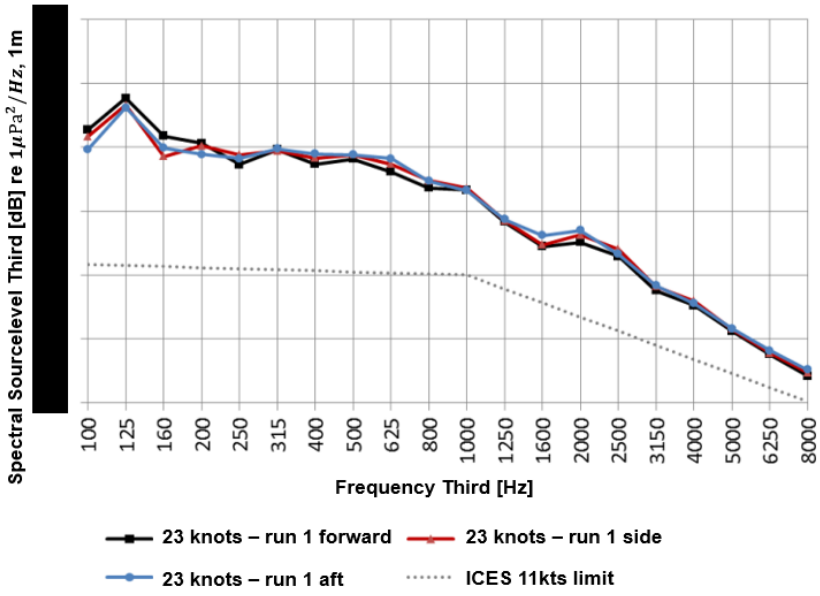

(b) Experiment for different averaging windows [96]

Fig. 145: 1/3 octave band comparison

For the simulation for the Red-Emi SCHOTTEL target case with the azimuthing unit, vortices and cavitation are given in Fig. 14. The SPL observed from the acoustic sensor of the measurement are given in Fig. 146 for the simulation in (a) and the experiment in (b) with respective trends indicated as dashed lines. This case illustrates a limitation of the approach with AMI sliding mesh interface in its current implementation. For both pressure and KFWH signals the AMI interpolation between rotating and stationary mesh produces high unphysical fluctuations over a large frequency range above $f > 100Hz$ in full scale. These effects are observed for other azimuthing propulsion testcases as well. Especially for the pressure probes there is an inverted linear trend yielding increasing amplitudes towards higher frequencies with an incline of $+10dB$ per $1 \cdot 10^3 Hz$, while the KFWH achieves a more physical decline with $-16dB$ per $1 \cdot 10^3 Hz$, while the measured decline is about $-20dB$ between $1 \cdot 10^3 < f < 1 \cdot 10^4 Hz$. For the KFWH the increase towards larger frequencies is caused by the loading component only, while the thickness appears to produce a more physical trend. However, both show the fluctuations over the complete frequency range above $f < 1000Hz$.

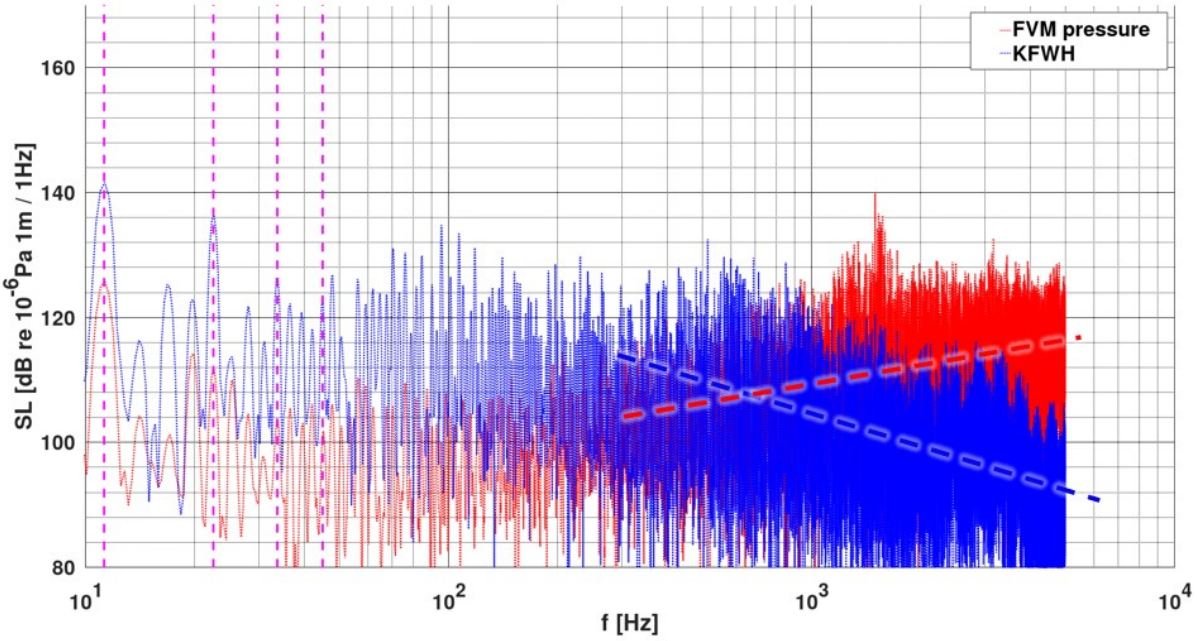

(a) Simulation narrowband

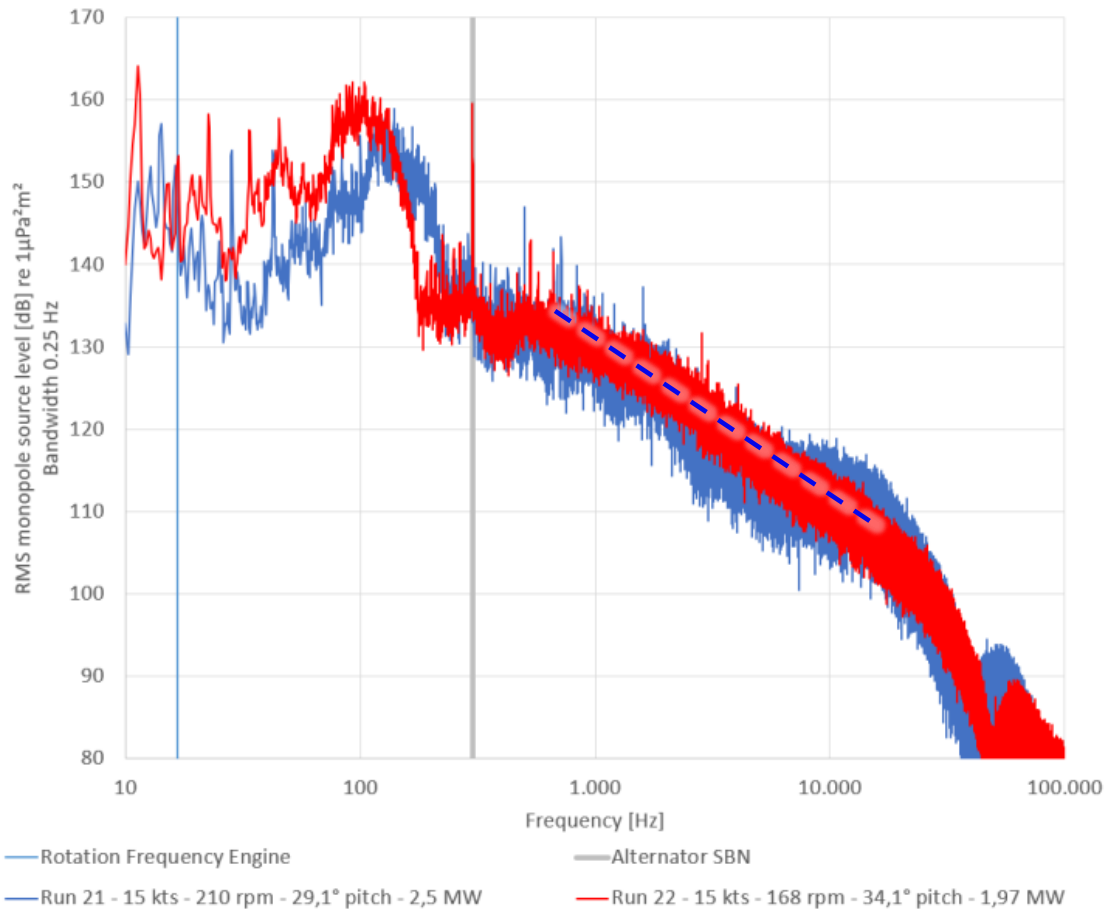

(b) Experiment for different averaging windows [97]

Fig. 146: Narrowband Red-Emi SCHOTTEL target case

In Fig. 147 is the representation of the received pressure level for the vessel passing the hydrophone, which is reconstructed for a line of observers parallel to the vessel direction of travel in the simulation. In this way the time dimension may be replaced by a geometric one. Here the large fluctuations over the small frequency range up to $f < 1000Hz$ are highlighted with the same colormap value range for both experiment and simulation. In (a) are the results from the pressure probes in the simulation and in (b) the obtained results from the KFWH method. For the pressure probes the coarsening of the mesh is visible in the results as the levels rapidly drop at a distance of $10m$ behind the vessel. This example shows that the KFWH method is required for observers in large distance to the vessel. While the experiment shows clear indication of propeller noise and a dependence on its direction, the full-scale simulation recreates the most relevant frequencies. The tonal machinery emissions appearing as horizontal lines in the measurement are not included in the simulation. There are many additional lines of unknown origin which are not as prominent in the measurement, however, it is valuable to compare simulation and measurement as hydrodynamic noise can be isolated in this way. It seems that much of the noise in the experiment visible at the closest point of approach (CPA) are thus caused by machinery and not the propulsor. Some peaks are visible below $200Hz$ at the propeller blade harmonics, which are increased as the vessel passes the hydrophone. Concluding, it may be possible to use the methods in full-scale over the frequency range from $10Hz$ to $1 \cdot 10^3 Hz$. However, the current implementation is susceptible to numerical noise caused by interpolation. In Fig. 148 the range from $0 - 100Hz$ is given in more detail with the shaft line harmonic and the first four propeller blade harmonics indicated with the vertical magenta lines. This representation proves that the propeller noise can be captured for a vessel passing and accurately predicts the propeller noise during the process.

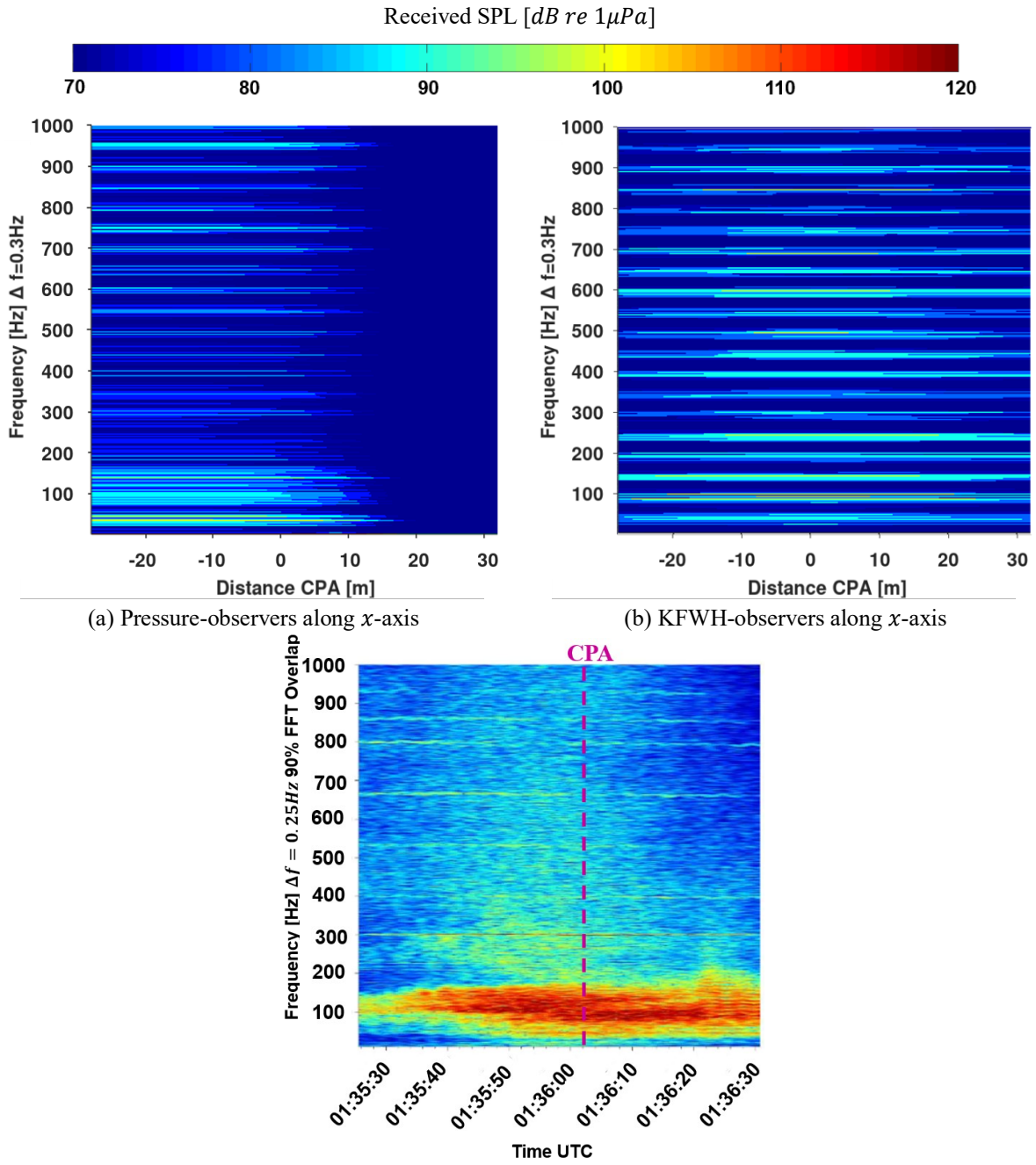

(a) Pressure-observers along x-axis

(b) KFWH-observers along x-axis

(c) Experiment along time axis [97]

Fig. 147: SPL during passing of the observer $0 - 1000Hz$

6.3 Summary

With the proposed methods the underwater acoustic effects can be resolved well on the structure of a vessel as well as the emissions into the fluid domain. As the FVM requires naturally fine geometrical discretization, higher data density compared to model tests is readily available, which can and should be utilized for the analysis of the interaction with the structure and the emissions into the fluid domain. An agreement with the pressure pulses on the hull is achieved within $\Delta p' > 0.2kPa$ for the first harmonic and acceptable agreement for higher harmonics for different vessel types and propellers. For open water propeller performance an agreement in the underwater signature with model scale tests within the margins of reproducibility of experiments is achieved. It is found that the simulation domain has a large influence on the achieved pressure pulses and signature and thus the domain should be constructed according to the model test setups or directly for the full-scale trial location. For full scale,

a good agreement is achieved with URN experiments with an accuracy of $\Delta SL < 10dB$ depending on the frequency. The KFWH method is necessary to evaluate URN at any distance from a passing vessel.

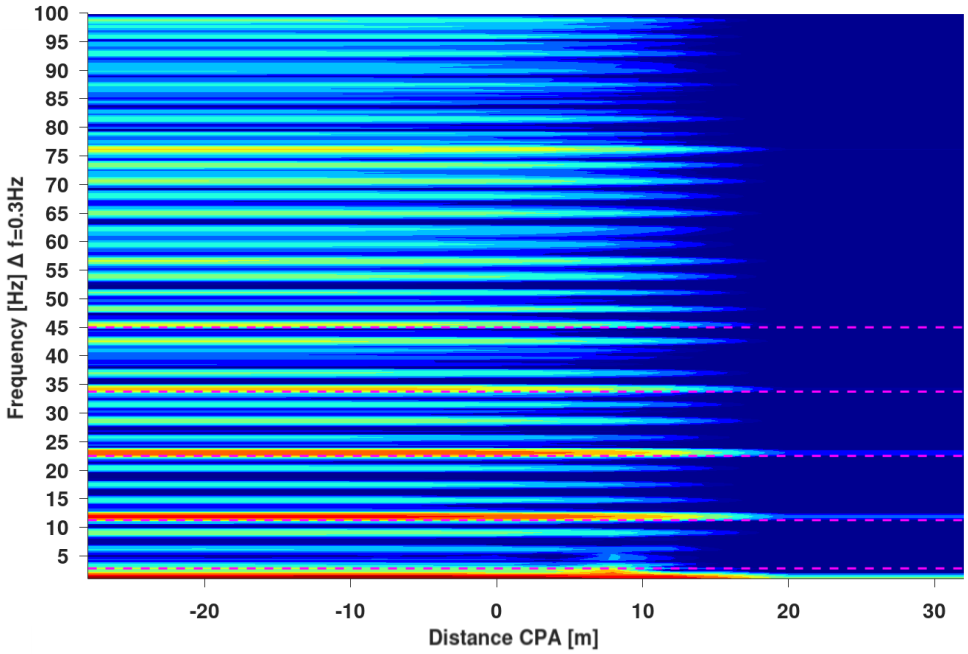

(a) Pressure-observers along x-axis

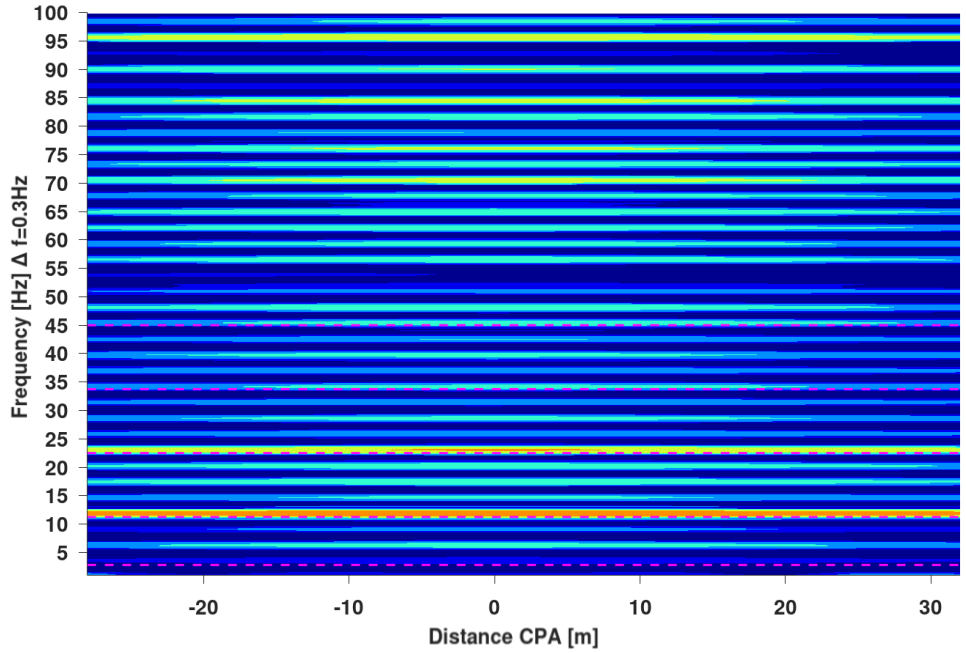

(b) KFWH-observers along x-axis

Fig. 148: SPL during passing of the observer $0 - 100Hz$

7 Discussion of the Results

In this final chapter the conclusions that can be drawn from the simulation results are summarized and discussed briefly, as well as the implications for the applicability of the discovered approach in an industry environment. The scientific contributions from the investigations to the body of knowledge are outlined. Of equal importance are the shortcomings of the approach, which are summarized and their possible remedies suggested as open questions for the work of future researchers.

7.1 Conclusions

7.1.1 Best Practice Findings

A best practice approach to obtain URN signatures of propulsor-hull combinations by considering surface and volumetric noise sources with the FVM in combination with VOF cavitation modelling and resolution of relevant turbulent length scales is successfully developed and validated in this study by applying appropriate mesh refinement techniques and acoustic evaluation models. With the turbulence modelling approach the relevant noise sources in the vicinity of the propeller blades and the propeller slipstream can be resolved and with the OpenFOAM Schnerr-Sauer cavitation model a good agreement with cavitation patterns from model scale tests on the propeller blades for suction side sheet cavities is achieved. With manual or a newly implemented automatic AMR techniques the cavitating trailing vortices and their interaction with obstacles in the propeller slipstream can be captured, however, the current implementation has limits, which either prevent noise evaluation or are incompatible with geometries that contain obstacles in the propeller slipstream. For inclined flow, a resource inefficient way to resolve trailing vortices without obstacles in the slipstream is found. Propeller induced FVM pressure fluctuations on the hull reach good agreement with experimental values and it is suggested in this work to utilize the FVM pressure information on active or passive surfaces, where it is calculated every timestep as part of the solution algorithm anyway, to obtain high density spatial and temporal information about the pressure field, which characterizes the acoustic sources. For the far-field noise signature, the FVM pressure, the FWH and KFWH acoustic analogy results are compared with model test results yielding good agreement for the FVM pressure and the KFWH method, however, the FVM pressure information dissipates on large meshes in coarser regions and is not available outside the FVM simulation domain. Thus the KFWH method, which respects the wave characteristics of the acoustic propagation that are becoming important in the acoustic far-field with $r > 3 \cdot \lambda$ is the preferred method and the only available method for observer locations outside the domain. For full-scale measurements an acceptable agreement with the KFWH method simulation results is reached for low frequencies $f < 100Hz$, however, noise in the pseudo-thickness term possibly generated by the sliding mesh interface leads to overprediction at higher frequencies in model and full scale.

Besides, procedures for starting and executing the acoustic evaluations are developed, including mesh and simulation quality control and convergence criteria that ensure the simulation results are appropriate for acoustic analysis. Turbulence resolution, stability and solution convergence require run time evaluation, however, high stability is not achieved with the selected approach and the solution method applied, which means automation in its current form is not attainable. For the OpenFOAM Schnerr-Sauer model a higher nuclei density leads to more details in the cavity morphology and topological dynamics, which in turn decreases stability and increases simulation resource effort.

With the one-time manual a-priori AMR a sufficient resolution for the cavitating trailing vortices of propellers may be reached with feasible mesh sizes in straight and with larger meshes additionally inclined flow conditions, however, obstacles in the slipstream cannot be considered. In this case an automatic runtime AMR approach is required, which leads to numerical instabilities originating from interpolation from coarsened and refined cells, preventing this approach from being utilized for the intended purpose of an acoustic analysis. An overset grid approach is eliminated beforehand from these analyses, as it suffers from the same issues as the a-priori approach in inclined flow and is thus not worth investigating.

The FWH-method in the Farassat or Farassat 1A formulation according Francescantonio, requires a closed surface without intersections, which is why simple shapes may be deducted from the acoustic source integration, i.e. the propeller shaft cylindrical intersection. It is found that the location of the permeable surface in FVM approaches, which has long been in discussion in academic context, is for a complex vessel-propulsor combination directly tied to the problem geometry for the investigated formulation of the FWH method, given by the underlying FVM mesh and the sliding mesh interface, which itself is posed by the geometry. Firstly, the mesh becomes coarser naturally the further the interrogation region is from the propulsor, and secondly the restriction remains that the surface should not be intersected by any other geometry as it is supposed to be closed, meaning the other boundary surfaces present in the simulation severely reduce any placement options, such as the vessel hull, shaft brackets and non-axisymmetric geometry near the propulsor such as a rudder. In the current implementation it may also not be placed inside the dynamic mesh region as the FVM cell to passive surface interpolation is determined at the simulation start time only. For a cylindrical permeable surface this results in only one possible positioning of the surface, which is outside the sliding mesh interface directly next to the interface, which in this work has been arbitrarily set to $1 \cdot 10^{-2} m$. Other shapes, such as cuboidal or spherical are not practical, as for the first, the distance to the source is not equal for instance at corners or on the face centers and the underlying FVM cell density has to be maintained up to the corners that are further away from the sliding mesh interface, and the second creates even more problematic restrictions regarding the placement due to the geometry of a sphere fitting around a cylinder in between the other boundaries. The KFWH control surface may not be placed directly behind the propeller, as it yields unphysical pseudo-thickness components due to the high pressure region. Thus, for cases with rudder the KFWH control surface cannot be placed between the propeller plane and the rudder, which means more control surface area eliminations are required to include shaft line and rudder intersection. While the KFWH method is validated for simple acoustic sources, its prediction quality mostly suffers from the underlying FVM hydrodynamic solution inaccuracies.

The numerical simulation domain setup has a large influence on the predicted acoustic pressure and a cavitation tunnel experimental setup, or a full-scale shallow water measurement may not be exchanged with any large or quasi-infinite domain geometry as it leads to different fluctuation levels.

7.1.2 Application of results

For industry application the most important aspect is resource economy and handling, which mainly pertains to stability during runtime and invariance to meshing. For the considered approach even with scale resolving simulations of complete ship-propulsor combinations, simulation times in the order of several weeks on 100 cores with about $3GHz$ CPUs are achieved, which includes at least 5 rotations in acoustically converged state for a clean frequency domain investigation of acoustic signatures. While this is still a considerable resource demand, it can be accepted for single investigations, such as validation of an initial and final propeller design or to obtain a noise prediction. Within the conducted research projects, different vessels, domain geometries and propeller designs are successfully compared regarding their signature. Once the methods are matured and find widespread use, it may replace model scale estimations of full-scale noise, with full-scale CFD simulations, which could potentially also serve for classification purposes in the far future. The handling on the other side is subpar, as the stability, especially of the cavitating part with scale resolved turbulence and during the cavitation startup procedure are poor and require manual adjustments in combination with constant monitoring of simulation convergence criteria. This limits an efficient automatization of the approach with the utilized solvers but this may be highly dependent on the respective software solution.

Practical results of this study include the knowledge of acoustic signatures of three vessels: a $P = 11.000kW$ mega yacht, a $P = 7800kW$ container feeder and a $P = 520kW$ wind turbine servicing catamaran given in Fig. 149. In addition, the acoustic emissions between the original P1595 and the improved P3193 are quantified, leading to the result that tip unloading regarding pitch and camber, increase of number of blades and a tip rake towards the pressure side are advantages for the reduction of noise. The propeller design achieves an effective suppression of the tip vortex and its cavitation by

splitting the tip vortex into several smaller vortices that refrain from merging into a combined vortex, helping to reduce volumetric noise sources in the propeller slipstream.

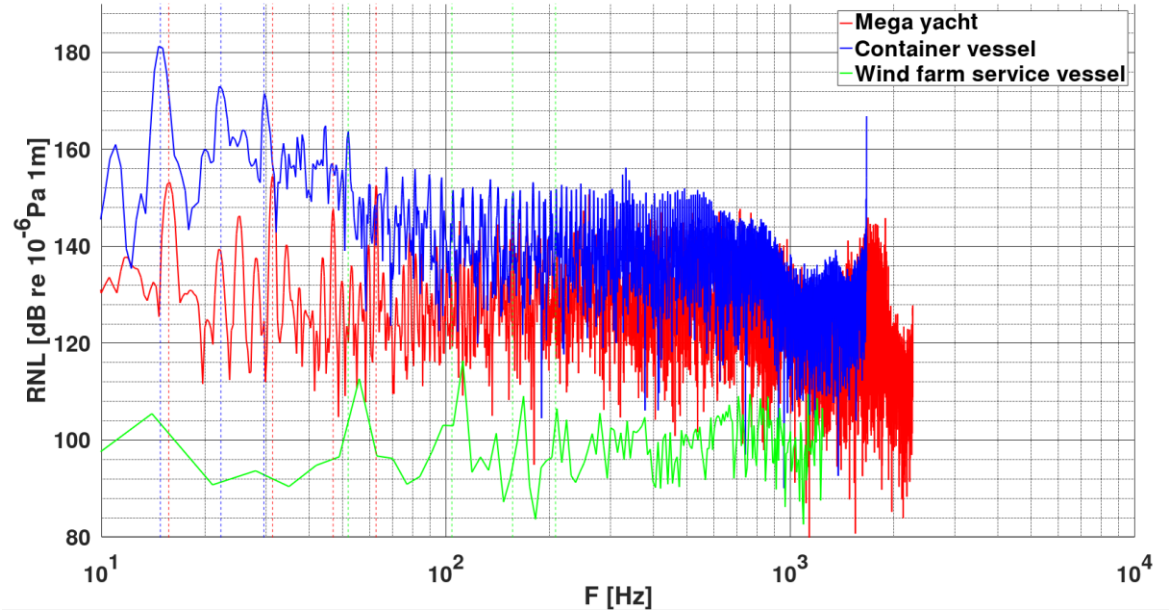

Fig. 149: Comparison of acoustic signatures of different vessel types

7.2 Scientific contributions

The contributions to the body of knowledge pertains to a deeper understanding of the underlying physics of noise sources. The topological and morphological analysis and investigation of temporal dynamics of wetted and cavitating tip vortices of complex lifting surfaces with a high resolution of details allows an insight into the formation physics. The interaction of propeller tip vortices with rudders is investigated, where for instance a circulation increase before the interaction with the rudder is detected. Trailing vortices of hydrofoils and propellers are investigated and an interior vapor flow structure is found in the simulations, which is not possible to detect in the experiment due to practical limitations in the setups. Furthermore, an improved understanding of noise sources for propulsor-hull combinations is gained and their scaling effects are for the first time quantified.

Another contribution relates to the improved engineering tools for URN prediction that are developed and validated. In this new approach high fidelity flow simulation methods with two-phases are combined with an acoustic analogy. Different evaluation and acoustic processing methods are developed for the near- and far-field on solid structures and for emission into the fluid domain. For both cases a standardized exchange format for application in the industry is introduced, which is particularly aimed towards transmitting hydrodynamic excitation into structure-borne noise simulations.

7.3 Future Work

In its current form, the approach is only moderately usable, as there are two primary issues identified on the technical side. Especially in full-scale it depends highly on the quality of the cells at the sliding interface and the interpolation errors during runtime. For the issue regarding the interpolation errors at the sliding mesh interface there are two possible paths to continue. Either the sliding mesh approach is abandoned in favor of volume based, instead of surface interpolation with the overset grid approach, or improved interpolation methods for the sliding mesh are explored. For the latter there is one implementation, which is supposed to reduce pressure fluctuations in the interpolation by enabling topology changes that establishes a 1-to-1 connectivity across the AMI. [98] Another relatively recently developed approach is non-conformal coupling, where the faces at the intersection are cut and new faces are created that are equal on both regions, which achieves a conservative interpolation. [99]

The local tip-vortex refinement with automated run-time AMR is currently producing unusable results for acoustic investigations, due to the cell-point interpolation during runtime between cell sizes for adapted regions. Although the approach manages to refine the trailing vortices of the propeller and its interaction with obstacles in the slipstream well, the implementation requires refinement regarding the mapping between timesteps and cell adaptions without increasing the calculation time significantly, as it is already at the upper limit of usability in an industry environment with current hardware.

Besides these technical shortcomings there are also several methodical issues. Concerns are raised regarding the VOF method only capturing cavitation regions spanning more than a cell volume and the OpenFOAM Schnerr-Sauer model, which accepts several simplifications that may affect the overall noise. In general, the quality of the achieved results depends highly on the type of cavitation. For off-design conditions bubble or cloud cavitation may be the prevalent forms of cavitation in which case the VOF method is not able to capture all contributions as single bubbles are not resolved. In case off-design URN is of interest, this may be investigated with Euler-Lagrange coupling, which have been proven to increase the noise emissions at medium frequencies. [42]

At the moment it is unclear whether the cavitation model for the VOF method plays a significant role in the application of these methods to actual ship-propulsor configurations, as there are no known studies on the effects for practical cases. This could be investigated in further work, and especially with respect to the question if the energy equation and microscopic compressibility effects that are often considered in academic studies [56] are worth resolving in an industry environment as this would fundamentally change the solver strategy. It is expected that the effects are relatively minute.

Finally, it may be worthwhile to investigate more than two-phases and include the free water surface in the simulation to achieve the correct wave pattern in the acoustic propulsion simulation and therefore accurate local hydrostatic pressure distributions. This technology may then also be utilized in maneuvering simulation setups to consider noise emissions.

An interesting spin-off topic sparked from the investigation of emissions on active and passive surfaces in the simulation in section 6.1 is to create pressure pulse prediction technologies based on estimations by reduced order models by utilizing the first few POD modes of the pressure. For this a large amount of propeller geometries would have to be the basis of the models, which at the moment may only be realized with BEM. In this study, it is observed that the POD modes seem to be relatively robust and independent of turbulence and cavitation physics. Therefore, simple RANS single-phase simulations may be used to collect data and adjust the results with only few reference simulations.

On the application side, the proposed methods can now be employed to investigate the effects of noise reduction measures for all types of propulsors such as conventional propellers, azimuthing propulsors or maneuvering devices such as tunnel thrusters or pump-jets and quantify them. The result of energy saving devices, e.g. propeller hub cap or inflow fins may be studied. Modifications of the propeller design can now also be analyzed with respect to their effect on noise emissions for instance by comparing noise optimized propeller designs with original designs. Also, advanced numerical methods could be applied to investigate the influence of air injection at the propeller surface or into the inflow of the propulsor. However, the latter study would again require a three phase investigation.

In a larger context in conjunction with the environmental interaction of anthropogenic shipping with the marine biology, different vessel types could be simulated to create cumulative noise maps depending on geographical regions.

8 References

[1] S. Turkmen, B. Aktas, M. Atlar, N. Sasaki, R. Sampson und W. Shi, „On-board measurement techniques to quantify underwater radiated noise level," *Ocean Engineering,* Bd. 130, pp. 166-175, 2017.

[2] G. V. Frisk, "Noiseonomics: The relationship between ambient noise levels in the sea and global economic trends," *Scientific Reports,* June 2012.

[3] J. Hildebrand, „Anthropogenic and natural sources of ambient noise in the ocean," *Marine Ecology Progress Series Geology*, 2009.

[4] R. Andrew, B. Howe, J. Mercer und M. Dzieciuch, „Ocean Ambient Sound: Comparing the 1960s with the 1990s for a Receiver off the California Coast," *Acoustics Research Letters Online,* Bd. 3(2), pp. 65-70, 2002.

[5] C. Erbe, „Underwater Acoustics: Noise and the Effects on Marine Mammals," in *Effects of Anthropogenic Noise on Animals*, JASCO Applied Sciences, 2018, pp. 227-309.

[6] B. M. Casper, P. S. Lobel und H. Y. Yan, „The hearing sensitivity of the little skate, Raja erinacea: A comparison of two methods," *Environmental Biology of Fishes,* 8 2003.

[7] B. K. Branstetter, J. S. Leger, D. Acton, J. Stewart, D. Houser, J. J. Finneran und K. Jenkins, „Killer whale (Orcinus orca) behavioral audiograms," *The Journal of the Acoustical Society of America,* 4 2017.

[8] N. Merchant, „Impacts of Underwater Noise on marine resources," in *Quieting Ships To Protect The Marine Environment: Technical Workshop*, London, 2019.

[9] Committee on Potential Impacts of Ambient Noise in the Ocean on Marine Mammals, „Ocean Noise and Marine Mammals," National Academies Press, Washington, DC, USA, 2003.

[10] S. Veirs, V. Veirs und J. Wood, „Ship noise extends to frequencies used for echolocation by endangered killer whales," PMCID: PMC4800784, 2016.

[11] ICES, „Underwater Noise of Research Vessels Review and Recommendations," ICES Cooperative Research Report No. 209, ISBN 978-87-7482-463-3, 1995.

[12] IMO, „IMO Resolution MSC.337(91), Code on Noise on Board Ships," 2012.

[13] IMO, „IMO Resolution MEPC.1/Circ833, Guidelines for the Reduction of Underwater Noise From Commercial Shipping to Address Adverse Impacts on Marine Life," 7 April 2014.

[14] EU, „Commission Decision 2010/477/EU," 2010.

[15] EU, „Commission Decision 2017/848/EU," 2017.

[16] EU, „Marine Strategy Framework Directives 2008/56/EC," 2008.

[17] DNV GL, "Silent Class Notation," DNV GL AS, Bærum, Norwegen, 2010.

[18] AQUO - achieve quieter oceans by shipping noise footprint reduction, *Full scale measurement of underwater radiated noise,* FP7 - Collaborative Project no 314227, 2014.

[19] R. E. A. Arndt, V. H. Arakeri and H. Higuchi, "Some observations of tip-vortex cavitation," *Journal of fluid mechanics,* pp. 269-289, 1991.

[20] E. J. Foeth, C. W. H. van Doorne, T. van Terwisga und B. Wieneke, „Time resolved PIV and flow visualization of 3D sheet cavitation," *Experiments in Fluids,* 2006.

[21] ITTC, „Model scale noise measurements," *Recommended Procedures and Guidelines,* pp. 7.4-02-01-05, 2014.

[22] SVA Potsdam GmbH, "Potsdam Propeller Test Case (PPTC) - Cavitation Tests with the Model Propeller VP1304," Report 3753, 2011.

[23] M. Felli, „Underlying Mechanisms of propeller wake interaction with a wing," *Journal of Fluid Mechanics,* Bd. 908, 2020.

[24] M. Felli, M. Falchi und G. Dubbioso, „Tomographic-PIV Survey of the Near-Field Hydrodynamic and Hydroacoustic Characteristics of a Marine Propeller," *Journal of Ship Research,* pp. 201-208, 2015.

[25] M. Felli und F. Di Felice, „Propeller wake analysis in nonuniform inflow by LDV phase sampling techniques," *Journal of Marine Science and Technology,* pp. 159-172, 2005.

[26] M. Felli, S. Grizzi and M. Falchi, "A novel approach for the isolation of the sound and pseudo-sound contributions from near-field pressure fluctuation measurements: Analysis of the hydroacoustic and hydrodynamic perturbation in a propeller-rudder system," *Exp Fluids,* 2014.

[27] S. Mäkiharju, C. Gabillet, B. Paik, N. Chang, M. Perlin und S. Ceccio, „Time-resolved two-dimensional x-ray densitometry of a two-phase flow downstream of a ventilated cavity," *Experiments in Fluids,* 20 June 2013.

[28] SVA Potsdam GmbH, „Messung der Kennwerte und induzierten Schallspektren eines oszillierenden Flügels (Profil NACA0012)," Schiffbau-Versuchsanstalt Potsdam GmbH, Potsdam, Germany, 2015.

[29] G. Tani, B. Aktas, M. Viviani and M. Atlar, "Two medium size cavitation tunnel hydro-acoustic benchmark experiment comparisons as part of a round robin test campaign," *Ocean Engineering,* p. 138 (2017) 179–207, 2017.

[30] J. Kimmerl, P. Mertes, V. Krasilnikov, K. Koushan, L. Savio, M. Felli, M. Abdel-Maksoud und N. Reichstein, „Experimental and Numerical Advances in Underwater Radiated Noise Prediction of Cavitating Propeller-Hull Combinations," Gyeongju, Korea, 2022.

[31] G. Tani, M. Viviani, M. Felli, F. H. Lafeber, T. Lloyd, B. Aktas, M. Atlar, H. Seol, J. Hallander, N. Sakamoto and H. Kamiirisa, "Round Robin Test on Radiated Noise of a Cavitating Propeller," in *Proceedings of the Sixth International Symposium on Marine Propulsors*, Rome, Italy, 26th-30th May 2019.

[32] ITTC, „Cavitation Induced Pressure Fluctuations Model Scale Experiments," *Recommendations and Guidelines,* pp. 7.5 – 02, 03 – 03.3, 2011.

[33] H. Hasenpflug, A. Homm, S. Schäl und L. Gilroy, „Evaluation of range standards for underwater radiated noise in beam aspect," in *Proceedings of the 23rd International Congress on Acoustics*, Aachen, Germany, 2019.

[34] D. Hannay und A. Hennessey, „Boundary Pass underwater listening station cabled hydrophone array system," *The Journal of the Acoustical Society of America,* Bd. 150, 2021.

[35] D. Wittekind, M. Schuster, N. Landsberg und L. Greitsch, „Analyzinh underwater radiated noise of a 3600 TEU containership," in *DAGA 2017*, Kiel, Germany, 2017.

[36] American National Standards Institute, *American National Standard - Quantities and Procedures for Description and Measurement of Underwater Sound from Ships – Part 1: General Requirements,* ANSI-ASA S12.64-2009/Part1, 2009.

[37] DIN, *Underwater acoustics - Quantities and procedures for description and measurement of underwater sound from ships - Part 1: Requirements for precision measurements in deep water used for comparison purposes,* DIN ISO 17208-1:2018-03, 2018.

[38] ITTC, „Underwater Noise from Ships, Full Scale Measurements," *Recommended Procedures and Guidelines,* pp. 7.5-04-04-01, 2017.

[39] R. Peric, Minimizing undesired wave reflection at the domain boundaries in flow simulations with forcing zones, Hamburg, Germany: Schriftenreihe Schiffbau, 2019.

[40] M. Lighthill, „On sound generated aerodynamically i. general theory," in *Proceedings of the Royal Society of London*, 1952.

[41] "Specialist Committee on Hydrodynamic Noise Final Report and Recommendations to the 28th ITTC," ITTC Report, 2017.

[42] A. K. Lidtke, *Predicting radiated noise of marine propellers using acoustic analogies and hybrid Eulerian-Lagrangian cavitation models,* University of Southampton, 2017.

[43] J. E. Ffowcs Williams und D. L. Hawkings, „Sound Generation by Turbulence and Surfaces in Arbitrary Motion," *Philosophical Transactions of the Royal Society of London. Series A, Mathematical and Physical Sciences,* pp. 321-342, 1969.

[44] F. Farassat, "Derivation of Formulations 1 and 1A of Farassat," NASA, 2007.

[45] S. Ianniello und E. Bernardis, „Farassat's Formulations in Marine Propeller Hydroacoustics," *International Journal of Aeroacoustics,* 2015.

[46] P. d. Francescantonio, „A New Boundary Integral Formulation For The Prediction Of Sound Radiation," *Journal of Sound and Vibration,* 1997.

[47] M. Cianferra, A. Petronio und V. Armenio, „Numerical prediction of ship propeller noise through acoustic analogy," in *Sixth International Symposium on Marine Propulsors*, Rome, Italy, 2019.

[48] A. Lidtke, S. Turnock und V. Humphrey, „Use of Acoustic Analogy for Marine Propeller Noise Characterisation," in *Fourth International Symposium on Marine Propulsors*, Austin, Texas, 2015.

[49] U. Göttsche, T. Lampe, M. Scharf and M. Abdel-Maksoud, "Evaluation of Underwater Sound Propagation of a Catamaran with Cavitating Propellers," in *Sixth International Symposium on Marine Propulsors*, Rome, Italy, 2019.

[50] S. Kim and S. A. Kinnas , "Prediction of Unsteady Developed Tip Vortex Cavitation and its Effect on the Induced Hull Pressures," in *Proceedings of the Sixth International Symposium on Marine Propulsors*, Rome, Italy, 2019.

[51] N. Yilmaz, M. Atlar and P. Fitzsimmons, "An Improved Tip Vortex Cavitation Model for Propeller-Rudder Interaction," in *10th International Cavitation Symposium*, Baltimore, USA, 2018.

[52] K. Shin und P. Andersen, „CFD Analysis of Propeller Tip Vortex Cavitation in Ship Wake Fields," in *10th International Symposium on Cavitation*, Baltimore, Maryland, USA, 2018.

[53] S. Sezen, M. Atlar und P. Fitzsimmons, „Prediction of cavitating propeller underwater radiated noise using RANS & DES-based hybrid method," *Ships and Offshore Structures,* Bd. 16, Nr. sup1, 2021.

[54] M. Liefvendahl und R. Bensow, „Simulation-Based Analysis of Flow-Generated Noise from Cylinders with Different Cross-Sections," in *32nd Symposium on Naval Hydrodynamics*, Hamburg, Germany, 2018.

[55] A. Lidtke, T. Lloyd und G. Vaz, „Acoustic modelling of a Propeller Subject to non-uniform inflow," in *Sixth International Symposium on Marine Propulsors*, Rome, Italy, 2019.

[56] V. Viitanen, T. Siikonen und A. Sanchez-Caja, „Cavitation on Model- and Full-Scale Marine Propellers: Steady and Transient Viscous Flow Simulations at Different Reynolds Numbers," *Journal of Marine Science and Engineering,* 2020.

[57] A. Posa, R. Broglia, M. Felli, M. Cianferra und V. Armenio, „Hydroacoustic analysis of a marine propeller using large-eddy simulation and acoustic analogy," *Journal of Fluid Mechanics,* Bd. 947, Nr. A46, 2022.

[58] W. Devenport, M. Rife, S. Liapis und G. Follin, „The structure and development of a wing tip-vortex," *Journal of Fluid Mechanics,* Bd. 312, pp. 67-106, 1996.

[59] J. Kimmerl, P. Mertes und M. Abdel-Maksoud, „Application of Large Eddy Simulation to Predict Underwater Noise of Marine Propulsors. Part 1 Cavitation Dynamics," *Journal of Marine Science and Engineering,* 2021.

[60] D. Fruman, P. Cerrutti, T. Pichon und P. Dupont, „Effect of hydrofoil planform on tip vortex roll-up and cavitation," *J. Fluids Eng.,* Bd. 117, pp. 162-169, 1995.

[61] J.-P. Franc und J.-M. Michel, Fundamentals of Cavitation, Springer Science & Business Media, 2006.

[62] J. Wu, H. Ma und M. Zhou, Vorticity and Vortex Dynamics, Berlin, Germany: Springer-Verlag, 2006.

[63] W. K. Blake, Mechanics of Flow-Induced Sound and Vibration, Volume 1: General Concepts and Elementary Sources, Academic Press, 2017.

[64] J. Geese, *Investigation of Adaptive Mesh Refinement Techniques for Trailing Vortices Generated by Complex Lifting Surfaces with OpenFOAM (Master Thesis),* Koblenz, Germany: Fachbereich Ingenieurwesen der Hochschule Koblenz, 2022.

[65] M. S. Plesset, „The Dynamics of Cavitation Bubbles," *J. Appl. Mech.,* pp. 277-282, Sep. 1949.

[66] J. Bosschers, Propeller Tip-Vortex Cavitation and its Broadband Noise, Renkum, Netherlands: University of Twente, 2018.

[67] P. Pennings, J. Westerweel und T. van Terwisga, „Cavitation tunnel analysis of radiated sound from the resonance of a propeller tip vortex cavity," *International Journal of Multiphase Flow,* pp. 83:1-11, 2016.

[68] S. Berger, „Numerical Analysis of Propeller-Induced Higher-Order Pressure Fluctuations on the Ship Hull," Schriftenreihe Schiffbau der Technischen Universität Hamburg-Harburg, Hamburg, 2018.

[69] J. Carlton, Marine Propellers and Propulsion, Oxford: Butterworth-Heinemann, 2007.

[70] U. Göttsche, Entwicklung einer numerischen Methode zur Vorhersage der hydroakustischen Schallabstrahlung von Schiffspropellern, Hamburg, Germany: Hamburg University of Technology, 2020.

[71] H. Söding, Vibrationen von Schiffen I (Lecture Notes), Hamburg, Germany: Institute for Shipbuilding of the Hamburg Technical University, 1987.

[72] J. Bolton, „ME 513: Engineering Acoustics," Purdue University, 2023. [Online]. Available: https://engineering.purdue.edu/ME513/. [Accessed: 16.08.2023].

[73] P. Davidson, Turbulence: An Introduction for Scientists and Engineers, Oxford University Press, 2015.

[74] L. F. Richardson, Weather Prediction by Numerical Processes, Cambridge: Cambridge University Press, 1922.

[75] S. B. Pope, Turbulent Flows, Cambridge: Cambridge University Press, 2000.

[76] P. Sagaut, Large Eddy Simulation for Incompressible Flows, New York: Springer, 2006.

[77] J. Smagorinsky, „General circulation experiments with the primitive equations: I. The basic experiment," *Monthly weather review,* Bd. 91, Nr. 3, pp. 99-164, 1963.

[78] G. Schnerr und J. Sauer, „Physical and Numerical Modeling of Unsteady Cavitation Dynamics," in *ICMF-2001, 4th International Conference on Multiphase Flow*, New Orleans, U.S.A., 2001.

[79] T. Rossing, Springer Handbook of Acoustics, New York: Springer Science+Business Media, 2007.

[80] J. Kimmerl, M. Abdel-Maksoud, M. Nataletti und L. Savio, „Acoustic Comparison of a Ship-Propeller Model in Cavitating Conditions with LES and FWH-Method," in *Seventh International Symposium on Marine Propulsors*, Wuxi, China, 2022.

[81] A. Gerasimov, „Quick Guide to Setting Up LES-type simulations," [Online]. Available: ANSYS Customer Portal. https://support.ansys.com/ [Accessed: 01.04.2020]

[82] G. Taylor, „The spectrum of Turbulence," *Proceedings of the Royal Society of London,* Bd. A164, pp. 476-490, 1938.

[83] V. Krasilnikov, "CFD modelling of hydroacoustic performance of marine propellers: Predicting propeller cavitation," in *Proceedings of the 22nd Numerical Towing Tank Symposium*, Tomar, Portugal, 2019.

[84] F. R. Menter, "Best Practice: Scale-Resolving Simulations in ANSYS CFD," ANSYS Germany GmbH, Nürnberg, Germany, 2015.

[85] G. Kuiper, "Cavitation Inception on Ship Propeller Models," Doctoral Thesis, TU Delft, Wageningen, Netherlands, 1981.

[86] J. Chow, G. Zilliac und P. Bradshaw, „Mean and Turbulence Measurements in the Near-field of a Wingtip Vortex," *AIAA Journal,* Bd. 35, Nr. 10, 1997.

[87] D. F. Feder, M. Dhone, N. Kornev und M. Abdel-Maksoud, „Comparison of different approaches tracking a wing-tip vortex," *Ocean Engineering,* Bd. 147, Nr. January 2018, pp. 659-675, 2018.

[88] E. Bensow, „Simulation of the unsteady cavitation on the Delft Twist11 foil using RANS, DES and LES," in *2nd International Symposium on Marine Propulsors, Workshop*, Hamburg, Germany, 2011.

[89] M. Felli, R. Camussi and F. Di Felice, "Mechanisms of evolution of the propeller wake in the transition and far fields," *Journal of Fluid Mechanics*, March 2011.

[90] J. Kimmerl, P. Mertes und M. Abdel-Maksoud, „Turbulence Modelling Capabilities of ILES for Propeller Induced URN Prediction," in *SNAME Maritime Convention 2020 - A Virtual Event*, 2020.

[91] J. Kimmerl und M. Abdel-Maksoud, „Visualization of Underwater Radiated Noise in the Near- and Far-Field of a Propeller-Hull Configuration Using CFD Simulation Results," *Journal of Marine Science and Engineering,* Bd. 11(4), p. 834, 2023.

[92] J. Kimmerl, P. Mertes und M. Abdel-Maksoud, „Application of Large Eddy Simulation to Predict Underwater Noise of Marine Propulsors. Part 2: Noise Generation," *Journal of Marine Science and Engineering,* Bd. 9, p. 778, 2021.

[93] P. Pennings, *Dynamics of Vortex Cavitation,* Delft: University Delft, 2016.

[94] E. Weitendorf, *Kavitationseinflüsse auf die vom Propeller induzierten Druckschwankungen,* Hamburg: Hamburg Technical University, Schriftenreihe Schiffbau, 1976.

[95] M. Nataletti, „Report ProNoVi EFD - model tests," SINTEF Ocean AS, Trondheim, Norway, 2020.

[96] DW-Shipconsult GmbH, „Unterwasserschallmessung [redacted]," DW-Shipconsult, Schwentinental, Germany, 2016.

[97] DW-Shipconsult GmbH, „Underwater Noise Measurements MV Lysoy," DW-Shipconsult, Schwentinental, Germany, 2023.

[98] S. Vilfayeau, „Latest Development in OpenFOAM and Industrial Applications," in *German OpenFoam User meetiNg (GOFUN)*, 2021.

[99] CFD Direct Ltd., „OpenFOAM Non-Conformal Coupling," CFD Direct Ltd., [Online]. Available: https://cfd.direct/openfoam/free-software/non-conformal-coupling/. [Accessed 13 04 2023].